

# The development of maleimide derived fluorophores for peptide- based applications

by

Jonathan Tristan Husband

**Supervisor: Rachel K. O'Reilly**

A thesis submitted to the University of Birmingham for the degree of  
Doctor of Philosophy



UNIVERSITY OF  
BIRMINGHAM

School of Chemistry

College of Engineering and Physical Sciences

University of Birmingham

February 2020

UNIVERSITY OF  
BIRMINGHAM

**University of Birmingham Research Archive**

**e-theses repository**

This unpublished thesis/dissertation is copyright of the author and/or third parties. The intellectual property rights of the author or third parties in respect of this work are as defined by The Copyright Designs and Patents Act 1988 or as modified by any successor legislation.

Any use made of information contained in this thesis/dissertation must be in accordance with that legislation and must be properly acknowledged. Further distribution or reproduction in any format is prohibited without the permission of the copyright holder.



# Abstract

Substituted maleimide fluorophores have been extensively used to study polymeric systems, as their optical properties are responsive to polymer environment and assembly. They are particularly effective as a result of their small size, and ease of functionalization. Furthermore, this makes them well-suited for peptide-based applications too, where fluorescence labelling is essential for tracking peptide therapeutics and disease diagnostics.

Initially in this work, the conjugation of maleimide precursors to enzymes is investigated as a turn-on fluorescence conjugation technique. However, despite the successful effective conjugation, the fluorescence of the conjugates was poor from solvent quenching interactions. Further work focused on improving aqueous fluorescence. Firstly, the dye imide substitution was investigated in an effort to prevent protic solvent quenching events, which led to insights into the fluorescence mechanism including improved solid-state fluorescence through preventing pi-pi interactions. Secondly, the synthesis of fluorescent amino acids was successfully undertaken for incorporation deeper into enzymes, where solvent quenching should be minimal. In addition, the synthesis of alkyne functionalized probes for the tagging and trapping of enzyme intermediates was completed and the subsequent compatibility of such dyes with cellular incubation conditions was proven.



## Thesis overview

The general concepts of the thesis and background literature are introduced in Chapter 1. This has been split into two broad categories: macromolecules with a focus on biological peptide-based entities and fluorescence and its applications in macromolecules.

Chapter 2 covers the investigation of maleimide fluorophores for the tagging of enzymes. It starts with exploring established dithiomaleimide-based conjugations and goes on to develop a new fluorescence conjugation technique through the formation of aminomaleimides. The efficiency of conjugation, conjugate fluorescence and the effect on enzyme integrity are all quantified.

The poor fluorescence of maleimides in water affected the applicability of work in Chapter 2, therefore, Chapter 3 investigates how chemical modifications to the maleimide fluorophore may improve fluorescence characteristics such as fluorescence in polar environments. Research led to observations of novel solid and solution state fluorescence behaviour and mechanistic insights into this phenomenon.

Chapter 4 focuses on the development and synthesis of a fluorescent maleimide-based amino acid for genetic incorporation into enzymes. Firstly, this would allow the incorporation of the dye deep into the enzyme structure, preventing quenching effects seen in Chapter 2. Secondly, this would have other applications such as active site monitoring and for the study of protein-protein interactions. Synthesis of four variants was completed and subsequent incorporation tests, by collaborators, have been successful for one activated amino acid.

In Chapter 5 the synthesis of maleimide based probes for studying enzyme mechanisms and intermediates in polyketide synthesis and non-ribosomal peptide

synthesis is completed, and their stability in enzyme expression media is established.

Finally, Chapter 6 covers a side-project which involved the synthesis of peptide-based monomers and chain transfer agents (CTA) for the templation of polymer assembly during aqueous polymerization induced self-assembly. Peptide CTAs universally led to aggregated assemblies however, this was used to synthesize peptide monomers which underwent PISA.

# Acknowledgements

Completing this period of my life has been the most fulfilling experience; I will be eternally grateful to my supervisor Rachel O'Reilly for the opportunity and her continued guidance and advice through the years. Your strive for world-class research and thoughtful critical analysis has shaped me greatly and your empathetic guidance throughout the move from Warwick to Birmingham is appreciated; without which I doubt I would be here today and for which I can say has helped me grow in so many different ways I never would have expected.

I must thank all of the O'Reilly group throughout the last nearly five years. You are all talented and personable scientists who have been truly a pleasure to work and collaborate with. I must firstly thank Dr Alice Hill, Dr Anne Mabire and in particular Dr Mat Robin, for helping me settle in and giving me great advice and mentorship throughout the first few years. Their experience has helped shape the Chemist that I am and the projects in this thesis. I must thank Samuel Nunez, Lucy Arkinstall, Dr Robert Keogh and Dr Maria Inam for their friendship and support through the early years and all group members for making my time here fun and welcoming, nearly all of you have had an impact on the science herein, for which I value greatly.

I must give a huge thank you to everyone who has given their time to help proof work included in this thesis, including Irem Akar, Chloe Antonen, Lucy Arkinstall, Yujie Xie, Dr Thomas Wilks, Dr Amanda Pearce, Spyridon Varlas, Dr John Husband and Gemma Cousins.

Finally, I must thank the most important people in my life, my Mum and Dad, Gran, Dominic and Jessica, and of course Gemma. I have been privileged to grow up in such a loving and supporting household, which challenged me to grow and led me to being able to be here today. Gemma your willingness to up and

move to Coventry (and then Hampton) and your constant love and company have helped me in being who I am today and has helped me so much through the pressures and challenges that life throws our way. I am hoping these years will pave the way for a bright and enjoyable future together.

## Declaration of authorship

This thesis is submitted to the University of Birmingham in support for the degree of Doctor of Philosophy. It has been composed by myself and has not been submitted in any previous application for any degree.

The work presented herein was carried out by the author except in the cases stated below (and highlighted again in each chapter):

- Chapter 2 – DSC measurements were conducted by Dr Malin Suurkuusk (TA instruments)
- Chapter 3 – Computational studies in support of fluorescence hypotheses were conducted by Dr Miquel Torrent-Sucarrat (University of the Basque Country).
- Chapter 4 – Genetic expression of amino acids and subsequent MALDI-ToF analysis in section 4.3.3 was conducted by Dr Joongoo Lee (Northwestern University).
- Chapter 5 – Coupling of the fluorescent dyes to enzyme probes and subsequent expression experiments in section 5.3.3 were completed by Dr Ina Wilkening, Dr Rob Jenkins and Panward Prasongpholchai, and their work is summarized for context.
- Chapter 6 – LogP<sub>oct</sub>/SA values were calculated by Prof. Robert Mathers (Penn State).

Parts of this thesis have been published by the author:

1. Husband, J. T.; Hill, A. C.; O'Reilly, R. K. Utilizing Functionalized Bromomaleimides for Fluorogenic Conjugation and PEGylation of Enzymes. *Polymer International*, **2019**, 68 (7), 1247–1254 (Chapter 2).
2. Husband, J. T.; Xie, Y.; Male, L.; Torrent-Sucarrat, M.; Wilks, T. R.; Stavros, V.; O'Reilly, R. K. Environment-independent solidification-induced

fluorescence in an aminomaleimide fluorophore. Chemical Science, *manuscript submitted*. (Chapter 3)

Alongside this work the author has contributed to other publications:

3. Hedir, G. G.; Arno, M. C.; Langlais, M.; Husband, J. T.; O'Reilly, R. K.; Dove, A. P. Poly(Oligo(Ethylene Glycol) Vinyl Acetate)s: A Versatile Class of Thermoresponsive and Biocompatible Polymers. *Angewandte Chemie International Edition*, **2017**, 56 (31), 9178-9182.
4. Xie, Y.; Husband, J. T.; Torrent-Sucarrat, M.; Yang, H.; Liu, W.; O'Reilly, R. K. Rational Design of Substituted Maleimide Dyes with Tunable Fluorescence and Solvafluorochromism. *Chemical Communications*, **2018**, 54 (27), 3339–3342.
5. Varlas, S.; Foster, J. C.; Georgiou, P. G.; Keogh, R.; Husband, J. T.; Williams, D. S.; O'Reilly, R. K. Tuning the Membrane Permeability of Polymersome Nanoreactors Developed by Aqueous Emulsion Polymerization-Induced Self-Assembly. *Nanoscale*, **2019**, 11 (26), 12643–12654.
6. Xie, Y.; Arno M. C.; Husband, J. T.; Torrent-Sucarrat, M.; O'Reilly, R. K. Photo Switchable barcoding: Manipulating the Fluorescence Lifetime at the Sub-Cellular Scale. *Nature Communications*, **2020**, 11 (1), 1-9.

# Contents

1.1	Biological macromolecules.....	3
1.1.1	Macromolecules .....	3
1.1.2	Proteins .....	4
1.1.2.1	Protein primary structure.....	4
1.1.2.2	Protein secondary structure .....	5
1.1.2.3	Protein tertiary structure .....	8
1.1.2.4	Protein quaternary structure .....	9
1.1.3	Peptide biosynthesis.....	10
1.1.4	Enzymes.....	12
1.1.5	Synthetic macromolecules.....	13
1.1.6	Self-assembly of polymer objects.....	13
1.1.7	Peptide-polymer complexation.....	15
1.1.8	Peptide encapsulation in polymer nanoparticles .....	16
1.1.9	Peptide-polymer conjugates .....	17
1.1.10	Peptide directed assembly.....	19
1.2	Fluorescence .....	22
1.2.1	Overview .....	22
1.2.2	Fluorescence labelling of biomolecules .....	23
1.3	Maleimides .....	27
1.3.1	Maleimide chemistry.....	27
1.3.2	Substituted maleimide fluorophores .....	28
1.3.3	Solvent dependent fluorescence.....	30
1.3.4	Applications of substituted maleimide fluorophores .....	31
1.3.5	Biomolecule-based applications of substituted maleimides .....	34
1.4	Summary .....	39
1.5	References .....	39
2.1	Abstract .....	47
2.2	Introduction .....	48
2.2.1	Enzyme conjugation <i>via</i> lysine and cysteine residues.....	48
2.2.2	PEGylation of enzymes and biomolecules .....	49
2.2.3	<b>Conjugation to <math>\alpha</math>-chymotrypsin</b> .....	51
2.2.4	Lysozyme variant conjugations .....	52
2.3	Results .....	54
2.3.1	Initial investigations into DBM conjugations to $\alpha$ -CT .....	54
2.3.2	Disulfide-based conjugations to human lysozyme.....	59
2.3.3	PEGylation thorough disulfide bridging.....	62
2.3.4	Amine targeted bromomaleimide conjugations.....	63
2.3.5	Fluorescence analysis of conjugates .....	67

2.3.6	Activity analysis of conjugates .....	68
2.4	Conclusions .....	71
2.5	Experimental .....	72
2.5.1	Instrumentation .....	72
2.5.2	Materials and chemicals .....	74
2.5.3	Small molecule synthesis .....	75
2.5.3.1	Synthesis of 3,4-bis(phenylthio)-1H-pyrrole-2,5-dione (2.1) .....	75
2.5.3.2	Synthesis of 2-3-dibromo-pyrrole-2,5-dione functionalized PEG <sub>350</sub> (2.2) ..	75
2.5.3.3	Synthesis of 3-bromo-1-methyl-1H-pyrrole-2,5-dione (2.3) .....	78
2.5.3.4	Synthesis of 3-bromo-1-(prop-2-yn-1-yl)-1H-pyrrole-2,5-dione (2.4) ...	78
2.5.3.5	Synthesis of 3-bromo-pyrrole-2,5-dione functionalized PEG <sub>800</sub> (2.5) .....	79
2.5.4	Enzyme conjugations .....	81
2.5.4.1	$\alpha$ -CT disulfide conjugation with M-DBM .....	81
2.5.4.2	$\alpha$ -CT lysine conjugation with alkyne-MBM .....	82
2.5.4.3	Human lysozyme disulfide conjugation with M-DBM .....	84
2.5.4.4	Human lysozyme lysine conjugated with alkyne MAM .....	85
2.5.4.5	$\alpha$ -CT lysine conjugation with M-DBM .....	86
2.5.4.6	HLZ lysine conjugation with M-DBM .....	88
2.5.4.7	$\alpha$ -CT lysine conjugation with M-MBM .....	89
2.5.4.8	HLZ lysine conjugation with M-MBM .....	89
2.5.4.9	$\alpha$ -CT conjugation with PEG-DBM <i>via</i> disulfide reduction .....	90
2.5.4.10	HLZ conjugation with PEG-DBM <i>via</i> disulfide reduction .....	91
2.5.4.11	$\alpha$ -CT lysine conjugation with PEG-MBM .....	93
2.5.4.12	HLZ lysine conjugation with PEG-MBM .....	94
2.5.5	Enzyme assays .....	96
2.5.5.1	$\alpha$ -Chymotrypsin <i>p</i> -nitroaniline hydrolysis assay .....	96
2.5.5.2	Human lysozyme EnzCheck® lysis assay .....	96
2.5.6	Quantum yield fluorescence analysis .....	97
2.5.7	Circular dichroism of DTM HLZ conjugate .....	98
2.6	References .....	100
3.1	Abstract .....	105
3.2	Introduction .....	106
3.2.1	Quenching of charge transfer fluorophores .....	106
3.2.2	Aggregation induced emission (AIE) .....	108
3.3	Results .....	111
3.3.1	The synthesis of imide functionalized maleimides with benzyl groups to reduce solvent quenching effects .....	111
3.3.2	The synthesis of bulky silyl derived aminomaleimides as sterically hindered maleimide fluorophores .....	114
3.3.3	Fluorescence analysis of benzyl functionalized maleimides .....	115
3.3.4	Fluorescence analysis of silyl functionalized maleimides .....	128



3.4	Conclusions .....	133
3.5	Experimental .....	134
3.5.1	Materials and instrumentation .....	134
3.5.2	Small molecule synthesis and characterization .....	135
3.5.2.1	1-phenyl-3-bromo-1H-pyrrole-2,5-dione (3.1) .....	135
3.5.2.2	1-benzhydryl-3-bromo-1H-pyrrole-2,5-dione (3.3) .....	137
3.5.2.3	3-bromo-1-trityl-1H-pyrrole-2,5-dione (3.5) .....	139
3.5.2.4	3,4-dibromo-1-trityl-1H-pyrrole-2,5-dione (3.6) .....	141
3.5.2.5	3-bromo-1-isopropyl-1H-pyrrole-2,5-dione (3.11) .....	143
3.5.2.6	General procedure for the synthesis of silyl functionalized bromomaleimides .....	145
3.5.2.7	3-bromo-1-(tert-butyldimethylsilyl)-1H-pyrrole-2,5-dione (3.17) ..	145
3.5.2.8	3,4-dibromo-1-(tert-butyldimethylsilyl)-1H-pyrrole-2,5-dione (3.18) ... .....	147
3.5.2.9	3-bromo-1-(tert-butyldiphenylsilyl)-1H-pyrrole-2,5-dione (3.19) ...	149
3.5.2.10	3,4-dibromo-1-(tert-butyldiphenylsilyl)-1H-pyrrole-2,5-dione (3.20) ... .....	151
3.5.2.11	General procedure for the synthesis of aminobromo- and monoaminomaleimides from bromomaleimides .....	153
3.5.2.12	1-isopropyl-3-(isopropylamino)-pyrrole-2,5-dione (3.12) .....	154
3.5.2.13	1-benzyl-3-(isopropylamino)-1H-pyrrole-2,5-dione (3.2) .....	156
3.5.2.14	1-benzhydryl-3-(isopropylamino)-1H-pyrrole-2,5-dione (3.4) .....	158
3.5.2.15	3-(isopropylamino)-1-trityl-pyrrole-2,5-dione (3.7) .....	160
3.5.2.16	3-bromo-4-(isopropylamino)-1-trityl-pyrrole-2,5-dione (3.8) .....	162
3.5.2.17	1-(tert-butyldimethylsilyl)-3-(isopropylamino)-pyrrole-2,5-dione (3.21) .....	164
3.5.2.18	3-bromo-1-(tert-butyldimethylsilyl)-4-(isopropylamino)-pyrrole-2,5- dione (3.22) .....	166
3.5.2.19	1-(tert-butyldiphenylsilyl)-3-(isopropylamino)-pyrrole-2,5-dione (3.23) .....	168
3.5.2.20	3-bromo-1-(tert-butyldiphenylsilyl)-4-(isopropylamino)-pyrrole-2,5- dione (3.24) .....	170
3.5.3	Fluorophore incorporation into PEG powders .....	172
3.6	References .....	173
4.1	Abstract .....	177
4.2	Introduction .....	178
4.2.1	Non-canonical amino acid incorporation into peptides .....	178
4.2.2	Fluorescent labelling of proteins through genetic incorporation .....	180
4.3	Results .....	183
4.3.1	Synthesis of an aminomaleimide-based amino acid for incorporation into aminoacyl tRNA .....	183
4.3.2	Synthesis of an activated aminomaleimide-based amino acid for flexizyme incorporation .....	189

4.3.3	Expression of peptides by ACM charged flexizymes .....	196
4.4	Conclusions .....	197
4.5	Future work .....	198
4.6	Experimental .....	200
4.6.1	Materials and instrumentation .....	200
4.6.2	Small molecule synthesis .....	201
4.6.2.1	3-bromo-1H-pyrrole-2,5-dione (4.1) .....	201
4.6.2.2	N-(((9H-fluoren-9-yl)methoxy)carbonyl)-N-(4-bromo-1-methyl-2,5-dioxo-2,5-dihydro-1H-pyrrol-3-yl)-L-lysine (4.4) .....	202
4.6.2.3	N-(4-bromo-1-methyl-2,5-dioxo-2,5-dihydro-1H-pyrrol-3-yl)-L-lysine (4.5) .....	204
4.6.2.4	3,4-dichloro-1H-pyrrole-2,5-dione (4.6) .....	207
4.6.2.5	3,4-dichloro-1-methyl-pyrrole-2,5-dione (4.7) .....	208
4.6.2.6	tert-butyl-(R)-2-((tert-butoxycarbonyl)amino)-5-((4-chloro-2,5-dioxo-2,5-dihydro-1H-pyrrol-3-yl)amino)pentanoate (4.8) .....	209
4.6.2.7	tert-butyl-(R)-2-((tert-butoxycarbonyl)amino)-5-((4-chloro-2,5-dioxo-2,5-dihydro-1H-pyrrol-3-yl)amino)pentanoate (4.9) .....	211
4.6.2.8	3,5-dinitrobenzyl 2-amino-5-((4-chloro-1-methyl-2,5-dioxo-2,5-dihydro-1H-pyrrol-3-yl)amino)pentanoate (4.10) .....	214
4.6.2.9	3,5-dinitrobenzyl 2-((tert-butoxycarbonyl)-amino)-5-((4-chloro-1-methyl-2,5-dioxo-2,5-dihydro-1H-pyrrol-3-yl)amino)pentanoate (4.11) .....	216
4.6.2.10	3,5-dinitrobenzyl 2-amino-5-((4-chloro-1-methyl-2,5-dioxo-2,5-dihydro-1H-pyrrol-3-yl)amino)pentanoate (4.12) .....	218
4.6.2.11	4,4'-(disulfanediylbis(methylene))dibenzoic acid (4.13) .....	221
4.6.2.12	di-tert-butyl (((4,4'-(disulfanediyl)-bis(methylene))bis(benzoyl))bis(azanediyl))bis(ethane-2,1-diyl))dicarbamate (4.14) .....	222
4.6.2.13	tert-butyl (2-(4-(mercaptomethyl)benzamido)ethyl)carbamate (4.15) .....	223
4.6.2.14	Boc-ABT-ACM-Boc-Orn (4.16) .....	223
4.6.2.15	ABT-ACM-Orn (4.17) .....	226
4.7	References .....	229
5.1	Abstract .....	233
5.2	Introduction .....	234
5.2.1	Probes for capturing enzyme intermediates .....	234
5.3	Results .....	238
5.3.1	Synthesis of alkyne functionalized maleimide fluorophores for utilization as enzyme intermediate probes .....	238
5.3.2	Studying the stability of maleimide fluorophores in cellular media .....	241
5.3.3	Evaluating the effectiveness of synthesized probes for detecting enzyme intermediates in natural product biosynthesis .....	251
5.4	Conclusions .....	254
5.5	Experimental .....	255
5.5.1.1	Materials .....	255

5.5.1.2	Instrumentation.....	255
5.5.1.3	Dye incubation in cellular growth media.....	257
5.5.2	Small molecule synthesis .....	258
5.5.2.1	3,4-bis(butylthio)-1H-pyrrole-2,5-dione (5.1).....	258
5.5.2.2	3,4-bis(butylthio)-1-(prop-2-yn-1-yl)-1H-pyrrole-2,5-dione (5.2) .....	259
5.5.2.3	3,4-dibromo-1-(prop-2-yn-1-yl)-1H-pyrrole-2,5-dione (5.3) .....	260
5.5.2.4	3-bromo-4-(ethylamino)-1-(prop-2-yn-1-yl)-1H-pyrrole-2,5-dione (5.4) .....	260
5.5.2.5	3-bromo-1-(prop-2-yn-1-yl)-1H-pyrrole-2,5-dione (5.5) .....	262
5.5.2.6	3-ethylamino-1-(prop-2-yn-1-yl)-1H-pyrrole-2,5-dione (5.6) .....	263
5.5.2.7	3-bromo-1-(prop-2-yn-1-yl)-1H-pyrrole-2,5-dione (5.7) .....	265
5.5.2.8	3-chloro-4-(ethylamino)-1-(prop-2-yn-1-yl)-1H-pyrrole-2,5-dione (5.8) .....	267
5.5.2.9	3-aminopropyl propiolate (5.11) .....	269
5.5.2.10	3-(3-bromo-2,5-dioxo-2,5-dihydro-1H-pyrrol-1-yl)propyl propiolate (5.12) .....	269
5.5.2.11	3-(3-(ethylamino)-2,5-dioxo-2,5-dihydro-1H-pyrrol-1-yl)propyl propiolate (5.13) .....	271
5.6	References .....	274
6.1	Abstract .....	277
6.2	Introduction .....	278
6.2.1	Polymerization-induced self-assembly (PISA) .....	278
6.2.2	Reversible addition-fragmentation chain-transfer (RAFT) polymerization...	280
6.2.3	Peptide synthesis .....	283
6.2.3.1	Preparation of synthetic peptides .....	283
6.2.3.2	Activation and amide bond formation.....	284
6.2.3.3	Sidechain protection .....	285
6.2.3.4	Resins used for SPPS .....	286
6.3	Results .....	288
6.3.1	Synthesis of peptide-functionalized chain transfer agents.....	288
6.3.2	Investigating aqueous PISA using a helical peptide-based PABTC macro-chain transfer agent.....	294
6.3.3	Investigating aqueous photo PISA using a random coil peptide-based PABTC chain transfer agent .....	297
6.3.4	Synthesis and aqueous PISA of peptide based acrylamide monomers .....	302
6.4	Conclusions .....	305
6.5	Experimental .....	306
6.5.1	Materials and instrumentation .....	306
6.5.1.1	Materials.....	306
6.5.1.2	Instrumentation.....	306
6.5.1.3	Photoreactor .....	309
6.5.2	Small molecule synthesis .....	310

6.5.2.1	PABTC .....	310
6.5.3	Peptide synthesis .....	311
6.5.3.1	General synthesis .....	311
6.5.3.2	Synthesis of CEPTA functionalized (ER) <sub>i+4</sub> peptide (6.1) .....	312
6.5.3.3	Synthesis of PABTC functionalized (ER) <sub>i+4</sub> peptide (6.2) .....	313
6.5.3.4	Synthesis of PABTC functionalized (RADA) <sub>4</sub> peptide (6.3) .....	314
6.5.3.5	Synthesis of PABTC functionalized EEE tagged (ER) <sub>i+4</sub> peptide (6.4) .....	315
6.5.3.6	Synthesis of PABTC functionalized RRR tagged KID-CREB peptide (6.5) .....	316
6.5.3.5	Synthesis of KID-CREB acrylamide monomer (6.6) .....	317
6.5.4	Aqueous PISA using peptide macro-CTAs .....	318
6.5.4.1	CTA 6.2 mediated polymerization of DAAM (P1-3) .....	318
6.5.4.2	CTA 6.4 mediated polymerization of DAAM (P4-5) .....	319
6.5.4.3	CTA 6.5 mediated photo-polymerization of DAAM (P6-7) .....	320
6.5.4.3	Aqueous photo-PISA of peptide-monomer using PEG <sub>2k</sub> CETPA macro-CTA ..	320
6.6	References .....	322
	Conclusions and future work.....	322

# List of Figures and Schemes

Figure 1.1: Make-up and classification of biological macromolecules and their respective monomers. ....	3
Figure 1.2: The structure of the twenty natural amino acids. ....	5
Figure 1.3: Cartoon representation of $\alpha$ -helix structure in manganin II (PDB: 1PEF). ....	6
Figure 1.4: Cartoon representation of antiparallel $\beta$ -helix structure in peptidyl-prolyl cis/trans isomerase (PDB: PIN1). ....	7
Figure 1.5: $\beta$ -turn type-II (top) in globin (PDB: 2BK9), and random coil (bottom) in indolicin (PDB: 1G89). ....	8
Figure 1.6: Example of protein folding pathways, from folding@home [CC BY-SA 3.0].	9
Figure 1.7: Cartoon representation of the barrel structure of GFP and a cut-away showing the chromophore. From PDB: 1GFL. <sup>30</sup> .....	10
Figure 1.8: Illustration of mRNA translation in peptide biosynthesis. ....	11
Figure 1.9: Examples of some common polymer compositions (left) and architectures (right) achievable through CRP. ....	14
Figure 1.10: The equation describing packing parameter, $p$ and an illustration of its effect on the morphology of assembled diblock copolymers. ....	15
Figure 1.11: Tuning the membrane permeability of PISA synthesized vesicles, reported by Varlas et al. <sup>83</sup> .....	17
Figure 1.12: Grafting through, from and to macromolecules. ....	18
Figure 1.13: Cyclic peptide-polymer based nanotubes developed by Perrier and co-workers. Reproduced from ref. <sup>102</sup> .....	20
Figure 1.14: Top: example structure of a peptide amphiphile developed by the Stupp group. <sup>122</sup> Bottom: giant nanotubes assembled from a peptide amphiphile. <sup>114</sup> .....	21
Figure 1.15: Jablonski diagram showing absorption and emission events in fluorescence and phosphorescence. ....	22
Figure 1.16: Illustration of selected GFP variants in their respective emission shades [CC BY-SA 3.0]. ....	25
Figure 1.17: Selected recently developed commercial small molecule fluorophores commonly used for fluorescence imaging. ....	26
Figure 1.18: Reported reactions of halogenated maleimides. ....	28
Figure 1.19: Approximate trends in fluorescence of substituted maleimides (with abbreviations) studied by Xie <i>et al.</i> <sup>146</sup> .....	29
Figure 1.20: FLIM of DTM labelled micelles in rat hippocampal tissue with fast-FLIM lifetime extractions for A) blood clot B) vascular tissue and C) red blood cells reported by Robin <i>et al.</i> <sup>161</sup> .....	32
Figure 1.21: Schematic representation showing the interaction between micelles and fluorescent dyes Nile Red and Rhodamine B. CLMs = core-labelled micelles, NLMs = non-labelled micelles. Figure reproduced from Robin <i>et al.</i> with permission. <sup>164</sup> .....	33
Figure 1.22: Confocal microscopy images of ABM tagged particles with (a) one ABM unimer addition and (b) two ABM unimer additions. Scale bar = 1000 nm. Reproduced from reference with permission. <sup>174</sup> .....	34
Figure 1.23: Maleimide (left) and bromomaleimide (right) thiol conjugation pathways, including post conjugation hydrolysis. ....	35
Figure 1.23: Illustration of DBM based stapling of $\alpha$ -helical BID. <sup>181</sup> .....	36
Figure 2.1: Commonly utilized protein conjugation techniques for lysine and cysteine targeting. ....	48
Figure 2.2: $\alpha,\beta$ -unsaturated- $\beta'$ -mono-sulfone functionalized PEG bridging of disulfide bonds. <sup>24</sup> .....	50
Figure 2.3: Polymerization of DMEMA by $\alpha$ -CT conjugated ATRP initiators. <sup>17</sup> .....	51

Figure 2.4: Topology of enzyme conjugated PEG (left) versus the incorrect, commonly assumed 'shroud' model (right). Figure reproduced from Pai <i>et al.</i> <sup>26</sup> .....	53
Scheme 2.1 Scheme of DBM disulfide bridging conjugations.....	54
Figure 2.5: MALDI-ToF spectra of purified M-DBM $\alpha$ -CT conjugate (red) against native $\alpha$ -CT (black). .....	54
Figure 2.6: MALDI-ToF spectra of M-DBM $\alpha$ -CT conjugates, at 10 mins (red), 90 mins (green) and after spin filtering (blue), against native $\alpha$ -CT (black).....	55
Figure 2.7: HPLC chromatogram of $\alpha$ -CT under various reaction conditions. ....	56
Figure 2.8: HPLC of the further optimized procedure with 220 nm and fluorescence detectors ( $\lambda_{\text{ex}}$ : 382 nm, $\lambda_{\text{em}}$ : 531 nm).....	57
Figure 2.9: Kyte-Doolittle plot of $\alpha$ -CT, including locations of disulfide bridges. ....	58
Figure 2.10: MALDI-ToF spectra of purified M-DTM HLZ conjugate (red) against native HLZ (black). ....	60
Figure 2.11: CD spectra of HLZ (black) and DTM-HLZ (red) in pH 6 phosphate buffer. 61	
Figure 2.12: DSC spectra of HLZ (black) and DTM HLZ (red) recorded in pH 6 PB buffer at approximately 0.5 mg/ml. Recorded by Malin Suurkuusk (TA instruments). ....	62
Scheme 2.2: Synthesis of PEG-DBM (2.2).....	62
Scheme 2.3: Synthesis of ABM and MAM conjugates using conjugating agents M-DBM, 2.3, 2.4 and 2.5.....	64
Figure 2.13: MALDI-ToF spectra of purified M-ABM HLZ conjugate (left, red) and alkyne-MAM conjugate (right, red) against native HLZ (black). ....	64
Figure 2.14: DSC spectra of HLZ (black) and MAM HLZ (red) recorded in pH 6 PB buffer at approximately 0.5 mg/ml. Recorded by Malin Suurkuusk (TA instruments). ....	66
Figure 2.15: Fluorescence emission of conjugates in pH 8.5 tris buffer. Left: alkyne-MAM HLZ conjugate (511 nm emission and 356 nm excitation), right: M-DTM HLZ conjugate (540 nm emission and 395 nm excitation). ....	66
Figure 2.16: (A) Initial activity of $\alpha$ -CT at time points against purified conjugates at t = 0 hr and (B) residual activities of native $\alpha$ -CT and conjugates (black = native enzyme; red = M-DTM conjugate; blue = alkyne-MAM conjugate; green = PEG-DTM conjugate; yellow = PEG-MAM conjugate). ....	69
Figure 2.17: The residual activity, by EnzChek® lysis assay, of native HLZ and conjugates when stored at (A) room temperature (B) 50 °C (black = native enzyme; red = M-DTM conjugate; blue = alkyne-MAM conjugate; green = PEG-DTM conjugate; yellow = PEG-MAM conjugate). ....	70
Figure 2.18: Elution gradient of water/acetonitrile used for enzyme analysis by HPLC. 74	
Figure 2.19: <sup>1</sup> H NMR spectrum of 2.2. ....	77
Figure 2.19: <sup>13</sup> C NMR spectrum of 2.2. ....	77
Figure 2.20: <sup>1</sup> H NMR spectrum of 2.5. ....	80
Figure 2.21: <sup>13</sup> C NMR spectrum of 2.5. ....	80
Figure 2.22: MALDI-ToF spectra of conjugate and native enzyme. ....	81
Figure 2.23: 2D excitation/emission spectrum of M-DTM $\alpha$ -CT conjugate in pH 6 buffer. ....	83
Figure 2.24: MALDI-ToF spectra of conjugate and native enzyme. ....	83
Figure 2.25: 2D excitation/emission spectrum of alkyne-MAM $\alpha$ -CT conjugate in pH 6 buffer. ....	83
Figure 2.26: MALDI-ToF spectra of conjugate and native enzyme. ....	84
Figure 2.27: 2D excitation/emission spectrum of M-DTM HLZ conjugate in pH 6 buffer. ....	85
Figure 2.28: MALDI-ToF spectra of conjugate and native enzyme. ....	86
Figure 2.29: 2D excitation/emission spectrum of M-DTM HLZ conjugate in pH 6 buffer. ....	86
Figure 2.30: MALDI-ToF spectra of conjugate and native enzyme. ....	87
Figure 2.31: Excitation/emission spectrum of methyl-MAM $\alpha$ -CT conjugate in pH 6 buffer. ....	87

Figure 2.32: MALDI-ToF of conjugate and native enzyme. ....	88
Figure 2.33: Excitation/emission spectrum of M-ABM HLZ conjugate in pH 8.5 buffer. 88	
Figure 2.34: MALDI-ToF spectra of conjugate and native enzyme. ....	89
Figure 2.35: MALDI-ToF spectra of conjugate and native enzyme. ....	90
Figure 2.36: MALDI-ToF spectra of conjugate and native enzyme. ....	91
Figure 2.37: Excitation/emission spectrum of PEG- <b>DTM</b> $\alpha$ -CT conjugate in pH 6 buffer. ....	91
Figure 2.38: MALDI-ToF spectra of conjugate and native enzyme. ....	92
Figure 2.39: Excitation/emission spectrum of PEG-DTM HLZ conjugate in pH 6 buffer. 92	
Figure 2.40: MALDI-ToF spectra of conjugate and native enzyme. ....	93
Figure 2.41: Excitation/emission spectrum of PEG- <b>MAM</b> $\alpha$ -CT conjugate in pH 6 buffer. ....	94
Figure 2.42: MALDI-ToF spectra of conjugate and native enzyme. ....	95
Figure 2.43: Excitation/emission spectrum of PEG-MAM HLZ conjugate in pH 6 buffer. 95	
Figure 2.44: Lysozyme standard curve. ....	97
Figure 2.45: UV-Vis (left) and fluorescence emission (right) spectra of DTM conjugate against quinine standard. ....	98
Figure 3.1: <b>Illustration of absorption and relaxation events in a generalized maleimide skeleton in different solvents. ISC = intersystem crossing, PR = photo recombination.</b> ....	106
Figure 3.2: Diagram of hypothesized EDPT mechanism for a maleimide solvated in MeOH. Electronic movement is indicated by the green dashed arrow and proton movement is indicated by the blue arrow. Reproduced from reference. <sup>8</sup> ....	108
Figure 3.3: Illustration of rotation-based relaxation of TPE (left), and the fluorescent aggregate state through RIM/RIR (right) ....	109
Figure 3.4: 2D Illustration of proposed interactions preventing solvent (R) hydrogen bonding in a phenyl substituted maleimide. ....	111
Scheme 3.1: Synthesis of mono- and bis-benzyl aminomaleimides 3.2 and 3.4 <i>via</i> intermediate MBMs 3.1 and 3.3. ....	112
Scheme 3.2: Synthesis of trityl MAM 3.7 and ABM 3.8. ....	113
Scheme 3.3: Synthesis of ABM/MAM dyes 3.9, 3.10, 3.12, 3.15 and 3.16 used for fluorescence controls. ....	113
Scheme 3.4: Synthesis of various silyl maleimides 3.21-3.24 <i>via</i> silyl bromomaleimide intermediates 3.17-3.20. ....	115
Figure 3.5: <b>Chart showing solution <math>\lambda_{\text{ex}}</math> (red) and <math>\lambda_{\text{em}}</math> (blue) of the benzyl maleimide series in various solvents. * Too weak for measurement.</b> ....	116
Figure 3.6: Chart showing solution and solid-state quantum yields of studied maleimide fluorophores; measured by either reference or absolute method, respectively. ....	118
Figure 3.7: HOMO isosurfaces of benzyl MAM series with their HOMO1 and NBO1 atomic integrations - representing the $\pi$ -conjugated structure of the aminomaleimide ring (lower $Q$ values indicate greater electron density on the maleimide ring) and the solution state absolute quantum yields (in diethyl ether). ....	119
Scheme 3.5: Schematic representation of the atom enumeration used in the simulation of NBO1 and HOMO1 orbitals. ....	119
Figure 3.8: Correlation between quantum yield, $\Phi_{\text{f}}(\%)$ , (in diethyl ether solution) and the atomic integration of HOMO1 along the $\pi$ conjugated structure of the aminomaleimide ring, $QHOMO1$ . ....	121
Figure 3.9 Fluorescence of Bz <sub>3</sub> MAM (3.7) in water/dioxane mixtures: emission at 470 nm (375 nm excitation) against water conten (left) and emission spectrum at 375 nm excitation at different percentages of water in dioxane (right). ....	122
Figure 3.10 CAM-B3LYP/6-311G(d,p) gradient isosurfaces with $s=0.5$ for the crystal structures of HMAM, BzMAM, Bz <sub>2</sub> MAM, and Bz <sub>3</sub> MAM with a blue-green-red colour scale from $-0.05 < \rho \text{ sign}(\lambda_2) < 0.05$ au. ....	125

Figure 3.11 LUMO isosurfaces overlaid on the obtained crystal structures of the benzyl functionalized series. ....	126
Figure 3.12 Chart displaying solid-state (darker colors) and PEG incorporated (lighter colors) absolute quantum yields. Error bars represent standard deviation over 3 repeats. ....	127
Figure 3.13. Spectrum displaying solution state emission of TBDPSiMAM (3.18) in various solvents ( $\lambda_{\text{ex}} = \lambda_{\text{max}}$ ). ....	128
Figure 3.14 Chart showing solution state quantum yields of silyl substituted maleimide fluorophores and control dyes; measured by reference method. ....	129
Figure 3.15 Illustration and modelling of hydrogen bonding interactions with TBDPSiMAM and methanol. ....	130
Figure 3.16: $^1\text{H}$ NMR spectrum of 3.1 (300 MHz, $\text{CDCl}_3$ ). ....	136
Figure 3.17: $^{13}\text{C}$ NMR spectrum of 3.1 (101 MHz, $\text{CDCl}_3$ ). ....	137
Figure 3.18: $^1\text{H}$ NMR spectrum of 3.3 (500 MHz, $\text{CDCl}_3$ ). ....	138
Figure 3.19: $^{13}\text{C}$ NMR spectrum of 3.3 (126 MHz, $\text{CDCl}_3$ ). ....	139
Figure 3.20: $^1\text{H}$ NMR spectrum of 3.5 (500 MHz, $\text{CDCl}_3$ ). ....	140
Figure 3.21: $^{13}\text{C}$ NMR spectrum of 3.5 (126 MHz, $\text{CDCl}_3$ ). ....	140
Figure 3.22: $^1\text{H}$ NMR spectrum of 3.6 (500 MHz, $\text{CDCl}_3$ ). ....	142
Figure 3.23: $^{13}\text{C}$ NMR spectrum of 3.6 (126 MHz, $\text{CDCl}_3$ ). ....	142
Figure 3.24: $^1\text{H}$ NMR spectrum of 3.11 (300 MHz, $\text{CDCl}_3$ ). ....	144
Figure 3.25: $^{13}\text{C}$ NMR spectrum of 3.11 (75 MHz, $\text{CDCl}_3$ ). ....	144
Figure 3.26: $^1\text{H}$ NMR spectrum of 3.17 (500 MHz, $\text{CDCl}_3$ ). ....	146
Figure 3.27: $^{13}\text{C}$ NMR spectrum of 3.17 (126 MHz, $\text{CDCl}_3$ ). ....	146
Figure 3.28: $^1\text{H}$ NMR spectrum of 3.18 (500 MHz, $\text{CDCl}_3$ ). ....	148
Figure 3.29: $^{13}\text{C}$ NMR spectrum of 3.18 (101 MHz, $\text{CDCl}_3$ ). ....	149
Figure 3.30: $^1\text{H}$ NMR spectrum of 3.19 (500 MHz, $\text{CDCl}_3$ ). ....	150
Figure 3.31: $^{13}\text{C}$ NMR spectrum of 3.19 (126 MHz, $\text{CDCl}_3$ ). ....	151
Figure 3.32: $^1\text{H}$ NMR spectrum of 3.20 (500 MHz, $\text{CDCl}_3$ ). ....	152
Figure 3.33: $^{13}\text{C}$ NMR spectrum of 3.20 (126 MHz, $\text{CDCl}_3$ ). ....	153
Figure 3.34: $^1\text{H}$ NMR spectrum of 3.11 (500 MHz, $\text{CDCl}_3$ ). ....	155
Figure 3.35: $^{13}\text{C}$ NMR spectrum of 3.11 (126 MHz, $\text{CDCl}_3$ ). ....	155
Figure 3.36: $^1\text{H}$ NMR spectrum of 3.2 (300 MHz, $\text{CDCl}_3$ ). ....	157
Figure 3.37: $^{13}\text{C}$ NMR spectrum of 3.2 (126 MHz, $\text{CDCl}_3$ ). ....	157
Figure 3.38: $^1\text{H}$ NMR spectrum of 3.4 (300 MHz, $\text{CDCl}_3$ ). ....	159
Figure 3.39: $^{13}\text{C}$ NMR spectrum of 3.4 (126 MHz, $\text{CDCl}_3$ ). ....	159
Figure 3.40: $^1\text{H}$ NMR spectrum of 3.7 (500 MHz, $\text{CDCl}_3$ ). ....	161
Figure 3.41: $^{13}\text{C}$ NMR spectrum of 3.7 (126 MHz, $\text{CDCl}_3$ ). ....	161
Figure 3.42: $^1\text{H}$ NMR spectrum of 3.8 (300 MHz, $\text{CDCl}_3$ ). ....	163
Figure 3.43: $^{13}\text{C}$ NMR spectrum of 3.8 (126 MHz, $\text{CDCl}_3$ ). ....	163
Figure 3.46: $^1\text{H}$ NMR spectrum of 3.22 (500 MHz, $\text{CDCl}_3$ ). ....	167
Figure 3.47: $^{13}\text{C}$ NMR spectrum of 3.22 (126 MHz, $\text{CDCl}_3$ ). ....	167
Figure 3.50: $^1\text{H}$ NMR spectrum of 3.24 (500 MHz, $\text{CDCl}_3$ ). ....	171
Figure 3.51: $^{13}\text{C}$ NMR spectrum of 3.24 (126 MHz, $\text{CDCl}_3$ ). ....	171
Figure 4.1: (A) Aminoacylation of tRNA with a uAA and (B) subsequent incorporation of the uAA into a peptide by a ribosome. ....	179
Figure 4.2: Illustration of flexizyme charging with a CME activated amino acid. ....	180
Figure 4.3: Fluorescently labelled amino acids that have been genetically expressed into proteins by the Schultz group. <sup>25-27</sup> ....	181
Scheme 4.1: Synthesis of MAM-Fmoc-lysine (4.3) via bromomaleimide (4.1). ....	183
Scheme 4.2: Synthesis of ABM-Fmoc-lysine 4.4 and attempted deprotection to ABM-lysine 4.5. ....	184
Figure 4.4: $^1\text{H}$ NMR spectrum of 4.5 (400 MHz, $\text{D}_2\text{O}$ ). ....	185
Scheme 4.3: Optimized synthesis of chlorinated maleimides 4.6 and 4.7. ....	187



Scheme 4.4: Synthesis of ACM- <i>N</i> $\alpha$ -Boc-OtBu-Ornithine 4.8 and deprotection to ACM-Ornithine 4.9.....	188
Figure 4.5: <sup>1</sup> H NMR spectrum of 4.9 (400 MHz, D <sub>2</sub> O).....	188
Figure 4.6: Fluorescence excitation (dashed line) and emission (full line) of 4.5 and 4.9 at 10 $\mu$ M in water.....	189
Scheme 4.5: Synthesis of DNB ester of ACM-Ornithine (4.12) <i>via</i> <i>N</i> -Boc-ACM-Ornithine (4.10).....	190
Scheme 4.6: Synthesis of disulfide ABT precursor (4.13) and subsequent synthesis of ABT thiol (4.15) <i>via</i> reduction of disulfide 4.14 formed by EDC coupling of EDA and 4.13.....	191
Figure 4.7: <sup>1</sup> H NMR spectrum of 4.17 (300 MHz, DMSO- <i>d</i> <sub>6</sub> ).....	193
Figure 4.8: Fluorescence excitation (dashed line) and emission (full line) of 4.12 and 4.17 at 10 $\mu$ M in water.....	194
Scheme 4.8: Suggested alternative synthesis of methyl-ACM-ABT-ornithine (4.17). ..	195
Figure 4.9: Location of W28 (yellow) and W109 (green) in HLZ, potential mutation targets for an ACM amino acid, with nearby active site for W109 (red). PDB structure: 1LZ1. <sup>40</sup> .....	199
Figure 4.10: <sup>1</sup> H NMR spectrum of 4.4 (500 MHz, DMSO- <i>d</i> <sub>6</sub> ).....	203
Figure 4.11: <sup>13</sup> C NMR spectrum of 4.4 (125 MHz, DMSO- <i>d</i> <sub>6</sub> ).....	203
Figure 4.12: <sup>1</sup> H NMR spectrum of 4.5 (400 MHz, D <sub>2</sub> O).....	205
Figure 4.13: <sup>13</sup> C NMR spectrum of 4.5 (101 MHz, D <sub>2</sub> O).....	205
Figure 4.14: HPLC chromatogram of prep-HPLC run (blue = 375 nm detector, red = acetonitrile% in water). .....	206
Figure 4.15: Fluorescence excitation and emission map of 4.5 in dioxane (5 $\mu$ M). ...	206
Figure 4.16: Fluorescence excitation and emission map of 4.5 in water (2.5 $\mu$ M)....	207
Figure 4.17: <sup>1</sup> H NMR spectrum of 4.8 (400 MHz, CDCl <sub>3</sub> ).....	210
Figure 4.18: <sup>13</sup> C NMR spectrum of 4.8 (101 MHz, DMSO- <i>d</i> <sub>6</sub> ).....	210
Figure 4.19: <sup>1</sup> H NMR spectrum of 4.9 (400 MHz, D <sub>2</sub> O).....	212
Figure 4.20: <sup>13</sup> C NMR spectrum of 4.9 (101 MHz, D <sub>2</sub> O).....	212
Figure 4.21: Fluorescence excitation and emission map of 4.9 in dioxane (1 $\mu$ M). ...	213
Figure 4.22: Fluorescence excitation and emission map of 4.9 in water (10 $\mu$ M)....	213
Figure 4.25: <sup>1</sup> H NMR spectrum of 4.11 (300 MHz, CDCl <sub>3</sub> ).....	217
Figure 4.26: <sup>13</sup> C NMR spectrum of 4.11 (101 MHz, CDCl <sub>3</sub> ).....	217
Figure 4.27: <sup>1</sup> H NMR spectrum of 4.12 (300 MHz, DMSO- <i>d</i> <sub>6</sub> ).....	219
Figure 4.28: <sup>13</sup> C NMR spectrum of 4.12 (101 MHz, DMSO- <i>d</i> <sub>6</sub> ).....	219
Figure 4.29: Fluorescence excitation and emission map of 4.12 in dioxane (5 $\mu$ M). .	220
Figure 4.30: Fluorescence excitation and emission map of 4.12 in water (2.5 $\mu$ M)...	220
Figure 4.31: <sup>1</sup> H NMR spectrum of 4.16 (400 MHz, DMSO- <i>d</i> <sub>6</sub> ).....	225
Figure 4.32: <sup>13</sup> C NMR spectrum of 4.16 (101 MHz, DMSO- <i>d</i> <sub>6</sub> ).....	225
Figure 4.34: <sup>13</sup> C NMR spectrum of 4.17 (101 MHz, D <sub>2</sub> O).....	227
Figure 4.35: Fluorescence excitation and emission map of 4.17 in dioxane (10 $\mu$ M). ..	228
Figure 4.36: Fluorescence excitation and emission map of 4.17 in water (2.5 $\mu$ M)...	228
Figure 5.1: Simplified mechanism of normal polyketide synthesis (black) and mechanism of trapping intermediates with probe (blue). .....	235
Figure 5.2: Illustration of normal non-ribosomal peptide synthesis (A) and capture of intermediates by chemical probe mimics (B) developed by Ho et. al. Figure reproduced from ref. <sup>2</sup> .....	236
Scheme 5.2: Synthesis of alkyne-ethylaminobromomaleimide 5.4. ....	239
Scheme 5.1: Synthesis of alkyne-dibutylthiomaleimide, 5.2. ....	238
Scheme 5.3: Synthesis of alkyne-ethylaminomaleimide 5.6. ....	239
Scheme 5.4: Synthesis of alkyne-ethylaminochloromaleimide 5.8. ....	239
Figure 5.3: <sup>1</sup> H NMR spectrum of 5.13 in CDCl <sub>3</sub> , with impurity circled.....	241

Figure 5.4: Structure and photo of fluorescence under UV illumination of ACM 5.4 after 24 hour incubation in cell media. ....	242
Figure 5.5: Structure and photo of fluorescence under UV illumination of ACM 5.8 after 24 hour incubation in cell media. ....	242
Figure 5.6: Fluorescence emission of 5.8 in 18.2 M $\Omega$ ·cm water over two weeks (375 nm excitation). ....	243
Figure 5.7: <b>Fluorescence emission (<math>\lambda_{\text{ex}} = 375 \text{ nm}</math> <math>\lambda_{\text{em}} = 500 \text{ nm}</math>)</b> of ACM 5.8 in non-sterile cell media. ....	244
Figure 5.8: Fluorescence emission ( $\lambda_{\text{ex}} = 375 \text{ nm}$ $\lambda_{\text{em}} = 500 \text{ nm}$ ) of ACM 5.8 in sterile cell media. ....	244
Figure 5.9: HPLC chromatograms of 5.8 in water over 14 days, with 254 nm detection (top) and 375 nm detection (bottom). ....	245
Figure 5.10: HPLC chromatograms of 5.8 in water over 14 days, recorded with a fluorescence detector (375 nm excitation and 500 nm emission). ....	246
Figure 5.11: HPLC chromatograms of 5.8 in SMM over 14 days, with 254 nm detection (top) and 375 nm detection (bottom). ....	246
Figure 5.12: HPLC chromatograms of 5.8 in YEME over 14 days, with 254 nm detection (top) and 375 nm detection (bottom). ....	247
Figure 5.13: HPLC chromatograms of 5.8 in TSB over 14 days, with 254 nm detection (top) and 375 nm detection (bottom). ....	247
Figure 5.14: GCMS chromatograms of 5.8 over 7 days extracted from water. ....	248
Figure 5.15: GCMS chromatograms of 5.8 over 7 days extracted from MYM. ....	249
Figure 5.16: GCMS chromatograms of 5.8 over 7 days extracted from SMM. ....	249
Figure 5.17: GCMS chromatograms of 5.8 over 7 days extracted from YEME. ....	250
Scheme 5.6: Synthesized maleimide functionalized intermediate probes by the Tosin group, from alkyne dyes 5.2 (top) and 5.8 (bottom) using CuAAC. ....	251
Figure 5.18: Proposed isolated intermediate and obtained mass spectrum in the probing of 6-MSA synthesis. ....	252
Figure 5.19: Three hypothesized species detected by MS-MS upon incubation of ACM probe with ACP and KS-CLF by the Tosin group. ....	253
Figure 5.20: Elution gradient of water/acetonitrile used for dye incubation analysis by HPLC. ....	256
Figure 5.21: Temperature gradient used for GCMS runs of 5.8. ....	257
Figure 5.22: $^1\text{H}$ NMR spectrum of 5.4 ....	261
Figure 5.23: $^{13}\text{C}$ NMR spectrum of 5.4 ....	262
Figure 5.24: $^1\text{H}$ NMR spectrum of 5.6 ....	264
Figure 5.25: $^{13}\text{C}$ NMR spectrum of 5.6 ....	264
Figure 5.26: $^1\text{H}$ NMR spectrum of 5.7 ....	266
Figure 5.27: $^{13}\text{C}$ NMR spectrum of 5.7 ....	266
Figure 5.28: $^1\text{H}$ NMR spectrum of 5.8 ....	268
Figure 5.29: $^{13}\text{C}$ NMR spectrum of 5.8 ....	268
Figure 5.30: $^1\text{H}$ NMR spectrum of 5.12 ....	270
Figure 5.31: $^{13}\text{C}$ NMR spectrum of 5.12 ....	271
Figure 5.32: $^1\text{H}$ NMR spectrum of 5.13 ....	272
Figure 5.33: $^{13}\text{C}$ NMR spectrum of 5.13 ....	273
Scheme 6.1: Illustrated representation of the dispersion PISA process. ....	278
Scheme 6.2: Illustration of PIESA reported by Cai <i>et al.</i> <sup>18</sup> ....	280
Scheme 6.3: Proposed RAFT mechanism. ....	282
Scheme 6.4: <b>Structure of generic RAFT agent, and empirical guide to R and Z-group selection for selected monomers, adapted from ref.<sup>33</sup></b> ....	276
Scheme 6.5: <b>Simplified scheme of the coupling step and selection of example activators and racemization reducing reagents.</b> ....	278
Scheme 6.6: Sequences of the three targeted peptide sequences. ....	289

Scheme 6.7: Unsuccessful synthesis of CETPA functionalized (ER) <sub>i+4</sub> peptide CTA 6.1.	290
Figure 6.1: DMF SEC (DRI) molecular weight distribution of PHPMA (DP = 50) polymerized using macro-CTA 6.1.	291
Figure 6.2: Circular dichroism spectra of (ER) <sub>i+4</sub> peptide CTA 6.2 and random coil peptide 6.5 conducted at 0.1 mg/mL in water.	292
Figure 6.3: A) Structure of PABTC functionalized RADA <sub>16</sub> peptide CTA 6.3. B) HPLC chromatogram after denaturing with 8 M guanidine.	293
Figure 6.4: DMF SEC (DRI) molecular weight distribution of PDAAm polymerized using macro-CTA 6.2.	294
Figure 6.6: A) Structure of macro-CTA 6.5 B) SEC (dashed = UV 309 nm, line = DRI) of P6 in THF.	298
Figure 6.7: A) Normalized THF SEC <i>M<sub>w</sub></i> distribution of P7 (dashed = 309 nm, line = DRI) B) crude DLS measurement of P7.	299
Figure 6.9: A) Synthesis of peptide side-chain monomer 6.6 B) HPLC of monomer 6.6 detected at 220 nm.	302
Figure 6.10: Typical elution gradient for peptide chromatography.	307
Figure 6.11: Photo of photoreactor set-up used for photo initiated polymerizations in this chapter.	309
Figure 6.13: HPLC chromatogram of 6.2.	313
Figure 6.14: HPLC chromatogram of 6.3 (conducted in an 8M guanidine solution to ensure solubility).	314
Figure 6.15: HPLC chromatogram of 6.4.	315

## List of Tables

<b>Table 2.1:</b> Approximate solvent accessible surface area of disulfide bonds calculated using PyMol (PDB: 4CHA).....	59
<b>Table 2.2.</b> Table showing number of attached units for disulfide conjugates observed by MALDI-ToF MS and standard deviation measured by Gaussian fit. ....	63
*= Gaussian fit not possible, observed discrete conjugates listed.....	63
<b>Table 2.3.</b> Table showing number of attached units for lysine/amine conjugates observed by MALDI-ToF MS and standard deviation measured by Gaussian fit. ....	65
<b>Table 2.4.</b> All measured $\lambda_{ex}/\lambda_{em}$ maximum, and recorded $\Phi_f(\%)$ for conjugates. ....	67
<b>Table 2.5:</b> Molar ellipticity difference of the DTM HLZ conjugate versus measured activity difference. ....	99
<b>Table 3.1</b> Hydrogen bonding data for solved crystals of the benzyl MAM series. *n.d. = not determined. <b>HMAM</b> i= 1-X, +Y, -1/2+Z; <b>BzMAM</b> i= 1-X, 1-Y, 1-Z; <b>Bz<sub>2</sub>MAM</b> i= 1-X, 1-Y, -Z; <b>Bz<sub>3</sub>MAM</b> i= +Y, +X, 1-Z.....	123
<b>Table 3.2</b> Solid state $\Phi_f$ and shortest maleimide crystal packing distances and angles for crystals of the benzyl MAM series. †Measured distance and angle between ring centroid of N1C1C2C3C4 and N1 <sup>i</sup> C1 <sup>i</sup> C2 <sup>i</sup> C3 <sup>i</sup> C4 <sup>i</sup> . *Angles between mean-plane created from atom selection N1C1C2C3C4 and N1 <sup>i</sup> C1 <sup>i</sup> C2 <sup>i</sup> C3 <sup>i</sup> C4 <sup>i</sup> . ‡ Distance between ring centroid of N1C1C2C3C4 and plane of N1 <sup>i</sup> C1 <sup>i</sup> C2 <sup>i</sup> C3 <sup>i</sup> C4 <sup>i</sup> . § Distance in horizontal shift between ring centroids of N1C1C2C3C4 and N1 <sup>i</sup> C1 <sup>i</sup> C2 <sup>i</sup> C3 <sup>i</sup> C4 <sup>i</sup> .....	124
<b>Table 3.3</b> Theoretical and observed fluorescence $\lambda_{ex/em}$ in methanol, used to calculate a probability of hydrogen bonding ( <i>P</i> ).....	131
<b>Table 4.1:</b> Summary of conditions attempted for the synthesis of dichloromaleimides <b>4.6</b> and <b>4.7</b> .....	186
<b>Table 6.1:</b> Selected side chain protection strategies employed in this chapter.....	286
<b>Table 6.2:</b> Structure of selected risin linkers, with their cleavage conditions and produced C-terminus.....	287
<b>Table 6.3:</b> Summary of $D_h$ , PD values and zeta potential values with deviation for assemblies formed <i>via</i> aqueous PISA, as determined by DLS analysis and .....	295
<b>Table 6.4:</b> Summary of $D_h$ , PD values and zeta potential with deviation for .....	297
<b>P4</b> in different pH buffers, as determined by DLS analysis and microelectrophoresis respectively.....	297
<b>Table 6.5:</b> $D_h$ , PD values, zeta potentials and observed size with deviations for <b>P4</b> , as determined by DLS analysis, microelectrophoresis and AFM respectively. ....	300
<b>Table 6.6:</b> Atom based octanol-water partition coefficients (ALogP98), calculated Connolly solvent accessible surface area (SA) and surface area normalized Log <i>P</i> (ALogP98/SA) for CTAs <b>6.2</b> and <b>6.5</b> . ....	301
<b>Table 6.7:</b> Summary of $D_h$ and PD values with deviation for <b>P8-11</b> , as determined by DLS analysis. *Signal too weak for analysis.....	303

## Abbreviations

A	Absorbance
ABM	Aminobromomaleimide
ABT	amino-derivatized benzyl thioester
ACM	Aminochloromaleimide
ACP	Acyl carrier protein
Ac	Acetate
ACQ	Aggregation caused quenching
AFM	Atomic force microscopy
AIE	Aggregation-induced emission
ATM	Aminothiomaleimide
ATRP	Atom transfer radical polymerization
Boc	<i>Tert</i> -butyloxycarbonyl
br	Broad peak in NMR spectrum
Bz	Benzyl
c	Concentration
CD	Circular dichroism
CDSA	Crystallization driven self-assembly
CETPA	4-cyano-4-[(ethylsulfanylthiocarbonyl)sulfanyl]pentanoic acid
CoA	Coenzyme A
CRP	Controlled radical polymerization
CTA	Chain transfer agent
CuAAC	Copper (I) catalyzed azide alkyne click
$D_h$	Hydrodynamic radius
$\bar{D}_M$	Molecular weight dispersity

d	Doublet in NMR spectrum
DAP	Diaminopimelic acid
DBM	Dibromomaleimide
DCM	Dichloromaleimide
DDAm	Diacetone acrylamide
DIAD	<i>N,N</i> -Diisopropylazodicarboxylate
DIC	<i>N,N</i> -Diisopropylcarbodiimide
DIPEA	<i>N,N</i> -Diisopropylethylamine
DLS	Dynamic light scattering
DMAEMA	2-(Dimethylamino)ethyl methacrylate
DMAP	4-Dimethylaminopyridine
DMF	<i>N,N</i> -Dimethylformamide
DMSO	Dimethylsulfoxide
DNA	Deoxyribonucleic acid
DNB	Dinitro benzyl
DP	Degree of polymerization
DRI	Differential refractive index
DSC	Differential scanning calorimetry
DTM	Dithiomaleimide
EDC	1-(3-Dimethylaminopropyl)-3-ethylcarbodiimide
EDPT	Electron driven proton transfer
em	Emission
Eq.	Equation
Equiv.	Equivalents
ESI-MS	Electrospray ionization mass spectrometry
Et	Ethyl

ex	Excitation
FLIM	Fluorescence-lifetime imaging microscopy
Fmoc	Fluorenylmethyloxycarbonyl
FRET	Förster resonance energy transfer
FTIR	Fourier transform infra-red
GC	Gas chromatography
GFP	Green fluorescent protein
HATU	Hexafluorophosphate Azabenzotriazole Tetramethyl Uronium
HEWL	Hen egg-white lysozyme
HLZ	Human lysozyme
HOBt	1-hydroxy-benzotriazole
HOMO	Highest occupied molecular orbital
HPLC	High-performance liquid chromatography
HPMA	2-Hydroxypropyl methacrylate
hr	Hour
HRMS	High-resolution mass spectrometry
hSOD	human superoxide dismutase
I	Initiator
iPr	Isopropyl
<i>J</i>	Observed NMR spectroscopy coupling constant
KID-CREB	Kinase independent domain of the cAMP response element binding protein
KS	Ketide synthesis/synthetase
l	Path length
LCST	Lower critical solution temperature
LUMO	Lowest unoccupied molecular orbital

M	Monomer
$M_n$	Number average molecular weight
$M_w$	Mass average molecular weight
m/z	Mass to charge ratio
MALDI-ToF	Matrix-assisted laser desorption/ionization time of flight spectroscopy
MAM	Monoaminomaleimide
MBM	Monobromomaleimide
Me	Methyl
min	Minute/s
MMA	Methyl methacrylate
mRNA	Messenger ribose nucleic acid
MS	Mass spectroscopy
MYM	Minimal yeast media
NBO	Natural bonding orbital
NHS	<i>N</i> -Hydroxysuccinimide
NMR	Nuclear magnetic resonance
NRPS	Non-ribosomal peptide synthesis
OCM	Alkoxychloromaleimide
OLED	Organic light-emitting diode
Orn	Ornithine
OXYMA	Ethyl cyanohydroxyiminoacetate
P	Poly
P/SA	Partition coefficient by surface area
$P_m$	Polymer with DP = m
$P_n$	Polymer with DP = n



PABTC	propionic acid butyl trithiocarbonate
Pbf	pentamethylhydrobenzofuran
PCT	Photo-induced charge transfer
PEG	Polyethylene glycol
Ph	Phenyl
PISA	Polymerization-induced self-assembly
PIESA	Polymerization-induced electrostatic self-assembly
ppm	Parts per million
RAFT	Reversible Addition Fragmentation Chain Transfer
ref	Reference
RIM	Restriction of intramolecular motion
RIV	Restriction of intramolecular vibration
RNA	Ribose nucleic acid
ROMP	Ring-opening metathesis polymerization
ROP	Ring-opening polymerisation
rt	Room temperature
s	Singlet in NMR spectrum
SA	Surface area
SDS-PAGE	sodium dodecyl sulfate–polyacrylamide gel electrophoresis
SEC	Size exclusion chromatography
SET-LRP	Single electron transfer living radical polymerisation
SMM	Simple malt media
SPPS	Solid-phase peptide synthesis
<sup>t</sup> Bu	<i>Tert</i> -butyl
T <sub>m</sub>	Melting temperature
TBDMSi	<i>Tert</i> -butyl dimethyl silane

TBDPSi	<i>Tert</i> -butyl diphenyl silane
TEM	Transition electron microscopy
TFA	Trifluoroacetic acid
THF	Tetrahydrofuran
TICT	Twisted intramolecular charge transfer
TLC	Thin layer chromatography
TMS	Dimethyl silane
TNT	Trinitrotoluene
TPE	Tetraphenylethylene
tRNA	Messenger ribose nucleic acid
Trt	Trityl
TSB	Tryptic soy broth
uAA	Unnatural amino acid
UV	Ultraviolet
v	volume
VA-044	2,2'-Azobis(2-(2-imidazolin-2-yl)propane dihydrochloride
vis	Visible
w%	Weight percentage
YEME	Yeast extract/Malt extract
Z	Chain transfer agent substituent
$\delta$	Chemical shift in NMR spectroscopy
$\alpha$ -CT	Alpha-Chymotrypsin
$\lambda$	Wavelength
$\Phi_f$	Quantum yield



# **Chapter 1:** Introducing applications of fluorescence for peptide-based macromolecules

# 1.1 Biological macromolecules

## 1.1.1 Macromolecules

Originally coined by Hermann Staudinger as 'high molecular compounds (in excess of 1,000 atoms)', macromolecules are these days regarded broadly as molecules of high molecular weight, made up from multiple lower molecular weight units.<sup>2</sup> They can be either of natural origins for example, biological macromolecules like proteins, carbohydrates and DNA; or synthetic, for example, synthetic polymers like plastics and rubbers.

Biology has relied upon macromolecules since the formation of microorganisms, initially relying upon RNA for information storage and catalysis, and lipids for protocell formation.<sup>3</sup> Contemporarily, biological macromolecules include proteins and enzymes comprised of amino acid subunits; DNA and RNA comprised of nucleic acid units; polysaccharides, polymers of sugars; and phospholipids derived from fatty acids (Figure 1.1). Proteins are highly functional

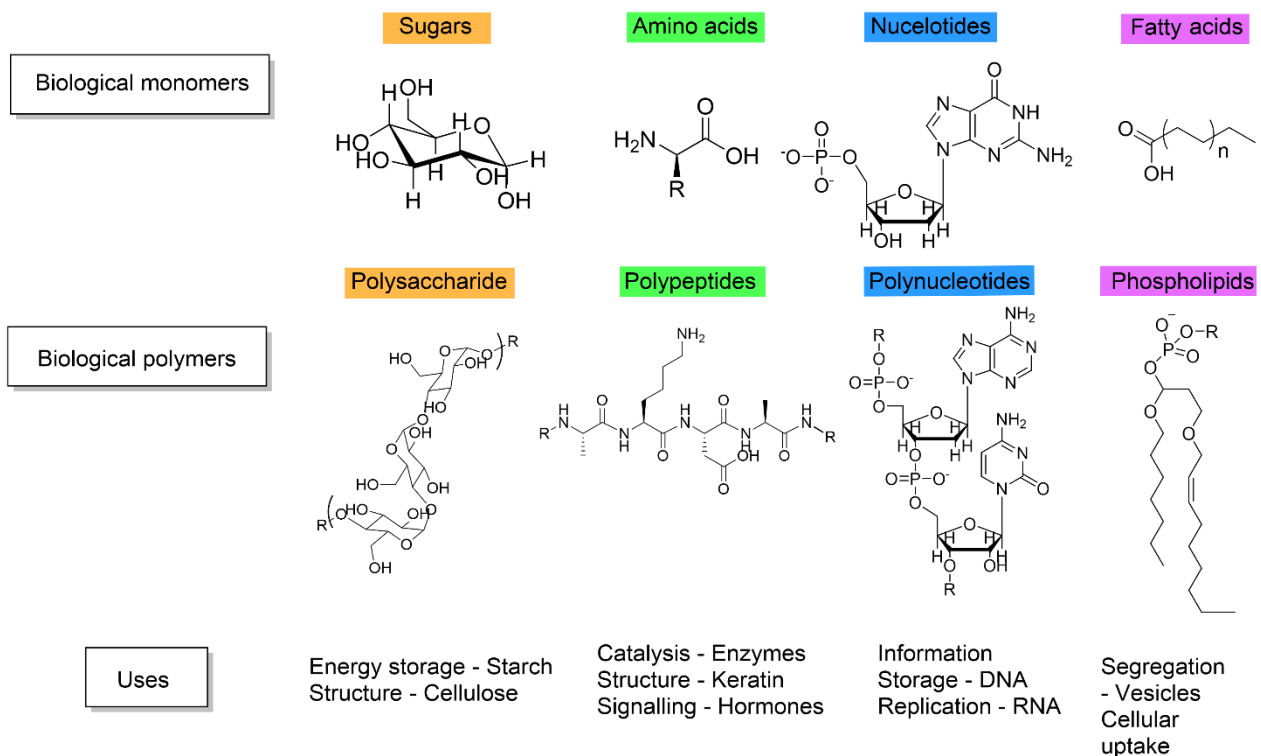


**Figure 1.1:** Make-up and classification of biological macromolecules and their respective monomers.

biological molecules performing a broad range of functions such as catalysis, stimuli response, molecule transportation and even providing structure. As such, they provide a major target for research into fields such as therapeutics and also materials for biological applications such as drug delivery vectors and tissue scaffolds.<sup>4,5</sup>

## 1.1.2 Proteins

### 1.1.2.1 Protein primary structure

Proteins are able to exhibit such a wide array of functionality as a result of their complex structural features. The determinant for this is the range of over 20 amino acids that comprise the sequence of units that makes up polypeptide chains. This sequence of units is defined as the proteins primary structure and is the first level of four generally agreed levels of organisation, the others being secondary, tertiary and quaternary.<sup>6</sup>

These amino acids contain a side chain pendant to a chiral carbon that lies between the peptidic bonds (Figure 1.2). In nature, this carbon is near universally the (S) or L- isomer, excluding glycine which is non-chiral. The side chain is highly viable and can contain a range of functionality and properties from hydrophilicity to aromaticity, large to small, and acidic to basic (Figure 1.2). The precise sequence of these is controlled during their synthesis *in vivo* from mRNA translation, and the sequence determines all higher levels of protein structure.

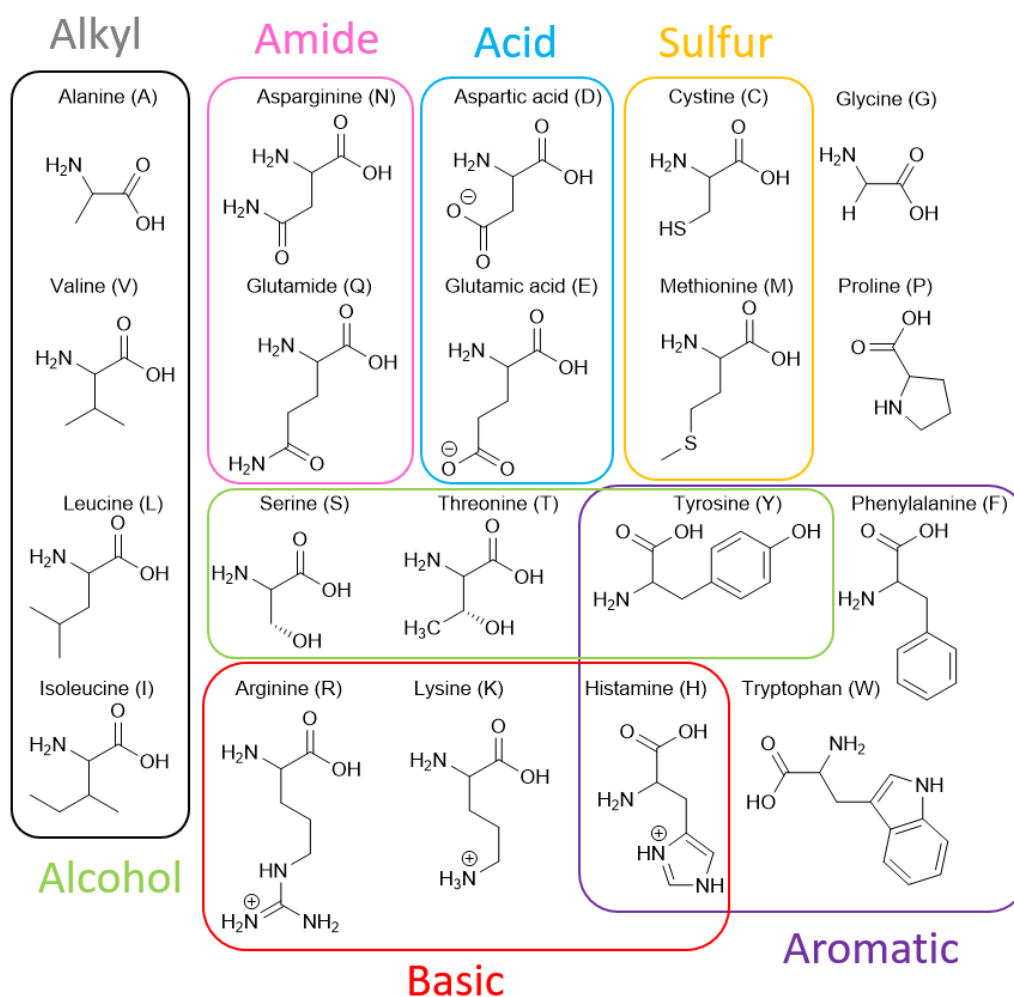


**Figure 1.2:** The structure of the twenty natural amino acids.

### 1.1.2.2 Protein secondary structure

The primary structure determines the three-dimensional shape preference of the chain in solution, which is mostly governed by hydrogen bonding between the peptidic bonds.<sup>7</sup> This shape preference leads to two main secondary structure features:  $\alpha$ -helices and  $\beta$ -sheets.

The  $\alpha$ -helix is a right handed helix, in which the backbone amide proton hydrogen bonds to a carbonyl C=O located 3 or 4 residues along the chain.<sup>8</sup> Despite being the most prevalent secondary structure in proteins, oligomeric polypeptide chains rarely exhibit strong helical character in solution, as a result of the entropic penalty associated with folding.<sup>9</sup> Even in large proteins, helix

backbone hydrogen bonds are weaker than those found in beta sheets and are readily attacked by water molecules.<sup>10</sup> However, when shielded from these interactions oligopeptides can readily adopt a strong helical character, for example in more hydrophobic environments such as membranes, or with the addition of cosolvents like trifluoroethanol.<sup>11,12</sup>

In an  $\alpha$ -helix, the amino acid side chains (R) point outwards and this R group character greatly influences the tendency of a chain to form a helix. Residues such as proline and glycine have very poor helix forming tendencies, proline because it cannot donate a backbone hydrogen and glycine because its conformational flexibility disfavours helix formation.<sup>10</sup> On the other end of the scale, alanine is the residue which most favours helix formation.

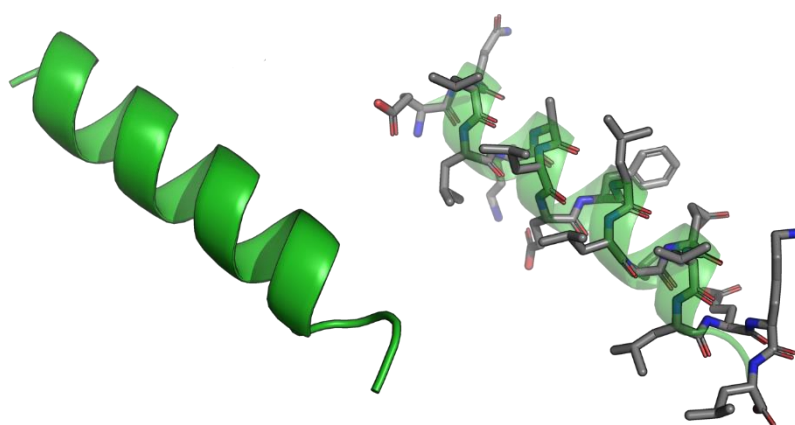


**Figure 1.3:** Cartoon representation of  $\alpha$ -helix structure in manganin II (PDB:1PEF).

$\beta$ -sheets are formed of multiple  $\beta$ -strands which are linearly aligned, in either parallel or anti-parallel directions. These strands are aligned through hydrogen bonding interactions, again between backbone amide groups, however, in  $\beta$ -sheets these are inter-strand bonding interactions.<sup>13</sup> These strands can either be aligned in the same direction, parallel (i.e. both C to N), or in opposite directions, anti-parallel. The hydrogen bonding interaction between parallel sheets is distorted from ideal geometries, however, the energetics of sheet formation are



indistinguishable between the two.<sup>14</sup> Often anti-parallel sheets are formed as a result of  $\beta$ -turns, or  $\beta$ -hairpins, which induce strand interactions within a continuous chain.<sup>15,16</sup> Hydrophobic residues can also provide favourable interactions between strands, increasing the stability of  $\beta$ -sheet and  $\beta$ -hairpin structures.<sup>17,18</sup>

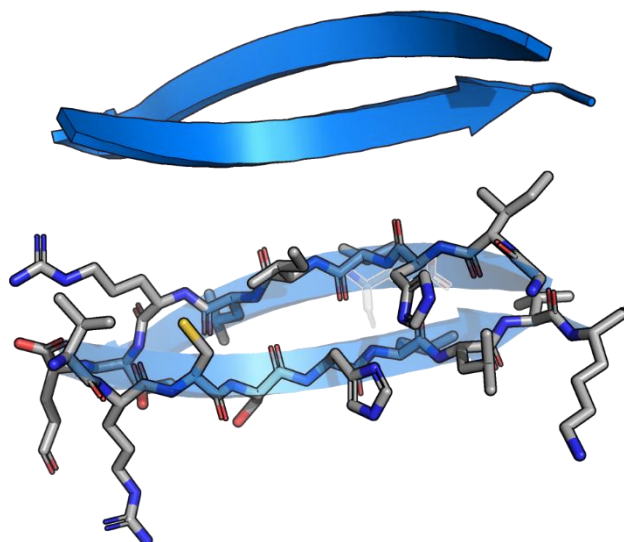


**Figure 1.4:** Cartoon representation of antiparallel  $\beta$ -helix structure in peptidyl-prolyl cis/trans isomerase (PDB:PIN1).

In addition to these two main categories of structure many rarer structural elements exist, for example  $3_{10}$  helices and  $\pi$ -helices are observed in a small number of proteins.<sup>19</sup> These helices are rare as they are inherently destabilizing and therefore when they occur they are typically integral to the functionality of a peptide.<sup>20</sup> The more common alternative structures are  $\beta$ -turns and random coils (Figure 1.5).  $\beta$ -turns are particularly unique as they provide a  $180^\circ$  turn in a peptide chain, often inducing anti-parallel  $\beta$ -sheet formation. Random coils are commonly observed in proteins, however, the term just defines a lack of preferred secondary structure rather than a particular configuration.<sup>21</sup>

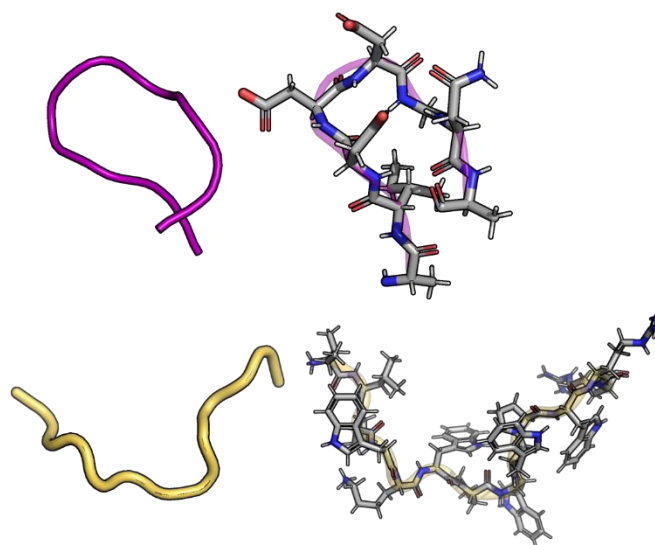


**Figure 1.5:**  $\beta$ -turn type-II (top) in globin (PDB:2BK9), and random coil (bottom) in indolicin (PDB:1G89).

#### 1.1.2.3 Protein tertiary structure

The tertiary structure of a protein describes the three-dimensional assembly of a complete peptide chain.<sup>22</sup> The interactions of side chains from different secondary structures will dictate the tertiary assembly. While residues in the final structure may be close together spatially, because of the complex nature of tertiary folding they may well be far apart in the peptide primary structure. Hydrophobic residues will drive core-based assembly, while charged polar residues will favour surface regions of the structure. Along with hydrophobicity driving forces, assembly is dictated by other R chain interactions such as ionic interactions, hydrogen bonding and even covalent bonds through disulfide linkages.<sup>23</sup> These driving forces mean that the native folded peptide structure has a lower Gibbs free energy than the unfolded peptide chain.<sup>23</sup> As a result, folding occurs spontaneously and a thermodynamically favoured state is reached, referred to as the protein's native configuration. While this state is near universally reached in biology, a systematic study for the lowest energy conformation would exceed the timescale of protein folding. It is understood that in reality, proteins fold

through multiple pathways that generally all lead to the lowest energy minima (Figure 1.6).<sup>24,25</sup>

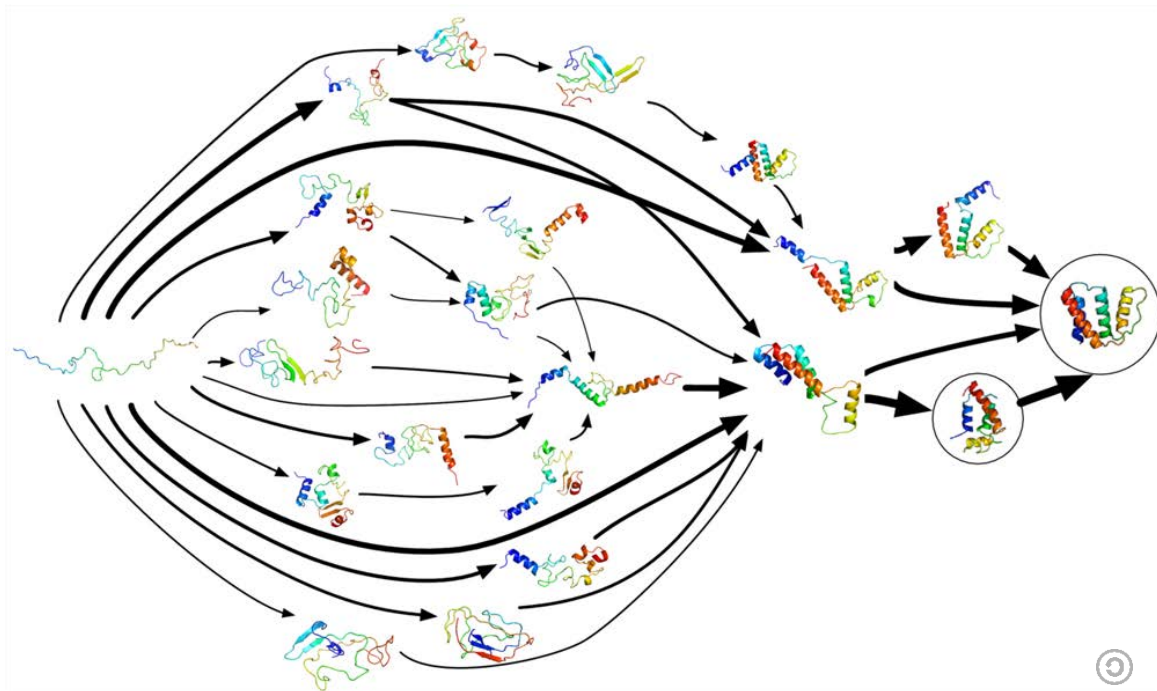


**Figure 1.6:** Example of protein folding pathways, from folding@home [CC BY-SA 3.0].

#### 1.1.2.4 Protein quaternary structure

Protein quaternary structure defines the arrangement of multiple peptide chains or units that form a functional complex. The simplest form of this is the dimer, where 2 protein units come together to form an active complex.<sup>26</sup> One common example, is the immunoglobulin A antibody, used for immune response in mucosal tissue.<sup>27</sup> The quaternary structure can also include the complexation of peptides with cofactors such as the heme group for oxygen binding in haemoglobin, or magnesium ions in DNA polymerase.<sup>28</sup> The quaternary structure and co-factors are essential for unique functions in many enzymes and even fluorescent proteins. For example, DsRed is a large barrel-shaped protein isolated

from *Discosoma coral*, in which the barrel-like assembly of  $\beta$ -sheets arranges into tetramers (Figure 1.7).<sup>29,30</sup>

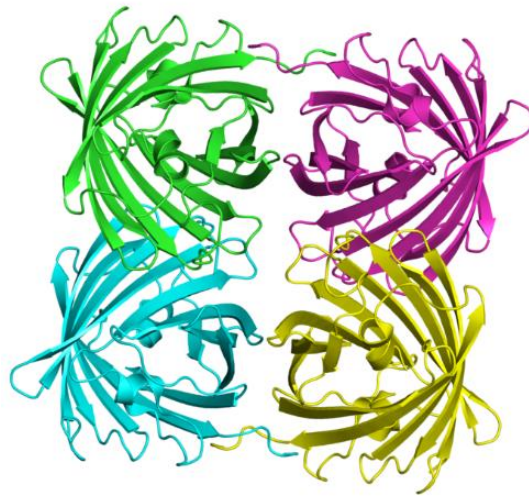


**Figure 1.7:** Cartoon representation of the tetrameric assembly of DsRed.

From PDB: 1G7K.<sup>30</sup>

### 1.1.3 Peptide biosynthesis

With protein structure and activity so dependent on amino acid sequence, the ability of cells to reliably and accurately synthesise peptide chains through *in vivo* peptide synthesis is essential for life. This sequence is determined by specific sequences of single strands of DNA known as template strands. The copying of this information from the template strand to a new RNA strand then occurs, a process known as transcription. Occurring in the cell nucleus, the duplexed DNA is 'unzipped' into its comprising strands *via* a helicase enzyme.<sup>31</sup> RNA polymerase then attaches to the template strands and reads from the 3' to 5' direction along the strand. As it reads, the synthesis of a complementary messenger RNA (mRNA) strand is completed from its 5' to 3' end. For eukaryotes, this mRNA can be recognised by the nuclear membrane and selectively released into the cytoplasm.<sup>32</sup> Here it can attach to a ribosome to undergo the second stage of protein biosynthesis, translation.

In translation the mRNA chain is read from the 5' end, which in turn initiates the synthesis of a chain of amino acids from the peptide *N*-terminus.<sup>32</sup> The synthesis requires the pre-activation of transfer RNAs (tRNA), in which an tRNA is acylated with the amino acid, facilitated by aminoacyl tRNA synthetases. These activated tRNAs, which code for triplets of RNA bases (known as codons), can bind to the ribosome when the decoding centre of the small ribosomal subunit reaches the corresponding complementary mRNA codon.<sup>33</sup> Upon binding, a peptide bond formation is catalyzed between the existing amino acid chain and the new tRNA bound amino acid, simultaneously releasing the tRNA (Figure 1.8). This process repeats until the ribosome comes across a stop codon (either UAA, UAG, or UGA). This stop codon causes binding of a release factor protein which terminates peptide synthesis, including complete disassembly of the tRNA/ribosome complex, and facilitates the release of the final peptide.<sup>34</sup>

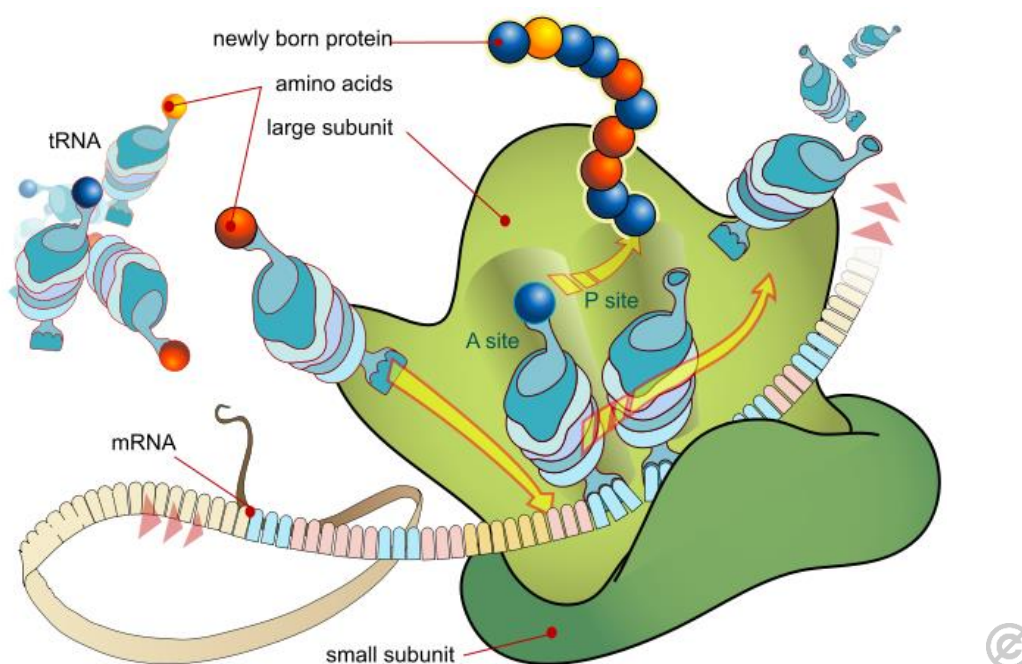


**Figure 1.8:** Illustration of mRNA translation in peptide biosynthesis.

While *in vivo* peptide synthesis is used in research,<sup>35</sup> the preparation of peptides at large scale is generally accepted to be easier through microwave-

assisted solid-phase peptide synthesis (SPPS). This is introduced further in Chapter 6, where SPPS is used to synthesize peptide macro-CTAs for polymerisation induced self-assembly (PISA).

#### 1.1.4 Enzymes

Broadly, enzymes are biological catalysts that facilitate chemical reactions. While generally regarded as peptides, enzymes can be RNA based, known as ribozymes. Ribozymes are increasingly regarded as the original enzyme, as researchers have shown they can catalyse their own synthesis which is an important step in the evolution of early pre-biotic systems.<sup>36,37</sup> In regards to peptide-based enzymes, they catalyse almost all known chemical processes in cells, most of which would otherwise be too slow to sustain life.<sup>38</sup> While the activity of an enzyme is usually based upon the functionality in the primary structure, or associated cofactor, it is the aforementioned folding into functional structures which activates the enzyme and facilitates catalysis. The classic example found in many enzymes is the catalytic triad, in which distant residues in the primary chain, when brought close together by folding, act as a catalytic unit. The classic example is the activity of proteases which are catalyzed by a trimer of aspartate (acid), histidine (base) and serine (nucleophile).<sup>39</sup> Significant research is focused on synthesizing artificial enzymes, to improve upon the rate achieved in nature. Such scaffolds that have been developed to achieve this include micellular polymers,<sup>40-42</sup> functionalized macrocycles,<sup>43</sup> and even artificial peptidic enzymes.<sup>44</sup>

Mechanistically, the active site of an enzyme catalyses the transformation of a substrate into a product. The way a substrate binds to the active site is loosely described by an induced fit approximation where, upon approaching the active site, a substrate induces structural changes in the enzyme until the substrate can be considered bound. Once bound, the energy level for the intermediate of the

reaction is lowered significantly, thus accelerating the reaction.<sup>38</sup> Measuring the rate of this process, or enzyme activity, is approximated by several kinetic models. The most widely used is the Michaelis-Menten approximation, which is suitable for diffusion-controlled pathways in which product formation is irreversible.<sup>45</sup>

#### 1.1.5 Synthetic macromolecules

For chemists, the goal of replicating biology's functionality and control of assembly is a formidable challenge. Synthetic materials that can efficiently replicate the shapes and functions of biologics could help develop novel therapeutics with reduced costs and the ability to introduce a greater range of functionality.<sup>46</sup> Synthetic macromolecules are diverse in chemical make-up, size and shape. Inorganic materials alone can be wide in nature ranging from metallic nanoparticles (such as iron and gold-based therapeutic conjugates,<sup>47,48</sup> and optically interesting quantum dots)<sup>49,50</sup> to inorganic polymers such as silicones<sup>51</sup> and sulfur-based polymers.<sup>52,53</sup> Arguably, more has been realized with organic-based chemistries, with plastics and polymers being well-established areas of research with large commercial sectors. In addition, new areas are developing from carbon nanotubes<sup>54</sup> to complex molecular machines pioneered by Nobel laureates Stoddart, Sauvage and Feringa, based upon assemblies such as rotaxanes and catenanes.<sup>55-57</sup> In regards to polymers in particular, the field of controlled radical polymerisation (CRP), with methods such as atom transfer radical polymerization (ATRP) and reversible activation fragmentation chain transfer polymerization (RAFT), has revolutionized macromolecular synthesis, allowing a much greater degree in control of organic nanoparticle synthesis.<sup>58</sup>

#### 1.1.6 Self-assembly of polymer objects

CRP has made steps towards replicating the assemblies seen in nature, through facilitating greater control of molecular weight and dispersity of synthetic

macromolecules, as well as the ability to create multi-block copolymers with a wide array of compatible functionality. The ability to precisely control the polymerization method has allowed a wide array of polymer architectures to be realized, from the simple chain block-copolymers (from gradient to statistical) to branched architectures like star-like assemblies and brush-like polymers (Figure 1.9).<sup>59</sup>

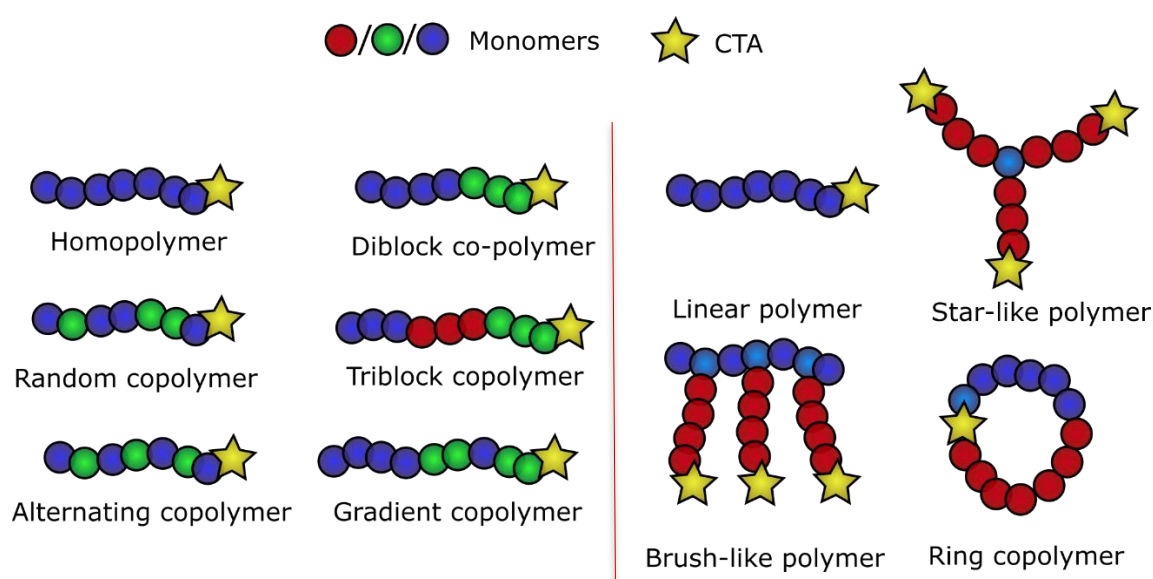


**Figure 1.9:** Examples of some common polymer compositions (left) and architectures (right) achievable through RAFT.

In a process analogous to peptide tertiary structure formation, block copolymers with sufficiently different blocks can phase separate, and assemble into structures through a process known as self-assembly. While this can occur in the bulk phase, it is more commonly utilized in a selective solvent (i.e. a solvent which is miscible with one block and immiscible with the other) where self-assembly still occurs, and the interfacial area between the solvophobic block and the solvent is minimized. The assembled morphology (for example spheres, cylinders or vesicles, Figure 1.10) depends primarily upon the relative volume fractions of each block, which in itself is affected by the solvent.<sup>60,61</sup> This can be



approximated by a parameter known as the packing parameter,  $p$ , developed by Ninham and co-workers.<sup>62,63</sup> This parameter relates the volume of the solvophobic tail ( $v$ ) to the solvophobic chain length ( $l_c$ ) and the surface area of the solvophilic chain at the particle-solvent interface ( $a_0$ ). Polymer chains with a low  $p$  ( $p < 1/3$ ) form highly curved structures such as spherical nanoparticles (Figure 1.10), while values of  $p$  approaching 1 form near-linear assemblies such as vesicles and bilayers. In practical applications,  $v$ ,  $l_c$  and  $a_0$  are difficult to calculate absolutely and therefore weight fractions of the blocks are often used as approximates.<sup>61</sup>

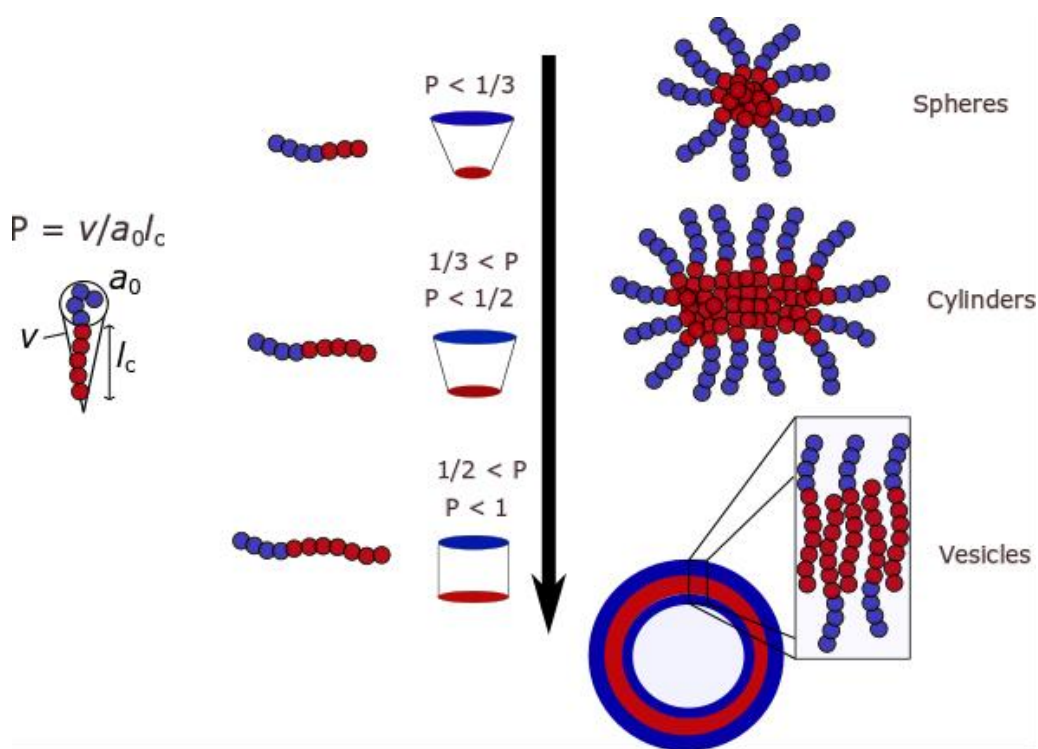


**Figure 1.10:** The equation describing packing parameter,  $p$  and an illustration of its effect on the morphology of assembled diblock copolymers.

### 1.1.7 Peptide-polymer complexation

While peptides are highly complex, monodisperse, functional therapeutics, synthesis of them on large scale is complex and economically challenging. They are also susceptible to degradation *in vivo* such as through proteolysis and

denaturing. Combining peptides with synthetic polymers can alleviate some of these issues; for example, polymers are far cheaper to synthesize and can add additional properties such as peptide stabilization and lowering immunogenicity,<sup>64,65</sup> or introduce a stimuli-response, such as to pH or light.<sup>66–68</sup> These benefits can be combined without covalent attachment, for instance polymer additives are often added to enzyme solutions to enhance stability (such as sugar-based polymers and ionic polymers which can stabilize the half-life of many enzymes through preventing protein-protein interactions).<sup>69–71</sup> The two main methods for forming polymer-peptide complexes is through covalent conjugation or encapsulation of the peptide therapeutic.

#### 1.1.8 Peptide encapsulation in polymer nanoparticles

One of these approaches is to encapsulate the peptide within a polymer vesicle. By encapsulating the therapeutic within a nanoparticle, similar effects of proteolytic and immunogenic protection can be achieved without reducing the activity of the encapsulated peptide.<sup>72</sup> Importantly, for encapsulated therapeutics to be effective, the substrates and products must diffuse through the polymer vesicle, or the therapeutic must be released in a controlled manner.<sup>73–75</sup> Some developed polymersome release triggers include pH,<sup>76</sup> pressure,<sup>77</sup> and chemical triggers, for example through disulfide cleavage<sup>78</sup> or sugar-binding by boronic acid functionalized polymers.<sup>79</sup>

Combination of multiple enzymes within separate vesicles can create nanoreactor cascades, in which the enzymes are prevented from interacting with each other thus retaining optimal activity and stability, in a process similar to cellular compartmentalization. This is a well-studied area and recent work has demonstrated: peptide incorporation into vesicle lumen, membrane and surface;<sup>80,81</sup> controlled disassembly of loaded vesicles;<sup>82</sup> three component enzyme

cascades;<sup>80</sup> and the precise control of vesicle permeability for substrate specificity (Figure 1.11).<sup>72,83</sup>

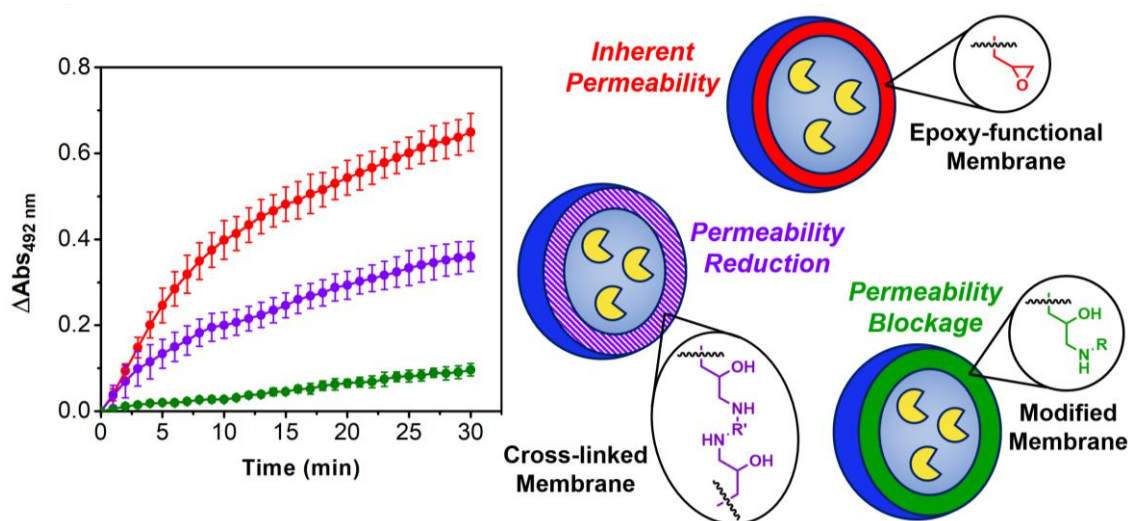


**Figure 1.11:** Tuning the membrane permeability of PISA synthesized vesicles by varying crosslinking chemistry (right), to give different dye release measured by  $\Delta A$  (left), reported by Varlas et al.<sup>83</sup>

### 1.1.9 Peptide-polymer conjugates

Covalent conjugation of polymers to peptides is a commonly undertaken, well understood procedure, which effectively creates hybrid materials overcoming the shortcomings of either component alone.<sup>84,85</sup> The most successful area of this is peptide PEGylation, in which the covalent attachment of polyethylene glycol (PEG) to peptides can improve various *in vivo* properties of the peptide, for example stability, immunogenicity and blood circulation time.<sup>86,87</sup> PEGylation will be discussed further in Chapter 2, but it is noteworthy that recent polymer research has focused on broadening the array of polymers for peptide conjugation resulting in the introduction of new properties and increased functionality.<sup>88</sup> This field has relied heavily upon the development of controlled radical polymerization techniques such as ATRP and RAFT to create realistic alternatives to PEG. This has also allowed the broadening of conjugation techniques from grafting to, to grafting

through and from.<sup>89</sup> Grafting to is the traditional modification of a peptide handle (such as lysine residues) or macromolecule with a reactive polymer (Figure 1.12). Handles and chemistries used to achieve this are discussed further in Chapter 2.

Grafting through utilizes peptide or macromolecule which has been modified with polymerizable functionality, such as acrylates or norbornenes.<sup>85</sup> Subsequent polymerization of these monomeric units leads to the formation of brush-like polymers, in which a polymer backbone is functionalized with arms of peptide (Figure 1.12). This process is commonly utilized to create novel materials such as thermoresponsive conjugates using elastin-like peptides,<sup>90,91</sup> enzyme degradable conjugates,<sup>92-94</sup> and materials with enhanced cellular uptake.<sup>95,96</sup>

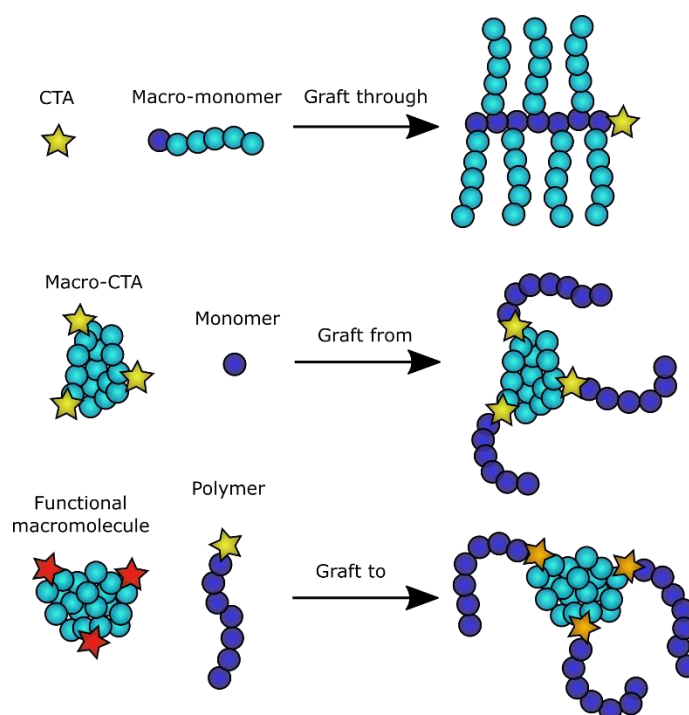


**Figure 1.12:** Illustration of grafting through, grafting from and grafting to a macromolecule, for example polymer or protein (light blue), using monomers or polymers (dark blue).

Finally, grafting from is the process of growing a polymer chain off a pre-functionalized macromolecule or peptide (Figure 1.12). Notably, there are a few advantages to this technique, in particular it does not require the tricky separation

of unreacted polymer from the conjugate, it does not require the large excess of reagents needed for grafting to, and it allows the synthesis of more hydrophobic polymeric conjugates, as monomers are typically more hydrophilic than their respective polymer units.<sup>97</sup> RAFT and single electron transfer living radical polymerization (SET-LRP) have been particularly successful in this area as they allow the utilization of peptide-based chain transfer agents under aqueous conditions.<sup>89,98</sup> In particular, it has been used for: the creation of cyclic peptide conjugates which exhibit unique stacking interactions;<sup>99</sup> the synthesis of active, more stable enzyme conjugates;<sup>100</sup> and temperature responsive bioactive peptide conjugates.<sup>98,101</sup>

#### 1.1.10 Peptide directed assembly

The ability of peptides to assemble into unique secondary and tertiary structures, as a result of their sequence specific nature, has been utilized in macromolecular chemistry to create novel and interesting architectures. The Perrier group have recently widely explored cyclic peptides as a powerful motif that assembles into stacked supramolecular nanotubes (Figure 1.13).<sup>102</sup> Their work has shown how nanotube length and functionality can be controlled;<sup>103,104</sup> how tubes can be responsive to pH, reducing conditions and host-guest interactions;<sup>103,105,106</sup> and how tubes can be used as drug delivery vectors.<sup>107,108</sup>

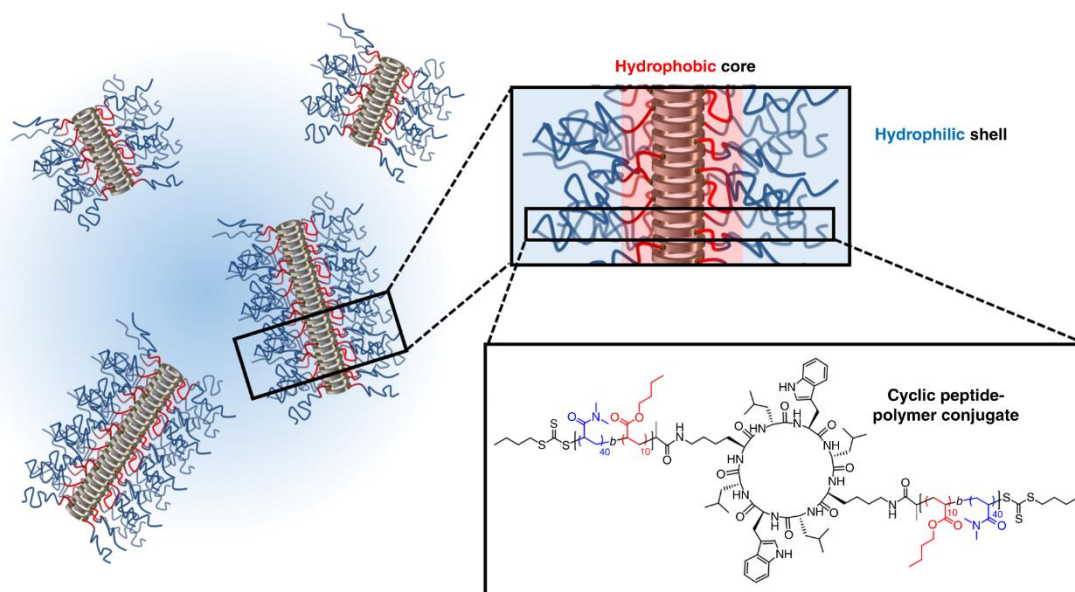


**Figure 1.13:** Cyclic peptide-polymer based nanotubes, which assemble through a combination of hydrophobicity and hydrogen bonding, developed by Perrier and co-workers. Reproduced from ref.<sup>102</sup> [CC BY 4.0].

Other novel assemblies commonly encountered with peptide conjugates are ribbons/lamella. Often these can be reached with a  $\beta$ -sheet forming domain, which dictates linear assemblies based upon hydrogen bonding and hydrophobic interactions. Such assemblies allow the creation of fibres,<sup>109</sup> nanotubes,<sup>110</sup> and self-healing hydrogels.<sup>111</sup> One field that has grown out of this area is peptide amphiphiles, which are short peptide units conjugated to alkyl chains, or aromatic moieties which aggregate under aqueous conditions to form long tubular structures (Figure 1.14).<sup>112,113</sup> Originally developed by the Stupp group, their work has shown how beta-sheet peptide domains dictate long range assembly, favouring the formation of nanotubes up to 0.1 mm in length.<sup>114–116</sup> These assemblies have been used as antimicrobial materials,<sup>117,118</sup> as scaffolds for cell support and even stem cell differentiation.<sup>119–121</sup>

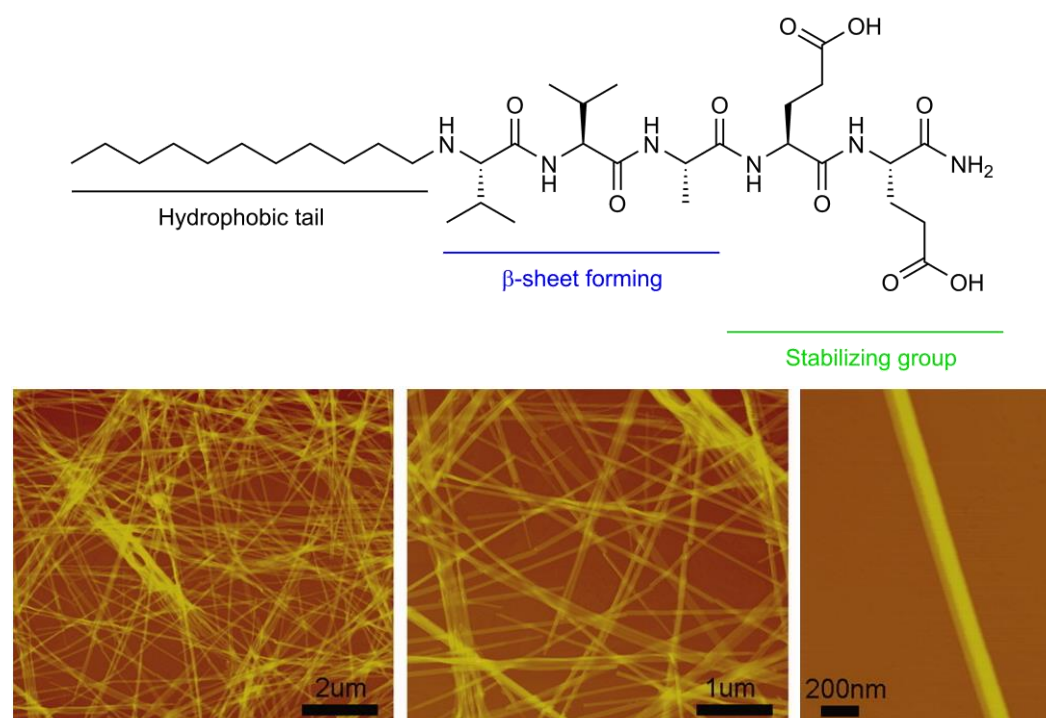


**Figure 1.14:** Top: example structure of a peptide amphiphile developed by the Stupp group.<sup>122</sup> Bottom: giant nanotubes, visualized by AFM, assembled from a peptide amphiphile.<sup>114</sup>

## 1.2 Fluorescence

### 1.2.1 Overview

Fluorescence has become an indispensable tool for the detection and analysis of a wide range of analytes. Commonly used in both the biological sciences and materials sciences, fluorescence is useful as a result of its unparalleled sensitivity; with fairly simple detection methods available, which are non-invasive and non-destructive.

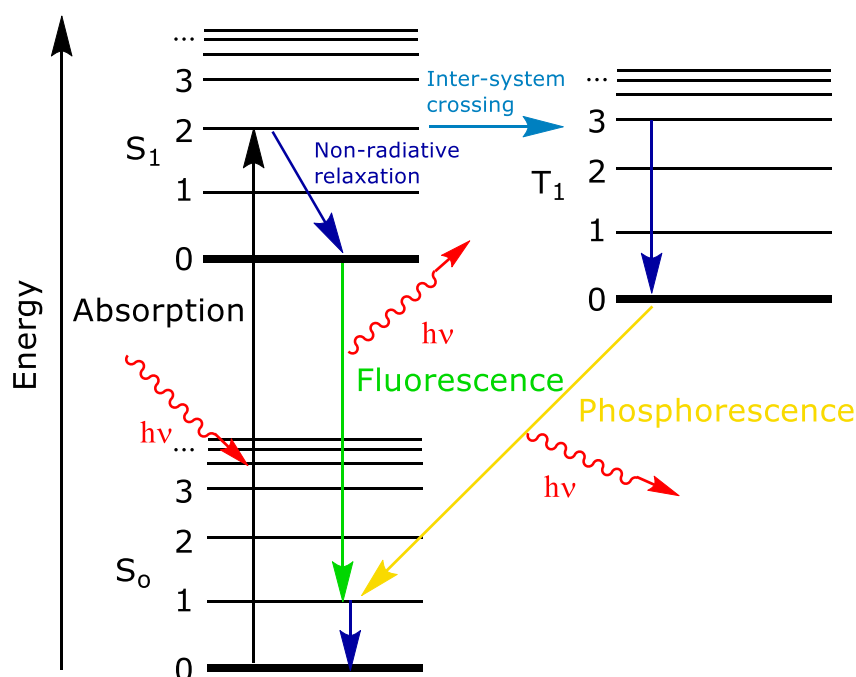


**Figure 1.15:** Jablonski diagram showing absorption and emission events in fluorescence and phosphorescence.

Specifically, fluorescence is the emission of a photon occurring when a molecule relaxes from an excited singlet state to the ground state. This higher energy state is reached through the absorption of a photon that matches the energy difference between the states. Often this is illustrated through a Jablonski diagram (Figure 1.15) which shows how a photon is absorbed from a ground energy state ( $S_0$ ) to an excited singlet state ( $S_n$ ). The molecule can then relax to a lower vibrational level within this singlet energy state through non-radiative



relaxation, followed by emission of a photon, as it relaxes to the  $S_0$  state. This emitted photon is lower in energy than the excited photon, and the time the molecule spends in the excited state before returning to the ground state is known as the fluorescence lifetime ( $\tau$ ). In most molecules, the energy gap between  $S_1$  and  $S_0$  is so small that relaxation can occur by non-radiative processes such as collision, and therefore emission does not occur. In rare cases the excited singlet state can transform into a triplet state, e.g.  $T_1$ , through intersystem crossing.<sup>123</sup> Once in this state, relaxation to the ground state can take orders of magnitude longer so that the emission, known as phosphorescence, occurs significantly later than absorption (from milliseconds to hours in phosphorescence compared to nanoseconds in fluorescence).<sup>124</sup> When emission of a photon follows other excitation processes it can be referred to by other terminology, for example, emission following chemical excitation is known as chemiluminescence.<sup>125</sup>

### 1.2.2 Fluorescence labelling of biomolecules

Fluorescence provides a unique way of imaging biomolecules *in vivo*. It is able to overcome limitations of other labelling techniques, such as radiolabelling or staining, as fluorescence is responsive to environmental conditions and dyes also tend to be easily synthesized or attached to targets.<sup>126</sup> There are several types of fluorophore that can be utilized in bioimaging, including fluorescent proteins that can be expressed with the target biomolecule, organic dyes that are comparatively small and more photostable,<sup>127</sup> as well as metal based fluorophores, for example europium (III) based complexes,<sup>128</sup> and newer quantum dot based imaging agents.<sup>129</sup> Each of these has its own advantages and disadvantages for particular applications and all are commonly used in biological research. The two types relied upon most for protein and DNA imaging are organic dyes and fluorescent proteins.<sup>127</sup>

A significant number of biology researchers rely upon fluorescent proteins. For biologists, the synthesis of fluorescent proteins is advantageous as they can easily be attached to any expressed peptide through expanding the genetic vector to express the fluorescent protein along with the target protein.<sup>127,130</sup> The original and most ubiquitous fluorescent protein is green fluorescent protein (GFP).<sup>29,131</sup> GFP is a 238 amino acid, 26.8 kDa protein, which has a characteristic barrel-like structure which includes the photoactive moiety (see section 1.1.2.4, Figure 1.7).<sup>30</sup> In water, GFP exhibits  $\lambda_{\text{max}}$  for excitation at 395 nm and 475 nm, and for emission at 509 nm, with a quantum yield\* of 79%. Since the expression of GFP a range of fluorescent proteins have been isolated (such as DsRed - *Discosoma* red fluorescent protein and *Aequorea* green fluorescent protein)<sup>132</sup> or developed through rationally introduced mutations or directed evolution (for example ultra-red fluorescent protein, mOrange and enhanced GFP (EGFP) – Figure 1.16).<sup>133,134</sup> All fluorescent proteins, while easy to synthesize, are very large molecules which may affect target properties,<sup>134</sup> and are generally prone to photobleaching in comparison to modern small molecule dyes.<sup>127</sup>

---

\*Quantum yield ( $\Phi_f$ ) is the ratio of absorbed photons to emitted photons, for example a  $\Phi_f$  = 50% signifies half of absorbed photons being re-emitted.

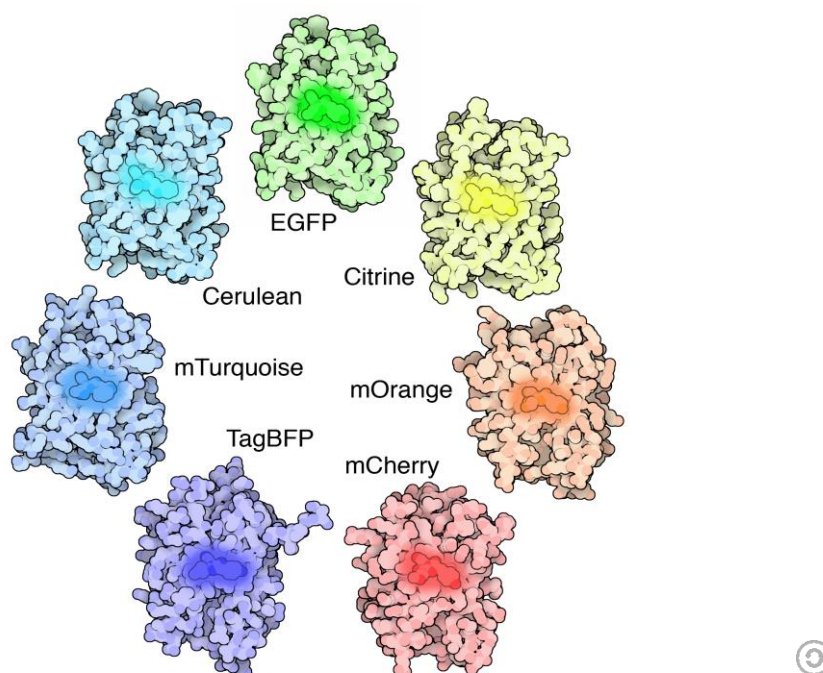


**Figure 1.16:** Illustration of selected GFP variants in their respective emission shades, showing the range of emissions achievable [CC BY-SA 3.0].

Organic, small molecule dyes are much more numerous and have experienced a significant growth of use in research as of recent.<sup>127</sup> In particular, dye lifetime, photostability and spectral window have been optimized for a great number of dyes;<sup>135</sup> many of which are commercially available and are easily conjugatable to the target of interest (the chemistries used to achieve this are discussed further in Chapter 2). This is particularly important for achieving good spatial and temporal monitoring of targets which requires increasingly large photostability of dyes, especially for techniques such as single-molecule imaging.<sup>136,137</sup> Classes of dye which have recently been developed towards these aims include Si-rhodamines,<sup>136</sup> as well as commercially available Alexa Fluor® and CyDyes® (Figure 1.17).<sup>138,139</sup> With this variety, a large range of optical properties and spectral windows are available to researchers for imaging. Notably, all these dyes are large, aromatic compounds; usually either hydrophobic in nature or

charged to allow water solubility, which has known consequences for the localization of the target.<sup>140</sup>

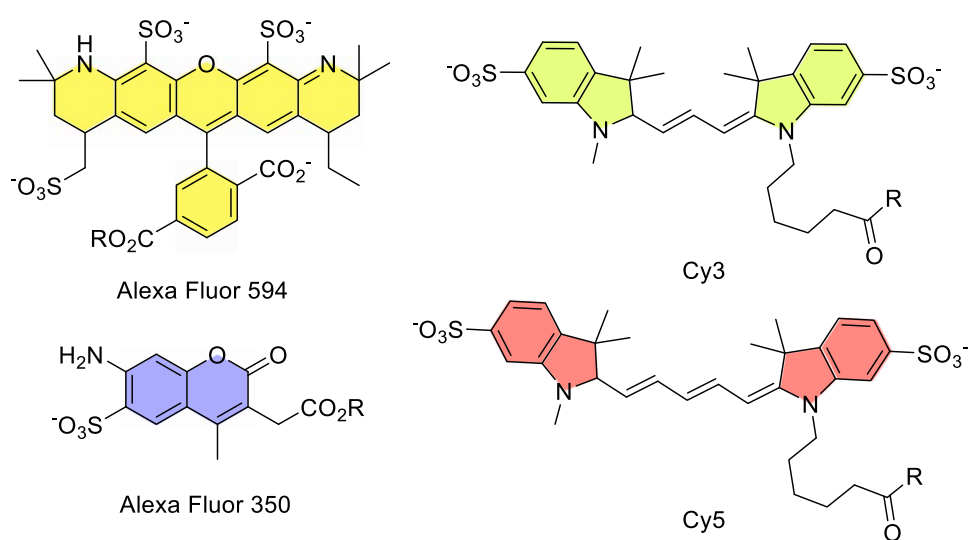


**Figure 1.17:** Selected recently developed commercial small-molecule fluorophores commonly used for fluorescence imaging.

## 1.3 Maleimide based fluorophores

### 1.3.1 Maleimide chemistry

Maleimides are unsaturated four carbon cyclic imides, which have been extensively researched as a tool for chain-end functionalization handles in polymer synthesis, and for protein modification. They undergo two highly efficient reactions: Michael addition with thiols, and Diels-Alder cycloadditions with dienophiles.<sup>141,142</sup> Recently, it has been shown that halogen substituted maleimides, such as monobromomaleimide (MBM) and dibromomaleimide (DBM), also undergo efficient reactions with thiols.<sup>143</sup> However, in these molecules the reaction proceeds *via* an addition elimination; retaining the double bond of the maleimide. Moreover, DBM can undergo a reaction with two equivalents of thiol to form a dithiomaleimide (DTM).<sup>144</sup> Halogenated maleimides are known to react with other nucleophiles, such as amines and alcohols (Figure 1.18).<sup>145-147</sup> Our group has pioneered the investigation of such substituted maleimides as efficient charge transfer fluorophores. Since originally reporting the fluorescence of DTMs as polymer tagging moieties,<sup>148</sup> our group has gone onto report the fluorescence properties of amino and alcohol substituted maleimides.<sup>149,150</sup>

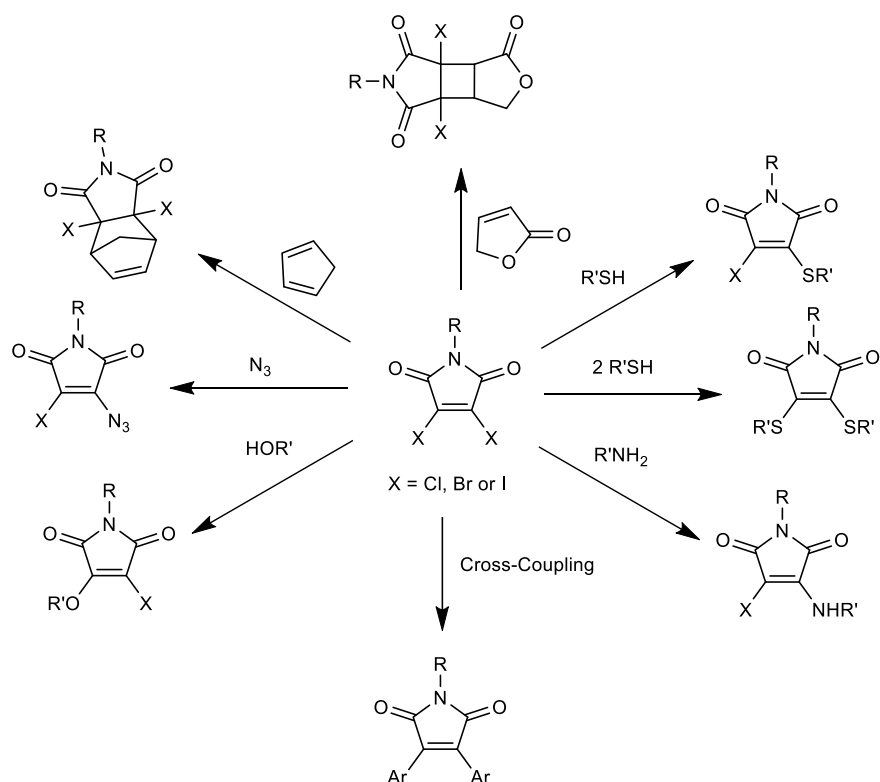


**Figure 1.18:** Reported reactions of dihalogenated maleimides.

### 1.3.2 Substituted maleimide fluorophores

Exhibiting a low lying  $\pi^*$  state, maleimides have historically been utilized as quenchers of fluorescence.<sup>151–153</sup> However, in 2013 Robin *et al.*<sup>148</sup> showed that substituted DTMs are a class of highly emissive fluorophore. It was discovered that DTM solubility and further functionalization could be easily varied through the selection of *N*- and *S*- substituents. Generally, the fluorophore has bright, solvent dependent emission around 500 nm and is quenched by aromatic thiol substitution (e.g. dithiophenolmaleimide).<sup>148</sup>

Following this, our group also showed that monoaminomaleimides (MAMs), and aminobromomaleimides (ABMs) - synthesized by addition-elimination reactions with monobromomaleimides and dibromomaleimides respectively- were also highly emissive.<sup>149</sup> These moieties have large Stokes shifts ( $\sim 100$  nm) and show solvent-dependent emission wavelengths and intensities, with polar protic

solvents causing a red shift and large reduction in emission intensity. This is explored further in the introduction to Chapter 3. In parallel to DTMs, ABMs and MAMs are also quenched by direct conjugation of aromatic amines to the maleimide ring.<sup>149</sup>

Most recently, our group completed a thorough study into the effect various substituents impart on the fluorescence of maleimide compounds (Figure 1.19).<sup>150</sup> In particular, it was shown that alcohol mono-functionalized chloromaleimides (OCMs) showed blue-shifted emission, and mixed di-substituted amino-thiol maleimides (ATMs) exhibit weaker red-shifted emission ( $\sim 560$  nm in diethyl ether versus  $\sim 480$  nm for ABMs).<sup>150</sup> These developments allow the use of different functionalities and chemistries for labelling, while broadening the window of dye excitation and emission. The exchange of halogens was also investigated, shown to be directly related to quantum yield where chlorine and hydrogen substitution led to highest  $\Phi_f$  (Figure 1.19).

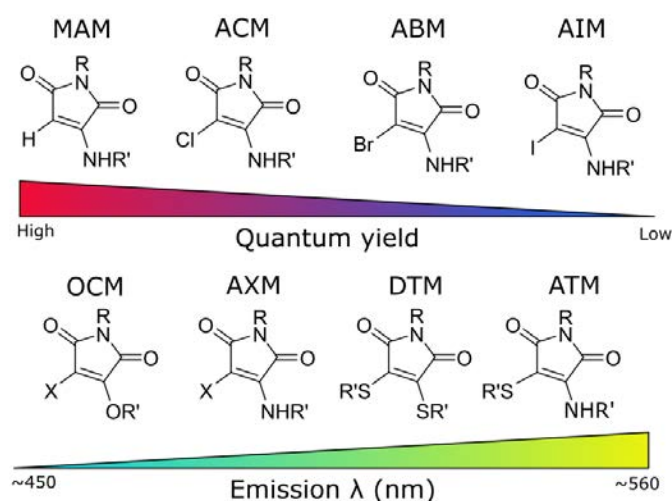


**Figure 1.19:** Approximate trends in fluorescence of substituted maleimides (with abbreviations) studied by Xie *et al.*<sup>146</sup>

### 1.3.3 Solvent dependent fluorescence

The fluorescence properties of a fluorophore are partially dependant on it's environment, but the degree to which this is true varies depending on the fluorophore in question.<sup>154</sup> For example, the temperature of a fluorophore normally directly relates to the fluorescence emission of a dye. This is because non-radiative processes that affect fluorescence are due to thermally dependent events (e.g. collisions, vibrations and rotations) and scale with thermal energy in a system, thus leading to a typical decrease in emission at higher temperature.<sup>154</sup> Note, delayed fluorescence in thermally activated delayed fluorophores can exhibit the reverse property due to reverse intersystem crossing being an energy activated process.<sup>155</sup>

Another environmental factor that effects fluorescence is the solvent, and probes in which emission wavelength is highly dependent upon solvent effects are termed solvatochromic. In general, the stabilization of the ground and excited state of a dye are going to be affected by interactions with the dipoles of the solvent, as the dipole of a molecule is different in its ground and excited state. Therefore, following an excitation event, the nearby solvent must reorganise to stabilize the new dipole. Depending on the polarity of the solvent this may be more or less effective, leading to differences in the stabilization of these excited states. Generally, more polar solvents lead to an increase in the stabilization of the excited state, and therefore dyes tend to exhibit a red-shifted emission in polar solvents.<sup>154,156</sup> Probes that undergo photoinduced charge transfer (PCT) are exceptional candidates as polarity probes. Such probes exhibit an electron-donating and electron-withdrawing group in conjugation. In such systems the dipole moment change upon excitation is usually relatively large.<sup>154,156</sup> Consequently, the solvent molecules must undergo a significantly larger amount



of reorganisation to relax the excited state, leading to large solvatochromic effects. The effects of solvent on maleimide dyes, in particular, will be discussed in the introduction to Chapter 3.

In addition to the solvent response, dyes can be designed to be responsive to other stimuli, for example, pH responsive probes are commonly found. Most probes are somewhat pH dependant, for example, fluorescein and rhodamine derivatives,<sup>157,158</sup> however types of fluorophores have been developed to exhibit extreme responses for pH, for example dyes which rely upon protonation or deprotonation to become fluorescent.<sup>159,160</sup>

#### 1.3.4 Fluorescence applications of substituted maleimides

Due to their promising fluorescent properties and uniquely small size, DTMs, MAMs, and ABMs have been researched extensively as polymer functionalization moieties in the O'Reilly group.<sup>144,148,161–164</sup> After originally reporting the use of DBM as a radical polymerisation compatible functionalization handle, which could be functionalized post-polymerization to form dithiomaleimide functionalized polymers,<sup>144</sup> Robin *et al.* subsequently, reported the fluorescence of DTM polymers. They showed how the fluorescence intensity, wavelength and lifetime of these polymers is dependent upon supramolecular assembly of the polymer.<sup>161</sup> The authors attributed this effect to the polymeric scaffold preventing both solvent and collisional quenching effects. The dye was applied to in-tissue studies in rat hippocampal tissue. In the region of a blood clot (Figure 1.20), micellar polymer could be differentiated from non-micellar polymer using fluorescence lifetime imaging microscopy (FLIM),<sup>161</sup> as the unimers exhibited much shorter fluorescence lifetimes.

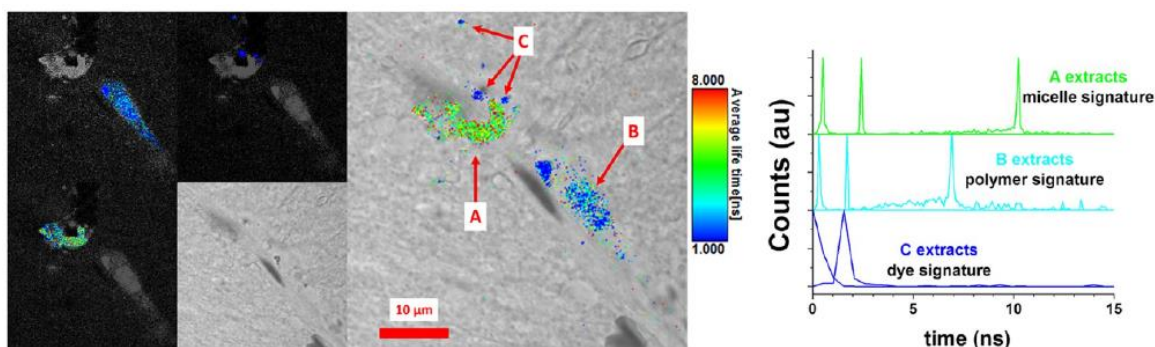


**Figure 1.20:** FLIM of DTM labelled micelles in rat hippocampal tissue with fast-FLIM lifetime extractions for A) blood clot B) vascular tissue and C) red blood cells reported by Robin *et al.*<sup>161</sup>

The presence of the DTM dye also allows detection of guest molecules by Förster resonance energy transfer (FRET). Robin *et al.* synthesized poly(triethylene glycol acrylate)-*b*-poly(*tert*-butyl acrylate) block co-polymer micelles which were labelled with a fluorescent DTM group in either the micelle core or shell.<sup>164</sup> Self-assembly of both shell and core labelled micelles could be identified by an increase in emission intensity, as a result of shielding of the DTM units from solvent quenching interactions. The unimer to micelle transition of the core-labelled micelles could also be distinguished through fluorescence lifetime measurements. By treating the core labelled micelles with a hydrophobic dye (Nile Red), FRET could be used to measure the uptake of dye into the micelle core as FRET occurs between the maleimide (donor) and Nile Red (acceptor). A hydrophilic dye (Rhodamine B), which was not taken up into the core, showed no FRET with the DTM micelles (Figure 1.21).<sup>164</sup>

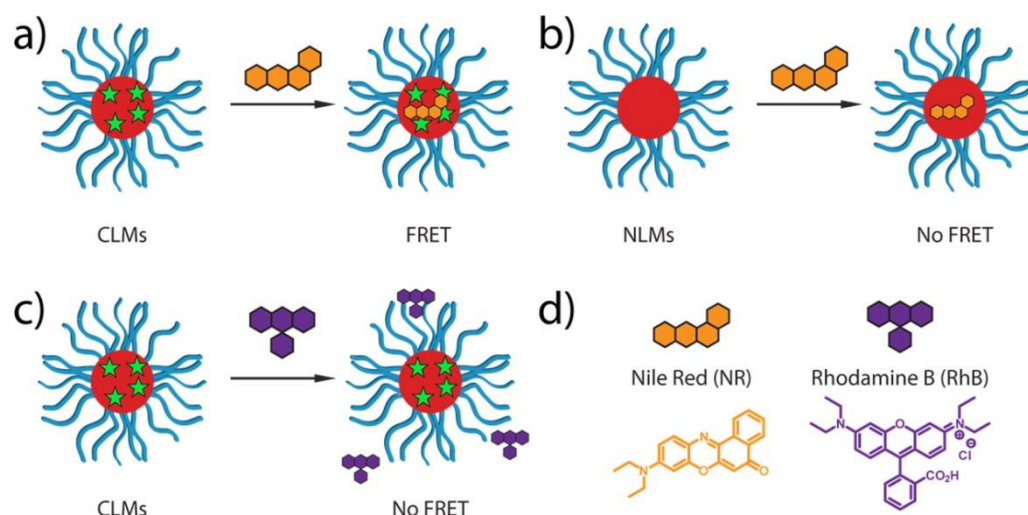


**Figure 1.21:** Schematic representation showing the interaction between micelles and fluorescent dyes Nile Red and Rhodamine B. CLMs = core-labelled micelles, NLMs = non-labelled micelles. Figure reproduced from Robin *et. al.* with permission.<sup>164</sup>

Maleimide fluorophores have also shown compatibility with ring-opening polymerisation (ROP),<sup>165,166</sup> ring-opening metathesis polymerisation (ROMP),<sup>167</sup> and SET-LRP.<sup>168,169</sup> Using DTMs and ABMs in these techniques has led to interesting functions and novel responsive materials. For example, DTM labelled polycaprolactone (PCL) polymers have been shown to exhibit mechanochemical responsive fluorescence, where fluorescence is responsive to sonication induced mechanical stress,<sup>170</sup> and ABM tagged micelles can show pH and CO<sub>2</sub> responsive fluorescence.<sup>166</sup> Despite containing sulfur atoms, DTMs have been shown to be stable to reducing conditions, leading DTM dyes to being used for labelling in pH<sup>171</sup> and glutathione<sup>172</sup> responsive drug delivery applications.

Other unique applications of maleimide dyes include monitoring crystallization driven self-assembly (CDSA), where the alternating incorporation of labelled and non-labelled polymer can create striking fluorescent crystals (Figure 1.22). They have also been used for labelling of silica nanoparticles for the

detection of copper ions,<sup>173</sup> and the surface labelling of thiol-terminated, emulsion templated, porous polymers.<sup>169</sup>

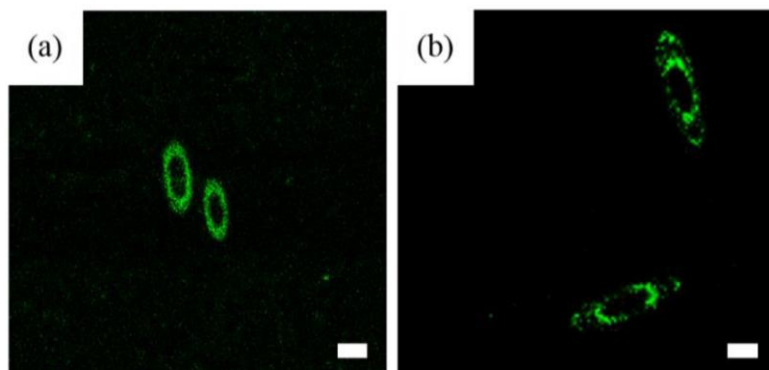


**Figure 1.22:** Confocal microscopy images of ABM tagged particles with (a) one ABM unimer addition with one fluorescent ring and (b) two ABM unimer additions with two fluorescent rings, illustrating how separate polymer blocks can be synthesized by CDSA and then visualized. Scale bar = 1000 nm.

Reproduced from reference with permission.<sup>174</sup>

### 1.3.5 Biomolecule based applications of substituted maleimides

Maleimides are well-known conjugation agents, often used in thiol-Michael additions, a class of click reaction. They are particularly reactive for this application as the highly electron withdrawn C=C bond is also under ring strain.<sup>175</sup> As a consequence, they have been heavily used in applications that require highly efficient chemistry, such as macromolecule labelling/conjugation.<sup>176</sup> This chemistry however, is susceptible to retro-Michael reaction; as the addition is reversible, and also prone to thiol exchange with biological thiols.<sup>177,178</sup> Many attempts have been made to overcome this which rely on the hydrolysis of the formed Michael product. This hydrolysed maleic amide is not susceptible to thiol-Michael pathways and thus traps the product, preventing retro-Michael thiol exchange (Figure 1.23).<sup>176</sup>

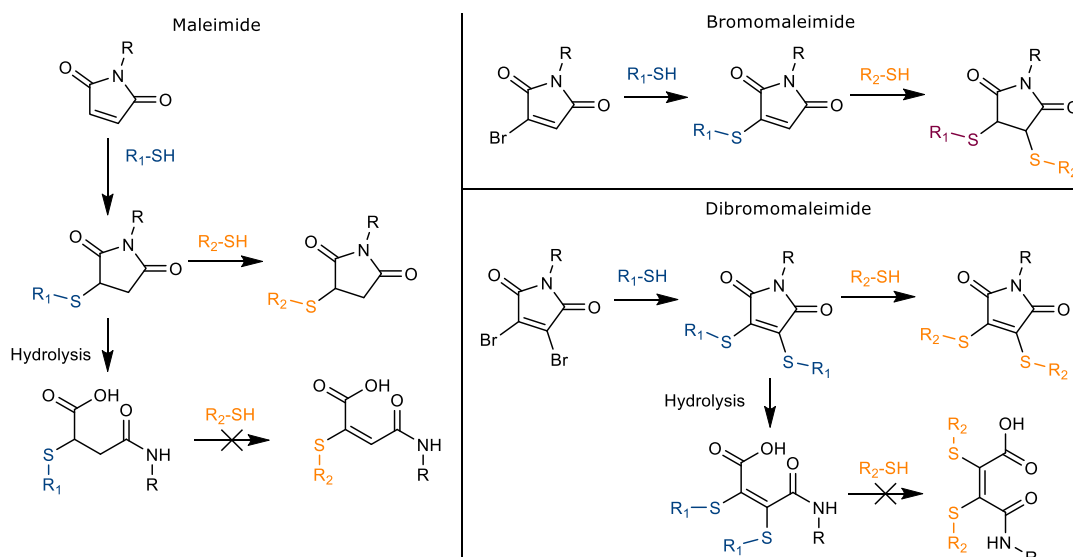


**Figure 1.23:** Maleimide (left) and bromomaleimide (right) thiol conjugation pathways, including post conjugation hydrolysis.

Recently, Caddick and co-workers have pioneered the use of halogenated maleimides, as next-generation maleimides for thiol based conjugations.<sup>143,179,180</sup> These substituted maleimides have been shown to be highly specific for cysteine, and can also be hydrolysed to prevent thiol exchange, a process that has been shown to cleave conjugates in blood serum (Scheme 1.23).<sup>181,182</sup> The group, however, has utilized the efficient thiol exchange of these substituted maleimides to enable targeted cleavage of conjugates *in vivo*, including for fluorophore and drug release.<sup>153</sup> Along with the Baker group, their research has focused extensively on the use of such dyes as antibody conjugation reagents, through reaction with reduced disulfide bonds, forming maleimide bridged conjugates.<sup>179,183</sup> In particular, by using this technique, up to four molecules of anti-cancer drug doxorubicin could be conjugated to a HER2 breast cancer targeting antibody trastuzumab.<sup>179</sup> Further work showed how different drugs could be conjugated, that conjugates were stable in blood serum conditions were selective and potent against HER2 expressing cell lines.<sup>183</sup>

Other biological applications for halogenated maleimides have been reported by other groups. One promising use is as a peptide stapling agent. Peptide stapling agents are alpha-helical peptides that are held together/constrained by a bridge between two residues, helping the helix achieve greater helical character.<sup>184</sup> Using dibromomaleimide, Wilson and co-workers showed the efficient bridging of two cysteine residues (Figure 1.24), creating helical peptides with increased bioactivity in two examples: BID a protein-protein interaction inhibitor, and RNase S a hydrolase.<sup>185</sup> Through stapling, the peptides were also shown to be drastically more resistant to proteolysis. Also, Chen *et al.* have shown how bromomaleimide disulfide bridging of virus-like particles can be used to create blood serum stable, fluorescently tagged particles.<sup>186</sup>

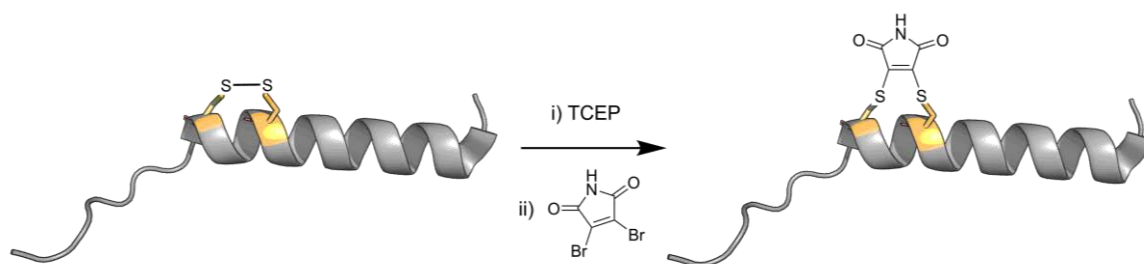


**Figure 1.23:** Illustration of DBM based stapling of α-helical BID.<sup>181</sup>

## 1.4 Summary

This introductory Chapter covers the general concepts behind the topics within this thesis. Firstly, an introduction into peptides and biological macromolecules was presented, as the structure of peptides and their functions underpins the work completed in Chapter 2 and Chapter 5, and the rules for peptide assembly form the basis for Chapter 6 which investigates peptides for dictating polymer assembly. State of the art research into peptide-based assembly for macromolecular applications was also introduced, for example, cyclic peptide driven assembly of nanotubes by the Perrier group<sup>102</sup> and peptide amphiphiles driving the assembly of nanofibers by the Stupp and Hamley groups.<sup>115-117</sup>

Secondly, the principles of fluorescence and its applications to labelling of macromolecules was introduced as Chapters 2 to 5 focus on developing maleimide fluorophores for peptide labelling and monitoring. To help give context, commonly used fluorescence proteins and small molecule probes are introduced, familiarizing the reader with current technology and the advantages and disadvantages of these, highlighting how these can be improved, work which will underpin this thesis.

As the potential solution to these issues, maleimides are finally introduced, covering their structure; current applications in peptides, including conjugation and peptide stapling,<sup>176,181</sup> and fluorescence properties, highlighting the expansive and high impact previous work in the group on polymer labelling.<sup>161-164</sup> This work has enabled the collection of unparalleled information from nanoparticles through fluorescence of maleimides, including in vivo assembly, polymer morphology and co-encapsulation of other dyes. Work in Chapters 2, 4 and 5 all relate to using these fluorophores in peptides as smaller and more appropriate dyes compared to

those currently used. In addition, Chapter 3 covers the bottom-up development of these dyes for these applications which relies heavily on the structure and functions introduced herein. Further explanation of the fluorescence quenching in aqueous conditions, as well as aggregation induced emission (AIE) that is serendipitously observed, is introduced in the Chapter itself.

The first work covered in this thesis is the conjugation of maleimide precursors to enzymes through a turn-on fluorescence conjugation. However, despite successful conjugation, the fluorescence of the conjugates was poor from quenching interactions with water, limiting applications compared to current labelling techniques presented here in the introduction. Further work, outlined in Chapter 3, focused on improving aqueous fluorescence which led to insights into the fluorescence mechanism including improved solid-state fluorescence through preventing pi-pi interactions. This AIE-like behaviour shows promise for improved performance in solid-state applications. In Chapter 4, the synthesis of fluorescent amino acids was successfully undertaken for incorporation deeper into enzymes through artificial expression techniques, where solvent quenching should be minimal and properties of the enzyme should be unaffected, unlike traditional labelling techniques presented in this introduction. In Chapter 5, the synthesis of alkyne functionalized probes for the tagging and trapping of enzyme intermediates was completed and the subsequent compatibility of such dyes with cellular incubation conditions was proven. And finally, Chapter 6, provides a novel method for dictating polymer assembly through peptide mediate interactions, introduced in this introduction.



## 1.5 References

- (1) Staudinger, H.; Fritsch, J. *Helv. Chim. Acta* 1922, 5, 785.
- (2) Jenkins, A. D.; Kratochvíl, P.; Stepto, R. F. T.; Suter, U. W. *Pure Appl. Chem.* 1996, 68, 2287.
- (3) Deamer, D. *Life* 2017, 7.
- (4) Sato, K.; Hendricks, M. P.; Palmer, L. C.; Stupp, S. I. *Chem. Soc. Rev.* 2018, 47, 7539.
- (5) Fosgerau, K.; Hoffmann, T. *Drug Discov. Today* 2015, 20, 122.
- (6) Eisenberg, D. *Proc. Natl. Acad. Sci.* 2003, 100, 11207.
- (7) Scholtz, J. M.; Baldwin, R. L. *Annu. Rev. Biophys. Biomol. Struct.* 1992, 21, 95.
- (8) Dunitz, J. D. *Angew. Chem. Int. Ed.* 2001, 40, 4167.
- (9) Creamer, T. P.; Rose, G. D. *Proc. Natl. Acad. Sci.* 1992, 89, 5937.
- (10) Nick Pace, C.; Martin Scholtz, J. *Biophys. J.* 1998, 75, 422.
- (11) Heyden, M.; Freites, J. A.; Ulmschneider, M. B.; White, S. H.; Tobias, D. *J. Soft Matter* 2012, 8, 7742.
- (12) Kentsis, A.; Sosnick, T. R. *Biochemistry* 1998, 37, 14613.
- (13) Sheu, S.-Y.; Yang, D.-Y.; Selzle, H. L.; Schlag, E. W. *Proc. Natl. Acad. Sci.* 2003, 100, 12683.
- (14) Gailer, C.; Feigel, M. J. *Comput. Aided Mol. Des.* 1997, 11, 273.
- (15) Kahn, M. *Synlett* 1993, 1993, 821.
- (16) Khakshoor, O.; Nowick, J. S. *Curr. Opin. Chem. Biol.* 2008, 12, 722.
- (17) Gellman, S. H. *Curr. Opin. Chem. Biol.* 1998, 2, 717.
- (18) Maynard, A. J.; Sharman, G. J.; Searle, M. S. *J. Am. Chem. Soc.* 1998, 120, 1996.
- (19) Hollingsworth, S. A.; Berkholz, D. S.; Karplus, P. A. *Protein Sci. Publ. Protein Soc.* 2009, 18, 1321.
- (20) Cooley, R. B.; Arp, D. J.; Karplus, P. A. *J. Mol. Biol.* 2010, 404, 232.
- (21) Smith, L. J.; Fiebig, K. M.; Schwalbe, H.; Dobson, C. M. *Fold. Des.* 1996, 1, R95.
- (22) Branden, C. I.; Tooze, J. *Introduction to Protein Structure*; 2 edition.; Garland Science: New York, 1998.
- (23) Alberts, B.; Johnson, A.; Lewis, J.; Raff, M.; Roberts, K.; Walter, P. *Mol. Biol. Cell* 4th Ed. 2002.
- (24) Ovchinnikov, S.; Kim, D. E.; Wang, R. Y.-R.; Liu, Y.; DiMaio, F.; Baker, D. *Proteins Struct. Funct. Bioinforma.* 2016, 84, 67.
- (25) **Evans, R.; Jumper, J.; Kirkpatrick, J.; Sifre, L.; Green, T.; Qin, C.; Žídek, A.; Nelson, S.; Bridgland, A.; Penedones, H.; Petersen, S.; Simonyan, K.; Crossan, S.; Jones, D.; Silver, D.; Kavukcuoglu, K.; Hassabis, D.; Senior, A.** *De novo structure prediction with deep-learning based scoring*; 2018.
- (26) Berg, J. M.; Tymoczko, J. L.; Stryer, L. *Biochemistry*; 5th edition.; W. H. Freeman and Company.: New York, 2002.
- (27) Fagarasan, S.; Honjo, T. *Nat. Rev. Immunol.* 2003, 3, 63.
- (28) Bollum, F. J. *J. Biol. Chem.* 1960, 235, 2399.
- (29) Tsien, R. Y. *Annu. Rev. Biochem.* 1998, 67, 509.
- (30) Yarbrough, D.; Wachter, R. M.; Kallio, L.; Matz, M. V. *Proc. Natl. Acad. Sci. U.S.A.* 2001, 98, 462.
- (31) Patel, S. S.; Donmez, I. *J. Biol. Chem.* 2006, 281, 18265.
- (32) Lengyel, P.; Söll, D. *Bacteriol. Rev.* 1969, 33, 264.

- (33) Schlutzen, F.; Tocilj, A.; Zarivach, R.; Harms, J.; Gluehmann, M.; Janell, D.; Bashan, A.; Bartels, H.; Agmon, I.; Franceschi, F.; Yonath, A. *Cell* 2000, *102*, 615.
- (34) Baggett, N. E.; Zhang, Y.; Gross, C. A. *PLOS Genet.* 2017, *13*, e1006676.
- (35) Hassouneh, W.; Zhulina, E. B.; Chilkoti, A.; Rubinstein, M. *Macromolecules* 2015, *48*, 4183.
- (36) Fedor, M. J.; Williamson, J. R. *Nat. Rev. Mol. Cell Biol.* 2005, *6*, 399.
- (37) Kruger, K.; Grabowski, P. J.; Zaug, A. J.; Sands, J.; Gottschling, D. E.; Cech, T. R. *Cell* 1982, *31*, 147.
- (38) Berg, J. M.; Tymoczko, J. L.; Stryer, L.; Berg, J. M.; Tymoczko, J. L.; Stryer, L. *Biochemistry*; 5th ed.; W H Freeman, 2002.
- (39) Hedstrom, L. *Chem. Rev.* 2002, *102*, 4501.
- (40) Sorella, G. L.; Strukul, G.; Scarso, A. *Green Chem.* 2015, *17*, 644.
- (41) Lestini, E.; Blackman, L. D.; Zammit, C. M.; Chen, T.; Williams, R. J.; **Inam, M.; Couturaud, B.; O'Reilly, R. K.** *Polym. Chem.* 2018, *9*, 820.
- (42) Peters, R. J. R. W.; Louzao, I.; Hest, J. C. M. *van Chem. Sci.* 2012, *3*, 335.
- (43) Raynal, M.; Ballester, P.; Vidal-Ferran, A.; Leeuwen, P. W. N. M. *van Chem. Soc. Rev.* 2014, *43*, 1734.
- (44) Donnelly, A. E.; Murphy, G. S.; Digianantonio, K. M.; Hecht, M. H. *Nat. Chem. Biol.* 2018, *14*, 253.
- (45) Johnson, K. A.; Goody, R. S. The Original Michaelis Constant: Translation of the 1913 Michaelis–Menten Paper  
<https://pubs.acs.org/doi/suppl/10.1021/bi201284u> (accessed Oct 2, 2019).
- (46) Mahon, C. S.; Fulton, D. A. *Nat. Chem.* 2014, *6*, 665.
- (47) Mody, V. V.; Siwale, R.; Singh, A.; Mody, H. R. *J. Pharm. Bioallied Sci.* 2010, *2*, 282.
- (48) Dadfar, S. M.; Roemhild, K.; Drude, N. I.; von Stillfried, S.; Knüchel, R.; Kiessling, F.; Lammers, T. *Adv. Drug Deliv. Rev.* 2019, *138*, 302.
- (49) Grundmann, M.; Christen, J.; Ledentsov, N. N.; Böhrer, J.; Bimberg, D.; **Ruvimov, ‡, S. S.; Werner, P.; Richter, U.; Gösele, U.; Heydenreich, J.; Ustinov, V. M.; Egorov, A. Yu.; Zhukov, A. E.; Kop'ev, P. S.; Alferov, Zh. I.** *Phys. Rev. Lett.* 1995, *74*, 4043.
- (50) SalmanOgli, A. *Cancer Nanotechnol.* 2011, *2*, 1.
- (51) Shit, S. C.; Shah, P. *Natl. Acad. Sci. Lett.* 2013, *36*, 355.
- (52) Parker, D. J.; Chong, S. T.; Hasell, T. *RSC Adv.* 2018, *8*, 27892.
- (53) Goethals, E. J. *J. Macromol. Sci. Part C* 1968, *2*, 73.
- (54) Baughman, R. H.; Zakhidov, A. A.; Heer, W. A. *de Science* 2002, *297*, 787.
- (55) Cheng, C.; McGonigal, P. R.; Schneebeli, S. T.; Li, H.; Vermeulen, N. A.; Ke, C.; Stoddart, J. F. *Nat. Nanotechnol.* 2015, *10*, 547.
- (56) Dietrich-Buchecker, C. O.; Jimenez-Molero, M. C.; Sartor, V.; Sauvage, J.-P. *Pure Appl. Chem.* 2003, *75*, 1383.
- (57) **Kistemaker, J. C. M.; Štacko, P.; Visser, J.; Feringa, B. L.** *Nat. Chem.* 2015, *7*, 890.
- (58) Matyjaszewski, K.; Spanswick, J. *Mater. Today* 2005, *8*, 26.
- (59) Hadjichristidis, N.; Hirao, A.; Tezuka, Y.; Du Prez, F., *Complex Macromolecular Architectures: Synthesis, Characterization, and Self-Assembly*; 1 edition.; Wiley, 2011.

- (60) Walther, A.; Goldmann, A. S.; Yelamanchili, R. S.; Drechsler, M.; Schmalz, H.; Eisenberg, A.; Müller, A. H. E. *Macromolecules* 2008, *41*, 3254.
- (61) Discher, D. E.; Eisenberg, A. *Science* 2002, *297*, 967.
- (62) Nagarajan, R. *Langmuir* 2002, *18*, 31.
- (63) Israelachvili, J. N.; Mitchell, D. J.; Ninham, B. W. *Biochim. Biophys. Acta BBA - Biomembr.* 1977, *470*, 185.
- (64) Ishizuka, F.; Chapman, R.; Kuchel, R. P.; Coureault, M.; Zetterlund, P. B.; Stenzel, M. H. *Macromolecules* 2018, *51*, 438.
- (65) Wan, X.; Zhang, J.; Yu, W.; Shen, L.; Ji, S.; Hu, T. *Process Biochem.* 2017, *52*, 183.
- (66) Li, M.; De, P.; Gondi, S. R.; Sumerlin, B. S. *Macromol. Rapid Commun.* 2008, *29*, 1172.
- (67) Bertrand, O.; Gohy, J.-F. *Polym. Chem.* 2016, *8*, 52.
- (68) Paik, B. A.; Mane, S. R.; Jia, X.; Kiick, K. L. *J. Mater. Chem. B* 2017, *5*, 8274.
- (69) Olsson, C.; Jansson, H.; Swenson, J. J. *Phys. Chem. B* 2016, *120*, 4723.
- (70) Mancini, R. J.; Lee, J.; Maynard, H. D. *J. Am. Chem. Soc.* 2012, *134*, 8474.
- (71) Andrianov, A. K.; Marin, A.; Chen, J. *Biomacromolecules* 2006, *7*, 394.
- (72) Blackman, L. D.; Varlas, S.; Arno, M. C.; Houston, Z. H.; Fletcher, N. L.; Thurecht, K. J.; Hasan, M.; Gibson, M. I.; O'Reilly, R. K. *ACS Cent. Sci.* 2018.
- (73) Bacinello, D.; Garanger, E.; Taton, D.; Tam, K. C.; Lecommandoux, S. *Eur. Polym. J.* 2015, *62*, 363.
- (74) Icart, L. P.; Souza, F. G. de; Lima, L. M. T. R. *bioRxiv* 2018, 262782.
- (75) Kim, M. R.; Feng, T.; Zhang, Q.; Chan, H. Y. E.; Chau, Y. *Polymers* 2019, *11*.
- (76) Lomas, H.; Canton, I.; MacNeil, S.; Du, J.; Armes, S. P.; Ryan, A. J.; Lewis, A. L.; Battaglia, G. *Adv. Mater.* 2007, *19*, 4238.
- (77) Gaitzsch, J.; Appelhans, D.; Wang, L.; Battaglia, G.; Voit, B. *Angew. Chem. Int. Ed.* 2012, *51*, 4448.
- (78) Cerritelli, S.; Velluto, D.; Hubbell, J. A. *Biomacromolecules* 2007, *8*, 1966.
- (79) Kim, K. T.; Cornelissen, J. J. L. M.; Nolte, R. J. M.; Hest, J. C. M. van *Adv. Mater.* 2009, *21*, 2787.
- (80) van Dongen, S. F. M.; Nallani, M.; Cornelissen, J. J. L. M.; Nolte, R. J. M.; van Hest, J. C. M. *Chem. – Eur. J.* 2009, *15*, 1107.
- (81) Vriezema, D. M.; Garcia, P. M. L.; Sancho Oltra, N.; Hatzakis, N. S.; Kuiper, S. M.; Nolte, R. J. M.; Rowan, A. E.; van Hest, J. C. M. *Angew. Chem. Int. Ed.* 2007, *46*, 7378.
- (82) Robbins, G. P.; Jimbo, M.; Swift, J.; Therien, M. J.; Hammer, D. A.; Dmochowski, I. J. *J. Am. Chem. Soc.* 2009, *131*, 3872.
- (83) Varlas, S.; Foster, J. C.; Georgiou, P. G.; Keogh, R.; Husband, J. T.; Williams, D. S.; O'Reilly, R. K. *Nanoscale* 2019, *11*, 12643.
- (84) Hermanson, G. T. In *Bioconjugate Techniques (Third edition)*; Academic Press: Boston, 2013; 1.
- (85) Gauthier, M. A.; Klok, H.-A. *Chem. Commun.* 2008, 2591.
- (86) Pasut, G.; Veronese, F. M. *Prog. Polym. Sci.* 2007, *32*, 933.
- (87) Hermanson, G. T. In *Bioconjugate Techniques (Third edition)*; Academic Press: Boston, 2013; 787.

- (88) Pelegri-O'Day, E. M.; Lin, E.-W.; Maynard, H. D. *J. Am. Chem. Soc.* 2014, **136**, 14323.
- (89) Wilson, P. *Macromol. Chem. Phys.* 2017, **218**, 1600595.
- (90) Ayres, L.; Vos, M. R. J.; Adams, P. J. H. M.; Shklyarevskiy, I. O.; van Hest, J. C. M. *Macromolecules* 2003, **36**, 5967.
- (91) Fernández-Trillo, F.; Duréault, A.; Bayley, J. P. M.; van Hest, J. C. M.; Thies, J. C.; Michon, T.; Weberskirch, R.; Cameron, N. R. *Macromolecules* 2007, **40**, 6094.
- (92) Wright, D. B.; Ramírez-Hernández, A.; Touve, M. A.; Carlini, A. S.; Thompson, M. P.; Patterson, J. P.; de Pablo, J. J.; Gianneschi, N. C. *ACS Macro Lett.* 2019, **8**, 676.
- (93) Wright, D. B.; Proetto, M. T.; Touve, M. A.; Gianneschi, N. C. *Polym. Chem.* 2019, **10**, 2996.
- (94) Sun, H.; Choi, W.; Zang, N.; Battistella, C.; Thompson, M.; Cao, W.; Zhou, X.; Forman, C.; Gianneschi, N. C. *Angew. Chem. Int. Ed.*
- (95) Blum, A. P.; Kammeyer, J. K.; Gianneschi, N. C. *Chem. Sci.* 2016, **7**, 989.
- (96) Silva, S.; Almeida, A. J.; Vale, N. *Biomolecules* 2019, **9**, 22.
- (97) Grover, G. N.; Maynard, H. D. *Curr. Opin. Chem. Biol.* 2010, **14**, 818.
- (98) Zhang, Q.; Li, M.; Zhu, C.; Nurumbetov, G.; Li, Z.; Wilson, P.; Kempe, K.; Haddleton, D. M. *J. Am. Chem. Soc.* 2015, **137**, 9344.
- (99) Larnaudie, S. C.; Brendel, J. C.; Jolliffe, K. A.; Perrier, S. J. *Polym. Sci. Part Polym. Chem.* 2016, **54**, 1003.
- (100) Falatach, R.; McGlone, C.; Al-Abdul-Wahid, M. S.; Averick, S.; Page, R. C.; Berberich, J. A.; Konkolewicz, D. *Chem. Commun.* 2015, **51**, 5343.
- (101) De, P.; Li, M.; Gondi, S. R.; Sumerlin, B. S. *J. Am. Chem. Soc.* 2008, **130**, 11288.
- (102) Rho, J. Y.; Cox, H.; Mansfield, E. D. H.; Ellacott, S. H.; Peltier, R.; Brendel, J. C.; Hartlieb, M.; Waigh, T. A.; Perrier, S. *Nat. Commun.* 2019, **10**, 1.
- (103) Catrouillet, S.; Brendel, J. C.; Larnaudie, S.; Barlow, T.; Jolliffe, K. A.; Perrier, S. *ACS Macro Lett.* 2016, **5**, 1119.
- (104) Danial, M.; Tran, C. M.-N.; Young, P. G.; Perrier, S.; Jolliffe, K. A. *Nat. Commun.* 2013, **4**, 1.
- (105) Hartlieb, M.; Catrouillet, S.; Kuroki, A.; Sanchez-Cano, C.; Peltier, R.; Perrier, S. *Chem. Sci.* 2019.
- (106) Song, Q.; Yang, J.; Rho, J. Y.; Perrier, S. *Chem. Commun.* 2019, **55**, 5291.
- (107) Larnaudie, S. C.; Sanchis, J.; Nguyen, T.-H.; Peltier, R.; Catrouillet, S.; Brendel, J. C.; Porter, C. J. H.; Jolliffe, K. A.; Perrier, S. *Biomaterials* 2018, **178**, 570.
- (108) Larnaudie, S. C.; Brendel, J. C.; Romero-Canelón, I.; Sanchez-Cano, C.; Catrouillet, S.; Sanchis, J.; Coverdale, J. P. C.; Song, J.-I.; Habtemariam, A.; Sadler, P. J.; Jolliffe, K. A.; Perrier, S. *Biomacromolecules* 2018, **19**, 239.
- (109) Liu, S.; Zhang, H.; Remy, R. A.; Deng, F.; Mackay, M. E.; Fox, J. M.; Jia, X. *Adv. Mater.* 2015, **27**, 2783.
- (110) ten Cate, M. G. J.; Severin, N.; Börner, H. G. *Macromolecules* 2006, **39**, 7831.
- (111) Clarke, D. E.; Pashuck, E. T.; Bertazzo, S.; Weaver, J. V. M.; Stevens, M. M. *J. Am. Chem. Soc.* 2017, **139**, 7250.
- (112) Cui, H.; Webber, M. J.; Stupp, S. I. *Pept. Sci.* 2010, **94**, 1.

- (113) Wakabayashi, R.; Suehiro, A.; Goto, M.; Kamiya, N. *Chem. Commun.* 2019, *55*, 640.
- (114) Cui, H.; Muraoka, T.; Cheetham, A. G.; Stupp, S. I. *Nano Lett.* 2009, *9*, 945.
- (115) Hendricks, M. P.; Sato, K.; Palmer, L. C.; Stupp, S. I. *Acc. Chem. Res.* 2017, *50*, 2440.
- (116) Hartgerink, J. D.; Beniash, E.; Stupp, S. I. *Proc. Natl. Acad. Sci.* 2002, *99*, 5133.
- (117) Edwards-Gayle, C. J. C.; Castelletto, V.; Hamley, I. W.; Barrett, G.; Greco, F.; Hermida-Merino, D.; Rambo, R. P.; Seitsonen, J.; Ruokolainen, J. *ACS Appl. Bio Mater.* 2019, *2*, 2208.
- (118) Chang, R.; Subramanian, K.; Wang, M.; Webster, T. J. *ACS Appl. Mater. Interfaces* 2017, *9*, 22350.
- (119) Webber, M. J.; Tongers, J.; Renault, M.-A.; Roncalli, J. G.; Losordo, D. W.; Stupp, S. I. *Acta Biomater.* 2010, *6*, 3.
- (120) Hellmund, K. S.; Koksche, B. *Front. Chem.* 2019, *7*.
- (121) Ji, W.; Álvarez, Z.; Edelbrock, A. N.; Sato, K.; Stupp, S. I. *ACS Appl. Mater. Interfaces* 2018, *10*, 41046.
- (122) Hartgerink, J. D.; Beniash, E.; Stupp, S. I. *Science* 2001, *294*, 1684.
- (123) Filatov, M. A.; Etzold, F.; Gehrig, D.; Laquai, F.; Busko, D.; Landfester, K.; Balushev, S. *Dalton Trans.* 2015, *44*, 19207.
- (124) In *Molecular Fluorescence*; John Wiley & Sons, Ltd, 2012; 1.
- (125) Schuster, G. B. *Acc. Chem. Res.* 1979, *12*, 366.
- (126) Ntziachristos, V. *Annu. Rev. Biomed. Eng.* 2006, *8*, 1.
- (127) Lavis, L. D. *Biochemistry* 2017, *56*, 5165.
- (128) Butler, S. J.; Lamarque, L.; Pal, R.; Parker, D. *Chem. Sci.* 2014, *5*, 1750.
- (129) Valizadeh, A.; Mikaeili, H.; Samiei, M.; Farkhani, S. M.; Zarghami, N.; kouhi, M.; Akbarzadeh, A.; Davaran, S. *Nanoscale Res. Lett.* 2012, *7*, 480.
- (130) Jung, D.; Min, K.; Jung, J.; Jang, W.; Kwon, Y. *Mol. Biosyst.* 2013, *9*, 862.
- (131) Prasher, D. C.; Eckenrode, V. K.; Ward, W. W.; Prendergast, F. G.; Cormier, M. J. *Gene* 1992, *111*, 229.
- (132) Gross, L. A.; Baird, G. S.; Hoffman, R. C.; Baldridge, K. K.; Tsien, R. Y. *Proc. Natl. Acad. Sci. U. S. A.* 2000, *97*, 11990.
- (133) Niu, W.; Guo, J. *Mol. BioSyst.* 2013, *9*, 2961.
- (134) Rodriguez, E. A.; Campbell, R. E.; Lin, J. Y.; Lin, M. Z.; Miyawaki, A.; Palmer, A. E.; Shu, X.; Zhang, J.; Tsien, R. Y. *Trends Biochem. Sci.* 2017, *42*, 111.
- (135) Gonçalves, M. S. T. *Chem. Rev.* 2009, *109*, 190.
- (136) Grimm, J. B.; English, B. P.; Chen, J.; Slaughter, J. P.; Zhang, Z.; Revyakin, A.; Patel, R.; Macklin, J. J.; Normanno, D.; Singer, R. H.; Lionnet, T.; Lavis, L. D. *Nat. Methods* 2015, *12*, 244.
- (137) Gong, W.; Das, P.; Samanta, S.; Xiong, J.; Pan, W.; Gu, Z.; Zhang, J.; Qu, J.; Yang, Z. *Chem. Commun.* 2019, *55*, 8695.
- (138) Berlier, J. E.; Rothe, A.; Buller, G.; Bradford, J.; Gray, D. R.; Filanoski, B. J.; Telford, W. G.; Yue, S.; Liu, J.; Cheung, C.-Y.; Chang, W.; Hirsch, J. D.; Beechem, J. M.; Haugland, R. P.; Haugland, R. P. *J. Histochem. Cytochem. Off. J. Histochem. Soc.* 2003, *51*, 1699.
- (139) Schwechheimer, C.; Röncke, F.; Schepers, U.; Wagenknecht, H.-A. *Chem. Sci.* 2018, *9*, 6557.

- (140) Simpson, J. D.; Smith, S. A.; Thurecht, K. J.; Such, G. *Polymers* 2019, **11**, 1441.
- (141) Northrop, B. H.; Frayne, S. H.; Choudhary, U. *Polym. Chem.* 2015, **6**, 3415.
- (142) Tawney, P. O.; Snyder, R. H.; Conger, R. P.; Leibbrand, K. A.; Stiteler, C. H.; Williams, A. R. *J. Org. Chem.* 1961, **26**, 15.
- (143) Tedaldi, L. M.; Smith, M. E. B.; Nathani, R. I.; Baker, J. R. *Chem. Commun.* 2009, 6583.
- (144) **Robin, M. P.; Jones, M. W.; Haddleton, D. M.; O'Reilly, R. K. ACS Macro Lett.** 2012, **1**, 222.
- (145) Karten, M. J.; Shapiro, S. L.; Isaacs, E. S.; Freedman, L. J. *Org. Chem.* 1965, **30**, 2657.
- (146) Katritzky, A. R.; Fan, W.-Q. *J. Heterocycl. Chem.* 1988, **25**, 901.
- (147) Lynch, D. M.; Crovetti, A. J. *J. Heterocycl. Chem.* 1972, **9**, 1027.
- (148) Robin, M. P.; Wilson, P.; Mabire, A. B.; Kiviahio, J. K.; Raymond, J. E.; **Haddleton, D. M.; O'Reilly, R. K. J. Am. Chem. Soc.** 2013, **135**, 2875.
- (149) Mabire, A. B.; Robin, M. P.; Quan, W.-D.; Willcock, H.; Stavros, V. G.; **O'Reilly, R. K. Chem. Commun.** 2015, **51**, 9733.
- (150) Xie, Y.; Husband, J. T.; Torrent-Sucarrat, M.; Yang, H.; Liu, W.; O'Reilly, R. K. *Chem. Commun.* 2018, **54**, 3339.
- (151) Chen, X.; Zhou, Y.; Peng, X.; Yoon, J. *Chem. Soc. Rev.* 2010, **39**, 2120.
- (152) Chen, Y.; Tsao, K.; De Francesco, É.; Keillor, J. W. *J. Org. Chem.* 2015, **80**, 12182.
- (153) Moody, P.; Smith, Mark. E. B.; Ryan, C. P.; Chudasama, V.; Baker, J. R.; Molloy, J.; Caddick, S. *ChemBioChem* 2012, **13**, 39.
- (154) In *Molecular Fluorescence*; John Wiley & Sons, Ltd, 2012; 109.
- (155) Penfold, T. J.; Dias, F. B.; Monkman, A. P. *Chem. Commun.* 2018, **54**, 3926.
- (156) Valeur, B.; Leray, I. In *New Trends in Fluorescence Spectroscopy: Applications to Chemical and Life Sciences*; Valeur, B.; Brochon, J.-C., Eds.; Springer Series on Fluorescence; Springer: Berlin, Heidelberg, 2001; 187.
- (157) Martynov, V. I.; Pakhomov, A. A.; Popova, N. V.; Deyev, I. E.; Petrenko, A. G. *Acta Naturae* 2016, **8**, 33.
- (158) Martin, M. M.; Lindqvist, L. *J. Lumin.* 1975, **10**, 381.
- (159) Qi, J.; Liu, D.; Liu, X.; Guan, S.; Shi, F.; Chang, H.; He, H.; Yang, G. *Anal. Chem.* 2015, **87**, 5897.
- (160) Tian, M.; Peng, X.; Fan, J.; Wang, J.; Sun, S. *Dyes Pigments* 2012, **95**, 112.
- (161) Robin, M. P.; Mabire, A. B.; Damborsky, J. C.; Thom, E. S.; Winzer-Serhan, U. H.; Raymond, J. E.; O'Reilly, R. K. *J. Am. Chem. Soc.* 2013, **135**, 9518.
- (162) Robin, M. P.; Raymond, J. E.; O'Reilly, R. K. *Mater. Horiz.* 2014, **2**, 54.
- (163) Smith, M. E. B.; Caspersen, M. B.; Robinson, E.; Morais, M.; Maruani, A.; Nunes, J. P. M.; Nicholls, K.; Saxton, M. J.; Caddick, S.; Baker, J. R.; Chudasama, V. *Org. Biomol. Chem.* 2015, **13**, 7946.
- (164) **Robin, M. P.; Osborne, S. A. M.; Pikramenou, Z.; Raymond, J. E.; O'Reilly, R. K. Macromolecules** 2016, **49**, 653.
- (165) Arno, M. C.; Inam, M.; Coe, Z.; Cambridge, G.; Macdougall, L. J.; Keogh, R.; Dove, A. P.; O'Reilly, R. K. *J. Am. Chem. Soc.* 2017, **139**, 16980.
- (166) Mabire, A. B.; Robin, M. P.; Willcock, H.; Pitto-Barry, A.; Kirby, N.; O'Reilly, R. K. *Chem. Commun.* 2014, **50**, 11492.

- (167) Varlas, S.; Keogh, R.; Xie, Y.; Horswell, S. L.; **Foster, J. C.; O'Reilly, R. K.** *J. Am. Chem. Soc.* 2019.
- (168) Tang, Z.; Wilson, P.; Kempe, K.; Chen, H.; Haddleton, D. M. *ACS Macro Lett.* 2016, 5, 709.
- (169) Eissa, A. M.; Wilson, P.; Chen, C.; Collins, J.; Walker, M.; Haddleton, D. M.; Cameron, N. R. *Chem. Commun.* 2017, 53, 9789.
- (170) Karman, M.; Verde-Sesto, E.; Weder, C.; Simon, Y. C. *ACS Macro Lett.* 2018, 7, 1099.
- (171) Bai, T.; Shao, D.; Chen, J.; Li, Y.; Xu, B. B.; Kong, J. J. *Colloid Interface Sci.* 2019, 552, 439.
- (172) Wang, H.; Xu, M.; Xiong, M.; Cheng, J. *Chem. Commun.* 2015, 51, 4807.
- (173) Cui, J.; Wang, S.; Huang, K.; Li, Y.; Zhao, W.; Shi, J.; Gu, J. *New J. Chem.* 2014, 38, 6017.
- (174) Inam, M. *Morphological Control in the Solution Crystallisation of Polymeric Nanoparticles*, University of Warwick, 2018.
- (175) Nair, D. P.; Podgórski, M.; Chatani, S.; Gong, T.; Xi, W.; Fenoli, C. R.; Bowman, C. N. *Chem. Mater.* 2014, 26, 724.
- (176) Ravasco, J. M. J. M.; Faustino, H.; Trindade, A.; Gois, P. M. P. *Chem. – Eur. J.* 2019, 25, 43.
- (177) Shen, B.-Q.; Xu, K.; Liu, L.; Raab, H.; Bhakta, S.; Kenrick, M.; Parsons-Reponte, K. L.; Tien, J.; Yu, S.-F.; Mai, E.; Li, D.; Tibbitts, J.; Baudys, J.; Saad, O. M.; Scales, S. J.; McDonald, P. J.; Hass, P. E.; Eigenbrot, C.; Nguyen, T.; Solis, W. A.; Fujii, R. N.; Flagella, K. M.; Patel, D.; Spencer, S. D.; Khawli, L. A.; Ebens, A.; Wong, W. L.; Vandlen, R.; Kaur, S.; Sliwkowski, M. X.; Scheller, R. H.; Polakis, P.; Junutula, J. R. *Nat. Biotechnol.* 2012, 30, 184.
- (178) Christie, R. J.; Fleming, R.; Bezabeh, B.; Woods, R.; Mao, S.; Harper, J.; Joseph, A.; Wang, Q.; Xu, Z.-Q.; Wu, H.; Gao, C.; Dimasi, N. J. *Controlled Release* 2015, 220, 660.
- (179) Schumacher, F. F.; Nunes, J. P. M.; Maruani, A.; Chudasama, V.; Smith, M. E. B.; Chester, K. A.; Baker, J. R.; Caddick, S. *Org. Biomol. Chem.* 2014, 12, 7261.
- (180) Forte, N.; Livanos, M.; Miranda, E.; Morais, M.; Yang, X.; Rajkumar, V. S.; Chester, K. A.; Chudasama, V.; Baker, J. R. *Bioconjug. Chem.* 2018, 29, 486.
- (181) Ryan, C. P.; Smith, M. E. B.; Schumacher, F. F.; Grohmann, D.; Papaioannou, D.; Waksman, G.; Werner, F.; Baker, J. R.; Caddick, S. *Chem. Commun.* 2011, 47, 5452.
- (182) Morais, M.; Nunes, J. P. M.; Karu, K.; Forte, N.; Benni, I.; Smith, M. E. B.; Caddick, S.; Chudasama, V.; Baker, J. R. *Org. Biomol. Chem.* 2017, 15, 2947.
- (183) Nunes, J. P. M.; Vassileva, V.; Robinson, E.; Morais, M.; Smith, M. E. B.; Pedley, R. B.; Caddick, S.; Baker, J. R.; Chudasama, V. *RSC Adv.* 2017, 7, 24828.
- (184) Wang, D.; Liao, W.; Arora, P. S. *Angew. Chem. Int. Ed.* 2005, 44, 6525.
- (185) Grison, C. M.; Burslem, G. M.; Miles, J. A.; Pils, L. K. A.; Yeo, D. J.; Imani, Z.; Warriner, S. L.; Webb, M. E.; Wilson, A. J. *Chem. Sci.* 2017, 8, 5166.
- (186) Chen, Z.; Boyd, S. D.; Calvo, J. S.; Murray, K. W.; Mejia, G. L.; Benjamin, C. E.; Welch, R. P.; Winkler, D. D.; Meloni, G.; **D'Arcy, S.**; Gassensmith, J. J. *Bioconjug. Chem.* 2017, 28, 2277.

## **Chapter 2:** Utilizing functionalized bromomaleimides for fluorogenic conjugation to enzymes



## 1.6 Abstract

Two efficient enzyme conjugation techniques have been explored by exploiting the reactions of bromomaleimides. The conjugations utilize monobromo- and dibromo-maleimides which have been reacted with reduced disulfide bonds or terminal amines in  $\alpha$ -chymotrypsin and human lysozyme. These reactions allow the formation of dithio- (DTM), monoamino- (MAM), and aminobromo- (ABM) maleimides, which are bright, solvent-dependent fluorophores that have a handle for further functionalization. The efficiency of the maleimide conjugation was monitored and the fluorescence of the resulting conjugates examined. The quantum yields of the maleimide conjugates have been calculated but are low due to solvent quenching effects. Catalytic activities of the conjugate enzymes have been compared to their respective native enzyme and no discernible effect of the conjugation on enzymatic activity or room temperature stability was observed. Additionally, one step PEGylation and fluorescent labelling of enzymes was investigated using PEG functionalized bromomaleimides.

## 1.7 Introduction

### 1.7.1 Enzyme conjugation *via* lysine and cysteine residues

Conjugation to amino acids in proteins is a widespread practice. It is used for many applications, including fluorophore incorporation,<sup>1,2</sup> biotinylation,<sup>3</sup> drug conjugates,<sup>4</sup> and radiolabelling.<sup>5</sup> The two most commonly accessed sites for conjugation are lysine residues and reduced cysteine residues. Among amine-reactive techniques, most commonly *N*-hydroxysuccinimide (NHS) activated esters are used for conjugation.<sup>6,7</sup> The technique requires activation of an acid group prior to conjugation, and due to the large number of lysine residues usually present in proteins, it is commonly difficult to control the location and number of modifications. Other lysine conjugation techniques include 1-ethyl-3-(3-dimethylaminopropyl)carbodiimide (EDC) coupling, and isocyanate and imidoester chemistries (Figure 2.1).

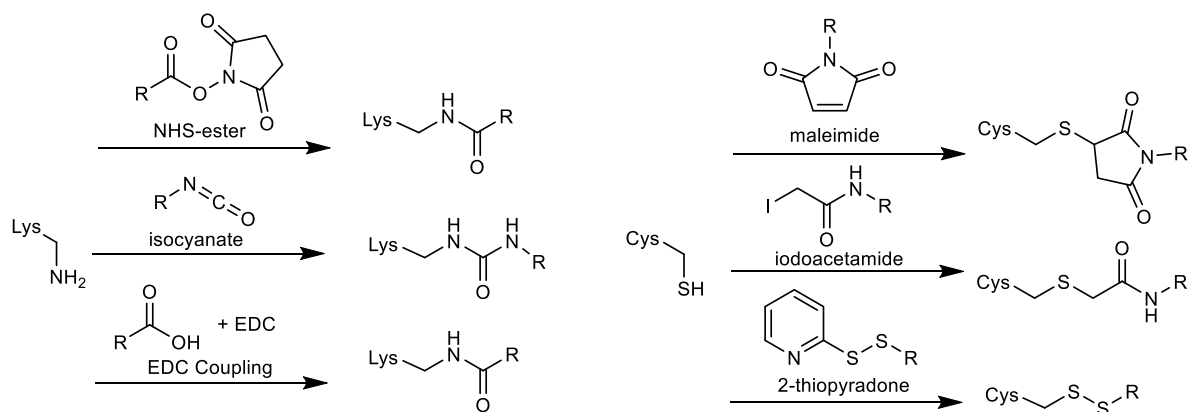


**Figure 2.1:** Commonly utilized protein conjugation techniques for lysine and cysteine targeting.

In order to facilitate a cysteine coupling, a reduced cysteine residue is required for functionalization. Cysteine is regarded as the most nucleophilic amino acid, towards soft electrophiles, in the majority of proteins and therefore is commonly regarded as the easiest to modify in a selective manner.<sup>6,8</sup> The most

widely used cysteine modification technique is maleimide conjugation, in which cysteine will undergo highly selective addition to the maleimide double bond.<sup>9</sup> Other cysteine conjugation methods include iodoacetamide chemistry, as well as utilizing disulfide exchange with, 2-dithiopyridine derivatives (Figure 2.1).<sup>10,11</sup>

### 1.7.2 PEGylation of enzymes and biomolecules

PEGylation is the process of chemically attaching polyethylene glycol (PEG) to molecules, such as drugs and therapeutic proteins. PEG can enhance the therapeutic properties of a molecule which can include better physical and thermal stability;<sup>12</sup> protection against degradation;<sup>13</sup> increased solubility;<sup>14</sup> longer half-life *in vivo*;<sup>15</sup> and even increased potency.<sup>16</sup> As of 2015, there were ten PEGylated proteins approved by the FDA for pharmaceutical use.<sup>17</sup> All of these are conjugated *via* lysine residues, the *N*-terminus or a cysteine residue.<sup>18</sup>

The effects of PEGylation on protein pharmacokinetics and pharmacodynamics can be difficult to predict. In fact, the amount of PEG and its location can negatively affect many properties of the therapeutic activity, including elimination and absorption.<sup>19</sup> Another major disadvantage of PEG is that it is non-biodegradable. Indeed, medium molecular weight PEG (40-60 kDa) can cause renal clearance problems and accumulation in the liver.<sup>20</sup> It should be noted that some degradable, or partially degradable PEG analogues, have been developed in the literature, which are expected to be cleared through the renal filtration system. This has been achieved through multiple strategies, for example, synthesizing a copolymer of PEG with degradable units such as PLA-PEG copolymers,<sup>21</sup> introducing hemiacetals through use of hydrogen peroxide and FeCl<sub>3</sub>,<sup>22</sup> or by developing fully degradable alternatives such as poly(ethylene oxide sulphide).<sup>23</sup>

In addition to degradable alternatives, there are many recent reports of alternative stabilizing polymers for peptide conjugation. Some of these include

polyzwitterions such as poly(amino acids) which exhibit tuneable degradation in addition to other benefits such as low toxicity and tuneable thermal properties<sup>24</sup> and sugar based polymers like the trehalose polymers reported by the Maynard group, which are not only degradable but also provided increased thermal stability in comparison to PEG.<sup>25</sup> Limitations of using alternatives includes a greater expense associate with controlled polymers and more challenges in getting FDA approval, as PEG has been classified to be Generally Regarded As Safe (GRAS) by the FDA.<sup>26</sup>

It should be noted that enzymes have been previously PEGylated *via* disulfide bridging, in the literature.<sup>27-29</sup> All reported methods have two steps in common: firstly, reduction of the disulfide to form two free cystine thiols; secondly, re-bridging of these thiols with a reagent. It used to be considered that an enzyme's native disulfides could not be modified because they were believed to be crucial to the enzyme's structure and function.<sup>28</sup> However, Brocchini *et al.*<sup>27</sup> have shown that bridging can be achieved by bis-alkylation utilizing an  $\alpha,\beta$ -unsaturated- $\beta'$ -mono-sulfone functionalized PEG reagent (Figure 2.2).

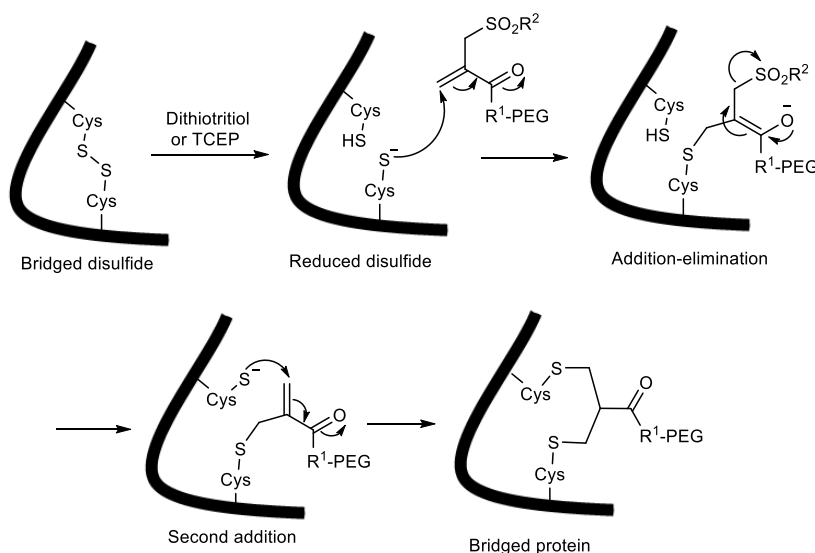


**Figure 2.2:**  $\alpha,\beta$ -unsaturated- $\beta'$ -mono-sulfone functionalized PEG bridging of disulfide bonds.<sup>27</sup>

### 1.7.3 Conjugation to $\alpha$ -chymotrypsin

$\alpha$ -Chymotrypsin ( $\alpha$ -CT) is a proteolysis enzyme, produced by the body in the pancreas and found in the duodenum. It has an activated serine residue, which helps it break down proteins and polypeptides, to aid with digestion.<sup>30</sup> Proteases like chymotrypsin are often used in laundry formulations<sup>31</sup> and chymotrypsin itself is used in cataract surgery.<sup>32</sup>

Chymotrypsin is most active at cleaving bonds where the carboxyl side of the amide bond is a large hydrophobic residue (for example tyrosine or tryptophan), as the aromatic side-chain can interact with chymotrypsin's 'hydrophobic pocket'.<sup>33</sup> Chymotrypsin contains such residues, and can, therefore, digest itself (autolysis), making it an interesting target for stabilization.<sup>34</sup>

$\alpha$ -CT has fourteen lysine residues and five disulfide bonds which can act as handles for conjugation.<sup>35</sup> Russell *et al.*<sup>34</sup> developed an atom transfer radical polymerization (ATRP) initiator (Figure 2.3) which was successfully conjugated to twelve lysine residues. They then polymerized *N,N*-dimethylaminoethyl methacrylate (DMAEMA), among other polymers, from these sites. When stored at pH 7, the CT-DMAEMA protein-polymer conjugate retained over 90% activity over 6 hours, compared with native  $\alpha$ -CT that retains only around 50% activity.<sup>34</sup> This was attributed to steric and electronic shielding and shows that conjugating certain polymers to  $\alpha$ -CT can lead to increased stability.

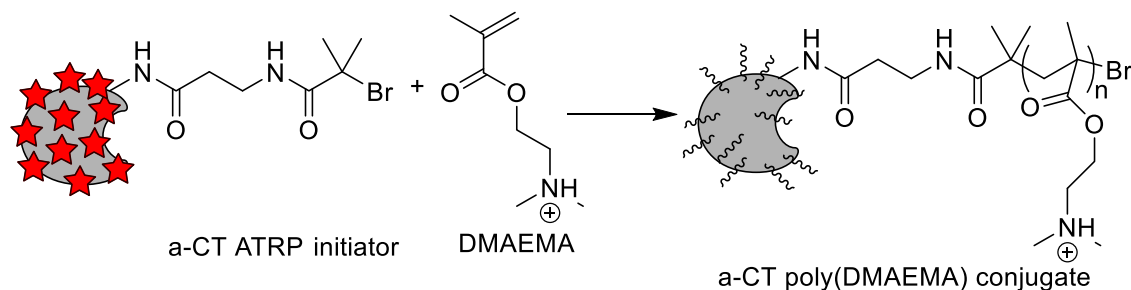


**Figure 2.3:** Polymerization of DMEMA by  $\alpha$ -CT conjugated ATRP initiators.<sup>17</sup>

#### 1.7.4 Lysozyme variant conjugations

Human lysozyme is a glycoside hydrolase and it performs  $\beta$ -1-4 glycosidic bond cleavage. By cleaving these bonds between N-acetylmuramic acid and N-acetyl-D-glucosamine residues in peptidoglycan bacterial cells walls, it can cause lysis and subsequent death of the cell.<sup>36</sup> As a consequence, lysozyme is critical to immune systems, for example, it kills bacteria in tears.<sup>37</sup>

Human lysozyme's structure and function is well characterized;<sup>35</sup> furthermore, the activity of the enzyme can be measured reliably by multiple assay methods making it a suitable target for this project.<sup>38-40</sup>

Lysozyme – most commonly hen egg white lysozyme (HEWL) - has been a frequent target of conjugation chemistry. CRP techniques such as RAFT<sup>41</sup> and SET-LRP<sup>42</sup> have been used to polymerize from lysozyme conjugated initiators. Both of these studies utilized succinimide-lysine coupling for the initial attachment. Lucius *et al.* showed that enzymatic activity was reduced as the conjugated polymer chain length increased.<sup>42</sup> However, when the enzyme was used to lyse negatively charged *M. lysodeikticus*, HEWL conjugated to the cationic polymer PDMAEMA showed an increase in activity. This was attributed to the "electrostatic attraction between the negatively charged cell wall and the positively charged polymer-conjugate."<sup>42</sup> The synthesis of PEGylated HEWL has also been reported.<sup>41</sup> Mono-PEGylated HEWL and mono-PEGylated human growth hormone were used to investigate the conformation of conjugated PEG in solution. The enzymes were analyzed by small-angle neutron scattering (SANS). The results showed that in this case, PEG behaves like a random coil adjacent to the protein, in contrast to the commonly assumed model of PEG encapsulating enzymes (Figure 2.4).<sup>44</sup>

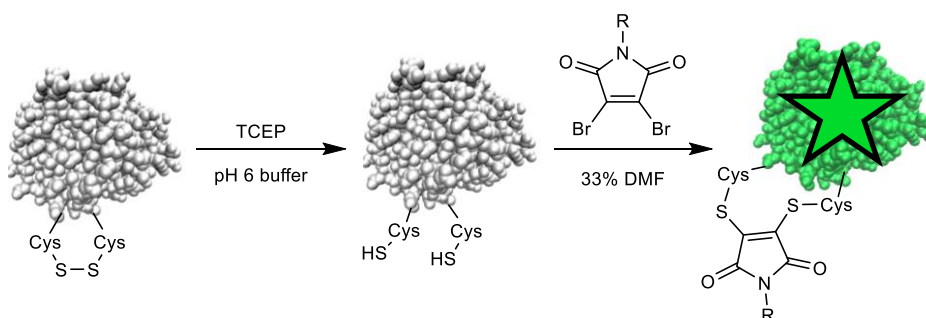


**Figure 2.4:** Topology of enzyme conjugated PEG (left) versus the incorrect, commonly assumed 'shroud' model (right). Figure reproduced from Pai *et al.*<sup>44</sup>

## 1.8 Results

### 1.8.1 Initial investigations into DBM bridging of $\alpha$ -CT

The first aim of this project was to investigate the bridging of disulfide bonds in  $\alpha$ -CT. *N*-methyldibromomaleimide (M-DBM) was chosen as the initial conjugating molecule, due to its small size and reported resistance to hydrolysis.<sup>46</sup> In addition, tris(2-carboxyethyl)phosphine (TCEP) was used to reduce the disulfides prior to conjugation (Scheme 2.1). Unusually for disulfide based conjugations, reacting M-DBM under an optimized protocol produced a singular conjugate with three DTMs conjugated as observed by matrix-assisted laser desorption/ionization-time of flight mass spectroscopy (MALDI-ToF MS - Figure 2.5). This result suggests that two of the disulfides are not solvent accessible and therefore, under such conditions, this conjugation technique allows for site-specific conjugation.



**Scheme 2.1** Scheme of DBM disulfide bridging conjugations.

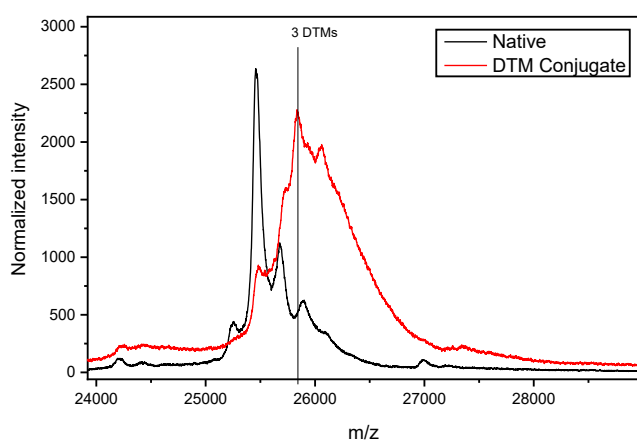


**Figure 2.5:** MALDI-ToF spectra of purified M-DBM  $\alpha$ -CT conjugate (red) against native  $\alpha$ -CT (black), showing formation of 3 DTM units.



A study into the progress of the conjugation with time, analyzed by MALDI-ToF, showed reaction of the native protein in 10 minutes, and the appearance of a strong band at around 25840 m/z representative of three DTMs per enzyme. However, after 90 minutes there is a large broad mass peak observed at around +700 m/z which corresponds to a conjugate with an average of 6.4 DTMs (Figure 2.6). It was thought that this may be caused by solvent or reagents becoming entrapped and desorbing with the enzyme. To test this hypothesis, the product enzyme was purified through a Bio-Spin® Column with Bio-Gel® P-30, which should allow removal of low molecular weight species (< 6000 Da) through centrifugation. The resultant purified enzyme was analyzed by MALDI-ToF (Figure 2.5) and the > 5 DTM peak is no longer present, suggesting that it was indeed caused by small molecule interference. It is noted that this could also be caused by side-product conjugates, which crash out upon conjugation and are therefore filtered off during the purification.

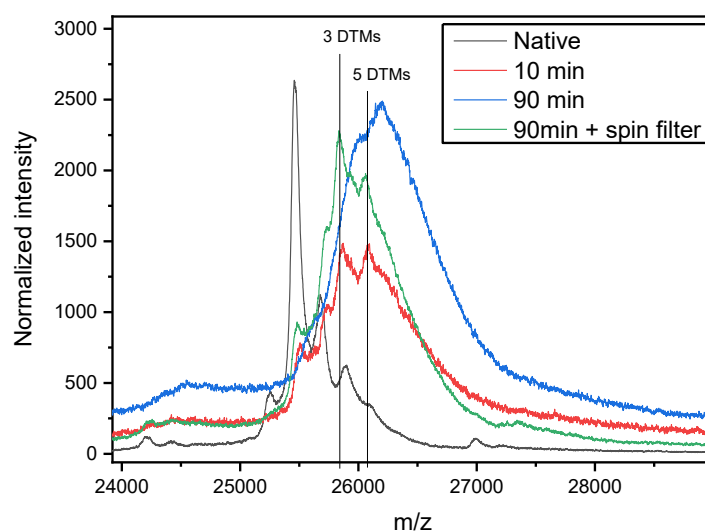


**Figure 2.6:** MALDI-ToF spectra of M-DBM  $\alpha$ -CT conjugates, at 10 mins (red), 90 mins (green) and after spin filtering (blue), against native  $\alpha$ -CT (black). Species above 5 DTM are clearly visible in the 90 min spectrum (blue) however, are removed in the spin filtered sample (green).

In an effort to obtain a quantitative analysis of the reaction, as well as to isolate the maximally conjugated species, high-performance liquid chromatography (HPLC) analysis of the conjugation was undertaken. After optimization of the method, HPLC chromatograms (Figure 2.7) were obtained for the conjugation mixture and other mixtures of reaction components ( $\alpha$ -CT with TCEP and  $\alpha$ -CT with MDBM without TCEP). Common to all chromatograms are numerous species eluted before 15 minutes followed by a broader peak at 15 minutes.

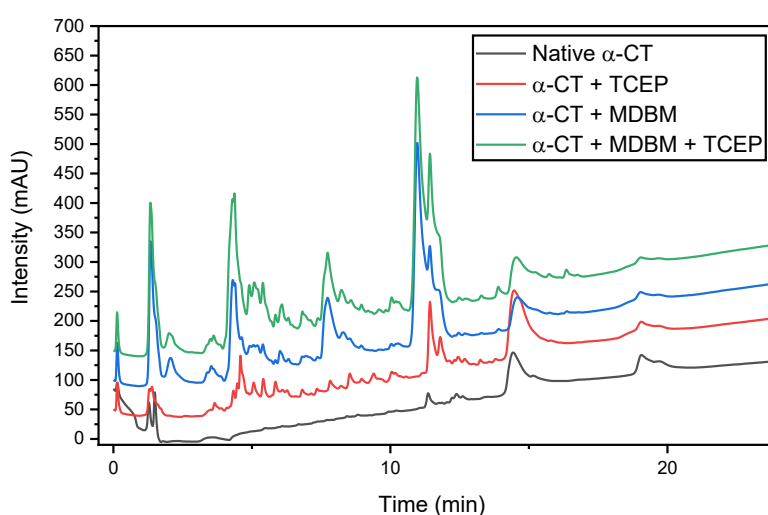


**Figure 2.7:** HPLC chromatogram of  $\alpha$ -CT under various reaction conditions, illustrating diiflucluty with autolysis to smaller species (< 14 min).

To identify these peaks, fractions were collected every minute and analyzed by MALDI-ToF MS. The results showed that no intact enzyme was observed until the 15-minute mark. The earlier peaks corresponded to smaller mass species (from 11-14 minutes), which could be attributed to digested and fragmented enzyme. HPLC analysis of the native enzyme that had been left in solution for several hours also showed an increase in signal intensities at 5-14 minutes, confirming this hypothesis.

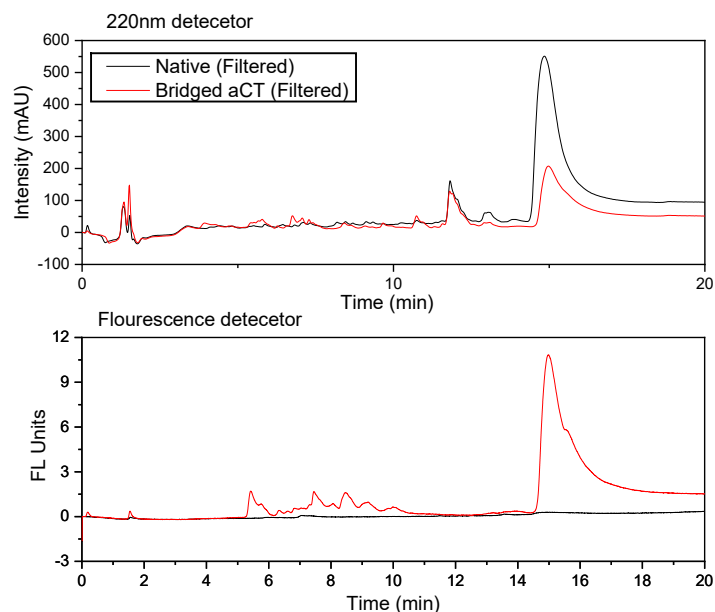


**Figure 2.8:** HPLC of the further optimized procedure with 220 nm and fluorescence detectors ( $\lambda_{\text{ex}}$ : 382 nm,  $\lambda_{\text{em}}$ : 531 nm).

Due to these impurities, it was decided to filter the samples and immediately HPLC the purified enzyme, using an optimized method (Figure 2.8). This did significantly reduce the signals that eluted before 14 minutes; however, separation of the unreacted native enzyme from the conjugated enzyme could still not be achieved. Positively, the conjugated enzyme produced a large fluorescence response in the fluorescence detector, making identification of conjugated species facile.

Sodium dodecyl sulfate polyacrylamide gel electrophoresis (SDS-PAGE) analysis of the conjugation was attempted. However, after multiple attempts, no fluorescence under a UV transilluminator was observed in the conjugated fragments and mass differentiation was difficult due to the small mass change upon M-DBM conjugation (Figure 2.22). For these reasons, SDS-PAGE analysis was determined to be an unsuitable method for characterizing this conjugation.

To ascertain whether the conjugation was residue-specific, analysis of the availability of the disulfides in  $\alpha$ -CT was undertaken. Firstly, a Kyte-Doolittle plot was drafted to establish if any of the disulfides were located in a particularly

hydrophobic or hydrophilic location in the enzyme (Figure 2.9). However, all disulfides lay across a neutral value and no significant conclusions could be drawn. To gain further insight, the solvent-accessible surface area of the enzyme was calculated using a crystal structure of the enzyme (from the Protein Data Bank: 4CHA)<sup>35</sup> and PyMol<sup>®</sup> software. It was clear that C1-C120 had the most solvent accessible surface area (Table 2.1) by this model, and C168-C182 and C191-220 displayed minimal to no solvent accessible surface area. This suggests that the C1-C122 bond is very likely to be the most reactive disulfide and that the C168-C182 and C191-220 bonds are the unmodified bonds. A trypsin digest was attempted to prove this hypothesis as this method would provide exact conjugation locations; however, as a consequence of  $\alpha$ -CT autolysis, this was excessively complex and not informative. Another method that could be used to gather information on site-specificity is MS proteomics (i.e. MS/MS), however investigation would be time and resource intensive.

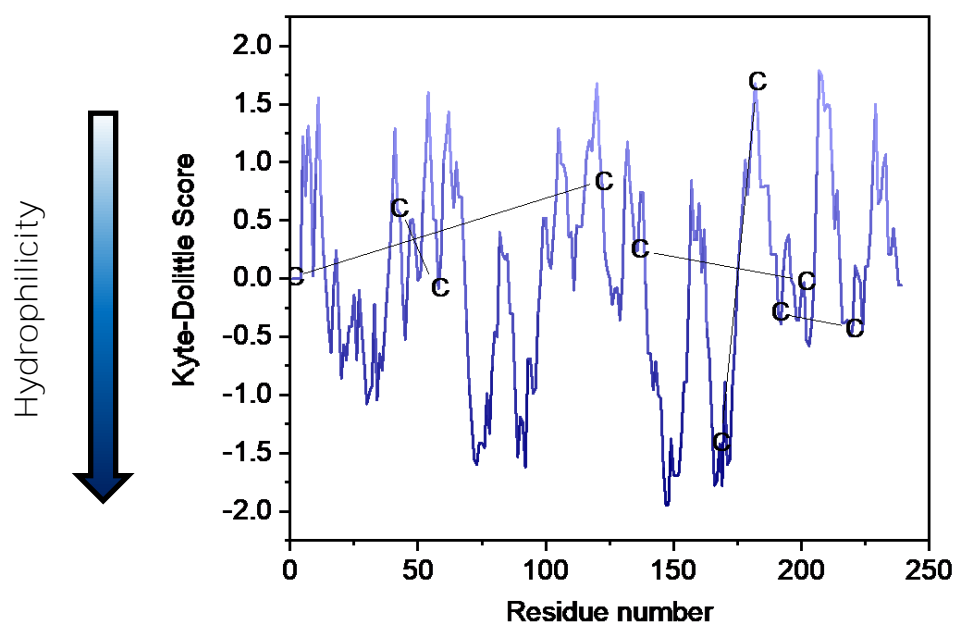


**Figure 2.9:** Kyte-Doolittle plot of  $\alpha$ -CT, showing approximate hydrophilicity of residues, including locations of disulfide bridges.

**Table 2.1:** Approximate solvent accessible surface area of disulfide bonds calculated using PyMol (PDB: 4CHA).

Disulfide	Surface area (Å)
C1-C120	122.0
C40-C57	19.1
C138-C200	17.5
C168-C182	0.5
C191-C220	0

The Baker and Caddick groups have preferentially used dithiomaleimides for the majority of their recent disulfide conjugations.<sup>46–48</sup> In some test reactions with TCEP they showed that both dibromomaleimides and dithiomaleimides react with TCEP, the reducing agent.<sup>48</sup> However, DBM showed a marginally greater reactivity with TCEP than dithiophenolmaleimide, hence their recent use of dithiophenolmaleimides. Therefore, it was decided to also investigate methyl-dithiophenolmaleimide as a conjugation agent. Using the same procedure as the M-DBM conjugation, no conjugation was observed with methyl-dithiophenolmaleimide (**2.1**) by MALDI-ToF analysis. Upon addition of DTM, the solution immediately went cloudy, indicative of DTM precipitating out of solution. Subsequent testing showed that a minimum of 30% DMF was required to solubilize dithiophenolmaleimide for the conjugation. Conjugations under these conditions did not produce any conjugated enzyme product. As a result of the harsher conditions required and lack of initial success, investigations into this method were no longer pursued.

### 1.8.2 Disulfide conjugations to human lysozyme

To ascertain that the bromomaleimide conjugations are applicable to a range of enzymes, human lysozyme was chosen as a second target for conjugation. Human lysozyme (HLZ) has four disulfide bonds as handles for

attachment, is smaller than  $\alpha$ -CT and does not perform autolysis.<sup>38</sup> Disulfide bridging to HLZ using M-DBM was undertaken using the same conditions as for  $\alpha$ -CT. In contrast to  $\alpha$ -CT, a distribution of 0-4 DTM species were observed by MALDI-ToF MS after purification (Figure 2.10). Interestingly, up to four DTMs can be formed per enzyme suggesting that all are solvent accessible, this which may be a result of the more hydrophilic nature of HLZ. However, as often observed in multi-site conjugation techniques,<sup>49</sup> only a distribution of differentially conjugated products was obtainable, indicating that the site-specific nature of this technique is limited. It should be noted that MALDI-ToF MS analysis of native HLZ showed a strong signal at around 14110 m/z, which does not match literature structures of HLZ, but has been observed by other groups.<sup>43</sup> However, the secondary peak at 14700 m/z correlates with published structures and therefore conjugation mass shifts were based upon this value.

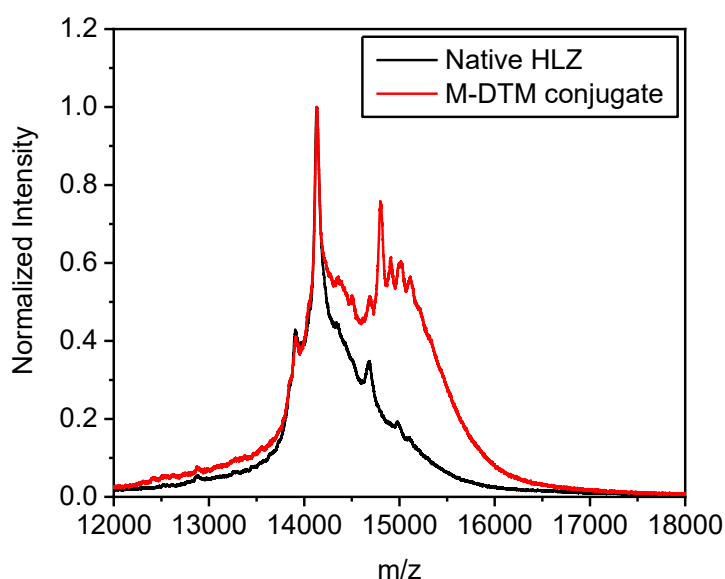


**Figure 2.10:** MALDI-ToF spectra of purified M-DTM HLZ conjugate (red) against native HLZ (black).

The retention of the tertiary structure of M-DTM HLZ was probed through circular dichroism (CD).  $\alpha$ -chymotrypsin exhibits a very poor CD signal in the

amide region for characterization,<sup>50</sup> and therefore CD analysis was undertaken on HLZ and the DTM HLZ conjugate. By recording the molar ellipticity  $-\Delta[\theta]_m$  at 222 nm, the  $\alpha$ -helicity of the enzyme can be measured. A negligible change in  $[\theta]_{222}$  was noted for the conjugate (97% of the native HLZ – Figure 2.11) and both CD spectra showed very similar structural features, indicating a minimal effect of conjugation on the tertiary structure of HLZ.

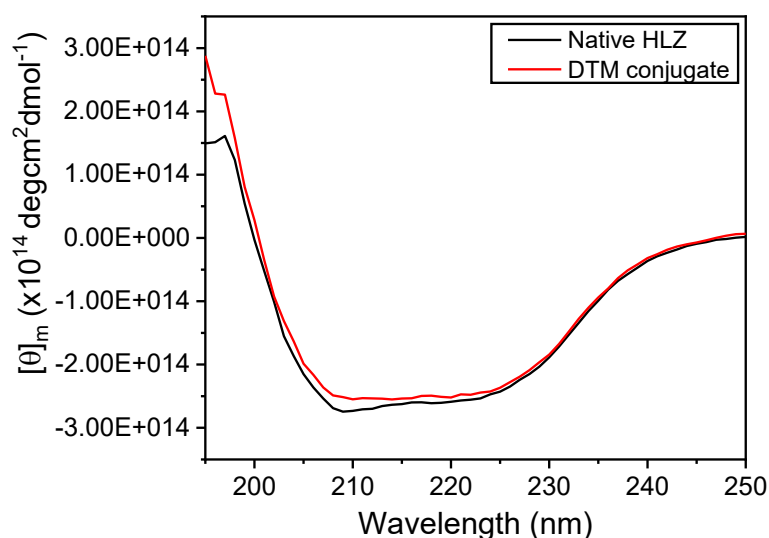


**Figure 2.11:** CD spectra of HLZ (black) and DTM-HLZ (red) in pH 6 phosphate buffer.

For further characterization, the denaturing temperature ( $T_m$ ) was measured for HLZ and the HLZ DTM conjugate, using differential scanning calorimetry (DSC). The  $T_m$  for the native enzyme was measured as 72.7 °C in pH 6 buffer, which compares well to previous literature.<sup>50</sup> For the HLZ DTM conjugate, multiple melts were observed (Figure 2.12), however, the major melt can be attributed to the singular DTM HLZ conjugate and was measured at 68.2 °C, suggesting a small loss in thermal stability upon DTM conjugation. The unresolved

melts observed below 68.2 °C could be attributed to conjugates with more than one DTM.

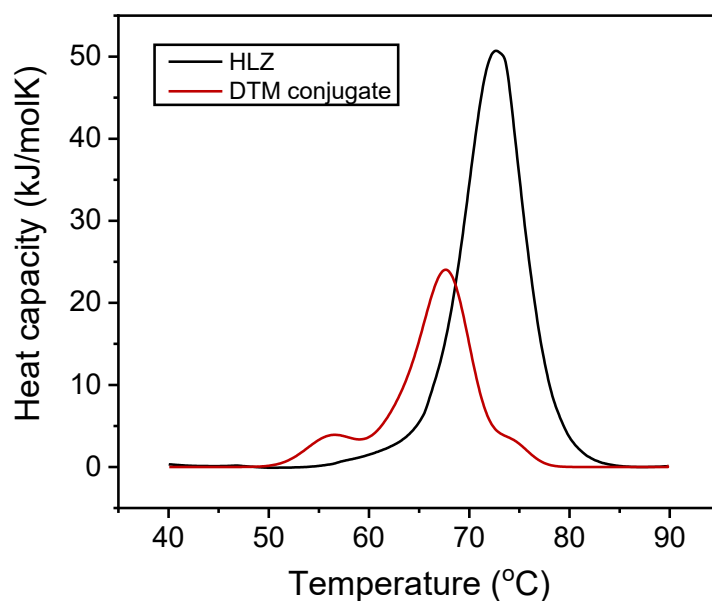
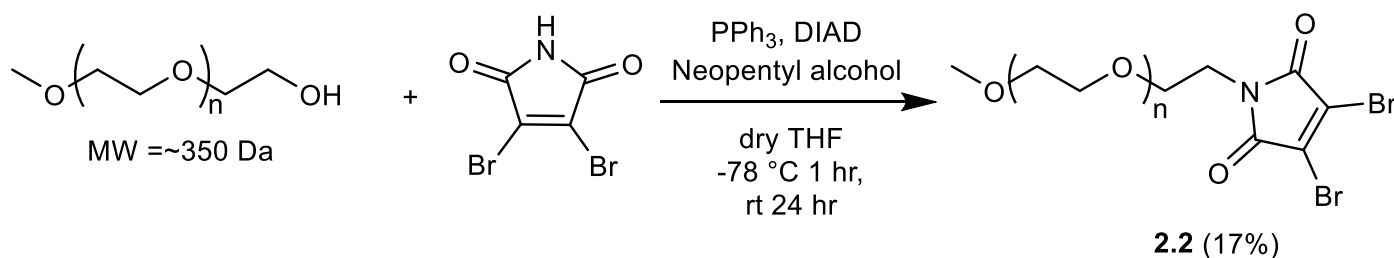


**Figure 2.12:** DSC spectra of HLZ (black) and DTM HLZ (red) recorded in pH 6 PB buffer at approximately 0.5 mg/ml. Recorded by Malin Suurkuusk (TA instruments).

### 1.8.3 PEGylation thorough disulfide bridging

To establish the effect of PEGylation *via* this disulfide bridging method on enzyme integrity, PEG-dibromomaleimide, PEG-DBM (**2.2**) was synthesized as a conjugation agent through a Mitsunobu reaction of hydroxyl-PEG<sub>350</sub> and DBM (Scheme 2.2).



**Scheme 2.2:** Synthesis of PEG-DBM (**2.2**).



PEGylation was attempted in pH 6 sodium phosphate buffer with a range of DMF concentrations from 0-33% v/v. MALDI-ToF MS analysis for the conjugation of both enzymes to PEG-DBM (**2.2**) showed that higher DMF concentration leads to higher degrees of PEG conjugation. For  $\alpha$ -CT conjugation, 33% v/v DMF conditions gave a mean, measured by Gaussian fit, of 1.8 attached PEG-DTM molecules (Table 2.2). However, the HLZ conjugate was observed to have a broader MALDI-ToF mass spectra (see 2.5.4.10), where an average of 2.0 PEG-DTMs per enzyme was observed (Table 2.2). It is hypothesized that the lower reactivity of the PEG-based conjugation can be attributed to the PEG chain providing steric hindrance to the conjugation through lowering chain end availability.

**Table 2.2.** Table showing number of attached units for disulfide conjugates observed by MALDI-ToF MS and standard deviation measured by Gaussian fit.

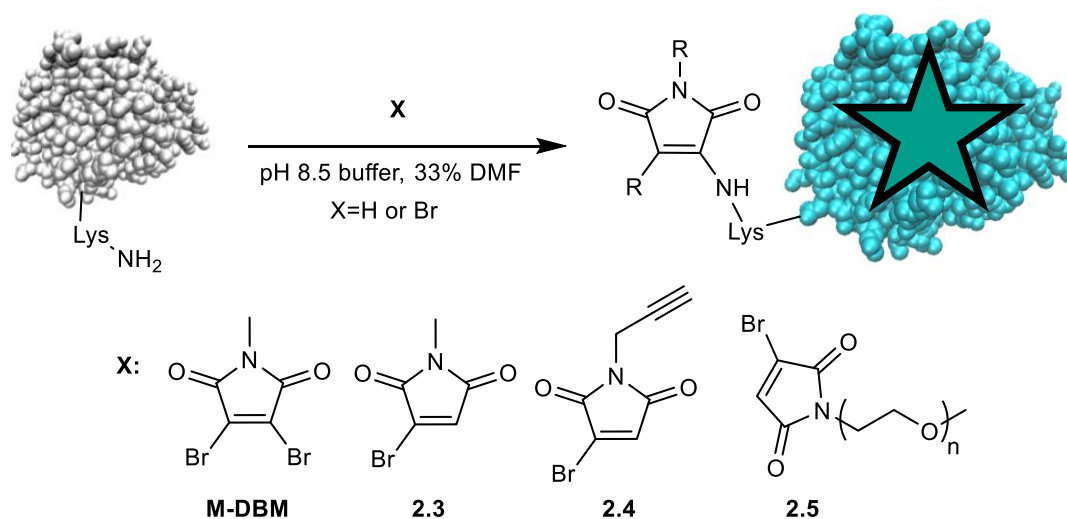
\*= Gaussian fit not possible, observed discrete conjugates listed.

Enzyme	Conjugate	# Attached
$\alpha$ -CT	M-DTM	3/5*
	PEG-DTM	1.8/5 $\pm$ 1.5
HLZ	M-DTM	0-4/4*
	PEG-DTM	2.0/4 $\pm$ 1.8

#### 1.8.4 Amine targeted bromomaleimide conjugations

Following the disulfide conjugations, conjugation utilizing lysine residues was investigated as a novel fluorogenic conjugation method. Using M-DBM the conditions of the conjugation were altered to mimic those in the synthesis of ABMs (Scheme 2.3). Conjugating to  $\alpha$ -CT overnight, in pH 8.5 tris buffer, resulted in a distribution of products as seen at around 26,600  $m/z$  by MALDI-ToF MS (Table 2.3 and section 2.5.4.2). The conjugation appears relatively slower than the thiol conjugations, which mirrors reaction rates observed in small molecule synthesis. One could hypothesize the polarizability of thiols makes them more nucleophilic

for these electrophiles. By completing a Gaussian fit of this peak an average of  $6.2 \pm 2.5$  ABMs per enzyme was observed. Through exposing HLZ to the same conditions, conjugation was also observed by MALDI-ToF MS with an average of  $2.7 \pm 2.3$  ABMs formed per enzyme from 6 amine handles (Table 2.3).



**Scheme 2.3:** Synthesis of ABM and MAM conjugates using conjugating agents M-DBM, **2.3**, **2.4** and **2.5**.

Our group has also shown the synthesis of MAMs under these conditions, producing a smaller more fluorescent dye. It was therefore decided to synthesize methyl-MBM (**2.3**), alkyne-MBM (**2.4**) and PEG-MBM (**2.5**) for conjugation. The alkyne substituent provides an opportunity for further functionalization, for example *via* copper-catalyzed azide-alkyne cycloaddition reactions (CuAAC).<sup>52</sup>

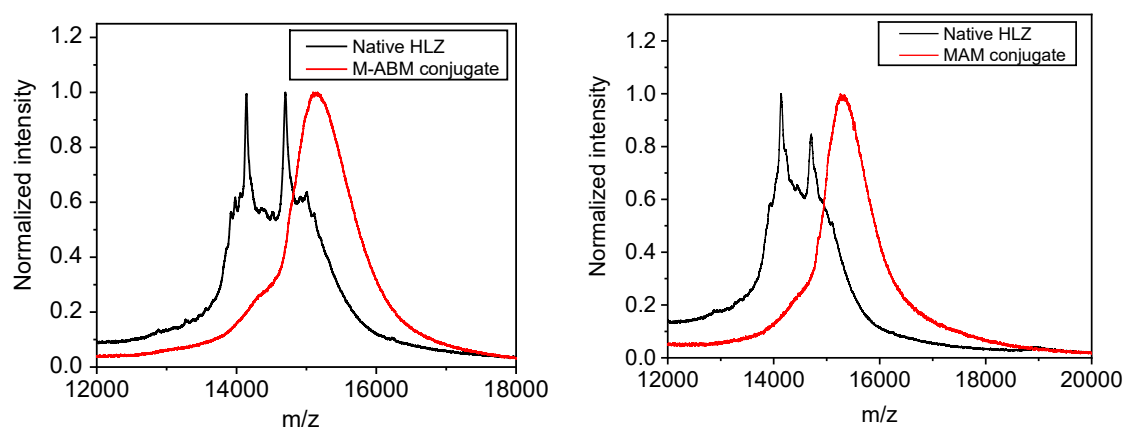


**Figure 2.13:** MALDI-ToF spectra of purified M-ABM HLZ conjugate (left, red) and alkyne-MAM conjugate (right, red) against native HLZ (black).

Conjugation of **2.3** and **2.4** was successful for both enzymes and subsequent MALDI-ToF MS analysis showed a distribution of products formed (Figure 2.13). Gaussian fits of the spectra are listed in Table 2.3, of note is the large distribution and deviation for conjugates, potentially due to trapped ions in the MALDI-ToF, but this highlights the poor site specificity and control in the conjugations. The reaction proved much more effective than the ABM reactions indicating conjugation of up to  $12.1 \pm 3.6$  MAMs for the  $\alpha$ -CT M-MAM conjugate. PEGylation using **2.4** was also successful; however, lower reactivity was again observed with an average of  $2.3 \pm 1.5$  PEG units attached on  $\alpha$ -CT and  $1.5 \pm 1.8$  on HLZ.

**Table 2.3.** Table showing number of attached units for lysine/amine conjugates observed by MALDI-ToF MS and standard deviation measured by Gaussian fit.

Enzyme	Conjugate	# Attached
$\alpha$ -CT	M-ABM	$6.2/17 \pm 2.5$
	M-MAM	$12.1/17 \pm 3.6$
	Alkyne-MAM	$11.2/17 \pm 1.8$
	PEG-MAM	$2.3/17 \pm 1.5$
HLZ	M-ABM	$2.7/6 \pm 2.3$
	M-MAM	$5.4/6 \pm 3.1$
	Alkyne-MAM	$4.9/6 \pm 2.5$
	PEG-MAM	$1.5/6 \pm 1.8$

To again help establish enzyme integrity the  $T_m$  of the MAM conjugate was investigated (Figure 2.14). For the M-MAM HLZ conjugate, a broad melt was observed as a consequence of many species being present. The average of these was measured at  $64.8^\circ\text{C}$ , suggesting a greater reduction in thermal stability compared to the DTM conjugate ( $68.2^\circ\text{C}$ ) as expected from a more modified conjugate.

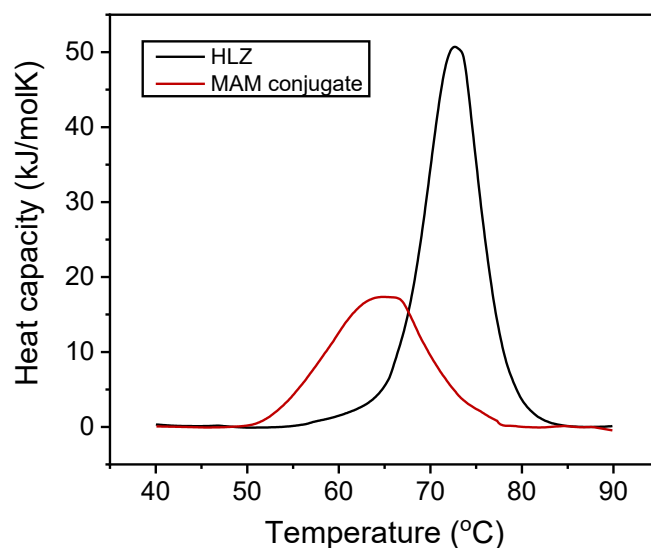


**Figure 2.14:** DSC spectra of HLZ (black) and MAM HLZ (red) recorded in pH 6 PB buffer at approximately 0.5 mg/ml. Recorded by Malin Suurkuusk (TA instruments).

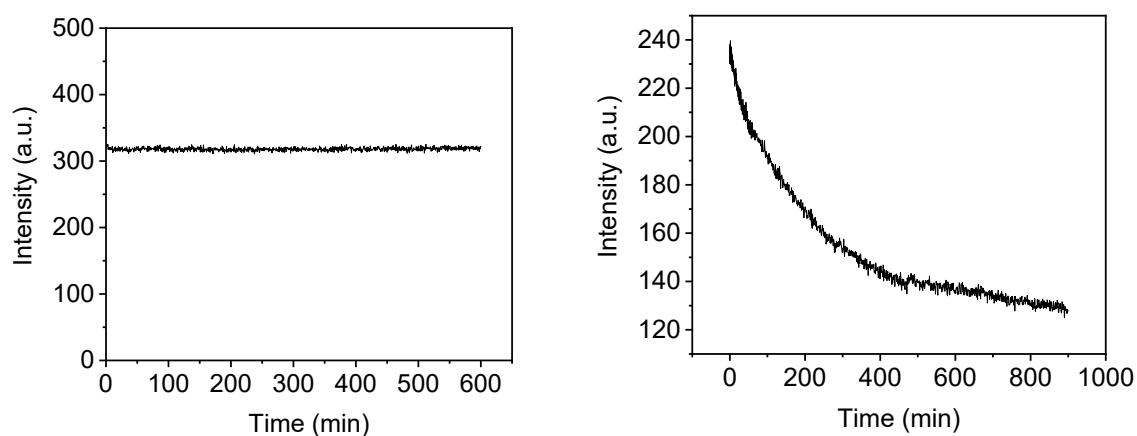


**Figure 2.15:** Fluorescence emission of conjugates in pH 8.5 tris buffer. Left: alkyne-MAM HLZ conjugate (511 nm emission and 356 nm excitation), right: M-DTM HLZ conjugate (540 nm emission and 395 nm excitation).

DTM conjugates have been shown to undergo hydrolysis at pH 8.5, dependent on structure, with half-lives as short as 16.5 minutes reported.<sup>53</sup> In order to ascertain the stability of MAM conjugates, the emission of alkyne-MAM HLZ was studied in pH 8.5 buffer. Under these conditions, no hydrolysis was

observed over 10 hours (Figure 2.15), whereas a significant reduction in emission was observed for an M-DTM HLZ conjugate control (Figure 2.15), this indicates greater resistance to hydrolysis in the MAM species and suggests no foreseeable hydrolysis under the conjugation conditions.

### 1.8.5 Fluorescence analysis of conjugates

To establish the fluorescence properties of conjugates, and therefore the turn-on nature of the conjugations, excitation/emission spectra were measured for all conjugates of both  $\alpha$ -CT and HLZ (Table 2.4). All recorded wavelengths were similar to those observed in water for small molecule species,<sup>51</sup> indicating retention of the maleimide motif.

**Table 2.4.** All measured  $\lambda_{\text{ex}}/\lambda_{\text{em}}$  maximum, and recorded  $\Phi_{\text{f}}(\%)$  for conjugates.

Enzyme	Conjugate	$\lambda_{\text{ex}}$ max(nm)	$\lambda_{\text{em}}$ max(nm)	$\Phi_{\text{f}}(\%)$
$\alpha$ -CT	M-DTM	382	532	-
	M-ABM	368	521	-
	M-MAM	368	530	-
	Alkyne-MAM	348	518	-
	PEG-DTM	386	528	-
	PEG-MAM	347	496	-
HLZ	M-DTM	395	540	$0.77 \pm 0.07$
	M-ABM	364	524	-
	M-MAM	364	521	-
	Alkyne-MAM	356	511	$0.69 \pm 0.04$
	PEG-DTM	408	538	$0.49 \pm 0.05$
	PEG-MAM	350	508	$1.43 \pm 0.24$

Small molecule MAMs have been shown to exhibit high (>59%) quantum yields in organic aprotic solvents; however, in water they are quenched significantly, exhibiting  $\Phi_{\text{f}} < 0.4\%$ .<sup>54</sup> Robin *et al.* have shown that by incorporating DTMs into nanostructures, shielding them from solvent quenching effects, the quantum yield can be restored (>30 %).<sup>55</sup> To investigate whether the same effect would be observed in enzymes, the quantum yield of two conjugates was

measured. The quantum yield of both MAM and DTM HLZ conjugates was measured in 18.2 MΩ.cm water, using a standard of quinine ( $\Phi_{\text{quinine}} = 59\%$ ). As shown in Table 2.4, the alkyne-MAM HLZ conjugate exhibited a quantum yield of  $\Phi_{\text{f}(\%)} = 0.7 \pm 0.04$  ( $\lambda_{\text{ex}} = 362$  nm) and the M-DTM HLZ conjugate of  $\Phi_{\text{f}(\%)} = 0.8 \pm 0.07$  ( $\lambda_{\text{ex}} = 365$  nm). The quantum yields for both conjugates have increased compared to the DTM and MAM small molecule analogues in water (all less than 0.4%);<sup>54</sup> however, the values were significantly lower than the fluorescent proteins currently used and would not meet the brightness requirements for applications such as fluorescence microscopy.<sup>56</sup> The quantum yield of the PEGylated HLZ samples were also measured to compare to the small molecule analogues. The PEG-DTM HLZ conjugate exhibited a quantum yield of  $\Phi_{\text{f}(\%)} = 0.5 \pm 0.05$  ( $\lambda_{\text{ex}} = 362$  nm), lower than the respective M-DTM conjugate. This could be attributed to the lower degree of conjugation observed for the polymer species. Theoretically, the most accessible and least shielded disulfide would be the most likely to undergo conjugation, leading to high solvent accessibility, and therefore fluorescence quenching, of the resulting maleimide moiety. In contrast, the PEG-MAM species exhibited a quantum yield of  $\Phi_{\text{f}(\%)} = 1.4 \pm 0.2$  ( $\lambda_{\text{ex}} = 364$  nm), double the quantum yield of the respective alkyne-MAM conjugate. In this case, despite exhibiting a lower degree of conjugation compared to the small molecule conjugate, it would appear the polymer chain provides a solvent shielding effect to the MAM dye.

### 1.8.6 Activity analysis of conjugates

To further establish the structural integrity of the conjugates and to check the catalytic activity of the DTM and MAM α-CT conjugates, their activity was measured using a *p*-nitroaniline hydrolysis assay (details in 2.5.5).<sup>57</sup> The initial velocity was measured and compared to the native enzyme after periods of time in solution. Results indicated a drop-in activity after conjugation for all conjugates

(Figure 2.16A). Indeed, it is notable that the activity is comparable to that of the native enzyme left in solution for the same time period as the conjugation and purification (6 hours for the DTM conjugates and 24 hours for the MAM conjugates). This indicates that the chemical modification itself has negligible effect on enzyme activity, which corroborates with the CD analysis of the DTM HLZ conjugate. Positively, the stability of the enzyme over 4 days was unaffected (Figure 2.16B), suggesting the conjugates have similar stability and autolysis rate to the native  $\alpha$ -CT.

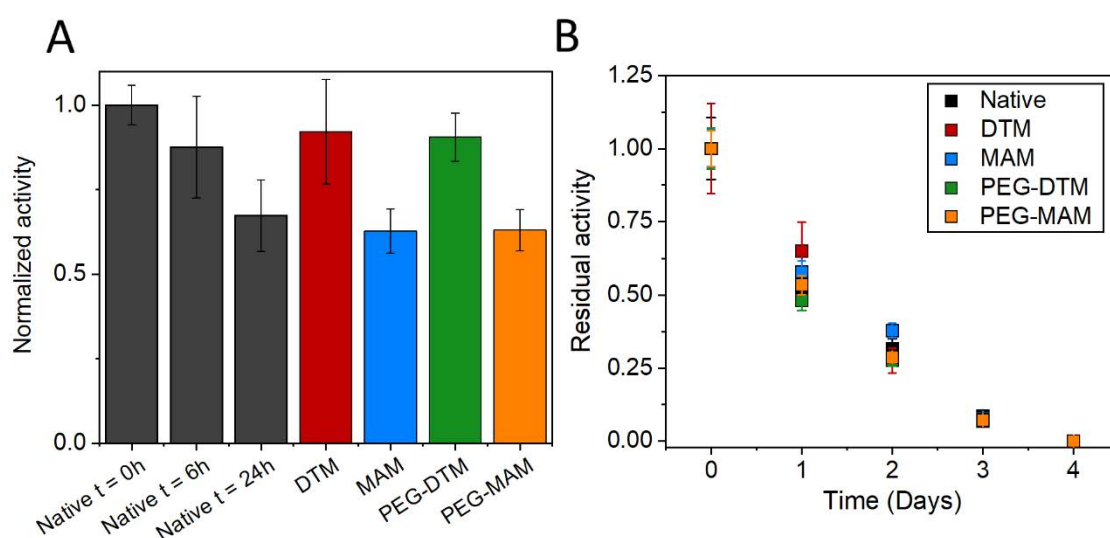


**Figure 2.16:** (A) Initial activity of  $\alpha$ -CT at time points against purified conjugates at t= 0 hr and (B) residual activities of native  $\alpha$ -CT and conjugates (black = native enzyme; red = M-DTM conjugate; blue = alkyne-MAM conjugate; green = PEG-DTM conjugate; yellow = PEG-MAM conjugate).

The HLZ conjugates were assayed by EnzChek® lysis to confirm their integrity. This assay relies on the lysis of fluorescein labelled *micrococcus lysodeikticus* cells, where upon cell lysis fluorescence signal increases.<sup>36</sup> When stored at room temperature the conjugates show no discernible difference in activity compared to native HLZ (Figure 2.17A). To discern whether any differences in stability are observed in more extreme conditions, the conjugates were also examined at 50 °C and their activity was measured at various time

intervals. It has been shown that under raised temperature storage the stability of native HLZ is negatively affected.<sup>58</sup> Results showed that the MAM conjugates showed only a minor decrease in activity over 7 days, comparable to that of the native enzyme. On the other hand, the DTM conjugates exhibited a decrease in activity. Specifically, the M-DTM conjugate lost all activity over 9 days compared to the native enzyme which retained 44% activity (Figure 2.17B). This indicates that disulfide re-bridging negatively affected enzyme stability at raised temperature, with the M-DTM conjugate, having the most DTM bridged disulfides, being least stable. This suggests that the stability of future DTM bio-conjugates should be carefully considered.

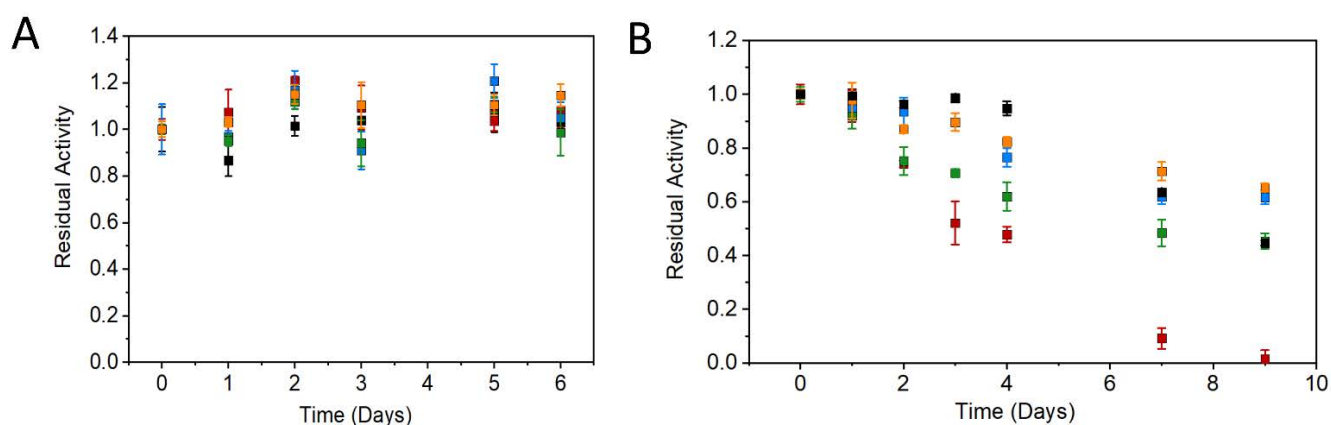


**Figure 2.17:** The residual activity, by EnzChek® lysis assay, of native HLZ and conjugates when stored at (A) room temperature (B) 50 °C (black = native enzyme; red = M-DTM conjugate; blue = alkyne-MAM conjugate; green = PEG-DTM conjugate; yellow = PEG-MAM conjugate).



## 1.9 Conclusions

In conclusion, enzyme conjugates have been synthesized by reacting dibromomaleimides and monobromomaleimides with reduced disulfides and free amines in human lysozyme and  $\alpha$ -chymotrypsin. Reactions of dibromomaleimides with reduced disulfides produced dithiomaleimide bridged enzyme conjugates, which showed fluorescence upon formation. Both  $\alpha$ -CT and HLZ DTM conjugates showed the same stability as the native enzyme when stored at room temperature, and exhibited negligible structural change by circular dichroism. However, at elevated temperature storage (50 °C) the HLZ DTM conjugates showed reduced stability, which corroborates with a decrease in the observed  $T_m$ , indicating this conjugation technique may have a destabilizing effect on some enzymes.

Reactions of dibromo- and monobromomaleimides with free amines in both enzymes produced fluorescent aminobromo- and monoaminomaleimide conjugates respectively. Monoaminomaleimides are shown to react with higher efficiency in both enzymes and conjugates are shown to be as stable as native enzymes at room temperature and at 50 °C, however, a decrease in  $T_m$  was observed by DSC analysis. Fluorescence analysis of all conjugated enzymes showed excitation and emission profiles comparable to small molecule studies; however, fluorescence quantum yields were low because of solvent quenching effects.

Both reactions were trialed as PEGylation methods using bromomaleimide functionalized PEG. Conjugation efficiency was detrimentally affected, attributed to the reduced availability of chain ends and steric hindrance. The PEG-MAM HLZ conjugate showed marginally increased fluorescence quantum yield attributed to solvent shielding effects of the short PEG chain.

## 1.10 Experimental

### 1.10.1 Instrumentation

NMR spectra were recorded on a Bruker Avance 300, a Bruker Avance III HD 400 or a Bruker Avance III HD 500 spectrometer at 298 K and at 300, 400 and 500 MHz respectively. Shifts are quoted in  $\delta$  in parts per million and quoted relative to the internal standard trimethylsilane (TMS) or the solvent peak.

High-Resolution Mass Spectra (HR-MS) were conducted on a Bruker UHR-Q-ToF MaXis spectrometer with electrospray ionization. MALDI-ToF MS was conducted on a Bruker Autoflex MALDI TOF/TOF spectrometer with a mass error of <5 ppm. Protein solution (2.0 mg/ml) was spotted on the MALDI plate followed by an equal volume of synaptic acid matrix (15 mg in 0.5 mL of water, 0.5 mL of acetonitrile and 1  $\mu$ L of trifluoroacetic acid (TFA)). The solvent was evaporated before recording the spectra and analysis using flexControl software. Gaussian fits were completed on conjugates which could be successfully fitted and full width at half maximum (FWHM) analysis was used to determine the standard deviation ( $\text{FWHM} = 2.355 \cdot \sigma$ ). It should be noted that MALDI-ToF MS analysis of native HLZ showed a strong signal at around 14110 m/z, which does not match literature structures of HLZ, but has been observed by other groups.<sup>40</sup> However, the secondary peak at 14692 m/z correlates with published structures and therefore conjugation mass shifts were based on this value.

Infrared spectra were recorded on neat samples using a Perkin Elmer Spectrum 100 FT-IR Spectrometer.

UV-Vis spectroscopy was carried out on a Perkin Elmer Lambda 35 UV/vis spectrometer or an Agilent Cary 60 UV-Vis Spectrometer at room temperature.

Fluorescence spectra were recorded using an Agilent Cary Eclipse Fluorescence spectrophotometer. Quartz cells with four polished sides (Starna) were used for fluorescence and UV-vis measurements.

Enzyme assays were conducted on a FLUOstar OPTIMA multi-well microplate reader according to the assay conditions for each individual enzyme. Human lysozyme room temperature activities were recorded on non-freeze-dried samples. Data was analyzed using OPTIMA analysis software.

Differential scanning calorimetry (DSC) analysis was performed on a TA Instruments Nano DSC. Blank runs were made with a buffer in both the sample and reference side. Each protein sample was run with a buffer in the reference side. Scans were made between 20 and 100 °C at 1 °C/min and a 600 s equilibration time was applied prior to each scan. Data is buffer subtracted (measured in pH 6 buffer at 0.5 mg/ml) and converted to molar heat capacity. The midpoint of the transitions was used to get an average  $T_m$  for each enzyme.

CD spectra were recorded on a J-720 CD spectrometer in 1 mM pH 6.0 phosphate buffer using a quartz cuvette with a path length of 0.1 cm. All experiments were run with ten acquisitions and recorded at 20 nm/min. The molar ellipticity was based upon protein concentration measured at 280 nm.

Reverse-phase high-performance liquid chromatography (RP-HPLC) was carried out using a 569223-U Discovery C18 column on a Varian 9250 with an autosampler. Sample detection was carried out using a photodiode array (PDA) detector and a fluorescence detector (382 nm excitation / 531 nm emission). The mobile phases used were (A) water with 0.04 % v/v TFA; B: MeCN (spectroscopy grade). A range of mobile phase gradients was investigated. The optimized gradient is shown below (Figure 2.18).

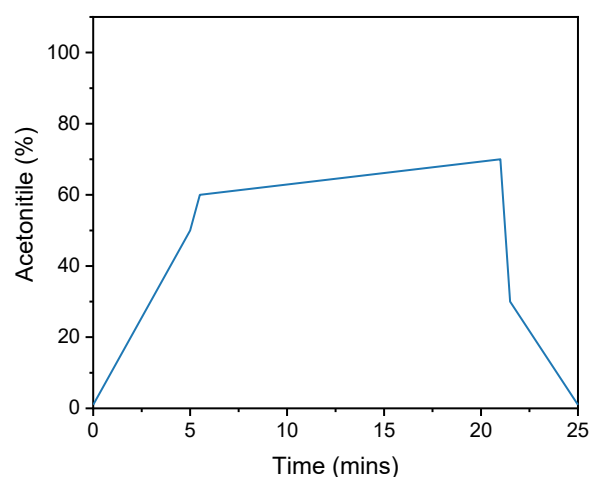


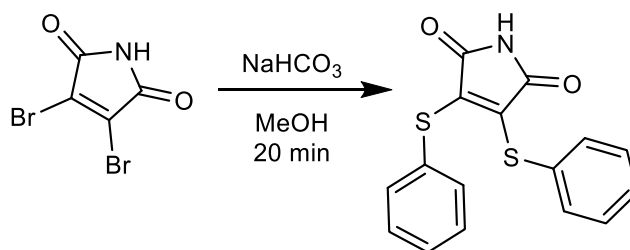
**Figure 2.18:** Elution gradient of water/acetonitrile used for enzyme analysis by HPLC.

### 1.10.2 Materials and chemicals

$\alpha$ -chymotrypsin (Type II from bovine pancreas, lyophilized powder) and human lysozyme (expressed in rice, lyophilized powder) were used as received from Sigma-Aldrich and stored in a freezer (at approximately  $-18^{\circ}\text{C}$ ). All other chemicals were obtained from either: Sigma Aldrich, Fisher Chemicals, Acros Chemicals, Alfa Aesar or IRIS biotech GmbH and used as received. Spin filters (MWCO 10 kDa) were obtained from Fisher Scientific.

### 1.10.3 Small molecule synthesis

#### 1.10.3.1 Synthesis of 3,4-bis(phenylthio)-1H-pyrrole-2,5-dione (2.1)



The synthesis of dithiophenolmaleimide (**2.1**) was based on a previously reported literature procedure.<sup>56</sup> In summary, dibromomaleimide (0.2 g, 0.78 mmol) and  $\text{NaHCO}_3$  was added to a round-bottom flask containing a stirrer bar and 15 mL of  $\text{MeOH}$ . To this thiophenol (0.19 g, 1.7 mmol) in 1 mL methanol was added, and an immediate yellow color formed. The reaction was stirred at room temperature for 20 mins. After which solvent was removed *in vacuo*, and the crude solid was purified by silica column by flash chromatography (8:2 petroleum ether 40-60 °C:  $\text{EtOAc}$ ) to yield a yellow solid **2.1** (177 mg, 57%).

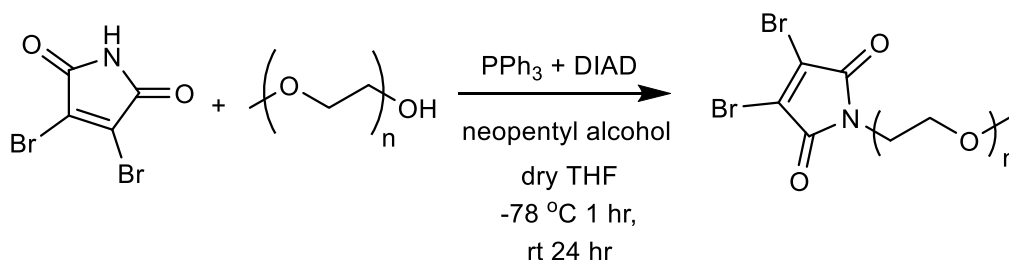
$^1\text{H}$  NMR ( $\text{DMSO}-d_6$ , 400 MHz, ppm)  $\delta$  = 7.30 – 7.18 (m, 10H,  $\text{ArH}$ ).

$^{13}\text{C}$  NMR ( $\text{DMSO}-d_6$ , 101 MHz, ppm)  $\delta$  = 168.03 (CO), 136.77 (CS), 131.23 (CH), 129.86 (C), 129.48 (CH), 128.36 (CH).

MS (ESI) -  $[\text{M}-\text{H}]^-$ : observed: 312.1 calculated: 312.0

Matches literature data.<sup>59</sup>

#### 1.10.3.2 2-3-dibromo-pyrrole-2,5-dione functionalized $\text{PEG}_{350}$ (2.2)



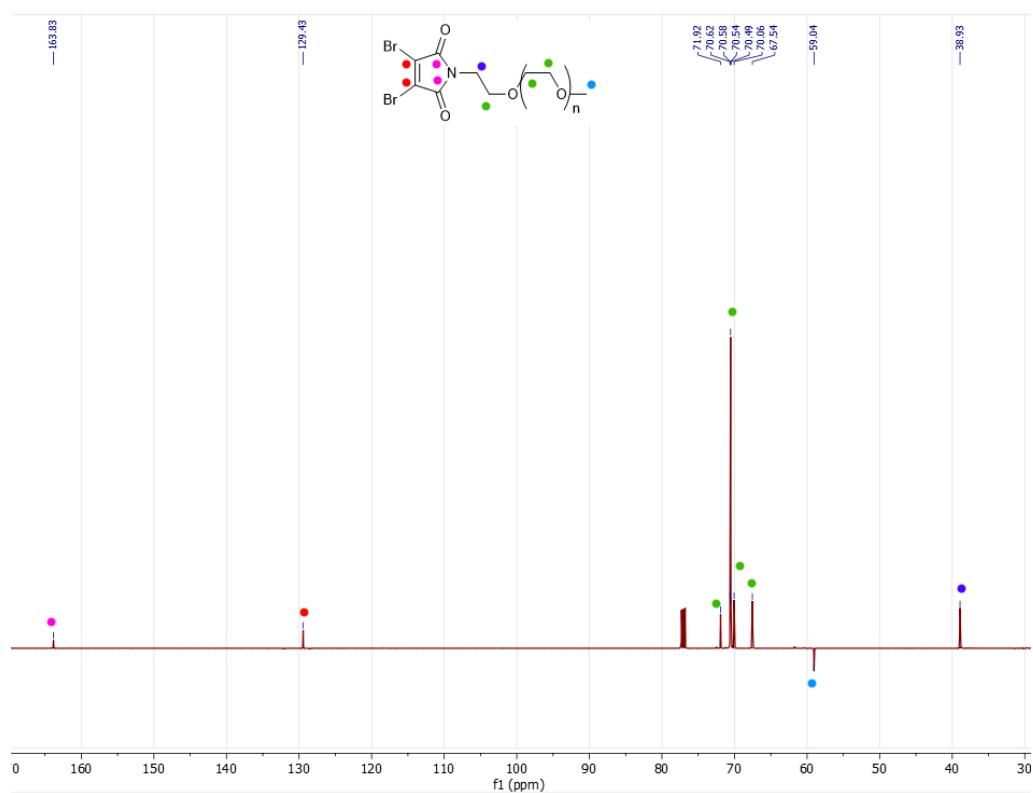
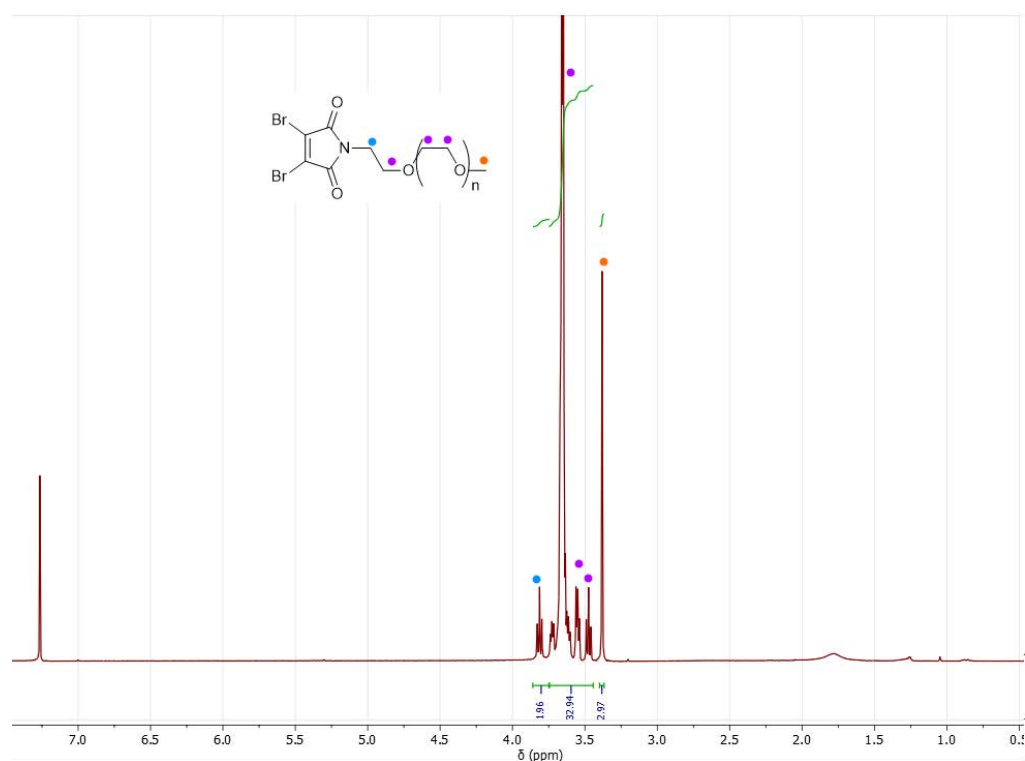
Triphenylphosphine (1.44 g, 5.5 mmol) was dissolved in dry tetrahydrofuran (100 mL) and cooled to -78 °C. Diisopropyl azodicarboxylate (1.14 mL, 5.5 mmol) was added dropwise and the solution was left to stir for 5 minutes. Methoxypoly(ethylene glycol) ( $M_n$  = 350 g/mol, 1.75 g, 5.5 mmol) was added dropwise to the cooled solution and left to stir for a further 5 minutes. Neopentyl alcohol (0.22 g, 2.5 mmol) was added and the solution was left to stir for a further 10 minutes. 3,4-dibromomaleimide (1.39 g, 5.5 mmol) was added to the solution and left to stir at -78 °C for 1 hour. The solution was allowed to warm to room temperature and left to stir for 24 hours. The solvent was removed *in vacuo*, and the resultant oil purified by silica column by flash chromatography (2:1 to 0:1 gradient of petroleum ether 40-60 °C : EtOAc) to yield a yellow oil **2.2** (287 mg, 17%).  $R_f$  (2:1 petroleum ether 40-60 °C : EtOAc): 0.1 to 0.4.

$^1\text{H}$  NMR ( $\text{CDCl}_3$ , 300 MHz, ppm)  $\delta$  = 3.82 (t,  $^3J_{\text{H-H}}$  = 5.6 Hz, 2H,  $\text{NCH}_2$ ), 3.71-3.53 (br m, 31H,  $\text{CH}_2\text{-CH}_2$ ), 3.38 (s, 3H,  $\text{CH}_3\text{-O}$ ).

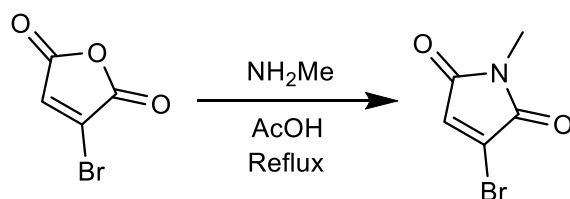
$^{13}\text{C}$  NMR ( $\text{CDCl}_3$ , 125 MHz, ppm)  $\delta$  = 163.8, 129.4, 71.9, 70.6-70.5, 70.1, 67.5, 59.0, 38.9

HR-MS (MaXis) -  $[\text{M}+\text{Na}]^+$  calculated  $m/z$  688.0764, observed  $m/z$  688.0768

FTIR ( $\text{cm}^{-1}$ ) -2872 ( $\nu_{\text{C-H}}$ ), 1716 ( $\nu_{\text{C=O}}$ ), 1104 ( $\nu_{\text{C-O}}$ )



### 1.10.3.3 Synthesis of 3-bromo-1-methyl-1H-pyrrole-2,5-dione (2.3)



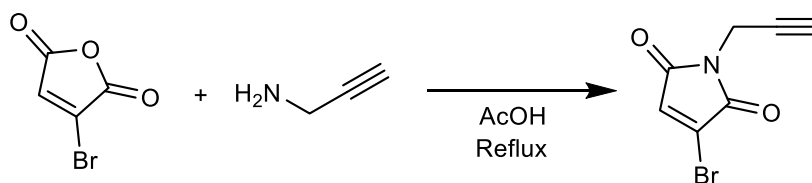
The synthesis was based on a previously reported literature procedure.<sup>57</sup> To a solution of bromomaleic anhydride (1 g, 5.65 mmol) in acetic acid (20 mL) was added methyl amine in ethanol (695  $\mu$ L, 5.65 mmol.) The solution was refluxed for 3 hours after which the solvent was removed *in vacuo*. The resultant solid was purified by silica column chromatography and eluted with 10% ethyl acetate in petroleum ether 40-60 °C to give a cream colored solid **2.3** (190 mg, 15%).  $R_f$ : 0.2.

$^1\text{H}$  NMR ( $\text{CDCl}_3$ , 500 MHz, ppm)  $\delta$  = 6.88 (s, 1H,  $\text{CHCBr}$ ), 4.33 (s, 3H,  $\text{NCH}_3$ ).

MS (ESI) -  $[\text{M}+\text{H}]^+$ : observed: 190.0 calculated: 189.9

Matches literature data.<sup>60</sup>

### 1.10.3.4 Synthesis of 3-bromo-1-(prop-2-yn-1-yl)-1H-pyrrole-2,5-dione (2.4)



The synthesis was based on a previously reported literature procedure.<sup>57</sup> To a solution of bromomaleic anhydride (1.2 g, 6.9 mmol) in acetic acid (15 mL) was added propargyl amine (432  $\mu$ L, 7.5 mmol.) The solution was refluxed for 6 hours after which the solvent was removed *in vacuo*. The resultant solid was purified by silica column chromatography and eluted with 100% dichloromethane ( $\text{CH}_2\text{Cl}_2$ ) to give a cream colored solid **2.4** (1.1 g, 78%),  $R_f$ (100%  $\text{CH}_2\text{Cl}_2$ ): 0.9.



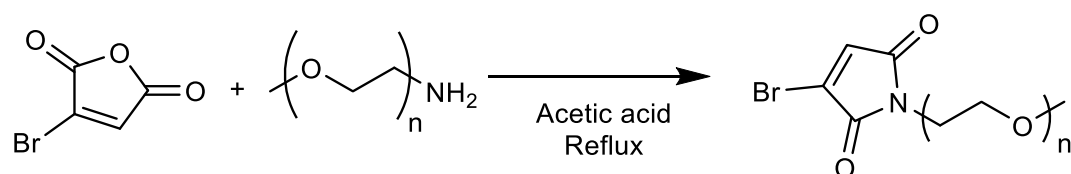
$^1\text{H}$  NMR ( $\text{CDCl}_3$ , 300 MHz, ppm)  $\delta$  = 6.39 (s, 1H,  $\text{CHCBr}$ ), 4.33 (d,  $^4J_{\text{H-H}}$  = 2.5Hz, 2H,  $\text{NCH}_2$ ) and 2.24 (t,  $^4J_{\text{H-H}}$  = 2.5Hz, 1H,  $\text{HC}\equiv\text{C}$ ).

$^{13}\text{C}$  NMR ( $\text{CDCl}_3$ , 75 MHz, ppm)  $\delta$  = 167.1 (CO), 162.1 (CO), 132.2 (CH), 131.7 (CBr), 76.4 ( $\text{CH}_2$ ), 72.1 (C) and 27.8 (CH).

HR-MS (MaXis) -  $[\text{M}+\text{Na}]^+$  calculated m/z 235.9318, observed m/z 235.9316

Matches literature data.<sup>57</sup>

#### 1.10.3.5 3-bromo-pyrrole-2,5-dione-functionalized PEG<sub>800</sub> (2.5)



Methoxypoly(ethylene glycol)-amine<sub>800</sub> ( $M_n$  = 800 g/mol, 0.48 g, 0.6 mmol) was added to 15 mL of acetic acid. Bromomaleic anhydride (0.13 g, 0.75 mmol) was added and the solution was refluxed at 114 °C overnight. The solvent was removed *in vacuo* and the resultant orange oil purified by flash chromatography on a silica column (2:1  $\text{CH}_2\text{Cl}_2$ :methanol) to give a viscous oil **2.5** that was ~90% functionalized with PEG, as determined by  $^1\text{H}$  NMR spectroscopy (0.403 g, 67%).  $R_f$  (2:1  $\text{CH}_2\text{Cl}_2$ :methanol): 0.05-0.35.

$^1\text{H}$  NMR ( $\text{CDCl}_3$ , 300 MHz, ppm)  $\delta$  = 6.88 (s, 0.9H,  $\text{CHCBr}$ ), 3.77 (t,  $^3J_{\text{H-H}}$  = 5.4Hz, 2H,  $\text{NCH}_2$ ), 3.68-3.53 (br m, 76H,  $\text{CH}_2\text{-CH}_2$ ), 3.38 (s, 3H,  $\text{CH}_3\text{-O}$ ).

$^{13}\text{C}$  NMR ( $\text{CDCl}_3$ , 125 MHz, ppm)  $\delta$  = 168.4 (CO), 165.3 (CO), 132.0 (CH), 131.4 (CBr), 71.9 ( $\text{CH}_2$ ), 70.6-70.5 (m,  $\text{CH}_2$ ), 70.1 ( $\text{CH}_2$ ), 67.7 ( $\text{CH}_3$ ), 38.08 ( $\text{CH}_2$ ).

HR-MS (MaXis) -  $[\text{M}+\text{Na}]^+$  calculated m/z 872.3250, observed m/z 872.3257

FTIR ( $\text{cm}^{-1}$ ) – 2824 ( $\nu_{\text{C-H}}$ ), 1720 ( $\nu_{\text{C=O}}$ ), 1106 ( $\nu_{\text{C-O}}$ ).

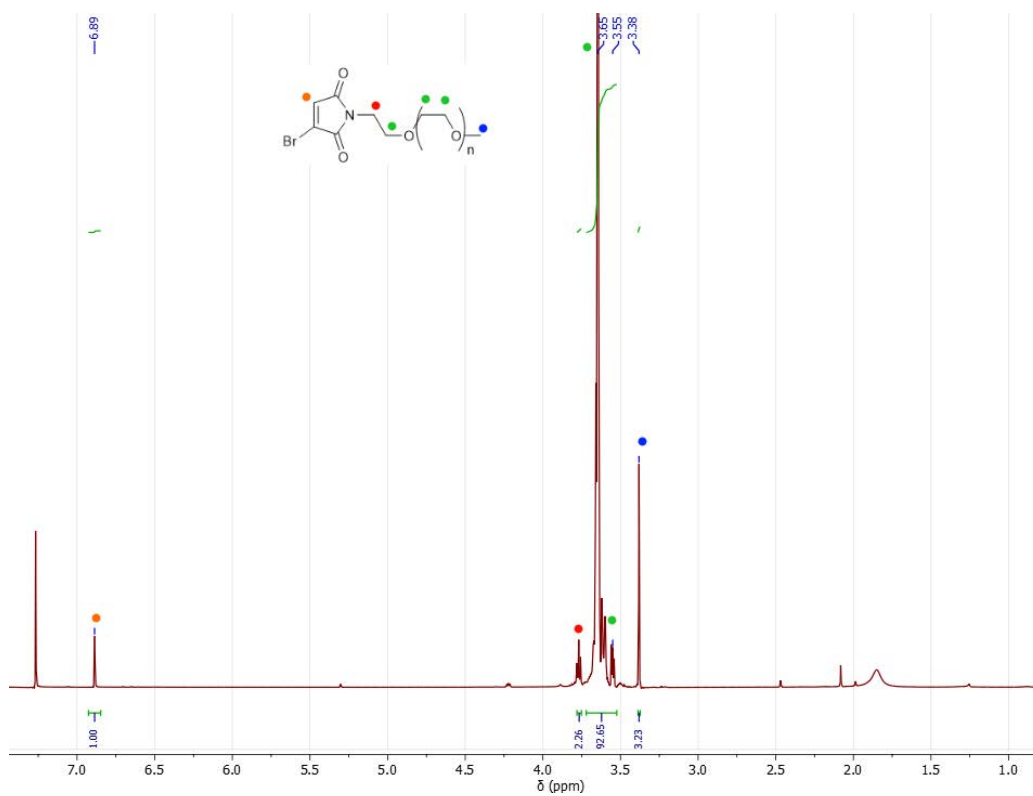


**Figure 2.20:** <sup>1</sup>H NMR spectrum of 2.5.

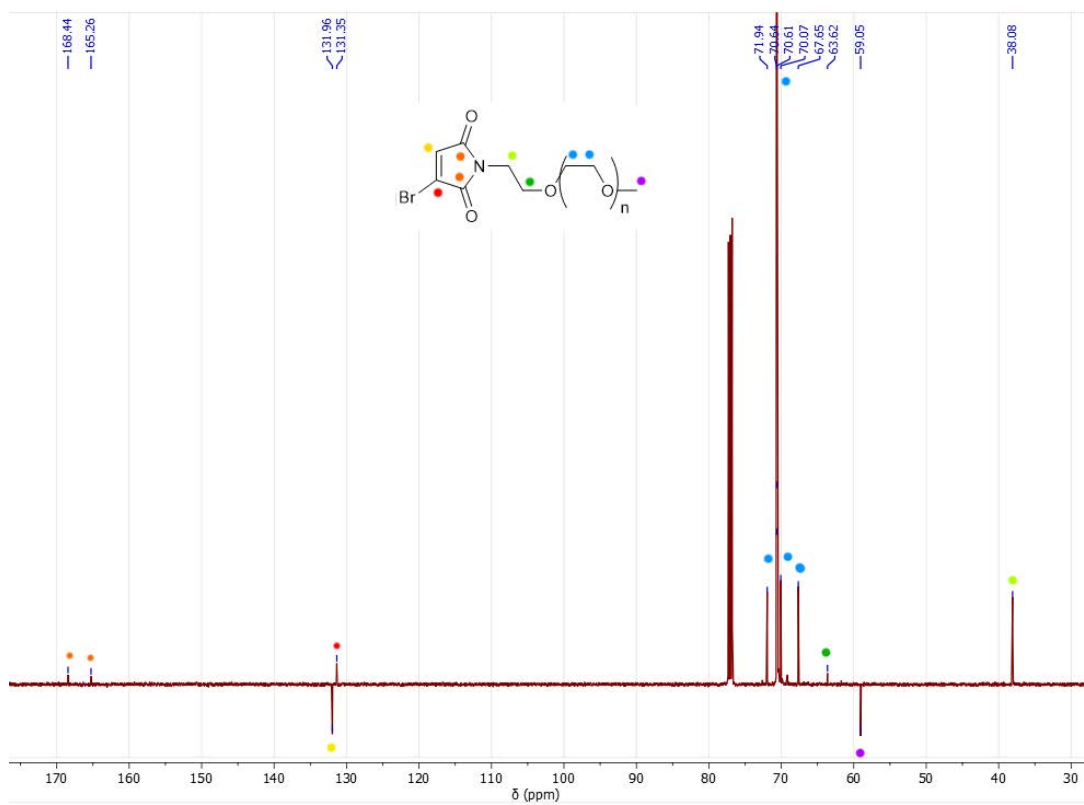
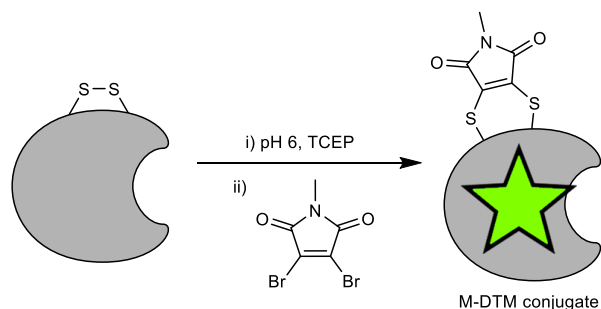


**Figure 2.21:** <sup>13</sup>C NMR spectrum of 2.5.

#### 1.10.4 Enzyme conjugations

##### 1.10.4.1 $\alpha$ -CT disulfide conjugation with M-DBM



3 mg (0.12  $\mu$ mol) of  $\alpha$ -CT was dissolved in 1.3 mL pH 6 phosphate buffer (0.1 M), followed by the addition of 0.1 mL tris(2-carboxyethyl)phosphine (TCEP) solution (4  $\mu$ mol in 18.2 M $\Omega$ .cm water). The reaction was vortexed and left to stir for 30 minutes. After this, a 0.1 mL of M-DBM (5  $\mu$ mol in DMF) was added and mixture vortexed. Maximum degree of conjugation, identified by MALDI-ToF MS analysis, was reached after 30 minutes. The crude enzyme was purified by ultrafiltration (AMICON® stirred cell) and freeze-dried.

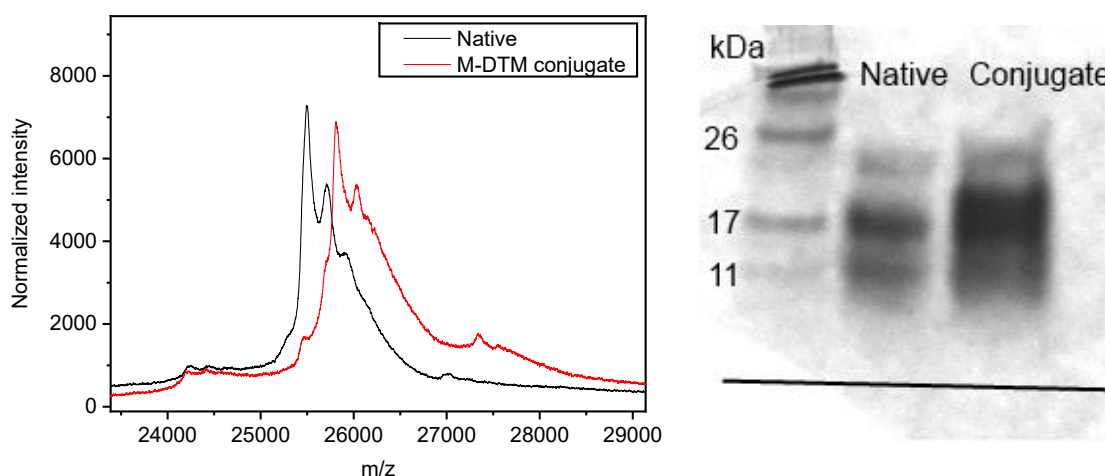


**Figure 2.22:** MALDI-ToF spectra of conjugate and native enzyme (left) and SDS-PAGE of conjugation (right).

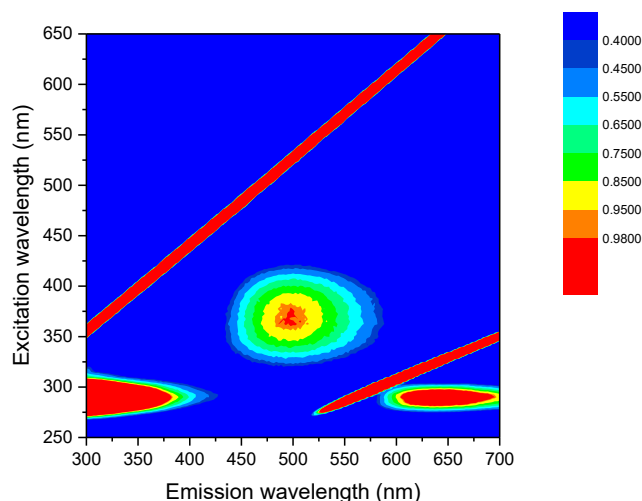
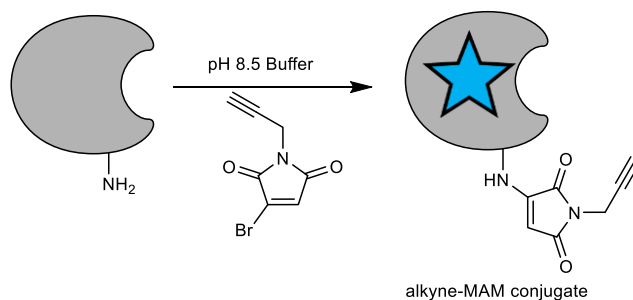


**Figure 2.23:** 2D excitation/emission spectrum of M-DTM  $\alpha$ -CT conjugate in pH 6 buffer.

#### 1.10.4.2 $\alpha$ -CT lysine conjugation with alkyne-MBM



3 mg (0.17  $\mu$ mol) of  $\alpha$ -CT was dissolved in 1 mL of 0.1 M pH 8.5 tris buffer. 0.5 mL of alkyne-DBM (**2.3**) solution (17  $\mu$ mol in DMF) was added and the solution vortexed. Maximum degree of conjugation, identified by MALDI-ToF MS analysis, was reached after leaving overnight (approximately 15 hours). The crude enzyme was purified by ultrafiltration (AMICON® stirred cell) and freeze-dried.

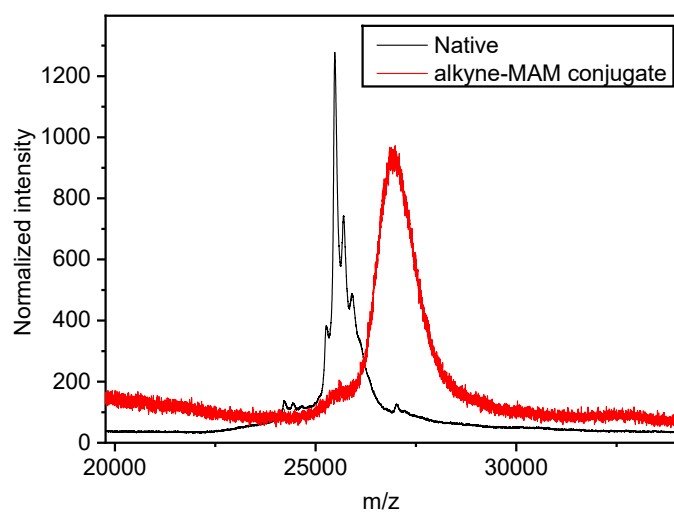


**Figure 2.24:** MALDI-ToF spectra of conjugate and native enzyme.

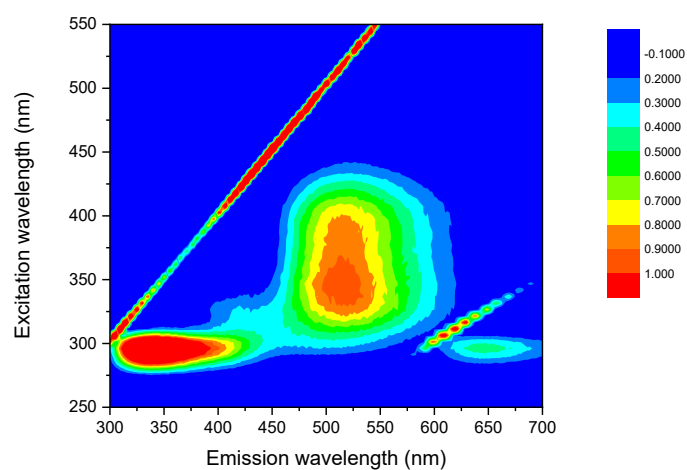
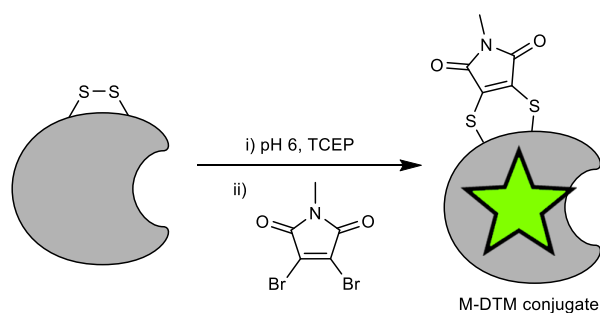


**Figure 2.25:** 2D excitation/emission spectrum of alkyne-MAM  $\alpha$ -CT conjugate in pH 6 buffer.

#### 1.10.4.3 Human lysozyme disulfide conjugation with M-DBM



3 mg (0.2  $\mu\text{mol}$ ) of HLZ was dissolved in 0.9 mL of 0.1 M pH 6 phosphate buffer, followed by addition of addition of 0.1 mL *tris*(2-carboxyethyl)phosphine (TCEP) (4.5  $\mu\text{mol}$  in 18.2 M $\Omega$ .cm water). The reaction was vortexed and left to stir for 30 minutes. After this, a 0.1 mL of M-DBM (6.3  $\mu\text{mol}$  in DMF) was added and mixture vortexed. Optimal conjugation identified by MALDI-ToF MS analysis was reached after 30 minutes. The crude enzyme was purified by ultrafiltration (AMICON® stirred cell) and freeze-dried.

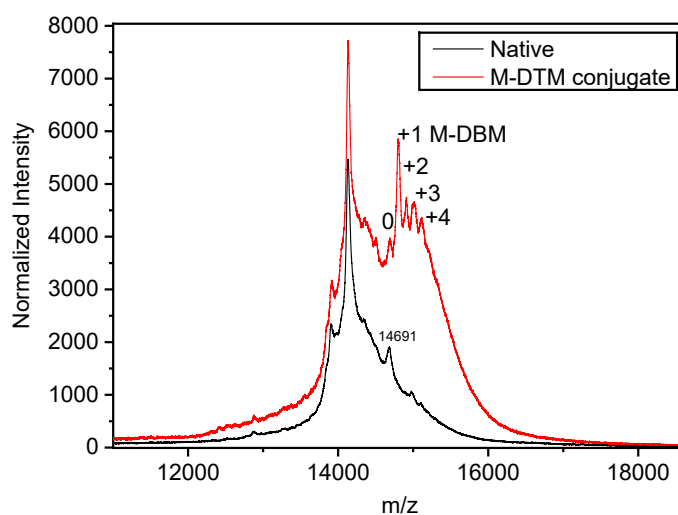


**Figure 2.26:** MALDI-ToF spectra of conjugate and native enzyme.

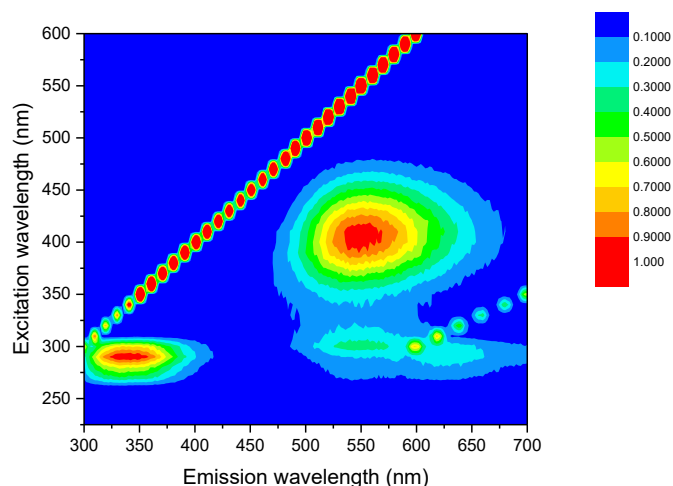
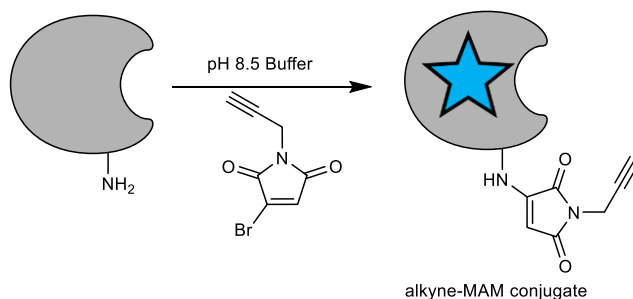


**Figure 2.27:** 2D excitation/emission spectrum of M-DTM HLZ conjugate in pH 6 buffer.

#### 1.10.4.4 Human lysozyme lysine conjugated with alkyne MAM



3 mg (0.2  $\mu$ mol) of human lysozyme was dissolved in 1 mL of 0.1 M pH 8.5 tris buffer. 0.5 mL of alkyne-DBM (**2.3**) solution (14  $\mu$ mol in DMF) was added and the solution vortexed. Maximum degree of conjugation, identified by MALDI-ToF MS analysis, was reached after leaving overnight (aproximetly 15 hours). The crude enzyme was purified by ultrafiltration (AMICON® stirred cell) and freeze-dried.

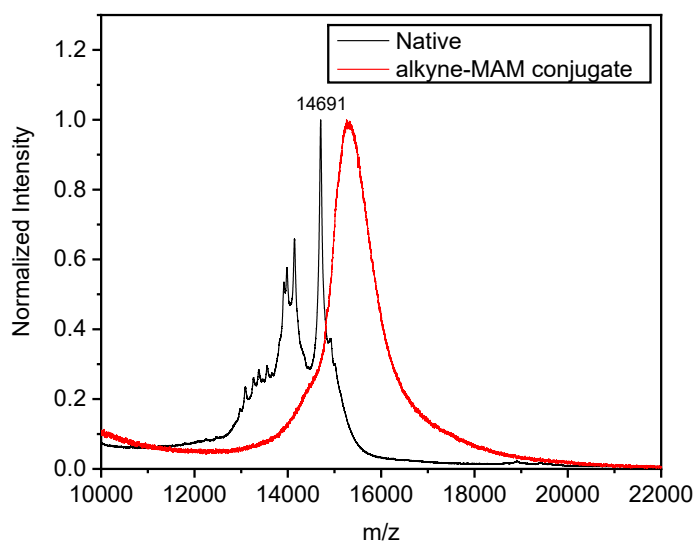


**Figure 2.28:** MALDI-ToF spectra of conjugate and native enzyme.

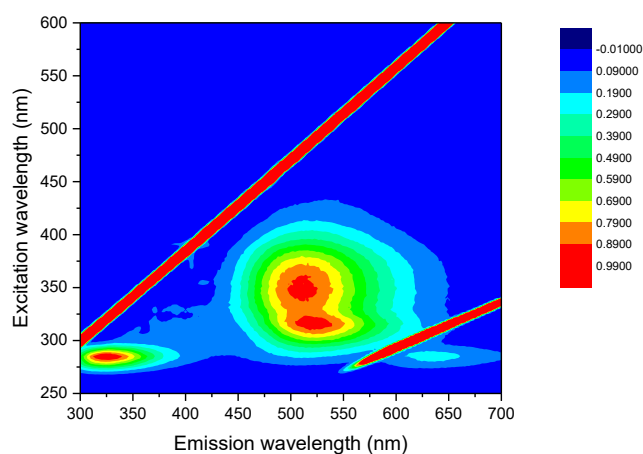
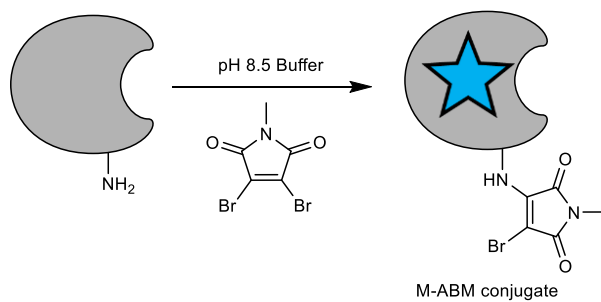


**Figure 2.29:** 2D excitation/emission spectrum of M-DTM HLZ conjugate in pH 6 buffer.

#### 1.10.4.5 $\alpha$ -CT lysine conjugation with M-DBM





ABM functionalized  $\alpha$ -CT was synthesized as per alkyne-MBM (2.6.3.2), without purification, using M-DBM.

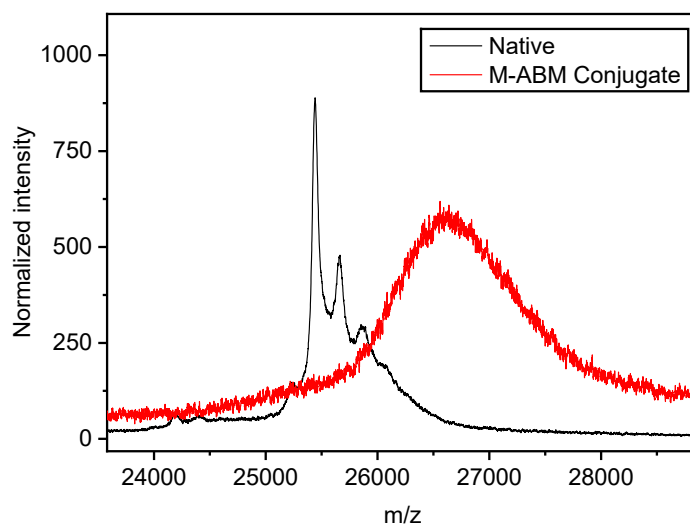


**Figure 2.30:** MALDI-ToF spectra of conjugate and native enzyme.

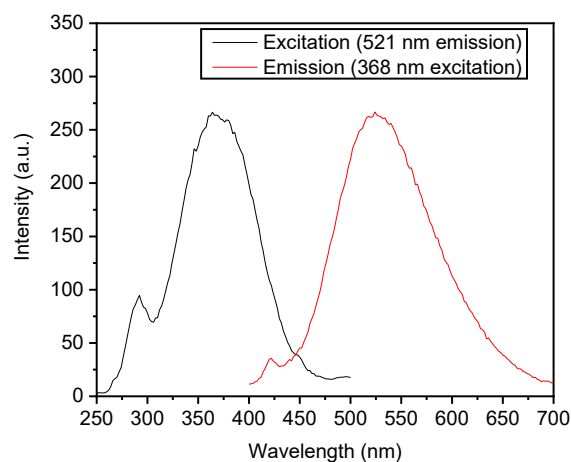
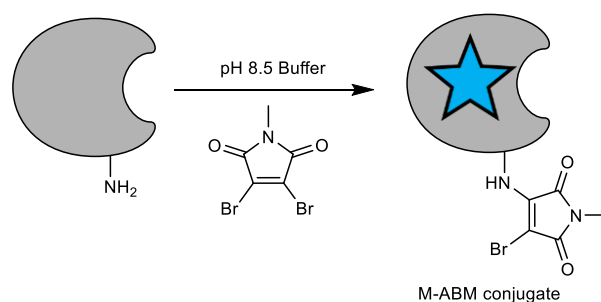


**Figure 2.31:** Excitation/emission spectrum of methyl-MAM  $\alpha$ -CT conjugate in pH 6 buffer.

#### 1.10.4.6 HLZ lysine conjugation with M-DBM



ABM functionalized HLZ was synthesized as per alkyne-MBM (2.6.3.4), without purification, using M-DBM.

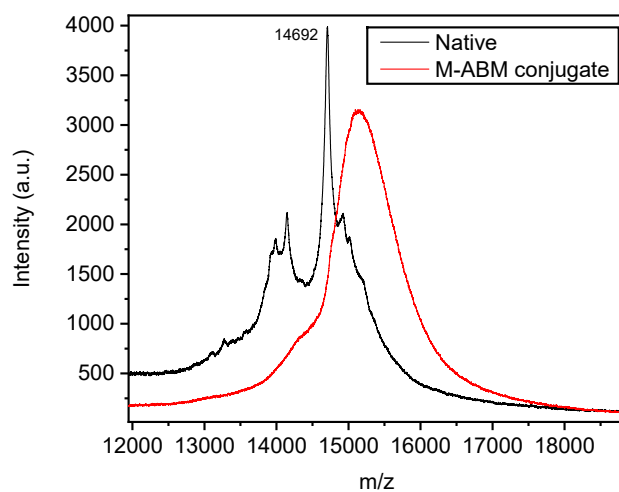


**Figure 2.32:** MALDI-ToF of conjugate and native enzyme.

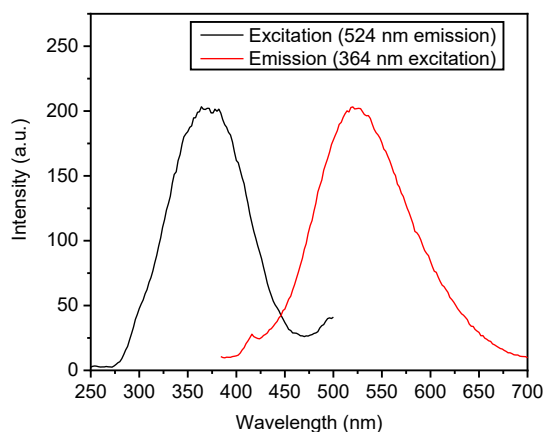
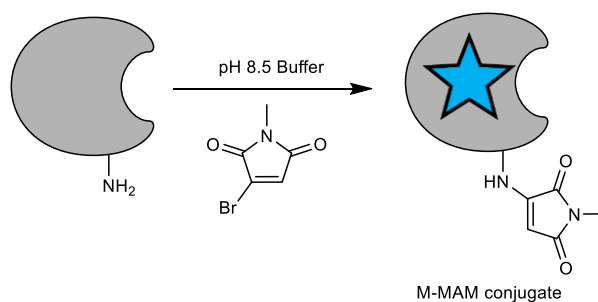


**Figure 2.33:** Excitation/emission spectrum of M-ABM HLZ conjugate in pH 8.5 buffer.

#### 1.10.4.7 $\alpha$ -CT lysine conjugation with M-MBM



MAM functionalized  $\alpha$ -CT was synthesized as per alkyne-MBM (**2.6.3.2**), without purification, using M-MBM (**2.3**)

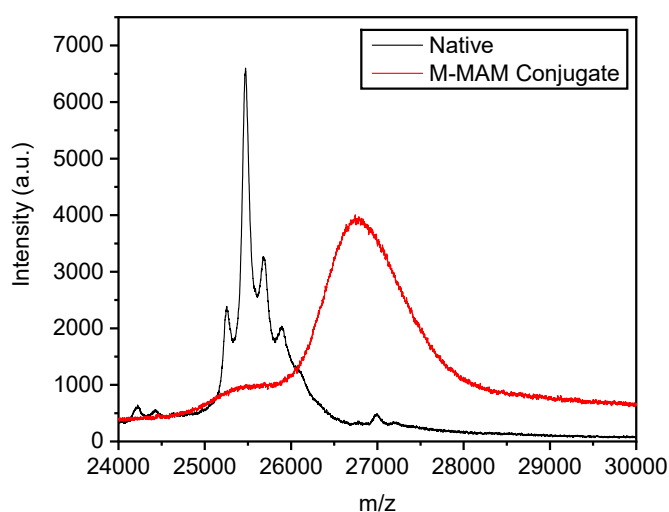
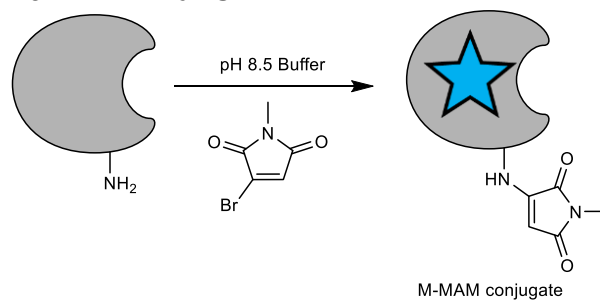


**Figure 2.34:** MALDI-ToF spectra of conjugate and native enzyme.

#### 1.10.4.8 HLZ lysine conjugation with M-MBM



MAM functionalized HLZ was synthesized as per alkyne-MBM (**2.6.3.4**), without purification, using M-MBM (**2.3**).

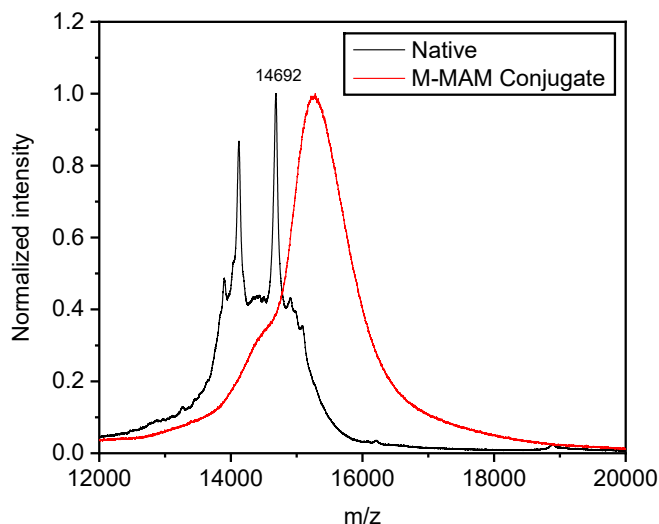
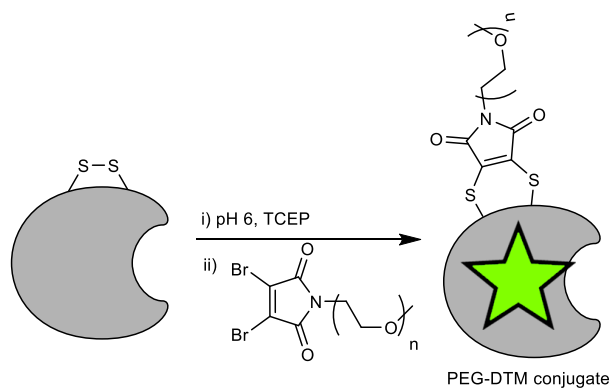


**Figure 2.35:** MALDI-ToF spectra of conjugate and native enzyme.

#### 1.10.4.9 $\alpha$ -CT conjugation with PEG-DBM *via* disulfide reduction



3 mg (0.17  $\mu$ mol) of  $\alpha$ -CT was dissolved in 0.9 mL of 0.1 M pH 6 phosphate buffer, followed by addition of 0.1 mL of TCEP solution (4  $\mu$ mol in 18.2 M $\Omega$ .cm water). The reaction was vortexed and left to stir for 30 minutes. After this, a 0.5 mL solution of PEG-DBM (**2.2**) (5  $\mu$ mol in DMF) was added, the solution vortexed and left to react for an hour. The crude enzyme was purified by ultrafiltration (AMICON® stirred cell) and freeze-dried.

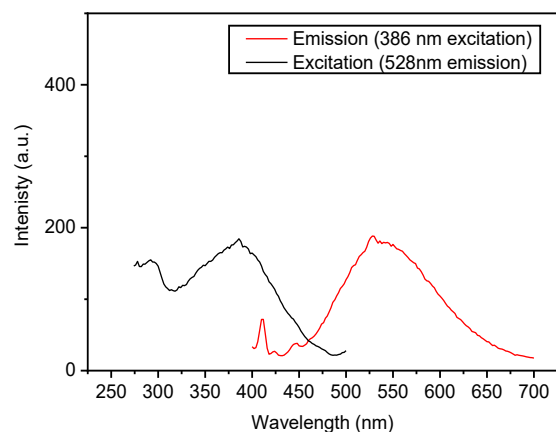


**Figure 2.36:** MALDI-ToF spectra of conjugate and native enzyme.

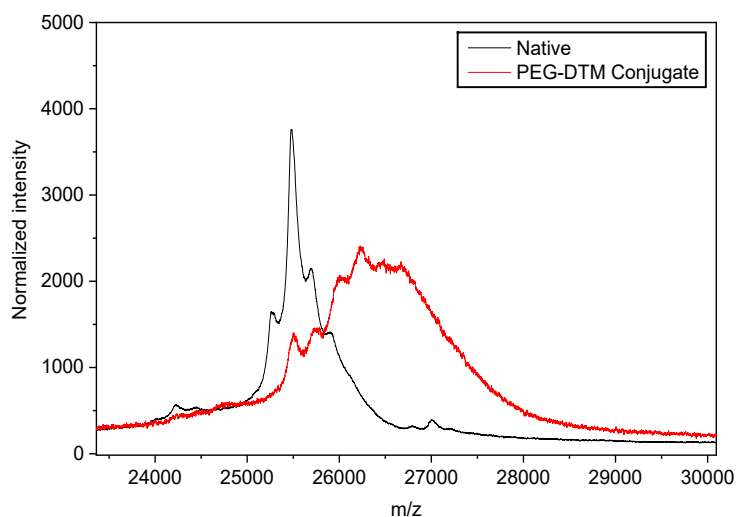
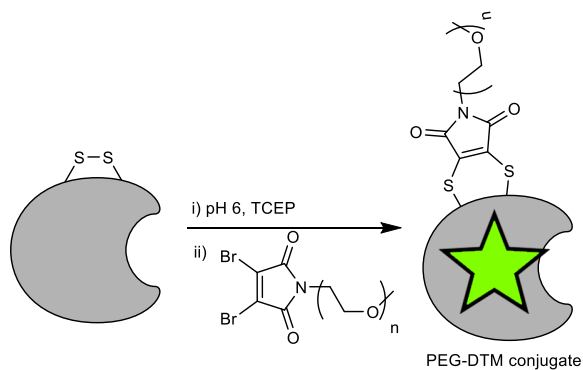


**Figure 2.37:** Excitation/emission spectrum of PEG-DTM α-CT conjugate in pH 6 buffer.

#### 1.10.4.10 HLZ conjugation with PEG-DBM *via* disulfide reduction



3 mg (0.2  $\mu$ mol) of HLZ was dissolved in 0.9 mL of 0.1M pH 6 phosphate buffer, followed by addition of 0.1 mL TCEP solution (4  $\mu$ mol in 18.2 M $\Omega$ .cm water). The reaction was vortexed and left to stir for 30 minutes. After this, a 0.5 mL solution 3.5 mg (5  $\mu$ mol) of PEG-DBM (**2.2**) in DMF was added and the reaction vortexed and left for an hour. The crude enzyme was purified by ultrafiltration (AMICON® stirred cell) and freeze-dried.

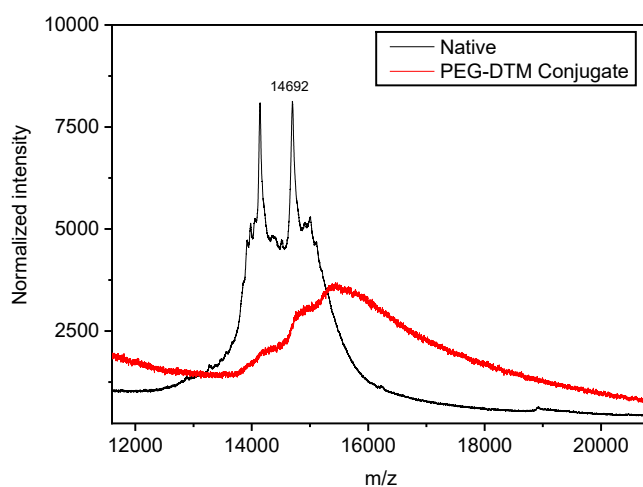


**Figure 2.38:** MALDI-ToF spectra of conjugate and native enzyme.

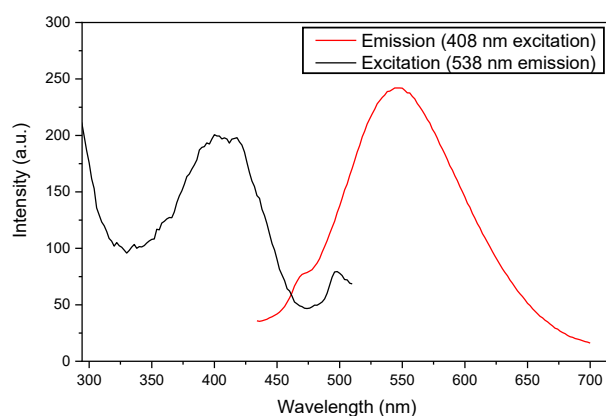
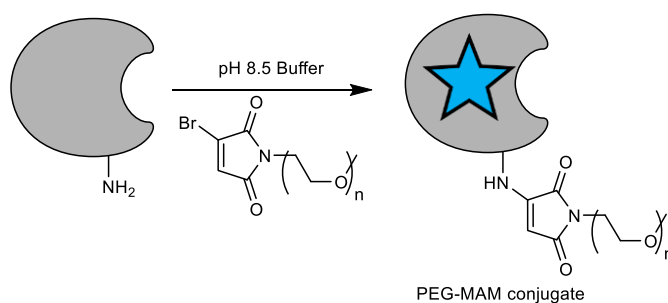


**Figure 2.39:** Excitation/emission spectrum of PEG-DTM HLZ conjugate in pH 6 buffer.

#### 1.10.4.11 $\alpha$ -CT lysine conjugation with PEG-MBM



3 mg (0.17  $\mu\text{mol}$ ) of  $\alpha$ -CT was dissolved in 0.9 mL of 0.1 M pH 8.5 phosphate buffer. To this, a 0.5 mL solution of PEG-MBM (**2.5**) (5  $\mu\text{mol}$  in DMF) was added and the reaction vortexed and left to react overnight. The crude enzyme was purified by ultrafiltration (AMICON® stirred cell) and freeze-dried.

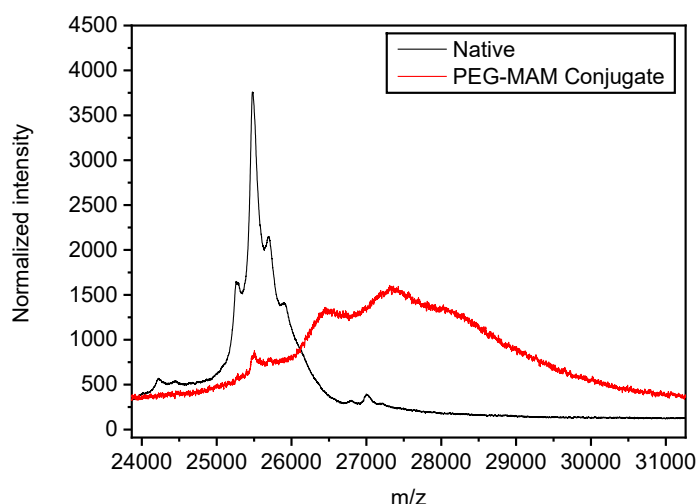


**Figure 2.40:** MALDI-ToF spectra of conjugate and native enzyme.

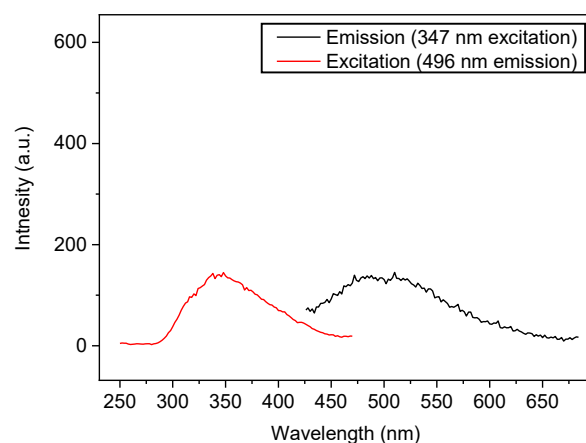
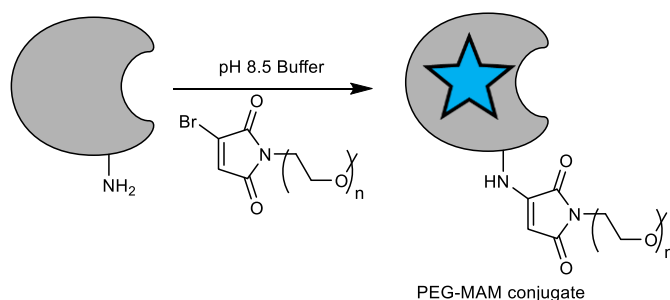


**Figure 2.41:** Excitation/emission spectrum of PEG-MAM  $\alpha$ -CT conjugate in pH 6 buffer.

#### 1.10.4.12 HLZ lysine conjugation with PEG-MBM



3 mg (0.2  $\mu$ mol) of HLZ was dissolved in 0.9 mL of 0.1 M pH 8.5 phosphate buffer. To this, a 0.5 mL solution of PEG-MBM (**2.5**) (5  $\mu$ mol in DMF) was added and the reaction vortexed and left to react overnight. The crude enzyme was purified by ultrafiltration (AMICON® stirred cell) and freeze-dried.



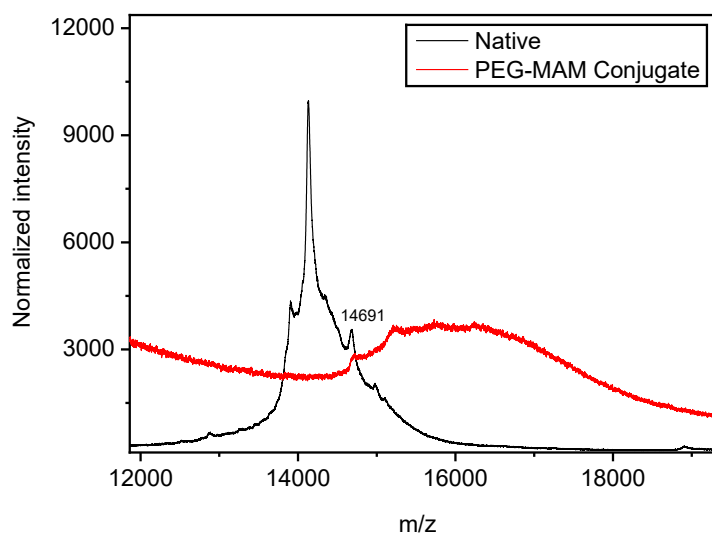


**Figure 2.42:** MALDI-ToF spectra of conjugate and native enzyme.

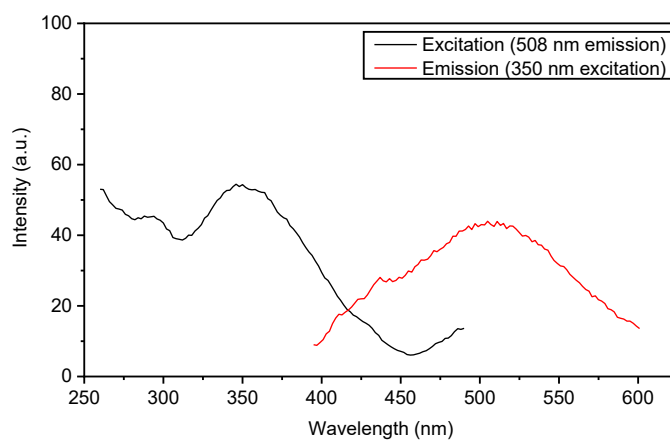


**Figure 2.43:** Excitation/emission spectrum of PEG-MAM HLZ conjugate in pH 6 buffer.

## 1.10.5 Enzyme assays

### 1.10.5.1 $\alpha$ -Chymotrypsin *p*-nitroaniline hydrolysis assay

Activity and stability of the enzyme and conjugates were assessed by analysis of the initial velocity changes in absorbance with time. Native  $\alpha$ -CT and conjugates (2  $\mu$ g/ml) were incubated in 0.1 M sodium phosphate buffer (pH 6) at 4 °C. 20  $\mu$ l aliquots of these solutions were added to 160  $\mu$ l of 0.1 M sodium phosphate buffer (pH 6) in a 96 well plate and 20  $\mu$ l of *N*-Succinyl-Ala-Ala-Pro-Phe *p*-nitroanilide in methanol (3 mg/ml) was added. Each sample was run in triplicate against buffer blanks. The initial rate of hydrolysis of the substrate was monitored through recording the rate of increase in absorption at 405 nm at 25 °C over 30 minutes. Background hydrolysis was subtracted to give initial rates of hydrolysis.

### 1.10.5.2 Human lysozyme EnzCheck® lysis assay

Lysozyme assays were carried out as reported in the literature<sup>36</sup>. DQ Lysozyme substrate stock suspension (1.0 mg/ml) was prepared according to the manufacturer, and aliquots were diluted to 50 mg/ml for each assay.

Prior to conjugate analysis, the substrate was used to generate a standard curve. 6 wells of a 96 well plate were filled with 50  $\mu$ l of 0.1 M sodium phosphate buffer (pH 6) followed by a solution of 50  $\mu$ l 500 U/mL of human lysozyme solution which was added to the first well. The solutions were mixed and 50  $\mu$ l was transferred into a second well. This was repeated over 5 wells, with the final 50  $\mu$ l from the 5<sup>th</sup> well discarded. To these solutions, 50  $\mu$ l of the 50 mg/ml substrate solution was added. These solutions in triplicate were incubated at 37 °C in a plate reader and emission at 530 nm (excitation at 492 nm) was recorded vs. time. From this, a value of 62.5 U/ml was identified as the concentration for future assays. The standard curve is plotted below (Figure 2.44).

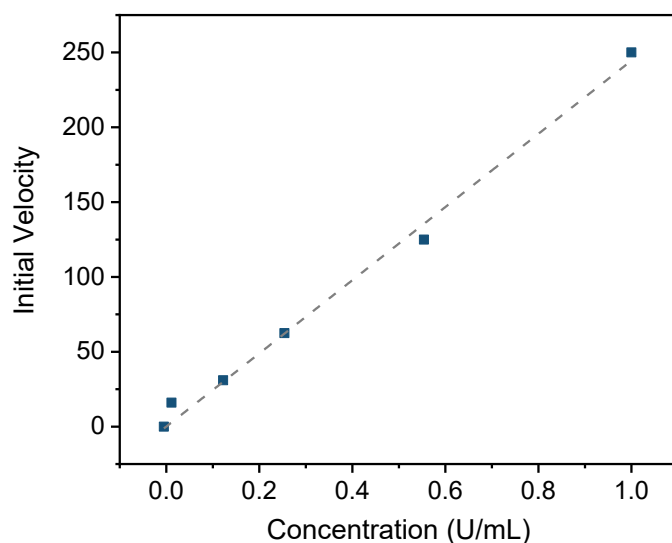


**Figure 2.44:** Lysozyme standard curve.

For the stability assay, Native human lysozyme and conjugates (2 mg/ml) were incubated in 0.1 M sodium phosphate buffer (pH 6) at 4 °C. Aliquots of these solutions were diluted to 0.005 mg/ml and 50  $\mu$ l of these solutions was pipetted onto a 96 well plate. To these solutions, 50  $\mu$ l of the 50 mg/ml substrate solution was added and these solutions, in triplicate, incubated at 37 °C in a plate reader. Analysis was carried out by measuring emission at 530 nm after 30 minutes, as per the manufacturer's protocol. Errors were measured as a standard deviation over all time points for each triplicate.

#### 1.10.6 Quantum yield fluorescence analysis

A solution of quinine sulfate dihydrate (15  $\mu$ mol) in 0.105 M perchloric acid, was used as a standard ( $\Phi_f$  quinine = 59%), and UV-Vis spectrum was recorded. The conjugate of interest was diluted to a concentration affording an absorbance <0.1 at the excitation wavelength determined by UV-Vis analysis. Both spectra were overlaid and the optimal excitation wavelength for the calculation was chosen to be the wavelength where the standard and the sample have the same absorption (Figure 2.45).

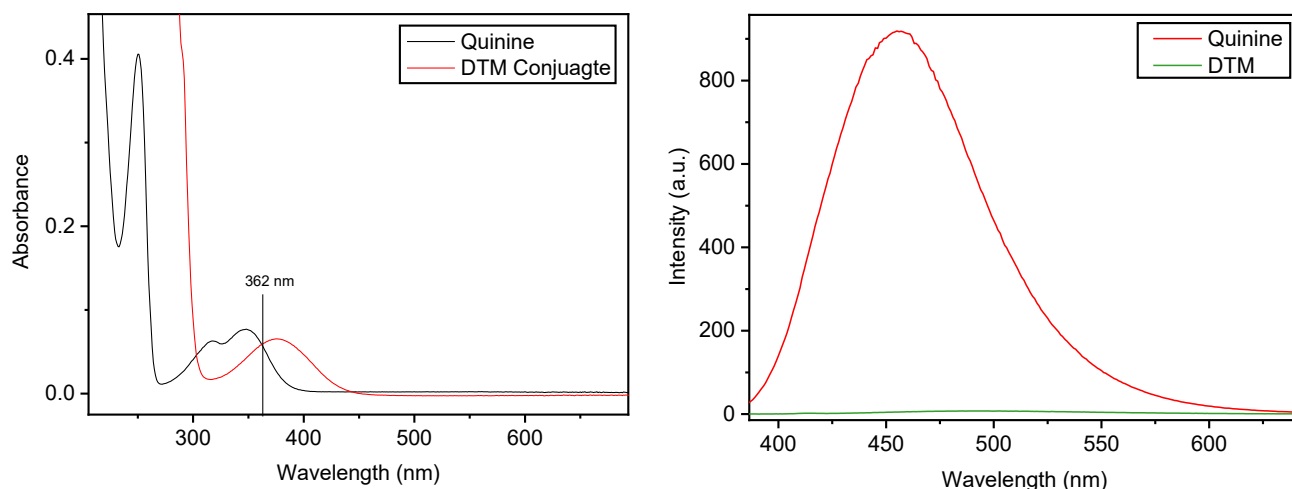


**Figure 2.45:** UV-Vis (left) and fluorescence emission (right) spectra of DTM conjugate against quinine standard.

Using 362 nm as the excitation wavelength for fluorescence, the emission of both samples was measured (Figure 2.45). To calculate the quantum yield Equation 1 is used, where  $F$ = Integral photon flux (emission integral),  $f$ = absorbance,  $n$ =refractive index of the solvent,  $\lambda_{em}$ = emission wavelength, conj=conjugate sample, and st=quinine standard.

$$\text{Equation 2.1: } \Phi_{f,conj} = \Phi_{f,st} \cdot \frac{F_{conj}}{F_{st}} \cdot \frac{f_{st}}{f_{conj}} \cdot \frac{n_{conj}^2(\lambda_{em})}{n_{st}^2(\lambda_{em})}$$

As the absorbance for the standard and sample match, it can be neglected ( $f_{st}/f_{conj}=1$ ). Refractive indices are found for the conjugate and quinine solvents at their respective average emission wavelengths (wavelength corresponding to the mean of the emission spectrum integration). The standard quantum yield  $\Phi_{f,st}(\Phi_{quinine}= 59\%)$  was used to calculate the relative fluorescence of each conjugate.

#### 1.10.7 Circular dichroism of DTM HLZ conjugate

Circular dichroism analysis was recorded for HLZ and the methyl DTM HLZ conjugate. By studying  $\Delta[\theta]_m$  at 222 nm the  $\alpha$ -helicity of the enzyme can be

measured. A small reduction in  $\Delta[\theta]_m$  was noted for the conjugate (97% of the native HLZ), which is similar to the difference by  $T = 0$  activity (96% - Table 2.5). This suggests there is a minimal reduction in enzyme integrity through conjugation of DTMs, the whole CD spectra also showed very similar structural features indicating good structure retention (Figure 2.11).

**Table 2.5:** Molar ellipticity difference of the DTM HLZ conjugate versus measured activity difference.

HLZ $[\theta]_{222}$	-2.54E+14 degcm <sup>2</sup> dmol <sup>-1</sup>
DTM HLZ $[\theta]_{222}$	-2.46E+14 degcm <sup>2</sup> dmol <sup>-1</sup>
$\Delta[\theta]_{222}$	97%
<b><math>\Delta</math>activity (t = 0)</b>	96%

## 1.11 References

- (1) Jung, D.; Min, K.; Jung, J.; Jang, W.; Kwon, Y. *Mol. Biosyst.* 2013, 9, 862.
- (2) Nanda, J. S.; Lorsch, J. R. In *Methods in Enzymology*; Lorsch, J., Ed.; Laboratory Methods in Enzymology: Protein Part A; Academic Press, 2014; Vol. 536, 87.
- (3) Kay, B. K.; Thai, S.; Volgina, V. V. *Methods Mol. Biol.* Clifton NJ 2009, 498, 185.
- (4) Gabor, F.; Wollmann, K.; Theyer, G.; Haberl, I.; Hamilton, G. *Anticancer Res.* 1994, 14, 1943.
- (5) Miao, Z.; Ren, G.; Liu, H.; Jiang, L.; Cheng, Z. *Bioconjug. Chem.* 2010, 21, 947.
- (6) Hermanson, G. T. In *Bioconjugate Techniques (Third edition)*; Academic Press: Boston, 2013; 1.
- (7) Stephanopoulos, N.; Francis, M. B. *Nat. Chem. Biol.* 2011, 7, 876.
- (8) Chalker, J. M.; Bernardes, G. J. L.; Lin, Y. A.; Davis, B. G. *Chem. – Asian J.* 2009, 4, 630.
- (9) Schelté, P.; Boeckler, C.; Frisch, B.; Schuber, F. *Bioconjug. Chem.* 2000, 11, 118.
- (10) Broyer, R. M.; Grover, G. N.; Maynard, H. D. *Chem. Commun.* 2011, 47, 2212.
- (11) Ranucci, E.; Ferruti, P.; Suardi, M. A.; Manfredi, A. *Macromol. Rapid Commun.* 2007, 28, 1243.
- (12) Suzuki, T.; Kanbara, N.; Tomono, T.; Hayashi, N.; Shinohara, I. *Biochim. Biophys. Acta BBA - Protein Struct. Mol. Enzymol.* 1984, 788, 248.
- (13) Cao, S.-G.; Zhao, Q.; Ding, Z.-T.; Ma, L.; Yu, T.; Wang, J.-H.; Feng, Y.; Cheng, Y.-H. *Ann. N. Y. Acad. Sci.* 1990, 613, 460.
- (14) Chen, R. H.-L.; Abuchowski, A.; Van Es, T.; Palczuk, N. C.; Davis, F. F. *Biochim. Biophys. Acta BBA - Enzymol.* 1981, 660, 293.
- (15) Kurtzberg, J.; Asselin, B.; Bernstein, M.; Buchanan, G. R.; Pollock, B. H.; Camitta, B. M. *J. Pediatr. Hematol. Oncol.* 2011, 33, 610.
- (16) Tsutsumi, Y.; Kihira, T.; Tsunoda, S.; Kanamori, T.; Nakagawa, S.; Mayumi, T. *Br. J. Cancer* 1995, 71, 963.
- (17) Gupta, V.; Bhavanasi, S.; Quadir, M.; Singh, K.; Ghosh, G.; Vasamreddy, K.; Ghosh, A.; Siahaan, T. J.; Banerjee, S.; Banerjee, S. K. *J. Cell Commun. Signal.* 2019, 13, 319.
- (18) Alconcel, S. N. S.; Baas, A. S.; Maynard, H. D. *Polym. Chem.* 2011, 2, 1442.
- (19) Veronese, F. M.; Mero, A.; Pasut, G. In *PEGylated Protein Drugs: Basic Science and Clinical Applications*; Veronese, F. M., Ed.; Milestones in Drug Therapy; Birkhäuser Basel, 2009; 11.
- (20) Knop, K.; Hoogenboom, R.; Fischer, D.; Schubert, U. S. *Angew. Chem. Int. Ed.* 2010, 49, 6288.
- (21) Couturaud, B.; Georgiou, P. G.; Varlas, S.; Jones, J. R.; Arno, M. C.; **Foster, J. C.; O'Reilly, R. K.** *Macromol. Rapid Commun.* 2019; 40, 1800460.
- (22) Reid, B.; Tzeng, S.; Warren, A.; Kozielski, K.; Elisseeff, J. *Macromolecules* 2010, 43, 9588.
- (23) Lee, Y.; Koo, H.; Jin, G.; Mo, H.; Cho, M. Y.; Park, J.-Y.; Choi, J. S.; Park, J. S. *Biomacromolecules* 2005, 6, 24.

- (24) B. A. Paik, S. R. Mane, X. Jia and K. L. Kiick, *J Mater Chem B*, 2017, 5, 8274–8288.
- (25) Y. Liu, J. Lee, K. M. Mansfield, J. H. Ko, S. Sallam, C. Wesdemiotis and H. D. Maynard, *Bioconjugate Chem.*, 2017, 28, 836–845
- (26) S. N. S. Alconcel, A. S. Baas and H. D. Maynard, *Polymer Chemistry*, 2011, 2, 1442–1448.
- (27) Brocchini, S.; Godwin, A.; Balan, S.; Choi, J.; Zloh, M.; Shaunak, S. *Adv. Drug Deliv. Rev.* 2008, 60, 3.
- (28) Smith, M. E. B.; Schumacher, F. F.; Ryan, C. P.; Tedaldi, L. M.; Papaioannou, D.; Waksman, G.; Caddick, S.; Baker, J. R. *J. Am. Chem. Soc.* 2010, 132, 1960.
- (29) Shaunak, S.; Godwin, A.; Choi, J.-W.; Balan, S.; Pedone, E.; Vijayarangam, D.; Heidelberger, S.; Teo, I.; Zloh, M.; Brocchini, S. *Nat. Chem. Biol.* 2006, 2, 312.
- (30) Appel, W. *Clin. Biochem.* 1986, 19, 317.
- (31) Valls, C.; Pujadas, G.; Garcia-Vallve, S.; Mulero, M. *Biochem. Mol. Biol. Educ.* 2011, 39, 280.
- (32) Harris, G. S. *Can. Med. Assoc. J.* 1961, 85, 186.
- (33) Vella, F. *Biochem. Educ.* 1990, 18, 154.
- (34) Cummings, C.; Murata, H.; Koepsel, R.; Russell, A. J. *Biomaterials* 2013, 34, 7437.
- (35) Tsukada, H.; Blow, D. M. *J. Mol. Biol.* 1985, 184, 703.
- (36) Dumoulin, M.; Johnson, R. J. K.; Bellotti, V.; Dobson, C. M. In *Protein Misfolding, Aggregation, and Conformational Diseases*; Uversky, V. N.; Fink, A. L., Eds.; Protein Reviews; Springer US, 2007; 285.
- (37) McDermott, A. M. *Exp. Eye Res.* 2013, 117, 53.
- (38) Artymiuk, P. J.; Blake, C. C. F. *J. Mol. Biol.* 1981, 152, 737.
- (39) Helal, R.; Melzig, M. F. *Pharm. - Int. J. Pharm. Sci.* 2008, 63, 415.
- (40) Ng, A.; Heynen, M.; Luensmann, D.; Subbaraman, L. N.; Jones, L. *Curr. Eye Res.* 2013, 38, 252.
- (41) Liao, Y. H.; Brown, M. B.; Martin, G. P. *J. Pharm. Pharmacol.* 2001, 53, 549.
- (42) Lucius, M.; Falatach, R.; McGlone, C.; Makaroff, K.; Danielson, A.; Williams, C.; Nix, J. C.; Konkolewicz, D.; Page, R. C.; Berberich, J. A. *Biomacromolecules* 2016, 17, 1123.
- (43) Zhang, Q.; Li, M.; Zhu, C.; Nurumbetov, G.; Li, Z.; Wilson, P.; Kempe, K.; Haddleton, D. M. *J. Am. Chem. Soc.* 2015, 137, 9344.
- (44) Pai, S. S.; Hammouda, B.; Hong, K.; Pozzo, D. C.; Przybycien, T. M.; Tilton, R. D. *Bioconjug. Chem.* 2011, 22, 2317.
- (45) Robin, M. P.; Osborne, S. A. M.; Pikramenou, Z.; Raymond, J. E.; O'Reilly, R. K. *Macromolecules* 2016, 49, 653.
- (46) Jones, M. W.; Strickland, R. A.; Schumacher, F. F.; Caddick, S.; Baker, J. R.; Gibson, M. I.; Haddleton, D. M. *Chem. Commun.* 2012, 48, 4064.
- (47) Collins, J.; Tanaka, J.; Wilson, P.; Kempe, K.; Davis, T. P.; McIntosh, M. P.; Whittaker, M. R.; Haddleton, D. M. *Bioconjug. Chem.* 2015, 26, 633.
- (48) Schumacher, F. F.; Nunes, J. P. M.; Maruani, A.; Chudasama, V.; Smith, M. E. B.; Chester, K. A.; Baker, J. R.; Caddick, S. *Org. Biomol. Chem.* 2014, 12, 7261.
- (49) Liu, M.; Tirino, P.; Radivojevic, M.; Phillips, D. J.; Gibson, M. I.; Leroux, J.-C.; Gauthier, M. A. *Adv. Funct. Mater.* 2013, 23, 2007.
- (50) Jibson, M. D.; Birk, Y.; Bewley, T. A. *Int. J. Pept. Protein Res.* 1981, 18, 26.

- (51) Booth, D. R.; Sunde, M.; Bellotti, V.; Robinson, C. V.; Hutchinson, W. L.; Fraser, P. E.; Hawkins, P. N.; Dobson, C. M.; Radford, S. E.; Blake, C. C. F.; Pepys, M. B. *Nature* 1997, **385**, 787.
- (52) Li, M.; De, P.; Gondi, S. R.; Sumerlin, B. S. *Macromol. Rapid Commun.* 2008, **29**, 1172.
- (53) Morais, M.; Nunes, J. P. M.; Karu, K.; Forte, N.; Benni, I.; Smith, M. E. B.; Caddick, S.; Chudasama, V.; Baker, J. R. *Org. Biomol. Chem.* 2017, **15**, 2947.
- (54) Mabire, A. B.; Robin, M. P.; Quan, W.-D.; Willcock, H.; Stavros, V. G.; **O'Reilly, R. K. Chem. Commun.** 2015, **51**, 9733.
- (55) Robin, M. P.; Mabire, A. B.; Damborsky, J. C.; Thom, E. S.; Winzer-Serhan, U. H.; **Raymond, J. E.; O'Reilly, R. K. J. Am. Chem. Soc.** 2013, **135**, 9518.
- (56) Shaner, N. C.; Steinbach, P. A.; Tsien, R. Y. *Nat. Methods* 2005, **2**, 905.
- (57) DelMar, E. G.; Largman, C.; Brodrick, J. W.; Geokas, M. C. *Anal. Biochem.* 1979, **99**, 316.
- (58) Avanti, C.; Saluja, V.; Streun, E. L. P. van; Frijlink, H. W.; Hinrichs, W. L. J. *PLOS ONE* 2014, **9**, e86244.
- (59) Schumacher, F. F.; Nobles, M.; Ryan, C. P.; Smith, M. E. B.; Tinker, A.; Caddick, S.; Baker, J. R. *Bioconj. Chem.* 2011, **22**, 132.
- (60) Smith, M. E. B.; Caspersen, M. B.; Robinson, E.; Morais, M.; Maruani, A.; Nunes, J. P. M.; Nicholls, K.; Saxton, M. J.; Caddick, S.; Baker, J. R.; Chudasama, V. *Org. Biomol. Chem.* 2015, **13**, 7946.





## **Chapter 3:** Designing maleimide derived fluorophores for improved fluorescence performance in aqueous environments

## 2.1 Abstract

In the previous Chapter, fluorescence quenching through hydrogen bonding interactions with water was observed in conjugated maleimide species. Based upon the principle of preventing this interaction, several ways of preventing this have been hypothesized and investigated. This Chapter covers the investigation into bulky imide substituents which are hypothesized to prevent H-bonding interactions through steric repulsion. This was achieved through introducing multiple benzyl groups to the imide and through using silylation reactions to produce silyl functionalized maleimides. Fluorescence analysis of the benzyl derivatives showed unexpected fluorescence behaviour, including what appeared to be aggregation induced emission (AIE) in a trityl-MAM. This observation is explored and explained through crystal structure analysis and computational simulation of electron distributions, which indicated a divergence from typical AIE mechanisms. Silyl derivatives indicated similar fluorescence properties to conventional maleimide fluorophores, however, the quantum yield of these was increased in methanol, attributed to successful shielding from solvent electron-driven proton transfer (EDPT).

## 2.2 Introduction

### 2.2.1 Quenching of charge transfer fluorophores

The properties of a fluorophore are greatly influenced by its environment, as discussed in Chapter 1. This is particularly true for photoinduced charge transfer dyes (PCT) such as aminomaleimide fluorophores,<sup>1,2</sup> hence they exhibit solvafluorochromism and have been particularly successful as sensing dyes in polymer-based applications.<sup>3-6</sup>

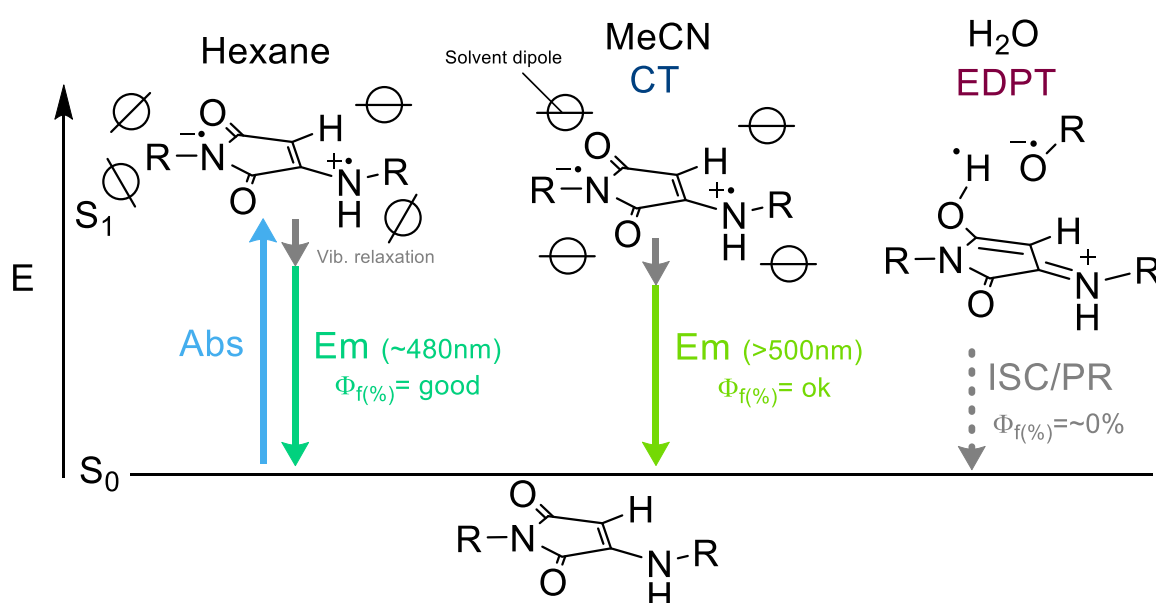


**Figure 3.1:** Illustration of absorption and relaxation events in a generalized maleimide skeleton in different solvents. ISC = intersystem crossing, PR = photo recombination.

Intramolecular charge transfer fluorophores are compounds which upon excitation become charge separated. In essence the excitation leads to a separation of charge - an acceptor (-ve) and a donor (+ve) group (Figure 3.1). If the molecule is in a planar configuration, the orbitals are aligned and fluorescence is electronically allowed, leading to high emission. However, this excitation forms a diradical: one radical existing in the ground state HOMO and one in the LUMO. To reduce columbic repulsion, the molecule may rotate around a single bond-forming a twisted intramolecular charge transfer state (TICT). This can lead to

electronic decoupling of the donor and acceptor before relaxation, which can forbid fluorescence emission or lead to red shifted emission.<sup>1,7+</sup> In a sufficiently fluid medium, solvent molecules can adjust to stabilize the shift in electronic distribution. The more polar the solvent, the more effective this stabilization is; which leads to this charge stabilization becoming more dominant in polar solvents such as water and methanol.

Concerning maleimide fluorophores in particular, a charge transfer quenching event occurs  $\sim 5$  ps post excitation, which is favoured by higher solvent polarity (Figure 3.1). However, the effect is still minimal for aminomaleimides in aprotic polar solvents such as acetonitrile (MeCN).<sup>2</sup> In addition, there is another quenching event in polar protic solvents. In protic solvents such as methanol, an electron driven proton transfer (EDPT) event also occurs leading to even greater quenching of fluorescence, and as a result, MAM dyes typically exhibit quantum yields ( $\Phi_f$ ) of around 1% in methanol and  $<0.1\%$  in water.<sup>2,9</sup> In such EDPT events, the movement of an electron from the solvent to the dye upon excitation, causes a charge difference which induces proton donation from the solvent.<sup>8</sup> This transfer leads to a neutral di-radical species, in which fluorescence is forbidden (Figure 3.2).

It is hypothesized that prevention of EDPT would lead to a marked increase in emission intensity in protic solvents.<sup>2</sup> Several changes to the maleimide motif to achieve this aim have been investigated and this Chapter will focus on using steric shielding of the carbonyl groups with the aim of preventing EDPT.

---

<sup>+</sup> Sometimes, this state can be fluorescent as a consequence of other effects, as observed for example, in DMABN (4-(dimethylamino)benzonitrile), which exhibits a TICT induced fluorochromic shift.<sup>7</sup>

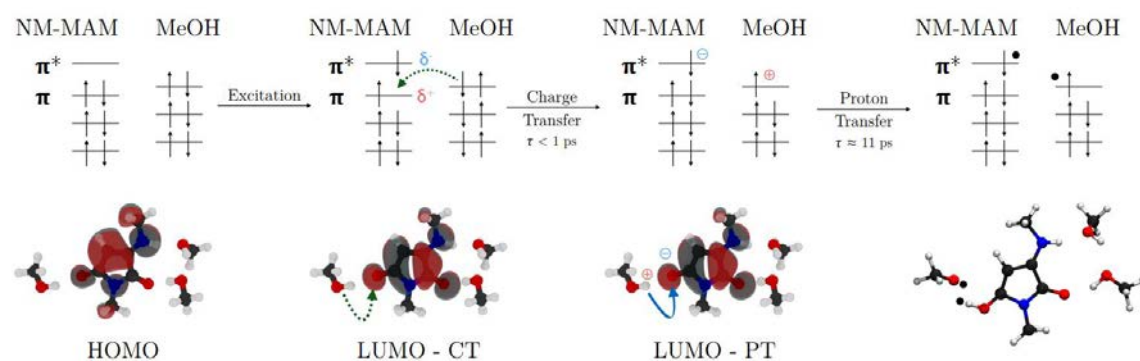


**Figure 3.2:** Diagram of hypothesized EDPT mechanism for a maleimide solvated in MeOH. Electronic movement is indicated by the green dashed arrow and proton movement is indicated by the blue arrow. Reproduced from reference.<sup>8</sup>

### 2.2.2 Aggregation induced emission (AIE)

Within this Chapter, a phenomenon analogous to aggregation induced emission (AIE) is serendipitously observed. AIE is a relatively recent but well-studied, area of fluorescence, especially in regard to materials applications.<sup>10</sup> Initially reported in 2001 by Tang and co-workers when studying phenyl substituted siloles,<sup>11</sup> AIE has now been observed in dyes from planar aromatics like tetraphenylethylene (TPE)<sup>12</sup> and arylated BODIPY variants<sup>13</sup> to metal complexes such as Au(I) thiolates.<sup>14</sup> AIE is in contrast to aggregation caused quenching (ACQ) which is the phenomenon that most conventional dyes exhibit.<sup>15</sup> In general ACQ occurs when dyes that are fluorescent in solution aggregate or crystallize, in a manner in which  $\pi$ - $\pi$  interactions are formed which cause self-quenching of fluorescence.<sup>15,16</sup> The major mechanism of AIE is through restriction of intramolecular motion (RIM) or restriction of intramolecular rotation (RIR). This RIM or RIR causes prevents the TICT quenching seen in solution,<sup>15</sup> for example TPE dyes in solution are not fluorescent as the aryl substituents are free to rotate which allows for non-radiative relaxation, however upon aggregation this rotation

and motion can no longer occur and thus the compound becomes fluorescent (Figure 3.3).<sup>17</sup> Very recently Tang and co-workers have reported a new version of RIM in which prevention of access to a dark state (caused by lone-pair  $\pi$  interactions) can be achieved upon aggregation or complexation of metal ions.<sup>18</sup>

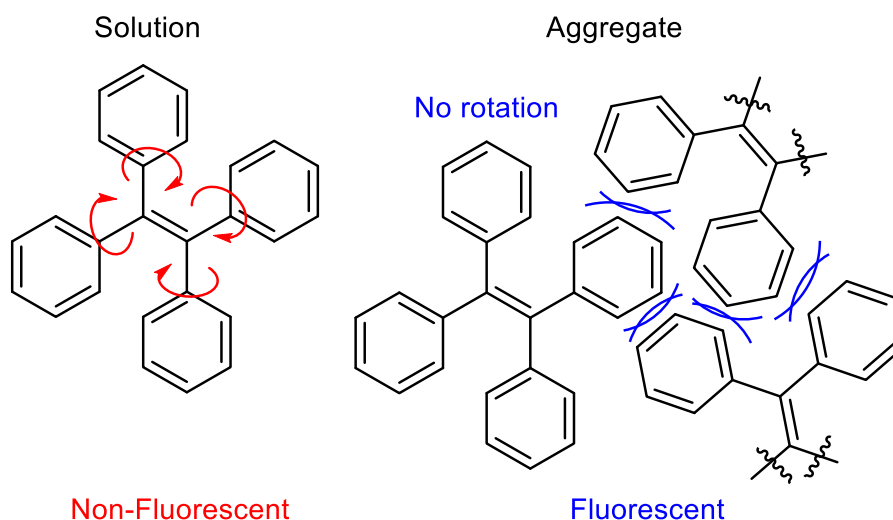


**Figure 3.3:** Illustration of rotation-based relaxation of TPE (left), and the fluorescent aggregate state through RIM/RIR (right).

Applications of AIE include OLED based applications, where a highly emissive species is required in the solid or film state,<sup>19</sup> to explosives detection in which highly emissive solids can be quenched upon contamination with aromatic explosives such as TNT and picric acid.<sup>20,21</sup>

In regard to maleimide based fluorophores, AIE can be observed through aromatic substitution of the dye as reported by the Tang group.<sup>22</sup> Substitution extends  $\pi$  conjugation beyond the maleimide ring through rotatable bonds which cause quenching in solution, however upon aggregation AIE can occur through restriction of these rotations. This has been applied to polymer-based materials to create condensation-based polymers which exhibited solid-state emission, and AIE behaviour at longer visible wavelengths ( $>600$  nm).<sup>23</sup> In both of these reports AIE

dyes exhibited solid-state  $\Phi_f < 40\%$ , which leaves room for improvement compared to other reported AIE dyes.<sup>10,22,23</sup>

A thorough investigation into imide substitution in maleimide dyes has not been reported and many questions still exist about maleimide fluorophores, including explaining their solid-state fluorescence behaviour. In this Chapter, a systematic study into the effect of imide functionalization of MAMs was conducted. It was anticipated that tuning substitution may not only aid with steric shielding from protic quenching events, but may also significantly affect the fluorescence mechanism, for example, from AIE to ACQ, along with potentially creating new  $\pi$ - $\pi$  or C-H- $\pi$  interactions in the aggregate state which have been shown to tune fluorescence in other dyes.<sup>24,25</sup>



## 2.3 Results

### 2.3.1 Synthesis of imide functionalized maleimides with benzyl groups to reduce solvent quenching effects

As a consequence of the poor fluorescence properties of previously synthesized conjugates in aqueous environments, it was decided to investigate maleimide derivatives that may undergo less quenching in aqueous environments. O'Reilly and co-workers have shown that quenching in polar environments can be a consequence of hydrogen bonding interactions with solvent protons.<sup>8</sup> Therefore, efforts will focus on preventing this interaction through the synthesis of sterically protected maleimides. Hypothetically, bulky imide substituents could provide steric hindrance to hydrogen bonding interactions, thus preventing quenching from protic solvents. Initially, phenyl substituted maleimides were targeted as the phenyl rings may also help introduce weak intra-molecular hydrogen bonding as shown in Figure 3.4.

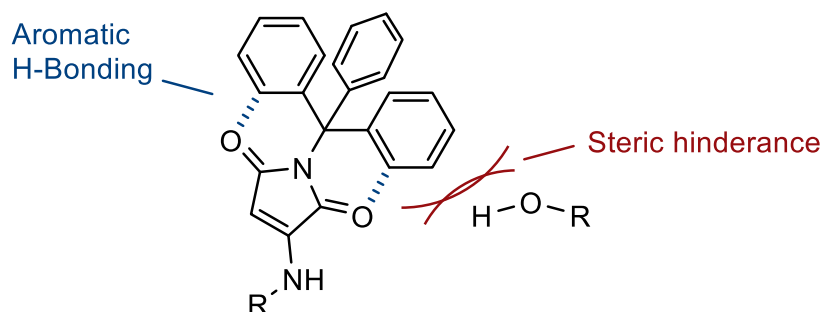
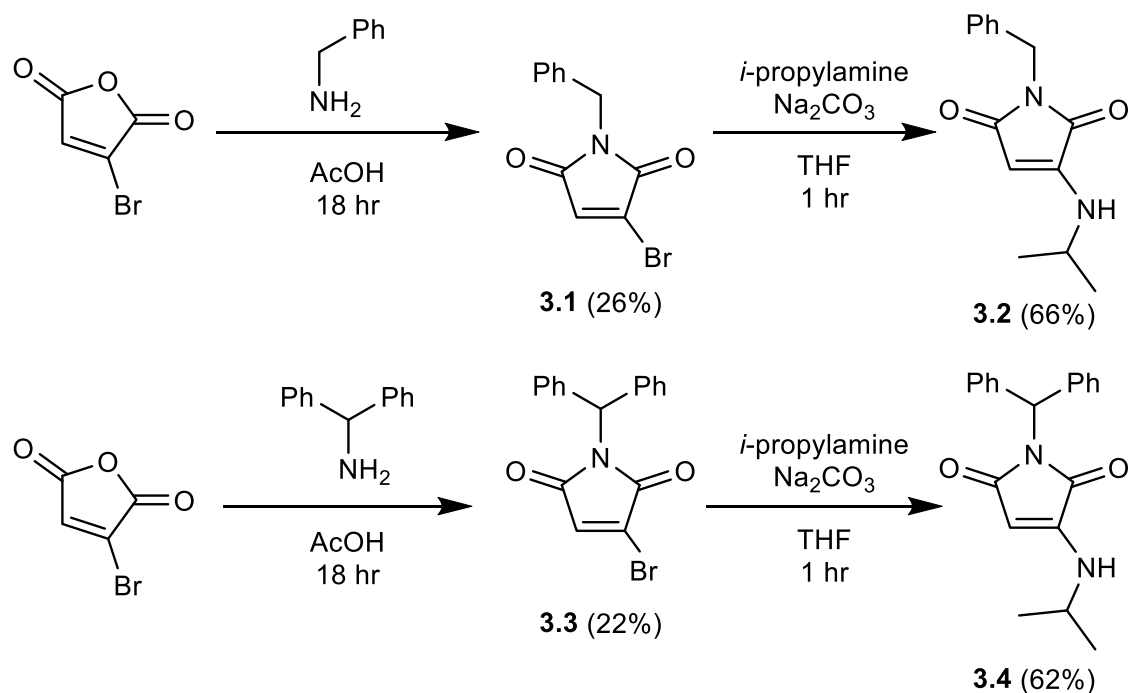


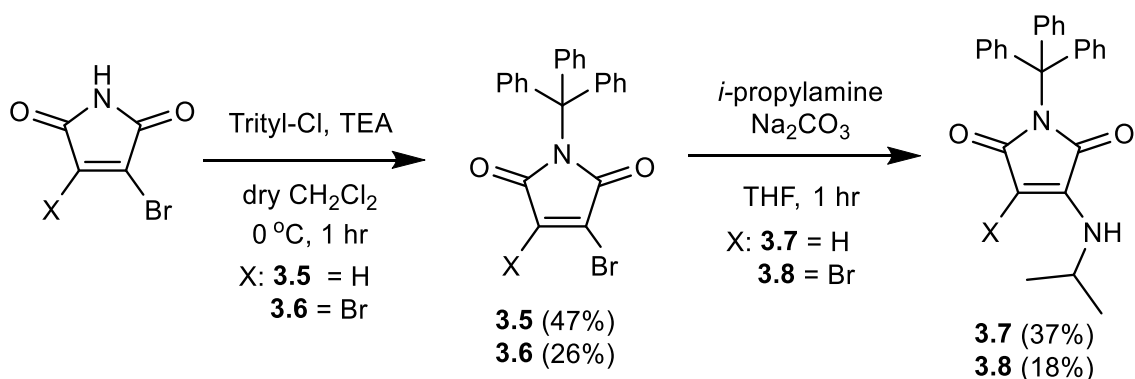
**Figure 3.4:** 2D Illustration of proposed interactions preventing solvent (R) hydrogen bonding in a phenyl substituted maleimide.

Mono-benzyl and bis-benzyl functionalized maleimides were successfully synthesized by reacting benzyl amine and diphenylmethanamine respectively (Scheme 3.1) with bromomaleicanhydride, under acidic reflux conditions reported by Tedaldi *et al.*<sup>26</sup>



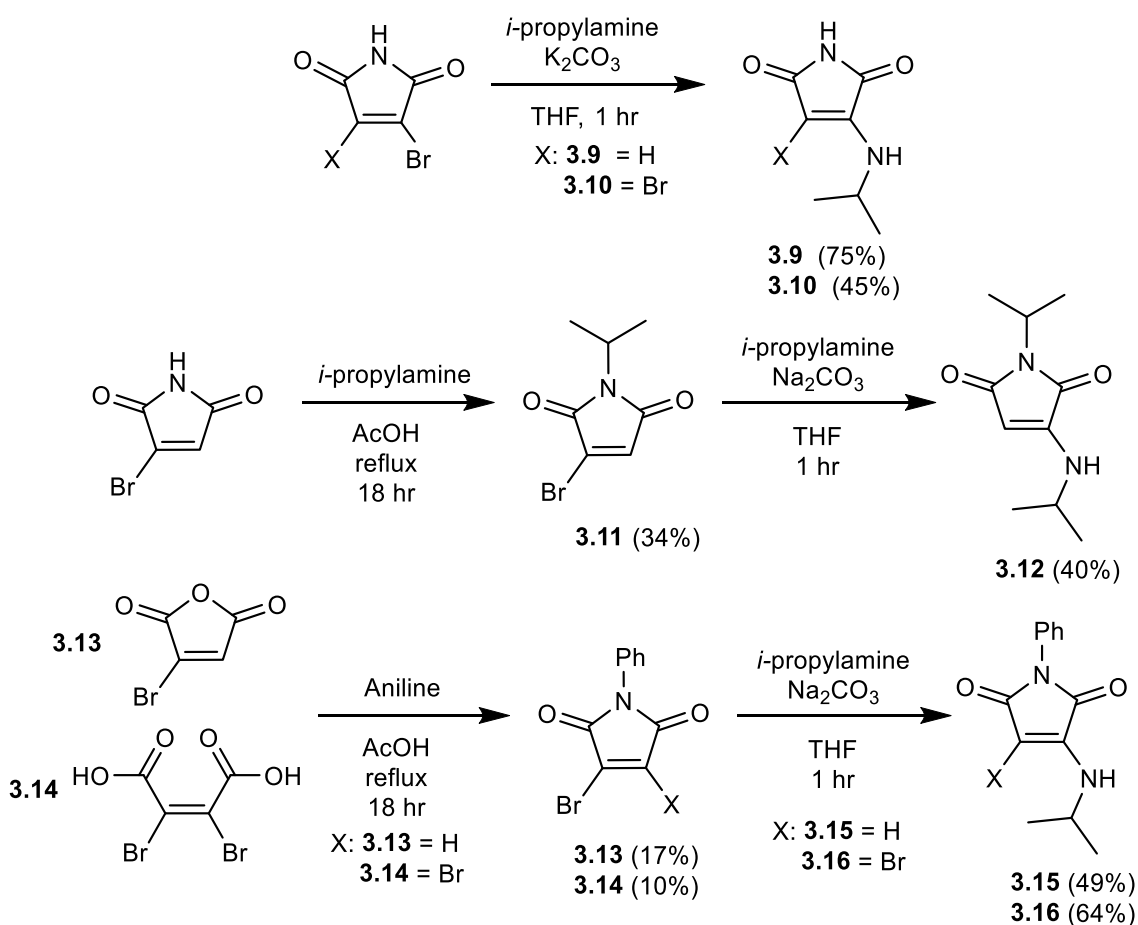
**Scheme 3.1:** Synthesis of mono- and bis-benzyl aminomaleimides **3.2** and **3.4** *via* intermediate MBMs **3.1** and **3.3**.

The reaction of tritylamine under the same conditions did not proceed, hypothesized to be a result of greater steric hindrance from the trityl group preventing nucleophilic attack on the anhydride. Typically alkyl halides are unreactive towards bromomaleimide nucleophiles,<sup>27</sup> unexpectedly however, the reaction of trityl chloride with MBM **2.1** and DBM did proceed (Scheme 3.2). This suggests an S<sub>N</sub>1 mechanism for such reactions, where a stable cation intermediate is required for attack of the maleimide to occur. This correlates with the poor nucleophilic nature of the imide group.



**Scheme 3.2:** Synthesis of trityl MAM **3.7** and ABM **3.8**.

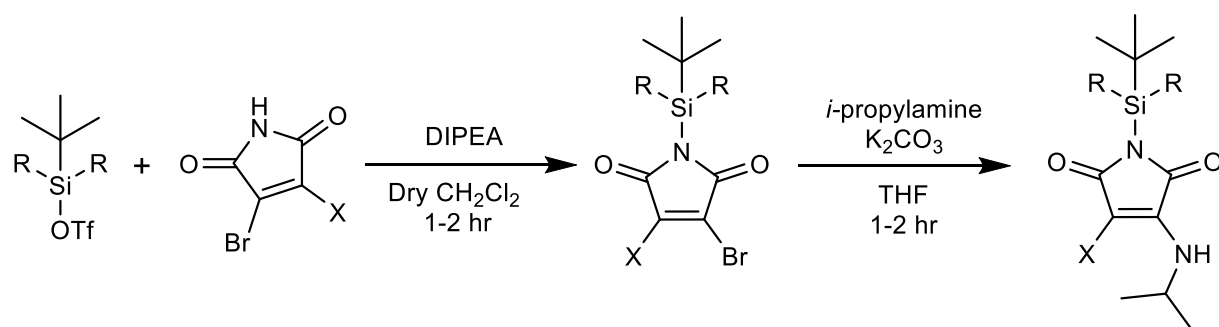
For comparison to previously studied maleimide fluorophores, five standards containing an isopropylamine donor group were synthesized (Scheme 3.3): HMAM (**3.9**), iPrMAM (**3.12**), PhMAM (**3.15**) PhABM (**3.16**), and HABM (**3.10**).



**Scheme 3.3:** Synthesis of ABM/MAM dyes **3.9**, **3.10**, **3.12**, **3.15** and **3.16** used for fluorescence controls.

### 2.3.2 The synthesis of bulky silyl derived aminomaleimides as sterically hindered maleimide fluorophores

It has been reported that silyl-maleimides can be formed through functionalization of the imide group,<sup>28</sup> and based upon this several silyl-aminomaleimides were targeted for synthesis. It was hoped that as well as giving more groups for steric hindrance, the silyl group may impart beneficial changes to the optical properties, for example Si-Rhodamines have been reported as near infrared dyes, which are highly stable to photo-bleaching.<sup>29,30</sup> Firstly, a *tert*-butyldimethylsilyl derivative was targeted, which would impart a large alkyl imide substituent for the study. The reaction of *tert*-butyldimethylsilyl trifluoromethanesulfonate was found to be successful with DBM and MBM under dry conditions (Scheme 3.4, **3.17-3.18**). These were successfully reacted with *i*-propylamine to give TBDMSi-MAM **3.21** and TBDMSi-ABM **3.22**. Based upon this, the reactions were repeated with *tert*-butyldiphenylsilyl trifluoromethanesulfonate, to give benzyl-silyl functionalized aminomaleimides (TBDPSi-MAM **3.23** and TBDPSi-ABM **3.24**). Reactions of trimethylsilyl chloride and triisopropylsilyl chloride were unsuccessful, suggesting either a more activated trifluoromethylsilyl group is required or a more substituted silyl reagent is required to stabilize the cation intermediate. Unfortunately, trimethylsilyl- or triisopropylsilyl-trifluoromethanesulfonate were not commercially available.



Intermediate	R=	X=	Yield
<b>3.17</b>	Me	H	18%
<b>3.18</b>	Me	Br	34%
<b>3.19</b>	Ph	H	65%
<b>3.20</b>	Ph	Br	20%

Product	R=	X=	Yield
<b>3.21</b>	Me	H	74%
<b>3.22</b>	Me	Br	47%
<b>3.23</b>	Ph	H	17%
<b>3.24</b>	Ph	Br	27%

**Scheme 3.4:** Synthesis of various silyl maleimides **3.21-3.24** *via* silyl bromomaleimide intermediates **3.17-3.20**.

### 2.3.3 Fluorescence analysis of benzyl substituted maleimides

To establish the effect of benzyl functionality on the optical properties of maleimides, the benzyl substituted dyes (**3.2**, **3.4**, **3.7** and **3.8**) synthesized in 3.3.1 were measured (single measurements) and compared to standard aminomaleimides HMAM (**3.9**) and iPrMAM (**3.12**) and PhMAM (**3.15**). The absorption and emission wavelengths of the series, from no benzyl substituents (HMAM, Figure 3.6) to three benzyl substituents (Bz<sub>3</sub>MAM) varied only a little, with the compounds all exhibiting similar  $\lambda_{\max}$  (Figure 3.5). It was noteworthy that all aromatic functionalized dyes exhibited smaller changes in  $\lambda_{\max}$  between solvents,

than the H and isopropyl imide functionalized dyes, suggesting a lesser influence from the environment in these dyes, as the charge transfer state is stabilized by interactions with polar solvents.<sup>1</sup> Meanwhile, Stokes shifts in the series varied little between dyes indicating similar HOMO-LUMO separation.

When studying the mono- and di-benzyl substituted MAMs, bright emission was noted in aprotic solvents, similar to HMAM, with comparable  $\lambda_{\text{ex/em}}$  maxima. In contrast, very little fluorescence was observed for the trityl-MAM (Bz<sub>3</sub>MAM – **3.7**) in apolar solvents, notably increased emission was observed in methanol and dimethyl sulfoxide (DMSO), seemingly inverting the trend observed in standard aminomaleimide fluorophores.

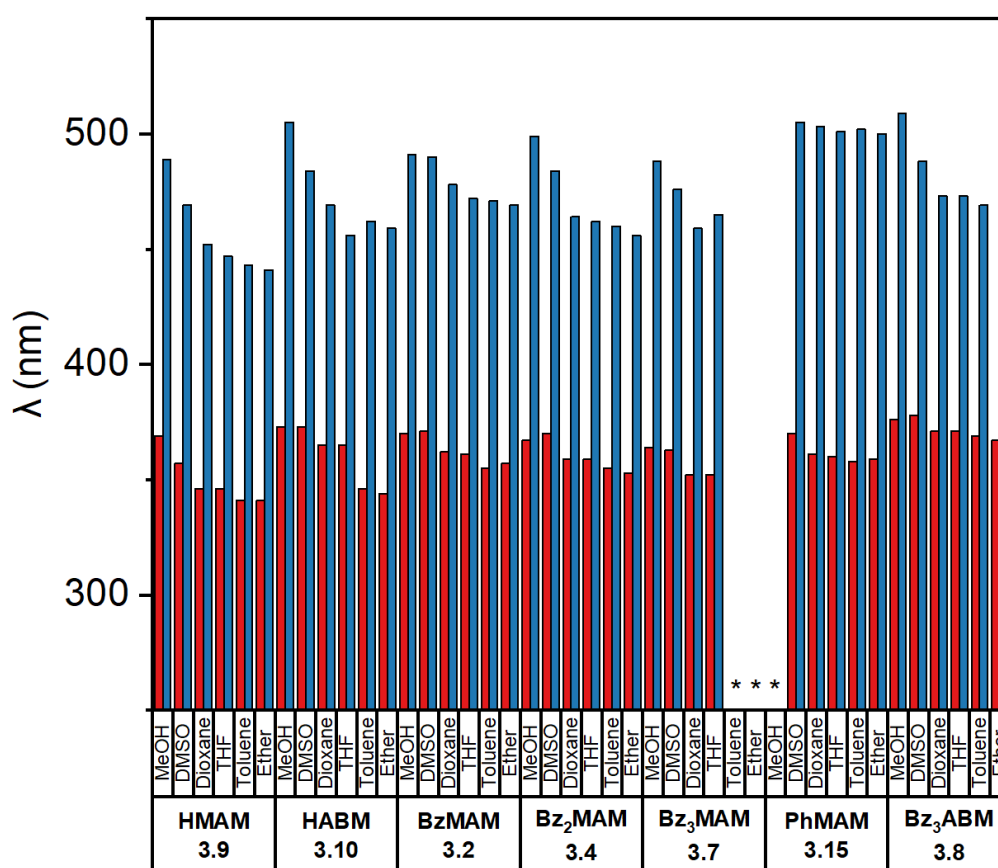


**Figure 3.5:** Chart showing solution excitation (red) and emission (blue)  $\lambda_{\text{max}}$  the benzyl maleimide series in various solvents, showing minimal variation in the series. \* Too weak for measurement.

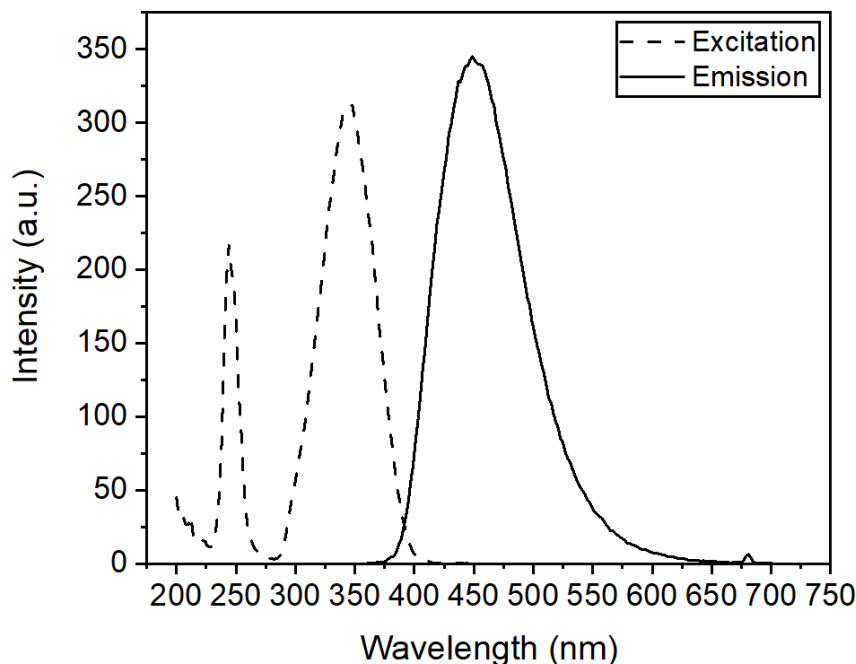


**Figure 3.6:** Example excitation and emission spectrum for **HMAM 3.9** in THF.

To quantify this, solution-state fluorescence quantum yield ( $\Phi_f$ ) analysis was undertaken for the series in a range of solvents (Figure 3.7). This confirmed initial observations, with BzMAM (**3.2**), Bz<sub>2</sub>MAM (**3.4**), HMAM (**3.9**), and iPrMAM (**3.12**) all exhibiting  $\Phi_{f(\%)}$  of 30-70% in non-polar solvents, and a significantly lower  $\Phi_f$  in DMSO and methanol. The slight decrease in  $\Phi_f$  displayed by iPrMAM (**3.12**) in all solvents could be attributed to the inductive effect of the isopropyl group. Likewise, PhMAM (**3.15**) was found to be non-fluorescent in solution, as previously reported for similar phenyl maleimides,<sup>9</sup> attributed to TICT in the solution state.

Most notably, however, Bz<sub>3</sub>MAM (**3.7**) exhibited increased  $\Phi_f$  in DMSO and methanol (11.3% and 3.8%) but significantly less in apolar solvents (all exhibited  $\Phi_{f(\%)} < 1.5\%$ ). This quenching in apolar solvents is perplexing as no direct conjugation of aromaticity to the maleimide ring is present based upon sp<sup>3</sup> hybridization theory, the usual cause of such quenching (as seen in PhMAM). To ascertain if the quenching may be a result of extension of the  $\pi$ -system beyond

the maleimide ring, modelling of the HOMO-LUMO isosurfaces was completed by Dr Miquel Torrent-Sucarrat (University of the Basque Country). The results of this are plotted in Figure 3.8.

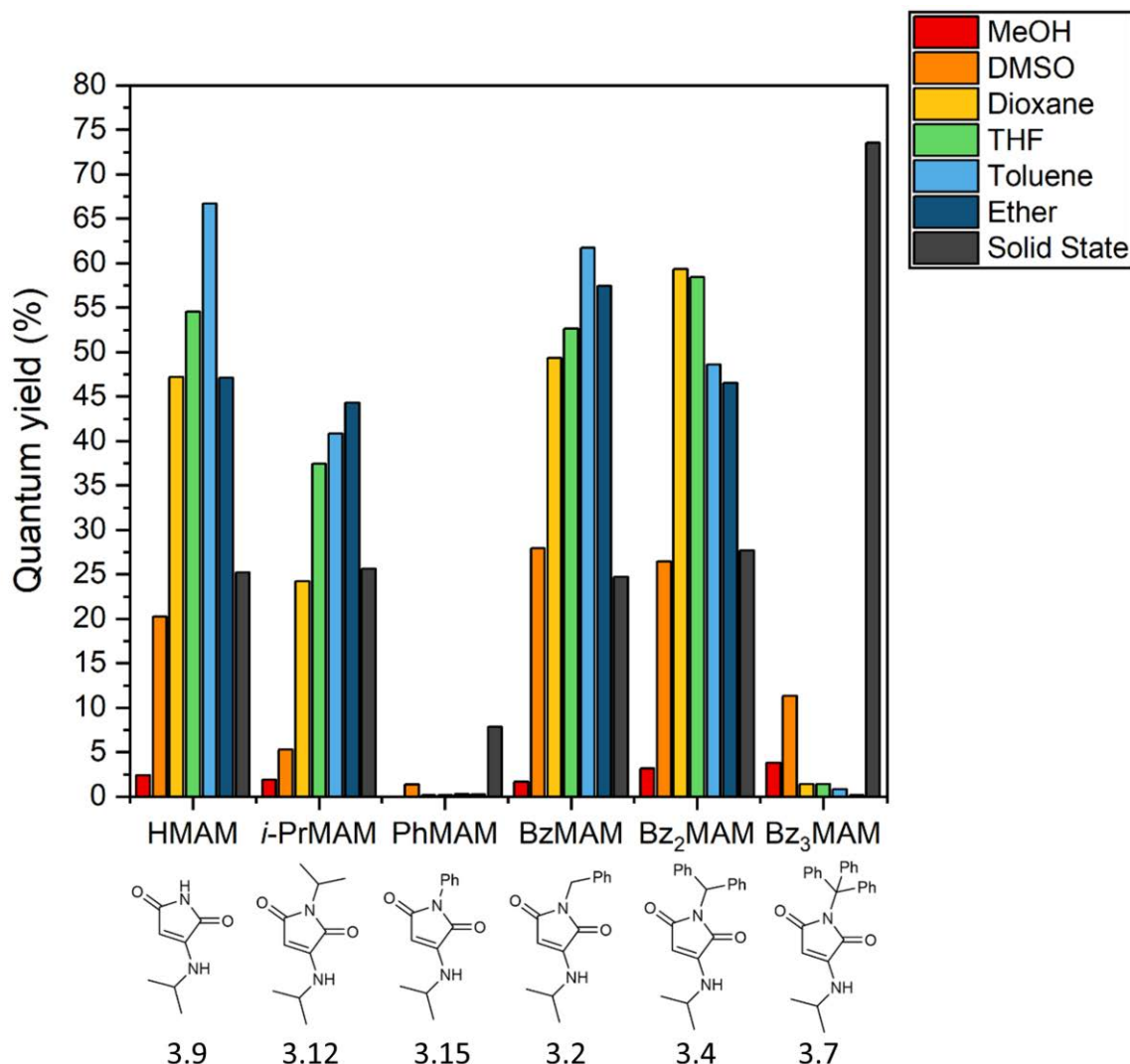


**Figure 3.7:** Chart of solution and solid-state quantum yields of studied maleimide fluorophores, showing poor solution fluorescence of PhMAM and Bz<sub>3</sub>MAM compared to the series. Recorded by either reference or absolute method, respectively.

This was numerically assessed through integration of electron density in the ring, in both the natural bonding orbital (NBO1) and the highest occupied molecular orbital (HOMO1). The electron density on the maleimide ring (Scheme 3.5), for NBO1 and HOMO1 were integrated and calculated as  $Q$  using equations

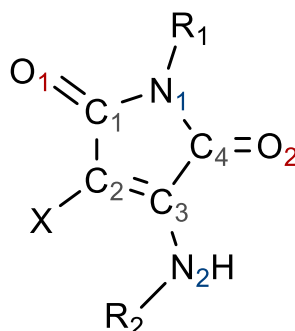


3.1 and 3.2. Lower  $Q$  values represent higher electron density on the maleimide ring and *vice versa*.

$$Q_{NBO1} = q_{NBO,C1} + q_{NBO,C2} + q_{NBO,C3} + q_{NBO,C4} + q_{NBO,O1} + \quad (\text{Eq. 3.1})$$

$$q_{NBO,O2}$$

$$Q_{HOMO1} = \int_{\Omega_{i=C1,C2,C3,C4,O1,O2}} \rho_{HOMO}(\vec{r}) w_i(\vec{r}) d\vec{r} \quad (\text{Eq. 3.2})$$



**Scheme 3.5:** Schematic representation of the atom enumeration used in the simulation of NBO1 and HOMO1 orbitals.

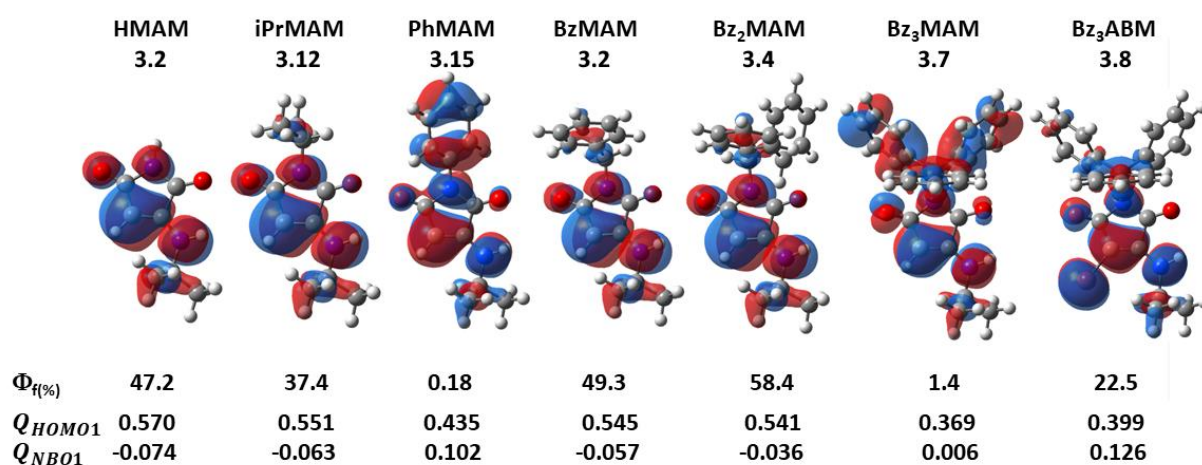


**Figure 3.8:** HOMO isosurfaces of benzyl MAM series with their HOMO1 and NBO1 atomic integrations - representing the  $\pi$ -conjugated structure of the aminomaleimide ring (lower  $Q$  values indicate greater electron density on the maleimide ring) and the solution state absolute quantum yields (in diethyl ether).

Based on the results obtained (Figure 3.8), we conclude that the imide substituent plays a crucial role in the electron distribution within the aminomaleimide ring and therefore, the resulting fluorescence emission of these

compounds. For instance, across the BzMAM, Bz<sub>2</sub>MAM, and Bz<sub>3</sub>MAM series, the HOMO isosurfaces and the electron density contributions of the substituents increase while exhibiting a corresponding decrease in the  $\pi$ -conjugated density on the aminomaleimide ring. This is visualized in Figure 3.8 where the HOMO1 of Bz<sub>3</sub>MAM is clearly located more towards the benzyl rings and this is shown by a high  $Q_{HOMO1}$ (0.006) compared to Bz<sub>2</sub>MAM (-0.036). This also correlates with a reduction in quantum yield in apolar solvents (58.4% to 1.4% in diethyl ether - Figure 3.8).

These results strongly suggest that the withdrawal of maleimide electron density across a quaternary carbon, leads to characteristic TICT quenching in solution. Moreover, within this series, the trityl group shows the largest electron-withdrawing character, which is evidenced by Bz<sub>3</sub>MAM also exhibiting the largest TICT quenching in solution. To explore this further analysis of a trityl-aminobromomaleimide analogue (Bz<sub>3</sub>ABM, **3.8**) was undertaken, in which the maleic proton is replaced by a bromine atom. Fluorescence analysis of this compound showed some quenching in apolar solvents, but not to the same degree as observed for Bz<sub>3</sub>MAM (for example, in toluene, the observed  $\Phi_f(\%)$  was 9.5% for the ABM and 1.39% for the MAM). By modelling the HOMO isosurface distribution of the compound, less electron density is located on the trityl group, which could be attributed to the electron-withdrawing character of the bromine atom (see Figure 3.8). It should be noted that the bromine atom is not included in the orbital integrations and therefore  $Q$  values are not comparable.

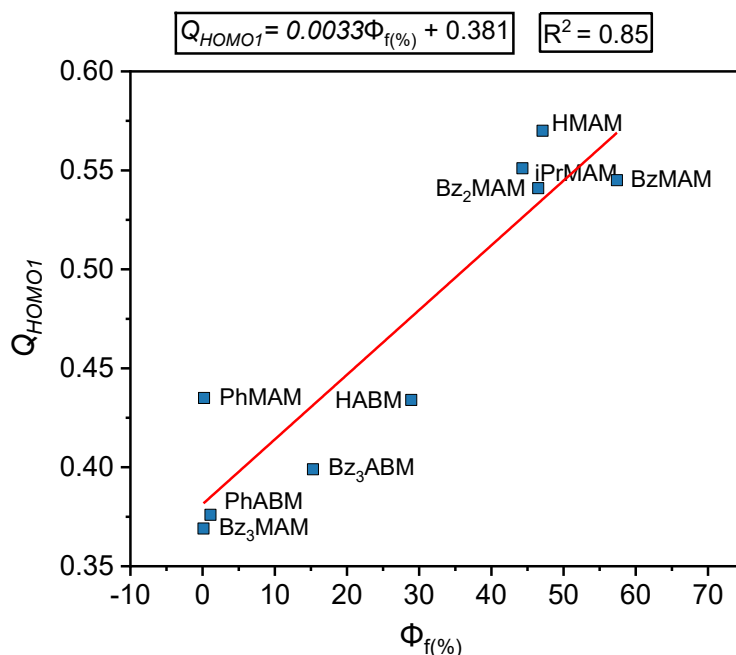


**Figure 3.9:** Correlation between quantum yield,  $\Phi_f(\%)$ , (in diethyl ether solution) and the atomic integration of HOMO1 along the  $\pi$  conjugated structure of the aminomaleimide ring,  $Q_{HOMO1}$ .

This phenomenon shows that the fluorescence intensity of maleimide dyes can be tuned through the withdrawal of electrons to or from aromatic groups. Specifically, conjugation of electron density above the imide is correlated well with a reduction in quantum yield in the solution state by linear fit,  $R^2 = 0.85$  (Figure 3.9). It could also be described by two quadrants in which a low  $Q_{HOMO}$  ( $< 0.45$ ) correlates to a low  $\Phi_f$  ( $< 30\%$ ) and a higher  $Q_{HOMO}$  ( $> 0.5$ ) correlates to a high  $\Phi_f$  ( $> 40\%$ ). Based upon this result, PhABM was analysed, which according to this theory should exhibit a higher  $\Phi_f$  in solution than PhMAM. Indeed, the bromine substituent did increase quantum yield in all solvents albeit the increase was small (for example from 1.3% to 3.6% in DMSO).

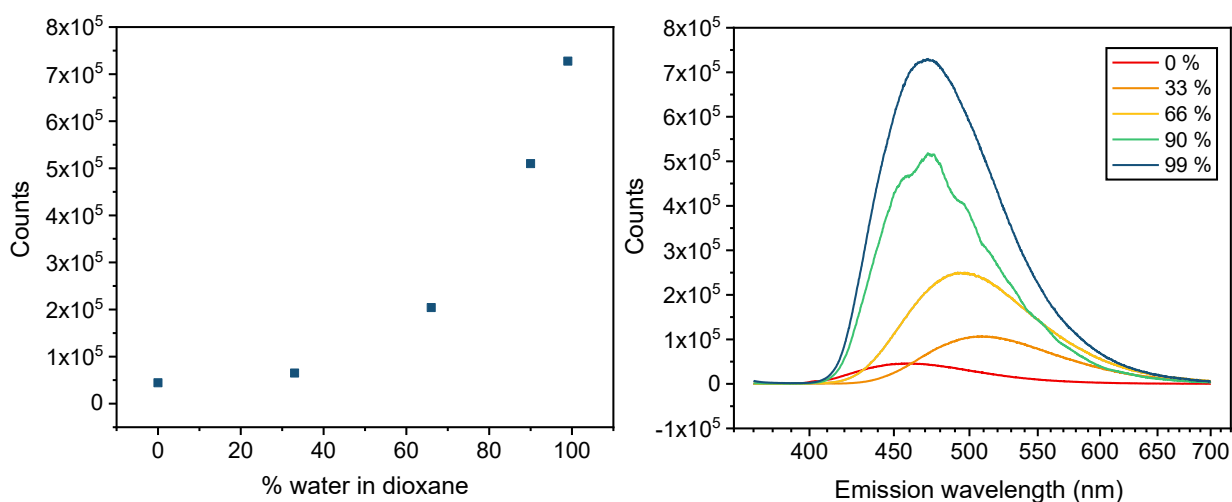


**Figure 3.10** Fluorescence of Bz<sub>3</sub>MAM (**3.7**) in water/dioxane mixtures: emission at 470 nm (375 nm excitation) against water content (left) and emission spectrum at 375 nm excitation at different percentages of water in dioxane (right).

In contrast to its solution state fluorescence, it was observed that Bz<sub>3</sub>MAM (**3.7**) was highly fluorescent in the solid-state. Therefore, it was decided to investigate any trends in solid-state fluorescence quantum yield for the series. BzMAM (**3.2**), Bz<sub>2</sub>MAM (**3.4**), HMAM (**3.9**), and iPrMAM (**3.12**) all exhibited  $\Phi_{f(\%)}$  around 25% (Figure 3.5). Notably however, Bz<sub>3</sub>MAM (**3.7**) showed very bright solid-state emission with a  $\Phi_{f(\%)}$  of 74% (Figure 3.7). To investigate the potential for AIE based applications, a solution of Bz<sub>3</sub>MAM (**3.7**) in dioxane was titrated with water to precipitate the dye. The low emission in dioxane gradually increased with increasing water content, as well as exhibiting a hypsochromic shift with increasing water content, indicative of fewer interactions with the solvent. In a water/dioxane (99/1) mixture, it exhibited over an eleven-fold increase in fluorescence emission compared to that exhibited in 100% dioxane, strongly suggesting AIE behaviour (Figure 3.10).

In an attempt to explain these observations, X-ray crystal structures were successfully obtained for the following compounds: BzMAM (**3.2**), Bz<sub>2</sub>MAM (**3.4**), HMAM (**3.9**), and Bz<sub>3</sub>MAM (**3.7**). From the molecular packing in the solved crystal structures, it was observed that HMAM, BzMAM, and Bz<sub>2</sub>MAM all form dimers connected by N–H···O bonds with bond lengths of 2.07 to 2.19 Å (Table 3.1). In HMAM, it was also notable that the imide N–H formed an extra hydrogen bonding dimer with the other carbonyl group; with an N–H···O bond length of 2.03 Å. In comparison, in Bz<sub>3</sub>MAM, the rings are no longer dimerized, possibly due to steric hindrances. Instead, maleimide rings form a chain of maleimide motifs with N–H···O bond lengths of 2.11 Å (Table 3.1).

**Table 3.1** Hydrogen bonding data for solved crystals of the benzyl MAM series.

\*n.d. = not determined. **HMAM** i= 1-X, +Y, -1/2+Z; **BzMAM** i= 1-X, 1-Y, 1-Z;

**Bz<sub>2</sub>MAM** i= 1-X, 1-Y, -Z; **Bz<sub>3</sub>MAM** i= +Y, +X, 1-Z.

Compound	Bonds	Length (dH-A) (Å)	Angle (°)	Form
HMAM 3.9	N2–H2···O1i	2.11 (±0.02)	167 (±2)	Dimer
	N1–H1···O2i	2.03 (±0.03)	170 (±3)	Imide H-Bond
BzMAM 3.2	N2–H2···O2i	2.19 (±0.02)	151.7 (±1.7)	Dimer
	H4···O1i	2.47 (±0.10)	174.2 (±0.8)	Dimer
Bz <sub>2</sub> MAM 3.4	N2–H2···O1i	2.07 (±0.04)	156 (±3)	Dimer
	N102–H102···O101i	2.11 (±0.04)	157 (±3)	Dimer
Bz <sub>3</sub> MAM 3.7	H3···O1i	2.92 (±0.04)	n.d.*	Chain
	N2–H2···O2i	2.14 (±0.06)	162 (±4)	Chain

**Table 3.2** Solid state  $\Phi_f$  and shortest maleimide crystal packing distances and angles for crystals of the benzyl MAM series. <sup>†</sup>Measured distance and angle between ring centroid of N1C1C2C3C4 and N1<sup>i</sup>C1<sup>i</sup>C2<sup>i</sup>C3<sup>i</sup>C4<sup>i</sup>. \*Angles between mean-plane created from atom selection N1C1C2C3C4 and N1<sup>i</sup>C1<sup>i</sup>C2<sup>i</sup>C3<sup>i</sup>C4<sup>i</sup>. <sup>‡</sup> Distance between ring centroid of N1C1C2C3C4 and plane of N1<sup>i</sup>C1<sup>i</sup>C2<sup>i</sup>C3<sup>i</sup>C4<sup>i</sup>. <sup>§</sup> Distance in horizontal shift between ring centroids of N1C1C2C3C4 and N1<sup>i</sup>C1<sup>i</sup>C2<sup>i</sup>C3<sup>i</sup>C4<sup>i</sup>.

Name	Solid state $\Phi_f(\%)$	Ring plane angle <sup>†</sup>	Ring centroid distance (Å) <sup>†</sup>	Inter plane distance (Å) <sup>†</sup>	Ring shift (Å) <sup>§</sup>	Ring to plane twist angle*	Ring to plane fold angle*
HMAM 3.9	25	9.8° (±0.14)	3.649 (±0.001)	3.520 (±0.001)	0.648 (±0.005)	23.1° (±0.04)	8.35° (±0.12)
BzMAM 3.2	25	0° (±0.07)	4.053 (±0.001)	3.519 (±0.002)	2.070 (±0.003)	0° (±0.07)	0° (±0.07)
Bz <sub>2</sub> MAM 3.4	28	0° (±0.05)	5.042 (±0.003)	2.764 (±0.009)	4.216 (±0.006)	0° (±0.205)	0° (±0.5)
Bz <sub>3</sub> MAM 3.7	74	13.0° (±0.3)	6.464 (±0.004)	5.885 (±0.007)	2.674 (±0.013)	150.1° (±0.7)	166.6° (±0.3)

It was hypothesized that steric hindrance arising from the trityl groups could be preventing the maleimide rings from coming in close proximity, reducing any intramolecular  $\pi$ - $\pi$  interactions that could be causing quenching in the aggregated state. The lack of N-H...O dimerization suggested that the rings may indeed be further separated. However, this can be further quantified through the measurement of maleimide ring distances to evaluate any  $\pi$ - $\pi$  interactions that may be present. HMAM and BzMAM both crystalized with anti-parallel off centre maleimide rings, where the maleimide rings are orientated at 180°, suggestive of  $\pi$ - $\pi$  stacking interactions.<sup>31,32</sup> The distance between rings is 3.707 Å in HMAM and 4.053 Å in BzMAM (Table 3.2), distances indicative of typical  $\pi$ - $\pi$  interactions.<sup>33,34</sup> In Bz<sub>2</sub>MAM, inter-ring centroid distances became larger at 5.042 Å, while the inter-plane distance decreased to 2.764 Å. This suggests an increase in the off-centre nature of the  $\pi$ - $\pi$  interactions. The shortest observed maleimide ring centroid

distance in obtained crystal structures was 6.464 Å for Bz<sub>3</sub>MAM, significantly higher than in the other crystals (Table 3.2).

To reveal this further, the visualization of noncovalent interactions (NCI) was performed (Figure 3.11). Clear  $\pi$ - $\pi$  stacking between the aminomaleimide rings is observed in the NCI isosurfaces of HMAM (**3.9**), BzMAM (**3.2**), and Bz<sub>2</sub>MAM (**3.4**). On the other hand, in Bz<sub>3</sub>MAM (**3.7**) the NCI plot became more diffuse and  $\pi$ - $\pi$  interactions are not observed; instead, above and below the maleimide rings sit methyl or benzyl groups of the neighbouring molecule. This can be visualized by plotting the HOMO or LUMO orbitals which show clear  $\pi$  overlap in all structures but Bz<sub>3</sub>MAM (Figure 3.12).

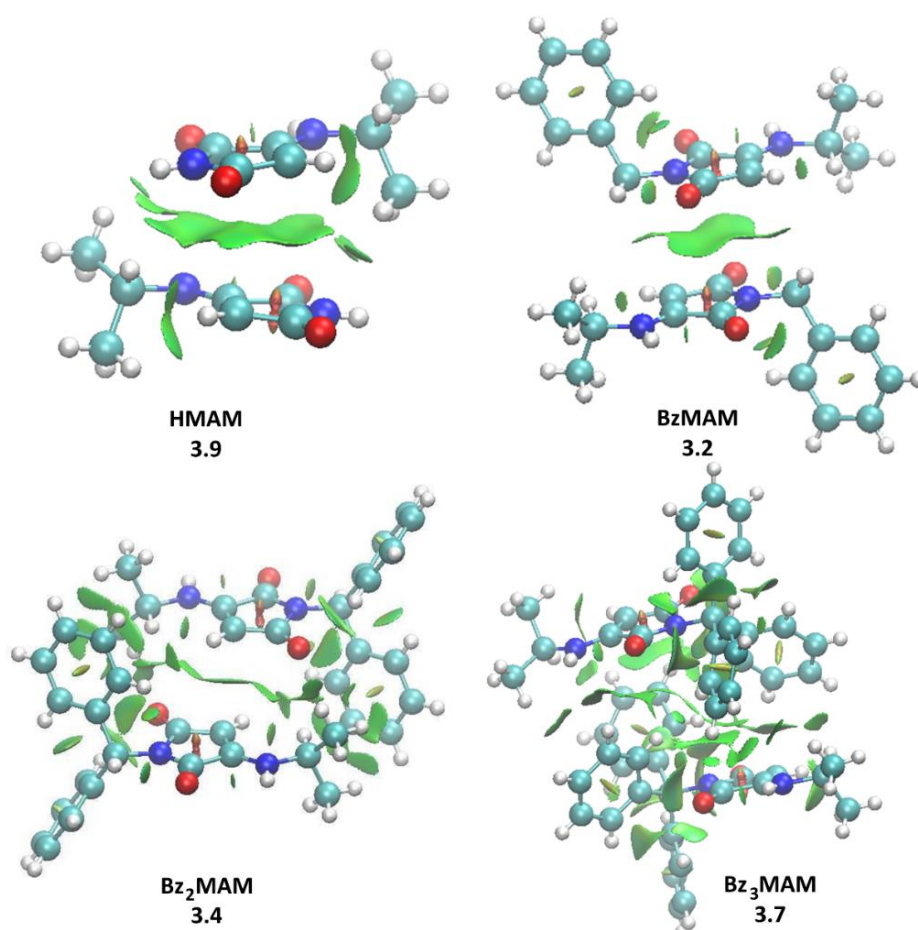


**Figure 3.11** CAM-B3LYP/6-311G(d,p) gradient isosurfaces with  $s=0.5$  for the crystal structures of HMAM (**3.9**), BzMAM (**2.3**), Bz<sub>2</sub>MAM (**3.4**), and Bz<sub>3</sub>MAM (**3.7**) with a blue-green-red colour scale from  $-0.05 < \rho \text{ sign}(\lambda_2) < 0.05$  au.

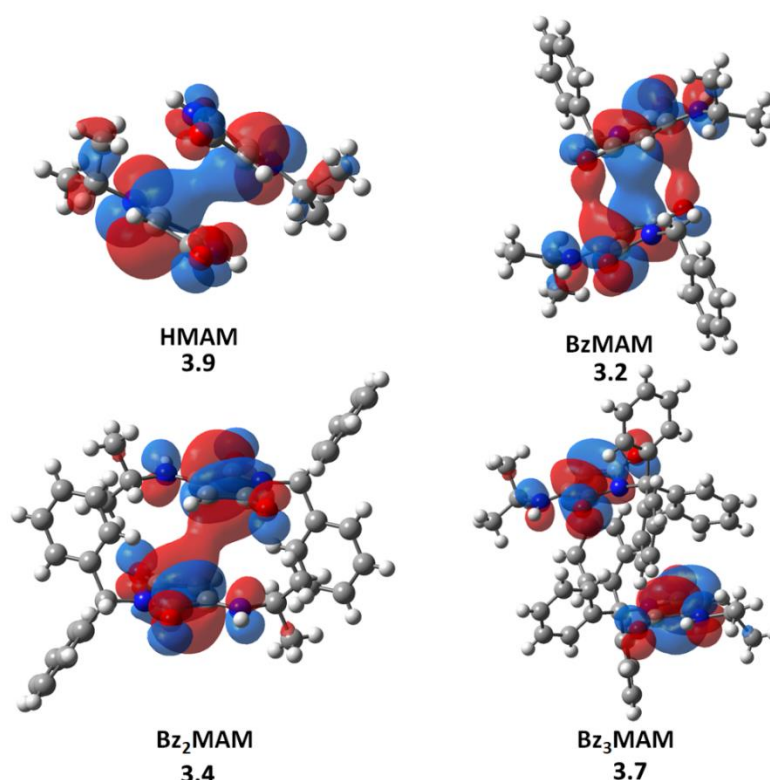


**Figure 3.12** LUMO isosurfaces overlaid on the obtained crystal structures of the benzyl functionalized series.

Despite the earlier AIE titration, the observation that the solid-state quantum yield may be negatively affected by  $\pi$ - $\pi$  interactions in the solid-state, and potentially hydrogen bonds between maleimide dimers, suggested that Bz<sub>3</sub>MAM is not exhibiting traditional AIE behavior. To probe this mechanism further, the series of dyes were drop cast with 12 kDa polyethylene glycol (PEG) to form dye incorporated powders. The absolute quantum yields of these powders were then measured to establish if the polymer chains provide shielding of  $\pi$ - $\pi$  and H-bonding interactions, thus increasing emission. As expected, the incorporation of dyes HMAM, BzMAM, and Bz<sub>2</sub>MAM into PEG led to an increase in emission, with an approximately two-fold increase in emission intensity observed for each dye, for example, the  $\Phi_{f(\%)}$  of HMAM increased from 25.3% to 49.4% (Figure 3.13). Bz<sub>3</sub>MAM however, showed a negligible increase in emission from 73.6% to 75.3%. These observations appear to confirm that prevention of  $\pi$ - $\pi$  interactions through



sterics increases fluorescence in the solid-state, and that this can be achieved covalently through dye substitution or non-covalently through polymer shielding.

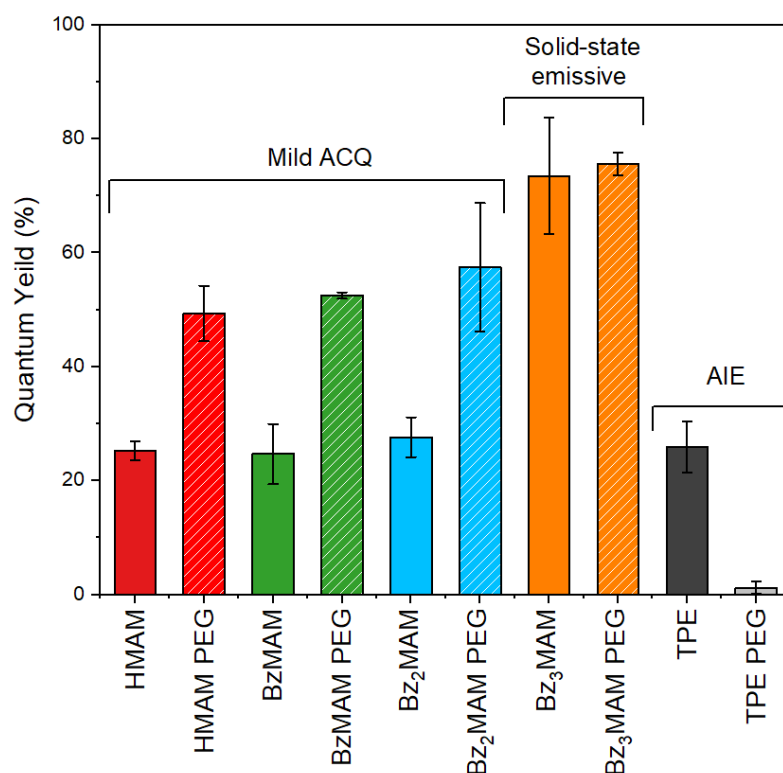


**Figure 3.13** Chart displaying solid-state (solid colors) and PEG incorporated (striped colors) absolute quantum yields. Error bars represent standard deviation over 3 repeats.

To ascertain if this phenomenon was unique to maleimides, a known AIE dye tetraphenylethylenealdehyde (TPE) was incorporated with PEG. Quantum yield analysis of this powder indicated a reduction in emission upon incorporation with PEG (25.9% to 1.5%). This is in corroboration with hypothesis on AIE dyes which suggests separation in the solid-state increases vibrational relaxation viability.<sup>35</sup> This suggests Bz<sub>3</sub>MAM exhibits purely solid-state emission in comparison to traditional AIE fluorophores and that these dyes could suit applications in material applications where separation in the solid-state maybe needed, for example explosives detection.<sup>36</sup> This puts doubt into previous reports on maleimide AIEgens,<sup>22</sup> and suggests future work should consider solid-state

separation to aid mechanistic understanding of AIE versus purely solid-state emission as seen here.

### 2.3.4 Fluorescence analysis of silyl substituted maleimides

In the hopes of realizing increased emission in protic solvents, the synthesised silyl derivatives were studied. The silyl derivatives appeared fluorescent, and were therefore analysed by steady-state fluorescence spectroscopy. All dyes showed emission in solution, with a slight blue shift compared to previous maleimide dyes - for example, TBDPSiMAM (**3.21**)  $\lambda_{\text{em}} = 458$  nm in dioxane (Figure 3.14), while BzMAM (**3.2**)  $\lambda_{\text{em}} = 469$  nm. Notably, emission in methanol appeared to be significantly higher than expected, suggesting improved emission under protic conditions. To evaluate any change in this regard,  $\Phi_f$  analysis was undertaken for the series in a range of solvents (Figure 3.15) and compared to HMAM (**3.9**), HABM (**3.10**) and iPrMAM (**3.12**) controls.

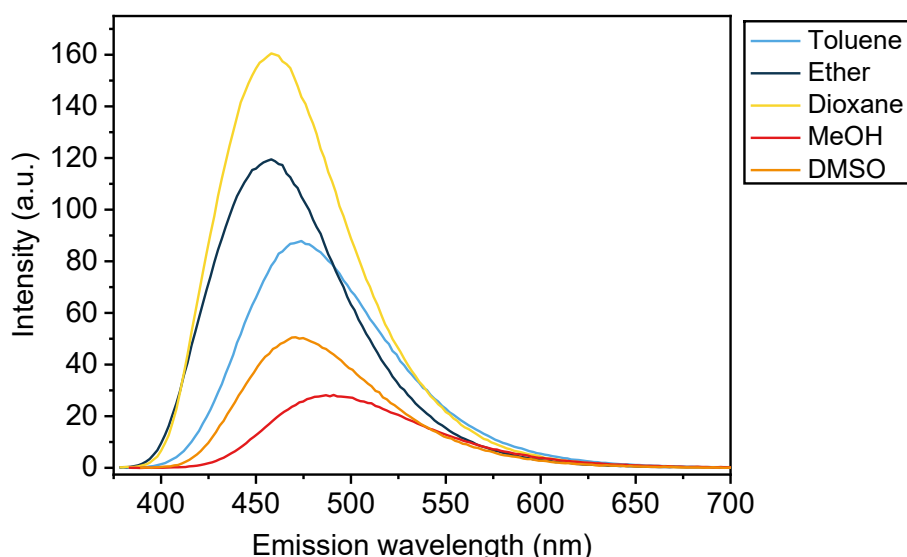


**Figure 3.14** Spectrum displaying solution state emission of TBDPSiMAM (**3.21**) in various solvents ( $\lambda_{\text{ex}} = \lambda_{\text{max}}$ ).

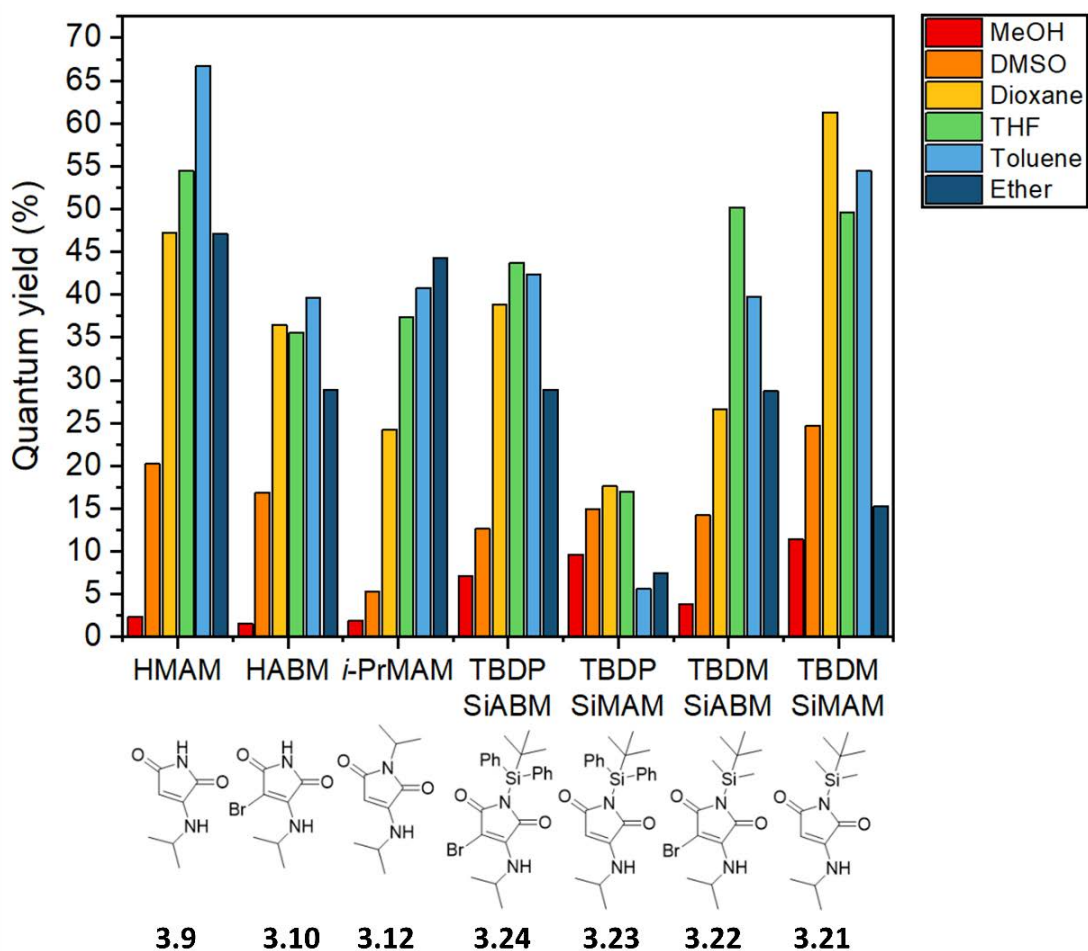


**Figure 3.15** Chart showing solution state quantum yields of silyl substituted maleimide fluorophores and control dyes; measured by reference method.

First impressions show similar quantum yields for the silyl derivatives in apolar solvents compared to the control maleimides. TBDPSiMAM (**3.23**) does show slightly reduced emission in these solvents, which could be attributed to partial withdrawal of electrons from the maleimide into the imide substituent, as seen in Bz<sub>3</sub>MAM (**3.7**). The observation that the analogous ABM, TBDPSiAbM (**3.24**), does not show reduced emission also corroborates this phenomenon as it was shown in the benzyl series that the bromine atom redistributed electrons back into the maleimide ring from imide substituents.

Comparing the polar solvent emission, however, it was clear that the quantum yield in methanol had increased. For the silyl-MAMs a  $\Phi_f(\%)$  of up to

11.4% (TBDMSiMAM) in methanol was recorded, a several fold increase from that recorded for the controls HMAM, HABM and iPrMAM ( $\Phi_{f(\%)}$  = 2.4%, 1.6% and 1.9% respectively). However, emission in DMSO was negligibly affected, indicating that the increase emission in methanol is from shielding of EDPT.<sup>2</sup> To confirm this, it was decided to model the theoretical emissions with various solvent interactions and compare these to the experimental data. By doing this we hope to eliminate any effects, the silyl substitution may be imparting. Collaborator Dr Miquel Torrent-Sucarrat modelled the theoretical  $\lambda_{ex/em}$  for the two silyl MAMs and for comparison HMAM and iPrMAM, when including zero, one or two explicit solvent molecules. These solvent molecules were considered to be bonding to either carbonyl or both (Figure 3.16).

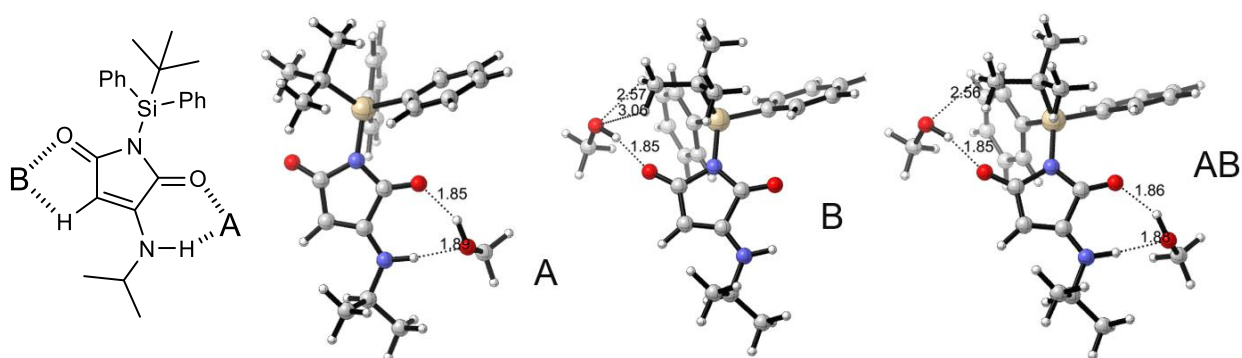


**Figure 3.16** Illustration and modelling of hydrogen bonding interactions with TBDPSiMAM and methanol.

**Table 3.3** Theoretical and observed fluorescence  $\lambda_{\text{ex/em}}$  in methanol, used to calculate a probability of hydrogen bonding ( $P$ ).

Compound	Calculated					Observed		
	H-Bonds	$\lambda_{\text{ex}}$ (nm)	$\lambda_{\text{em}}$ (nm)	$\Delta\lambda$ (nm)	P	$\lambda_{\text{ex}}$ (nm)	$\lambda_{\text{em}}$ (nm)	$\Delta\lambda$ (nm)
HMAM 3.9	None	316.0	418.9	102.9	0.66	369	489	120
	A	328.9	451.6	122.7				
	B	322.4	430.9	108.5				
	AB	334.9	463.8	128.9				
iPrMAM 3.12	None	326.8	444.4	117.6	1.23	369	519	150
	A	338.3	474.4	136.1				
	B	334.4	458.2	123.8				
	AB	346.8	490.3	143.6				
TBDPSi-MAM 3.23	None	316.1	416.5	100.4	0.45	353	467	114
	A	326.7	434.9	108.3				
	B	320.3	423.3	103.1				
	AB	332.5	456.2	123.7				
TBDMSi-MAM 3.22	None	316.1	417.7	101.7	0.28	363	473	110
	A	328.6	448.5	119.9				
	B	323.8	434.2	110.4				
	AB	336.4	465.8	129.4				

Using these optimised geometries, the theoretical  $\lambda_{\text{ex/em}}$  and thereby Stokes shift,  $\Delta\lambda$ , was calculated and compared to experimental observations (Table 3.3). Measured Stokes shifts of silyl-maleimides were smaller than controls and emission was blue-shifted (467 nm for TBDPSi-MAM and 489 nm for HMAM). Both these indicate fewer interactions with solvent as red-shifted emission is directly correlated to interactions with polar solvents due to the stabilization of the CT state.<sup>2</sup> To establish a more quantifiable parameter the simulated data was fitted to a quadratic equation (Eq. 3.3) and solved for the measured values to establish a probability of hydrogen bonding,  $P$ . In this we let  $z$  be the empirical measurement of Stokes shift,  $u_0$  is the numerically estimated Stokes shift with no hydrogen bonding interactions,  $u_a$  and  $u_b$  are the estimated Stokes shifts with hydrogen bonding occurring at either side A or B, finally,  $u_{ab}$  is the calculated Stokes shift

for both hydrogen bonding events occurring at A and B. Both hydrogen bonding events A and B are assumed to be of equal probability. Assuming this, the positive real root of  $P$  can be solved to give an average rate/probability of hydrogen bonding occurring.

$$p^2(u_{ab}) + p(1 - p)(u_a + u_b) + ((1 - p)^2 * u_0) - z = 0 \text{ (Eq. 3.3)}$$

The trend observed in  $P$  values correlates well with the observed trend in Stokes shift and suggests that the bulky silyl groups are indeed providing protection from solvent quenching interactions. iPrMAM has the largest Stokes shift (150 nm) and  $P$  value at 1.23, suggesting the greatest influence of solvent. With a  $P$  value over 1, this suggests either an error with the theoretical modelled values or that more than two H-bonding events per molecule are occurring on average, which could be envisioned. At the other end of the scale, TBDMSi-MAM shows the lowest Stokes shift (110 nm) and the lowest  $P$  value (0.23). The combination of trend in Stokes shift and estimated  $P$  values suggests successful shielding against EDPT in methanol. Unfortunately, these compounds are not water-soluble and the increase in size negates the benefit of maleimide dyes being small, neutral fluorophores. Therefore, the use of these dyes for peptide-based applications, such as fluorescent labelling, will not be investigated further.

## 2.4 Conclusions

To summarize, the effect of imide substitution on the emission of maleimide fluorophores has been explored, through introduction of aryl and silyl groups. In general, direct conjugation of an aromatic group to the maleimide unit quenches fluorescence in solution. However, this quenching is also observed in a trityl functionalized dye where electron density is withdrawn through a quaternary carbon. This same dye also appeared to exhibit AIE as the quantum yield significantly increased to 79% in the aggregate state. However, by analyzing the crystal structures of the series, including measuring  $\pi$ - $\pi$  separation and modelling the NCI and HOMO-LUMO isosurfaces, it is clear that most dyes exhibit mild aggregation caused quenching as a cause of  $\pi$ - $\pi$  and H-bonding interactions. However, in Bz<sub>3</sub>MAM the presence of a bulky trityl group simply prevents such interactions leading to the impressive solid-state quantum yield. This was proven further through polymer powder incorporation which increased the emission of all non-shielded dyes, suggesting that 'AIE' effects can be amplified through increasing dye separation in the solid-state, an important consideration when designing AIE probes for macromolecular applications.

In regards to the silyl derivatives, the steric hindrance introduced through silyl derivatives has been shown to increase fluorescence emission in polar protic solvents, with a  $\Phi_{\text{f}(\%)}$  up to 11% in MeOH. The reduced interaction with solvent is also exhibited by reduced Stokes shift in silyl-maleimides, and expressed as an estimated probability of hydrogen bonding or  $P$ .

## 2.5 Experimental

### 2.5.1 Materials and instrumentation

All chemicals were obtained from either: Sigma Aldrich, Fisher Chemicals, Acros Chemicals, Carbosynth or Alfa Aesar and used as received.

NMR spectra were recorded on a Bruker Advance 300, a Bruker Advance III HD 400 or a Bruker Advance III HD 500 spectrometer at 300, 400 and 500 MHz respectively. Shifts are quoted in  $\delta$  in parts per million (ppm) and quoted relative to the internal standard trimethylsilane (TMS) or the solvent peak.

High Resolution Mass Spectra (HR-MS) were conducted by Dr Lijiang Song (University of Warwick) on a Bruker UHR-Q-ToF MaXis spectrometer with electrospray ionization, or by Dr Christopher Williams (University of Birmingham) on a Waters Xevo G2-XS.

Infrared spectra were recorded on neat samples using a Perkin Elmer Spectrum 100 FT-IR Spectrometer. UV-Vis spectroscopy was carried out on a Perkin Elmer Lambda 35 UV/vis spectrometer or an Agilent Cary 60 UV-Vis Spectrometer at room temperature.

Fluorescence emission and excitation spectrum were obtained with an Edinburgh Instruments FS5 Spectrofluorometer in quartz 3.5 mL cuvettes for liquid samples (Starna Cell, Type: 3/Q/10), and analyzed in Fluoracle (Edinburgh Instruments) and Origin 2019 (Origin Labs). Solution state quantum yield analysis was based on a previously reported literature procedure.<sup>37</sup> In short, a solution of quinine sulfate dihydrate (15  $\mu\text{mol}$ ) in 0.105 mol/L perchloric acid was used a standard ( $\Phi_{\text{quinine}} = 59\%$ ), from which a UV-visible spectrum was recorded. The sample was diluted until the absorbance was between 0.05 - 0.1 and then the emission spectra at  $\lambda_{\text{max}}$  was measured.

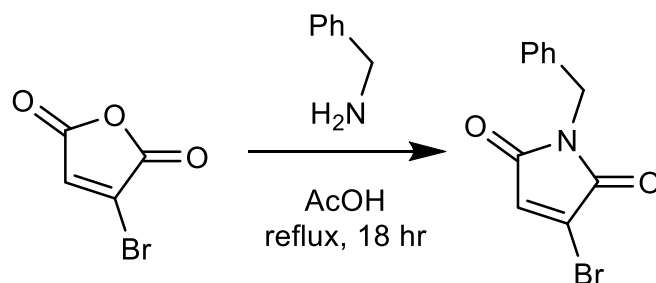


For solid-state fluorescence, absolute fluorescence quantum yields were recorded with an integrating sphere set up. The dye solid was crushed into a fine powder, and approximately 1-10 mg of the dye was placed onto a circular solid-state holder for analysis. All dyes were recorded with 375 nm excitation; with a 7-8 nm excitation slit and 0.1-0.2 nm emission slit width. Dyes were measured in triplicate and the mean and standard deviation ( $\sigma$ ) recorded.

Crystals were grown by dissolving several milligrams of the dye in around 5 mL of  $\text{CH}_2\text{Cl}_2$ /hexane, in a small vial with a lid. This was placed in a sealed jar quarter filled with hexane. A needle was placed into the vial to allow solvent exchange with the jar reservoir. This was left on a windowsill for 2-4 weeks until crystals were observed. The datasets for HMAM, BzMAM, Bz<sub>2</sub>MAM and Bz<sub>3</sub>MAM were measured on an Agilent SuperNova diffractometer using an Atlas detector. Structures were collected and solved by Dr Louise Male. More information on the structures can be found in the publication. CCDC1955637 – CCDC1955640 contain the supplementary crystallographic data for this Chapter. These can be obtained free of charge from The Cambridge Crystallographic Data Centre *via* [www.ccdc.cam.ac.uk/data\\_request/cif](http://www.ccdc.cam.ac.uk/data_request/cif).

## 2.5.2 Small molecule synthesis and characterization

### 2.5.2.1 1-phenyl-3-bromo-1H-pyrrole-2,5-dione (3.1)



Bromomaleic anhydride (1 g, 5.6 mmol) was dissolved in acetic acid (25 mL) in a round bottom flask containing a stirrer bar. To this benzylamine (642 mg, 6.4 mmol) was slowly added. This was refluxed for 4 hours and then left to cool.

The solvent is removed *in vacuo* and then purified by silica column chromatography and eluted with 20% CHCl<sub>3</sub> in hexane. The product was obtained as a yellow powder (984 mg, 26%).

<sup>1</sup>H NMR (300 MHz, CDCl<sub>3</sub>, ppm) δ = 7.38 – 7.28 (m, 5H, ArH), 6.87 (s, 1H, CH), 4.71 (s, 2H, CH<sub>2</sub>).

<sup>13</sup>C NMR (101 MHz, CDCl<sub>3</sub>, ppm) δ = 168.21 (CO), 165.04 (CO), 135.63 (CH), 131.92 (CBr), 131.51 (ArC), 128.80 (ArC), 128.62 (ArC), 128.14 (ArC), 42.40 (CH<sub>2</sub>).

HR-MS (MaXis) - [M+Na<sup>+</sup>] – calculated m/z 265.9813, observed m/z 265.9817;

FTIR (cm<sup>-1</sup>) - 3093 (ν<sub>Ar-H</sub>), 2933 (ν<sub>C-H</sub>), 1705 (ν<sub>C=O</sub>).

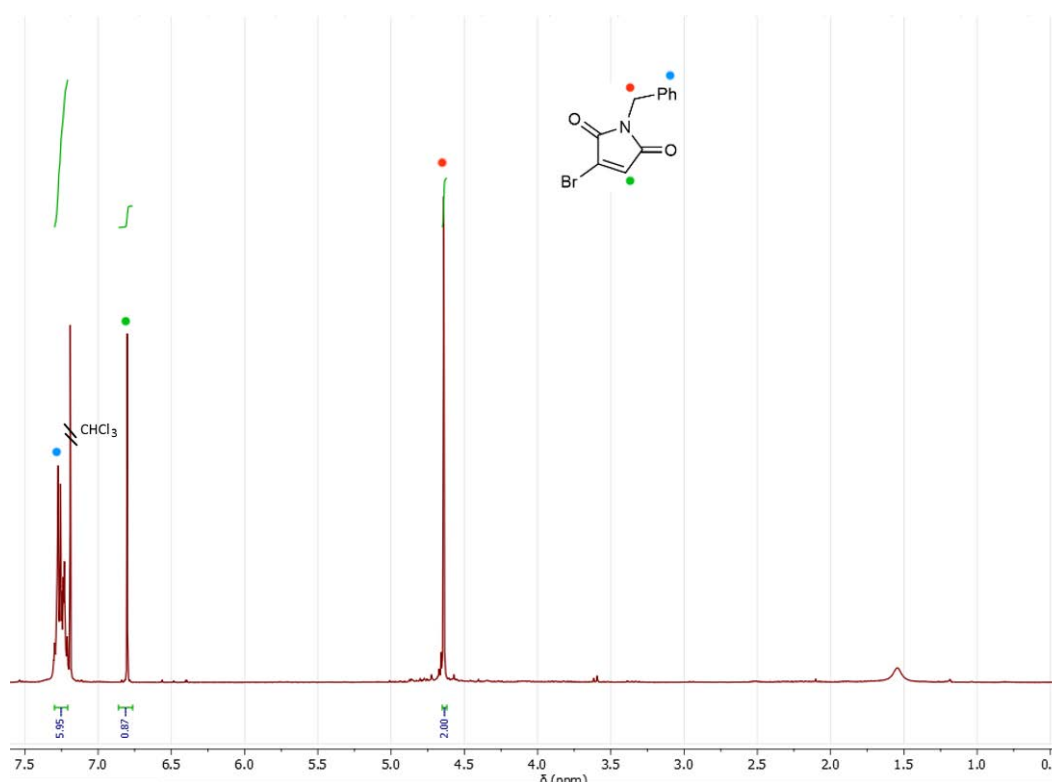


**Figure 3.17:** <sup>1</sup>H NMR spectrum of **3.1** (300 MHz, CDCl<sub>3</sub>).

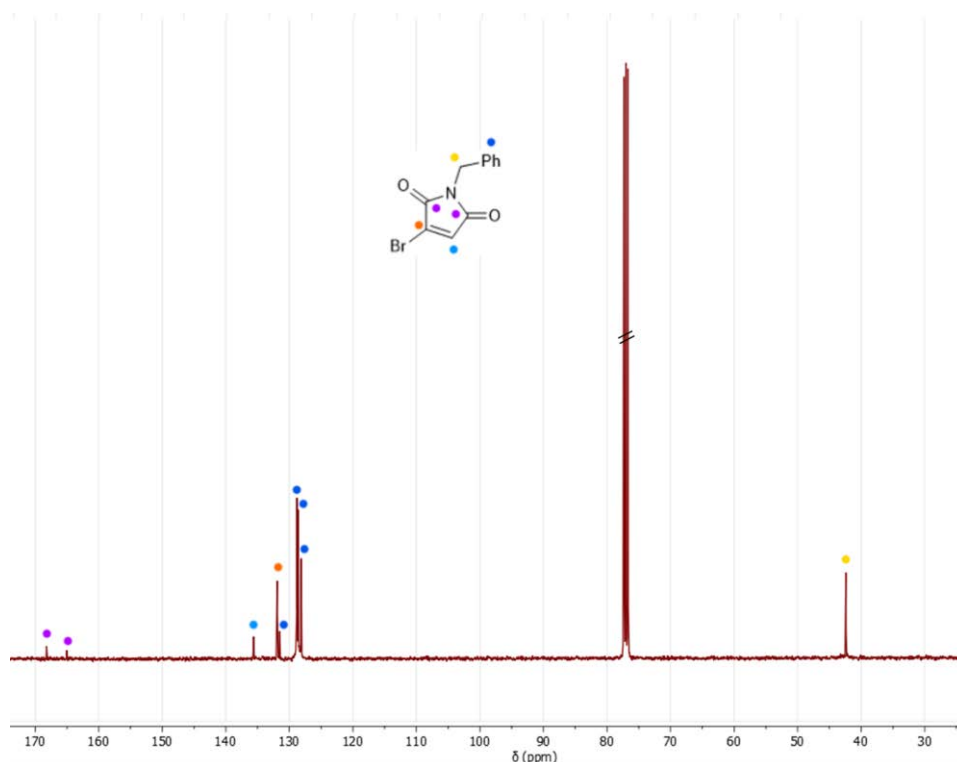
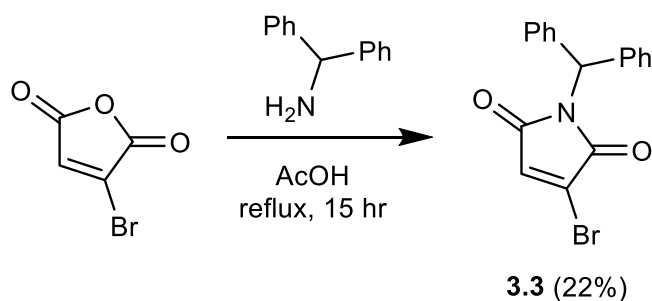


**Figure 3.18:**  $^{13}\text{C}$  NMR spectrum of **3.1** (101 MHz,  $\text{CDCl}_3$ ).

#### 2.5.2.2 1-benzhydryl-3-bromo-1H-pyrrole-2,5-dione (**3.3**)



Bromomaleic anhydride (1 g, 5.6 mmol) was dissolved in acetic acid (25 mL) in a round bottom flask containing a stirrer bar. To this diphenylmethanamine (1.03 g, 5.6 mmol) was slowly added. This was refluxed for 15 hours and then left to cool. The solvent is removed *in vacuo* and then the orange solid was purified by silica column chromatography and eluted with 10% diethyl ether in hexane ( $R_f = 0.1$ ). The product was obtained as a yellow powder (415 mg, 22%).

$^1\text{H}$  NMR (500 MHz,  $\text{CDCl}_3$ , ppm)  $\delta$  = 7.48 – 7.17 (m, 10H, ArH), 6.89 (s, 1H, CH), 6.54 (s, 1H, ArCH).

$^{13}\text{C}$  NMR (126 MHz,  $\text{CDCl}_3$ , ppm)  $\delta$  = 168.1 (CO), 164.9 (CO), 137.6 (CH), 131.8 (CBr), 131.5 (CAr), 128.6 (ArC), 128.5 (ArC), 128.0 (ArC), 58.6 (CH).

HR-MS (MaXis) -  $[\text{M}+\text{Na}^+]$  – calculated  $m/z$  363.9944 observed  $m/z$  363.9942;

FTIR ( $\text{cm}^{-1}$ ) – 3096 ( $\nu_{\text{Ar-H}}$ ), 2910 ( $\nu_{\text{C-H}}$ ), 1705 ( $\nu_{\text{C=O}}$ ), 1656 ( $\nu_{\text{C=O}}$ ).

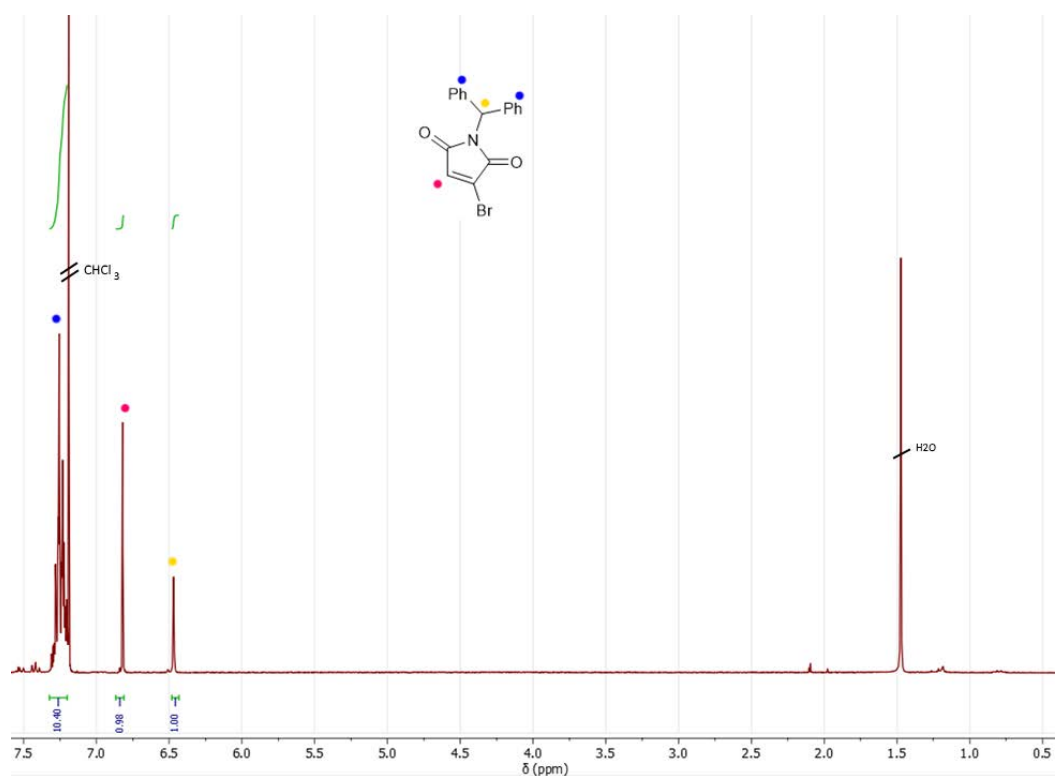


**Figure 3.19:**  $^1\text{H}$  NMR spectrum of **3.3** (500 MHz,  $\text{CDCl}_3$ ).

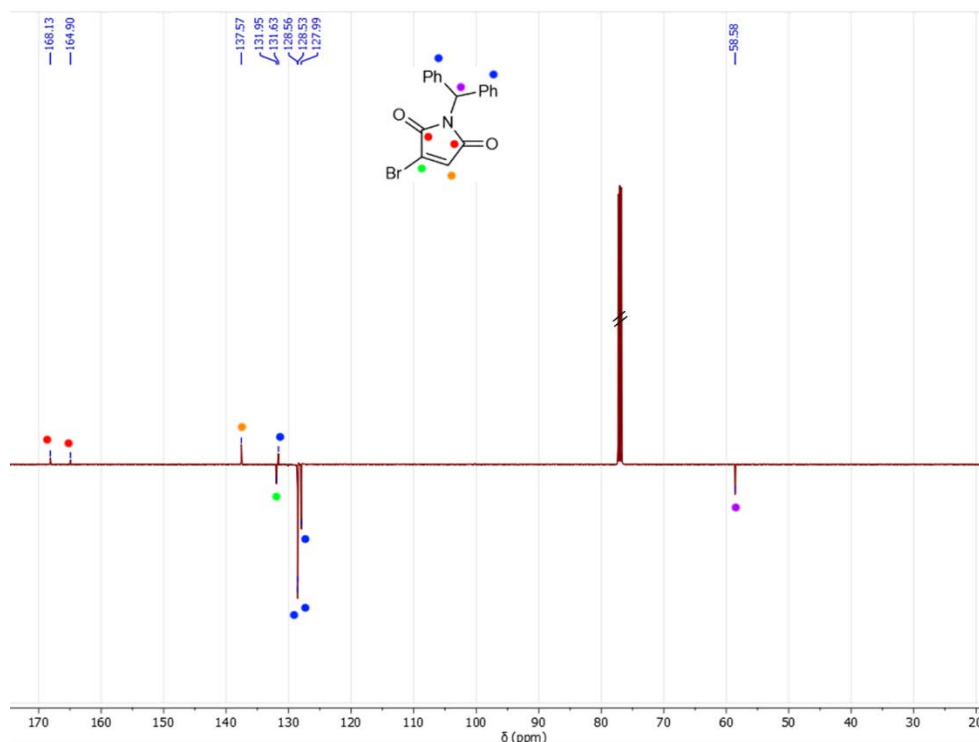
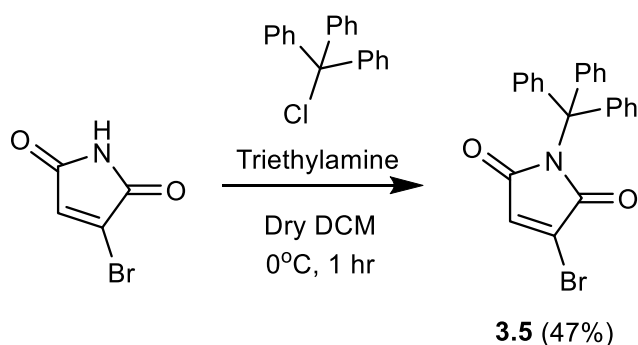


**Figure 3.20:**  $^{13}\text{C}$  NMR spectrum of **3.3** (126 MHz,  $\text{CDCl}_3$ ).

#### 2.5.2.3 3-bromo-1-trityl-1H-pyrrole-2,5-dione (**3.5**)



Under dry conditions, a solution of monobromomaleimide (**2.1**, 0.25 g) and trityl chloride (0.42 g) in dry  $\text{CHCl}_2$  was cooled to 0 °C. To this, triethylamine (160 mg) was added gradually. After 1 h the reaction was dried. The crude product was isolated *via* column chromatography using 2-3% EtOAc in petroleum ether as the eluent to afford cream solid (580 mg, 47%).

$^1\text{H}$  NMR (500 MHz,  $\text{CDCl}_3$ , ppm)  $\delta$  = 7.38 (d,  $^3J_{\text{HH}}$  = 7.5 Hz, 6H), 7.32 – 7.14 (m, 9H), 6.76 (s, 1H).

$^{13}\text{C}$  NMR (126MHz,  $\text{CDCl}_3$ , ppm)  $\delta$  = 168.4 (CO), 165.1 (CO), 142.0 (CBr), 132.6 (CH), 131.9 (CAr), 128.6 (CAr), 127.7 (CAr), 127.0 (CAr), 76.4 (C).

HR-MS (MaXis) -  $[\text{M}+\text{Na}^+]$  – calculated m/z 440.0257 observed m/z 440.0256;

FTIR ( $\text{cm}^{-1}$ ) - 3096 ( $\nu_{\text{C-H}}$ ), 1707 ( $\nu_{\text{C=O}}$ ), 1686 ( $\nu_{\text{C=O}}$ ).

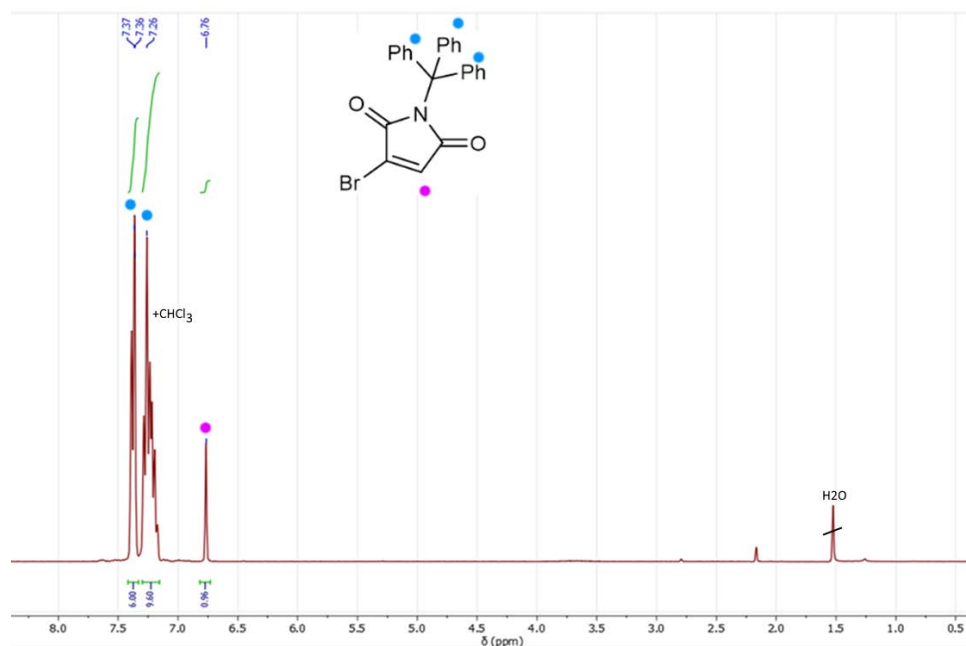


**Figure 3.21:**  $^1\text{H}$  NMR spectrum of **3.5** (500 MHz,  $\text{CDCl}_3$ ).

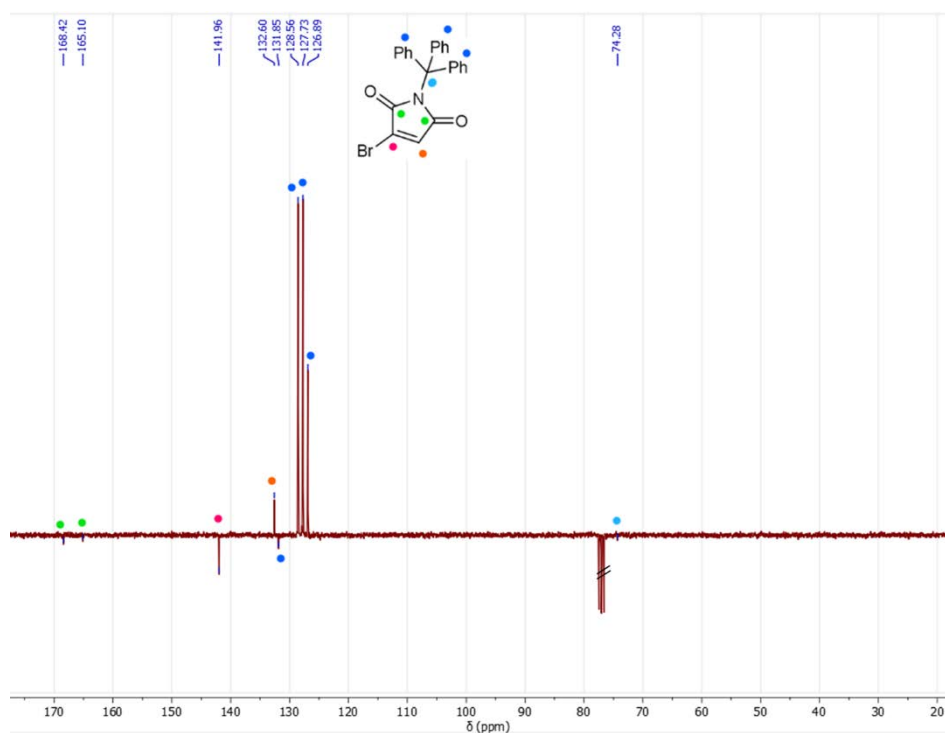
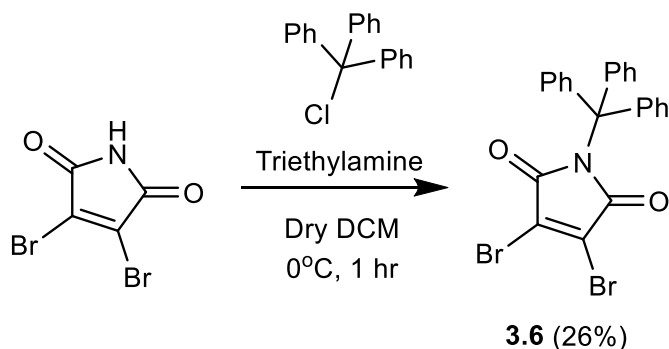


**Figure 3.22:**  $^{13}\text{C}$  NMR spectrum of **3.5** (126 MHz,  $\text{CDCl}_3$ ).

#### 2.5.2.4 3,4-dibromo-1-trityl-1H-pyrrole-2,5-dione (3.6)



Under dry conditions, a solution of dibromomaleimide (0.5 g) and trityl chloride (0.6 g) in dry  $\text{CHCl}_2$  was cooled to  $0^\circ\text{C}$ . To this, triethylamine (218  $\mu\text{l}$ ) was added gradually. After 1 h 15 min the reaction was dried. The crude product was isolated *via* column chromatography using 5% EtOAc in petroleum ether as the eluent, to afford cream solid (240 mg, 26%).

$^1\text{H}$  NMR (400 MHz,  $\text{CDCl}_3$ , ppm)  $\delta$  = 7.31 – 7.21 (m, 5H, ArH).

$^{13}\text{C}$  NMR (101 MHz,  $\text{CDCl}_3$ , ppm)  $\delta$  = 163.7 (CO), 141.7 (CBr), 130.2 (CAr), 128.5 (CAr), 127.8 (CAr), (CAr), 127.0 (CAr), 75.2 (CN).

HR-MS (Xevo) -  $[\text{M}+\text{Na}^++\text{MeOH}]$  – calculated m/z 549.9624 observed m/z 549.9611;

FTIR ( $\text{cm}^{-1}$ ) – 3056 ( $\nu_{\text{C-H}}$ ), 1716 ( $\nu_{\text{C=O}}$ )

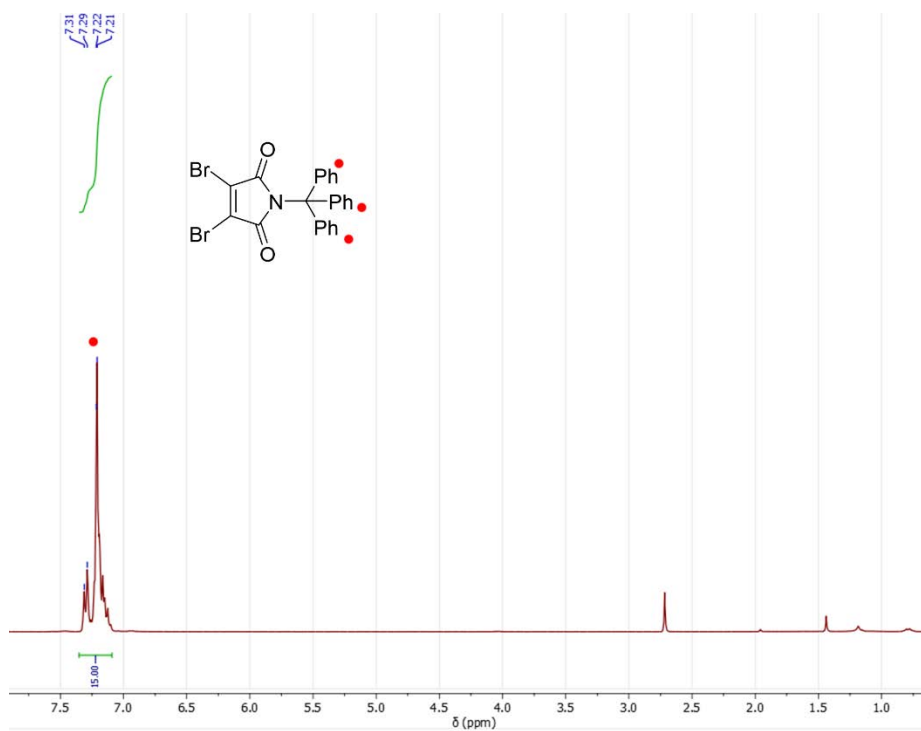


**Figure 3.23:** <sup>1</sup>H NMR spectrum of **3.6** (500 MHz, CDCl<sub>3</sub>).

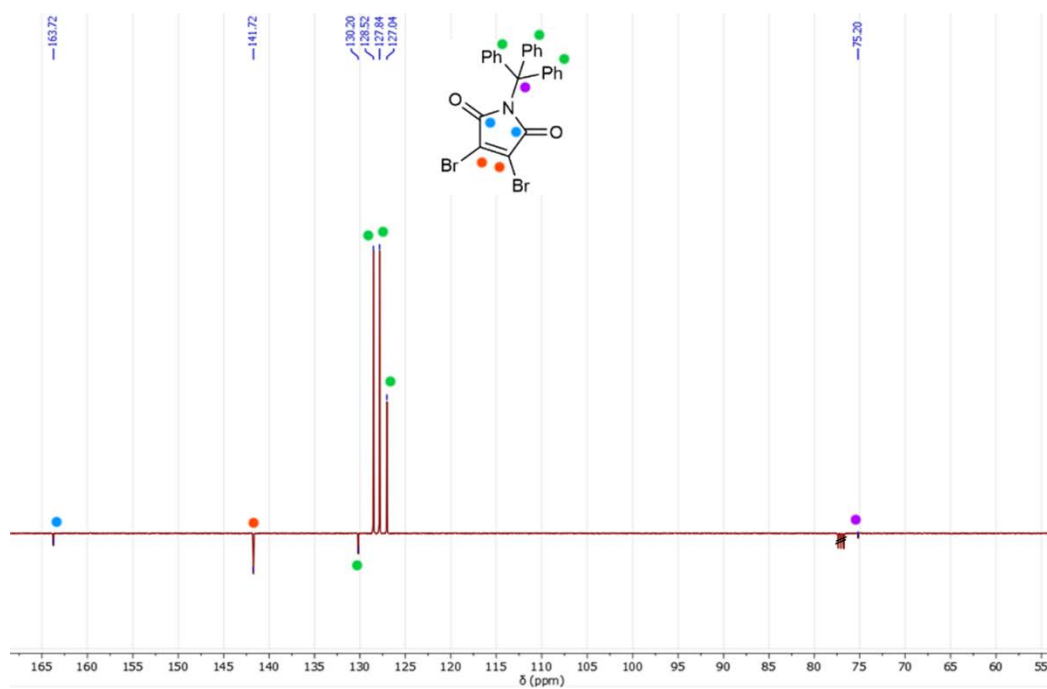
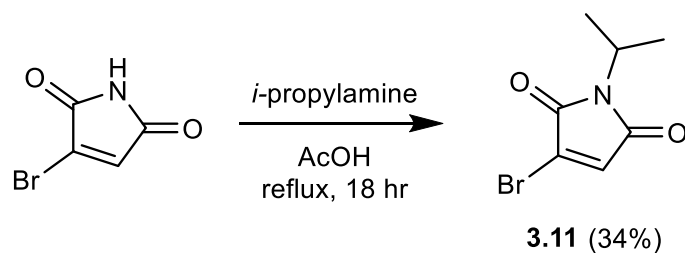


**Figure 3.24:** <sup>13</sup>C NMR spectrum of **3.6** (126 MHz, CDCl<sub>3</sub>).



#### 2.5.2.5 3-bromo-1-isopropyl-1H-pyrrole-2,5-dione (3.11)



Overnight, a solution of bromomaleimide (**2.1**, 1 g) and isopropyl amine (480  $\mu$ l) in acetic acid (25 ml) was refluxed at 118  $^{\circ}$ C. After, the reaction was dried *in vacuo* with the addition of toluene. The crude product was isolated *via* column chromatography using 10-20% EtOAc in petroleum ether as the eluent to afford cream solid (409 mg, 34%).

$^1\text{H}$  NMR (300 MHz,  $\text{CDCl}_3$ , ppm)  $\delta$  = 6.82 (s, 1H, CH), 4.39 (Hept.,  $^3J_{\text{HH}}$  = 6.8 Hz, 1H, CH), 1.41 (d,  $^3J_{\text{HH}}$  = 6.8 Hz, 6H,  $\text{CH}_3$ ).

$^{13}\text{C}$  NMR (75 MHz,  $\text{CDCl}_3$ , ppm)  $\delta$  = 169.0 (CO), 164.9 (CO), 131.7 (CH), 131.1 (CBr), 43.8 (CH), 20.1 ( $\text{CH}_3$ ).

HR-MS (MaXis) -  $[\text{M}+\text{Na}^+]$  - calculated m/z 216.9738 observed m/z 216.9736;

FTIR ( $\text{cm}^{-1}$ ) - 2974 ( $\nu_{\text{C-H}}$ ), 1705 ( $\nu_{\text{C=O}}$ ), 1690 ( $\nu_{\text{C=O}}$ )

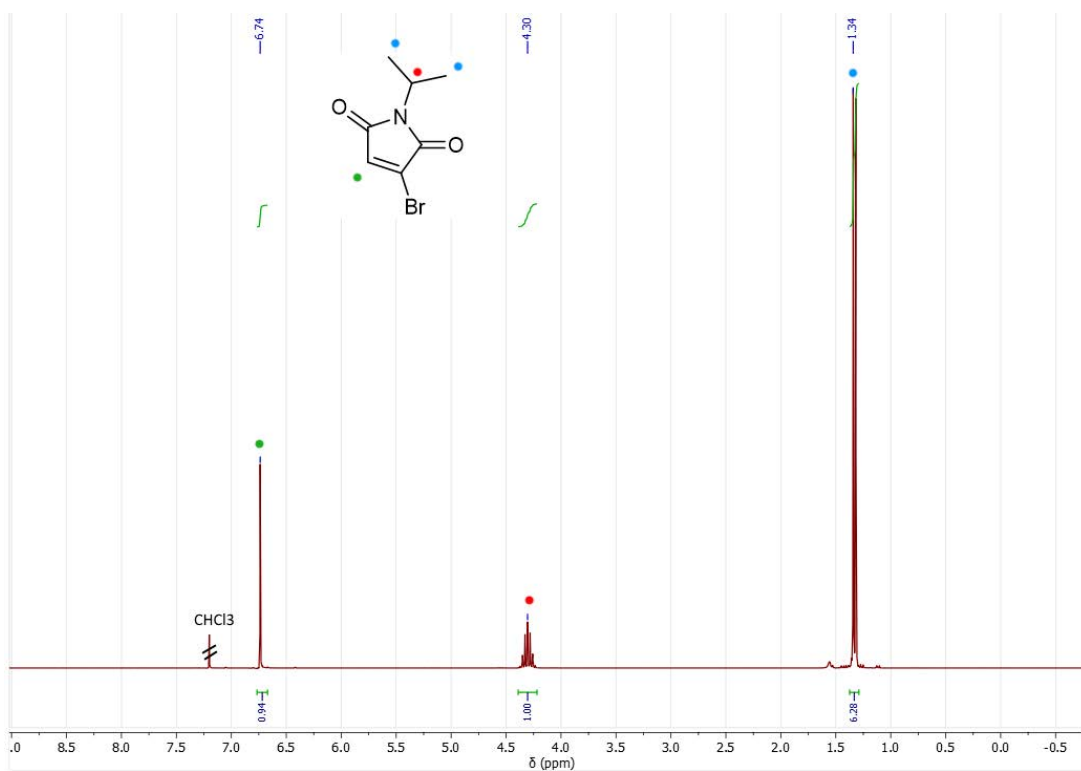


**Figure 3.25:**  $^1\text{H}$  NMR spectrum of **3.11** (300 MHz,  $\text{CDCl}_3$ ).

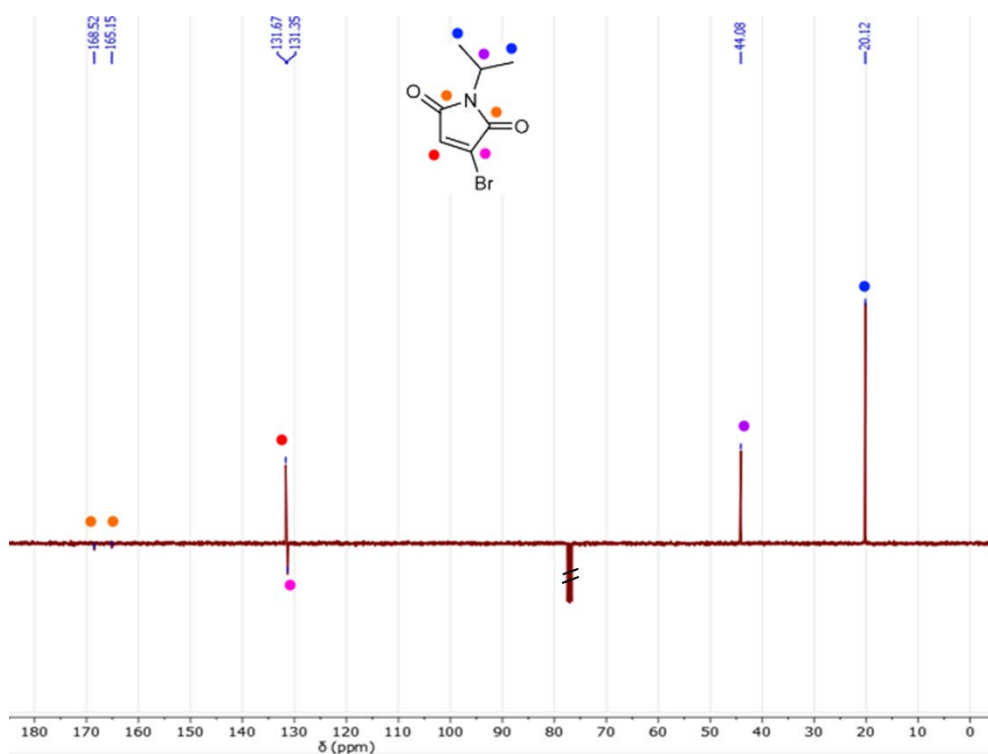
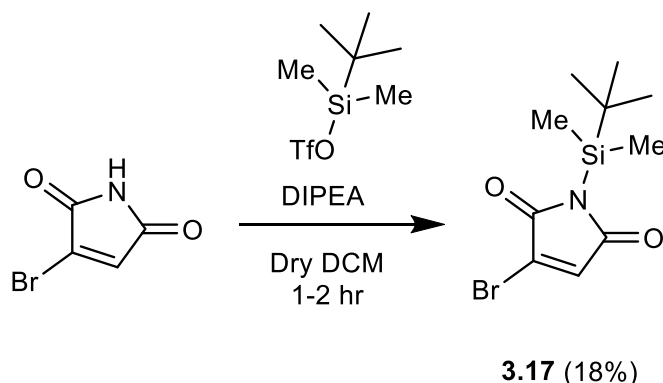


**Figure 3.26:**  $^{13}\text{C}$  NMR spectrum of **3.11** (75 MHz,  $\text{CDCl}_3$ ).

**2.5.2.6** General procedure for the synthesis of silyl functionalized bromomaleimides.

The reactions followed a similar protocol to Prishchcenko *et al.*<sup>28</sup> In summary, the bromomaleimide was dissolved into dry CH<sub>2</sub>Cl<sub>2</sub> under dry conditions. To this DIPEA (2.1 equiv.) was added followed by the trifluoromethyl silyl reagent (1.1 equiv.). The reaction was left for 1-2 hours, before purification.

**2.5.2.7** 3-bromo-1-(tert-butyldimethylsilyl)-1H-pyrrole-2,5-dione (3.17)



The crude product obtained from the general procedure, was purified *via* silica column chromatography using 10% EtOAc in petroleum ether as the eluent to afford a white solid (197 mg, 20 %).

<sup>1</sup>H NMR (500 MHz, CDCl<sub>3</sub>, ppm) δ = 6.83 (s, 1H, CH), 0.92 (s, 9H, CH<sub>3</sub>), 0.43 (s, 6H, CH<sub>3</sub>).

<sup>13</sup>C NMR (101 MHz, CDCl<sub>3</sub>, ppm) δ = 173.8 (CO), 170.5 (CO), 134.0 (CH), 133.4 (CBr), 26.1 (CH<sub>3</sub>), 25.7 (CH<sub>3</sub>), 18.9 (CH).

HR-MS (Xevo) - [M+Na<sup>+</sup>+MeOH] - calculated m/z 549.9624 observed m/z 549.9611;

FTIR (cm<sup>-1</sup>) - 3056 (ν<sub>C-H</sub>), 1716 (ν<sub>C=O</sub>)

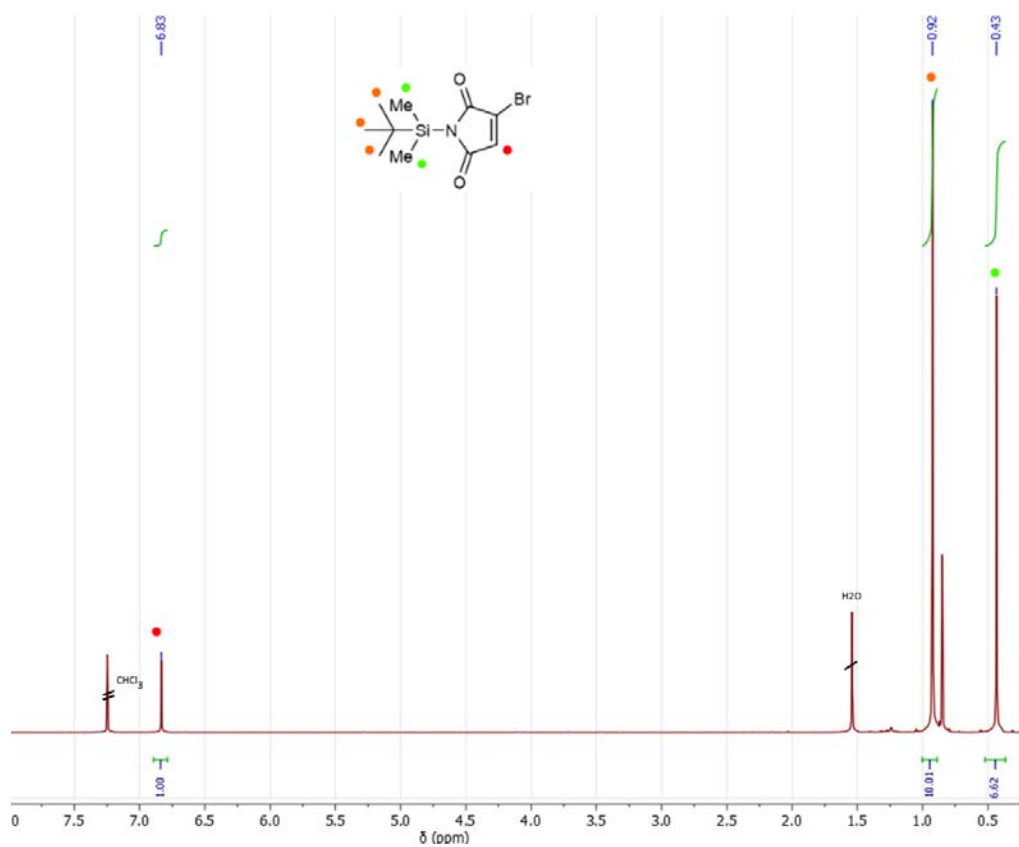


**Figure 3.27:** <sup>1</sup>H NMR spectrum of **3.17** (500 MHz, CDCl<sub>3</sub>).

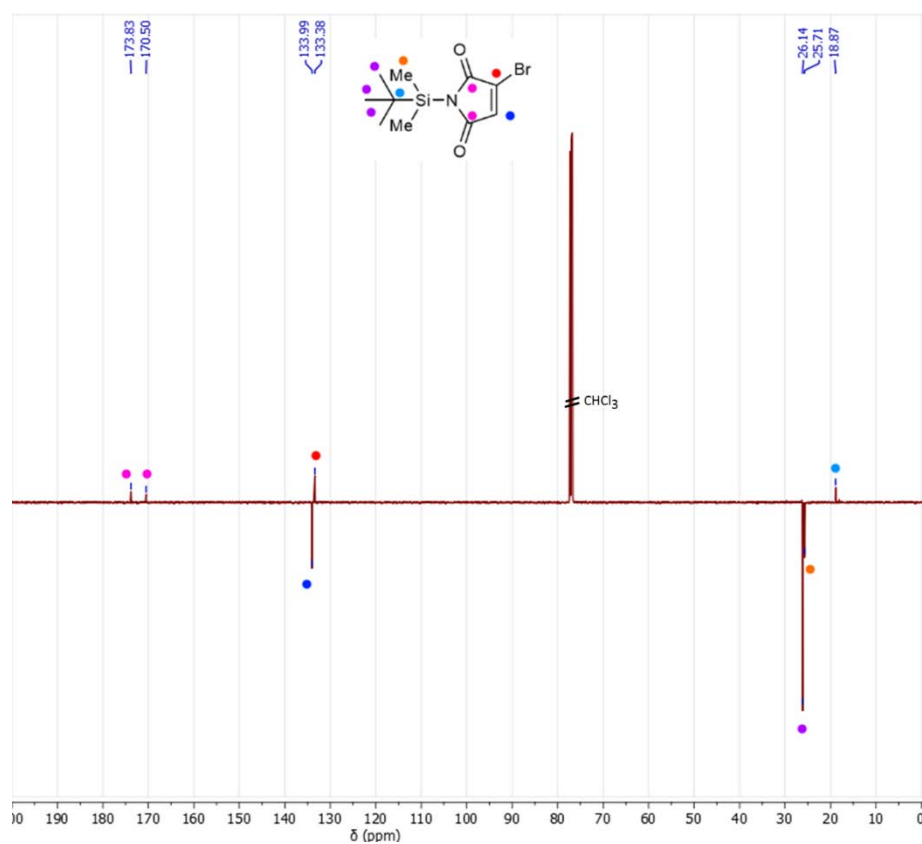
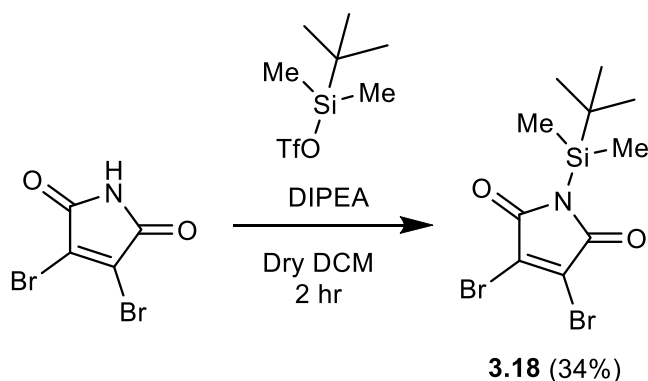


**Figure 3.28:** <sup>13</sup>C NMR spectrum of **3.17** (126 MHz, CDCl<sub>3</sub>).

**2.5.2.8** 3,4-dibromo-1-(tert-butyldimethylsilyl)-1H-pyrrole-2,5-dione (3.18)



The crude product obtained from the general procedure, was purified *via* silica column chromatography using hexane as the eluent to afford a white solid (245 mg, 34 %).

$^1\text{H}$  NMR (500 MHz,  $\text{CDCl}_3$ , ppm)  $\delta$  = 6.83 (s, 1H, CH), 0.92 (s, 9H,  $\text{CH}_3$ ), 0.43 (s, 6H,  $\text{CH}_3$ ).

$^{13}\text{C}$  NMR (101 MHz,  $\text{CDCl}_3$ , ppm)  $\delta$  = 168.8 (CO), 131.6 (CBr), 26.1 ( $\text{CH}_3$ ), 18.89 ( $\text{CCH}_3$ ), -4.59 ( $\text{CH}_3$ ).

HR-MS (Xevo) -  $[\text{M}+\text{NH}_3^+]$  – calculated m/z 384.9577 observed m/z 384.9576,

FTIR ( $\text{cm}^{-1}$ ) - 3052 ( $\nu_{\text{C-H}}$ ), 1708 ( $\nu_{\text{C=O}}$ )

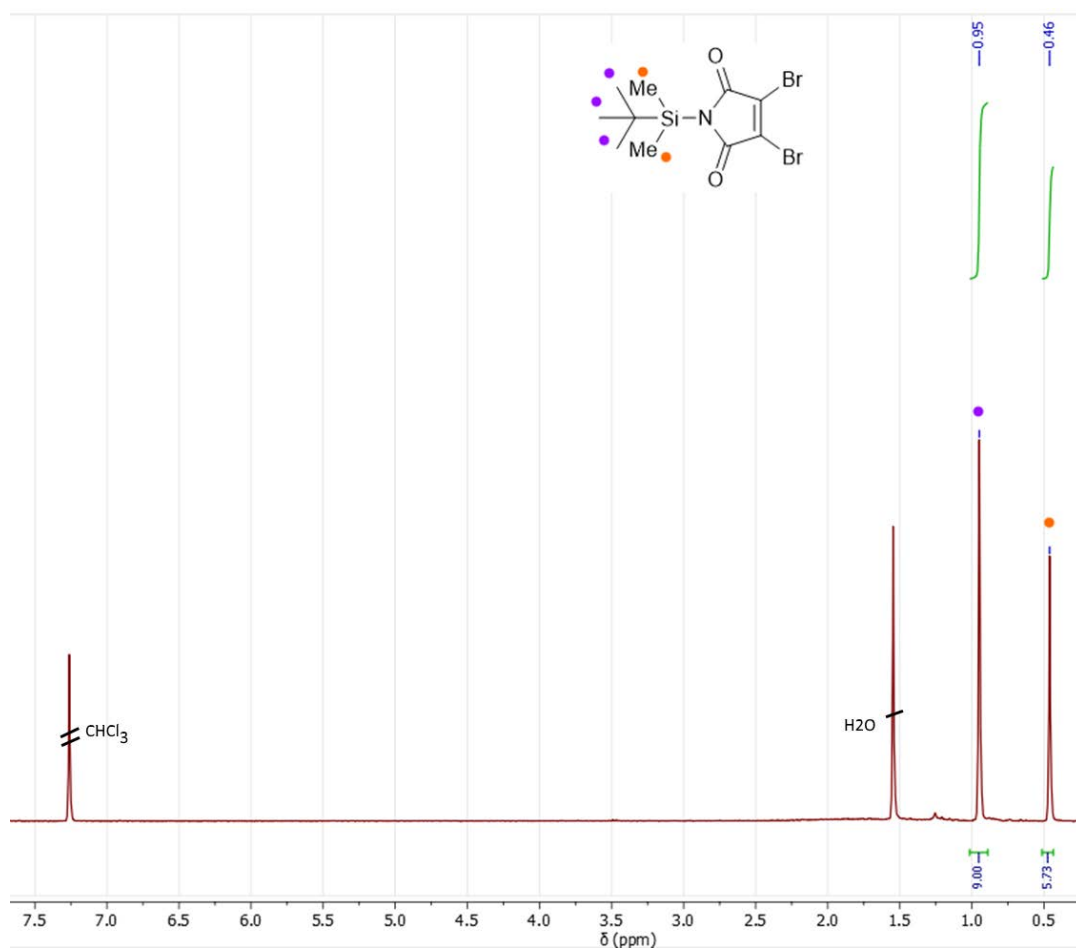


**Figure 3.29:**  $^1\text{H}$  NMR spectrum of **3.18** (500 MHz,  $\text{CDCl}_3$ ).

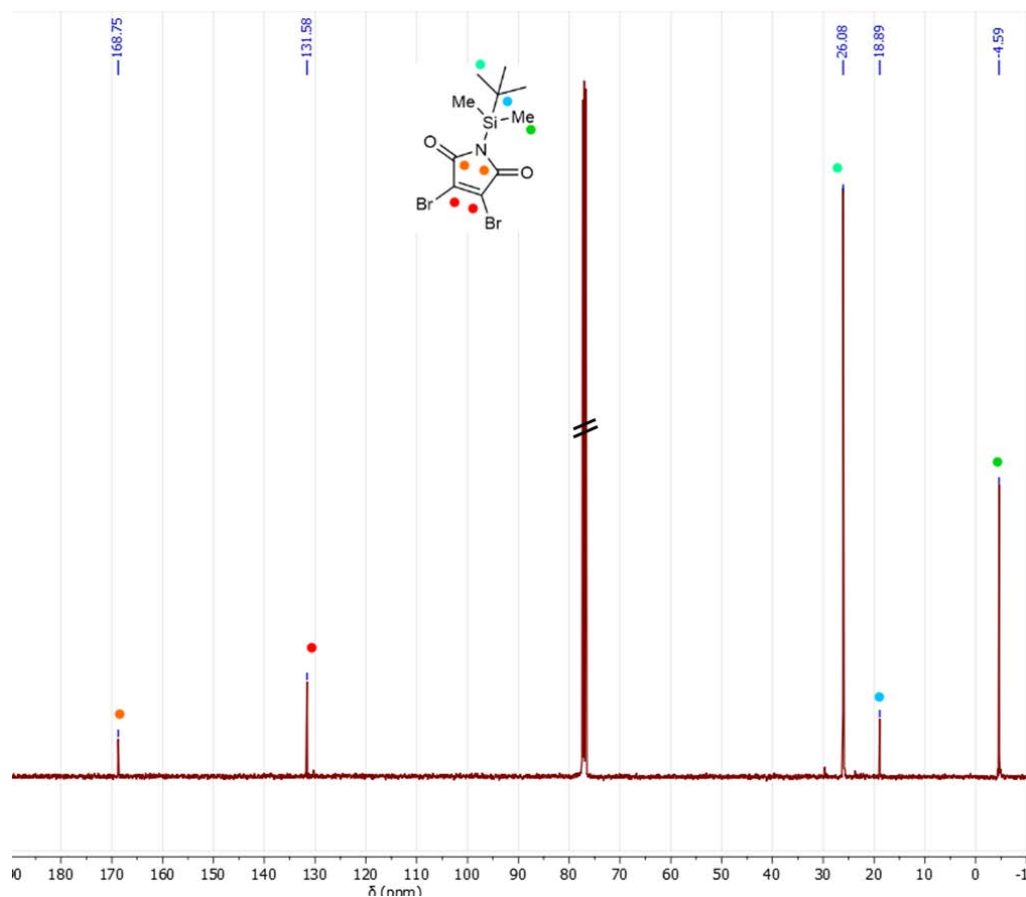
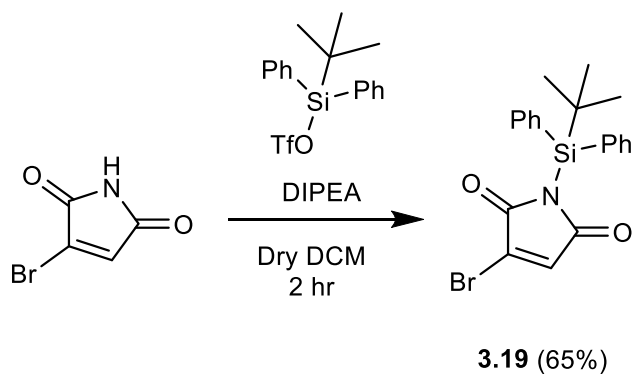


**Figure 3.30:**  $^{13}\text{C}$  NMR spectrum of **3.18** (101 MHz,  $\text{CDCl}_3$ ).

#### 2.5.2.9 3-bromo-1-(tert-butyldiphenylsilyl)-1H-pyrrole-2,5-dione (3.19)



The crude product obtained from the general procedure, was purified *via* silica column chromatography using hexane as the eluent to afford a white solid (703 mg, 65 %).

$^1\text{H}$  NMR (500 MHz,  $\text{CDCl}_3$ )  $\delta$  = 7.60 (d,  $^3J_{\text{HH}}$  = 7.3 Hz, 4H, ArH), 7.38 (m, 6H, ArH), 6.89 (s, 1H, CH), 1.21 (s, 9H,  $\text{CH}_3$ ).

$^{13}\text{C}$  NMR (126MHz,  $\text{CDCl}_3$ , ppm)  $\delta$  = 170.76 (CO), 167.4 (CO), 136.8 (CH), 135.0 (CAr), 134.0 (CAr), 131.4 (CBr), 129.6 (CAr), 128.0 (CAr), 27.0 (C), 19.15 ( $\text{CH}_3$ ).

HR-MS (MaXis) -  $[\text{M}+\text{Na}^+]$  - calculated m/z 436.0339 observed m/z 436.0342;

FTIR ( $\text{cm}^{-1}$ ) - 3050 ( $\nu_{\text{C-H}}$ ), 1708 ( $\nu_{\text{C=O}}$ ), 1690 ( $\nu_{\text{C=O}}$ )

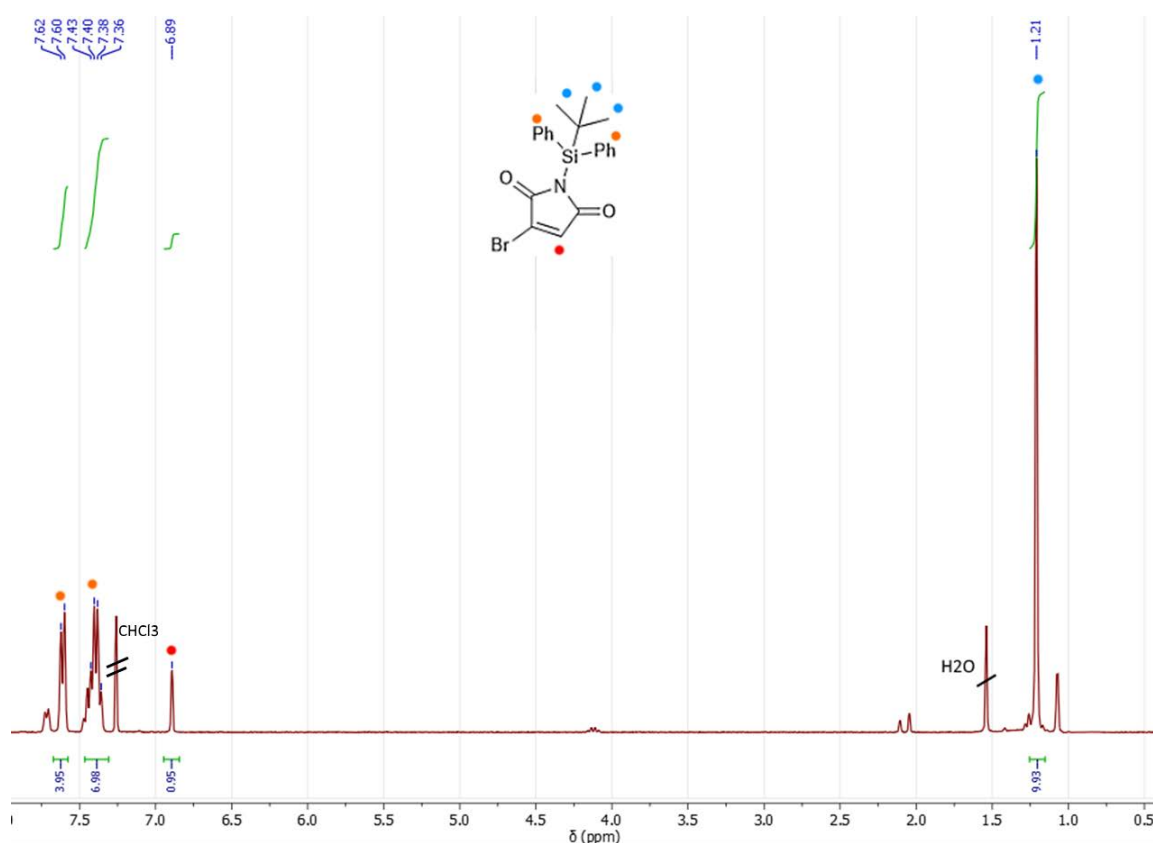


**Figure 3.31:**  $^1\text{H}$  NMR spectrum of **3.19** (500 MHz,  $\text{CDCl}_3$ ).



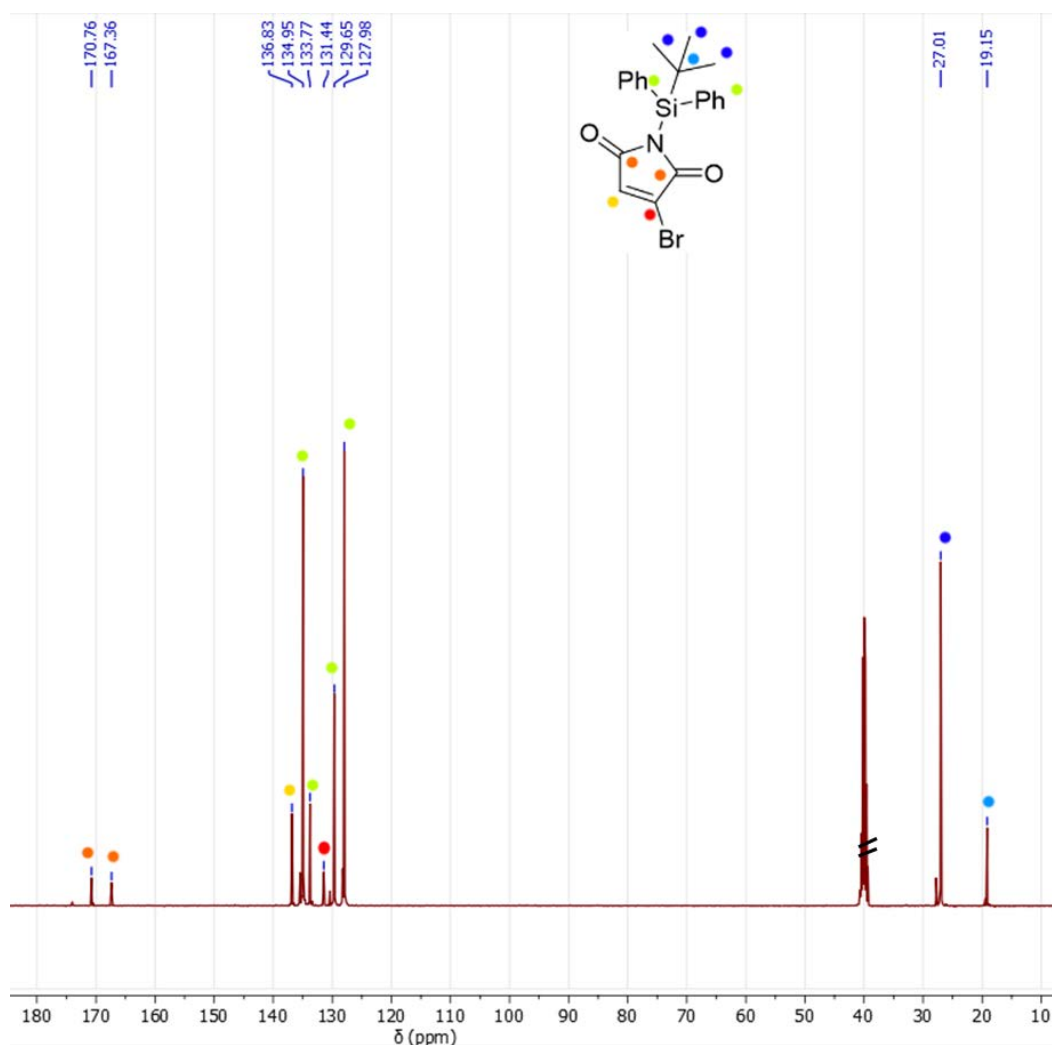
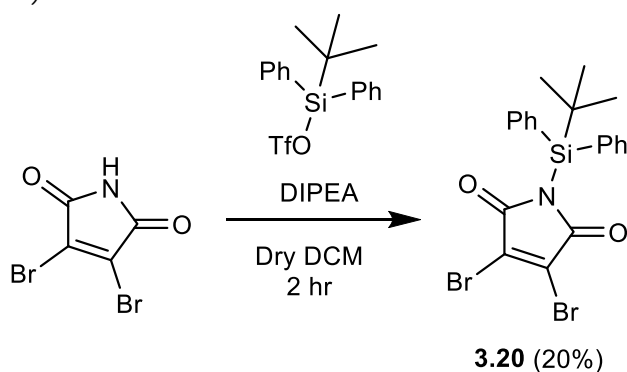


**Figure 3.32:**  $^{13}\text{C}$  NMR spectrum of **3.19** (126 MHz,  $\text{CDCl}_3$ ).

**2.5.2.10** 3,4-dibromo-1-(tert-butyldiphenylsilyl)-1H-pyrrole-2,5-dione (**3.20**)



The crude product obtained from the general procedure, was purified *via* silica column chromatography using hexane as the eluent to afford a white solid (197 mg, 20 %).

$^1\text{H}$  NMR (500 MHz,  $\text{CDCl}_3$ , ppm)  $\delta$  = 7.54 (d,  $^3J_{\text{HH}}$  = 7.4 Hz, 1H), 7.39 (t,  $^3J_{\text{HH}}$  = 7.4 Hz, 1H), 7.32 (t,  $^3J_{\text{HH}}$  = 7.4 Hz, 1H), 1.15 (s, 2H).

$^{13}\text{C}$  NMR (126 MHz,  $\text{CDCl}_3$ , ppm)  $\delta$  = 168.2 (CO), 135.5 (CAr), 131.9 (CAr), 130.6 (CBr), 130.3 (CAr), 127.9 (CAr), 27.8 ( $\text{CMe}_3$ ), 19.7 ( $\text{CH}_3$ ).

HR-MS (Xevo) -  $[\text{M}+\text{NH}_3^+]$  - calculated m/z 508.9896 observed m/z 508.9911,

FTIR ( $\text{cm}^{-1}$ ) - 2941 ( $\nu\text{C-H}$ ), 2859 ( $\nu\text{C-H}$ ), 1705 ( $\nu\text{C=O}$ ), 1679 ( $\nu\text{C=O}$ ).

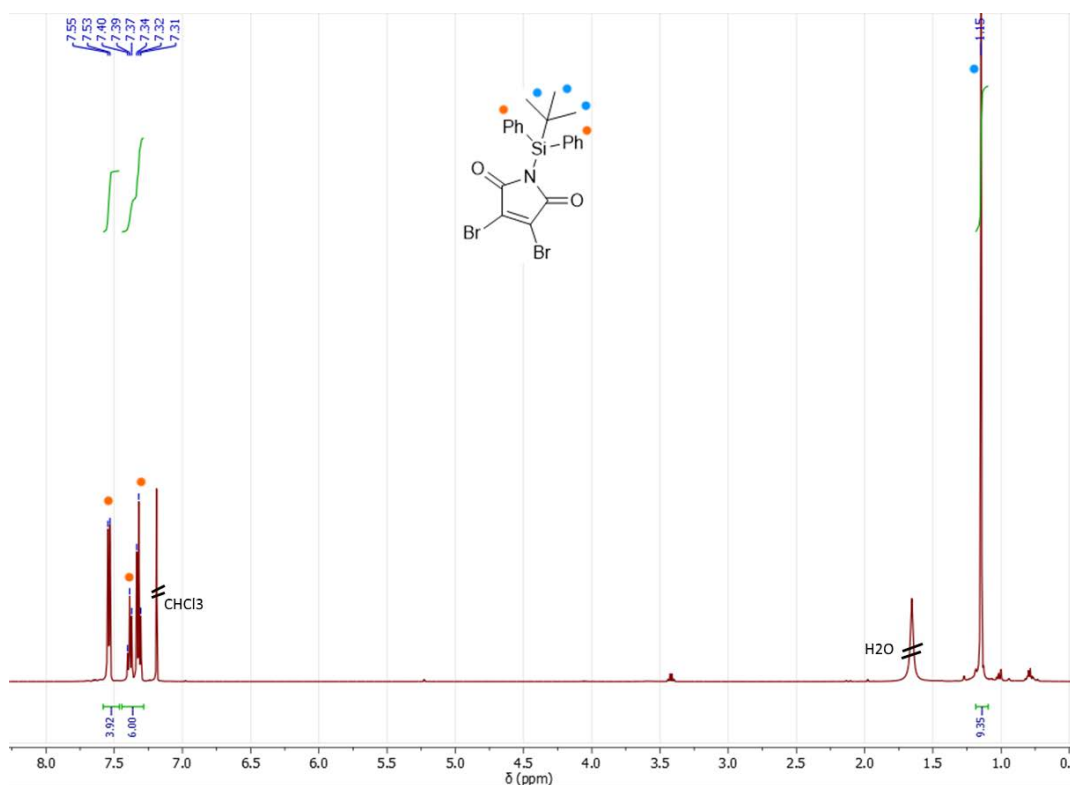


**Figure 3.33:**  $^1\text{H}$  NMR spectrum of **3.20** (500 MHz,  $\text{CDCl}_3$ ).

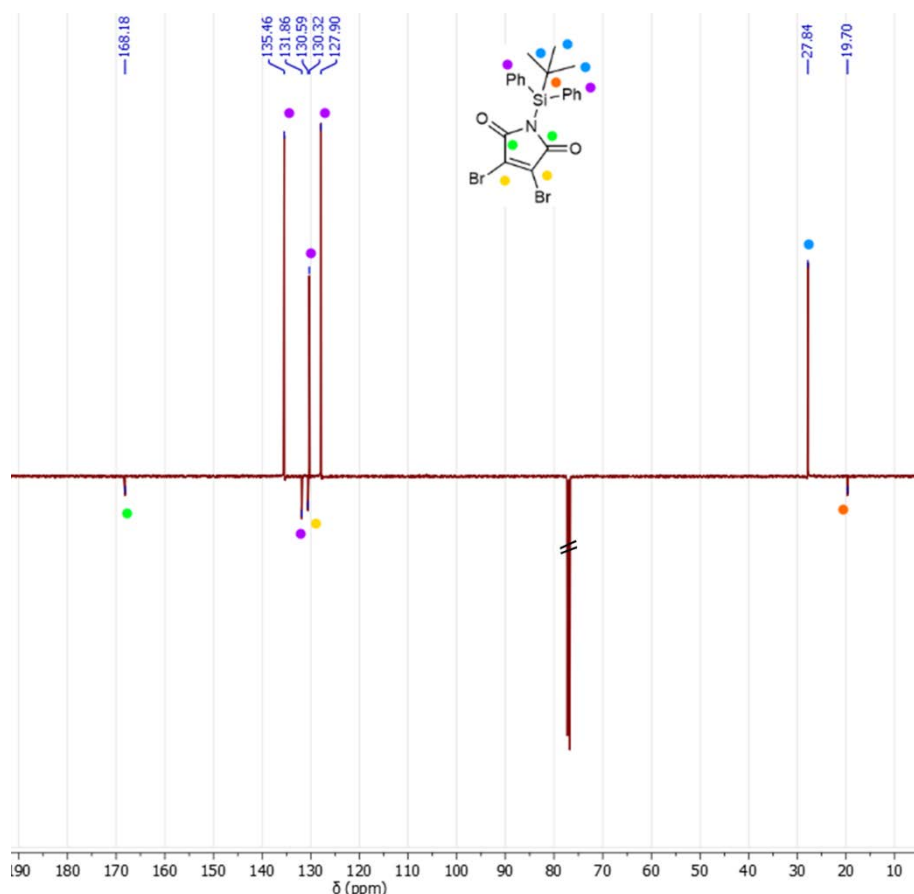
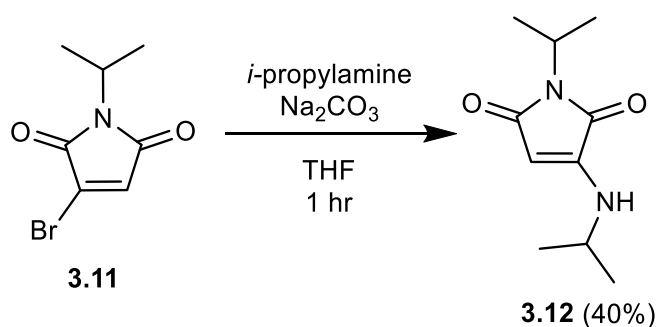


**Figure 3.34:**  $^{13}\text{C}$  NMR spectrum of **3.20** (126 MHz,  $\text{CDCl}_3$ ).

#### 2.5.2.11 General procedure for the synthesis of aminobromo- and monoaminomaleimides from bromomaleimides

The reactions were based of a previously reported procedure.<sup>9</sup> For all reactions the bromomaleimide (1 equiv.), was dissolved in THF with sodium carbonate (2 equiv.). To this a solution of amine in THF (1.05-1.1 equiv.) was added dropwise over 30 min. After 40 min – 1 hour the reaction mixture was filtered, the filtrate collected and the solvent was removed *in vacuo*. The resultant residue was then purified *via* column chromatography on silica gel, generally with a petroleum ether/ethyl acetate eluent system.

### 2.5.2.12 1-isopropyl-3-(isopropylamino)-pyrrole-2,5-dione (3.12)



The crude product synthesized by the above procedure was purified using silica column chromatography with an eluent of 5% ethyl acetate in petroleum ether, to isolate a yellow solid (107 mg, 40%).

$^1\text{H}$  NMR (300 MHz,  $\text{CDCl}_3$ )  $\delta$  = 5.19 (s, 1H), 4.75 (s, 1H), 4.30 (dt,  $^3J_{\text{HH}}$  = 13.9, 7.0 Hz, 1H), 3.51 (dq,  $^3J_{\text{HH}}$  = 13.1, 6.5 Hz, 1H), 1.39 (d,  $^3J_{\text{HH}}$  = 6.9 Hz, 6H), 1.27 (d,  $^3J_{\text{HH}}$  = 6.5 Hz, 6H)

$^{13}\text{C}$  NMR (126 MHz,  $\text{CDCl}_3$ , ppm)  $\delta$  = 172.7 (CO), 167.6 (CO), 147.8 (CNH), 83.8 (CH), 46.2 (CH), 42.3 (CH), 21.9 ( $\text{CH}_3$ ), 20.2 ( $\text{CH}_3$ )

HR-MS (MaXis) -  $[\text{M}+\text{Na}^+]$  – calculated m/z 219.1104 observed m/z 219.1109;

FTIR ( $\text{cm}^{-1}$ ) - 2974 ( $\nu_{\text{C-H}}$ ), 1698 ( $\nu_{\text{C=O}}$ ), 1636 ( $\nu_{\text{C=O}}$ )

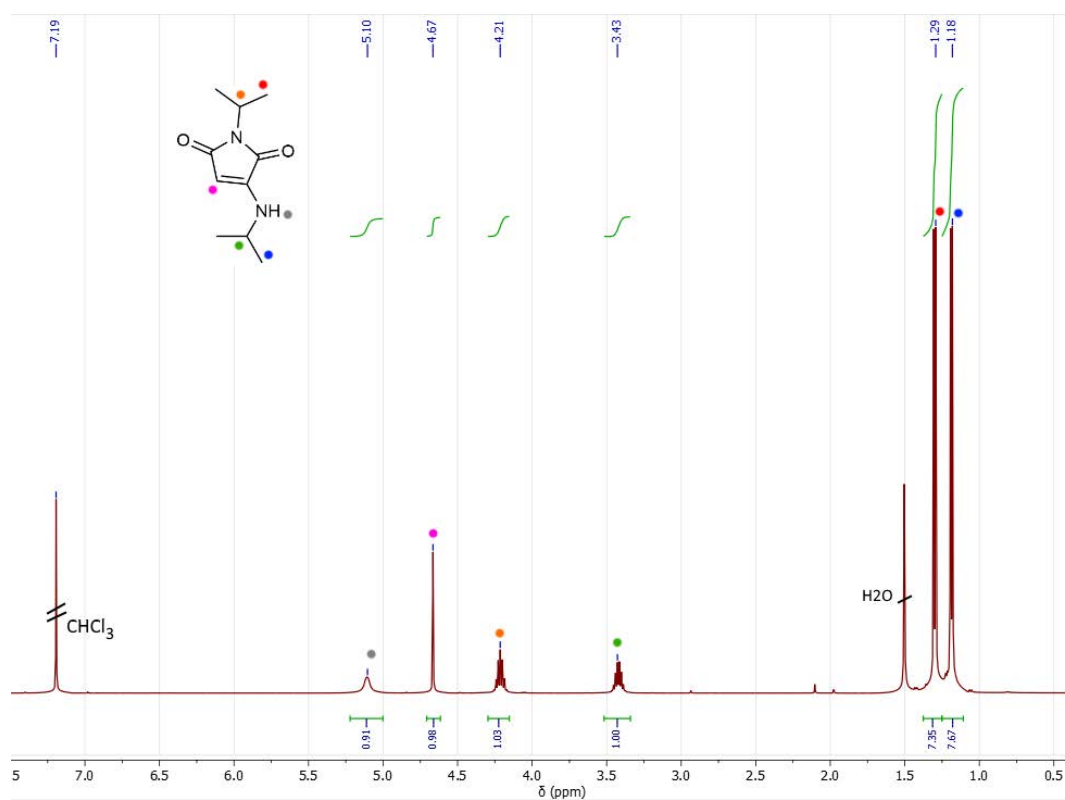


**Figure 3.35:** <sup>1</sup>H NMR spectrum of **3.11** (500 MHz, CDCl<sub>3</sub>).

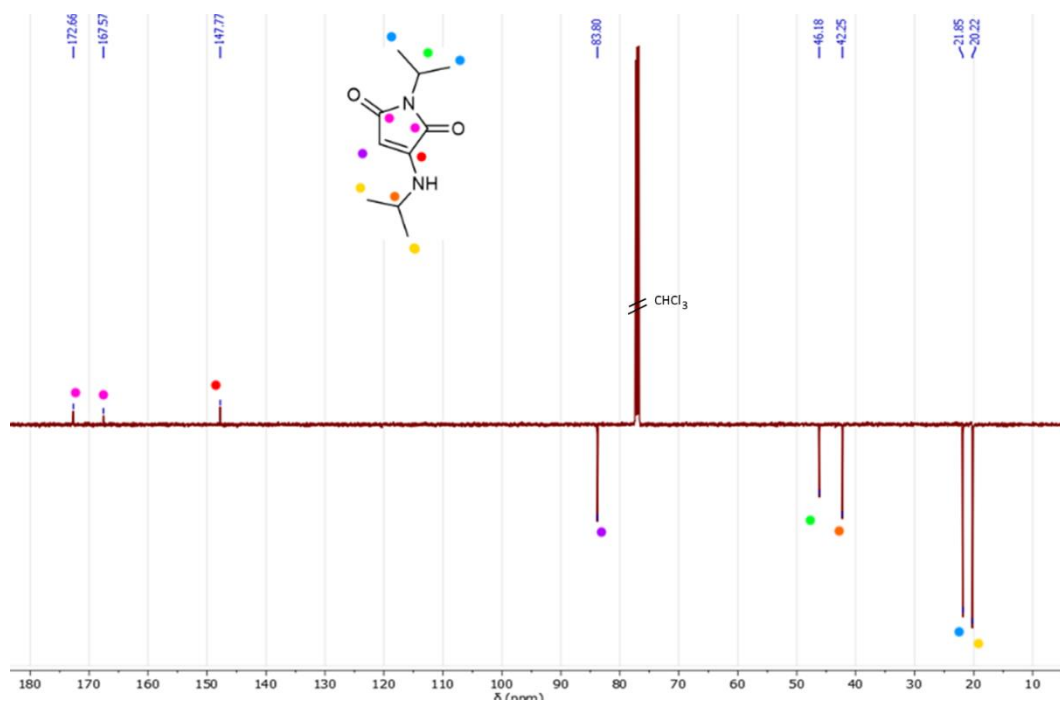
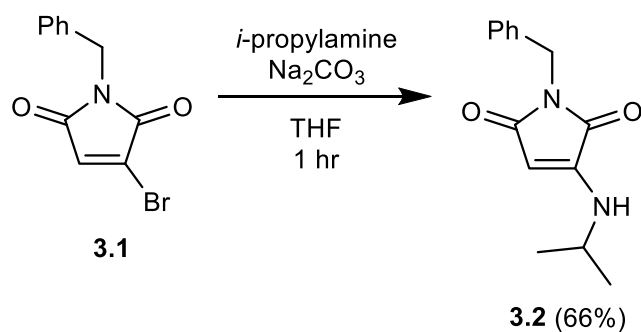


**Figure 3.36:** <sup>13</sup>C NMR spectrum of **3.11** (126 MHz, CDCl<sub>3</sub>).

### 2.5.2.13 1-benzyl-3-(isopropylamino)-1H-pyrrole-2,5-dione (3.2)



The crude product obtained by the general procedure was purified by silica column chromatography (30% EtOAc in petroleum ether) to afford a yellow solid (227 mg, 66 %).

$^1\text{H}$  NMR (300 MHz,  $\text{CDCl}_3$ )  $\delta$  = 7.37-7.28 (m, 5H), 5.29 (br, 1H), 4.82 (br d,  $^3J_{\text{HH}}$  = 13.1 Hz, 1H), 4.65 (s, 2H), 3.51 (dq,  $^3J_{\text{HH}}$  = 13.1, 6.5 Hz, 1H), 1.27 (d,  $^3J_{\text{HH}}$  = 6.5 Hz, 9H).

$^{13}\text{C}$  NMR (126 MHz,  $\text{CDCl}_3$ , ppm)  $\delta$  = 172.9 (CO), 167.5 (CO), 148.5 (CNH), 136.5 (CAr), 127.4-128.7 (m, ArC), 84.4 (CH), 46.1 (CH), 41.0 ( $\text{CH}_2$ ), 21.8 ( $\text{CH}_3$ )

HR-MS (MaXis) -  $[\text{M}+\text{Na}^+]$  – calculated  $m/z$  267.1104 observed  $m/z$  267.1104;

FTIR ( $\text{cm}^{-1}$ ) - 3103 ( $\nu_{\text{Ar-H}}$ ), 2971 ( $\nu_{\text{C-H}}$ ), 1698 ( $\nu_{\text{C=O}}$ ), 1621 ( $\nu_{\text{C=O}}$ )

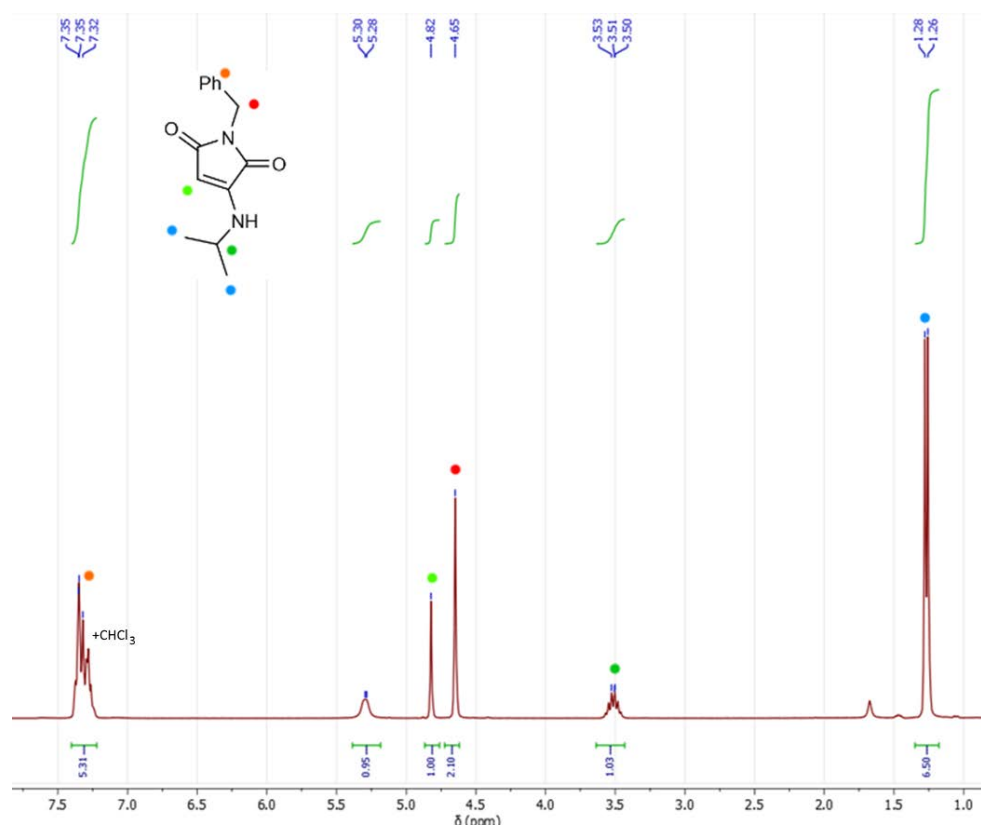


**Figure 3.37:**  $^1\text{H}$  NMR spectrum of **3.2** (300 MHz,  $\text{CDCl}_3$ ).

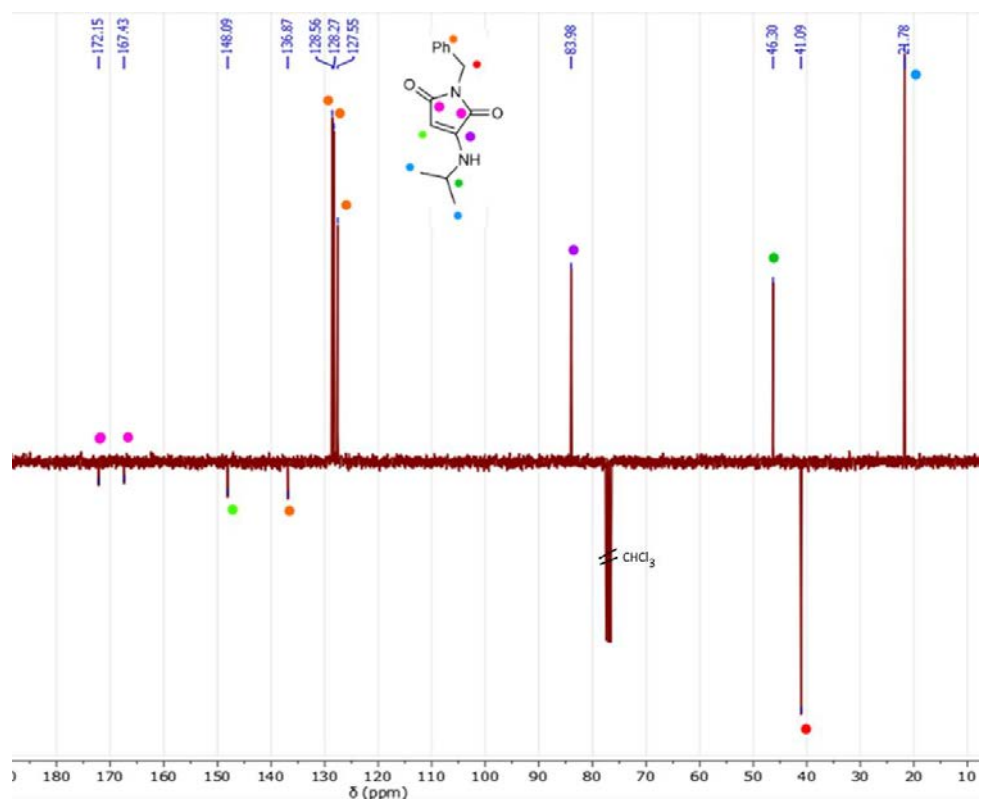
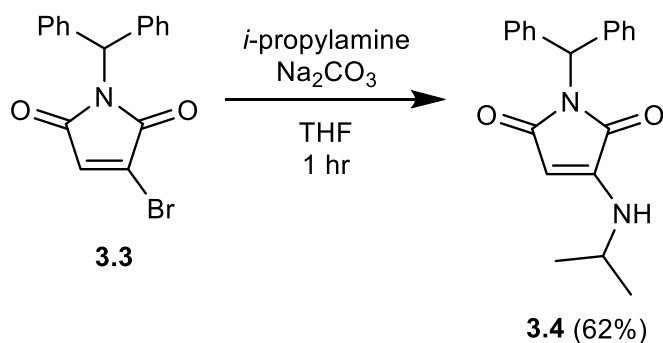


**Figure 3.38:**  $^{13}\text{C}$  NMR spectrum of **3.2** (126 MHz,  $\text{CDCl}_3$ ).

2.5.2.14 1-benzhydryl-3-(isopropylamino)-1H-pyrrole-2,5-dione (3.4)



The crude product obtained by the general procedure was purified by silica column chromatography (10% EtOAc in petroleum ether) to afford a deep yellow solid (198 mg, 62 %).

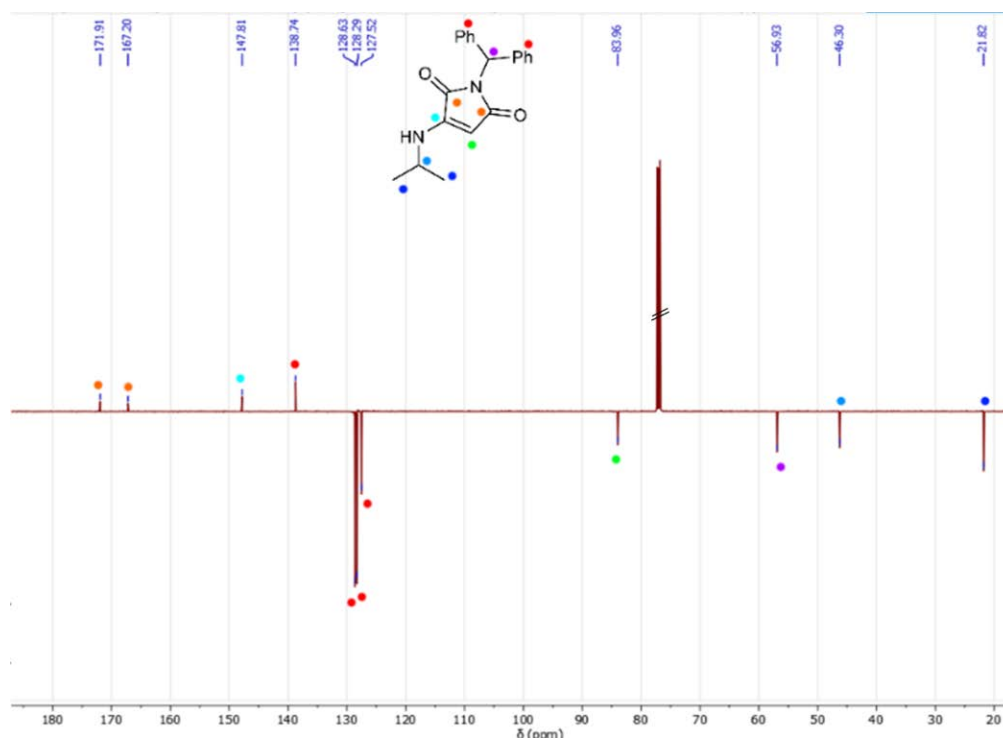
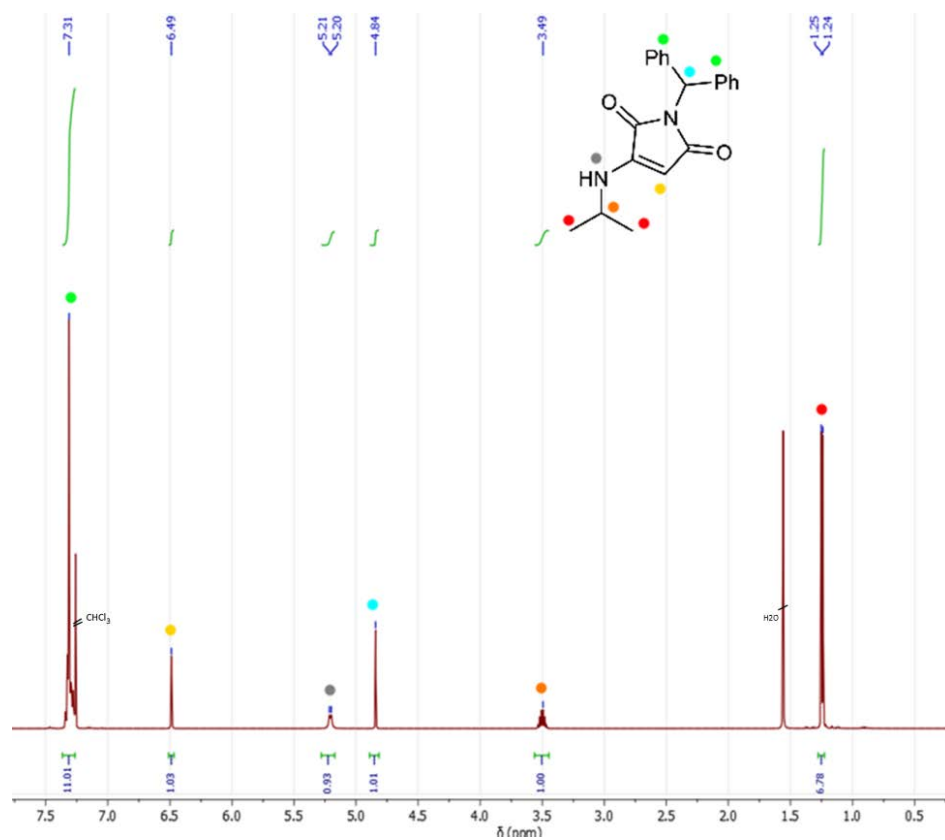
$^1\text{H}$  NMR (300 MHz,  $\text{CDCl}_3$ , ppm)  $\delta$  = 7.28 (m, 10H, ArH), 6.49 (s, 1H, ArCH), 5.19 (s, 1H, NH), 4.84 (s, 1H, CH), 3.51 (dt,  $^3J_{\text{HH}}$  = 6.5 Hz, 1H, CH), 1.25 (d,  $^3J_{\text{HH}}$  = 6.5 Hz, 6H,  $\text{CH}_3$ ).

$^{13}\text{C}$  NMR (126 MHz,  $\text{CDCl}_3$ , ppm)  $\delta$  = 171.91 (CO), 167.20 (CO), 147.81(CN), 138.7 (CAr), 128.6 (CAr), 128.3 (CAr), 127.5 (CAr), 84.0 (CH), 56.9 (CH), 46.3 (CH), 21.8 ( $\text{CH}_3$ ).

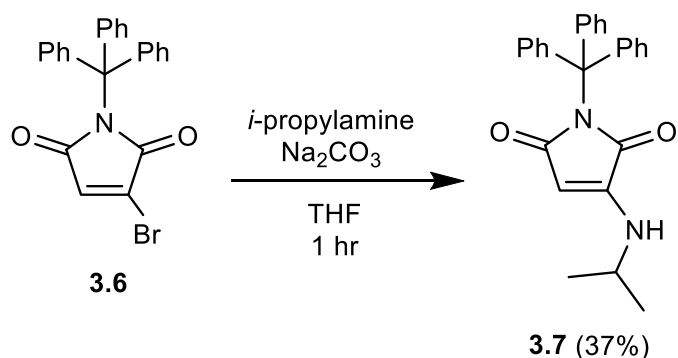
HR-MS (MaXis) -  $[\text{M}+\text{Na}^+]$  - calculated m/z 343.1417 observed m/z 343.1422;

FTIR ( $\text{cm}^{-1}$ ) – 2973 ( $\nu_{\text{C-H}}$ ), 1704 ( $\nu_{\text{C=O}}$ ), 1634 ( $\nu_{\text{C=O}}$ ).





### 2.5.2.15 3-(isopropylamino)-1-trityl-pyrrole-2,5-dione (3.7)



The crude product obtained by the general procedure was purified by silica column chromatography (5% EtOAc in petroleum ether) to afford a lime yellow solid (36 mg, 37 %).

$^1\text{H}$  NMR (500 MHz,  $\text{CDCl}_3$ )  $\delta$  = 7.33 (s, 6H), 7.11-7.20 (m, under solvent peak), 5.02 (d, 1H), 4.68 (s, 1H), 3.37 (m, 1H), 1.13 (s, 6H).

$^{13}\text{C}$  NMR ( $\text{CDCl}_3$ , 126 MHz, ppm)  $\delta$  = 172.1 (CO), 168.0 (CO), 147.5 (CN), 142.9 (ArC), 128.8 (ArC), 127.4 (ArC), 126.5 (ArC), 85.7 (CH), 72.9 (CPh<sub>3</sub>), 46.1 (CH), 21.8 (CH<sub>3</sub>).

HR-MS (MaXis) -  $[\text{M}+\text{Na}^+]$  - calculated m/z 419.1703 observed m/z 419.1730;

FTIR ( $\text{cm}^{-1}$ ) - 3018 ( $\nu_{\text{Ar-H}}$ ), 2983 ( $\nu_{\text{C-H}}$ ), 1700 ( $\nu_{\text{C=O}}$ ), 1624 ( $\nu_{\text{C=O}}$ )

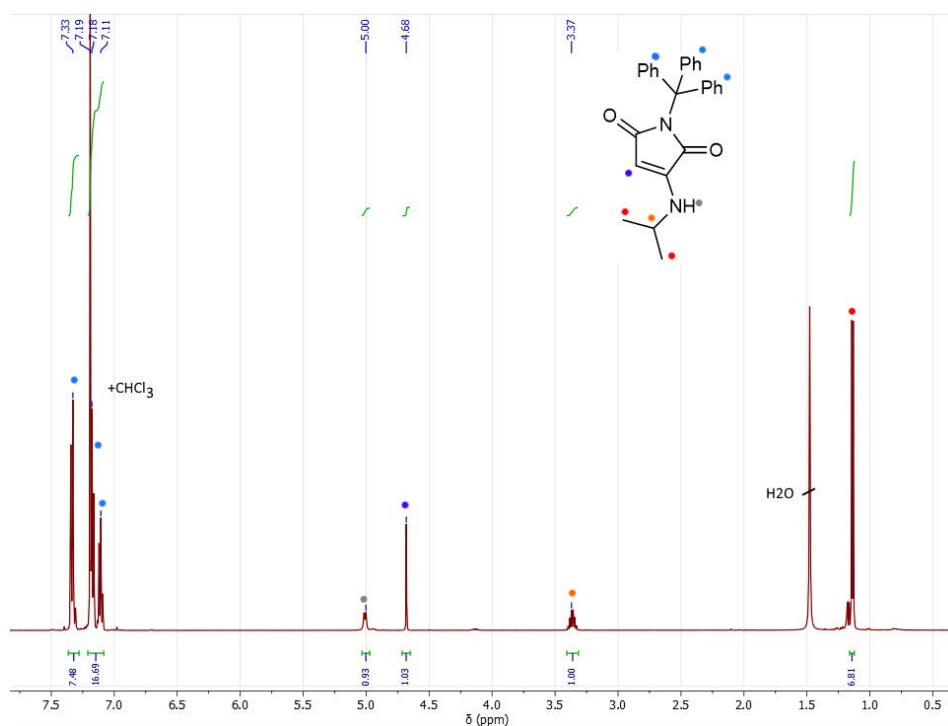


**Figure 3.41:** <sup>1</sup>H NMR spectrum of **3.7** (500 MHz, CDCl<sub>3</sub>).

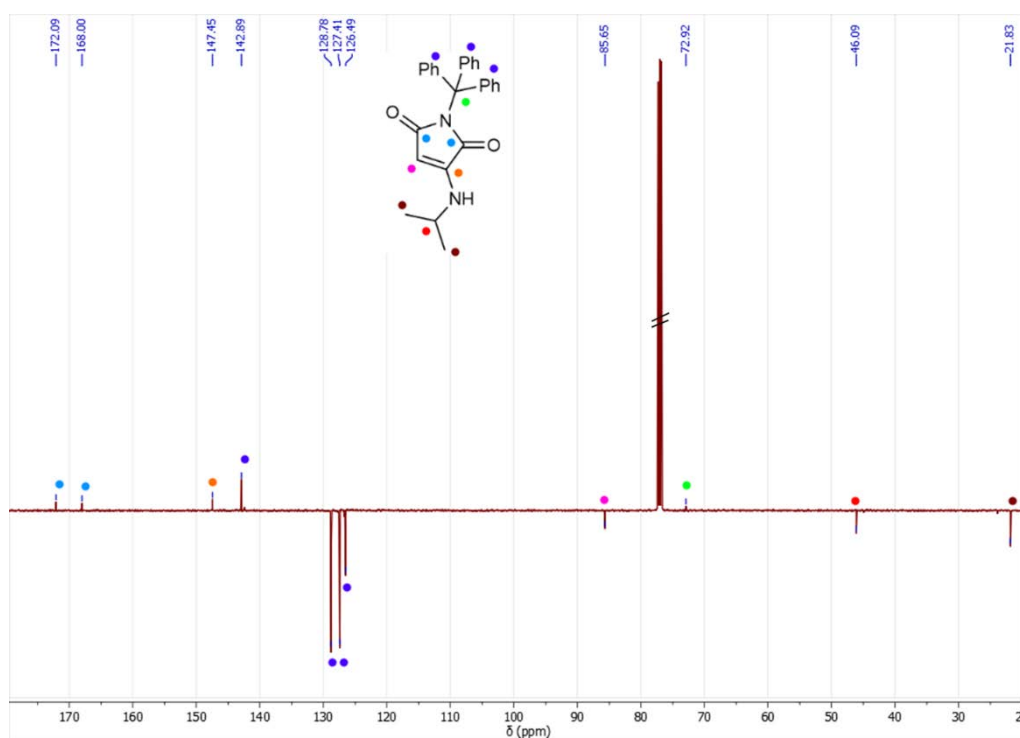
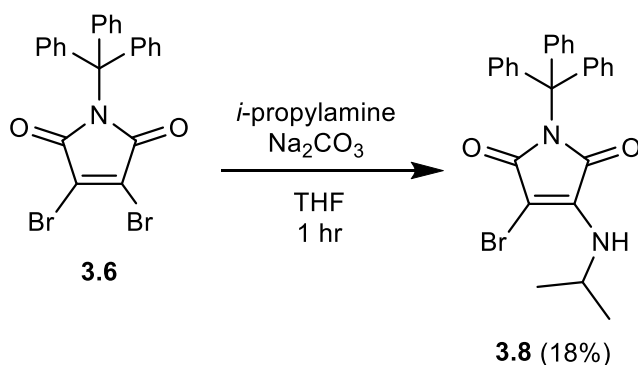


**Figure 3.42:** <sup>13</sup>C NMR spectrum of **3.7** (126 MHz, CDCl<sub>3</sub>).

2.5.2.16 3-bromo-4-(isopropylamino)-1-trityl-pyrrole-2,5-dione  
(3.8)



The crude product obtained by the general procedure was purified by silica column chromatography (2-3% EtOAc in petroleum ether) to afford a lime yellow solid (16 mg, 9%).

$^1\text{H}$  NMR (300 MHz,  $\text{DMSO}-d_6$ , ppm)  $\delta$  = 7.38 – 7.00 (m, 15H, ArH), 5.06 (d,  $J$  = 8.9 Hz, 1H, NH), 4.33 – 4.08 (m, 1H, CH), 1.17 (d,  $^3J_{\text{HH}}$  = 6.6 Hz, 6H,  $\text{CH}_3$ ).

$^{13}\text{C}$  NMR (126 MHz,  $\text{CDCl}_3$ , ppm)  $\delta$  = 171.1 (CO), 162.4 (CO), 146.9 (CN), 142.4 (CBr), 128.7 (CAr), 128.0 (CAr), 127.3 (CAr), 126.7 (CAr), 44.7 (CH), 21.8 ( $\text{CH}_3$ ).

HR-MS (MaXis) -  $[\text{M}+\text{Na}^+]$  - calculated  $m/z$  497.0838 observed  $m/z$  497.0841;

FTIR ( $\text{cm}^{-1}$ ) – 2966 ( $\nu_{\text{C-H}}$ ), 1704 ( $\nu_{\text{C-H}}$ ), 1620 ( $\nu_{\text{C-H}}$ ).

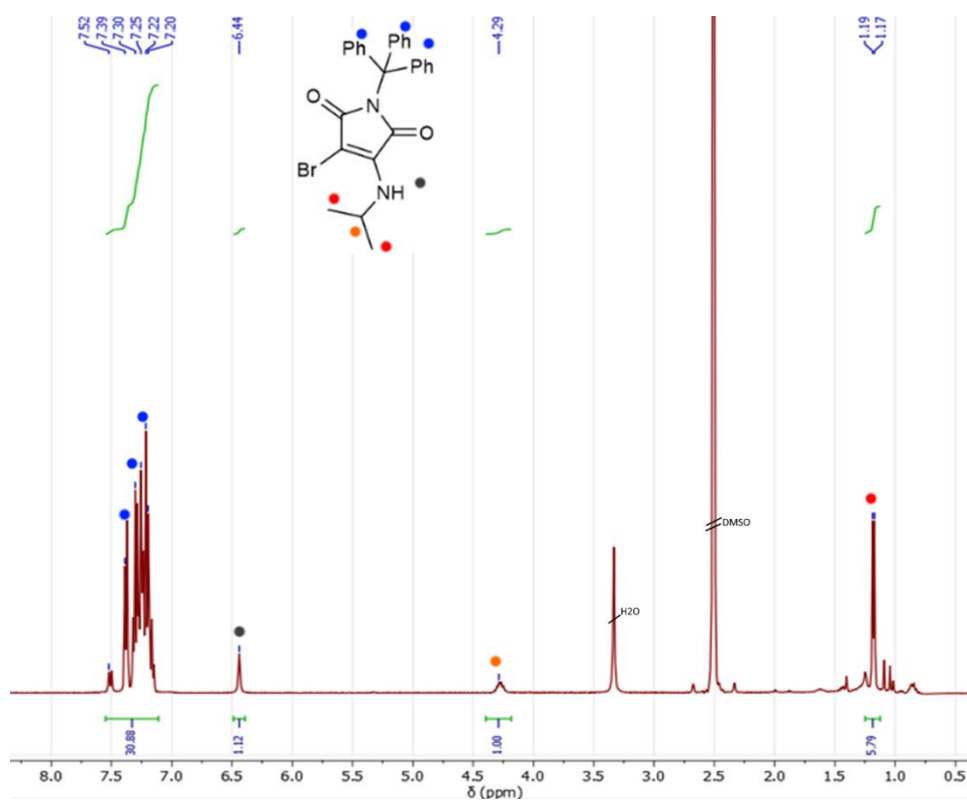


**Figure 3.43:**  $^1\text{H}$  NMR spectrum of **3.8** (300 MHz,  $\text{CDCl}_3$ ).

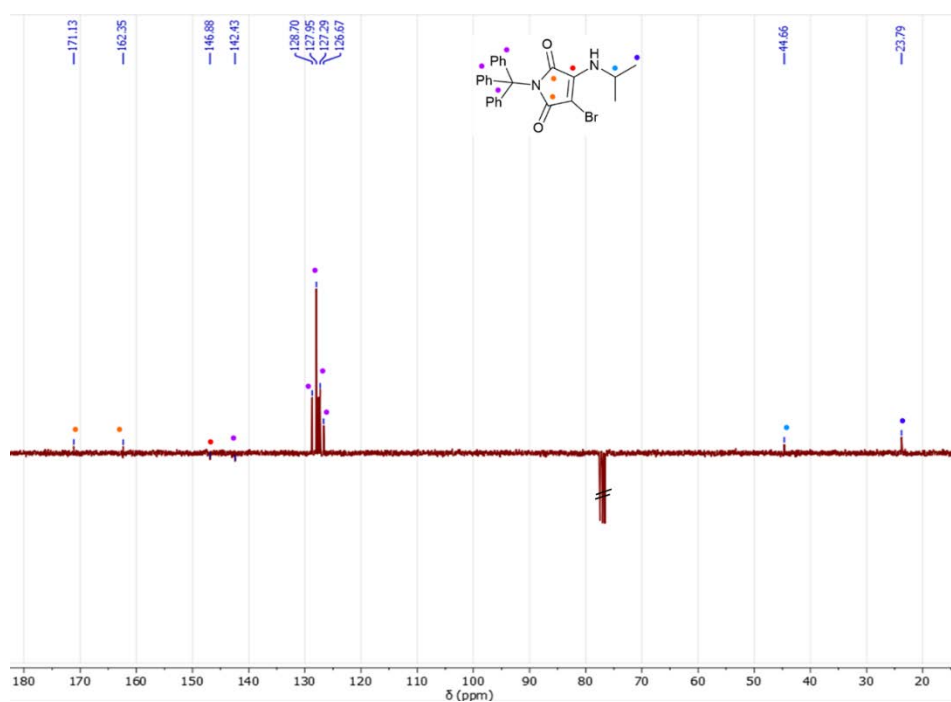
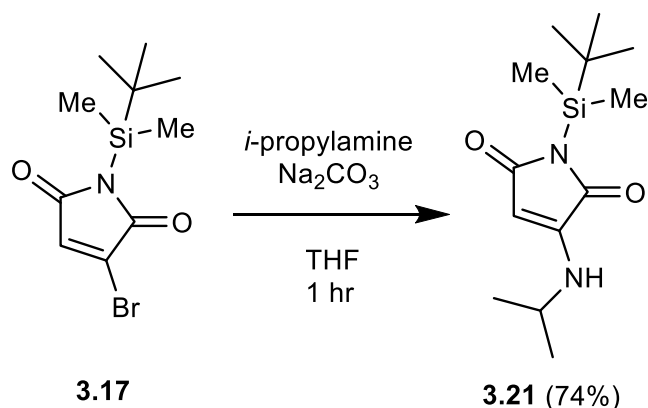


**Figure 3.44:**  $^{13}\text{C}$  NMR spectrum of **3.8** (126 MHz,  $\text{CDCl}_3$ ).

**2.5.2.17** 1-(tert-butyldimethylsilyl)-3-(isopropylamino)-pyrrole-2,5-dione (3.21)



The crude product obtained from the general procedure, was purified *via* silica column chromatography using 5% EtOAc in petroleum ether as the eluent to afford clear pale yellow crystals (67 mg, 74 %).

$^1\text{H}$  NMR (500 MHz,  $\text{CDCl}_3$ , ppm)  $\delta$  = 5.09 (d,  $^3J_{\text{HH}}$  = 5.7 Hz, 1H, CH), 4.83 (s, 1H, NH), 3.50 (m, 1H, CH), 1.24 (dd,  $^3J_{\text{HH}}$  = 5.6 Hz, 9H,  $\text{CH}_3$ ), 0.94 (s, 9H,  $\text{CH}_3$ ), 0.41 (s, 6H,  $\text{CH}_3$ ).

$^{13}\text{C}$  NMR (126MHz,  $\text{CDCl}_3$ , ppm)  $\delta$  = 177.4 (CO), 173.4 (CO), 148.9 (CN), 87.2 (CH), 46.3 (CH), 26.3 ( $\text{CH}_3$ ), 21.8 ( $\text{CH}_3$ ), 18.9 (CH), -4.4 ( $\text{SiCH}_3$ )

HR-MS (MaXis) -  $[\text{M}+\text{Na}^+]$  - calculated m/z 291.1499 observed m/z 291.1502;

FTIR ( $\text{cm}^{-1}$ ) – 2972 ( $\nu_{\text{C-H}}$ ), 2938 ( $\nu_{\text{C-H}}$ ), 1697 ( $\nu_{\text{C=O}}$ ), 1627 ( $\nu_{\text{C=O}}$ ).

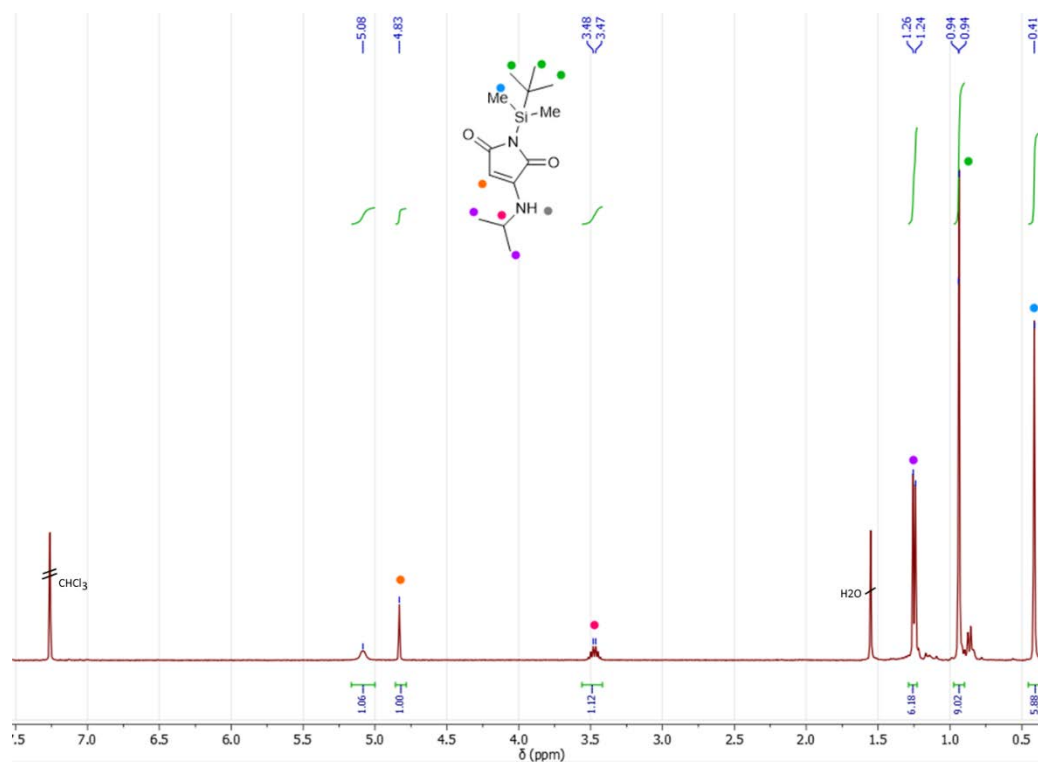


**Figure 3.45:** <sup>1</sup>H NMR spectrum of **3.21** (300 MHz, CDCl<sub>3</sub>).

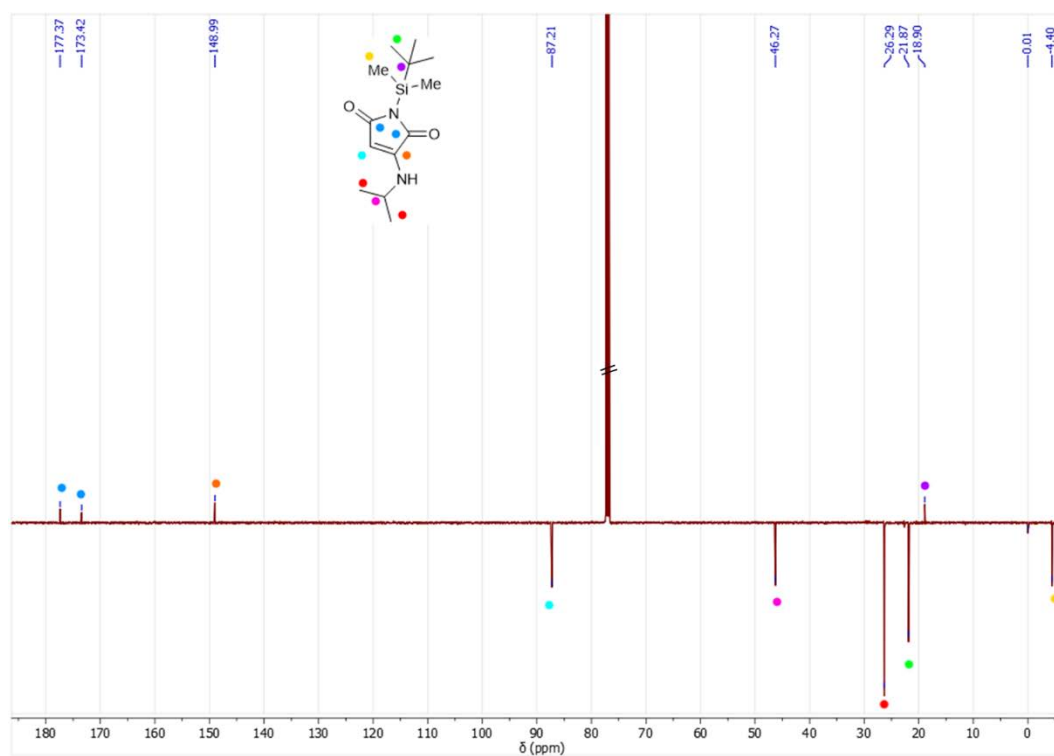
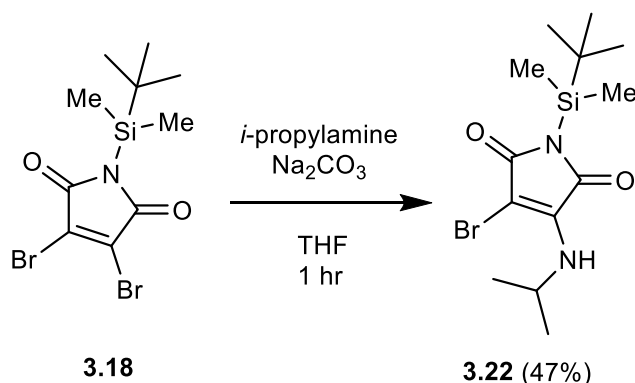


**Figure 3.46:** <sup>13</sup>C NMR spectrum of **3.21** (126 MHz, CDCl<sub>3</sub>).

**2.5.2.18** 3-bromo-1-(tert-butyldimethylsilyl)-4-(isopropylamino)-pyrrole-2,5-dione (3.22)



The crude product obtained from the general procedure, was purified *via* silica column chromatography using 100% petroleum ether as the eluent to afford a yellow solid (110 mg, 47 %).

$^1\text{H}$  NMR (500 MHz,  $\text{CDCl}_3$ )  $\delta$  5.14 (br, 1H, NH), 4.3 (m, 1H, CH), 1.27 (t,  $^3J_{\text{HH}} = 9.1$  Hz, 6H,  $\text{CH}_3$ ), 0.94 (s, 9H,  $\text{CCH}_3$ ), 0.42 (s, 6H,  $\text{SiCH}_3$ ).

$^{13}\text{C}$  NMR ( $\text{CDCl}_3$ , 126MHz, ppm)  $\delta$  = 172.2 (CO), 171.3 (CO), 143.2 (CNH), 44.5 (CH), 26.2 (CH), 23.8 ( $\text{CH}_3$ ), 18.8 ( $\text{CMe}_3$ ), 20.22 ( $\text{CH}_3$ ), -4.4 ( $\text{SiCH}_3$ )

HR-MS (MaXis) -  $[\text{M}+\text{Na}^+]$  - calculated  $m/z$  369.0604 observed  $m/z$  369.0601;

FTIR ( $\text{cm}^{-1}$ ) - 2960 ( $\nu_{\text{C-H}}$ ), 1701 ( $\nu_{\text{C=O}}$ ), 1634 ( $\nu_{\text{C=O}}$ )



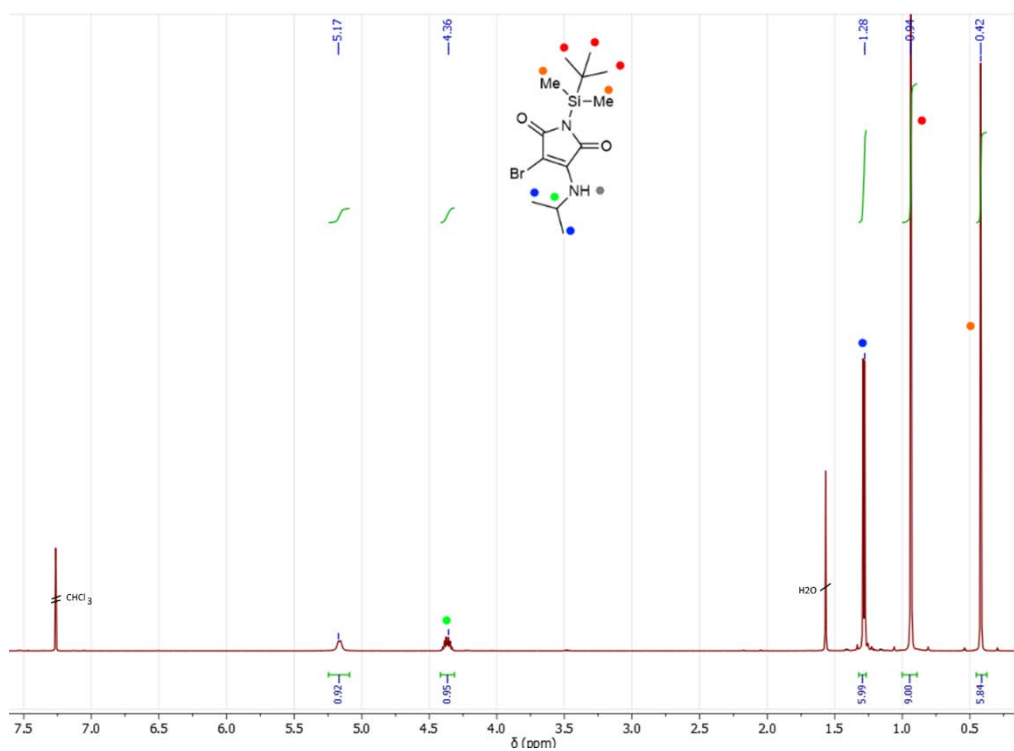


**Figure 3.47:**  $^1\text{H}$  NMR spectrum of **3.22** (500 MHz,  $\text{CDCl}_3$ ).

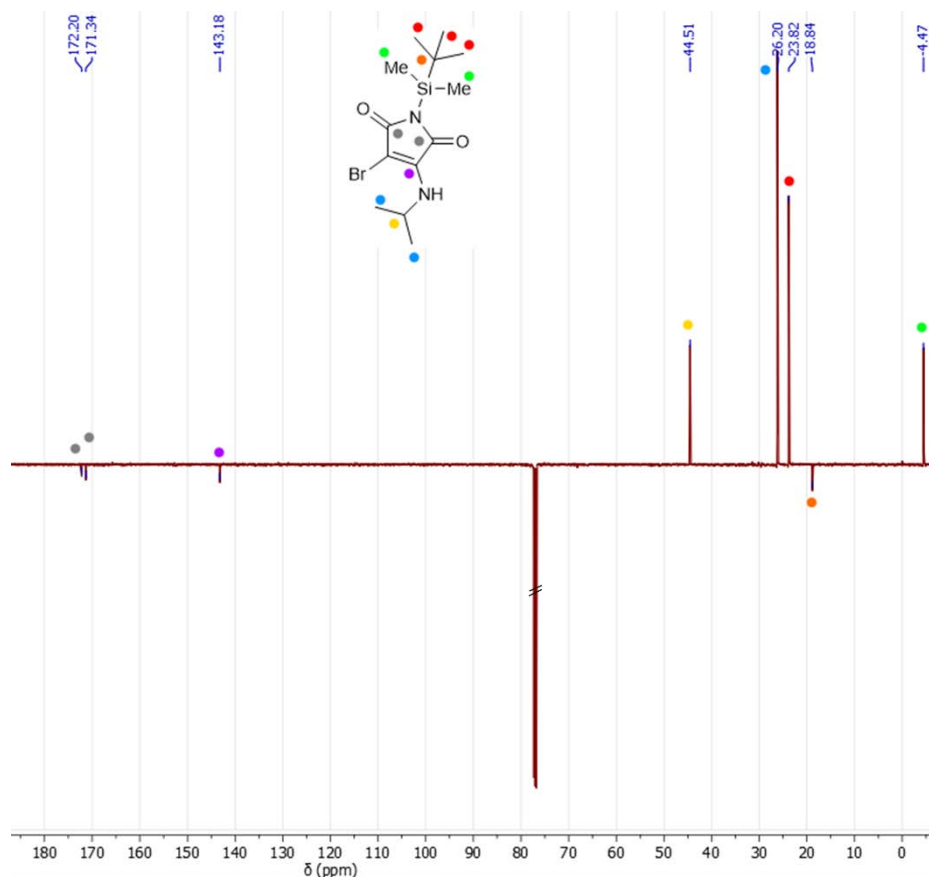
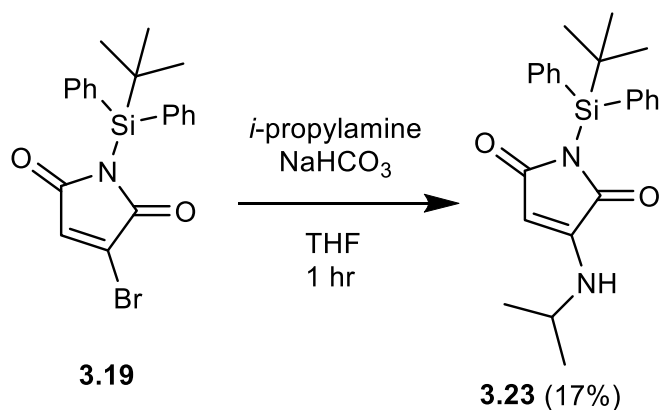


**Figure 3.48:**  $^{13}\text{C}$  NMR spectrum of **3.22** (126 MHz,  $\text{CDCl}_3$ ).

**2.5.2.19** 1-(tert-butyldiphenylsilyl)-3-(isopropylamino)-pyrrole-2,5-dione (3.23)



The crude product obtained from the general procedure, was purified *via* silica column chromatography using 5% EtOAc in petroleum ether as the eluent to afford a pale yellow solid (53 mg, 17 %).

$^1\text{H}$  NMR (500 MHz,  $\text{CDCl}_3$ , ppm)  $\delta$  = 7.61 (d,  $^3J_{\text{HH}}$  = 6.9 Hz, 4H, ArH), 7.45 – 7.30 (q,  $^3J_{\text{HH}}$  = 6.9 Hz, 6H, ArH), 5.12 (d,  $^3J_{\text{HH}}$  = 7.0 Hz, 1H, NH), 4.90 (s, 1H, CH), 3.57 – 3.42 (m, 1H, CH), 1.27 – 1.17 (m, 15H,  $\text{CH}_3$ ).

$^{13}\text{C}$  NMR (126 MHz,  $\text{CDCl}_3$ , ppm)  $\delta$  = 176.9 (CO), 172.7 (CO), 149.3 (CN), 136.3 (CAr), 134.3 (CAr), 132.6 (CAr), 130.0 (CAr), 127.7 (CAr), 127.3 (CAr), 87.4 (CH), 46.8 (CH), 28.0 ( $\text{CH}_3$ ), 26.7 (CH), 22.0 ( $\text{CH}_3$ ).

HR-MS (MaXis) -  $[\text{M}+\text{Na}^+]$  - calculated m/z 415.1812 observed m/z 415.1813;

FTIR ( $\text{cm}^{-1}$ ) – 2941 ( $\nu\text{C-H}$ ), 2859 ( $\nu\text{C-H}$ ), 1694 ( $\nu\text{C=O}$ ), 1623 ( $\nu\text{C=O}$ ).

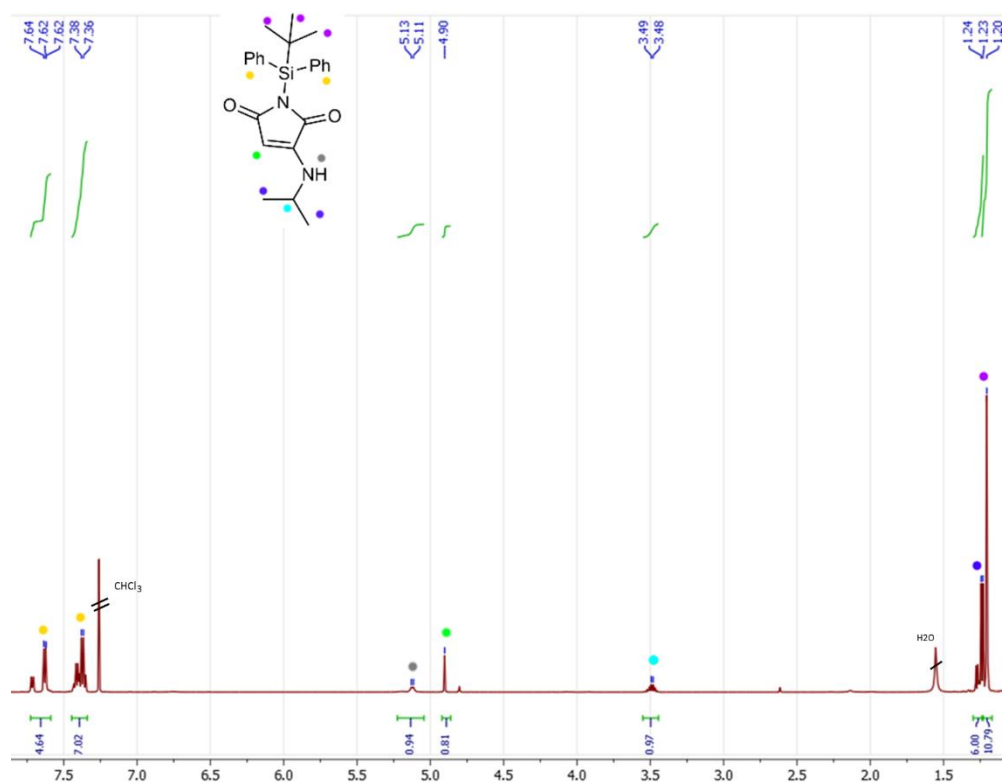


**Figure 3.49:** <sup>1</sup>H NMR spectrum of **3.23** (500 MHz, CDCl<sub>3</sub>).

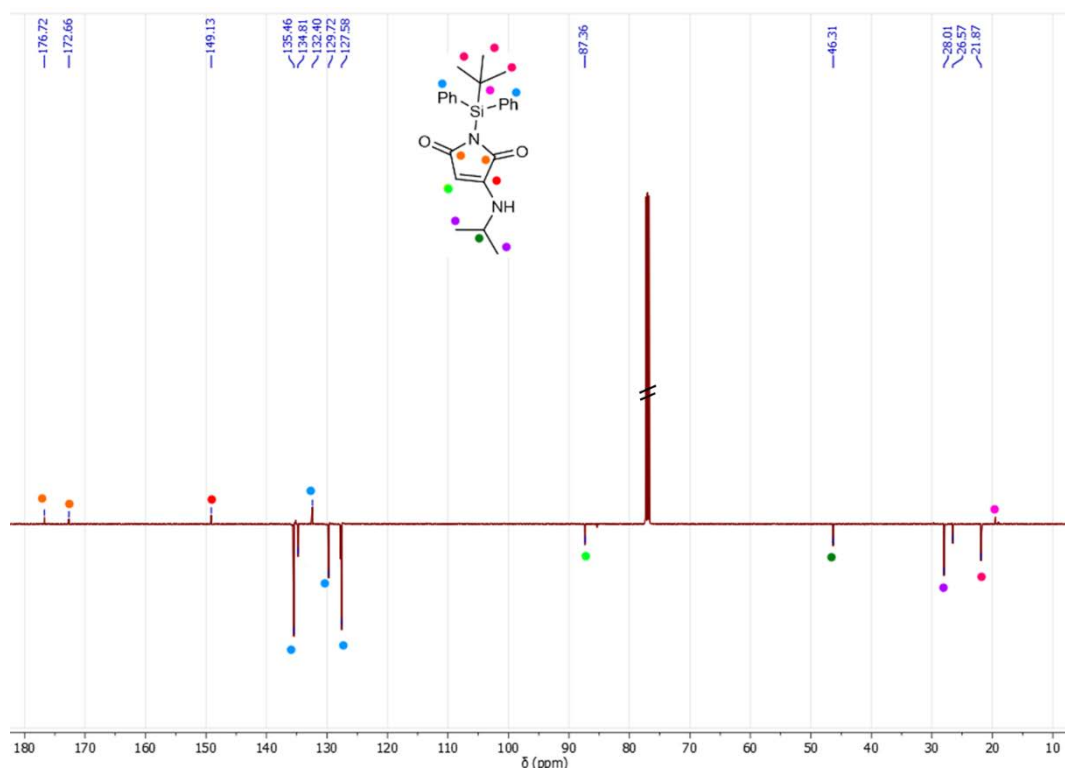
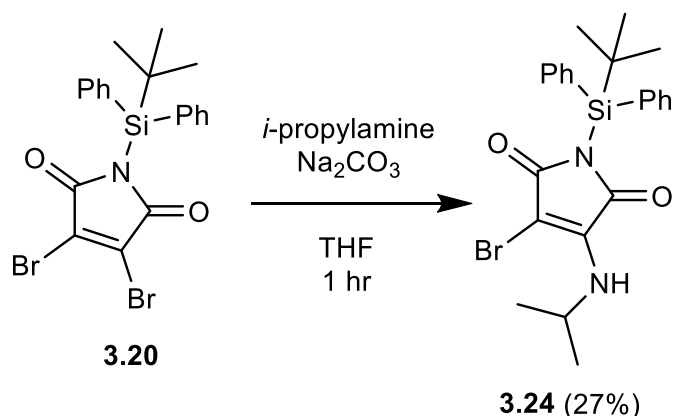


**Figure 3.50:** <sup>13</sup>C NMR spectrum of **3.23** (126 MHz, CDCl<sub>3</sub>).

2.5.2.20 1-(tert-butyldiphenylsilyl)-3-(isopropylamino)-pyrrole-2,5-dione (3.24)



The crude product obtained from the general procedure, was purified *via* silica column chromatography using 5% EtOAc in petroleum ether as the eluent to afford a pale yellow solid (17 mg, 27 %).

$^1\text{H}$  NMR (500 MHz,  $\text{CDCl}_3$ , ppm)  $\delta$  = 7.60 (d,  $^3J_{\text{HH}}$  = 7.7 Hz, 4H, ArH), 7.40 (m, 6H, ArH), 5.16 (d,  $^3J_{\text{HH}}$  = 12.2 Hz, 1H, NH), 4.44 – 4.33 (m, 1H, CH), 1.27 (t,  $^3J_{\text{HH}}$  = 7.3 Hz, 6H,  $\text{CH}_3$ ), 1.21 (s, 9H,  $\text{CCH}_3$ ).

$^{13}\text{C}$  NMR (75 MHz,  $\text{CDCl}_3$ , ppm)  $\delta$  = 135.5 (CAr), 129.9 (CAr), 127.7 (CAr), 28.0 ( $\text{CH}_3$ ), 23.8 ( $\text{CH}_3$ ).

HR-MS (MaXis) -  $[\text{M}+\text{Na}^+]$  – calculated m/z 493.0920 observed m/z 493.0901;

FTIR ( $\text{cm}^{-1}$ ) – 3019 ( $\nu_{\text{Ar-C-H}}$ ), 2964 ( $\nu_{\text{C-H}}$ ), 1701 ( $\nu_{\text{C=O}}$ ), 1636 ( $\nu_{\text{C=O}}$ )

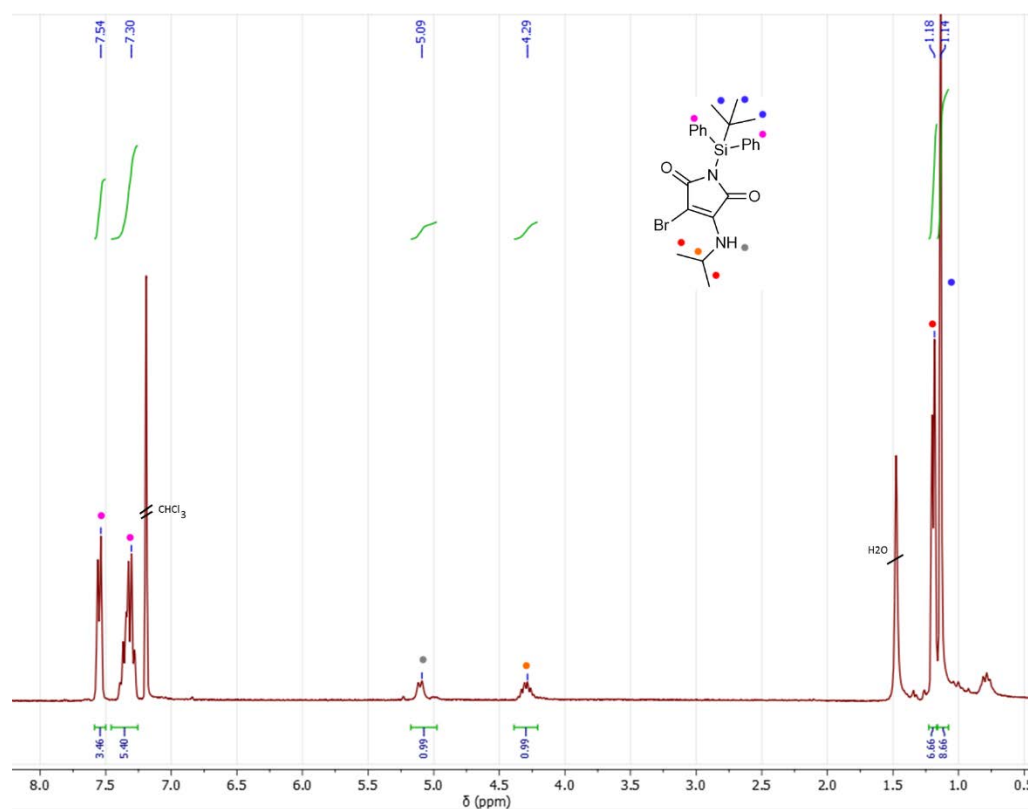


**Figure 3.51:** <sup>1</sup>H NMR spectrum of **3.24** (500 MHz, CDCl<sub>3</sub>).

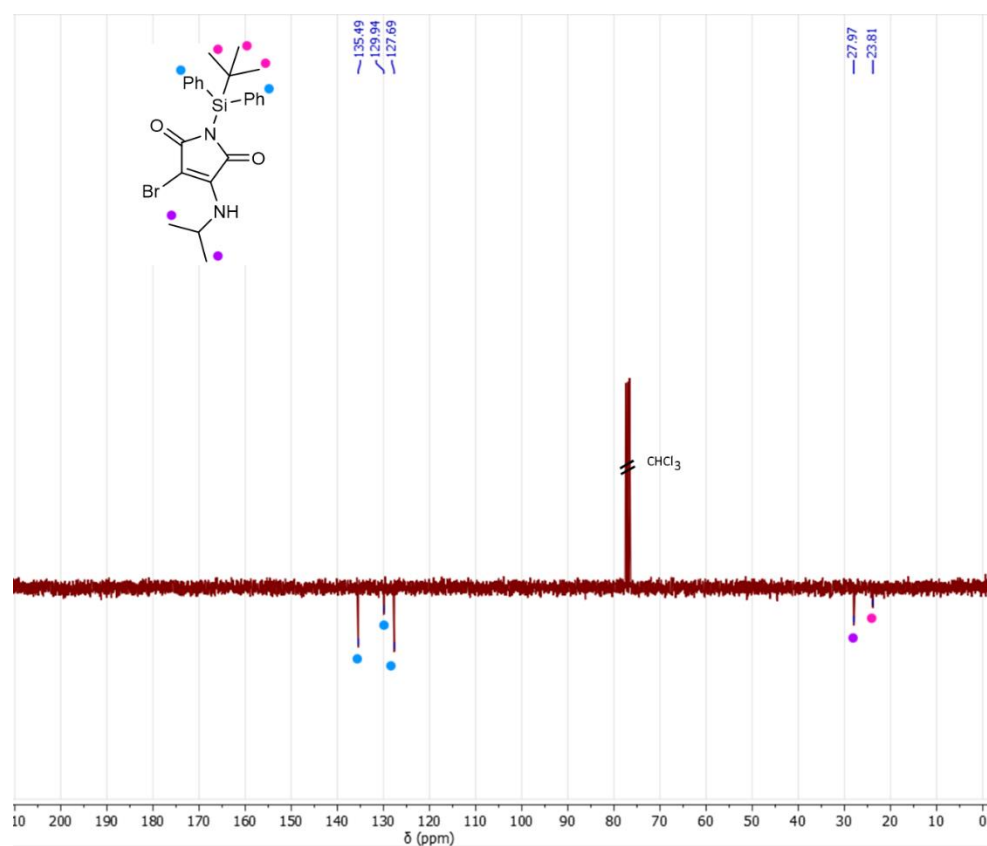


**Figure 3.52:** <sup>13</sup>C NMR spectrum of **3.24** (126 MHz, CDCl<sub>3</sub>).

### 2.5.3 Fluorophore incorporation into PEG powders

Fluorophore containing PEG powders were prepared as follows. Firstly, PEG (12 kDa) was dissolved into chloroform (20 mg/mL). To this, the selected MAM or 4-(1,2,2-Triphenylvinyl)benzaldehyde was added at 0.1 mg/mL and this solution was dropped into a circular mould of approx. 1 cm depth. The chloroform was left to evaporate, and the resultant powder was then added to the fluorimeter solid-state holder for analysis. Powders without MAM were also prepared using the same method, and used as scattering controls for the absolute quantum yield analysis.

## 2.6 References

- (1) In *Molecular Fluorescence*; Wiley-Blackwell, 2012; 109.
- (2) Staniforth, M.; Quan, W.-D.; Karsili, T. N. V.; Baker, L. A.; O'Reilly, R. K.; Stavros, V. G. *J. Phys. Chem. A* 2017, *121*, 6357.
- (3) Xie, Y.; Husband, J. T.; Torrent-Sucarrat, M.; Yang, H.; Liu, W.; O'Reilly, R. K. *Chem. Commun.* 2018, *54*, 3339.
- (4) Robin, M. P.; Mabire, A. B.; Damborsky, J. C.; Thom, E. S.; Winzer-Serhan, U. H.; Raymond, J. E.; O'Reilly, R. K. *J. Am. Chem. Soc.* 2013, *135*, 9518.
- (5) Robin, M. P.; Osborne, S. A. M.; Pikramenou, Z.; Raymond, J. E.; O'Reilly, R. K. *Macromolecules* 2016, *49*, 653.
- (6) Mabire, A. B.; Brouard, Q.; Pitto-Barry, A.; Williams, R. J.; Willcock, H.; Kirby, N.; Chapman, E.; O'Reilly, R. K. *Polym. Chem.* 2016, *7*, 5943.
- (7) Haberhauer, G.; Gleiter, R.; Burkhart, C. *Chem. – Eur. J.* 2016, *22*, 971.
- (8) Quan, W.-D. The design, construction and characterisation of self-assembled biomimetic multi-chromophoric photosystems, University of Warwick, 2017.
- (9) Mabire, A. B.; Robin, M. P.; Quan, W.-D.; Willcock, H.; Stavros, V. G.; O'Reilly, R. K. *Chem. Commun.* 2015, *51*, 9733.
- (10) Mei, J.; Leung, N. L. C.; Kwok, R. T. K.; Lam, J. W. Y.; Tang, B. Z. *Chem. Rev.* 2015, *115*, 11718.
- (11) Luo, J.; Xie, Z.; Lam, J. W.; Cheng, L.; Chen, H.; Qiu, C.; Kwok, H. S.; Zhan, X.; Liu, Y.; Zhu, D.; Tang, B. Z. *Chem. Commun.* 2001, *18*, 1740.
- (12) Zhao, Z.; Lam, J. W. Y.; Tang, B. Z. *J. Mater. Chem.* 2012, *22*, 23726.
- (13) Loudet, A.; Burgess, K. *Chem. Rev.* 2007, *107*, 4891.
- (14) Luo, Z.; Yuan, X.; Yu, Y.; Zhang, Q.; Leong, D. T.; Lee, J. Y.; Xie, J. J. *Am. Chem. Soc.* 2012, *134*, 16662.
- (15) Hong, Y.; Lam, J. W. Y.; Tang, B. Z. *Chem. Soc. Rev.* 2011, *40*, 5361.
- (16) Li, K.; Wang, J.; Li, Y.; Si, Y.; He, J.; Meng, X.; Hou, H.; Tang, B. Z. *Sens. Actuators B Chem.* 2018, *274*, 654.
- (17) Yang, Z.; Qin, W.; Leung, N. L. C.; Arseneault, M.; Lam, J. W. Y.; Liang, G.; Sung, H. H. Y.; Williams, I. D.; Tang, B. Z. *J. Mater. Chem. C* 2015, *4*, 99.
- (18) Tu, Y.; Liu, J.; Zhang, H.; Peng, Q.; Lam, J. W. Y.; Tang, B. Z. *Angew. Chem.* 2019, *131*, 15053.
- (19) Li, Y.; Xu, Z.; Zhu, X.; Chen, B.; Wang, Z.; Xiao, B.; Lam, J. W. Y.; Zhao, Z.; Ma, D.; Tang, B. Z. *ACS Appl. Mater. Interfaces* 2019, *11*, 17592.
- (20) Panigrahi, A.; Sahu, B. P.; Mandani, S.; Nayak, D.; Giri, S.; Sarma, T. K. *J. Photochem. Photobiol. Chem.* 2019, *374*, 194.
- (21) Wu, Y.; Qin, A.; Tang, B. Z. *Chin. J. Polym. Sci.* 2017, *35*, 141.
- (22) Zhu, Q.; Ye, Z.; Yang, W.; Cai, X.; Tang, B. Z. *J. Org. Chem.* 2017, *82*, 1096.
- (23) Imoto, H.; Fujii, R.; Naka, K. *Eur. J. Org. Chem.* 2019, *2019*, 3086.
- (24) Xie, Z.; Yu, T.; Chen, J.; Ubba, E.; Wang, L.; Mao, Z.; Su, T.; Zhang, Y.; Aldred, M. P.; Chi, Z. *Chem. Sci.* 2018, *9*, 5787.
- (25) Shao, Y.; Yin, G.-Z.; Ren, X.; Zhang, X.; Wang, J.; Guo, K.; Li, X.; Wesdemiotis, C.; Zhang, W.-B.; Yang, S.; Zhu, M.; Sun, B. *RSC Adv.* 2017, *7*, 6530.
- (26) Tedaldi, L. M.; Smith, M. E. B.; Nathani, R. I.; Baker, J. R. *Chem. Commun.* 2009, *43*, 6583.

- (27) Robin, M. P. Bromo and thio maleimides for functionalisation and fluorescent labelling of polymers and polymer nanoparticles, University of Warwick, 2014.
- (28) Prishchenko, A. A.; Livantsov, M. V.; Novikova, O. P.; Livantsova, L. I.; Petrosyan, V. S. *Heteroat. Chem.* 2012, *23*, 138.
- (29) Fu, M.; Xiao, Y.; Qian, X.; Zhao, D.; Xu, Y. *Chem. Commun.* 2008, 1780.
- (30) Koide, Y.; Urano, Y.; Hanaoka, K.; Piao, W.; Kusakabe, M.; Saito, N.; Terai, T.; Okabe, T.; Nagano, T. *J. Am. Chem. Soc.* 2012, *134*, 5029.
- (31) R. Martinez, C.; L. Iverson, B. *Chem. Sci.* 2012, *3*, 2191.
- (32) Hunter, C. A.; Sanders, J. K. M. *J. Am. Chem. Soc.* 1990, *112*, 5525.
- (33) Hunter, C. A.; Lawson, K. R.; Perkins, J.; Urch, C. J. *J. Chem. Soc. Perkin Trans.* 2001, *2*, 651.
- (34) Riwar, L.-J.; Trapp, N.; Kuhn, B.; Diederich, F. *Angew. Chem. Int. Ed.* 2017, *56*, 11252.
- (35) Chen, Y.; Lam, J. W. Y.; Kwok, R. T. K.; Liu, B.; Tang, B. Z. *Mater. Horiz.* 2019, *6*, 428.
- (36) Zhou, H.; Chua, M. H.; Tang, B. Z.; Xu, J. *Polym. Chem.* 2019, *10*, 3822.
- (37) Würth, C.; Grabolle, M.; Pauli, J.; Spieles, M.; Resch-Genger, U. *Nat. Protoc.* 2013, *8*, 1535.





## **Chapter 4:** Synthesis of aminomaleimide functionalized fluorescent amino acids for incorporation into peptides through codon re-allocation techniques

### 3.1 Abstract

The uniquely small size of maleimide dyes means that there are numerous novel applications for them in enzyme-based research where larger dyes would not be appropriate. It is hypothesized herein that these dyes could be incorporated into buried residues of enzymes without disturbing enzyme integrity, a challenge currently unrealized. This chapter will focus on synthesizing non-canonical amino acids functionalized with aminomaleimide dyes for genetic expression into peptides. Four probes were targeted: two zwitterionic amino acids for traditional tRNA orthogonal synthetase incorporation, and two activated ester variants for flexizyme based incorporation. Difficulties were encountered with the synthesis of un-activated aminomaleimides, mainly a result of purification and solubility issues. However, aminobromomaleimide functionalized lysine and aminochloromaleimide functionalized ornithine were synthesized successfully and the former was isolated using preparative HPLC. In regards to the activated compounds, the activated dinitrobenzyl (DNB)-ester variant was synthesized successfully over four steps. Unfortunately, incorporation into peptides was poor and therefore a more water-soluble amino-derivatized benzyl thioester (ABT) ester variant was targeted. Synthesis of this ABT derivative was successful over an eight-step divergent synthesis through reaction of a synthesized ABT group with previously realized ACM-ornithine. This compound has been sent to collaborators and has been successfully incorporated into peptides mediated through cell-free flexizyme based expression.

## 3.2 Introduction

### 3.2.1 Non-canonical amino acid incorporation into peptides

Polypeptides have a wide variety of structures and functions, yet nature has a toolbox of only 20 standard amino acids for their synthesis. However, over 500 examples of rare non-canonical amino acids have been observed in nature, for example, selenocystine and *D*-serine.<sup>1,2</sup> The observation of these rarer amino acids has led researchers to focus on synthesizing novel amino acids which may impart useful novel functions to peptides.<sup>3</sup> These unnatural amino acids (uAA) can be incorporated by *in vivo* protein biosynthesis *via* processes such as amber suppression.<sup>4,5</sup> In this process a stop codon (specifically UAG) is re-assigned to a new uAA. This is achieved through derivatization of the tRNA/synthetase pair, which recognizes this codon, through aminoacylation of tRNA with the new uAA.<sup>5</sup> This process is catalyzed by an orthogonal aminoacyl tRNA synthase (Figure 4.1). This process requires directed evolution of this enzyme towards the aim of specifically recognizing the new unnatural amino acid over all other natural amino acids that will be present in expression media. Once achieved, this uAA functionalized tRNA/synthetase pair can then be utilized in translation of peptides; instead of stopping the synthesis at a UAG codon, the uAA is incorporated and translation can continue (Figure 4.1B). A limitation of this methodology, is that the amino acid must fit into the active site of an extensively evolved orthogonal synthetase, hence limiting the introduction of some non-natural amino acids.<sup>5</sup>

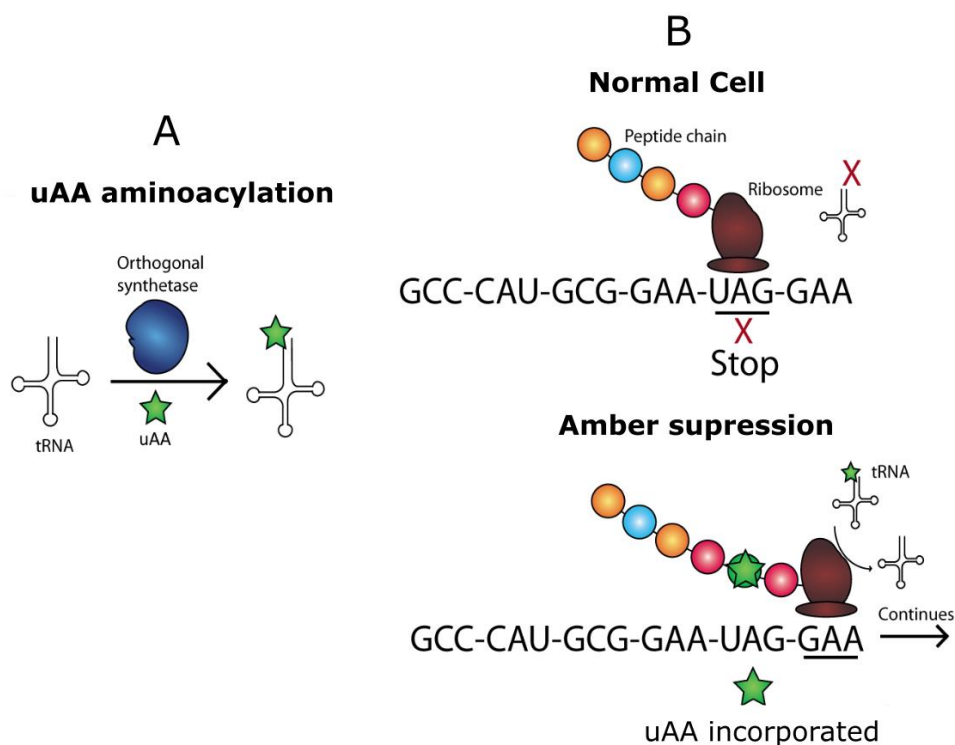


**Figure 4.1:** (A) Aminoacylation of tRNA with a uAA and (B) subsequent incorporation of the uAA into a peptide by a ribosome.

Recently, new machinery has been developed to overcome this hurdle. One such technology is flexizymes, which are ribozymes that have been developed to catalyze the aminoacylation step.<sup>6,7</sup> They are evolved to recognize only activated amino acids ensuring that only the desired amino acid will be acylated (Figure 4.2). Two activating groups that have been successfully utilized for this include cyanomethyl esters (CME) and 3,5-dinitrobenzyl esters.<sup>7</sup>

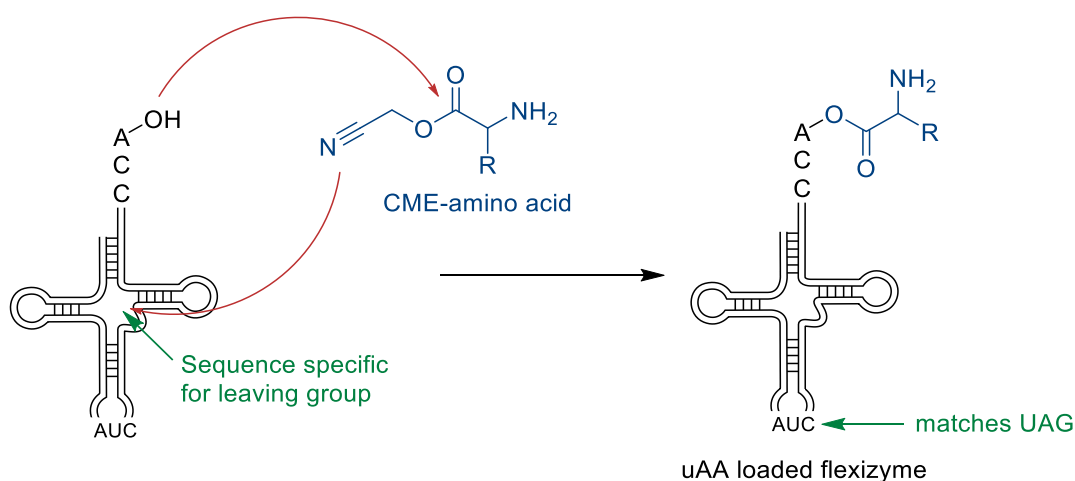


**Figure 4.2:** Illustration of flexizyme charging with a CME activated amino acid.

### 3.2.2 Fluorescent labelling of proteins through genetic incorporation

Fluorescent labelling of proteins is a widespread practice. It is used for many applications, including studying intracellular trafficking,<sup>8,9</sup> tracking cellular uptake,<sup>10</sup> measuring conformational changes,<sup>11–13</sup> and environmental sensing.<sup>14</sup> Commonly this is achieved by conjugating fluorescent proteins to the target.<sup>15</sup> Not only may the large size of such proteins have a significant effect on the properties and function of the target, but they are prone to photobleaching.<sup>16,17</sup> Another strategy is to conjugate a small molecule fluorophore to the studied protein *via* an amino acid residue.<sup>18,19</sup> Often this is achieved by incorporating a non-natural amino acid into the protein through genetic expression, which can then be selectively conjugated to a dye, for example, azide functionalized amino acids can be modified using CuAAC.<sup>20–23</sup>

The incorporation of fluorescent dyes genetically, eliminating the need for conjugation, is seen as the best way to site selectively label proteins, as tricky purification steps can be avoided, and side reactions can be eliminated.<sup>24</sup> The

Schultz group has successfully genetically incorporated several dyes including dansyl,<sup>25</sup> 7-hydroxycoumarin<sup>26</sup> and prodan<sup>27</sup> (Figure 4.3).

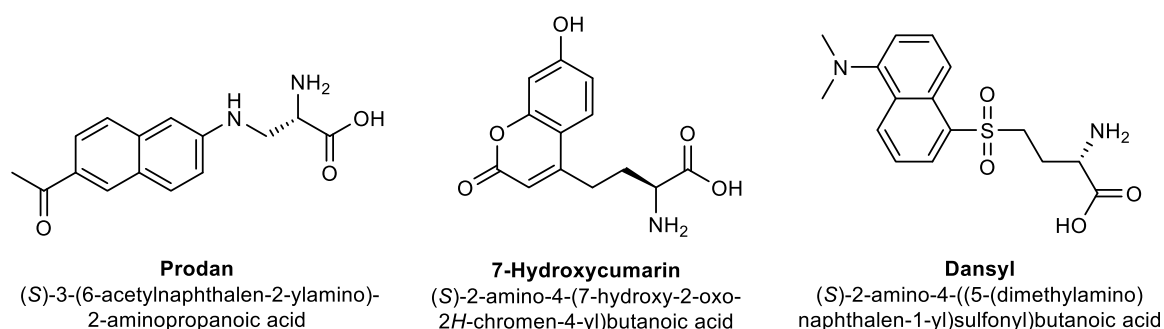


**Figure 4.3:** Fluorescently labelled amino acids that have been genetically expressed into proteins by the Schultz group.<sup>25–27</sup>

These dyes were utilized for various applications, for example, the dansyl labelled amino acid was incorporated into human superoxide dismutase (hSOD) using an amber nonsense codon and corresponding orthogonal tRNA/aminoacyl-tRNA synthetase pair.<sup>25</sup> The denaturing of the labelled enzyme could be measured by studying fluorescence emission wavelength and intensity. Notably, the expressed amino acids are incorporated at solvent-accessible residues, such as in place of Gln-16 and Trp-33 in hSOD.

Genetic expression could theoretically allow incorporation of residues anywhere in an enzyme sequence - dependent on enzyme-specific factors - so that the maleimide dye could theoretically be buried deep within the tertiary structure where it would be shielded from the solvent, and where traditional conjugations would not be able to target. It could also be site-specifically incorporated for applications such as active site labelling, and for studying protein-protein interactions, a topic of great importance to research into protein aggregation related diseases such as Creutzfeldt–Jakob disease (CJD) and Alzheimer's.<sup>28,29</sup> The goal of this chapter will be to synthesize aminomaleimide

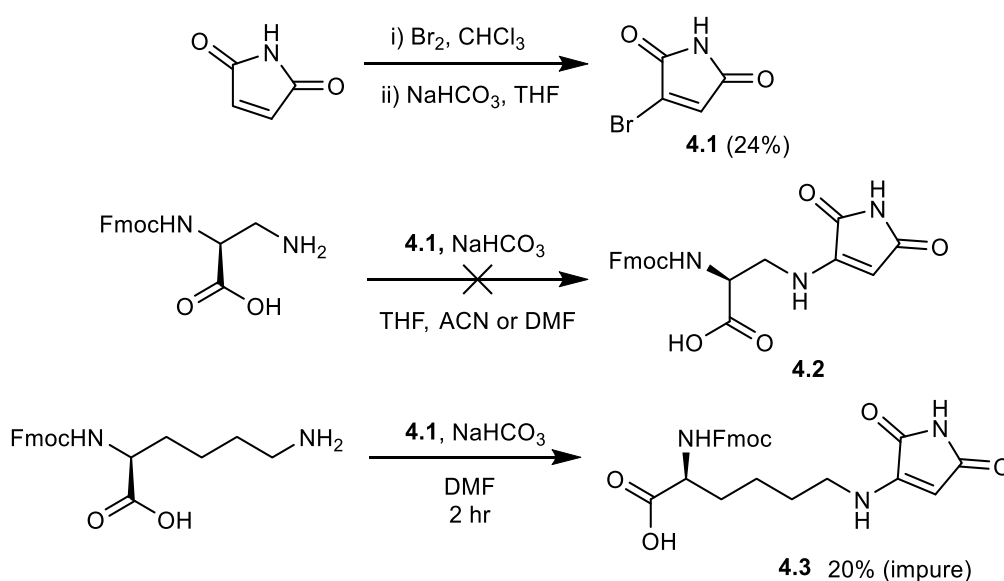
functionalized amino acids for genetic expression testing, towards applications such as these. Initially, this will focus on synthesis of zwitterionic amino acids for expression through an orthogonal aminoacyl tRNA synthetase catalyzed ligation to tRNA.



## 3.3 Results

### 3.3.1 Synthesis of an aminomaleimide based amino acid for incorporation into aminoacyl tRNA

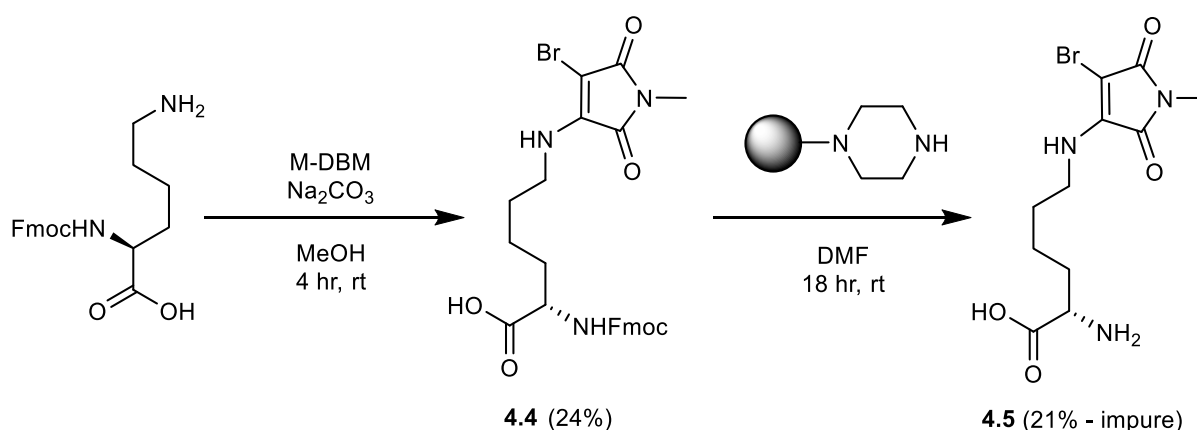
Aminoacyl tRNA synthetase catalyzes the formation of aminoacyl tRNA between the reaction of an amino acid and the 2'- or the 3'-OH of the final nucleotide at the 3' tRNA end.<sup>11</sup> This is the target for initial incorporation, and therefore a maleimide functionalized unnatural amino acid suitable for this application was targeted. As DTMs have shown to be susceptible to thiol exchange,<sup>30</sup> which could easily occur in cellular growth media, an aminomaleimide product was designed.



**Scheme 4.1:** Synthesis of MAM-Fmoc-lysine (**4.3**) via bromomaleimide (**4.1**).

The first targets were MAM variants which are smaller than their corresponding halogenated maleimide dyes and were theorized to be simply synthesized from functionalization of readily available amino functionalized amino acids for example: lysine or DAP (2,3-diaminopropionic acid). Initially monobromomaleimide (**4.1**) was synthesized as per a literature procedure,<sup>31</sup> for reaction with Fmoc protected amino acids (Scheme 4.1).

The reaction of **4.1** with both Fmoc-DAP and Fmoc-lysine, did not proceed appreciably in either THF or acetonitrile with  $\text{NaHCO}_3$  as a base. The reaction of Fmoc-lysine did proceed in DMF, however, only a yield of 20% could be obtained (which also contained residual DMF). It was decided to focus on the reaction of *N*-methyl-dibromomaleimide (M-DBM) with Fmoc-lysine, because of these issues. O'Reilly and co-workers have found that the allylic hydrogen on monobromomaleimide can be more reactive than the bromine analogue.<sup>32</sup> In addition, the methyl imide was targeted to prevent imide nucleophilicity. The reaction of M-DBM with Fmoc-lysine in the presence of  $\text{Na}_2\text{CO}_3$  in MeOH gave **4.4** in 24% isolated yield (Scheme 4.2). Unexpectedly, it was noted that precipitation of dibenzofulvene occurred during the reaction, suggesting a cause for the poor yield could be unexpected Fmoc deprotection.



**Scheme 4.2:** Synthesis of ABM-Fmoc-lysine **4.4** and attempted deprotection to ABM-lysine **4.5**.

Deprotection of **4.4** was attempted under several conditions including piperidine in THF and in 1:1 mixture of piperidine : DMF (v/v). However, all conditions explored resulted in a poor yield (1-10%) of impure ABM-lysine (**4.5**), which could not be successfully purified by extraction or column chromatography. It has been reported in the literature that piperidine-dibenzofulvene adducts can

form in these reactions.<sup>33</sup> In these cases piperazine loaded polystyrene can be utilized to scavenge any dibenzofulvene adducts.<sup>34</sup> Thus, resin-bound piperazine was treated with **4.4**, which produced ABM-lysine (**4.5**) in 21% yield, but at only 67% purity according to <sup>1</sup>H NMR spectroscopy. A preparative HPLC purification method was developed, and this achieved successful isolation of 52 mg of pure compound **4.5**, pure by <sup>1</sup>H NMR spectroscopy (Figure 4.4).

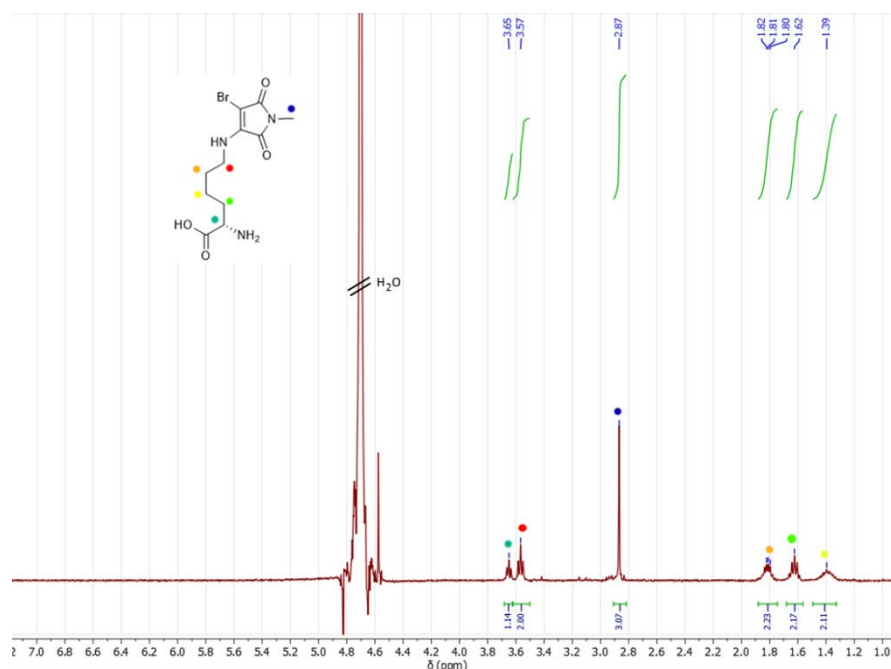


**Figure 4.4:** <sup>1</sup>H NMR spectrum of **4.5** (400 MHz, D<sub>2</sub>O).

During this time, work in the group developed aminochloromaleimides (ACMs) which are smaller, more fluorescent and less reactive towards some nucleophiles than their ABM analogues.<sup>35</sup> As a result of this and the issues encountered above with Fmoc chemistry, a new synthetic route was proposed through the reaction of a synthesized dichloromaleimide (**4.6** or **4.7**) with *N*-Boc-O<sup>t</sup>Bu-ornithine. This route requires the large scale synthesis of chlorinated maleimides. However, while syntheses of chlorinated maleimides have been reported in the literature,<sup>36,37</sup> attempts at repeating them were unsuccessful with low yields. Therefore, investigation into optimizing the synthesis of both H-DCM

(**4.6**) and M-DCM (**4.7**), both suitable for ornithine substitution, was conducted (Table 4.1).

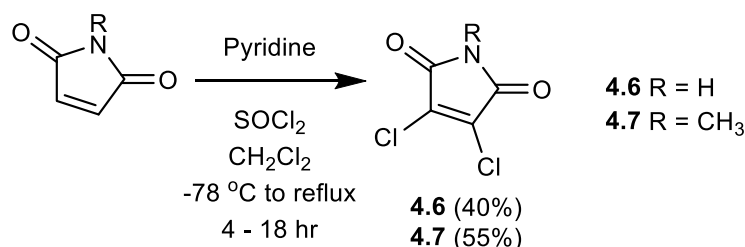
Initially, a synthesis from dichloromaleic acid using methyl ammonia was attempted as reported by Nirogi *et al.* (entry 1).<sup>37</sup> However this resulted in a fluorescent yellow solid isolated as the major product, identified to be methylamino-*N*-methylmaleimide, the double substitution product.

**Table 4.1:** Summary of conditions attempted for the synthesis of dichloromaleimides **4.6** and **4.7**.

Prod	#	Reactant	Conditions	Temp/ Time	Notes	Yield (%)	Ref.
4.7	1	Dichloromaleic anhydride	MeNH <sub>2</sub> .HCl, CH <sub>3</sub> COOK, AcOH	110 °C, 4 hr	Double addition preferred	4%	37
4.7	2	Dichloromaleic anhydride	MeNH <sub>2</sub> .HCl, AcOH	100 °C, 8 hr	Low conversion	2%	
4.7	3	Dichloromaleic anhydride	MeNH <sub>2</sub> (2 M in toluene), AcOH	110 °C, 4 hr	Double addition preferred	6%	
4.7	4	Methyl-maleimide	SOCl <sub>2</sub> , pyridine	0 °C 1 hr, to 75 °C 1 hr	Violent pyridine addition + messy HCl workup	5%	36
4.6	5	Maleimide	SOCl <sub>2</sub> , pyridine	0 °C 1 hr, to 75 °C 1 hr	No HCl work-up	21%	
4.6	6	Maleimide	SOCl <sub>2</sub> , DMAP	0 °C 1 hr, to 75 °C 3 hr	No conversion by TLC	0%	
4.6	7	Maleimide	SOCl <sub>2</sub> , pyridine, CH <sub>2</sub> Cl <sub>2</sub>	-78 °C 1 hr, to 75 °C 4 hr	Diluted pyridine addition was less violent	40%	
4.7	8	Methyl-maleimide	SOCl <sub>2</sub> , pyridine, CH <sub>2</sub> Cl <sub>2</sub>	-78 °C 1 hr, to 75 °C 18 hr	No brown colour formed	55%	

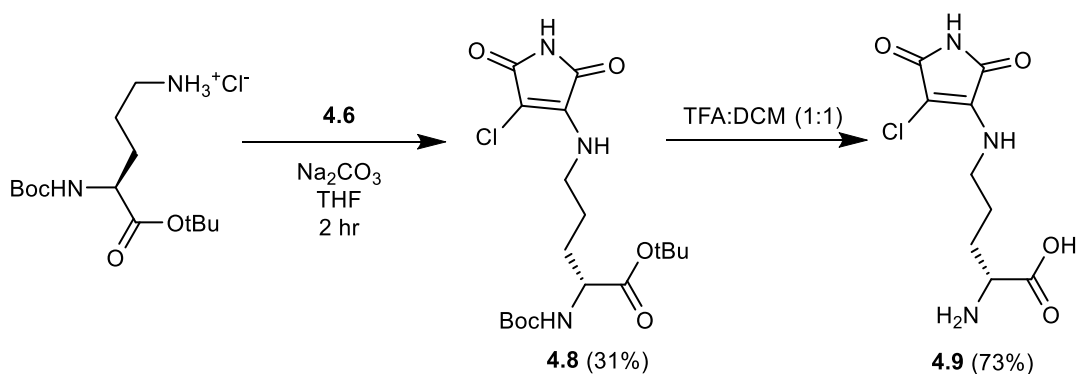
It was hypothesized that the presence of base favoured chloro- substitution over imide substitution, thus leading to the observation of significant side product. However, removal of base led to very slow conversion when using the methylammonium HCl salt (entry 2), and when used as the free base in solution double addition was again observed (entry 3).

Another literature protocol had been reported, which involved the chlorination of maleimide species using thionyl chloride.<sup>36</sup> This synthesis was attempted and it was noted that upon addition of piperidine to thionyl chloride a violent reaction took place, resulting in a brown precipitate (entries 4-5). Cooling to -78 °C for the piperidine addition, and adding the piperidine dropwise and diluted in CH<sub>2</sub>Cl<sub>2</sub> avoided formation of the precipitate, and the isolated yield from the reaction could be considerably increased to around 50% (entries 7-8 and Scheme 4.3).



**Scheme 4.3:** Optimized synthesis of chlorinated maleimides **4.6** and **4.7**.

Having obtained **4.6** in a reliably sufficient yield, its reaction with *N*-Boc-O<sup>t</sup>Bu-Ornithine was attempted (Scheme 4.4). Using previously developed aminomaleimide synthesis conditions, specifically with base in THF for an hour, formation of the protected ACM functionalized amino acid **4.8** was successful, in fair yield (32%). Longer reaction times led to imide substitution side reactions. The convenient one-step deprotection of **4.8**, to form ACM amino acid **4.9**, was completed in TFA/CH<sub>2</sub>Cl<sub>2</sub> (1:1) over 4 hours. Compound **4.9** was characterized by <sup>1</sup>H NMR spectroscopy (Figure 4.4.5), <sup>13</sup>C NMR spectroscopy (Figure 4.20), high resolution mass spectroscopy and infrared spectroscopy.



**Scheme 4.4:** Synthesis of ACM-*N*α-Boc-*O*<sup>t</sup>Bu-Ornithine **4.8** and deprotection to ACM-Ornithine **4.9**.

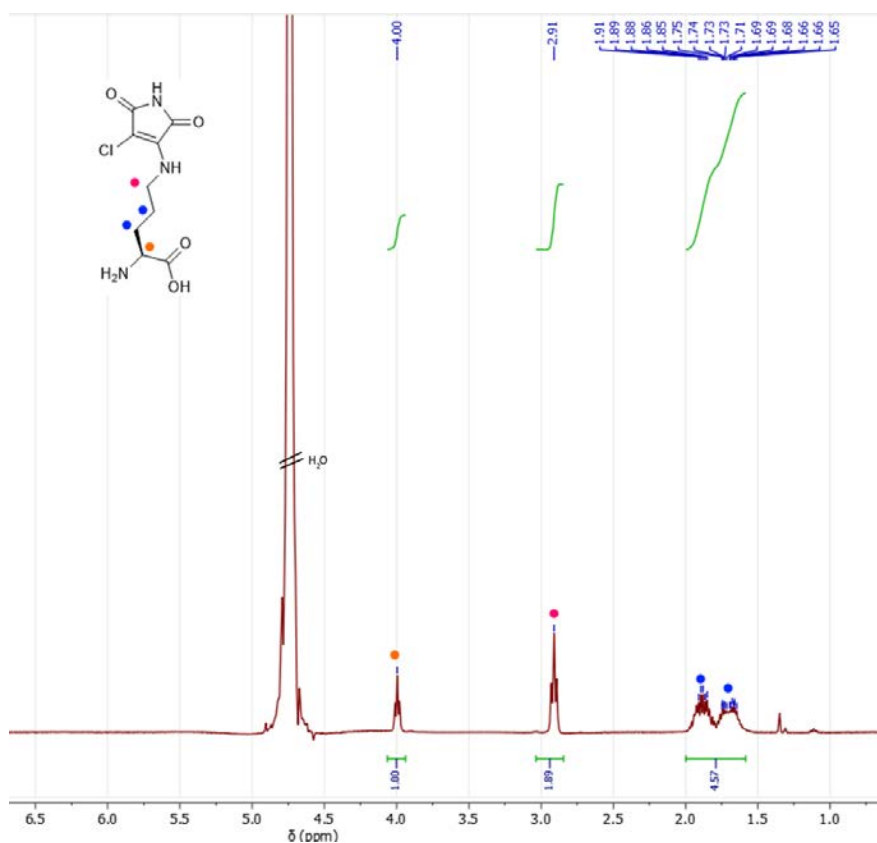


**Figure 4.5:** <sup>1</sup>H NMR spectrum of **4.9** (400 MHz, D<sub>2</sub>O).

Fluorescence excitation and emission were recorded for both **4.9** and **4.5** to ensure they exhibited suitable fluorescence for the application. Both dyes showed fluorescence with characteristic  $\lambda_{\text{max}}$  and weak emission in water (Figure 4.6), as expected from maleimide fluorophores.

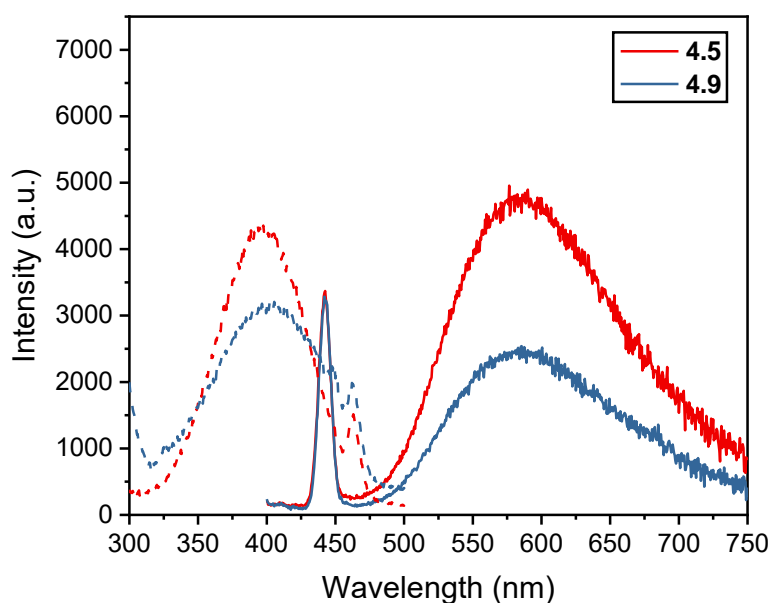
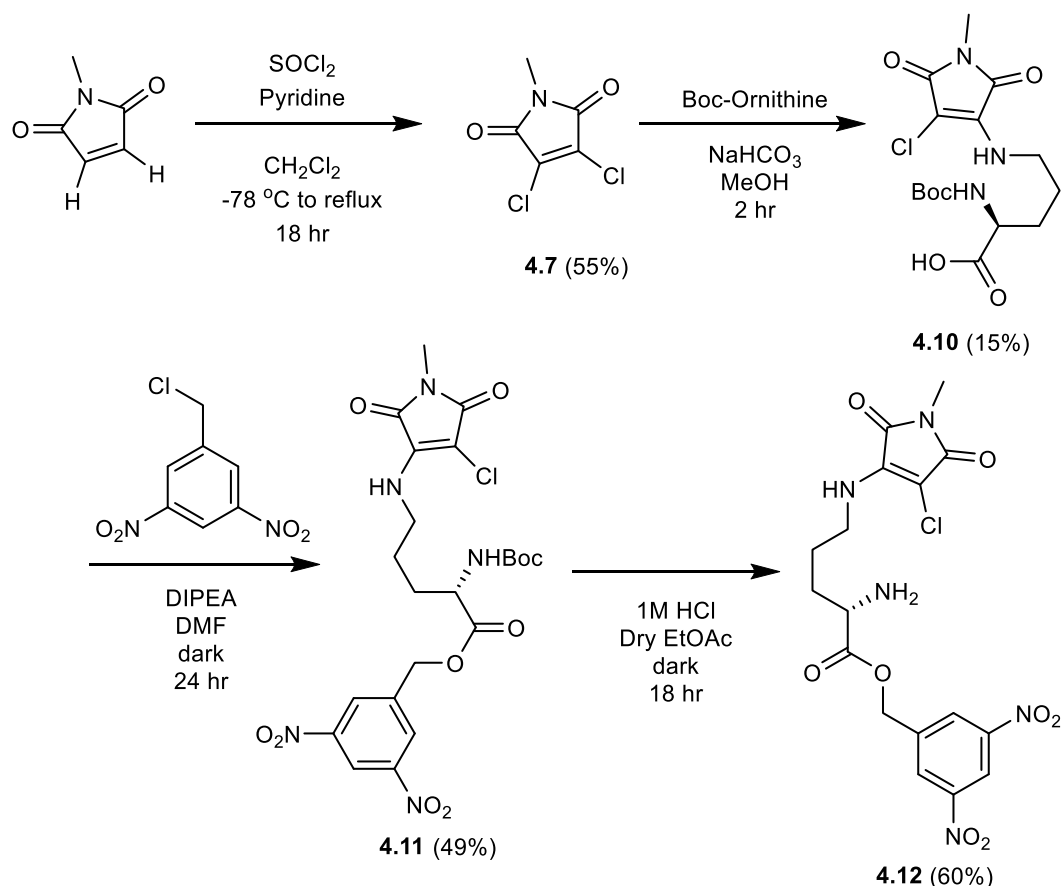


**Figure 4.6:** Fluorescence excitation (dashed line) and emission (full line) of **4.5** and **4.9** at 10  $\mu$ M in water.

### 3.3.2 Synthesis of an activated aminomaleimide based amino acid for flexizyme incorporation

Flexizyme based methods of tRNA acylation have recently been developed as discussed in the introduction, and this technique can save a considerable amount of time in the expression and optimization stages, compared to tRNA synthetase based expression. Unfortunately, compounds **4.4** and **4.9** are not compatible with flexizyme based incorporation techniques and therefore a new synthetic target was required. Loading of the flexizyme with an amino acid requires activation of the carboxylic acid *via* a water-soluble activated ester. Early work had shown the dinitrobenzyl (DNB) activating group to be effective and generally easy to synthesize.<sup>38</sup> Therefore, the dinitrobenzyl ester of compound **4.8** was targeted, by synthesis through an *N* $_{\alpha}$ -Boc-ACM-ornithine intermediate (Scheme 4.5).

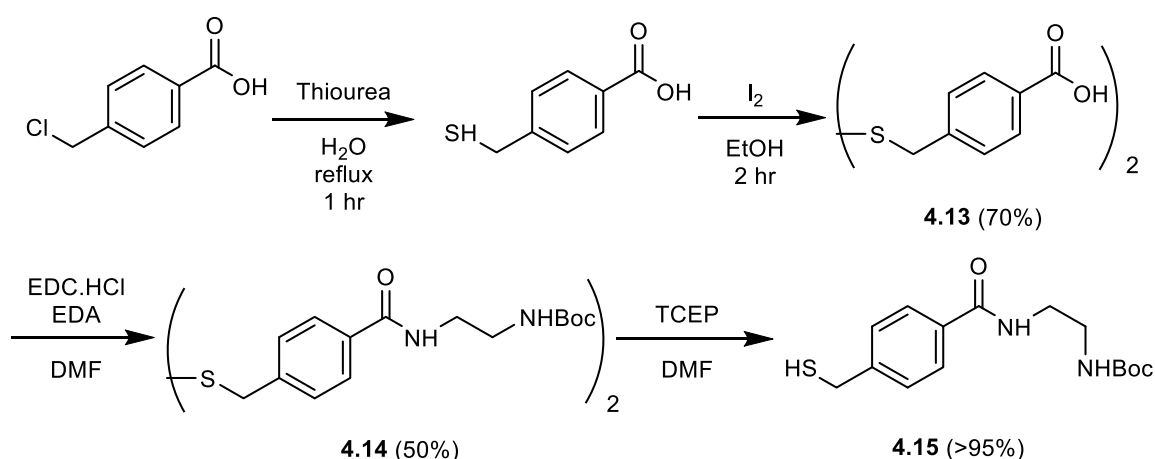
The synthesis of M-DCM, **4.7**, was targeted to help add stability to the maleimide, while also preventing the imide from acting as a nucleophile. The new chlorination reaction developed for **4.6** was found to also work well for this derivative producing **4.7** in 55% yield. This was used to functionalize *N*<sub>α</sub>-Boc-ornithine to form *N*<sub>δ</sub>-methyl-ACM-*N*<sub>α</sub>-Boc-ornithine, **4.10**, however the yield for this reaction was again low (15%). To create the DNB ester, **4.10** was reacted with 3,5-dinitrobenzyl chloride, under basic conditions in the dark, which formed DNB ester, **4.11**, in 49% yield. Finally, the deprotection of **4.11** was completed through treatment with 1 M HCl in dry ethyl acetate, overnight in the dark. The product precipitated and could be isolated through centrifugation to produce the product amino acid **4.12** in 60% yield.



**Scheme 4.5:** Synthesis of DNB ester of ACM-Ornithine (**4.12**) via *N*-Boc-ACM-Ornithine (**4.10**).

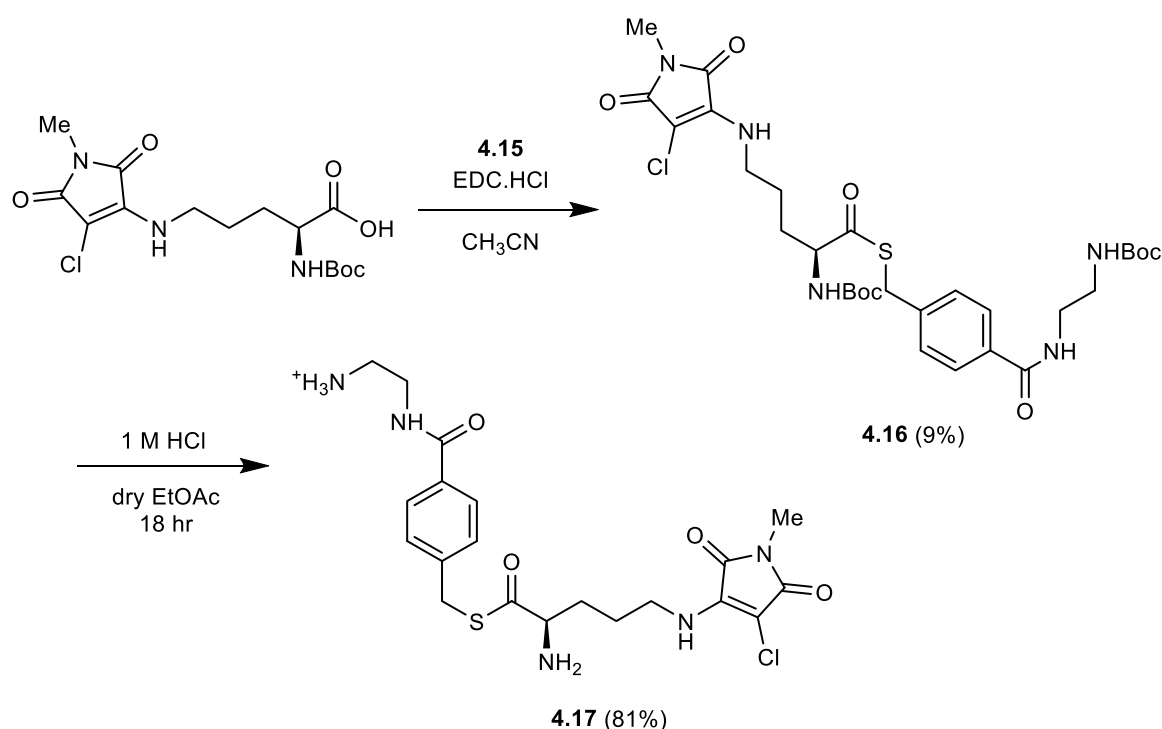


Activated amino acid, **4.12**, was sent to collaborators for flexizyme incorporation evaluation. Unfortunately, only partial *N*-terminal incorporation could be achieved, and no mid-chain incorporation – attributed to poor solubility of the hydrolysis product in water. During the development of this synthesis, the group had increased success with a new amino-derivatized benzyl thioester (ABT) activating ester. As a result, the synthesis of an ABT activated ACM functionalized amino acid was targeted, in the hopes of increased flexizyme charging. To achieve this the ABT activating group was synthesized based on a literature procedure.<sup>39</sup> Modifications were made to this protocol primarily as a result of solubility issues not described in the manuscript. Formation of disulfide acid **4.13** was successfully reproduced in 70% yield over 2 steps (Scheme 4.6). However, this product was not soluble in dioxane as described and therefore reaction of **4.13** with ethylenediamine (EDA) was conducted in DMF using an EDC coupling (Scheme 4.6). The purified disulfide **4.14** was then reduced with TCEP to form the free thiol ABT **4.15** in >95% yield.



**Scheme 4.6:** Synthesis of disulfide ABT precursor (**4.13**) and subsequent synthesis of ABT thiol (**4.15**) *via* reduction of disulfide **4.14** formed by EDC coupling of EDA and **4.13**.

The previously synthesized methyl-ACM-*N*-Boc-ornithine **4.10** was then coupled with **4.15** and EDC.HCl to give the Boc protected ABT thioester ACM-ornithine **4.16** in 9% yield (Scheme 4.7). TLC analysis (hexane : ethyl acetate) of this reaction indicated the formation of many products, with several yellow and UV active species observed. Helpfully, only one new fraction was fluorescent, thus isolation could be completed *via* silica column chromatography. The isolated product **4.16** was reacted with 1 M HCl in EtOAc under dry conditions to give the final ABT activated amino acid **4.17** in 81% yield, which could be isolated by simple centrifugation of the crude solution resulting from the precipitation of **4.17**. Amino acid **4.17** was characterized again by  $^1\text{H}$  NMR spectroscopy (Figure 4.7),  $^{13}\text{C}$  NMR spectroscopy (Figure 4.34), high resolution mass spectroscopy and infrared spectroscopy.



**Scheme 4.7:** Synthesis of methyl-ACM-ABT-ornithine (**4.17**) *via* a Boc-ABT intermediate (**4.16**).

Analogously to previously synthesized dyes, optical characterization of the activated amino acids **4.12** and **4.17** was undertaken, to ensure the dye exhibited characteristic maleimide fluorescence properties. Excitation and emission wavelengths closely matched expected maleimide values for both dyes with quenched red-shifted emission in water ( $\sim 550$  nm – Figure 4.8). For **4.12**, no obvious effect of the dinitrobenzyl ester on fluorescence emission is observed, although this would not be present in the expressed peptide in-any-event.

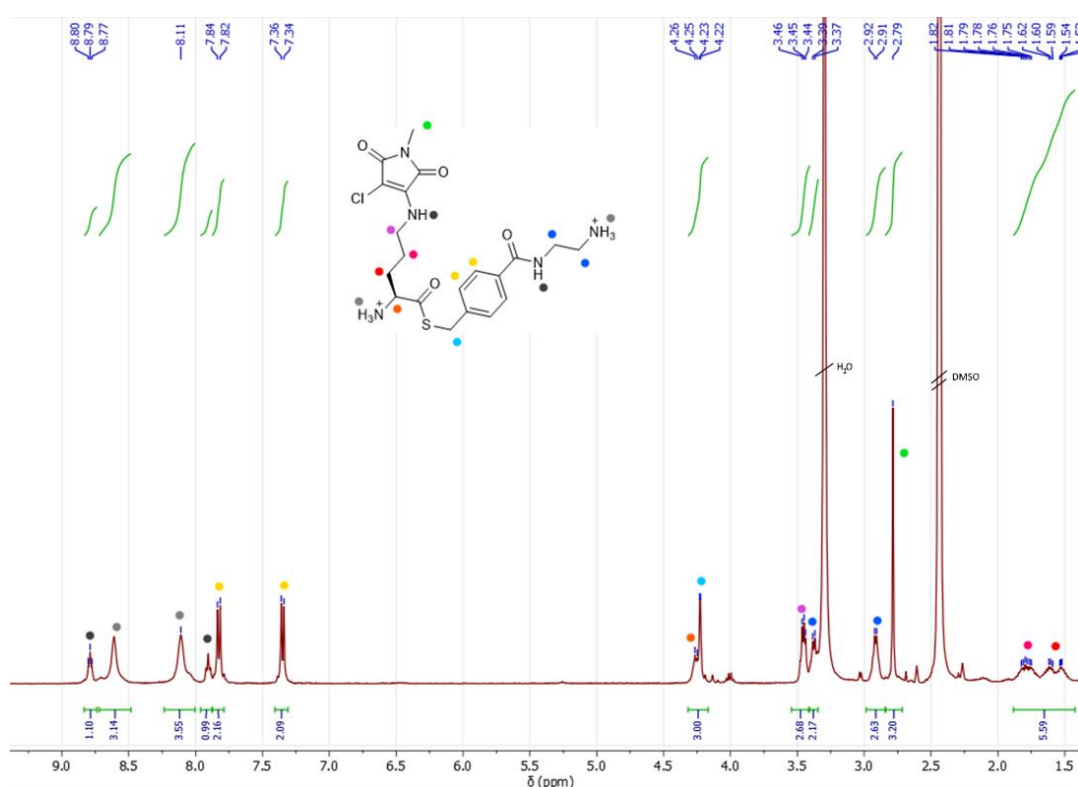


**Figure 4.7:** <sup>1</sup>H NMR spectrum of **4.17** (300 MHz, DMSO-*d*<sub>6</sub>).

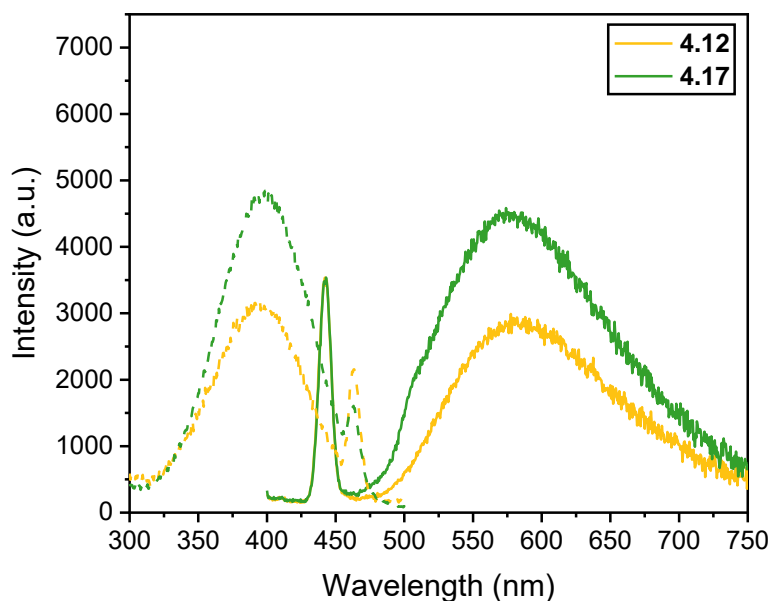
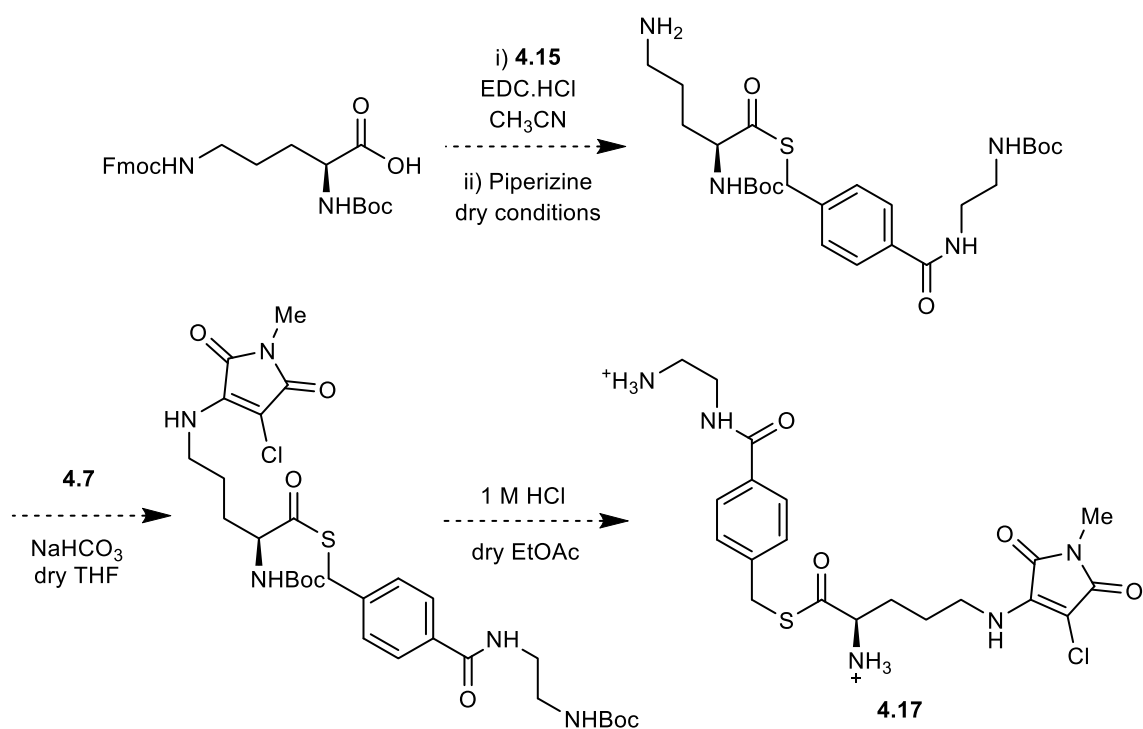


**Figure 4.8:** Fluorescence excitation (dashed line) and emission (full line) of **4.12** and **4.17** at 10  $\mu\text{M}$  in water.

While synthesis was successful in a yield sufficient for initial testing of flexizyme charging, future scale-up may be required for use *in vitro*. To achieve this, optimization of the ornithine ABT coupling in the synthesis of **4.16** is suggested. On the other hand, it may be convenient to redesign the synthesis so that the ornithine-ABT coupling is higher yielding, such a route is suggested in Scheme 4.8.



**Scheme 4.8:** Suggested alternative synthesis of methyl-ACM-ABT-ornithine (**4.17**).

### 3.3.3 Expression of peptides by ACM charged flexizymes

Activated amino acids (**4.12**) and (**4.17**) were both sent to Dr Joongoo Lee of the Jewett group (Northwestern University, IL) for initial incorporation tests using their PURExpress cell-free system.<sup>39,40</sup> In summary of their work, **4.12** exhibited poor charging efficiency which was attributed to poor solubility of the DNB ester group. However, **4.17** did successfully couple to the 3'-end of two flexizymes: fMet(CAU) tRNA and Pro1E2(GGU) tRNA. These charged flexizymes were then both added to the PURExpression system and the subsequent product peptides were isolated and characterized by MALDI-ToF (Figure 4.9). While the ACM containing peptides did not appear to be the major products, ACM containing peptides were seen for both C-terminal and N-terminal incorporation sequences.

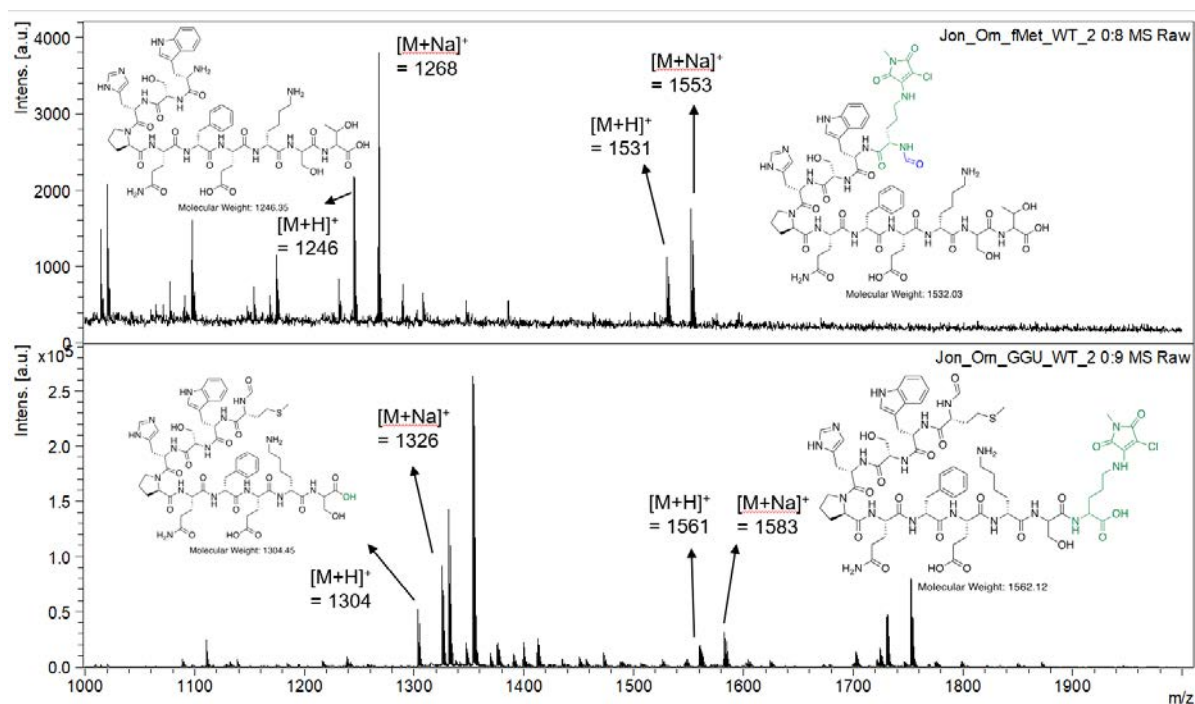


**Figure 4.9:** MALDI-ToF spectra of purified peptides obtained by PURExpression with amino acid **4.17** charged (top) fMet(CAU) tRNA and (bottom) Pro1E2(GGU) tRNA (recorded by Dr Joongoo Lee, Northwestern).

## 3.4 Conclusions

In conclusion, the synthesis of four new unnatural amino acids has been realized. The fluorescence of these has been confirmed in both water and dioxane, and while water quenching effects were strong these were expected and potentially beneficial for some applications, for example the monitoring of denaturing or protein-protein interactions. Incorporation of a DNB activated modified amino acid into flexizyme based amino-acylation led to poor incorporation efficiencies, while an ABT activated amino has led to successful expression of an ACM amino acid in peptides at N-terminal and C-terminal residues.

## 3.5 Future work

As genetic expression of an ACM amino acid has been realized, using a flexizyme based tRNA charging technique, there are several research targets that could be investigated. Firstly, incorporation at buried residues should be targeted, where emission should be high due to prevention of quenching interactions with water. Likely candidates for replacement by an ACM amino acid are large buried aromatic residues, such as tyrosine and tryptophan. If the tertiary structure of the enzyme can be retained upon the incorporation of the ACM amino acid, along with enzyme activity, many applications could be realized. This will be particularly powerful as a result of the ACMs uniquely sensitive fluorescence emission to protic solvents. For example, as buried ACMs will be shielded from the solvent, they will be highly emissive while protein tertiary structure is retained, but upon denaturing and unfolding the ACM will be exposed to water and be quenched. Therefore, enzyme integrity will be directly relatable to fluorescence emission and in addition, fluorescence lifetime may be even more informative of enzyme configuration as small changes in nearby residues may impart changes to fluorescence lifetime. An example buried residue for mutation could be W28 in HLZ (Figure 4.10), which is completely solvent inaccessible and an enzyme of familiarity to the group. More complex applications can also be envisioned, such as incorporating the dye near to the active site of an enzyme to visualize docking of substrates or inhibitors. Through expulsion of water from the active site upon substrate binding, fluorescence intensity and lifetime will increase giving an enzyme activity or inhibition responsive fluorescence emission. Such a residue in HLZ could be W109 which is located on the opposite side of the pocket to the nucleophilic aspartic acid residue (Figure 4.10).



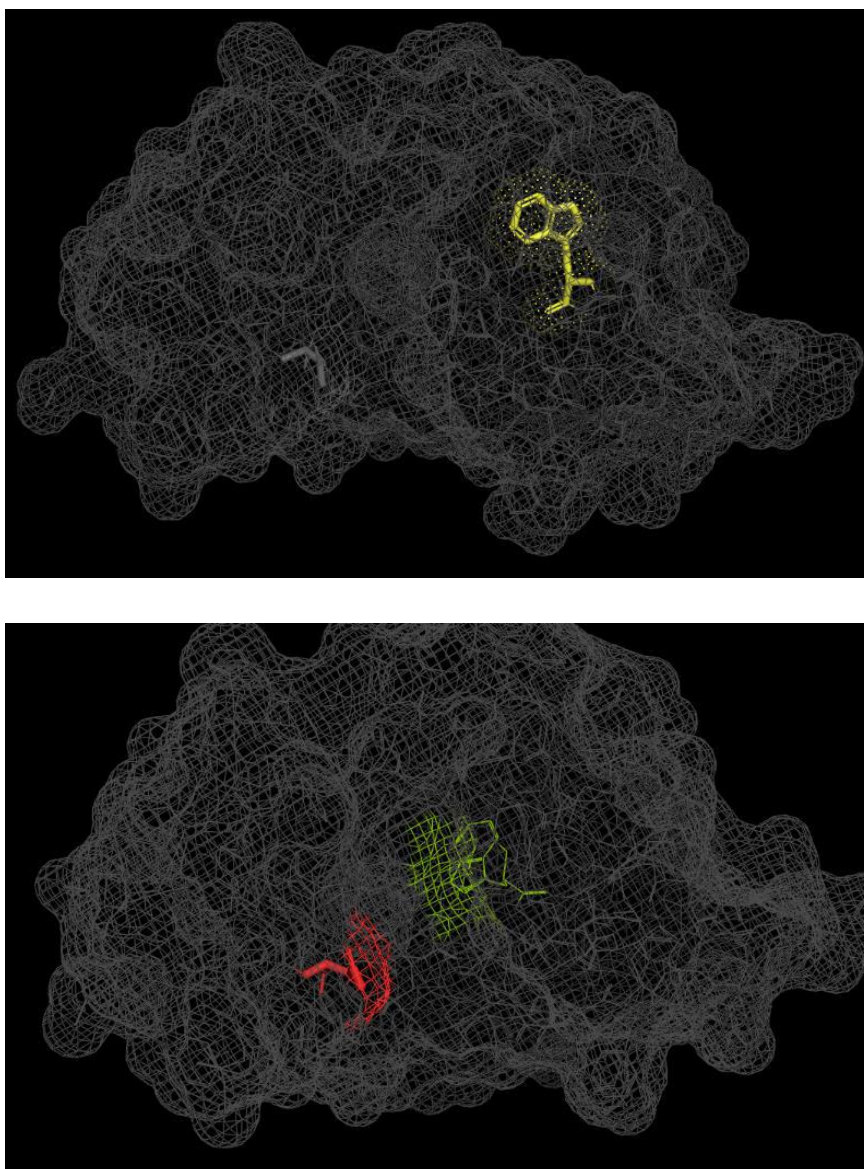


**Figure 4.10:** Location of W28 (yellow) and W109 (green) in HLZ, potential mutation targets for an ACM amino acid, with nearby active site for W109 (red). PDB structure: 1LZ1.<sup>41</sup>

## 3.6 Experimental

### 3.6.1 Materials and instrumentation

Amino acids were received from BACHEM or Iris Biotech. All other chemicals were obtained from either: Sigma Aldrich, Fisher Chemicals, Acros Chemicals, Carbosynth or Alfa Aesar and used as received.

NMR spectra were recorded on a Bruker Advance 300, a Bruker Advance III HD 400 or a Bruker Advance III HD 500 spectrometer at 300, 400 and 500 MHz respectively. Shifts are quoted in  $\delta$  in parts per million (ppm) and quoted relative to the solvent peak.

High Resolution Mass Spectra (HR-MS) were conducted by Dr Lijiang Song (University of Warwick) on a Bruker UHR-Q-ToF MaXis spectrometer with electrospray ionization, or By Dr Chi Tsang or Dr Christopher Williams (University of Birmingham) on a Waters Xevo G2-XS.

FTIR spectroscopy was carried out using an Agilent Technologies Cary 630 FTIR spectrometer. 16 Scans from 600 to 4000  $\text{cm}^{-1}$  were taken at a resolution of 4  $\text{cm}^{-1}$ , and the spectra were corrected for background absorbance.

UV-Vis spectroscopy was performed on Evolution 350 UV-Vis spectrophotometer equipped with Xenon Flash Lamp light source and Dual Matched Silicon Photodiode detectors.

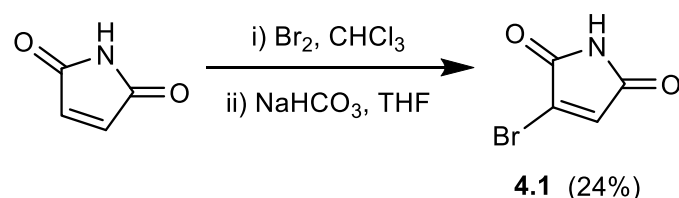
Fluorescence emission and excitation spectrum were obtained with an Edinburgh Instruments FS5 Spectrofluorometer in quartz 3.5 mL cuvettes for liquid samples (Starna Cell, Type: 3/Q/10), and analyzed in Fluoracle (Edinburgh Instruments) and Origin 2019 (Origin Labs).

Prep-HPLC was carried out on an Agilent 1260 infinity system on an ACE C18 150 x 21.1mm column using a water (0.03% formic acid): acetonitrile (0.03%

formic acid) gradient. Specific methods are given specifically in each molecules experimental method.

### 3.6.2 Small molecule synthesis

#### 3.6.2.1 3-bromo-1H-pyrrole-2,5-dione (4.1)



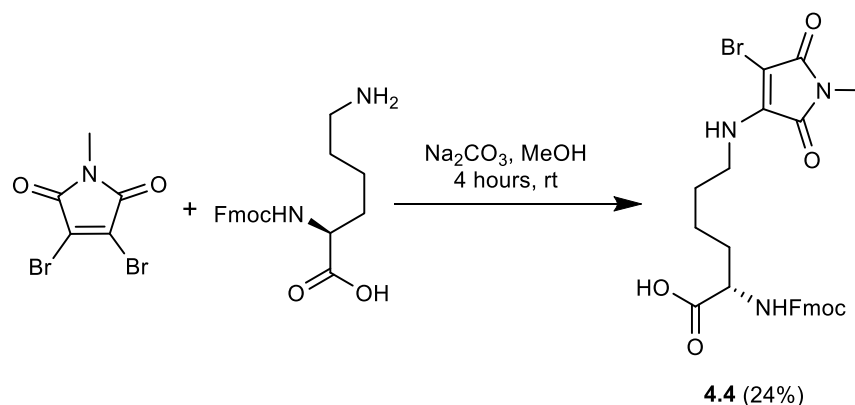
The synthesis was based on a previously reported literature procedure.<sup>31</sup> Maleimide (10 g, 0.102 mol) and bromine (20 g, 0.13 mol) were solubilized in chloroform (200 ml) and were refluxed for 1 hour. The solution was cooled to precipitate a product. The product was filtered and washed with very cold chloroform, to afford 16.4 g (40%) of 2,3-dibromosuccinimide. Subsequently, 12 g (0.046 mol) of 2,3-dibromosuccinimide was dissolved in THF, and to this NaHCO<sub>3</sub> (4.3 g, 0.051 mol) was added. The mixture was refluxed for 2 hours. Solvent was removed *in vacuo* and the product was re-dissolved in ethyl acetate (EtOAc) and this was washed with water and brine, and then dried over MgSO<sub>4</sub>. Solvent removal *in vacuo* afforded the product as a pale yellow solid (60%). R<sub>f</sub> (9:1 petroleum ether: EtOAc): 0.45.

<sup>1</sup>H NMR (DMSO-*d*<sub>6</sub>, 400 MHz, ppm):  $\delta$  = 11.28 (br, 1H, NH) 7.31 (s, 1H, CH);

MS (ESI) - [M+H]<sup>+</sup>: observed: 175.9 calculated: 175.9

Matches literature data.<sup>31</sup>

**3.6.2.2** *N*-(((9H-fluoren-9-yl)methoxy)carbonyl)-*N*-(4-bromo-1-methyl-2,5-dioxo-2,5-dihydro-1H-pyrrol-3-yl)-L-lysine (**4.4**)



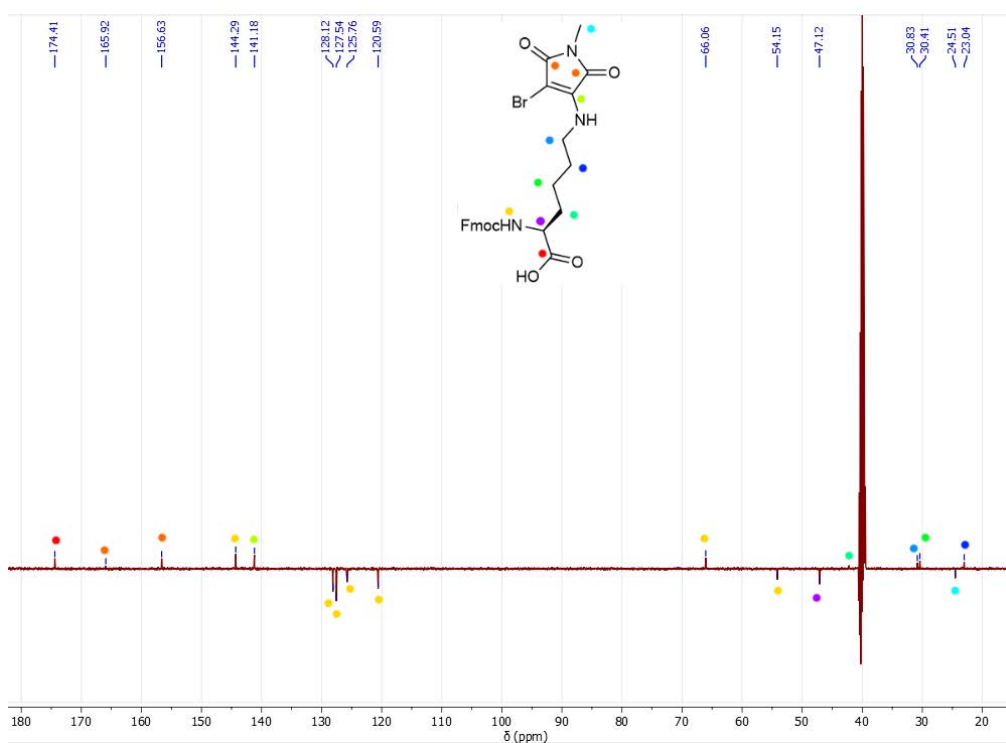
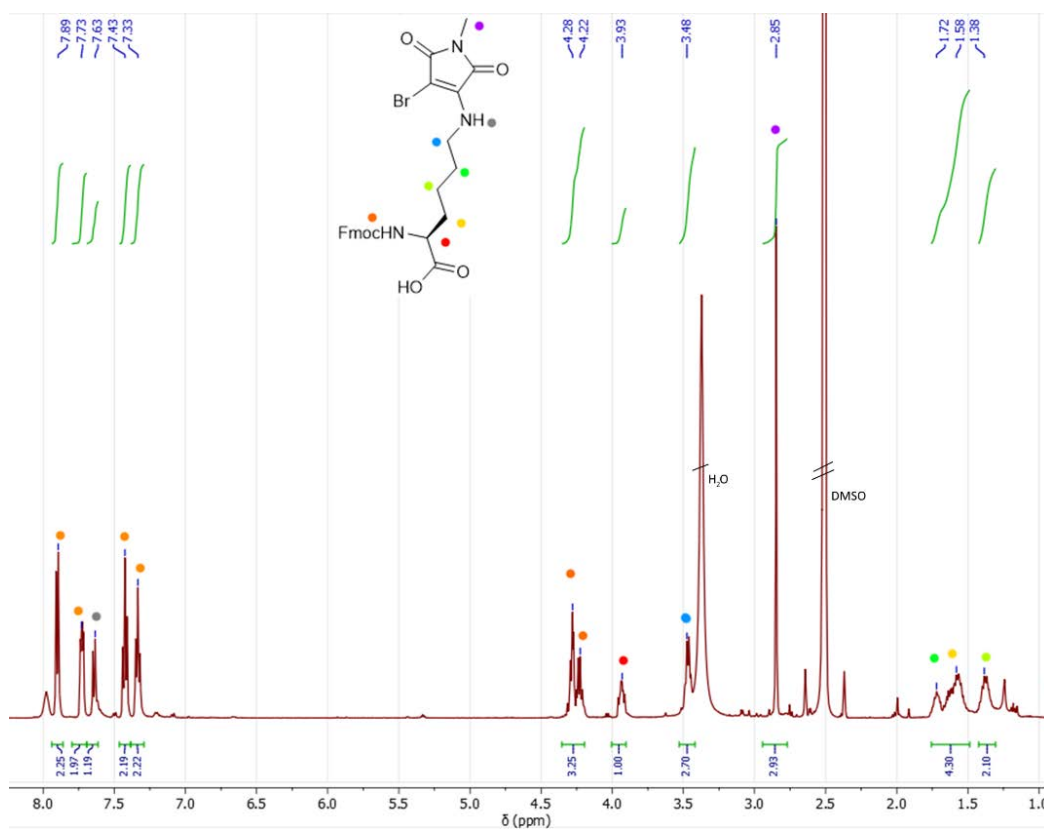
To a solution of dibromomaleimide (2 g, 7.4 mmol) in methanol (100 ml) was added Fmoc-lysine-OH (2.2 g, 6 mmol) and  $K_2CO_3$  (1.24 g, 9 mmol). The solution was stirred for 3 hours after which the solution was filtered to remove salts and the filtrate was evacuated *in vacuo*. The resultant solid was purified by silica column chromatography and eluted with a mixture of EtOAc: petroleum ether: acetic acid (10:10:1) ( $R_f$  = 0.20 – broad). The product was obtained as a yellow solid **4.4** (24%).

$^1H$  NMR (500 MHz,  $DMSO-d_6$ , ppm)  $\delta$  = 7.90 (d,  $^3J_{HH}$  = 7.5 Hz, 2H, ArH), 7.80 – 7.69 (m, 2H, ArH), 7.64 (d,  $^3J_{HH}$  = 8.0 Hz, 1H, NH), 7.43 (t,  $^3J_{HH}$  = 7.5 Hz, 2H, ArH), 7.33 (t,  $^3J_{HH}$  = 7.5 Hz, 2H, ArH), 4.35 – 4.19 (m, 3H, CH +  $CH_2$ ), 3.93 (dt,  $^3J_{HH}$  = 8.6, 4.8 Hz, 1H,  $CH_2$ ), 3.47 (t,  $^3J_{HH}$  = 7.2 Hz, 2H,  $CH_2$ ), 2.85 (s, 3H,  $CH_3$ ), 1.76 – 1.49 (m, 4H,  $CH_2$ ), 1.38 (m, 2H,  $CH_2$ ).

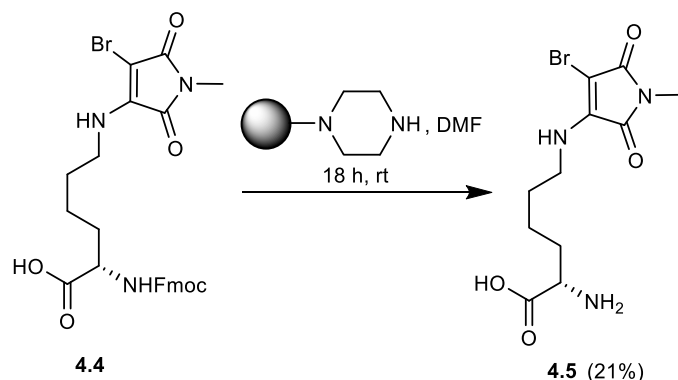
$^{13}C$  NMR (125 MHz,  $DMSO-d_6$ , ppm)  $\delta$  = 174.4 (CO), 166.0 (CO), 156.6 (CO), 144.3 (COON), 141.2 (CN), 128.1 (CAr), 127.5 (CAr), 125.7 (CAr), 120.9 (CAr), 66.1 (CH), 54.2 ( $CH_2$ ), 47.1 (CH), 42.3 ( $CH_2$ ), 30.8 ( $CH_2$ ), 30.8 ( $CH_2$ ), 24.5 ( $CH_3$ ), 23.0 ( $CH_2$ ).

HR-MS (MaXis):  $[M+H]^+$  calculated  $m/z$  555.1004 observed  $m/z$  – 555.0083;

FTIR ( $cm^{-1}$ ): 3320 ( $\nu_{O-H}$ ), 2900 ( $\nu_{C-H}$ ), 1704 ( $\nu_{C=O}$ ), 1643 ( $\nu_{C=O}$ ).



### 3.6.2.3 *N*-(4-bromo-1-methyl-2,5-dioxo-2,5-dihydro-1H-pyrrol-3-yl)-L-lysine (**4.5**)



Piperazine functionalized polystyrene resin (3.5 g, 3.5 mmol) was swollen with DMF (5 ml) in an end-capped syringe. ABM-Fmoc-Lysine **4.4** (300 mg, 0.5 mmol) was dissolved in DMF (5 mL) and added to the syringe. The vessel was stirred overnight. The resin was then washed with DMF and water to collect product. The solvent was removed *in vacuo* to produce a yellow solid, which was isolated by prep-HPLC to give a yellow solid **4.5** (52 mg isolated). The eluent used was a gradient of acetonitrile in water, see HPLC chromatogram (Figure 4.17) for exact composition.

$^1\text{H}$  NMR (300 MHz,  $\text{D}_2\text{O}$ , ppm)  $\delta$  = 3.65 (t,  $^3J_{\text{HH}}$  = 6.2 Hz, 1H, CH), 3.57 (t,  $^3J_{\text{HH}}$  = 7.0 Hz, 2H,  $\text{CH}_2$ ), 2.87 (s, 3H,  $\text{CH}_3$ ), 1.82 (dd,  $^3J_{\text{HH}}$  = 10.4, 5.7 Hz, 2H,  $\text{CH}_2$ ), 1.72 – 1.57 (m, 2H,  $\text{CH}_2$ ), 1.46 – 1.28 (m, 2H,  $\text{CH}_2$ ).

$^{13}\text{C}$  NMR (101 MHz,  $\text{D}_2\text{O}$ , ppm)  $\delta$  = 174.7 (CO), 171.4 (CO), 166.8 (CO), 145.1 (CN), 54.6 ( $\text{CH}_2$ ), 41.9 (CH), 26.3 ( $\text{CH}_2$ ), 23.8 ( $\text{CH}_2$ ), 21.4 ( $\text{CH}_3$ ).

HR-MS (Xevo):  $[\text{M}+\text{H}]^+$  calculated  $m/z$  262.0595 observed  $m/z$  262.0602;

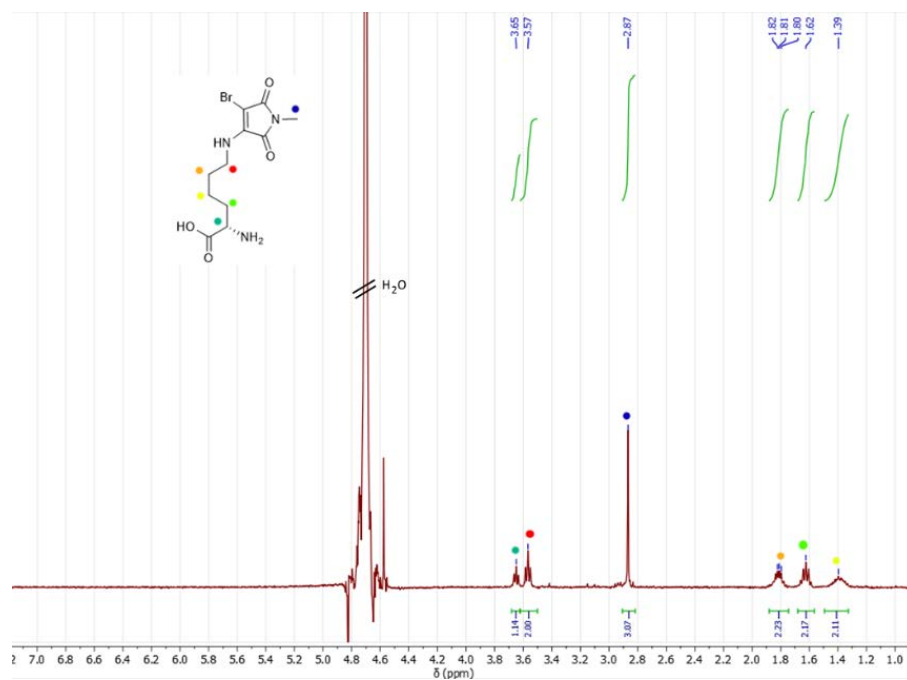


**Figure 4.13:**  $^1\text{H}$  NMR spectrum of **4.5** (400 MHz,  $\text{D}_2\text{O}$ ).

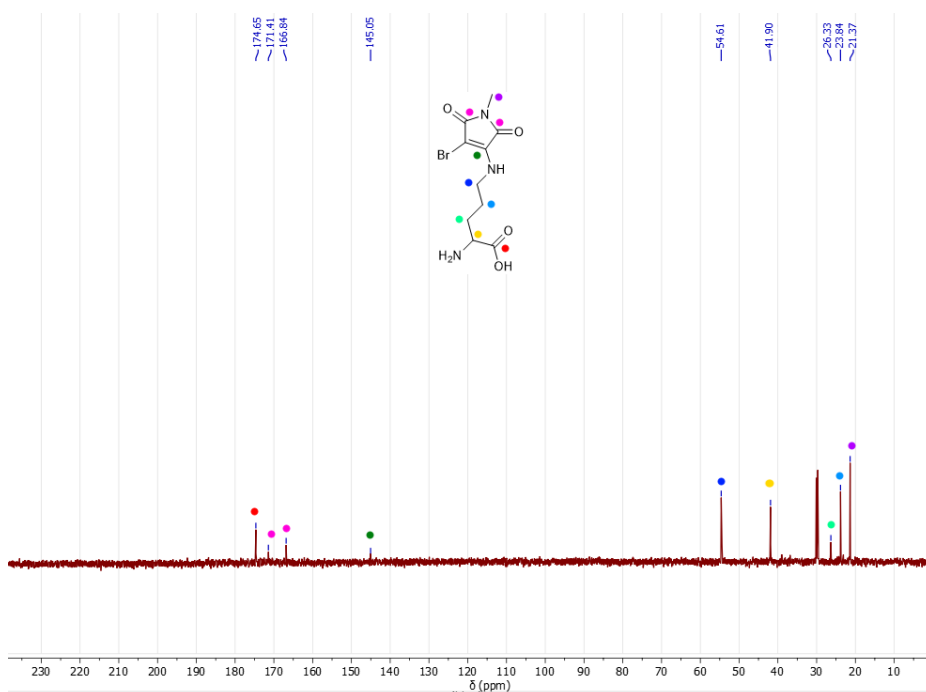


**Figure 4.14:**  $^{13}\text{C}$  NMR spectrum of **4.5** (101 MHz,  $\text{D}_2\text{O}$ ).

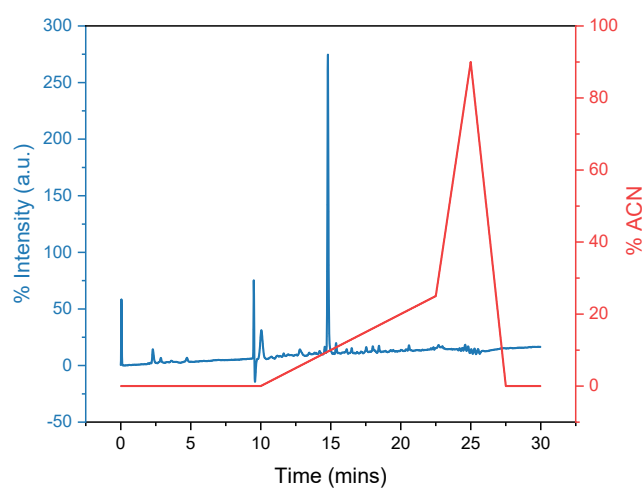


**Figure 4.15:** HPLC chromatogram of prep-HPLC run (blue = 375 nm detector, red = acetonitrile% in water).

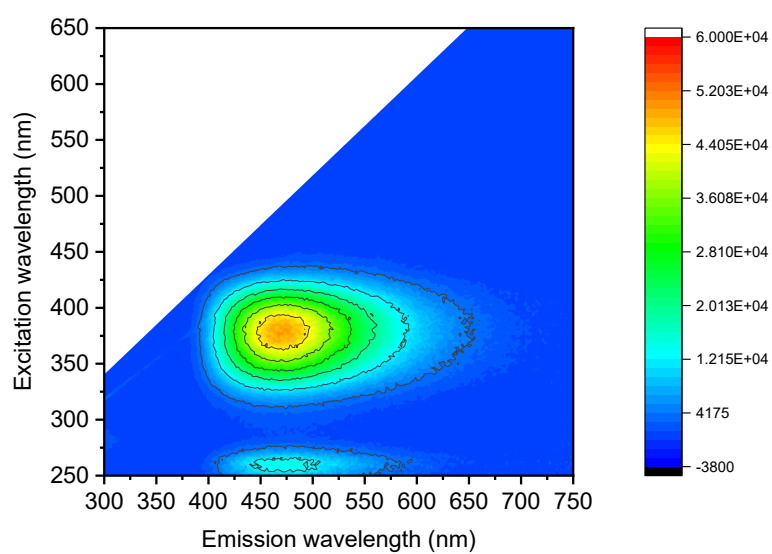


**Figure 4.16:** Fluorescence excitation and emission map of **4.5** in dioxane (5  $\mu$ M).



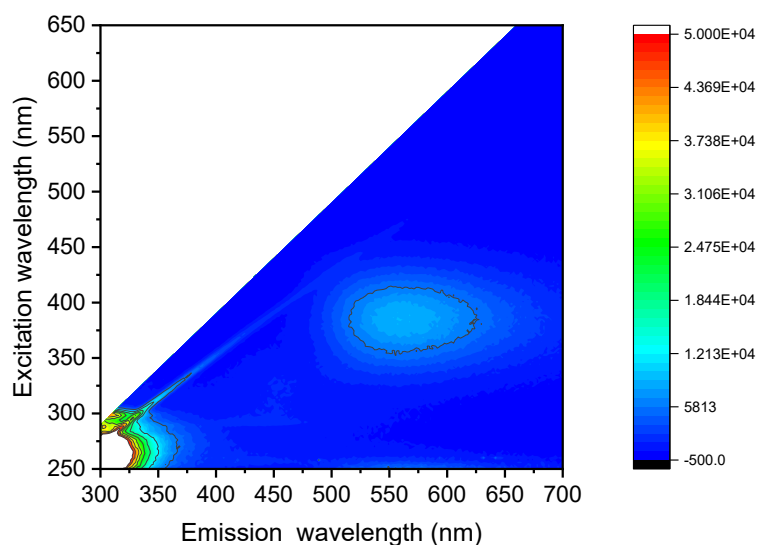
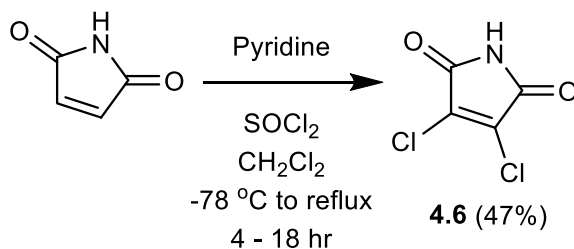


**Figure 4.17:** Fluorescence excitation and emission map of **4.5** in water (2.5  $\mu\text{M}$ ).

#### 3.6.2.4 3,4-dichloro-1H-pyrrole-2,5-dione (4.6)



The synthesis was developed from a previously reported protocol.<sup>36</sup> Initially, maleimide (15 g, 0.15 mol) was added to a 500 mL round bottom flask, which contained 100 mL of freshly distilled thionyl chloride and a magnetic stirrer bar. This solution was put onto a dry ice/acetone bath to cool. To this a solution of pyridine in dichloromethane (2.7 M pyridine in 50 mL  $\text{CH}_2\text{Cl}_2$ ) was added dropwise over 30 mins. This was left for another hour on the dry ice bath and left to warm to room temperature over 4 hours. The solution was then refluxed at  $78^\circ\text{C}$  overnight. After being left to cool, volatiles were removed *in vacuo*. The solid mixture was then washed with ethyl acetate and brine three times. The ethyl

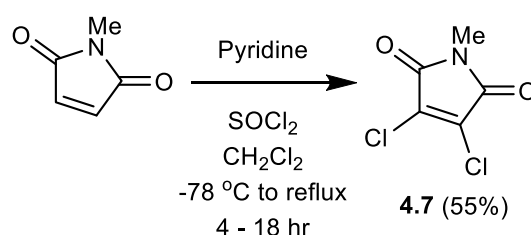
acetate layer was collected and dried *in vacuo*. This solid was recrystallized in hot toluene to produce clear lime colored crystals of **4.6** (9.81 g, 40 %).

$^{13}\text{C}$  NMR ( $\text{CDCl}_3$ , 101 MHz, ppm)  $\delta$  = 162.09 (CO), 134.15 (CCI).

HR-MS (Xevo) -  $[\text{M}+\text{H}^+]$  – calculated m/z 165.9463 observed m/z 165.9470;

Matches literature data.<sup>36</sup>

### 3.6.2.5 3,4-dichloro-1-methyl-pyrrole-2,5-dione (4.7)



The synthesis was developed from a previously reported protocol.<sup>36</sup> Initially, Methyl maleimide (7 g, 63 mmol) was added to a 250 mL round bottom flask, which contained 100 mL of freshly distilled thionyl chloride and a magnetic stirrer bar. This solution was put onto a dry ice/acetone bath to cool. To this a solution of pyridine in dichloromethane (2.7 M pyridine in 50 mL  $\text{CH}_2\text{Cl}_2$ ) was added dropwise over 30 mins. This was left for another hour on the dry ice bath and left to warm to room temperature over 4 hours. The solution was then refluxed at  $78\text{ }^\circ\text{C}$  overnight. After being left to cool, volatiles were removed *in vacuo*. The solid mixture was then purified by silica column chromatography with a diethyl ether: petroleum ether (1:3) eluent. The fractions containing product were combined and dried slowly *in vacuo*, to produce a clear crystals of **4.7** (6.03 g, 55%).

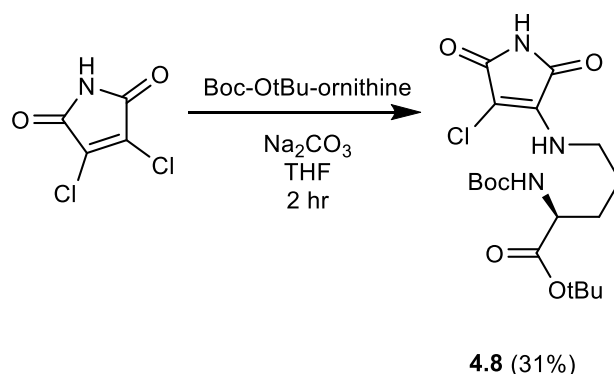
$^1\text{H}$  NMR (300 MHz,  $\text{CDCl}_3$ , ppm)  $\delta$  = 3.16 (s, 3H, Me).

$^{13}\text{C}$  NMR (101 MHz,  $\text{CDCl}_3$ , ppm)  $\delta$  = 163.08 (CO), 133.36 (CCI), 25.09 ( $\text{CH}_3$ ).

HR-MS (Xevo) -  $[\text{M}+\text{H}^+]$  – calculated m/z 179.9619 observed m/z 179.9618;

Matches literature data.<sup>36</sup>

**3.6.2.6** tert-butyl-(R)-2-((tert-butoxycarbonyl)amino)-5-((4-chloro-2,5-dioxo-2,5-dihydro-1H-pyrrol-3-yl)amino)pentanoate (**4.8**)



Firstly, DCM **4.6** (8.6 mmol, 1.45 g) was dissolved into 40 mL of THF. To this  $\text{Na}_2\text{CO}_3$  (17 mmol, 1.8 g) was added. A solution of *O*<sup>*t*</sup>*Bu*-*N*-Boc-ornithine (2.5 g, 8.6 mmol) in 25 mL of THF was added to a dropping funnel. Over 10 minutes this was added dropwise to the stirred solution of base and  $\text{CH}_2\text{Cl}_2$ . This was left for another 90 minutes, after which it was filtered to remove base and the residual THF was washed with brine three times and dried *in vacuo*. The crude solid was purified by silica column chromatography with a 10-20% ethyl acetate eluent in hexane, to elute the yellow product. This was dried *in vacuo* to afford yellow solid **4.8** (1.09 g, 31%).

$^1\text{H}$  NMR (400 MHz,  $\text{CDCl}_3$ , ppm)  $\delta$  = 7.23 (br, 1H), 5.50 (br, 1H), 5.09 (br d,  $^3J_{\text{HH}}$  = 7.9 Hz, 1H), 4.14 (m, 2H), 3.58 (q,  $^3J_{\text{HH}}$  = 4.1 Hz, 2H), 1.89 – 1.60 (m, 4H), 1.40 s, 6H), 1.38 (s, 6H). Spectrum peaks are broader and poorly resolved than expected attributed to partial aggregation in the NMR solvent.

$^{13}\text{C}$  NMR (101 MHz,  $\text{DMSO}-d_6$ , ppm)  $\delta$  = 171.62 (CO), 168.19 (CO), 166.00 (CO), 161.83 (CO), 155.46 (CO), 141.67 (CN), 80.17 ( $\text{CMe}_3$ ), 77.99 ( $\text{CMe}_3$ ), 54.07 ( $\text{CH}_2$ ), 41.51 ( $\text{CH}_2$ ), 28.14 ( $\text{CH}_3$ ), 27.64 ( $\text{CH}_2$ ), 27.57 ( $\text{CH}_3$ ), 26.93 ( $\text{CH}_2$ ).

HR-MS (Xevo) -  $[\text{M}+\text{H}^+]$  –calculated  $m/z$  398.1095 observed  $m/z$  398.1094;

FTIR ( $\text{cm}^{-1}$ ): 2929 ( $\nu_{\text{C-H}}$ ), 1772 ( $\nu_{\text{C=O}}$ ), 1708( $\nu_{\text{C=O}}$ ), 1667 ( $\nu_{\text{C=O}}$ ), 1649 ( $\nu_{\text{C=O}}$ ).

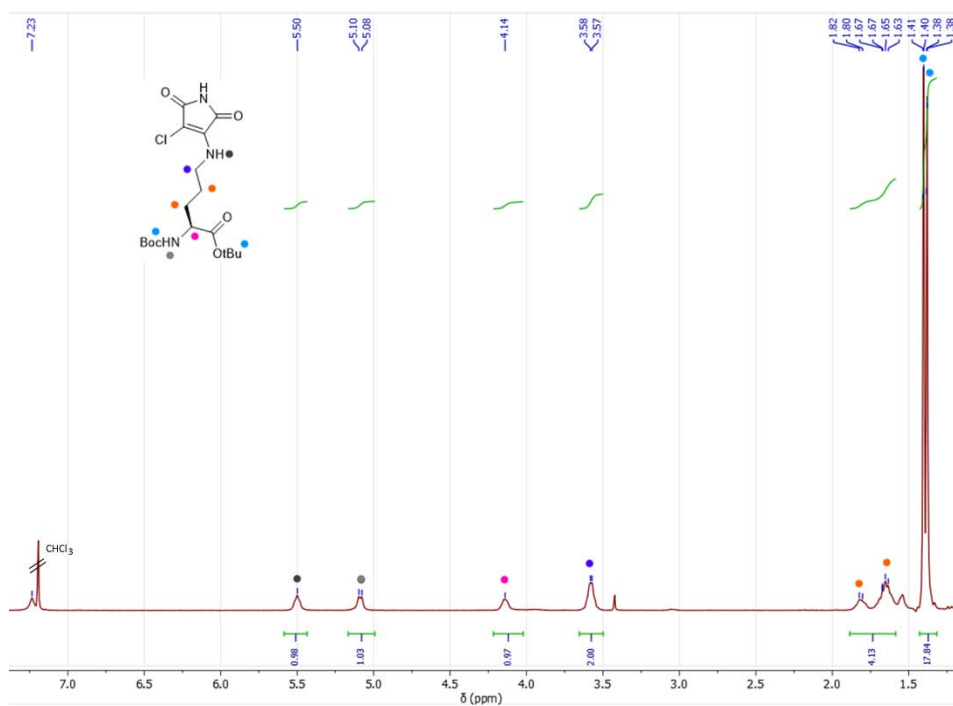


**Figure 4.18:** <sup>1</sup>H NMR spectrum of **4.8** (400 MHz, CDCl<sub>3</sub>).

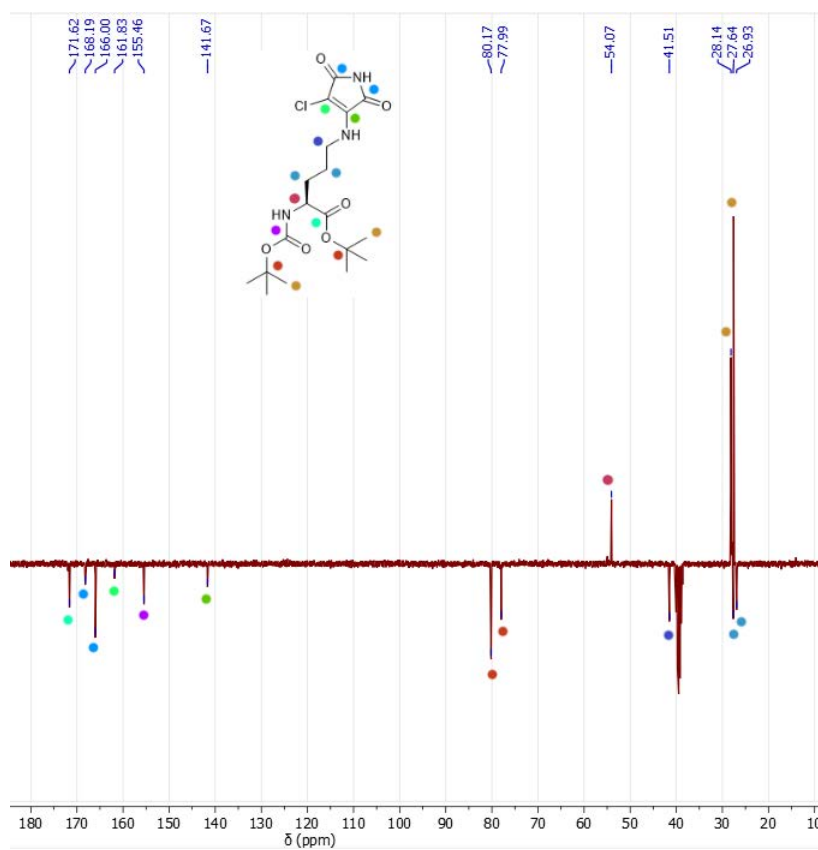
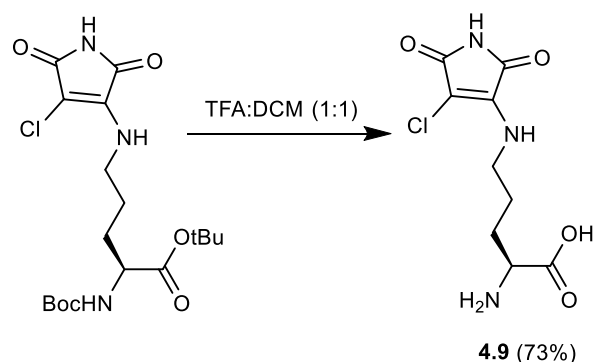


**Figure 4.19:** <sup>13</sup>C NMR spectrum of **4.8** (101 MHz, DMSO-*d*<sub>6</sub>).

**3.6.2.7** tert-butyl-(R)-2-((tert-butoxycarbonyl)amino)-5-((4-chloro-2,5-dioxo-2,5-dihydro-1H-pyrrol-3-yl)amino)pentanoate (**4.9**)



ACM-*N*-Boc-Ornithine (**4.8**, 150 mg, 0.35 mmol) was added to a round bottom flask with 9 mL CH<sub>2</sub>Cl<sub>2</sub>. To this 1 mL of trifluoroacetic acid (TFA) was added. This was stirred with a magnetic stirrer for 24 hours. After which the solution was washed with water and the aqueous layer was separated and dried *in vacuo* to yield yellow solid **4.9** (10 mg, 73%).

<sup>1</sup>H NMR (400 MHz, D<sub>2</sub>O, ppm) δ = 4.00 (t, <sup>3</sup>J<sub>HH</sub> = 6.1 Hz, 1H), 3.01 – 2.83 (t, <sup>3</sup>J<sub>HH</sub> = 6.2 Hz, 3H), 2.03 – 1.52 (m, 4H).

<sup>13</sup>C NMR (101 MHz, D<sub>2</sub>O, ppm) δ = 174.33 (CO), 171.53 (CO), 166.89 (CO), 142.59 (CN), 54.41 (CH<sub>2</sub>), 41.56 (CH), 27.35 (CH<sub>2</sub>), 25.92 (CH<sub>2</sub>).

FTIR (cm<sup>-1</sup>): 2933 (ν<sub>C-H</sub>), 1768 (ν<sub>C=O</sub>), 1716 (ν<sub>C=O</sub>), 1656 (ν<sub>C=O</sub>).

HR-MS (Xevo) - [M+H<sup>+</sup>] – calculated m/z 262.0595, observed m/z 262.0594;

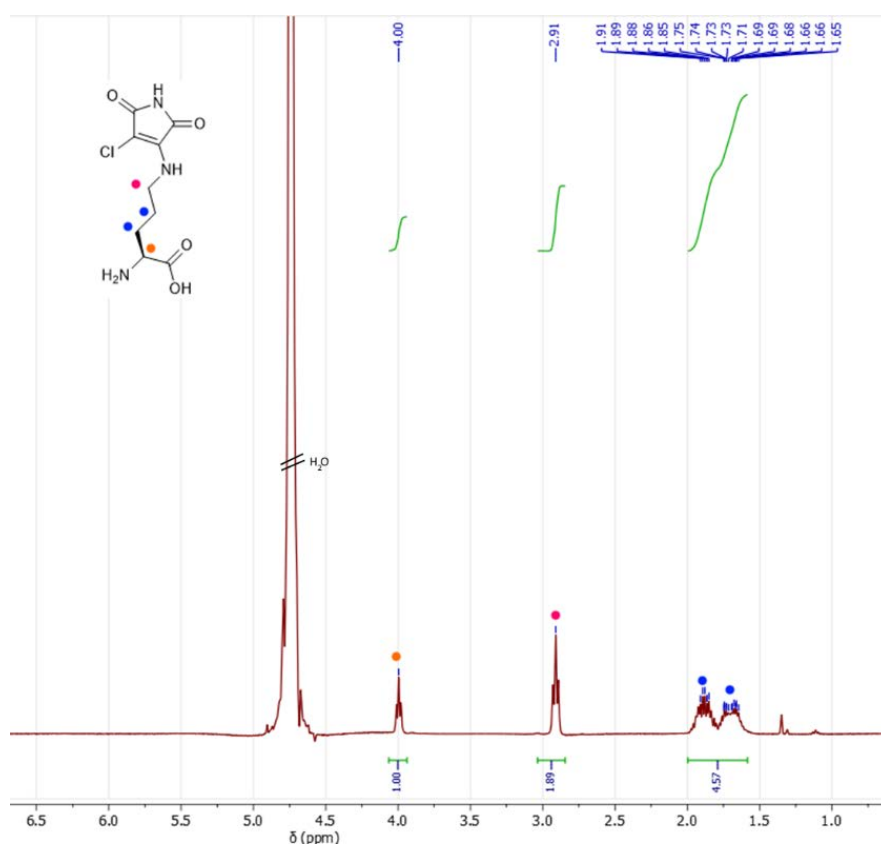


**Figure 4.20:**  $^1\text{H}$  NMR spectrum of **4.9** (400 MHz,  $\text{D}_2\text{O}$ ).

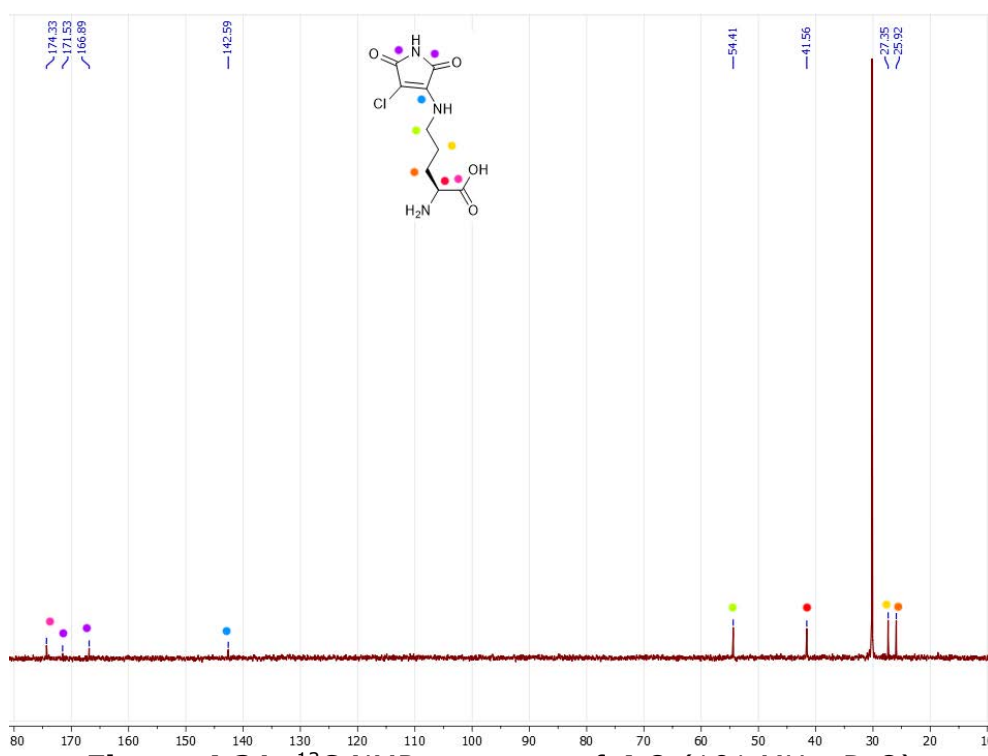


**Figure 4.21:**  $^{13}\text{C}$  NMR spectrum of **4.9** (101 MHz,  $\text{D}_2\text{O}$ ).

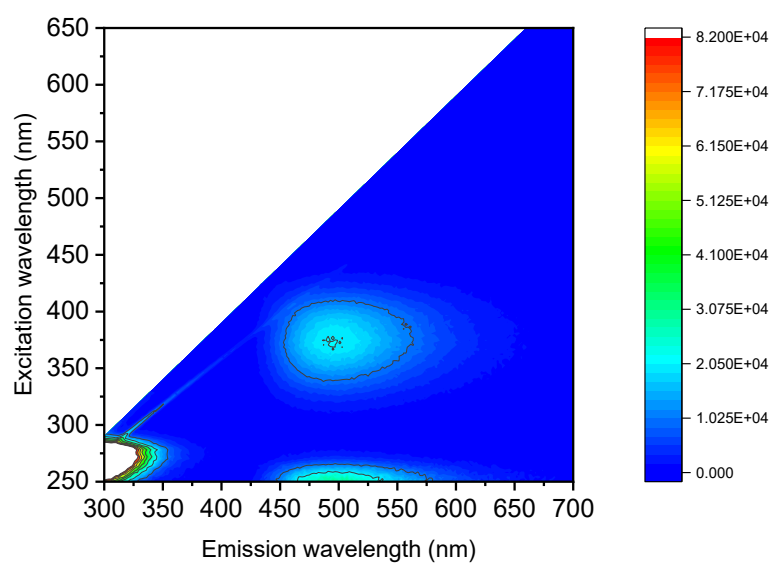


**Figure 4.22:** Fluorescence excitation and emission map of **4.9** in dioxane (1  $\mu$ M).

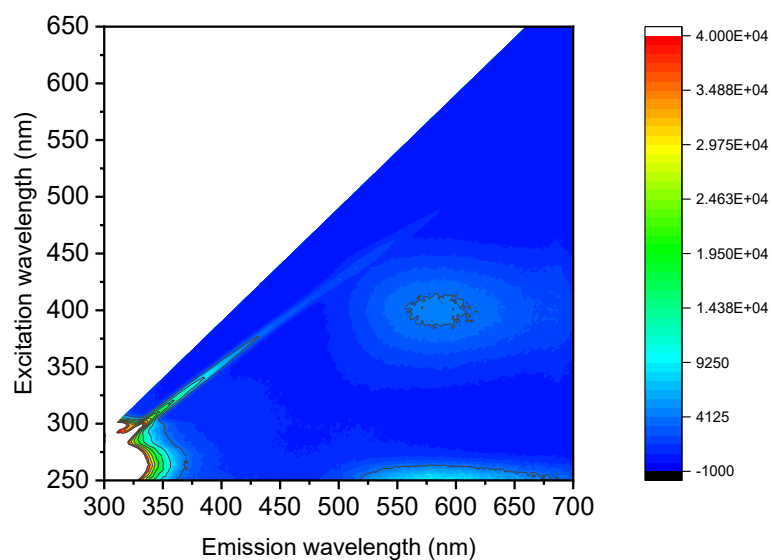
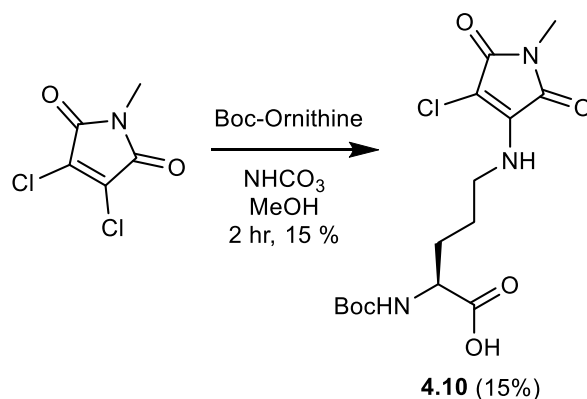


**Figure 4.23:** Fluorescence excitation and emission map of **4.9** in water (10  $\mu$ M).

**3.6.2.8** 3,5-dinitrobenzyl 2-amino-5-((4-chloro-1-methyl-2,5-dioxo-2,5-dihydro-1H-pyrrol-3-yl)amino)pentanoate (4.10)



Firstly, DCM **4.7** (23 mmol, 8 g) was dissolved into 100 mL of methanol. To this  $\text{NaHCO}_3$  (34 mmol, 2.85 g) was added. A solution of *O*-Boc-Ornithine (4.13 g, 23 mmol) in 50 mL of methanol was added to a dropping funnel. Over 10 minutes this was added dropwise to the stirred solution of base and ACM. This was left for another 90 minutes, after which it was filtered to remove base and dried *in vacuo*. The crude solid was purified by silica column chromatography with an ethyl acetate eluent to elute side products followed by ethyl acetate with 1 % MeOH/acetic acid added to elute the yellow product. This was dried *in vacuo* to afford yellow solid **4.10** (1.11 g, 15%).

$^1\text{H}$  NMR (300 MHz,  $\text{DMSO}-d_6$ , ppm)  $\delta$  = 7.96 (t,  $^3J_{\text{HH}}$  = 5.5 Hz, 1H), 7.15 (d,  $^3J_{\text{HH}}$  = 8.0 Hz, 1H), 3.93 (m, 1H), 3.52 (m, 2H), 2.91 (s, 3H), 1.81 – 1.56 (m, 4H), 1.44 (s, 9H).

$^{13}\text{C}$  NMR (101 MHz,  $\text{DMSO}-d_6$ , ppm)  $\delta$  = 174.5 (CO), 168.0 (CO), 165.5 (CO), 156.0 (COO), 142.2 (CN), 78.5 (CCH<sub>3</sub>), 53.7 (CH), 42.2 (CH<sub>2</sub>), 28.7 (CCH<sub>3</sub>), 28.2 (CH<sub>2</sub>), 27.6 (CH<sub>2</sub>), 24.3 (CH<sub>3</sub>)

HR-MS (Xevo) -  $[\text{M}+\text{Na}^+]$  – calculated  $m/z$  398.1095 observed  $m/z$  398.1094;

FTIR ( $\text{cm}^{-1}$ ) - 3379 ( $\nu_{\text{O-H}}$ ), 2929 ( $\nu_{\text{C-H}}$ ), 1742 ( $\nu_{\text{C=O}}$ ), 1705 ( $\nu_{\text{C=O}}$ ), 1653 ( $\nu_{\text{C=O}}$ ).



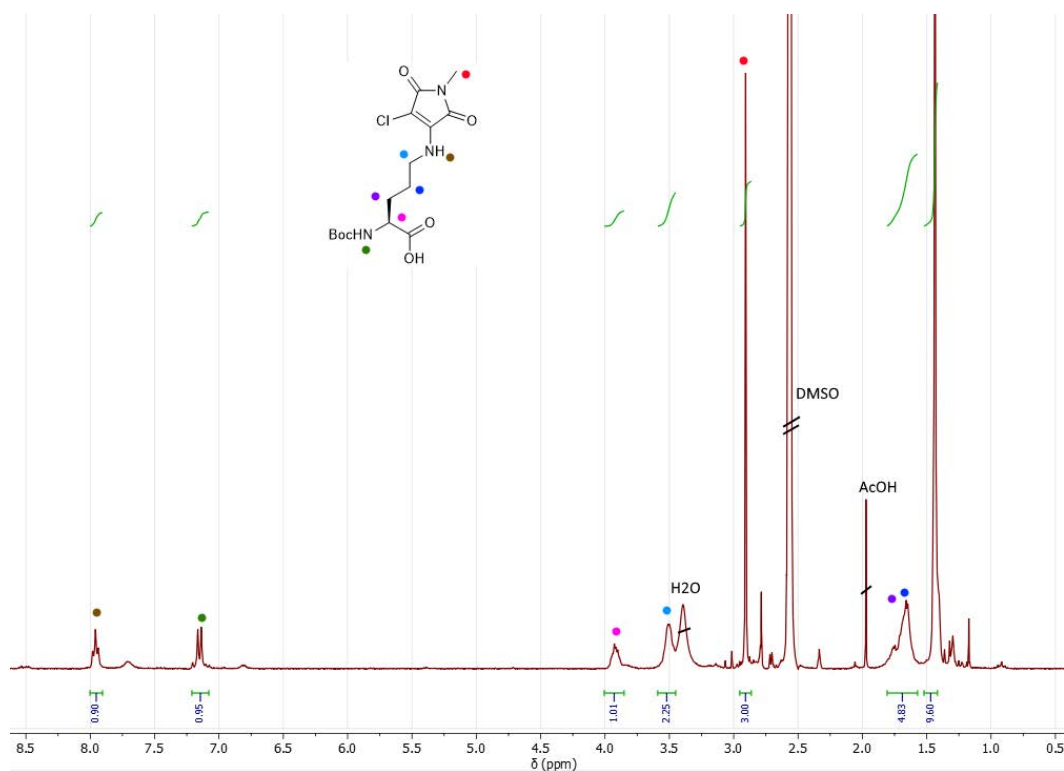


**Figure 4.24:** <sup>1</sup>H NMR spectrum of **4.10** (300 MHz, DMSO-*d*<sub>6</sub>).

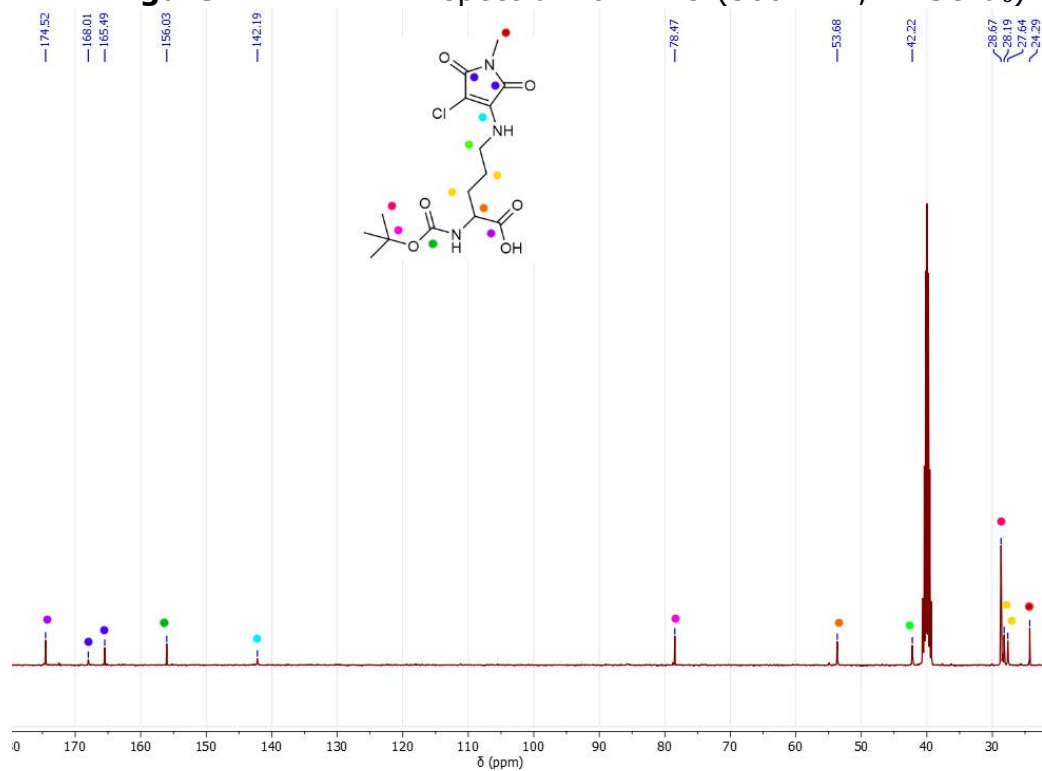
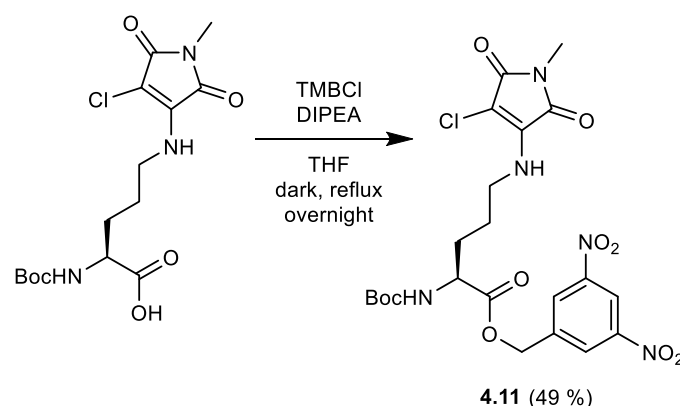


**Figure 4.25:** <sup>13</sup>C NMR spectrum of **4.10** (300 MHz, DMSO-*d*<sub>6</sub>).

**3.6.2.9** 3,5-dinitrobenzyl 2-((tert-butoxycarbonyl)-amino)-5-((4-chloro-1-methyl-2,5-dioxo-2,5-dihydro-1H-pyrrol-3-yl)amino)pentanoate (4.11)



Firstly, the modified amino acid **4.10** (2.6 mmol, 1 g) was dissolved into 20 mL of acetonitrile. This was kept in the dark and to it diisopropylethylamine (5.2 mmol, 0.67 g) was added. The reaction mixture was stirred and to this dinitrobenzyl chloride (5.2 mmol, 1.3 g). This was heated at reflux for 18 hours after which it was concentrated *in vacuo*. The crude solid was purified by silica column chromatography with an ethyl acetate/petroleum ether gradient eluent (10% ethyl acetate to 50% ethyl acetate). This was dried *in vacuo* to afford yellow solid **4.11** (706 mg, 49%).

$^1\text{H}$  NMR (300 MHz,  $\text{CDCl}_3$ , ppm)  $\delta$  = 9.03 (t,  $^3J_{\text{HH}}$  = 2.1 Hz, 1H), 8.56 (d,  $^3J_{\text{HH}}$  = 2.1 Hz, 2H), 5.38 (m, 3H), 5.02 (br d,  $^3J_{\text{HH}}$  = 8.2 Hz, 1H), 4.40 (m, 1H), 3.64 (m, 2H), 3.00 (s, 3H), 1.97 (s, 1H), 1.78 (m, 2H), 1.43 (s, 9H).

$^{13}\text{C}$  NMR (101 MHz,  $\text{CDCl}_3$ , ppm)  $\delta$  = 172.0 (CO), 167.7 (CO), 165.6 (CO), 155.4 (COO), 148.7 (CAr), 140.3 (CAr), 139.7 (CN), 127.9 (CAr), 118.8 (CAr), 80.7 (CCH<sub>3</sub>), 64.7 (CH<sub>2</sub>), 53.0 (CH), 42.4 (CH<sub>2</sub>), 29.5 (CH<sub>2</sub>), 28.2 (CCH<sub>3</sub>), 27.0 (CH<sub>2</sub>), 24.3 (CH<sub>3</sub>)

HR-MS (Xevo) -  $[\text{M}+\text{H}^+]$  - calculated m/z 578.1266 observed m/z 578.1267;

FTIR ( $\text{cm}^{-1}$ ) - 2940 ( $\nu_{\text{C-H}}$ ), 1746 ( $\nu_{\text{C=O}}$ ), 1708 ( $\nu_{\text{C=O}}$ ), 1649 ( $\nu_{\text{C=O}}$ ), 1530 ( $\nu_{\text{N=O}}$ ),

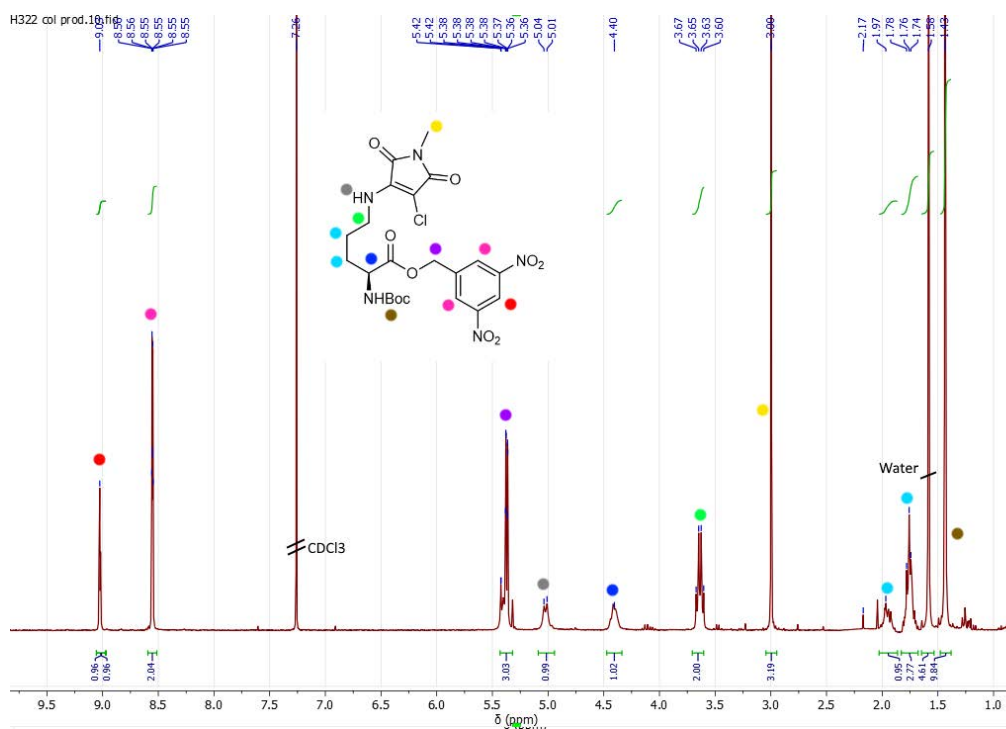


**Figure 4.26:**  $^1\text{H}$  NMR spectrum of **4.11** (300 MHz,  $\text{CDCl}_3$ ).

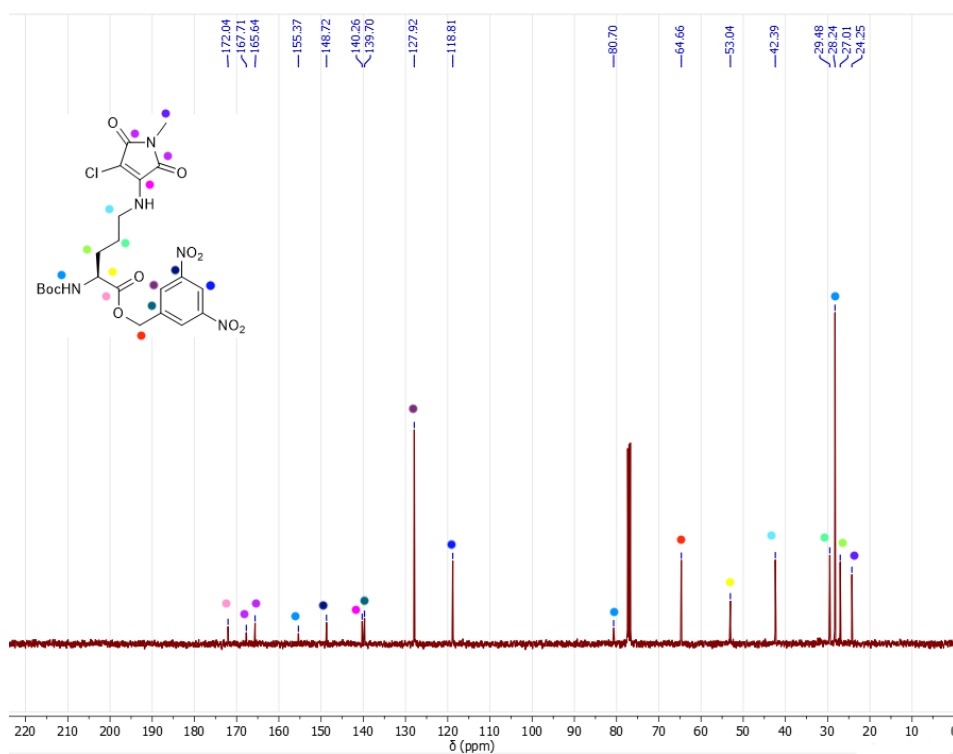
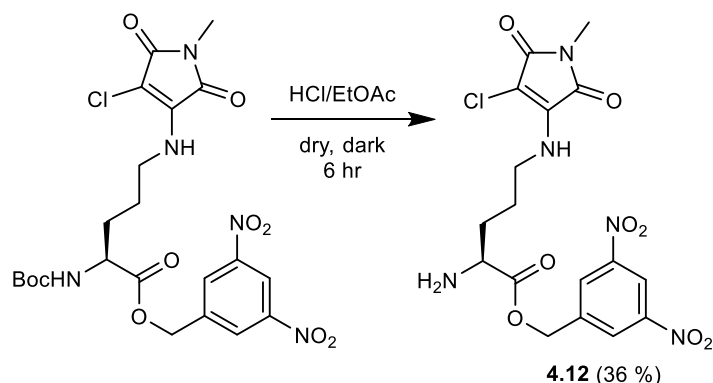


**Figure 4.27:**  $^{13}\text{C}$  NMR spectrum of **4.11** (101 MHz,  $\text{CDCl}_3$ ).

**3.6.2.10** 3,5-dinitrobenzyl 2-amino-5-((4-chloro-1-methyl-2,5-dioxo-2,5-dihydro-1H-pyrrol-3-yl)amino)pentanoate (**4.12**)



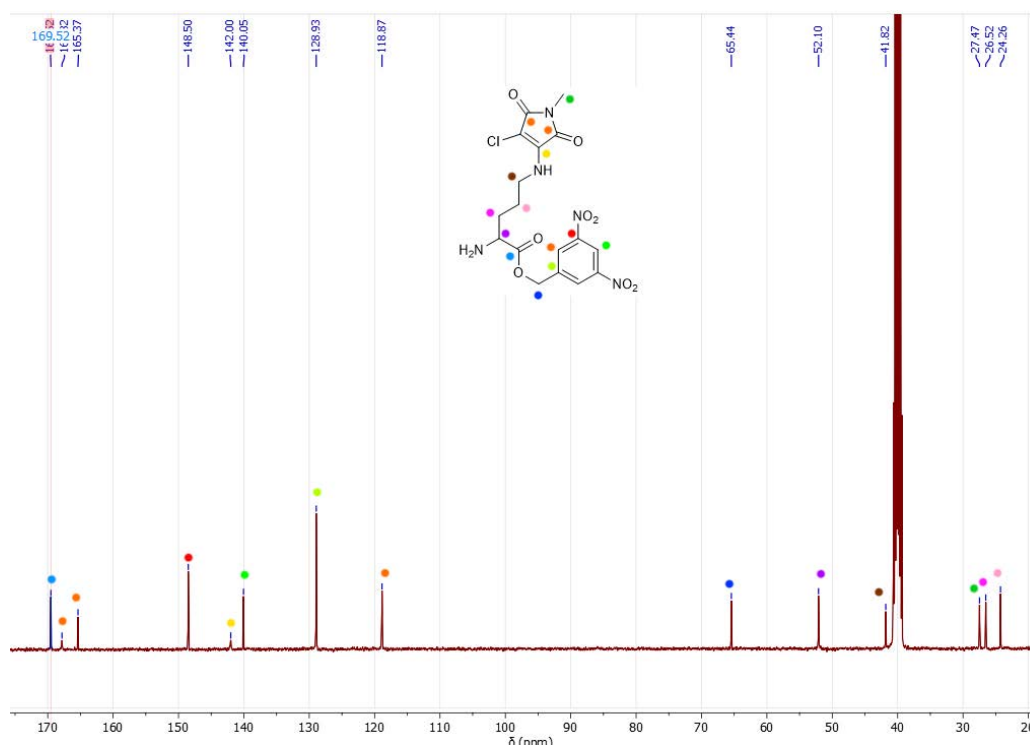
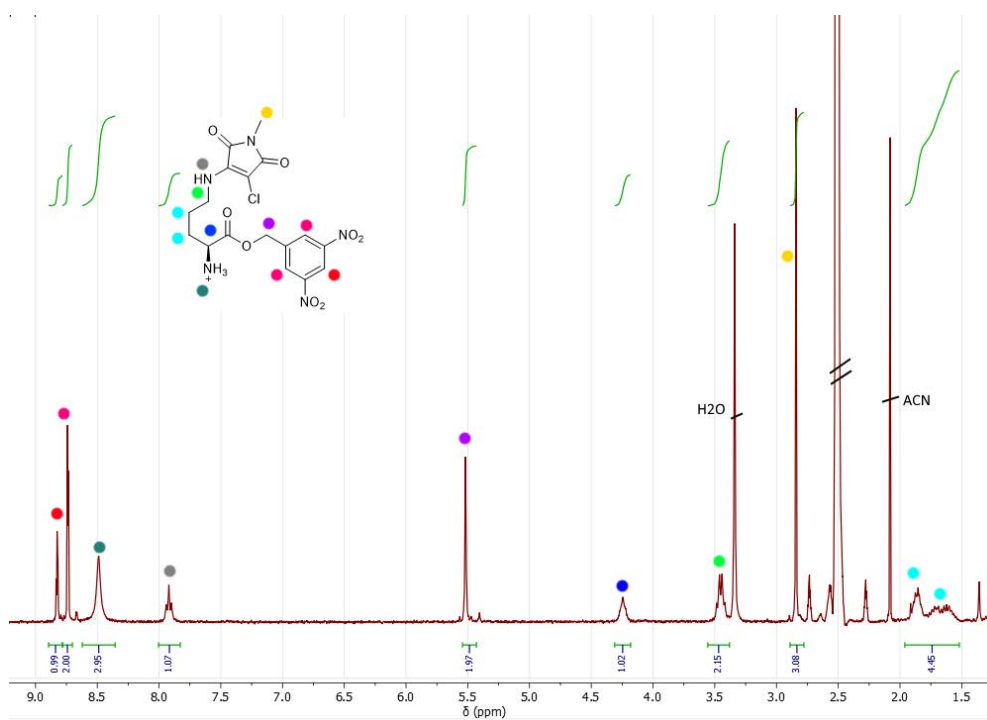
DNB-ACM-Boc-Orn (**4.11**, 300 mg, 0.54 mmol) was added to a dried round bottom flask containing 8 mL of 1M HCl in dry ethyl acetate and a magnetic stirrer. This was sealed and stirred overnight after which the volatiles were removed. This was dissolved into acetonitrile (10 mL) and precipitated with the addition of diethyl ether (100 mL). This was filtered and dried to yield a yellow solid **4.12** (90 mg, 36%).

$^1\text{H}$  NMR (300 MHz, DMSO- $d_6$ , ppm)  $\delta$  = 8.82 (t,  $^3J_{\text{HH}}$  = 2.1 Hz, 1 H), 8.74 (d,  $^3J_{\text{HH}}$  = 2.1 Hz, 2 H), 7.92 (t,  $^3J_{\text{HH}}$  = 6.6 Hz, 1 H), 5.52 (s, 2 H), 4.23 (t,  $^3J_{\text{HH}}$  = 6.2 Hz, 1 H), 3.45 (q,  $^3J_{\text{HH}}$  = 6.6 Hz, 2 H), 2.84 (s, 3 H), 1.96 – 1.50 (m, 5 H).

$^{13}\text{C}$  NMR (101 MHz, DMSO- $d_6$ , ppm)  $\delta$  = 169.52 (COO), 167.82 (CO), 165.37 (CO), 148.50 (CAr), 142.00 (CAr), 140.05 (CNH), 128.93 (CAr), 118.87 (CAr), 65.44 ( $\text{CH}_2$ ), 52.10 (CH), 41.82 ( $\text{CH}_2$ ), 27.47 ( $\text{CH}_2$ ), 26.52 ( $\text{CH}_2$ ), 24.26 ( $\text{CH}_3$ ).

HR-MS (Xevo) -  $[\text{M}+\text{H}^+]$  - calculated m/z 456.0922 observed m/z 456.0922

FTIR ( $\text{cm}^{-1}$ ) –3353 ( $\nu_{\text{N-H}}$ ), 2933 ( $\nu_{\text{C-H}}$ ), 1746 ( $\nu_{\text{C=O}}$ ), 1705 ( $\nu_{\text{C=O}}$ ), 1649 ( $\nu_{\text{C=O}}$ ), 1534 ( $\nu_{\text{N=O}}$ ),



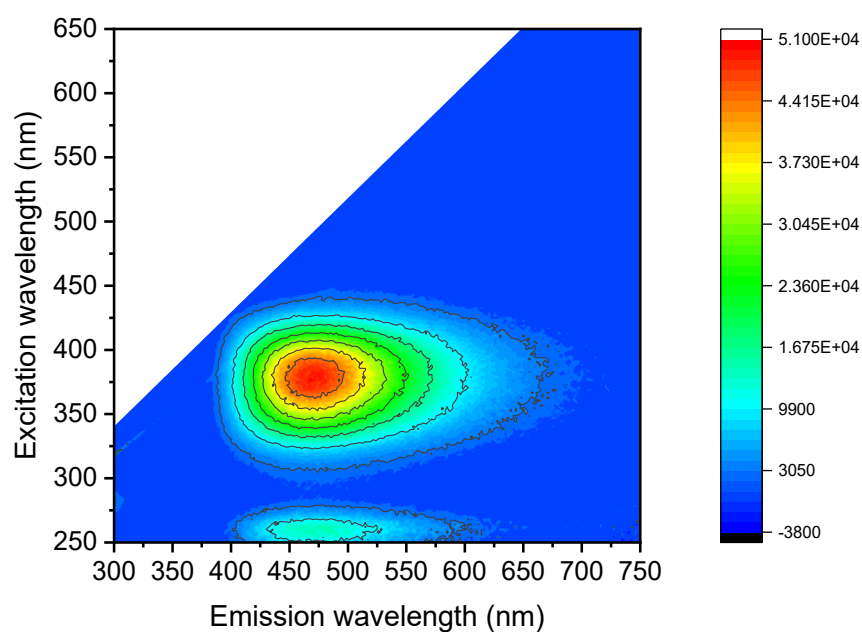


**Figure 4.30:** Fluorescence excitation and emission map of **4.12** in dioxane (5 μM).

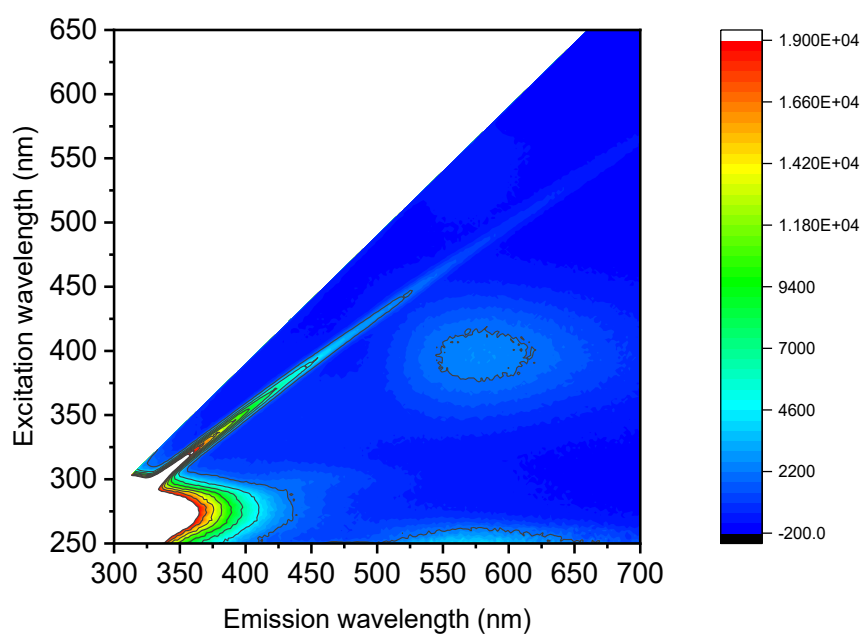
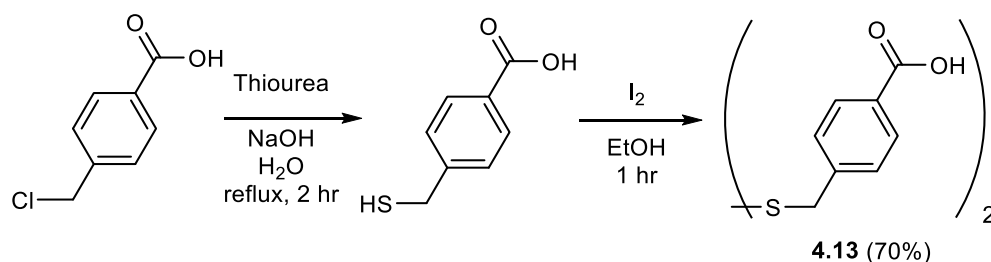


**Figure 4.31:** Fluorescence excitation and emission map of **4.12** in water (2.5 μM).

### 3.6.2.11 4,4'-(disulfanediybis(methylene))dibenzoic acid (4.13)



The synthesis was repeated as per a literature protocol.<sup>39</sup> A solution of 4-chloromethylbenzoic acid (10 g, 58 mmol) was added to 120 mL of 18.2 MΩ·cm water, followed by thiourea (6.6 g, 87 mmol). This was heated to reflux for two hours.

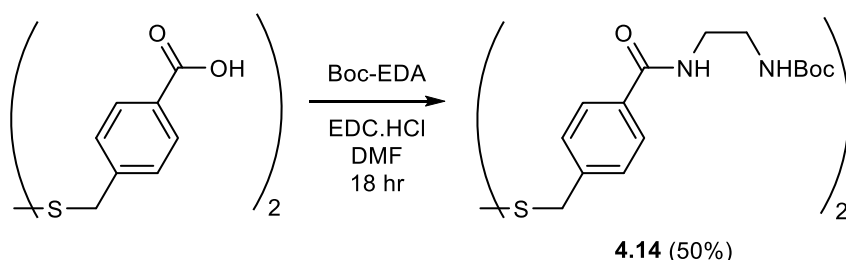
To this was added NaOH (70 mL of 10% w/v in water). This was heated to reflux for an hour, followed by cooling to room temperature in an ice bath. This solution was acidified until pH < 2 using concentrated HCl. The white precipitate was filtered and isolated. This was washed with water and dried *in vacuo*. This was dissolved into ethanol (150 mL), and to this iodine was added until the orange colour remained. This was left for an hour, after which sodium thiosulfate was added until the colour disappeared again. Volatiles were removed *in vacuo*, and the solid was rinsed thoroughly with water and dried to give solid **4.13** (9.1 g, 67%).

<sup>1</sup>H NMR (DMSO-*d*<sub>6</sub>, 300 MHz, ppm) δ = 7.91 (d, <sup>3</sup>*J*<sub>HH</sub> = 8.1 Hz, 1H), 7.39 (d, <sup>3</sup>*J*<sub>HH</sub> = 8.1 Hz, 1H), 3.83 (s, 1H).

MS (ESI) - [M+H<sup>+</sup>] – calculated m/z 335.0 observed m/z 335.0

Matches literature data.<sup>39</sup>

**3.6.2.12** di-tert-butyl (((4,4'-(disulfanediyl-bis(methylene))bis(benzoyl))bis(azanediyl))bis(ethane-2,1-diyl))dicarbamate (4.14)



Solid **4.13** (7 g, 2.1 mmol), was added to a round bottom flask with a magnetic stirrer, followed by 50 mL of DMF. To this solution *N*-Boc-ethylene diamine (3.8 g, 2.4 mmol) was added, followed by EDC.HCl (3.72 g, 2.4 mmol). This was left to stir overnight followed by concentration *in vacuo*. The solid was dissolved in CH<sub>2</sub>Cl<sub>2</sub> and washed with NaHCO<sub>3</sub> solution, 1 M HCl and brine three times. This was dried *in vacuo* and purified by silica column chromatography on a 12 g RediSep R<sub>f</sub> silica flash column and eluted with an CH<sub>2</sub>Cl<sub>2</sub> and methanol (0-10%) gradient eluent on a CombiFlash R<sub>f</sub>+ Lumen by Teledyne, to produce an off white solid **4.14** (6.1 g, 50%).

<sup>1</sup>H NMR (400 MHz, CDCl<sub>3</sub>, ppm) δ = 12.55 (d, <sup>3</sup>J<sub>HH</sub> = 7.9 Hz, 2H), 12.10 (d, <sup>3</sup>J<sub>HH</sub> = 8.3 Hz, 2H), 8.07 (s, 2H), 8.03 (d, <sup>3</sup>J<sub>HH</sub> = 6.1 Hz, 2H), 7.86 (t, <sup>3</sup>J<sub>HH</sub> = 6.2 Hz, 2H), 6.12 (d, <sup>3</sup>J<sub>HH</sub> = 1.2 Hz, 9H).

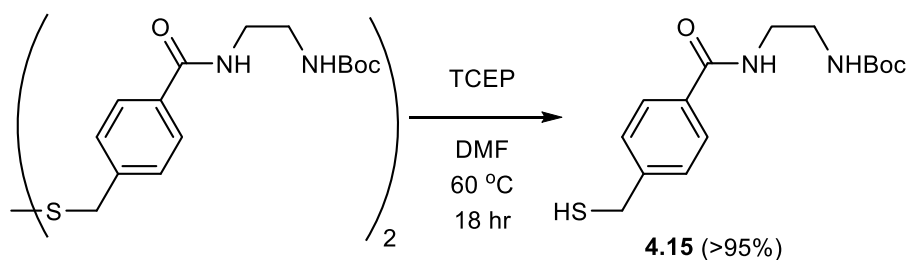
<sup>13</sup>C NMR (101 MHz, DMSO-*d*<sub>6</sub>, ppm) δ = 166.52 (CON), 156.21 (COON), 141.03 (CAr), 140.17 (CS), 133.93 (CAr), 129.66 (CAr), 127.80 (CAr), 78.14 (CBoc), 42.01 (CH<sub>2</sub>), 41.37 (CH<sub>2</sub>), 28.70 (CH<sub>3</sub>).

HR-MS (Xevo) - [M+H<sup>+</sup>] – calculated m/z 619.2624 observed m/z 619.2618;

Matches literature data.<sup>39</sup>



### 3.6.2.13 tert-butyl (2-(4-(mercaptomethyl)benzamido)ethyl)carbamate (4.15)



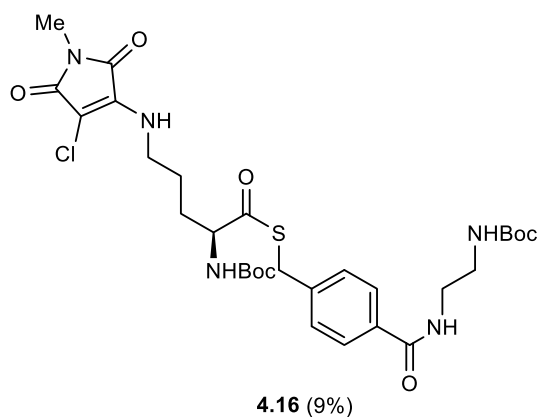
6 g of solid **4.14** (9.6 mmol), was dissolved in ethanol (150 mL) and heated to 60 °C to ensure dissolution. To this TCEP (3 g, 12 mmol) was added and the reaction was left overnight at 60 °C. This was dried and dissolved into CH<sub>2</sub>Cl<sub>2</sub>, and washed with water and brine three times. The CH<sub>2</sub>Cl<sub>2</sub> was removed *in vacuo* to yield white solid **4.15** (5.8 g, >95%).

<sup>1</sup>H NMR (DMSO-*d*<sub>6</sub>, 300 MHz, ppm) δ = 7.84 (d, <sup>3</sup>*J*<sub>HH</sub> = 8.0 Hz, 2H), 7.47 (d, <sup>3</sup>*J*<sub>HH</sub> = 8.2 Hz, 2H), 3.83 (d, <sup>3</sup>*J*<sub>HH</sub> = 7.9 Hz, 2H), 3.33 (q, <sup>3</sup>*J*<sub>HH</sub> = 6.1 Hz, 2H), 3.16 (q, <sup>3</sup>*J*<sub>HH</sub> = 6.1 Hz, 2H), 1.44 (s, 9H).

MS (ESI) - [M+H<sup>+</sup>] – calculated m/z 311.1 observed m/z 311.1;

Matches literature data.<sup>39</sup>

### 3.6.2.14 S-(4-((2-((tert-butoxycarbonyl)amino)ethyl)carbamoyl)benzyl) 2-((tert-butoxycarbonyl)amino)-5-((4-chloro-1-methyl-2,5-dioxo-2,5-dihydro-1H-pyrrol-3-yl)amino)pentanethioate (4.16)



Boc-Ornithine (**4.10**, 100 mg, 0.32 mmol) was added to 25 mL of acetonitrile in a round bottom flask with a magnetic stirrer. To this EDC.HCl (180 mg, 0.47 mmol) was added followed by Boc-ABT (**4.15**, 120 mg, 0.32 mmol). This was stirred overnight after which solvent was removed *in vacuo*. The crude yellow solid dissolved in ethyl acetate and washed with water and brine three times. To the organic layer was added iodine until an orange colour remained. Boc-ABT precipitated, and sodium thiosulfate was added until the colour of iodine disappeared. This solution was filtered and then concentrated and purified by silica column chromatography with an CH<sub>2</sub>Cl<sub>2</sub> eluent to elute side products followed by CH<sub>2</sub>Cl<sub>2</sub> with 5 % MeOH added to elute the yellow product. This was dried *in vacuo* to afford yellow solid **4.16** (85 mg, 9%).

<sup>1</sup>H NMR (400 MHz, DMSO-*d*<sub>6</sub>, ppm) δ = 8.47 (t, <sup>3</sup>J<sub>HH</sub> = 5.4 Hz, 1H), 7.96 (t, <sup>3</sup>J<sub>HH</sub> = 6.4 Hz, 1H), 7.81 (d, <sup>3</sup>J<sub>HH</sub> = 8.0 Hz, 2H), 7.73 (d, <sup>3</sup>J<sub>HH</sub> = 7.9 Hz, 1H), 7.40 (d, <sup>3</sup>J<sub>HH</sub> = 8.3 Hz, 2H), 6.97 (t, <sup>3</sup>J<sub>HH</sub> = 5.7 Hz, 1H), 4.23 – 4.07 (m, 3H), 3.58 – 3.42 (m, 2H), 3.33 (q, <sup>3</sup>J<sub>HH</sub> = 6.1 Hz, 2H), 3.15 (q, <sup>3</sup>J<sub>HH</sub> = 7.3, 6.6 Hz, 2H), 2.91 (s, 3H), 1.85 – 1.53 (m, 5H), 1.45 (s, 7H), 1.43 (s, 11H).

<sup>13</sup>C NMR (101 MHz, DMSO-*d*<sub>6</sub>, ppm) δ = 202.53 (CS), 168.01 (CO), 166.44 (CNO), 165.48 (CO), 156.19 (CBoc), 155.92 (CBoc), 142.35 (CNH), 141.56 (CAr), 133.71 (CAr), 128.93 (CAr), 127.84 (CAr), 79.18 (CBoc), 78.13 (CBoc), 60.86 (CH<sub>2</sub>), 42.06 (CH<sub>2</sub>), 31.98 (CH), 29.00 (CH<sub>2</sub>), 28.69 (CBoc), 28.65 (CBoc), 28.23 (CH<sub>2</sub>), 27.33 (CH<sub>2</sub>), 24.30 (CH<sub>3</sub>)

HR-MS (Xevo) - [M+Na<sup>+</sup>] – calculated m/z 690.2340 observed m/z 690.2336;

FTIR - 2959 (ν<sub>C-H</sub>), 1705 (ν<sub>C=O</sub>), 1686 (ν<sub>C=O</sub>), 1653 (ν<sub>C=O</sub>), 1641 (ν<sub>C=O</sub>)

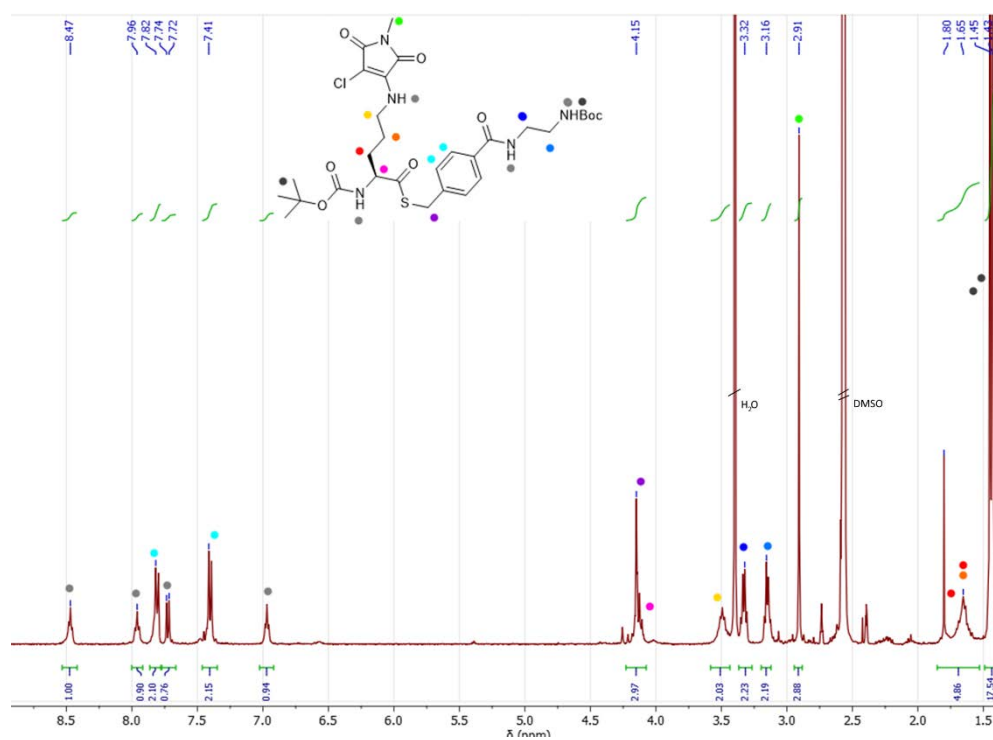


**Figure 4.32:** <sup>1</sup>H NMR spectrum of **4.16** (400 MHz, DMSO-*d*<sub>6</sub>).

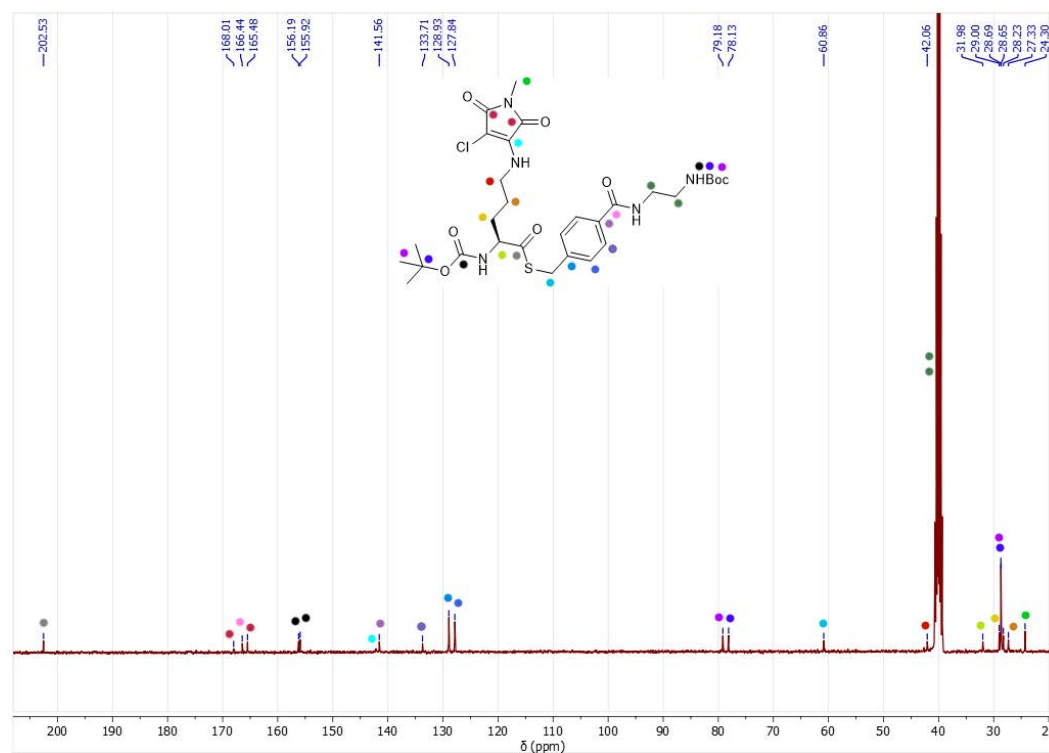
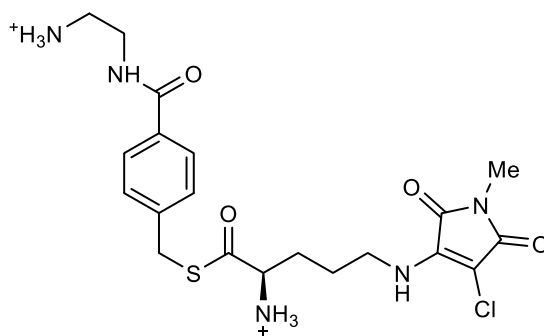


**Figure 4.33:** <sup>13</sup>C NMR spectrum of **4.16** (101 MHz, DMSO-*d*<sub>6</sub>).

**3.6.2.15** S-(4-((2-aminoethyl)carbamoyl)benzyl) 2-amino-5-((4-chloro-1-methyl-2,5-dioxo-2,5-dihydro-1H-pyrrol-3-yl)amino)pentanethioate (4.17)



**4.17** (81%)

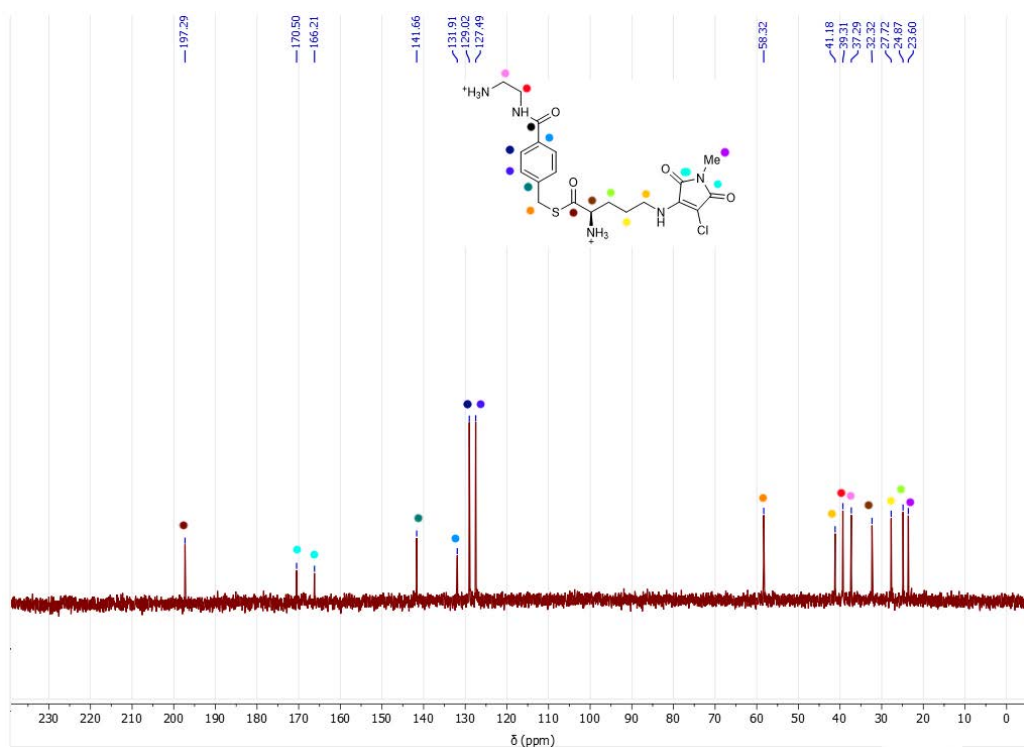
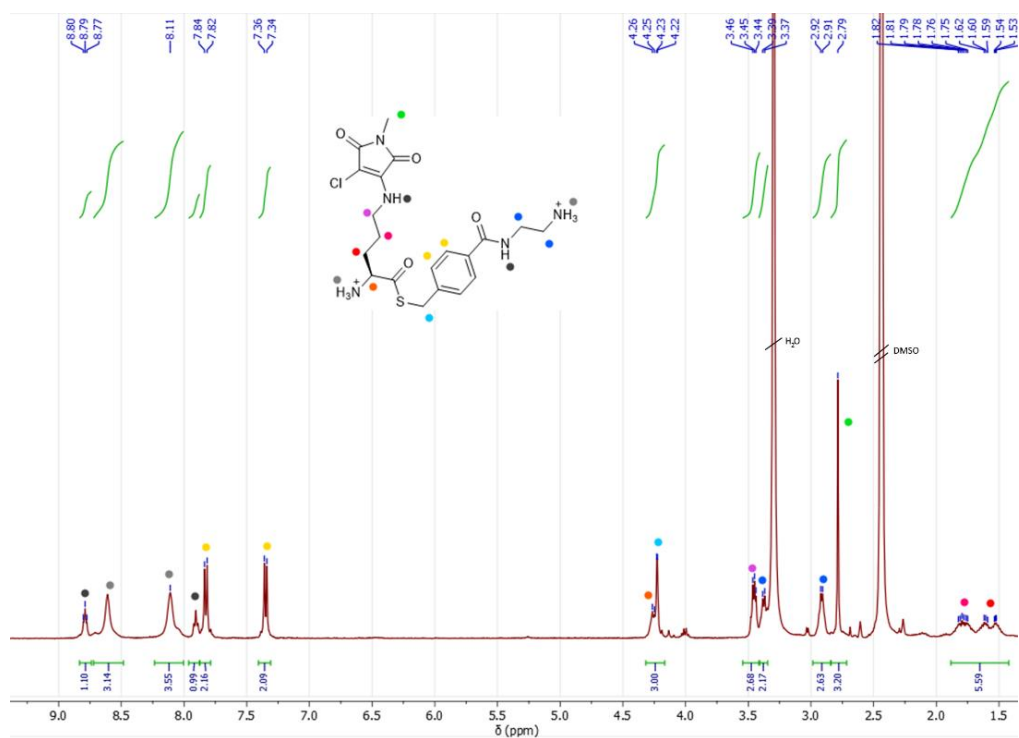
Boc-ABT-ACM-Boc-Orn (**4.16**, 75 mg, 0.11 mmol) was added to a dried round bottom flask containing 5 mL of 1M HCl in dry ethyl acetate and a magnetic stirrer. This was sealed and stirred overnight after which the solution was transferred to a falcon tube and centrifuged. This was decanted, re-solvated in ethyl acetate (10 mL) and centrifuged twice more. After three centrifuges the solid was dried *in vacuo* to yield a yellow solid **4.17** (41 mg, 81%).

$^1\text{H}$  NMR (300 MHz, DMSO- $d_6$ , ppm)  $\delta$  = 8.83 – 8.74 (t, 1H), 8.61 (br, 3H), 8.11 (br, 4H), 7.91 (t,  $^3J_{\text{HH}}$  = 6.7 Hz, 1H), 7.83 (d,  $^3J_{\text{HH}}$  = 8.2 Hz, 2H), 7.35 (d,  $^3J_{\text{HH}}$  = 8.1 Hz, 2H), 4.23 (d,  $^3J_{\text{HH}}$  = 2.5 Hz, 3H), 3.46 (q,  $^3J_{\text{HH}}$  = 5.1, 4.3 Hz, 3H), 3.38 (d,  $^3J_{\text{HH}}$  = 6.6 Hz, 2H), 2.91 (q,  $^3J_{\text{HH}}$  = 6.0 Hz, 3H), 2.79 (s, 3H), 1.88 – 1.42 (m, 6H).

$^{13}\text{C}$  NMR (101 MHz, D $_2$ O, ppm)  $\delta$  = 197.29, 170.50, 166.21, 141.66, 131.91, 129.02, 127.49, 58.32, 41.18, 39.31, 37.29, 32.32, 27.72, 24.87, 23.60.

HR-MS (Xevo) -  $[\text{M}+\text{H}^+]$  – calculated m/z 468.1472 observed m/z 468.1474;

FTIR - 2959 ( $\nu_{\text{C-H}}$ ), 1705 ( $\nu_{\text{C=O}}$ ), 1653 ( $\nu_{\text{C=O}}$ ), 1649 ( $\nu_{\text{C=O}}$ )



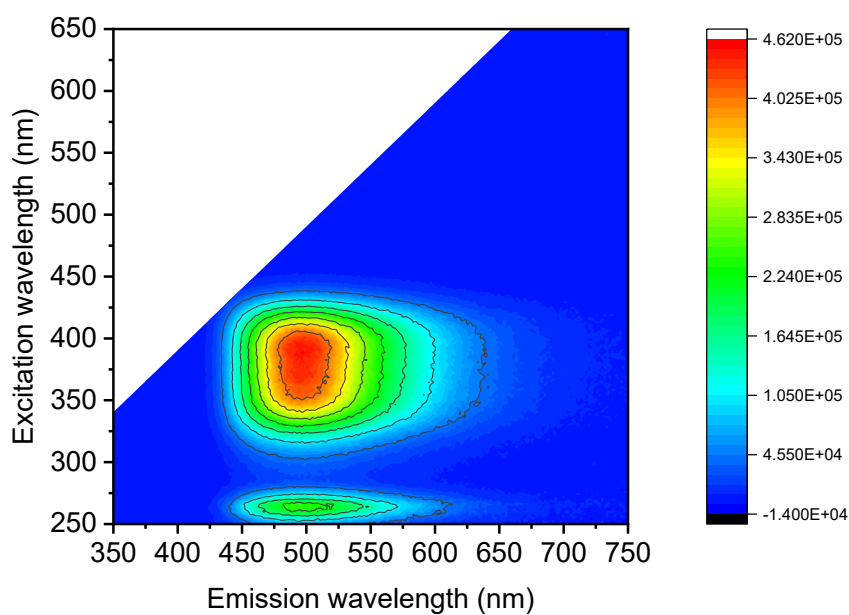


**Figure 4.36:** Fluorescence excitation and emission map of **4.17** in dioxane (10  $\mu\text{M}$ ).

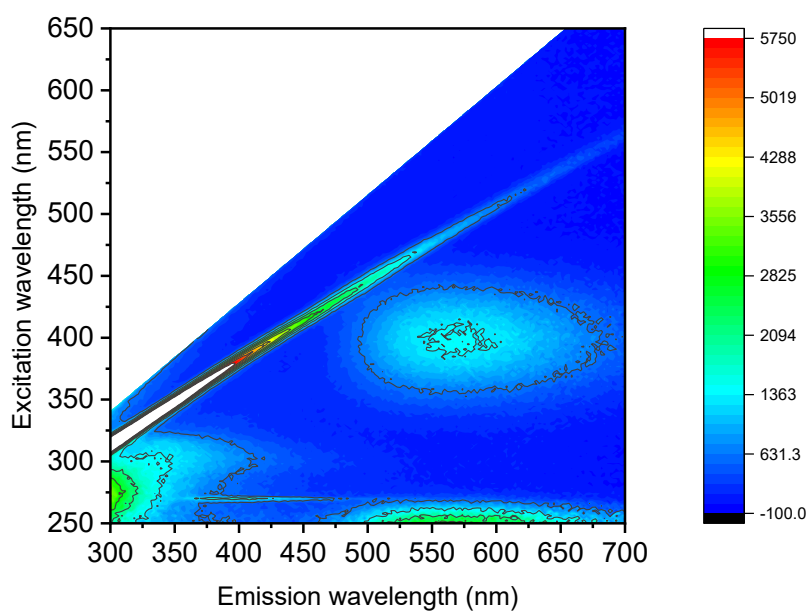


**Figure 4.37:** Fluorescence excitation and emission map of **4.17** in water (2.5  $\mu\text{M}$ ).

## 3.7 References

- (1) Gonzalez-Flores, J.; Shetty, S. P.; Dubey, A.; Copeland, P. R. *Biomol. Concepts* 2013, *4*, 349.
- (2) Wagner, I.; Musso, H. *Angew. Chem. Int. Ed. Engl.* 1983, *22*, 816.
- (3) Noren, C. J.; Anthony-Cahill, S. J.; Griffith, M. C.; Schultz, P. G. *Science* 1989, *244*, 182.
- (4) Goodman, H. M.; Abelson, J.; Landy, A.; Brenner, S.; Smith, J. D. *Nature* 1968, *217*, 1019.
- (5) Wals, K.; Ova, H. *Front. Chem.* 2014, *2*, 15.
- (6) Murakami, H.; Ohta, A.; Ashigai, H.; Suga, H. *Nat. Methods* 2006, *3*, 357.
- (7) Ohuchi, M.; Murakami, H.; Suga, H. *Curr. Opin. Chem. Biol.* 2007, *11*, 537.
- (8) Watson, P.; Jones, A. T.; Stephens, D. J. *Adv. Drug Deliv. Rev.* 2005, *57*, 43.
- (9) Ivanchenko, S.; Röcker, C.; Oswald, F.; Wiedenmann, J.; Nienhaus, G. U. *J. Biol. Phys.* 2005, *31*, 249.
- (10) Zheng, S.; Zhang, G.; Li, J.; Chen, P. R. *Angew. Chem. Int. Ed.* 2014, *53*, 6449.
- (11) Wang, K.; Sachdeva, A.; Cox, D. J.; Wilf, N. M.; Lang, K.; Wallace, S.; Mehl, R. A.; Chin, J. W. *Nat. Chem.* 2014, *6*, 393.
- (12) Kajihara, D.; Abe, R.; Iijima, I.; Komiyama, C.; Sisido, M.; Hohsaka, T. *Nat. Methods N. Y.* 2006, *3*, 923.
- (13) Royer, C. A. *Chem. Rev.* 2006, *106*, 1769.
- (14) Yang, M.; Song, Y.; Zhang, M.; Lin, S.; Hao, Z.; Liang, Y.; Zhang, D.; Chen, P. R. *Angew. Chem. Int. Ed.* 2012, *51*, 7674.
- (15) Sato, M.; Ozawa, T.; Inukai, K.; Asano, T.; Umezawa, Y. *Nat. Biotechnol.* 2002, *20*, 287.
- (16) Henderson, J. N.; Ai, H.; Campbell, R. E.; Remington, S. J. *Proc. Natl. Acad. Sci.* 2007, *104*, 6672.
- (17) Borrmann, A.; Milles, S.; Plass, T.; Dommerholt, J.; Verkade, J. M. M.; Wießler, M.; Schultz, C.; Hest, V.; M, J. C.; Delft, V.; L, F.; Lemke, E. A. *ChemBioChem* 2012, *13*, 2094.
- (18) Ariyasu, S.; Hayashi, H.; Xing, B.; Chiba, S. *Bioconjug. Chem.* 2017, *28*, 897.
- (19) Ratner, V.; Kahana, E.; Eichler, M.; Haas, E. *Bioconjug. Chem.* 2002, *13*, 1163.
- (20) Sachdeva, A.; Wang, K.; Elliott, T.; Chin, J. W. *J. Am. Chem. Soc.* 2014, *136*, 7785.
- (21) Nguyen, D. P.; Elliott, T.; Holt, M.; Muir, T. W.; Chin, J. W. *J. Am. Chem. Soc.* 2011, *133*, 11418.
- (22) Plass, T.; Milles, S.; Koehler, C.; Szymański, J.; Mueller, R.; Wießler, M.; Schultz, C.; Lemke, E. A. *Angew. Chem. Int. Ed.* 2012, *51*, 4166.

- (23) Moatsou, D.; Li, J.; Ranji, A.; Pitto-Barry, A.; Ntai, I.; Jewett, M. C.; **O'Reilly, R. K. *Bioconjug. Chem.* 2015, 26, 1890.**
- (24) Kim, Y.; Ho, S. O.; Gassman, N. R.; Korlann, Y.; Landorf, E. V.; Collart, F. R.; Weiss, S. *Bioconjug. Chem.* 2008, 19, 786.
- (25) Summerer, D.; Chen, S.; Wu, N.; Deiters, A.; Chin, J. W.; Schultz, P. G. *Proc. Natl. Acad. Sci.* 2006, 103, 9785.
- (26) Wang, J.; Xie, J.; Schultz, P. G. *J. Am. Chem. Soc.* 2006, 128, 8738.
- (27) Lee, H. S.; Guo, J.; Lemke, E. A.; Dimla, R. D.; Schultz, P. G. *J. Am. Chem. Soc.* 2009, 131, 12921.
- (28) Liu, W.; Wu, A.; Pellegrini, M.; Wang, X. *Sci. Rep.* 2015, 5, 14344.
- (29) Gonzalez, M. W.; Kann, M. G. *PLoS Comput. Biol.* 2012, 8, 12.
- (30) Jones, M. W.; Strickland, R. A.; Schumacher, F. F.; Caddick, S.; Baker, J. R.; Gibson, M. I.; Haddleton, D. M. *Chem. Commun.* 2012, 48, 4064.
- (31) Tedaldi, L. M.; Smith, M. E. B.; Nathani, R. I.; Baker, J. R. *Chem. Commun.* 2009, 6583.
- (32) Robin, M. P. Bromo and thio maleimides for functionalisation and fluorescent labelling of polymers and polymer nanoparticles, University of Warwick, 2014.
- (33) Fields, Gregg B. In *Peptide Synthesis Protocols*; Pennington, Michael W.; Dunn, Ben M., Eds.; Methods in Molecular Biology; Humana Press, 1995; 17.
- (34) **Carpino, L. A.; Williams, J. R.; Łopusiński, A. J. *Chem. Soc., Chem. Commun.* 1978, 450.**
- (35) Xie, Y.; Husband, J. T.; Torrent-Sucarrat, M.; Yang, H.; Liu, W.; **O'Reilly, R. K. *Chem. Commun.* 2018, 54, 3339.**
- (36) Relles, H. M. *J. Org. Chem.* 1972, 37, 3630.
- (37) Nirogi, R.; Dwarampudi, A.; Kambhampati, R.; Bhatta, V.; Kota, L.; Shinde, A.; Badange, R.; Jayarajan, P.; Bhyrapuneni, G.; Dubey, P. K. *Bioorg. Med. Chem. Lett.* 2011, 21, 4577.
- (38) Morimoto, J.; Hayashi, Y.; Iwasaki, K.; Suga, H. *Acc. Chem. Res.* 2011, 44, 1359.
- (39) Niwa, N.; Yamagishi, Y.; Murakami, H.; Suga, H. *Bioorg. Med. Chem. Lett.* 2009, 19, 3892.
- (40) Tuckey, C.; Asahara, H.; Zhou, Y.; Chong, S. *Curr. Protoc. Mol. Biol.* 2014, 108, 16.31.1.
- (41) **Artymiuk, P. J.; Blake, C. C. F. *J. Mol. Biol.* 1981, 152, 737–762.**





## **Chapter 5:** Synthesis of maleimide based fluorescent probes for investigation of enzyme mechanisms and intermediates

## 4.1 Abstract

The environmental sensing abilities of maleimide dyes, along with their significantly smaller size compared to fluorophores currently used in biological research, means that there are numerous novel applications in this field. This Chapter focuses on the synthesis of various alkyne functionalized maleimide dyes for use in probing the biosynthesis of natural products, a collaborative project with the group of Manuela Tosin. Various alkyne functionalized maleimides were synthesized for coupling with azide containing probes, which have been shown by the Tosin group to capture intermediates in natural product biosynthesis. A range of alkyne maleimides were synthesized, including a DTM, ACM and an activated alkyne MAM. Their ability to capture intermediates has been initially evaluated by the Tosin group (University of Warwick). As these dyes will be used *in vivo*, we wanted to establish the stability of these moieties to cellular incubation conditions including various cell growth media. To achieve this, dyes were incubated in the broths over several days at raised temperature and under sterile and non-sterile conditions to mimic a range of incubation conditions. GCMS, HPLC and fluorescence analysis all indicated no loss of dye integrity and that no dye adducts were forming, suggesting full stability to broth ingredients under raised temperature conditions, indicating a promising future for the dye in these applications.

## 4.2 Introduction

### 4.2.1 Probes for capturing enzyme intermediates

For the first part of this Chapter, the synthesis of maleimide based probes for studying enzyme catalyzed biosynthesis, was undertaken. Such probes could improve detection of intermediates in the synthesis of various natural products and could provide more information into understanding how many important biomolecules are synthesized *in vivo*.<sup>1,2</sup> The probes are substrate mimics and have been used to elucidate the mechanism of several enzymatic pathways that utilize acyl carrier proteins (ACPs), including non-ribosomal peptide synthetases (NRPS)<sup>3</sup> and polyketide synthetases (PKS).<sup>4,5</sup> Such pathways require ACPs to shuttle intermediates between local catalytic domains, a process which leads to a diverse range of natural products.<sup>6</sup>

The Tosin group have pioneered work in this field through the development of chemical probes that aid in the capture and identification of intermediates in such biosynthetic pathways.<sup>1,2,7,8</sup> The probes are designed to mimic the natural substrate, however they are functionalized to prevent product formation and aid characterization and isolation of intermediates. This provides insight into substrate flexibility and provides a mechanism for the synthesis of novel compounds through diversification of unnatural substrates. Initial research was focused on probing polyketide biosynthesis to obtain unnatural functionalized intermediates, concentrating on the well understood biosynthetic pathway of polyketide formation catalyzed by polyketide synthase (PKS). The group synthesized non-hydrolysable malonate analogues (Figure 5.1) which would be recognized by PKS and undergo polyketide differentiation pathways with the aid of ACP.<sup>7</sup> Off-loading of products from ACP is naturally achieved through a nucleophilic PKS based cysteine residue with the aid of NADPH;<sup>9</sup> however this process cannot occur in the

mutant probes. Therefore, the intermediate species are derivatives of the modified probes, and can be isolated and characterized by LCMS. These studies proved tolerance and processing of unnatural analogues, in addition to providing kinetic insights into the assembly and the amenability of polyketides to further structural modifications.<sup>1,8</sup>

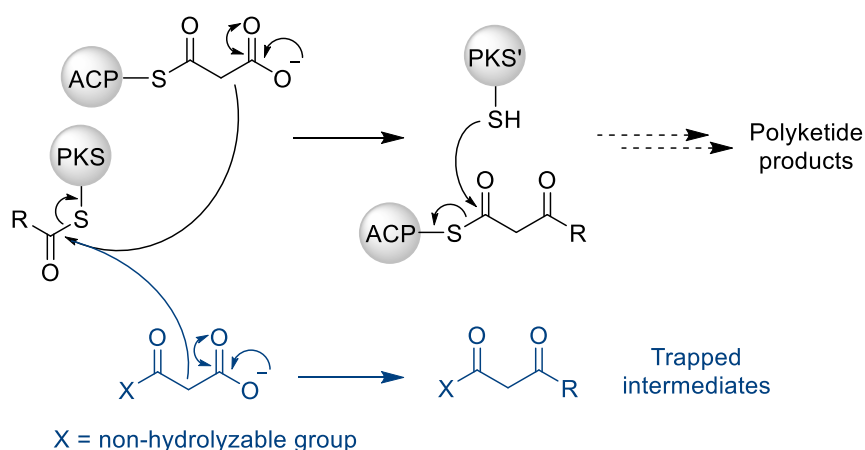


**Figure 5.1:** Simplified mechanism of normal polyketide synthesis (black) and mechanism of trapping intermediates with probe (blue).

After studying PKS and the kinetic transformation of intermediates in polyketide assembly, the group has focused on a new variant of probes for the elucidation of nonribosomal peptide synthesis.<sup>2</sup> Specifically, they have probed the synthesis of echinomycin in cultures of *S. lasaliensis* through a new generation of chain transfer termination probes (Figure 5.2). Several intermediate peptide species were captured by these probes, which provided new information on the biosynthetic pathway and substrate flexibility/specificity.<sup>2</sup>

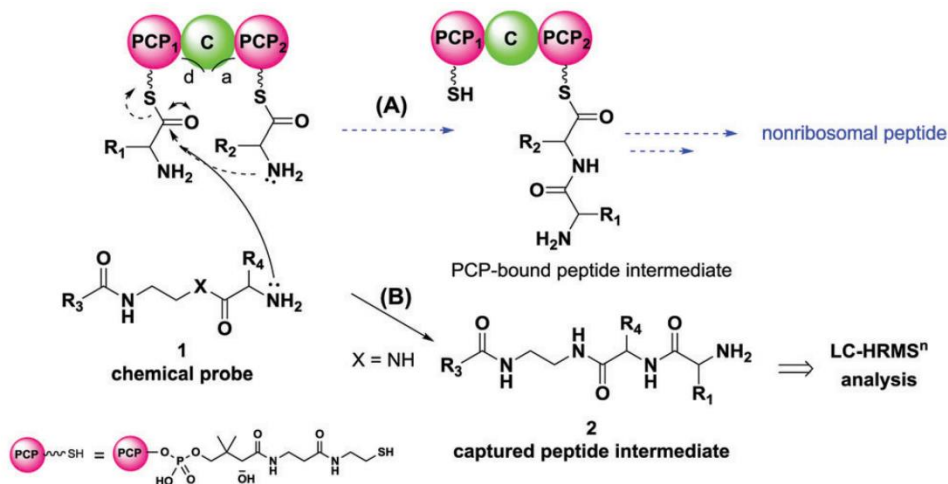


**Figure 5.2:** Illustration of normal non-ribosomal peptide synthesis (A) and capture of intermediates by chemical probe mimics (B), also a target of this Chapter, developed by Ho *et al.* Figure reproduced from ref.<sup>2</sup>

Based upon this earlier work it was hypothesized that the small size of maleimide fluorophores would allow for attachment to these probes, without affecting their intermediate capture ability. As the probes would now be tagged with a fluorophore, the process of isolation and detection of off-loaded intermediates in such complex systems should be easier through being able to utilize UV and fluorescence detection. The environmental response of the dye, along with its wide lifetime range, may also find future applications in the monitoring of kinetics in these multi-step syntheses. Therefore, the first goal of this Chapter was to synthesize maleimide based alkynes for reaction with azide functionalized probes previously developed by the Tosin group, to create maleimide tagged probes for *in vivo* testing.

The second goal of this Chapter was to establish that the maleimide motif was stable to the complex environment of cell expression media. This will be established by incubating the dye in commonly used cell media, under the conditions used for the intermediate trapping conditions, including at raised temperature. The contents of such bacterial expression media are extremely

complex and include sugars, proteins, amino acids, vitamins, sulfates and more depending on the media.<sup>10</sup> The cell expression media is essential for the growth of *E. Coli* used to express the enzymes studied.<sup>11</sup> If it were to be found that the maleimide was susceptible to degradation or reaction under these conditions, then the dyes will not be reliably useful in the isolation of intermediates, as the probes need to be isolatable at the end of the experiment.

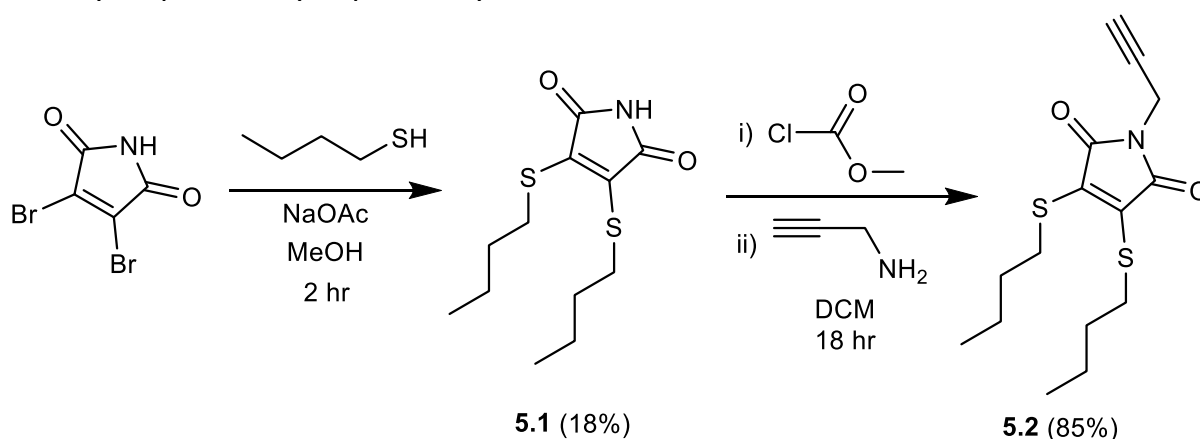
## 4.3 Results

### 4.3.1 Synthesis of alkyne functionalized maleimide fluorophores for utilization as enzyme intermediate probes

To attach the maleimide motifs to the biosynthesis probe, Copper(I)-catalyzed alkyne-azide cycloaddition (CuAAC) was chosen due to its high selectivity and reliability, and its proven effectiveness for previous probe functionalization.<sup>1</sup> Therefore, maleimide motifs (DTM, MAM, ABM and ACM) were designed with alkyne functionality at the imide position.

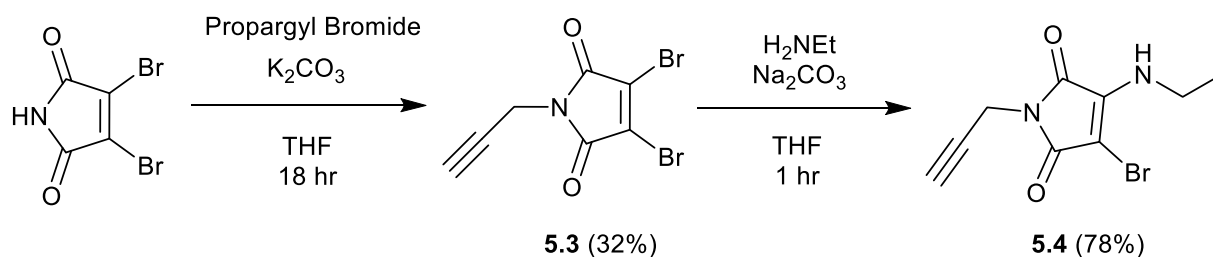
Initially, DTM and ABM dyes were targeted as they were the most studied dyes at the initiation of the project. The formation of alkyne-dibutylthiomaleimide (**5.1**) was achieved *via* the formation of intermediate DTM **5.2** (Scheme 5.1). Formation of alkyne-DBM could be achieved, however subsequent treatment with butanethiol led to derivatization of the alkyne in preference to DBM substitution.

On the other hand, formation of ABM alkyne-ethylaminobromomaleimide (**5.4**) could be achieved over two steps from alkyne-DBM (**5.3**) (Scheme 5.2), similarly to previously reported synthesis.<sup>12</sup>



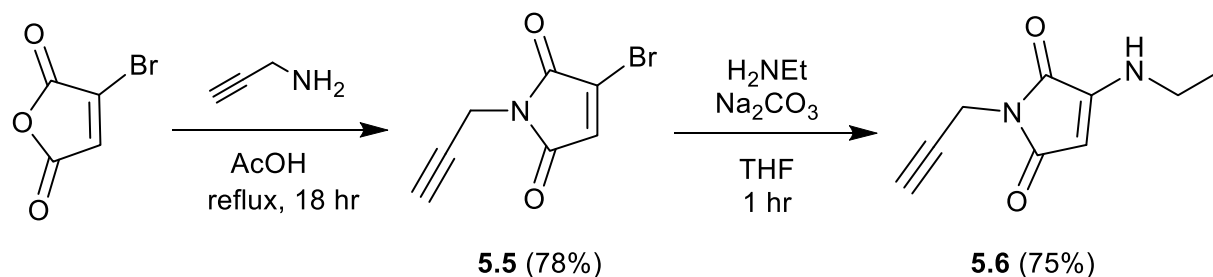
**Scheme 5.1:** Synthesis of alkyne-dibutylthiomaleimide, **5.2**.





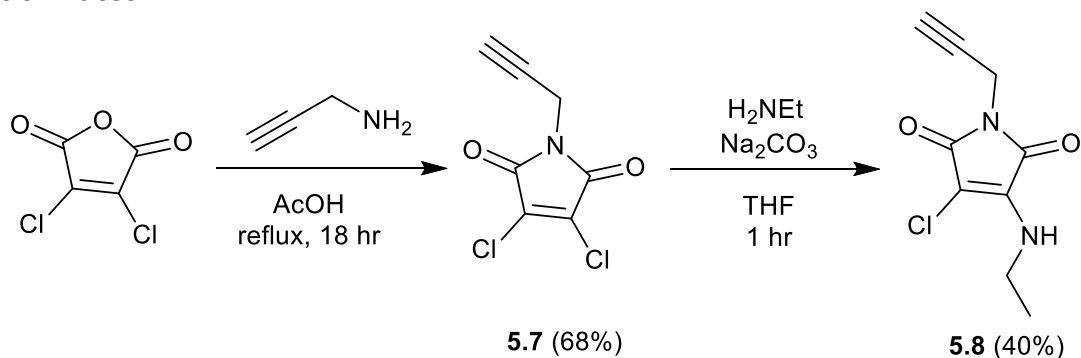
**Scheme 5.2:** Synthesis of alkyne-ethylaminobromomaleimide **5.4**.

While less stable and more reactive,<sup>13</sup> monoaminomaleimides are smaller and brighter than ABM analogues. Therefore, alkyne-monoaminomaleimide **5.6** was also synthesized, *via* intermediate alkyne-MBM **5.5**, for study in these applications (Scheme 5.3).



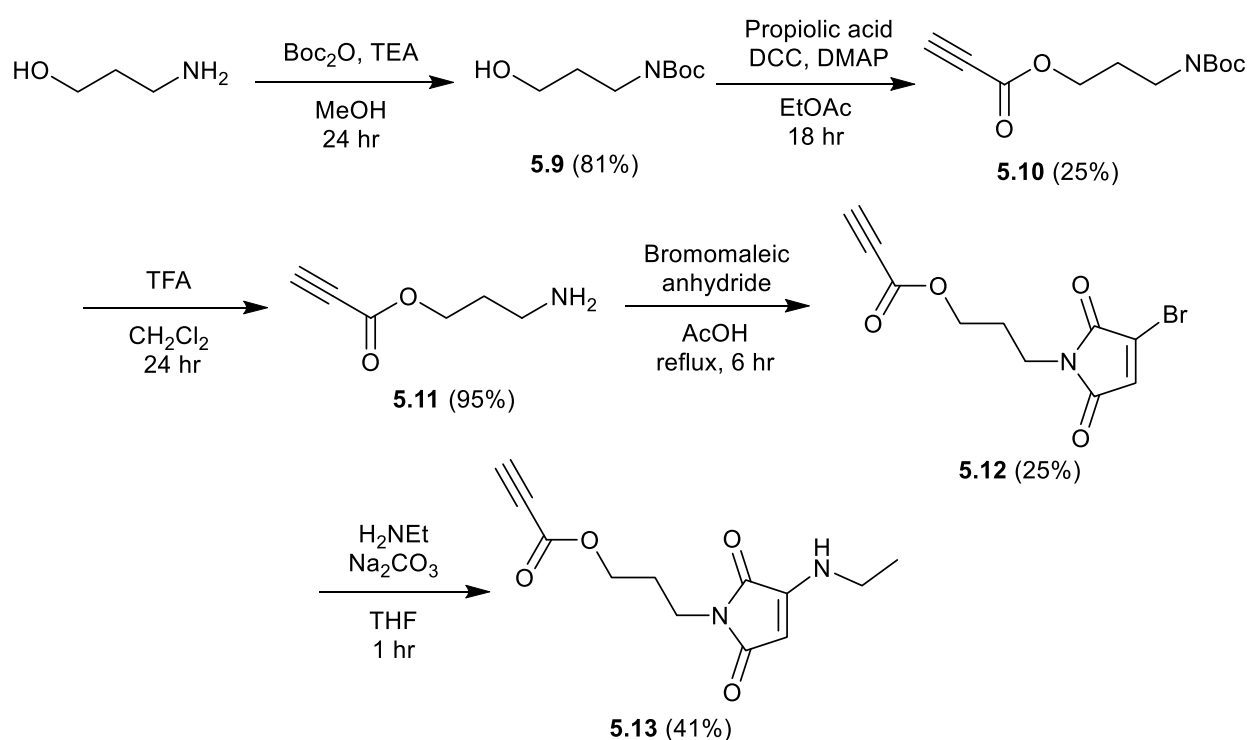
**Scheme 5.3:** Synthesis of alkyne-ethylaminomaleimide **5.6**.

During the course of this project aminochloromaleimides (ACMs) were developed by our group,<sup>14</sup> and were found to be a good compromise between the stability of ABMs, and the improved brightness and size of MAMs. Therefore, synthesis of ACM alkyne probe **5.8** was subsequently developed (Scheme 5.4) with the hypothesis that this dye could produce the most promising intermediate detection rates.



**Scheme 5.4:** Synthesis of alkyne-ethylaminochloromaleimide **5.8**.

Finally, the synthesis of an activated alkyne probe was undertaken to potentially facilitate a higher yielding probe formation step, while also removing the need for copper catalysts which requires removal prior to enzyme incorporation. Towards this, an activated alkyne amine **5.11** was synthesized according to a literature method,<sup>15</sup> which was subsequently reacted with bromomaleic anhydride and then ethylamine to form the activated alkyne MAM product **5.13** (Scheme 5.5). <sup>1</sup>H and <sup>13</sup>C NMR analysis indicated the presence of a small impurity (Figure 5.3) which integrated to < 5% by <sup>1</sup>H NMR. A smaller amount of impurity was later noticed in the <sup>1</sup>H NMR of **5.12**. This is attributed to derivatization of the previous alkyne **5.11**, forming an unidentified vinyl side-product. Alkynes are known to react with nucleophiles, for example alcohols, under basic conditions.<sup>16,17</sup> It was not envisioned that this impurity would affect the coupling reaction, and therefore this was used for coupling to the azide-probe without further purification.



**Scheme 5.5:** Synthesis of activated alkyne-ethylaminomaleimide **5.13**.

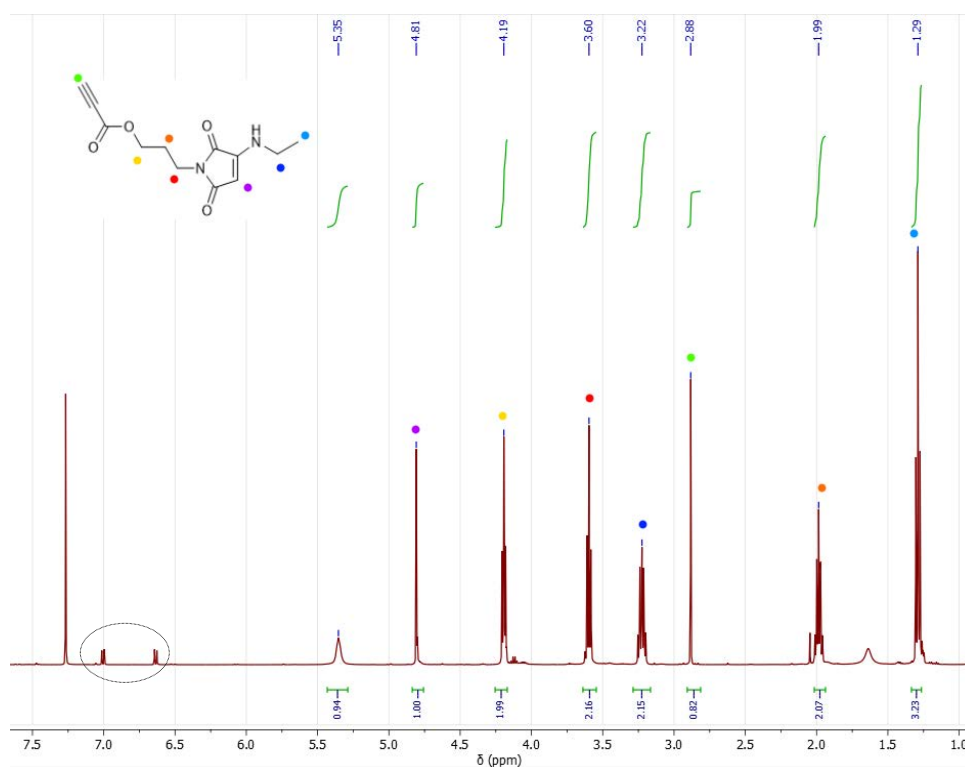


**Figure 5.3:**  $^1\text{H}$  NMR spectrum of **5.13** in  $\text{CDCl}_3$ , with impurity circled.

#### 4.3.2 Studying the stability of maleimide fluorophores in cellular media

As discussed in the introduction, the dyes will be incubated in *E. Coli* growth media and therefore, the tolerance of substituted maleimides to such media was investigated. Degradation or reaction of the probe with chemical species in the broths would lead to significant complication of the analysis, and loss of probe efficiency. To achieve this, precursor ABM **5.4** was chosen as a model for incubation. This was placed into four cell media formulations, along with a deionized water control. These were:

- SMM – Supplemented minimal media.<sup>18</sup>
- MYM – Minimal yeast media.<sup>2</sup>
- YEME – Yeast and malt extract broth.<sup>19</sup>
- TSB – Tryptic soy broth.<sup>20</sup>

The dissolved dye was then incubated at 30 °C to replicate the conditions of the *in vivo* experiments that will be used to trap enzyme intermediates. However, after an initial test over a day, emission of the dye in YEME under UV illumination was clearly exhausted (Figure 5.4), suggesting loss of integrity of the probe. YEME medium contains yeast and malt cell extracts, therefore the contents are too complex to identify a cause for this phenomenon.



**Figure 5.4:** Structure and photo of fluorescence under UV illumination of ACM **5.4** after 24 hour incubation in cell media, showing YEME quenching.

As these initial results indicated poor stability of the ABM probe to YEME and research in the group had moved onto more stable ACM probes, we incubated ACM **5.8** under the same conditions. After initial incubation for 24 hours, UV illumination showed that emission of the dye was visible in YEME (Figure 5.5), unlike for the ABM. Therefore, the dye was incubated over two weeks in the broths and progress of the incubation was monitored by fluorescence emission, GCMS and HPLC.



**Figure 5.5:** Structure and photo of fluorescence under UV illumination of ACM **5.8** after 24 hour incubation in cell media.

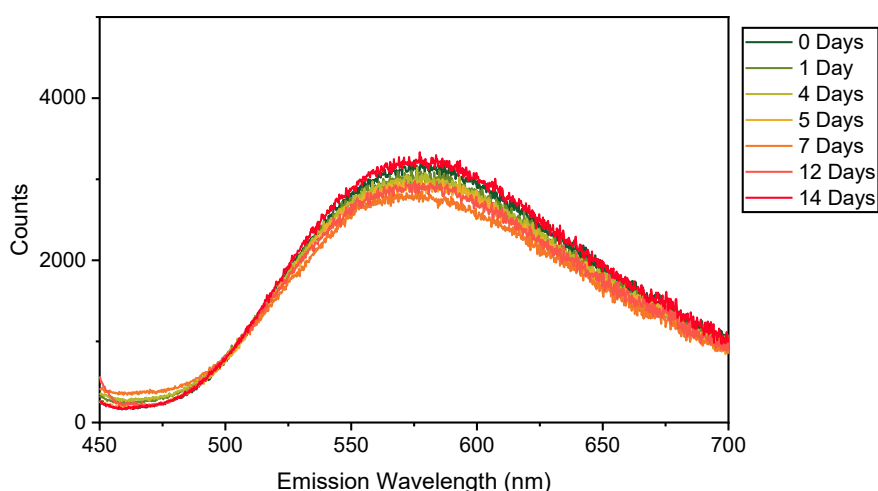


**Figure 5.6:** Fluorescence emission of **5.8** in 18.2 MΩ·cm water over two weeks (375 nm excitation), illustrating retention of fluorescence.

In regards to the fluorescence analysis, the dye incubated in 18.2 MΩ·cm water showed very good retention of emission over 14 days (Figure 5.6). This was also true for MYM, YEME and TSB broths, all showing negligible change in fluorescence emission. On the other hand, incubation in SMM led to fluorescence emission increasing over the period of the study significantly (Figure 5.7). Two hypotheses were proposed for this phenomenon. Firstly, the dye was aggregating slowly in the broth causing aggregation enhanced emission; or secondly, that bacteria was growing in the sample providing a more hydrophobic environment for the dye, thus increasing emission. To eliminate the second hypothesis the study was repeated under sterile conditions, however, the same phenomenon was observed with incubation in SMM, albeit to a significantly lower degree (Figure 5.8). Based upon this the cause for these observations is still unclear, but *in vitro* studies will use other broths to alleviate any concerns.

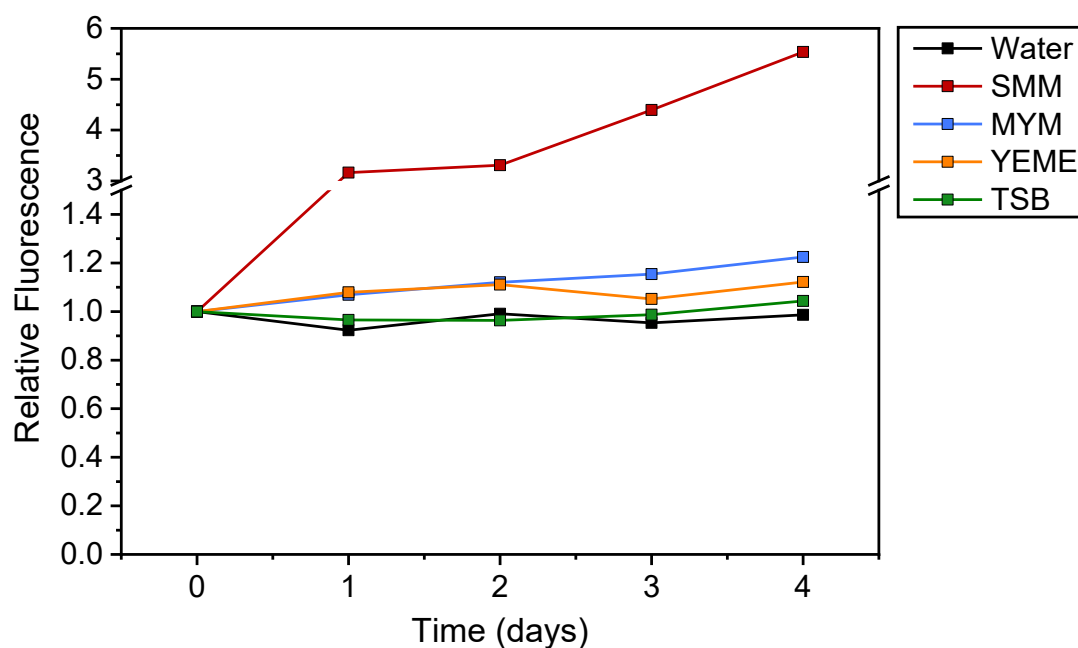


**Figure 5.7:** Fluorescence emission ( $\lambda_{\text{ex}} = 375 \text{ nm}$   $\lambda_{\text{em}} = 500 \text{ nm}$ ) of ACM 5.8 in non-sterile cell media, showing the increase in fluorescence in SMM. Note that the y-axis is split and has different scales for the upper and lower part of the axes.

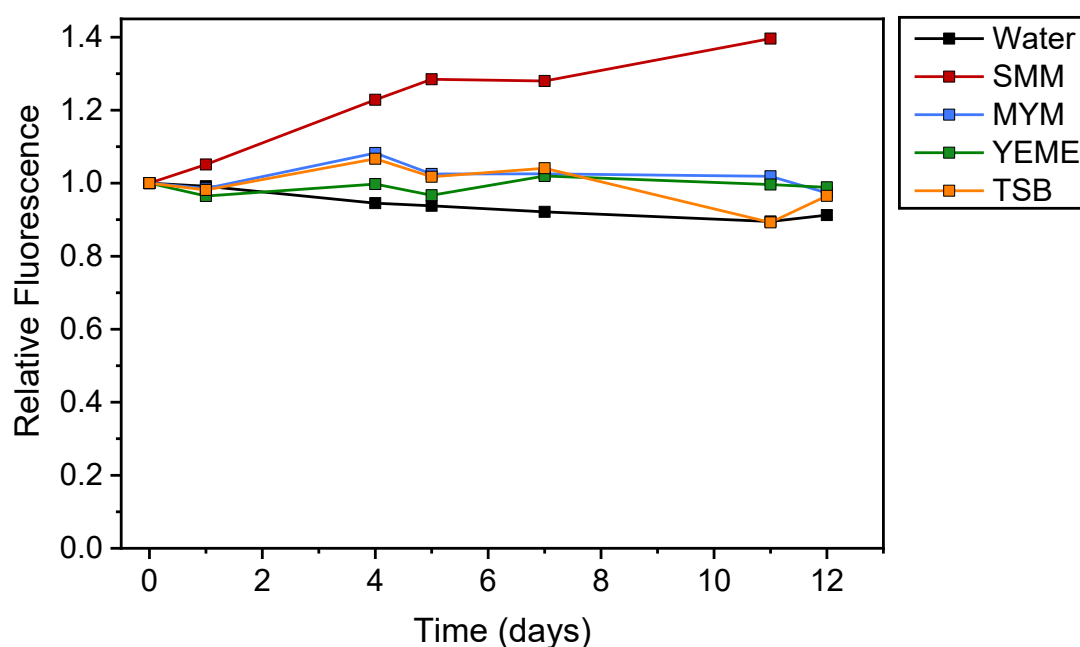


**Figure 5.8:** Fluorescence emission ( $\lambda_{\text{ex}} = 375 \text{ nm}$   $\lambda_{\text{em}} = 500 \text{ nm}$ ) of ACM 5.8 in sterile cell media. Note the increase in fluorescence for SMM is lower in magnitude than for the dye under non-sterile conditions (Figure 5.7).

HPLC was conducted on the broths during the incubation period to establish integrity of the dye – additional peaks in the 375 nm region would suggest derivatization of the dye (for example reaction of the alkyne), whereas absorbance at other wavelengths may suggest loss of integrity of the maleimide motif. The water control showed dye elution at around 15.5 minutes, which continued for 14 days (Figure 5.9). Positively, no additional peaks could be seen in the dye or UV region, suggesting full retention of the maleimide structure corroborating fluorescence results. The fluorescence detector (375 nm excitation and 500 nm emission) also confirmed this peak was fluorescent (Figure 5.10), however possibly due to the poor emission in aqueous solution, this detector did show slightly more noise.

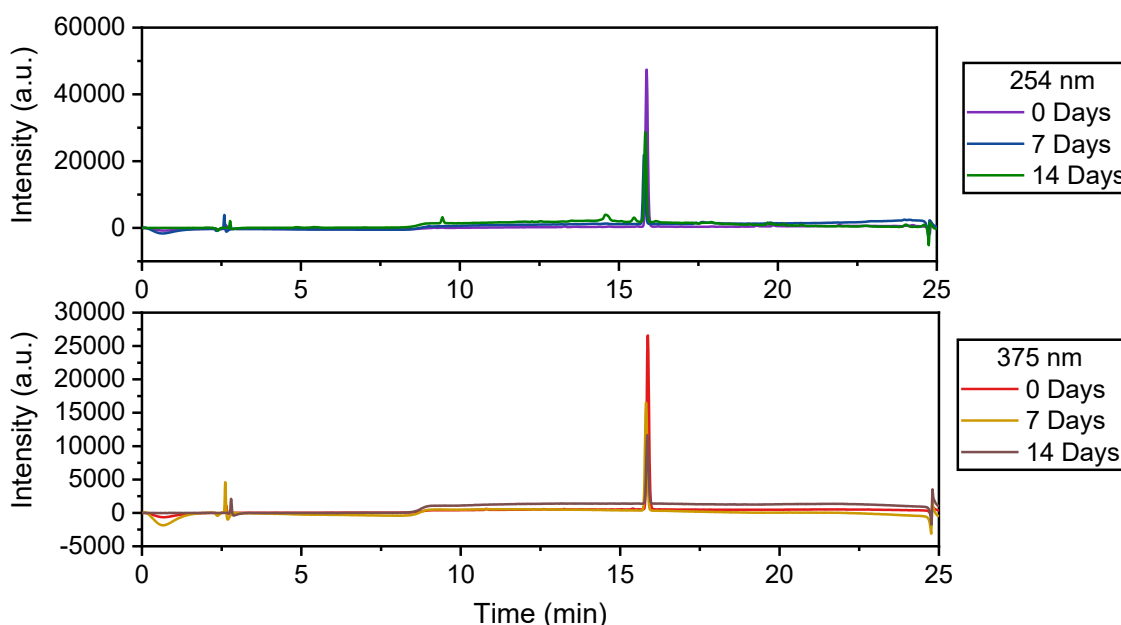


**Figure 5.9:** HPLC chromatograms of **5.8** in water over 14 days, with 254 nm detection (top) and 375 nm detection (bottom).

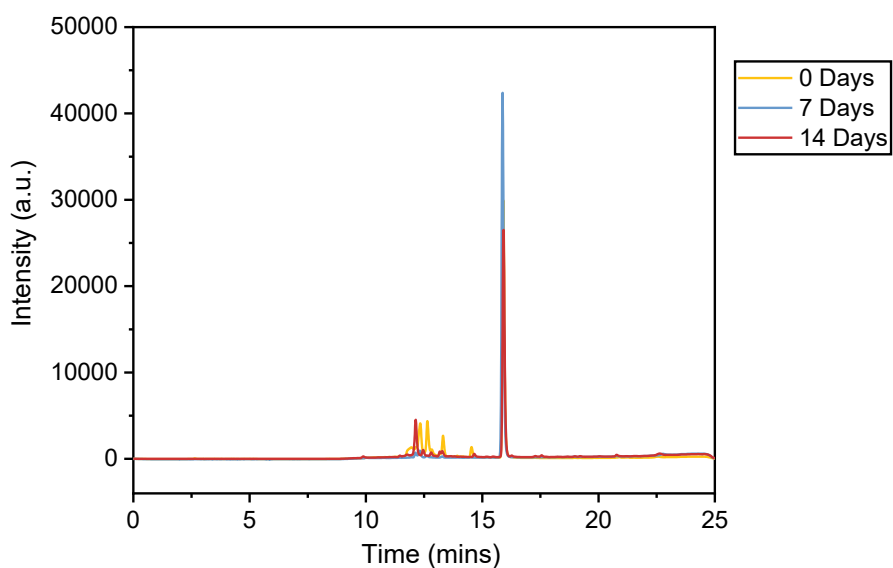


**Figure 5.10:** HPLC chromatograms of **5.8** in water over 14 days, recorded with a fluorescence detector (375 nm excitation and 500 nm emission).

HPLCs were also run of the dye incubated in the other broths and the obtained chromatograms suggested complete integrity of the dye across all broths (Figure 5.11 – Figure 5.13).

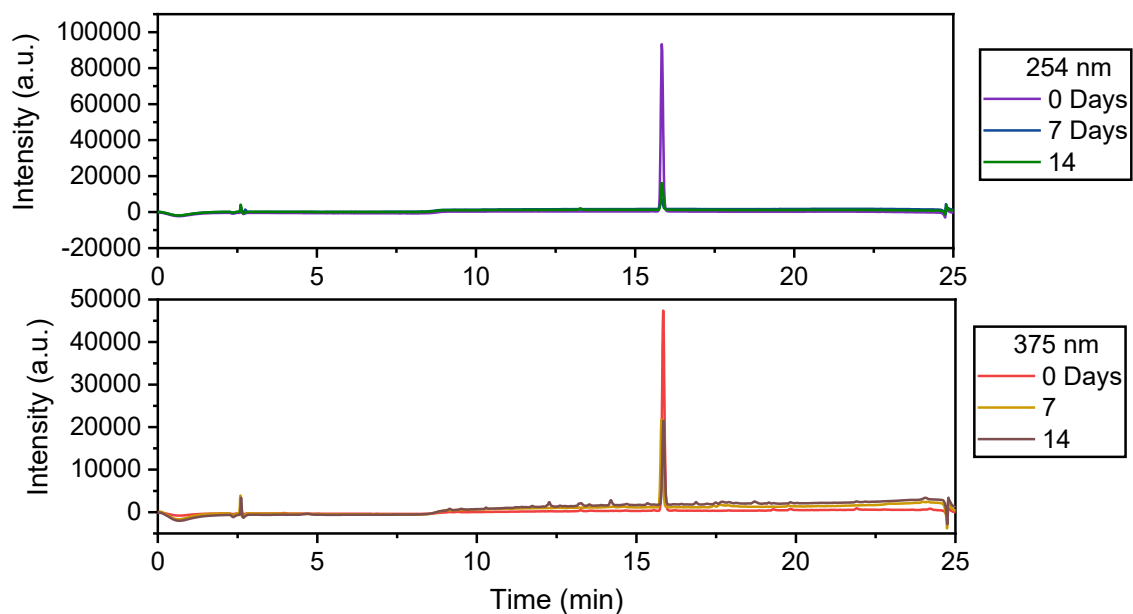


**Figure 5.11:** HPLC chromatograms of **5.8** in SMM over 14 days, with 254 nm detection (top) and 375 nm detection (bottom).



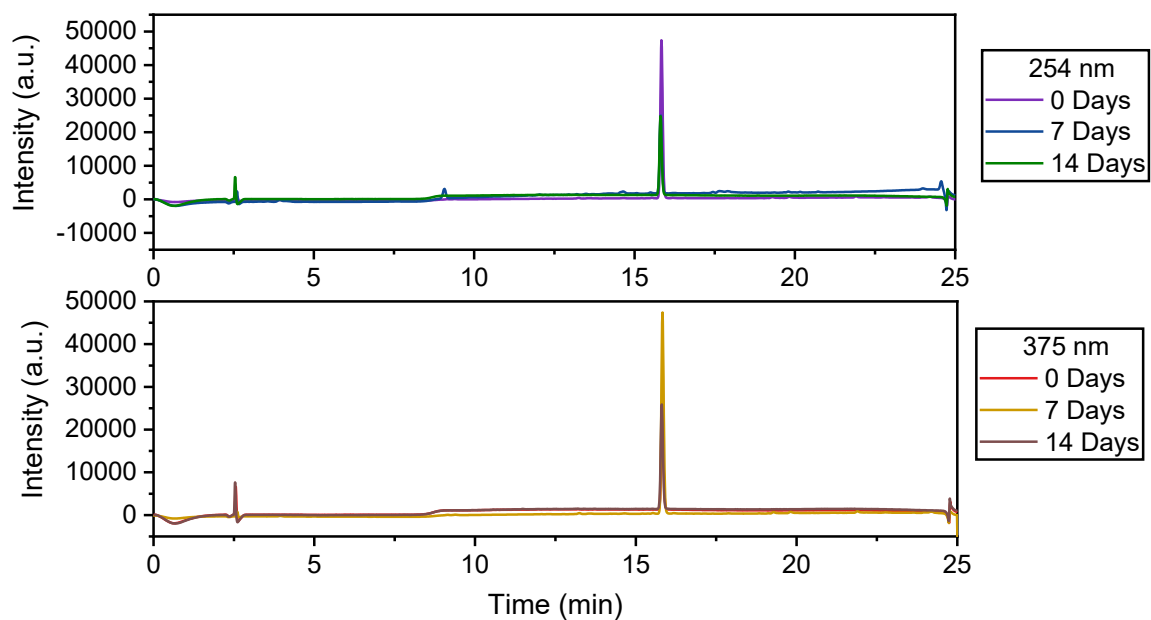


**Figure 5.12:** HPLC chromatograms of **5.8** in YEME over 14 days, with 254 nm detection (top) and 375 nm detection (bottom).

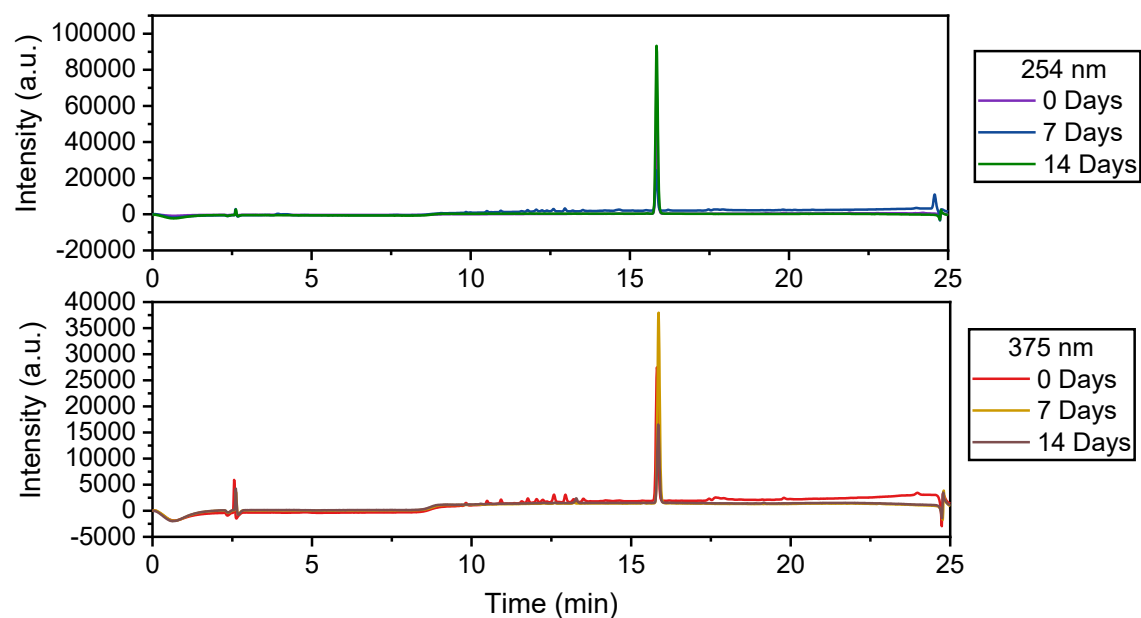


**Figure 5.13:** HPLC chromatograms of **5.8** in TSB over 14 days, with 254 nm detection (top) and 375 nm detection (bottom).

While HPLC and fluorescence emission both suggested good purity and stability in cell media, it was posited that a mass-based characterization technique would also be useful to detect the existence of side products that may not be water-soluble or UV active. Therefore, samples from the study were extracted with  $\text{CH}_2\text{Cl}_2$  and then analyzed by GCMS. GCMS analysis indicated only pure dye was observable over the duration of the study for all broths (Figure 5.14-5.17), corroborating the conclusion that the dye is stable in the cell media under incubation conditions. The day 0 chromatograms are from the unincubated alkyne **5.8** as a control.

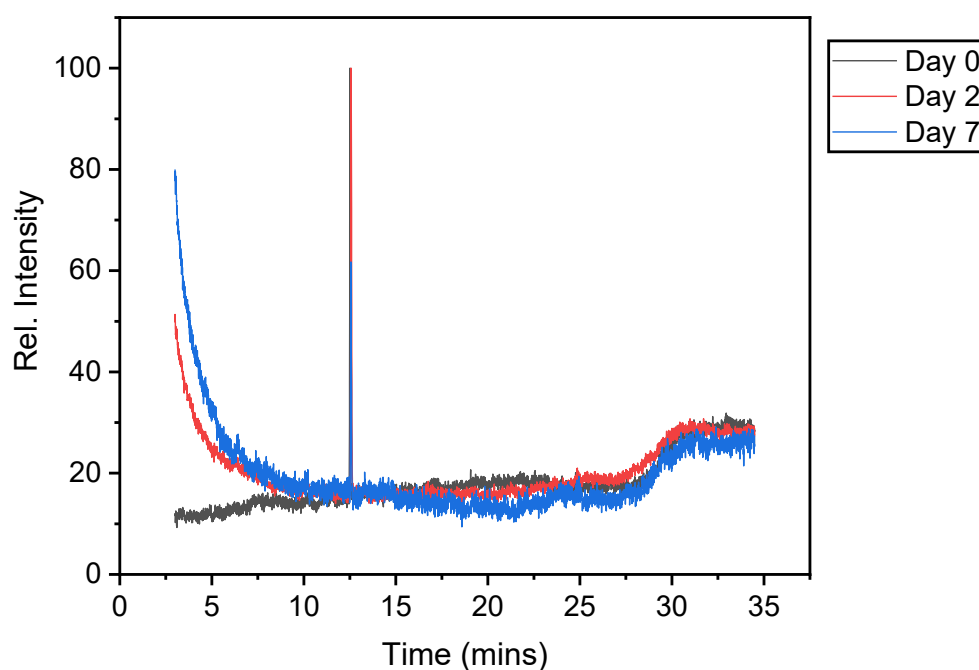


**Figure 5.14:** GCMS chromatograms of **5.8** over 7 days extracted from water.

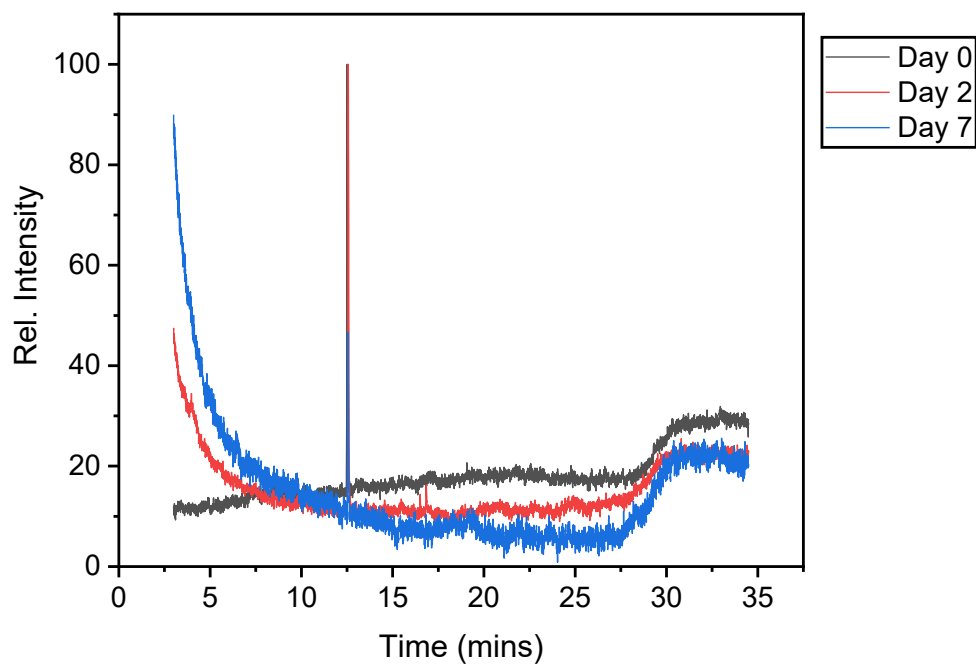


**Figure 5.15:** GCMS chromatograms of **5.8** over 7 days extracted from MYM.

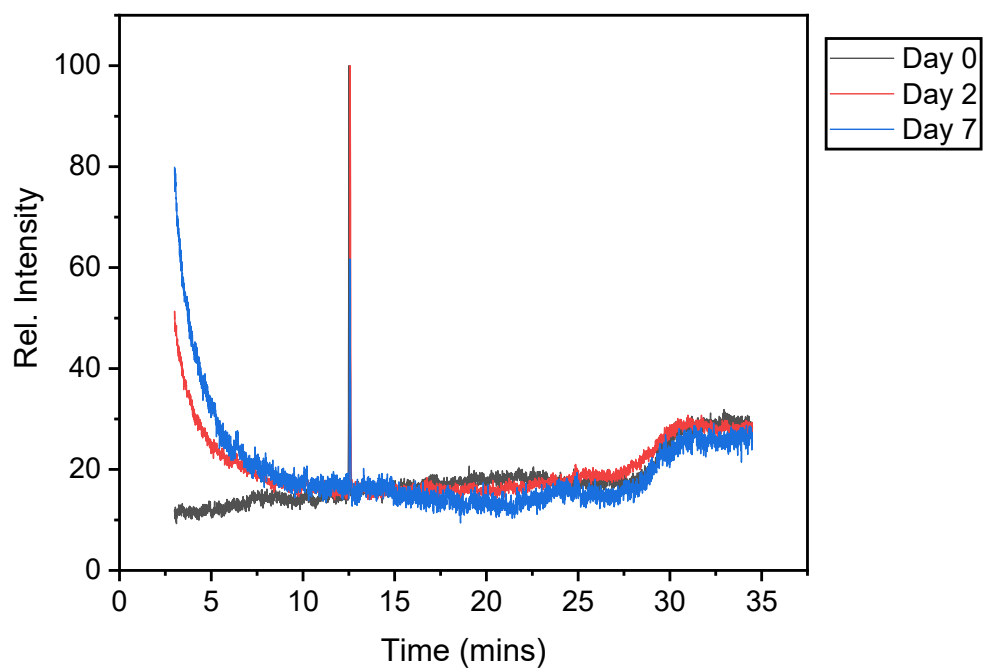


**Figure 5.16:** GCMS chromatograms of **5.8** over 7 days extracted from SMM.

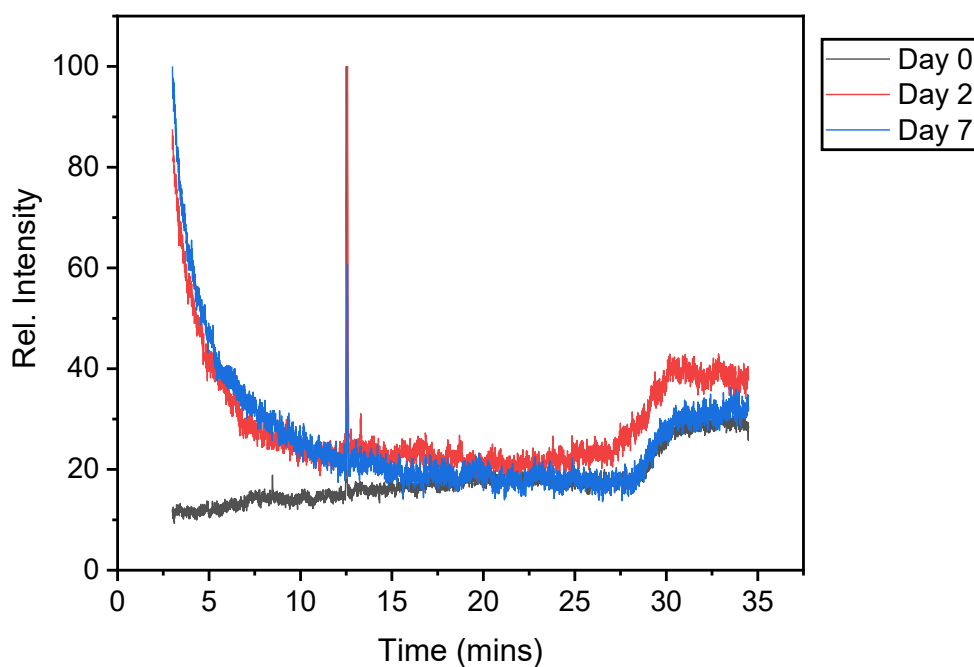
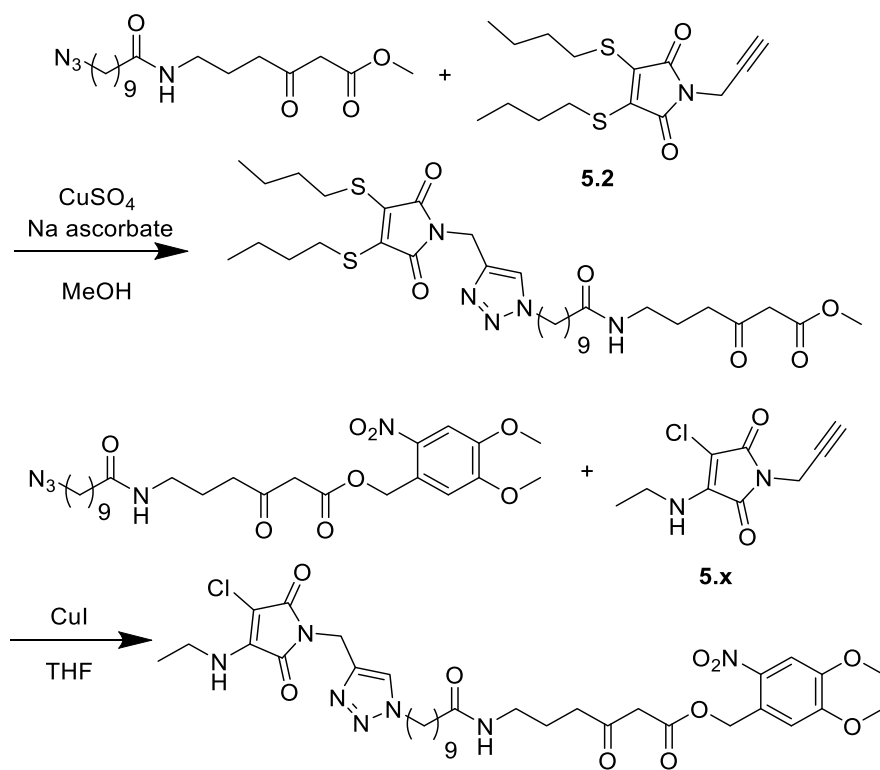


**Figure 5.17:** GCMS chromatograms of **5.8** over 7 days extracted from YEME.

With no identifiable impurities forming in any of the analytical techniques used for the study and dye integrity remaining under all conditions, it is concluded that the dye is highly suitable for use in enzyme trapping experiments. Not only do these results suggest the dye is a good candidate for this study, but this suggests that the dye will be suitable for other cellular expression applications such as those discussed in Chapter 4.

### 4.3.3 Evaluating the effectiveness of synthesized probes for detecting enzyme intermediates in natural product biosynthesis

Evaluation of the dyes for intermediate capture was completed by the Tosin group. Firstly, dyes were coupled to their azide functionalized intermediate probe through CuAAC (Scheme 5.6). This was completed by Dr Ina Wilkening for alkyne-DTM **5.2** and activated alkyne **5.13**, however, conversion was low for copper-free click of activated alkyne-DTM **5.13** and therefore only **5.2** was investigated. Alkyne-ACM **5.8** has also been successfully coupled (by Dr Rob Jenkins) to a photo-labile nitrobenzyl protected azide probe for *in vitro* studies (Scheme 5.6).



**Scheme 5.6:** Synthesized maleimide functionalized intermediate probes by the Tosin group, from alkyne dyes **5.2** (top) and **5.8** (bottom) using CuAAC.

To validate the use of the dye in a known system, the *in vivo* polyketide synthesis of 6-methylsalicylic acid (6-MSA) was investigated, the system previously studied by the Tosin group,<sup>1</sup> using the DTM functionalized probe **5.2**. Using this, probe the group were able to identify a putative off-loaded triketide

intermediate, through fragments observed by LCMS-MS (Figure 5.18). This intermediate is analogous to that observed using the standard probes, suggesting compatibility of the fluorophore with the *in vivo* system.

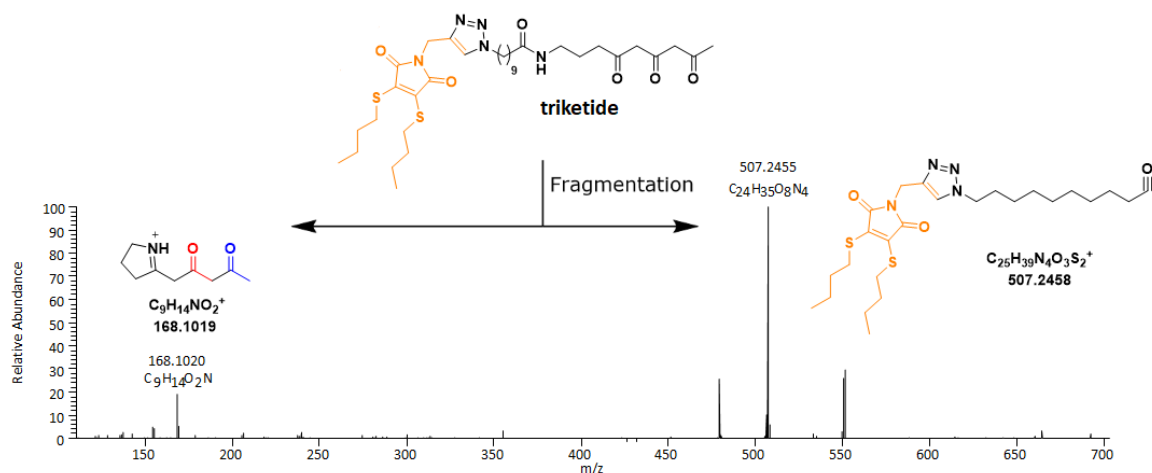


**Figure 5.18:** Proposed isolated intermediate and obtained mass spectrum in the probing of 6-MSA synthesis.

To help identify intact biosynthetic intermediates captured by the fluorescent probe, an *in vitro* system is under investigation using the ACM functionalized photolabile protected probe. Preliminary investigations were completed on an iterative type II polyketide synthetase. These were the biosynthesis of SEK4 and SEK4b using malonyl-CoA, ACP and KS-CLF protein (from *S. coelicolor*).<sup>21</sup> By substituting the malonyl-CoA with our probe we hope to capture intermediates in this synthesis. Panward Prasongpholchai from the Tosin group completed incubation of our ACM probe after photolysis with ACP and KS-CLF, and could identify a few promising putative intermediates, including a dehydrated pentaketide species (Figure 5.19). Work is ongoing into investigating this further, however, these initial results suggest the dye has promising compatibility with enzyme intermediate capturing. Future work may include studying the fluorescence lifetime when bound and unbound to enzymes, with the long term goal of studying kinetics of these processes.

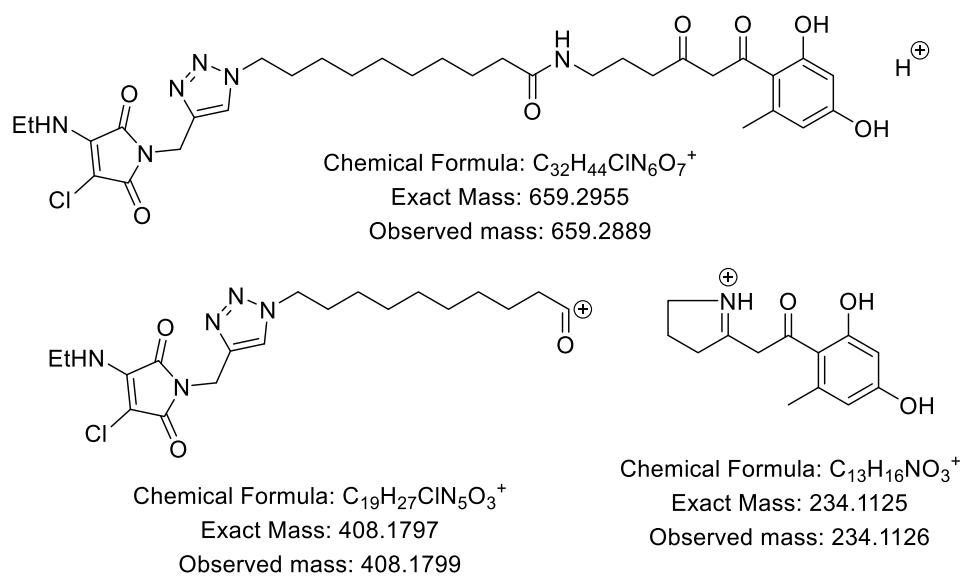


**Figure 5.19:** Three hypothesized species detected by MS-MS upon incubation of ACM probe with ACP and KS-CLF by the Tosin group.

## 4.4 Conclusions

This Chapter covers the application of maleimide fluorophores to the field of isolating enzyme intermediates, with the goal of increasing sensitivity and ease of isolation and identification of intermediates. Towards this aim alkyne functionalized maleimide have been synthesized for CuAAC coupling with azide functionalized probes developed by the Tosin group. Successful efficient coupling was observed for both the DTM and ACM alkynes, and the Tosin group had preliminary success in isolating offloaded intermediates using these coupled probes. To check for compatibility with enzymatic media, which are also relevant to *in vivo* expression of amino acids developed in Chapter 4, ACM alkyne was tested for degradation and stability in several cellular media: YEME, SMM, MYM and TSB. Fluorescence, HPLC and GCMS analysis all indicated complete compatibility with all broths under cellular incubation conditions, excluding an unusual fluorescence phenomenon observed during incubation in SMM, hypothesized to be a result of dye aggregation.



## 4.5 Experimental

### 4.5.1.1 Materials

All chemicals were obtained from either: Sigma Aldrich, Fisher Chemicals, Acros Chemicals, Carbosynth or Alfa Aesar and used as received. Sterilized growth mediums TSB, YEME, SMM and MYM were prepared and provided by Mr Rob Jenkins.

### 4.5.1.2 Instrumentation

NMR spectra were recorded on a Bruker Advance 300, a Bruker Advance III HD 400 or a Bruker Advance III HD 500 spectrometer at 300, 400 and 500 MHz respectively. Shifts are quoted in  $\delta$  in parts per million (ppm) and quoted relative to the internal standard trimethylsilane (TMS) or the solvent peak.

High Resolution Mass Spectra (HR-MS) were conducted by Dr Lijiang Song on a Bruker UHR-Q-ToF MaXis spectrometer with electrospray ionization.

Infrared spectra were recorded on neat samples using a Perkin Elmer Spectrum 100 FT-IR Spectrometer.

UV-Vis spectroscopy was carried out on a Perkin Elmer Lambda 35 UV/vis spectrometer or an Agilent Cary 60 UV-Vis Spectrometer at room temperature. Fluorescence emission and excitation spectrum were obtained with an Edinburgh Instruments FS5 Spectrofluorometer in quartz 3.5 mL cuvettes (Starna Cell, Type: 3/Q/10), and analyzed in Fluoracle (Edinburgh Instruments) and Origin 2019 (Origin Labs).

Reverse-phase high pressure liquid chromatography (HPLC) analysis was performed on a modular Shimadzu instrument with the following modules: CBM-20A system controller, LC-20AD solvent delivery module, SIL-20AC HT autosampler, CTO-20AC column oven, SPD-M20A photodiode array UV-Vis detector, RF-20A spectrofluorometric detector and a FRC-10 fraction collector (not

used). Chromatography was performed on a Shim-pack GISS 5  $\mu\text{m}$  C18 (4.6 $\times$ 125mm) reverse phase column heated at 30  $^{\circ}\text{C}$ . Flow rate was set at 0.8 mL/min and the products were eluted using a gradient of 18.2 M $\Omega\cdot\text{cm}$  water and acetonitrile. A typical elution gradient is shown in Figure 5.20.

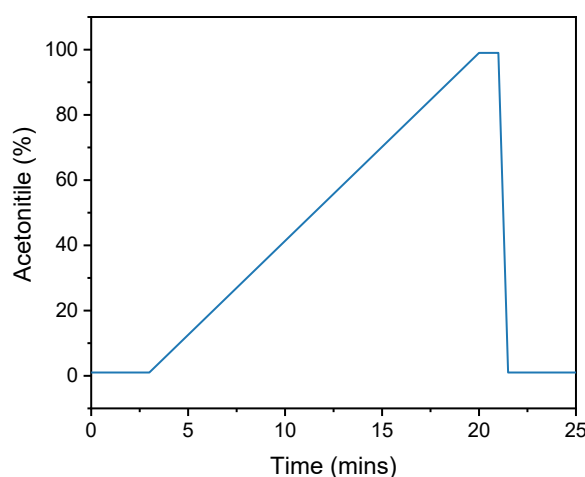


**Figure 5.20:** Elution gradient of water/acetonitrile used for dye incubation analysis by HPLC.

Gas chromatography-mass spectrometry (GCMS) was performed on a Shimadzu GCMS QP2010 SE system with a Zebron ZB-5HT Inferno $^{\circledR}$  column of 30 m length and 0.25 mm I.D. Samples were prepared by extraction from 5-10 mL of incubation solution 1:1 with  $\text{CH}_2\text{Cl}_2$ . The injector temperature was 350  $^{\circ}\text{C}$  with 1.0  $\mu\text{L}$  injection volume (splitless). The helium carrier gas flow rate was set at (20.6 mL/min), with a column flow rate of 1.6 mL/min. MS detection was used with selective ion scanning of 1.5-1000  $m/z$ . The typical temperature gradient for runs is shown in Figure 5.21, after one or two blank runs were completed before each batch to reset/clean the column.

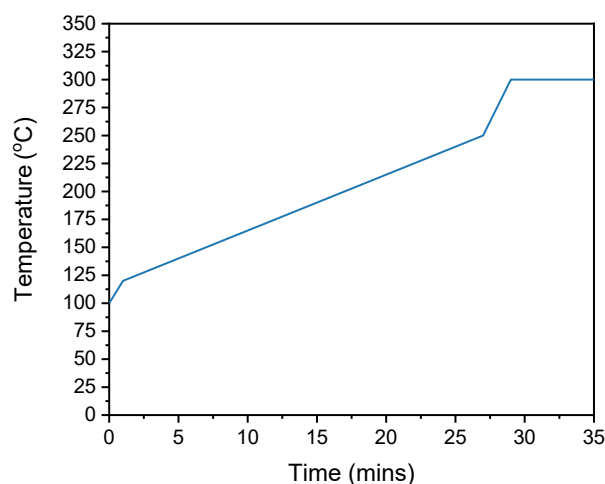


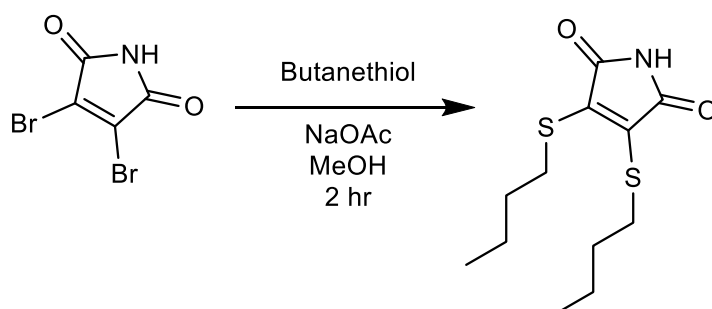
**Figure 5.21:** Temperature gradient used for GCMS runs of **5.8**.

#### 4.5.1.3 Dye incubation

Dyes were dissolved in 15 mL of either water or the sterilized broth at 0.5 mg/mL in 15 mL centrifuge tubes. These were placed in an incubator at 30 °C with 5% CO<sub>2</sub> supply. Aliquots of 1 mL were taken after time periods and diluted to 3 mL with water for fluorescence analysis. These were then extracted with 3 mL of CH<sub>2</sub>Cl<sub>2</sub> for GCMS analysis. 1 mL of this was dried *in vacuo* and re-solvated in 2 mL of 18.2 MΩ·cm water for HPLC analysis.

## 4.5.2 Small molecule synthesis

### 4.5.2.1 3,4-bis(butylthio)-1H-pyrrole-2,5-dione (5.1)



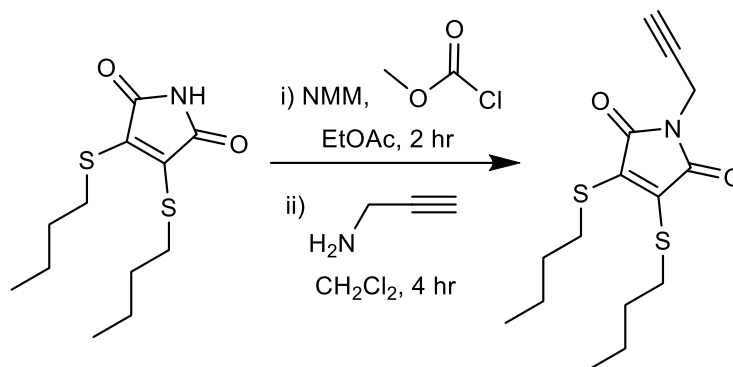
Dibromomaleimide (2 g, 7.8 mmol) was added to a round bottom flask containing a stirrer bar and 80 mL of methanol. To this NaOAc (1.4 g, 17.2 mmol) and secondly, butanethiol (1.58 g, 17.2 mmol) was added. The solution was stirred for 2 hours followed by removal of volatiles using evaporation. The obtained oil was purified by silica column chromatography in a petroleum ether and ethyl acetate gradient (0% EtOAc to 8%). The fractions containing product were dried *in vacuo* to yield yellow solid **5.1** (344 mg, 18%).

<sup>1</sup>H NMR (300 MHz, CDCl<sub>3</sub>, ppm)  $\delta$  = 3.29 (t, <sup>3</sup>J<sub>HH</sub> = 7.3 Hz, 2H, CH<sub>2</sub>), 1.73 – 1.61 (q, <sup>3</sup>J<sub>HH</sub> = 7.3 Hz, 2H, CH<sub>2</sub>), 1.45 (q, <sup>3</sup>J<sub>HH</sub> = 7.2 Hz, 2H, CH<sub>2</sub>), 0.93 (t, <sup>3</sup>J<sub>HH</sub> = 7.2 Hz, 3H, CH<sub>3</sub>)

<sup>13</sup>C NMR (75 MHz, CDCl<sub>3</sub>, ppm)  $\delta$  = 166.1 (CO), 136.7 (CS), 32.5 (CH<sub>2</sub>), 31.4 (CH<sub>2</sub>), 21.6 (CH<sub>2</sub>), 13.6 (CH<sub>3</sub>);

Matches literature data.<sup>22</sup>

#### 4.5.2.2 3,4-bis(butylthio)-1-(prop-2-yn-1-yl)-1H-pyrrole-2,5-dione (5.2)



This two-step procedure was based on a literature protocol.<sup>23</sup> Initially, compound **5.1** was dissolved into 20 mL of ethyl acetate in a round bottom flask with a stirrer bar. To this *N*-methyl morpholine (111 mg, 1.1 mmol) was added and secondly, methyl chloroformate (114 mg, 1.2 mmol). Immediate precipitation of a solid was noted, along with a purple color appearing. This was left to stir for 2 hours, followed by washing with water and brine three times. The organic layer was dried *in vacuo* and was used directly for the next step.

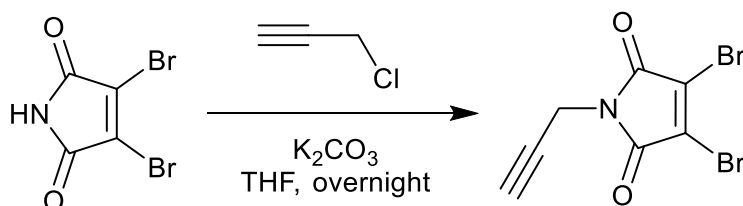
Next, this intermediate was added to a round bottom flask containing a stirrer bar and 40 mL of  $\text{CHCl}_3$ . To this propylamine (96.6  $\mu\text{L}$ , 1.5 mmol) was added slowly. This was left to stir for 4 hours and then directly loaded onto silica. This was purified by silica column chromatography using a petroleum ether and ethyl acetate gradient (0% EtOAc to 10%). This was dried *in vacuo* to yield a yellow solid **5.2** (387 mg, 85%).

$^1\text{H}$  NMR (400 MHz,  $\text{CDCl}_3$ , ppm)  $\delta$  = 4.27 (t,  $^4J_{\text{HH}}$  = 2.1 Hz, 2H,  $\text{CH}_2$ ), 3.41 – 3.22 (t,  $^3J_{\text{HH}}$  = 7.3 Hz 2H,  $\text{CH}_2$ ), 2.22 (s,  $^4J_{\text{HH}}$  = 2.0 Hz, 1H, CH), 1.64 (p,  $^3J_{\text{HH}}$  = 7.4 Hz, 2H,  $\text{CH}_2$ ), 1.52 – 1.38 (m, 2H,  $\text{CH}_2$ ), 0.93 (t,  $^3J_{\text{HH}}$  = 7.3 Hz, 3H,  $\text{CH}_3$ ).

$^{13}\text{C}$  NMR (101 MHz,  $\text{CDCl}_3$ , ppm)  $\delta$  = 165.3 (CO), 136.0 (CS), 71.5 (CH), 32.5 ( $\text{CH}_2$ ), 31.6 ( $\text{CH}_2$ ), 27.5 ( $\text{CH}_2$ ), 21.7 ( $\text{CH}_2$ ), 13.6 ( $\text{CH}_3$ )

Matches literature data.<sup>23</sup>

4.5.2.3 3,4-dibromo-1-(prop-2-yn-1-yl)-1H-pyrrole-2,5-dione (5.3)



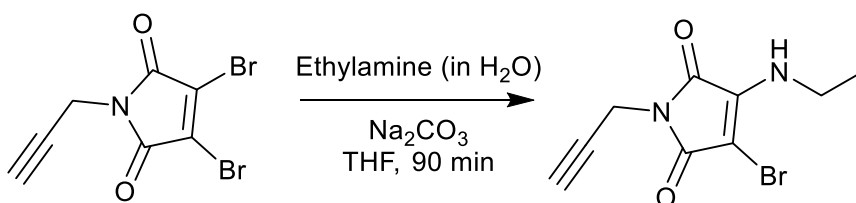
Dibromomaleimide (1 g, 3.9 mmol) was added to a round bottom flask containing a stirrer bar and 10 mL of THF. To this  $K_2CO_3$  (0.59 g, 4.3 mmol) was added and the solution stirred. Finally, propargyl chloride (80 % in THF – 410  $\mu$ L, 4.3 mmol) was added dropwise to the solution and this was left overnight. This was filtered and then dried *in vacuo* to yield solid **5.3** (360 mg, 32 %).

$^1H$  NMR (400 MHz,  $CDCl_3$ , ppm)  $\delta$  = 4.38 (d,  $^4J_{HH}$  = 2.5 Hz, 2H,  $CH_2$ ), 2.27 (t,  $^4J_{HH}$  = 2.5 Hz, 1H,  $CH$ ).

$^{13}C$  NMR (101 MHz,  $CDCl_3$ , ppm)  $\delta$  = 162.6 (CO), 129.81 (CBr), 76.05 (C), 72.57 (CH), 28.59 ( $CH_2$ ).

Matches literature data.<sup>24</sup>

4.5.2.4 3-bromo-4-(ethylamino)-1-(prop-2-yn-1-yl)-1H-pyrrole-2,5-dione (5.4)



Initially, compound **5.3** (300 mg, 1 mmol) was dissolved in THF (20 mL). To this  $Na_2CO_3$  was added (265 mg, 2.5 mmol) followed by ethylamine solution (68 % in  $H_2O$  – 47  $\mu$ L, 1.05 mmol), after which a color change from clear to yellow

was observed. After 90 mins of stirring the solution, it was filtered to remove base and then dried *in vacuo*. This solid was washed with  $\text{CHCl}_3$  and water three times and then dried with addition and filtration of  $\text{MgSO}_4$ . This solid was purified by column chromatography using a 10 : 1 petroleum spirits : ethyl acetate eluent. The product was dried *in vacuo* to yield yellow solid **5.4** (201 mg, 78%).

$^1\text{H}$  NMR (500 MHz,  $\text{CDCl}_3$ , ppm)  $\delta$  = 4.28 (d,  $^4J_{\text{HH}}$  = 2.5 Hz, 2H), 3.71 (p,  $^3J_{\text{HH}}$  = 7.2 Hz, 2H), 2.22 (t,  $^4J_{\text{HH}}$  = 2.5 Hz, 1H), 1.32 (t,  $^3J_{\text{HH}}$  = 7.2 Hz, 3H).

$^{13}\text{C}$  NMR (126 MHz,  $\text{CDCl}_3$ , ppm)  $\delta$  = 166.3 (CO), 165.0 (CO), 143.4 (CN), 71.6 ( $\text{CH}_2$ ), 38.2 ( $\text{CH}_2$ ), 27.5 (CH), 16.0 ( $\text{CH}_3$ ).

MS (ESI) -  $[\text{M}+\text{H}^+]$  – calculated m/z 280.0 observed m/z 279.9;

FTIR ( $\text{cm}^{-1}$ ) – 3333 ( $\nu_{\text{C-H}}$ ), 2977 ( $\nu_{\text{C-H}}$ ), 2130 ( $\nu_{\text{C}\equiv\text{C}}$ ), 1706 ( $\nu_{\text{C=O}}$ ), 1643 ( $\nu_{\text{C=O}}$ ).

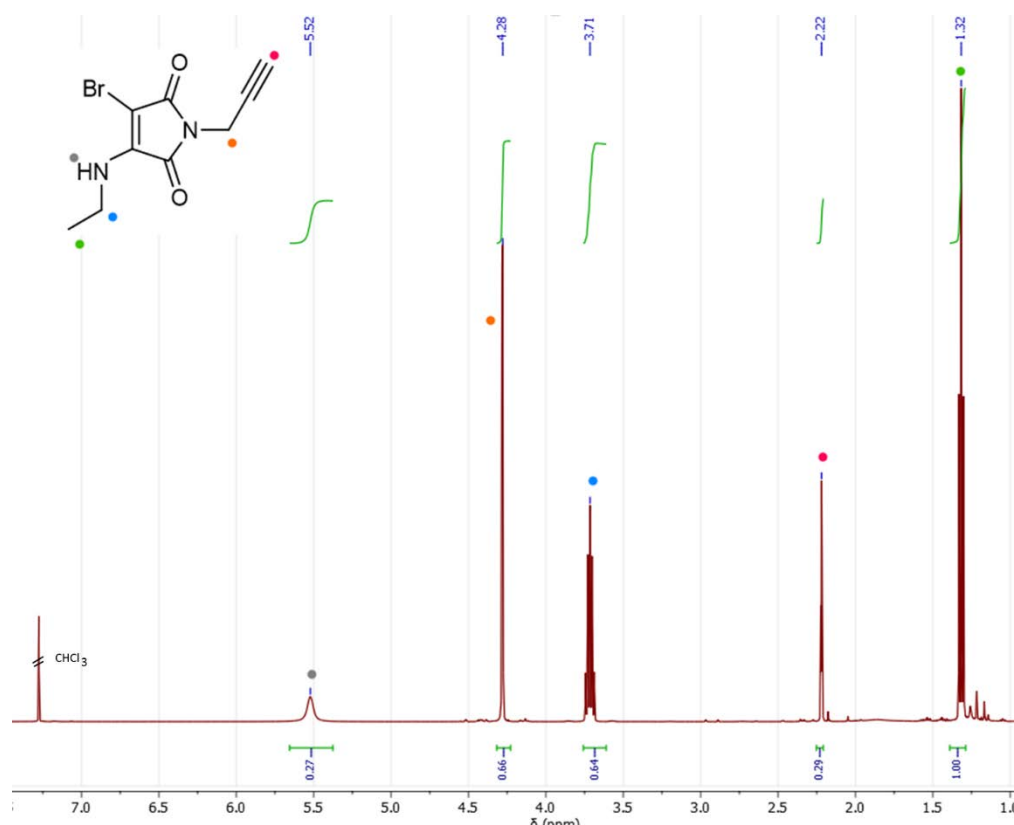


**Figure 5.22:**  $^1\text{H}$  NMR spectrum of **5.4**

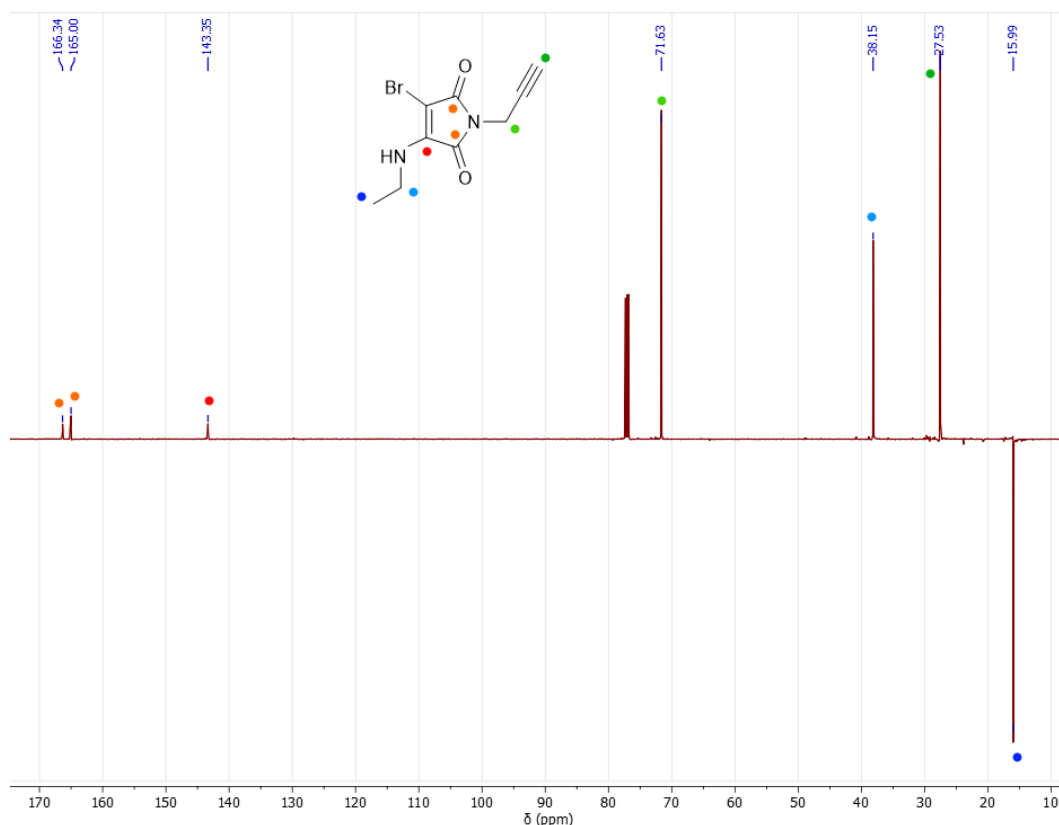
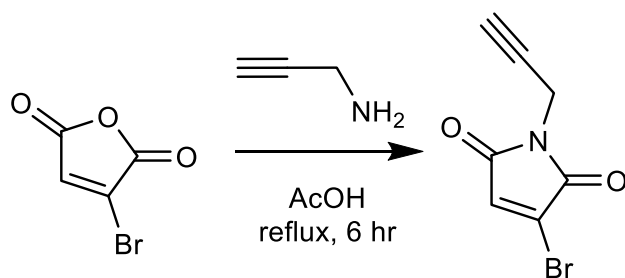


**Figure 5.23:**  $^{13}\text{C}$  NMR spectrum of **5.4**

#### 4.5.2.5 3-bromo-1-(prop-2-yn-1-yl)-1H-pyrrole-2,5-dione (**5.5**)



Propargyl amine (0.16 mL, 2.3 mmol) was added slowly to a stirred solution of bromomaleicanhydride (1.2 g, 6.9 mmol) in acetic acid (15 mL). This was then heated to reflux for 6 hours, after which solvent was removed *in vacuo* with the aid of toluene azeotrope. The dried crude solid purified by column chromatography using a 100%  $\text{CH}_2\text{Cl}_2$  eluent. This was dried *in vacuo* to yield yellow solid **5.5** (1.13 g, 78%).

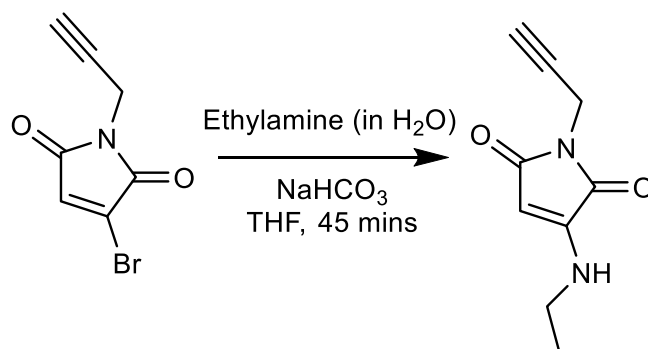


$^1\text{H}$  NMR (300 MHz,  $\text{CDCl}_3$ , ppm)  $\delta$  = 6.93 (s, 1H), 4.34 (d,  $^4J_{\text{HH}}$  = 2.5 Hz, 2H), 2.24 (t,  $^4J_{\text{HH}}$  = 2.5 Hz, 1H).

$^{13}\text{C}$  NMR (101 MHz,  $\text{CDCl}_3$ , ppm)  $\delta$  = 167.0 (CO), 164.0 (CO), 132.2 (CH), 131.7 (CBr), 76.8 (C), 72.0 (CH), 27.7 ( $\text{CH}_2$ )

Matches literature data.<sup>25</sup>

#### 4.5.2.6 3-ethylamino-1-(prop-2-yn-1-yl)-1H-pyrrole-2,5-dione (5.6)



Compound **5.5** (0.5 g, 2.3 mmol) was dissolved in 50 mL of THF in a round bottom flask with a stirrer bar. To this  $\text{NaHCO}_3$  was added (210 mg, 4.1 mmol) followed by ethylamine solution (68 % in  $\text{H}_2\text{O}$  – 110  $\mu\text{L}$ , 12.3 mmol), after which a color change from clear to yellow was observed immediately. After 45 mins this reaction was filtered and then dried *in vacuo*. The crude solid was purified by silica column chromatography with a  $\text{CH}_2\text{Cl}_2$ /petroleum ether eluent (75%  $\text{CH}_2\text{Cl}_2$ ). This was dried *in vacuo* to afford yellow solid **5.6** (104 mg, 75%).

$^1\text{H}$  NMR (300 MHz,  $\text{CDCl}_3$ , ppm)  $\delta$  = 5.35 (br, 1H, NH), 4.86 (s, 1H, CH), 4.25 (d,  $^4J_{\text{HH}}$  = 2.5 Hz, 2H,  $\text{CH}_2$ ), 3.24 (m, 2H,  $\text{CH}_2$ ), 2.19 (t,  $^4J_{\text{HH}}$  = 2.5 Hz, 1H, CH), 1.29 (t,  $^3J_{\text{HH}}$  = 7.3 Hz, 3H,  $\text{CH}_3$ ).

$^{13}\text{C}$  NMR (101 MHz,  $\text{CDCl}_3$ , ppm)  $\delta$  = 170.8 (CO), 166.5 (CO), 149.3 (CN), 84.4 (CH), 77.6 (C), 71.1 (CH), 39.1 ( $\text{CH}_2$ ), 26.5 ( $\text{CH}_2$ ), 13.7 ( $\text{CH}_3$ ).

HR-MS (Xevo) -  $[\text{M}+\text{H}^+]$  – calculated m/z 179.0821 observed m/z 179.0820;

FTIR ( $\text{cm}^{-1}$ ) – 3300 ( $\nu_{\text{C-H}}$ ), 2977( $\nu_{\text{C-H}}$ ), 2131 ( $\nu_{\text{C}\equiv\text{C}}$ ), 1704 ( $\nu_{\text{C=O}}$ ), 1644 ( $\nu_{\text{C=O}}$ ).

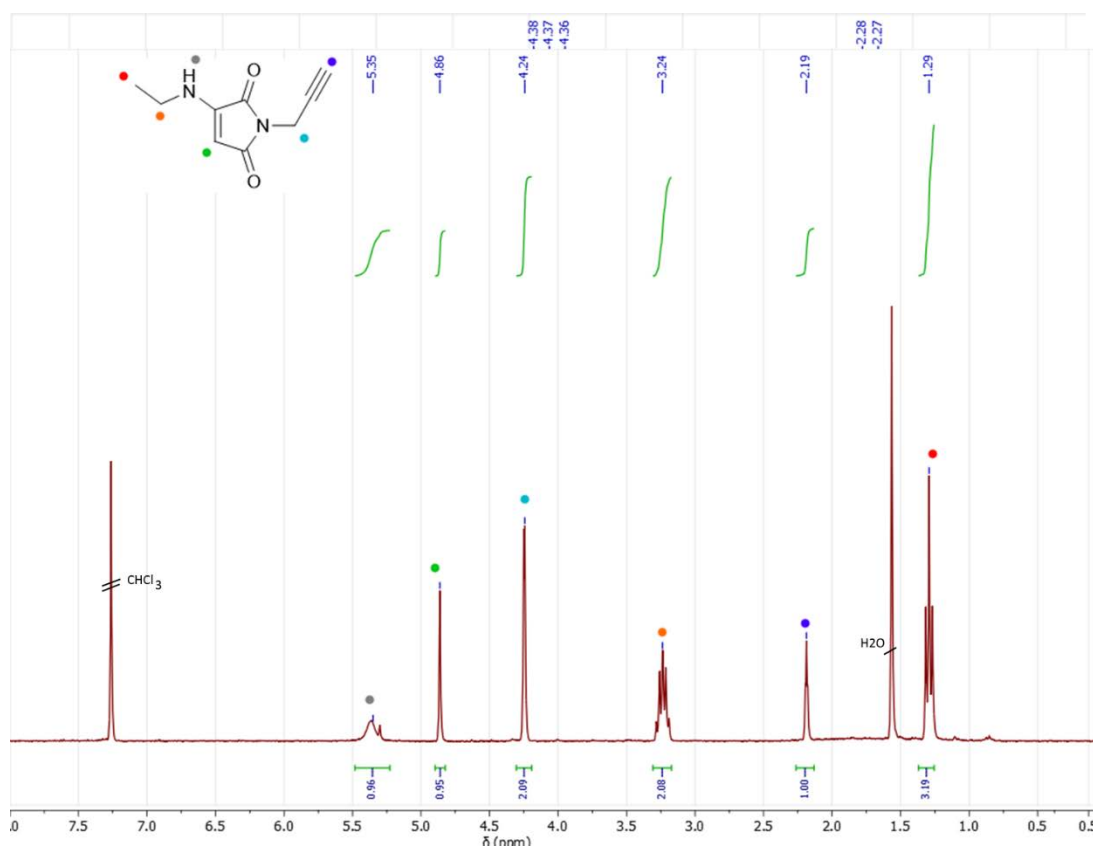


**Figure 5.24:**  $^1\text{H}$  NMR spectrum of **5.6**

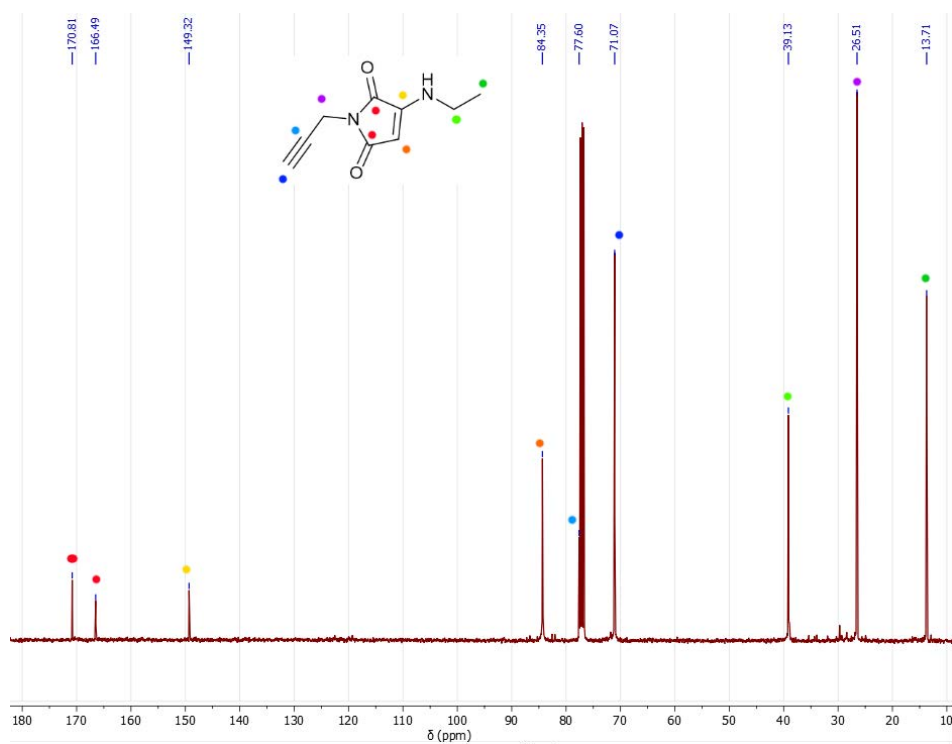
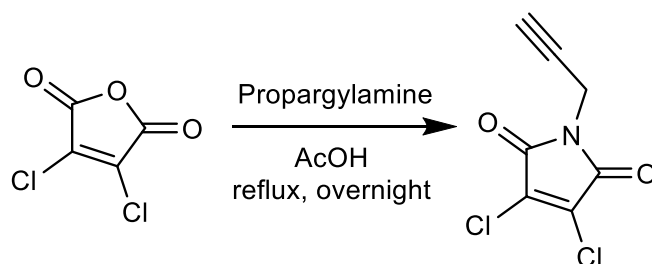


**Figure 5.25:**  $^{13}\text{C}$  NMR spectrum of **5.6**

#### 4.5.2.7 3-bromo-1-(prop-2-yn-1-yl)-1H-pyrrole-2,5-dione (5.7)



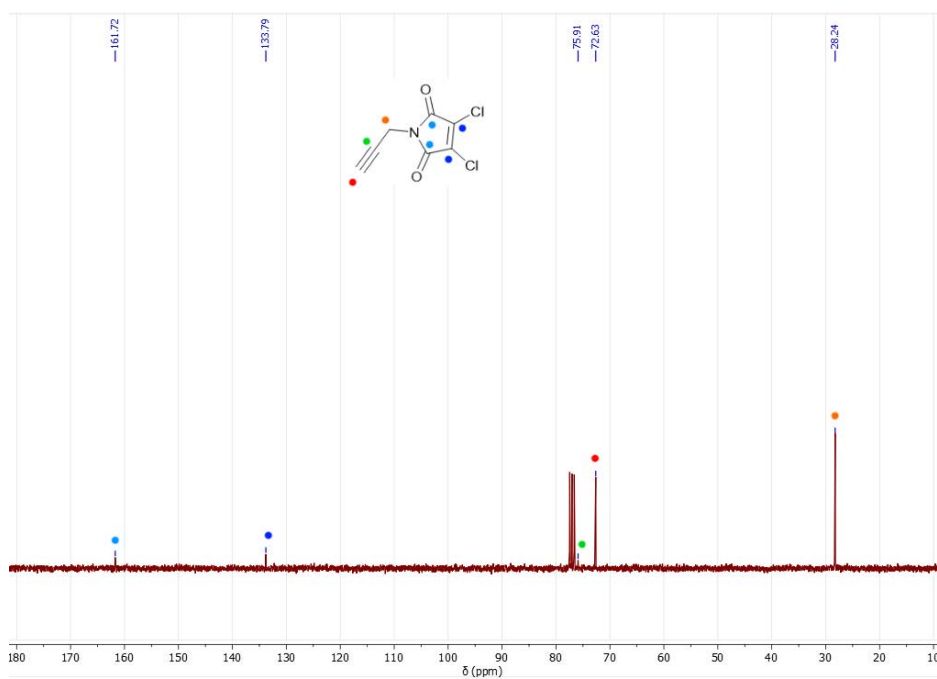
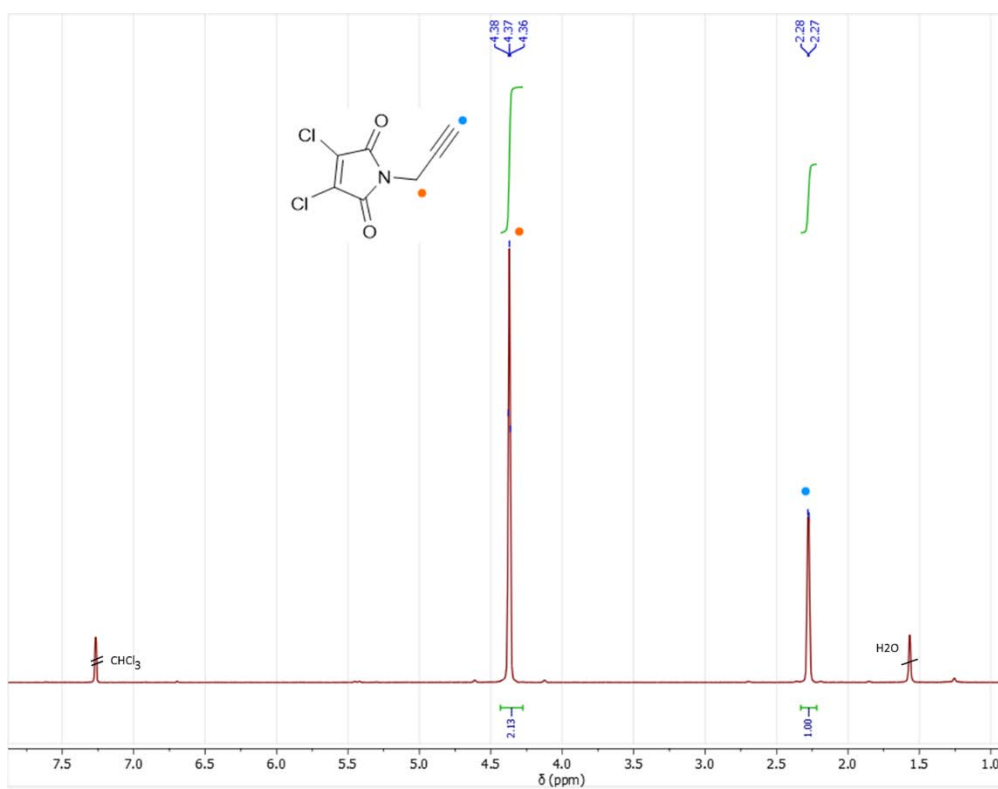
To a solution of acetic acid (15 mL) was added dichloromaleic anhydride (1 g, 6.1 mmol) and a stirrer bar. To this propargylamine (390  $\mu$ l, 6.1 mmol) was added and the solution was heated to reflux overnight, attached to a condenser. After this, the dark solution was dried *in vacuo* with the aid of toluene azeotrope. This solid was purified by column chromatography using a 1 : 2 petroleum spirits : ethyl acetate eluent. The product was dried *in vacuo* to yield yellow solid **5.7** (723 mg, 60%).

$^1\text{H}$  NMR (300 MHz,  $\text{CDCl}_3$ , ppm)  $\delta$  = 4.37 (t,  $^4J_{\text{HH}}$  = 2.3 Hz, 2H), 2.28 (d,  $^4J_{\text{HH}}$  = 2.4 Hz, 1H).

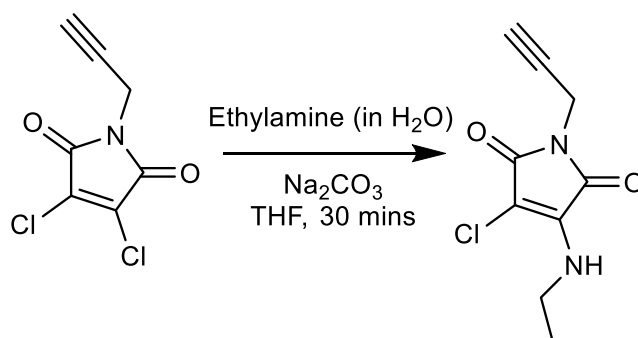
$^{13}\text{C}$  NMR (101 MHz,  $\text{CDCl}_3$ , ppm)  $\delta$  = 161.7 (CO), 133.8 (CCl), 75.91 (C), 72.63 (CH), 28.24 ( $\text{CH}_2$ ).

HR-MS (Xevo) -  $[\text{M}+\text{H}^+]$  – calculated m/z 203.9619 observed m/z 203.9625;

FTIR ( $\text{cm}^{-1}$ ) –3254 ( $\nu_{\text{C-H}}$ ), 2130 ( $\nu_{\text{C}\equiv\text{C}}$ ), 1704 ( $\nu_{\text{C=O}}$ ), 1664 ( $\nu_{\text{C=O}}$ ).



**4.5.2.8** 3-chloro-4-(ethylamino)-1-(prop-2-yn-1-yl)-1H-pyrrole-2,5-dione (**5.8**)



To start, compound **5.7** (500 mg, 2.5 mmol) was dissolved in THF (20 mL). To this Na<sub>2</sub>CO<sub>3</sub> was added (530 mg, 5 mmol) followed by ethylamine solution (68 % in H<sub>2</sub>O – 140 µL, 2.5 mmol), on which a colour change from clear to yellow was observed. After 30 mins of stirring the solution, it was filtered to remove base and then dried *in vacuo*. This solid was purified by column chromatography using a 10 : 1 petroleum spirits : ethyl acetate eluent. This was dried *in vacuo* to yield yellow solid **5.8** (197 mg, 40%).

<sup>1</sup>H NMR (300 MHz, CDCl<sub>3</sub>, ppm) δ = 5.35 (br, 1H, NH), 4.27 (d, <sup>4</sup>J<sub>HH</sub> = 2.5 Hz, 2H, CH<sub>2</sub>), 3.68 (p, <sup>3</sup>J<sub>HH</sub> = 7.1 Hz, 2H, CH<sub>2</sub>), 2.21 (t, <sup>4</sup>J<sub>HH</sub> = 2.5 Hz, 1H, CH), 1.31 (t, <sup>3</sup>J<sub>HH</sub> = 7.2 Hz, 3H, CH<sub>3</sub>).

<sup>13</sup>C NMR (126 MHz, CDCl<sub>3</sub>, ppm) δ = 166.3 (CO), 164.6 (CO), 140.6 (CN), 71.6 (CH), 38.2 (CH<sub>2</sub>), 27.3 (CH<sub>2</sub>), 16.1 (CH<sub>3</sub>).

HR-MS (Xevo) - [M+H<sup>+</sup>] – calculated m/z 213.0431 observed m/z 213.0433;

FTIR (cm<sup>-1</sup>) – 3249 (ν<sub>C-H</sub>), 2119 (ν<sub>C≡C</sub>), 1705 (ν<sub>C=O</sub>), 1688 (ν<sub>C=O</sub>)

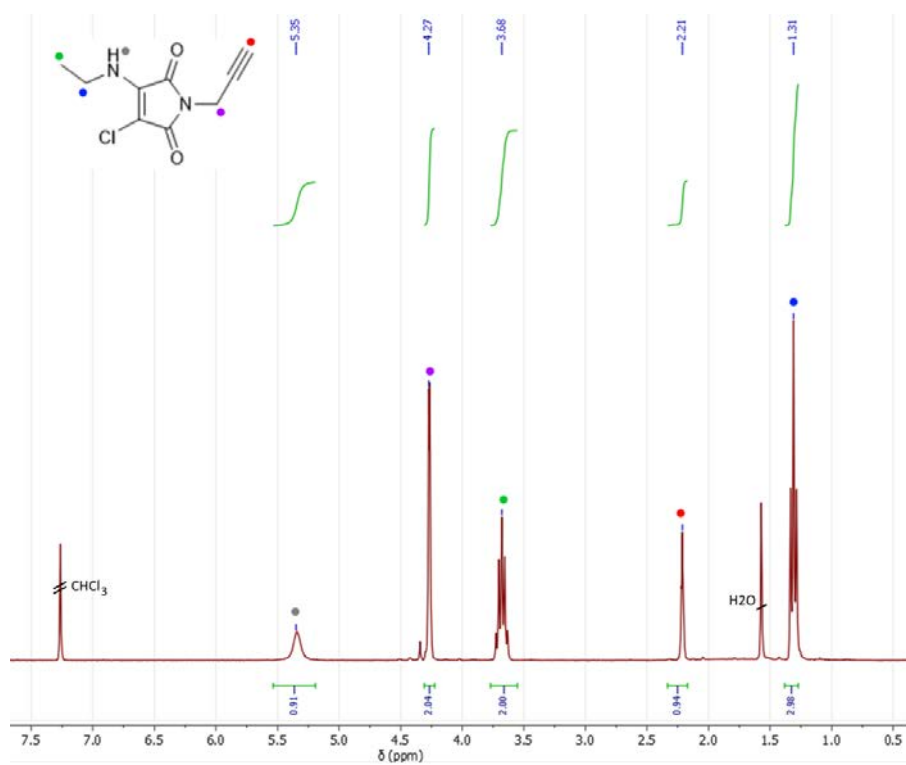


**Figure 5.28:** <sup>1</sup>H NMR spectrum of **5.8**

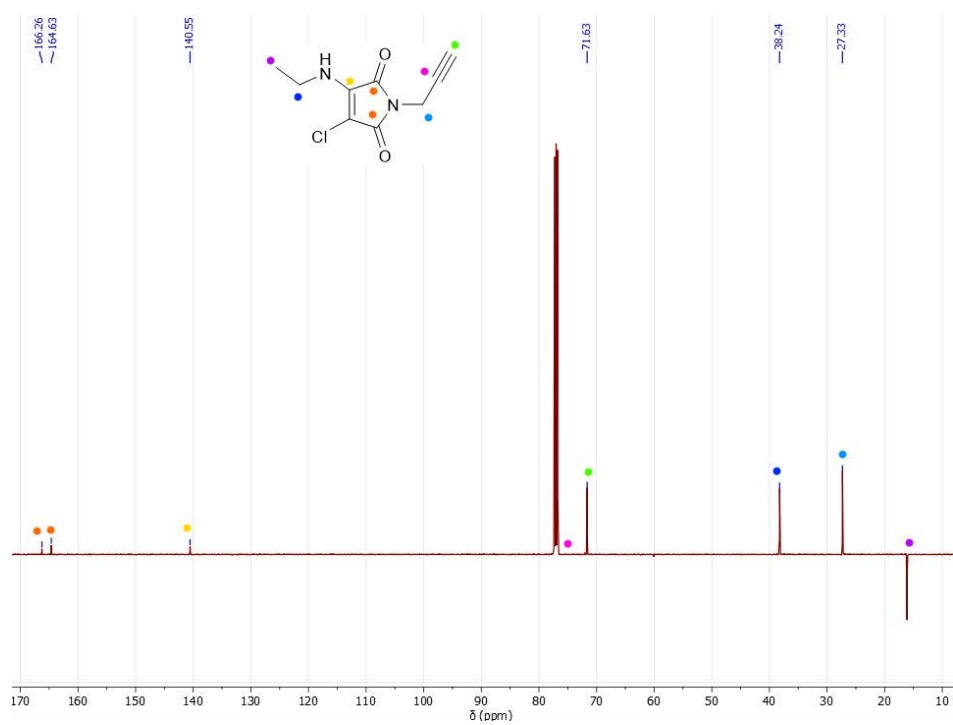
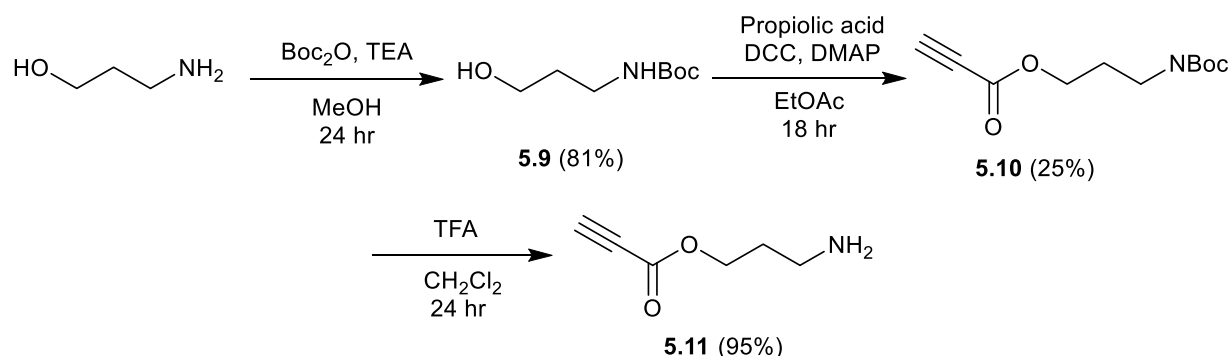


**Figure 5.29:** <sup>13</sup>C NMR spectrum of **5.8**

#### 4.5.2.9 3-aminopropyl propiolate (5.11)



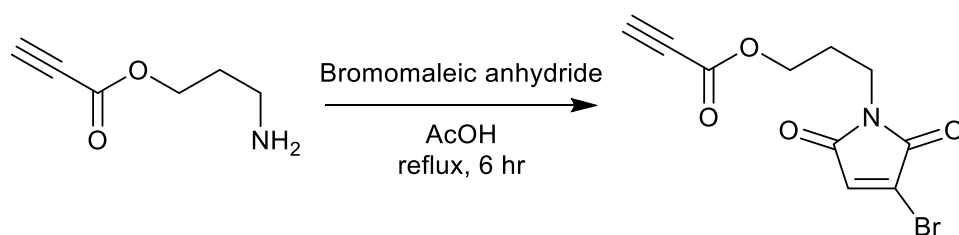
The synthesis of alkyne **5.11** was completed as previously reported, over 3 steps with no alterations to the procedure. The final product contained a residual amount of methanol.<sup>15</sup>

$^1\text{H}$  NMR (300 MHz,  $\text{CDCl}_3$ , ppm)  $\delta$  = 4.26 (t,  $^3J_{\text{HH}}$  = 5.9 Hz, 2H), 3.22 (q,  $^3J_{\text{HH}}$  = 6.0 Hz, 2H), 2.89 (s, 1H), 1.89 (q,  $^3J_{\text{HH}}$  = 6.0 Hz, 2H), 1.44 (s, 9H).

MS (ESI)  $[\text{M}+\text{H}^+]$  calculated  $m/z$  127.1 observed  $m/z$  127.1

Matches literature data.<sup>15</sup>

#### 4.5.2.10 3-(3-bromo-2,5-dioxo-2,5-dihydro-1H-pyrrol-1-yl)propyl propiolate (5.12)



Bromomaleic anhydride (**2.4**, 1.2 g, 6.9 mmol) was dissolved into 15 mL of acetic acid in a round bottom flask with stirrer bar. To this compound **5.11** (0.95 g, 7.1 mmol) was added and the mixture was stirred and heated to reflux (117 °C) for 6 hours. This was dried *in vacuo* to yield a crude oil which was purified by silica

column chromatography in  $\text{CHCl}_3$ . This was dried *in vacuo* to afford yellow solid **5.12** (477 mg, 25%).

$^1\text{H}$  NMR (400 MHz,  $\text{CDCl}_3$ , ppm)  $\delta$  = 6.89 (s, 1H, CH), 4.21 (t,  $^3J_{\text{HH}}$  = 6.1 Hz, 2H,  $\text{CH}_2$ ), 3.71 (t,  $^3J_{\text{HH}}$  = 6.8 Hz, 2H,  $\text{CH}_2$ ), 2.90 (s, 1H, CH), 2.02 (m, 2H,  $\text{CH}_2$ ).

$^{13}\text{C}$  NMR (126 MHz,  $\text{CDCl}_3$ , ppm)  $\delta$  = 168.4 (CO), 165.3 (CO), 152.4 (COO), 131.9 (CH), 131.5 (CBr), 75.1 (C), 74.4 (CH), 63.5 ( $\text{CH}_2$ ), 35.9 ( $\text{CH}_2$ ), 27.2 ( $\text{CH}_2$ ).

HR-MS (maXis) -  $[\text{M}+\text{H}^+]$  - calculated  $m/z$  307.9527 observed  $m/z$  307.9529;

FTIR - 3245 ( $\nu_{\text{C-H}}$ ), 2115 ( $\nu_{\text{C}\equiv\text{C}}$ ), 1703 ( $\nu_{\text{C=O}}$ ),

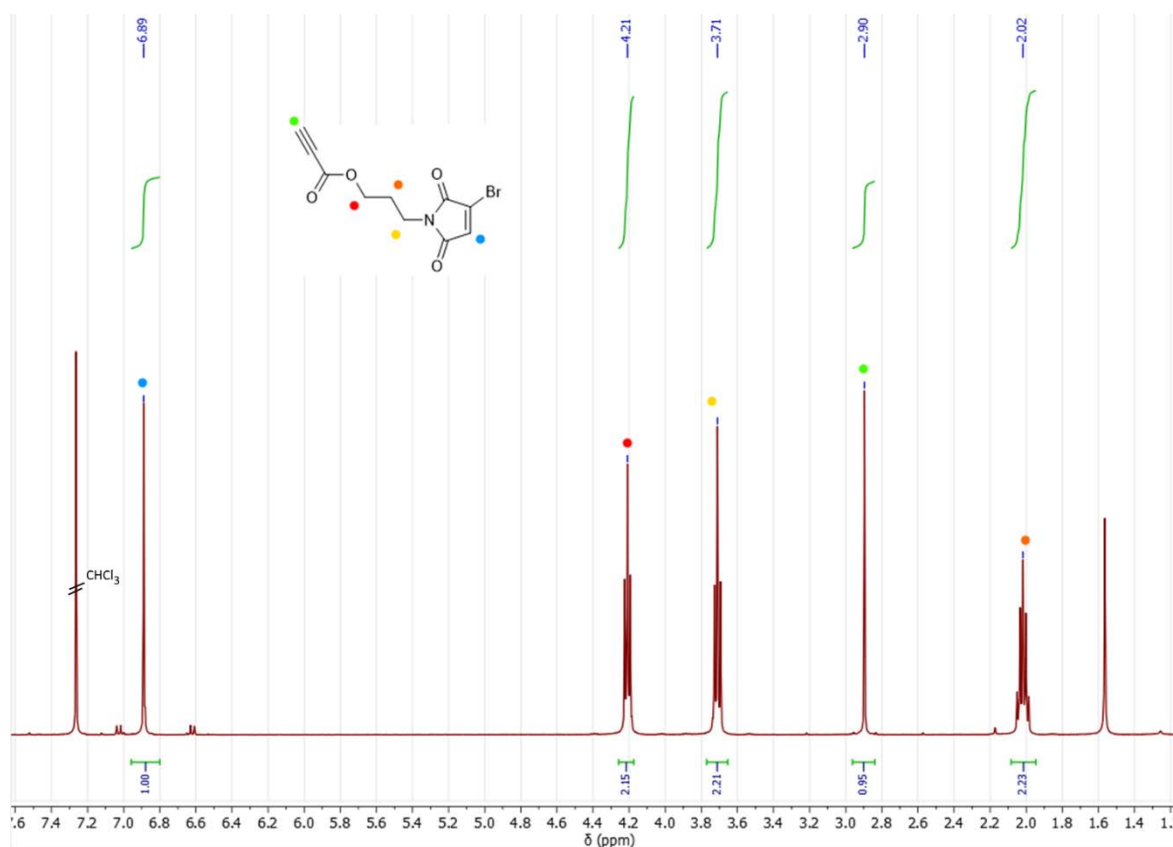


**Figure 5.30:**  $^1\text{H}$  NMR spectrum of **5.12**



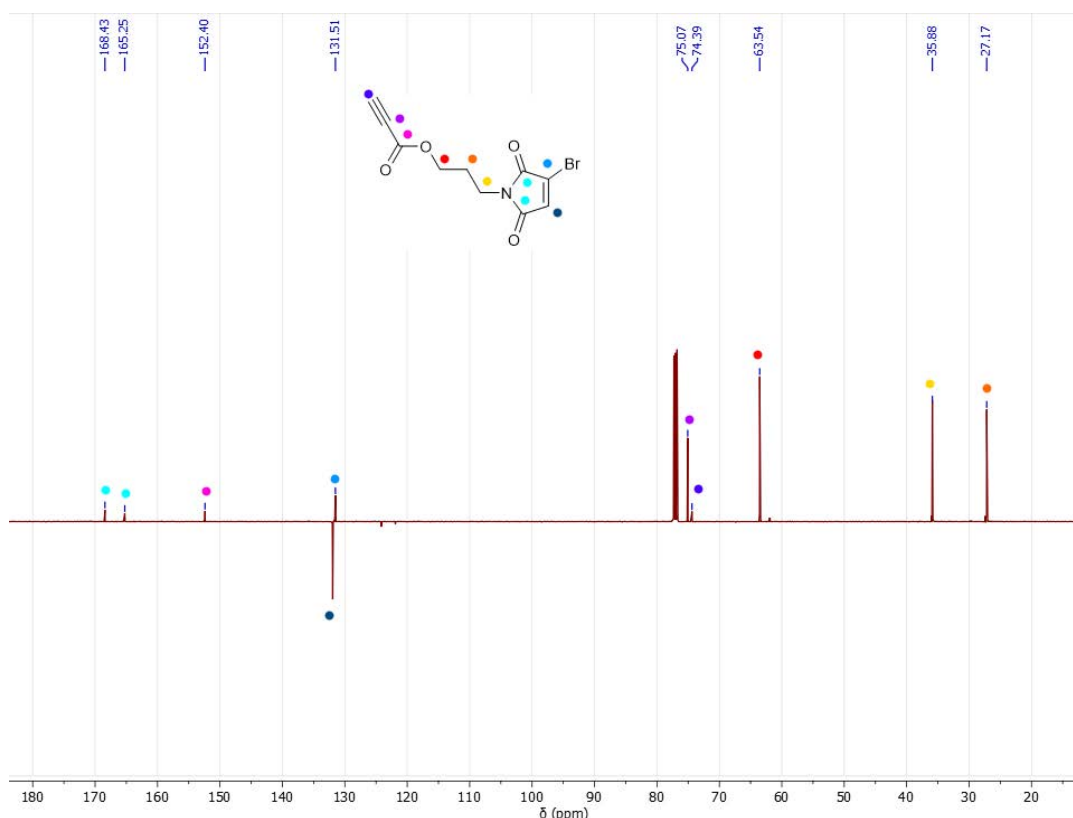
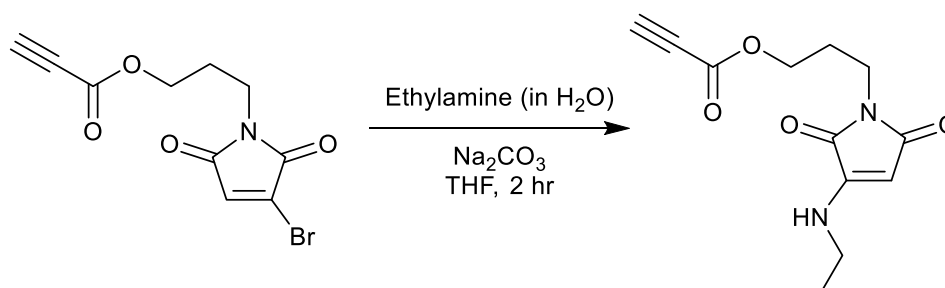


**Figure 5.31:**  $^{13}\text{C}$  NMR spectrum of **5.12**

#### 4.5.2.11 3-(3-(ethylamino)-2,5-dioxo-2,5-dihydro-1H-pyrrol-1-yl)propyl propiolate (**5.13**)



Firstly, ethylamine solution (68% in water, 120  $\mu\text{L}$ , 1.4 mmol) was added to a round bottom flask containing THF (20 mL) and a stirrer bar. To this  $\text{Na}_2\text{CO}_3$  (3.5 mmol, 280 mg) was added followed by alkyne **5.12** (400 mg, 1.4 mmol). This was left for two hours, after which it was filtered to remove base and dried *in vacuo*. The crude solid was purified by silica column chromatography in  $\text{CHCl}_2$ . This was dried *in vacuo* to afford yellow solid **5.13** (145 mg, 41%) which contained

a residual impurity (<5% by  $^1\text{H}$  NMR), however would hypothetically not affect the next coupling step.

$^1\text{H}$  NMR (500 MHz,  $\text{CDCl}_3$ , ppm)  $\delta$  = 5.35 (br t, 1H, NH), 4.81 (s, 1H, CH), 4.19 (t,  $^3J_{\text{HH}}$  = 6.3 Hz, 2H,  $\text{CH}_2$ ), 3.60 (t,  $^3J_{\text{HH}}$  = 6.7 Hz, 2H,  $\text{CH}_2$ ), 3.23 (dt,  $^3J_{\text{HH}}$  = 7.3 Hz, 6.9 Hz, 2H,  $\text{CH}_2$ ), 2.88 (s, 1H), 1.99 (p,  $^3J_{\text{HH}}$  = 6.5 Hz, 2H,  $\text{CH}_2$ ), 1.29 (t,  $^3J_{\text{HH}}$  = 7.3 Hz, 3H,  $\text{CH}_3$ ).

$^{13}\text{C}$  NMR (126 MHz,  $\text{CDCl}_3$ , ppm)  $\delta$  = 172.25 (CO), 167.48 (CO), 152.61 (COO), 149.06 (CH), 84.07 (CN), 74.77 (CH), 74.59 (CC), 63.68 ( $\text{CH}_2$ ), 39.06 ( $\text{CH}_2$ ), 34.28 ( $\text{CH}_2$ ), 27.57 ( $\text{CH}_2$ ), 13.77 ( $\text{CH}_2$ ).

HR-MS (maXis) -  $[\text{M}+\text{H}^+]$  – calculated m/z 250.1032 observed m/z 250.1033;

FTIR – 3326 ( $\nu_{\text{C-H}}$ ), 2108 ( $\nu_{\text{C}\equiv\text{C}}$ ), 1715 ( $\nu_{\text{C=O}}$ ), 1664 ( $\nu_{\text{C=O}}$ ),

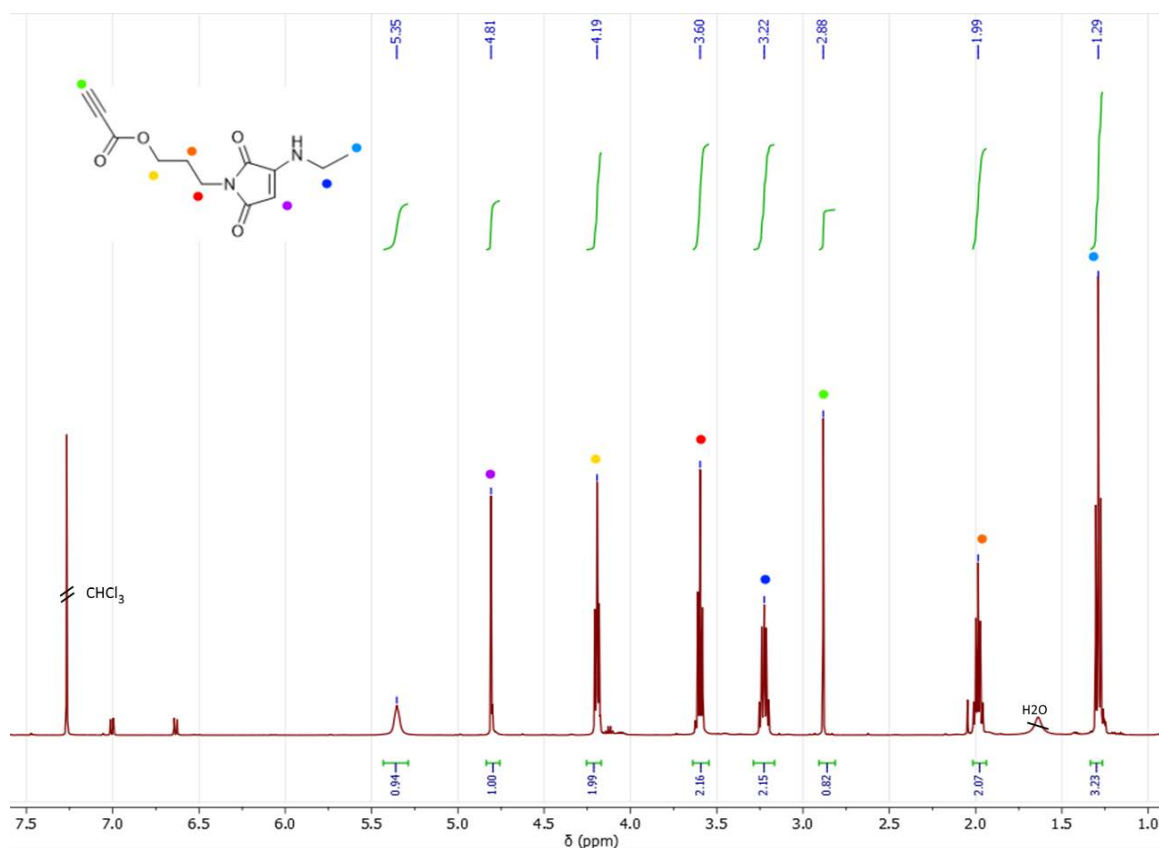


**Figure 5.31:**  $^1\text{H}$  NMR spectrum of **5.13**

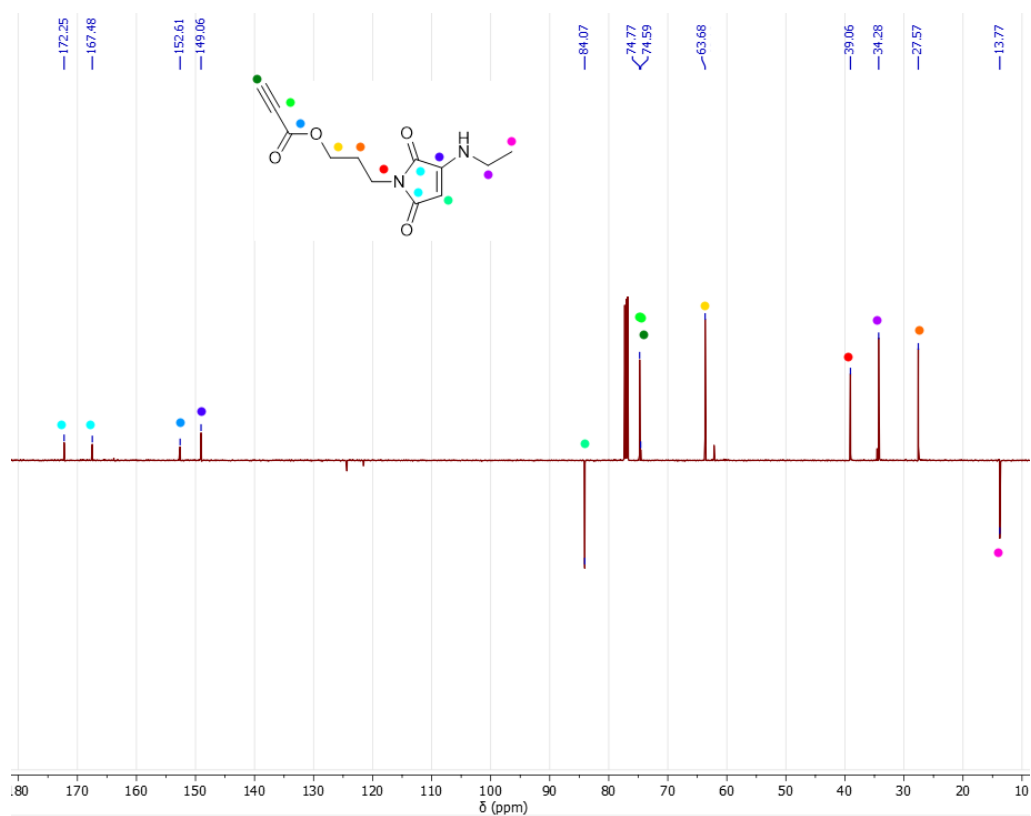


**Figure 5.33:** <sup>13</sup>C NMR spectrum of **5.13**

## 4.6 References

- (1) Wilkening, I.; Gazzola, S.; Riva, E.; Parascandolo, J. S.; Song, L.; Tosin, M. *Chem. Commun.* 2016, 52, 10392.
- (2) Ho, Y. T. C.; Leng, D. J.; Ghiringhelli, F.; Wilkening, I.; Bushell, D. P.; Köstner, O.; Riva, E.; Havemann, J.; Passarella, D.; Tosin, M. *Chem. Commun.* 2017, 53, 7088.
- (3) Sundlov, J. A.; Shi, C.; Wilson, D. J.; Aldrich, C. C.; Gulick, A. M. *Chem. Biol.* 2012, 19, 188.
- (4) Worthington, A. S.; Hur, G. H.; Meier, J. L.; Cheng, Q.; Moore, B. S.; Burkart, M. D. *ChemBioChem* 2008, 9, 2096.
- (5) Worthington, A. S.; Rivera, H.; Torpey, J. W.; Alexander, M. D.; Burkart, M. D. *ACS Chem. Biol.* 2006, 1, 687.
- (6) Gulick, A. M.; Aldrich, C. C. *Nat. Prod. Rep.* 2018, 35, 1156.
- (7) Tosin, M.; Spiteller, D.; Spencer, J. B. *ChemBioChem* 2009, 10, 1714.
- (8) Riva, E.; Wilkening, I.; Gazzola, S.; Li, W. M. A.; Smith, L.; Leadlay, P. F.; Tosin, M. *Angew. Chem. Int. Ed.* 2014, 53, 11944.
- (9) Du, L.; Lou, L. *Nat. Prod. Rep.* 2010, 27, 255.
- (10) Studier, F. W. *Protein Expr. Purif.* 2005, 41, 207.
- (11) Sivashanmugam, A.; Murray, V.; Cui, C.; Zhang, Y.; Wang, J.; Li, Q. *Protein Sci. Publ. Protein Soc.* 2009, 18, 936.
- (12) Wang, H.; Xu, M.; Xiong, M.; Cheng, J. *Chem. Commun.* 2015, 51, 4807.
- (13) Robin, M. P. *Bromo and thio maleimides for functionalisation and fluorescent labelling of polymers and polymer nanoparticles*, University of Warwick, 2014.
- (14) Xie, Y.; Husband, J. T.; Torrent-Sucarrat, M.; Yang, H.; Liu, W.; O'Reilly, R. K. *Chem. Commun.* 2018, 54, 3339.
- (15) Mehlich, J.; Ravoo, B. J. *Org. Biomol. Chem.* 2011, 9, 4108.
- (16) Ireland, R. E.; Wipf, P.; Xiang, J. N. J. *Org. Chem.* 1991, 56, 3572.
- (17) Patel, M.; Sushmita; Verma, A. K. *Indian J. Heterocycl. Chem.* 2018, 28, 169.
- (18) Amberg, D. C. ***Methods in yeast genetics : a Cold Spring Harbor Laboratory course manual***; 2005 ed.; Cold Spring Harbor Laboratory Press,: Cold Spring Harbor, N.Y. :, 2005.
- (19) Kieser, T.; Bibb, M. J.; Buttner, M. J.; Chater, K. F.; Hopwood, D. A. *Practical Streptomyces genetics*; The John Innes Foundation: Norwich, 2000.
- (20) *BAM Media M154: Trypticase (Tryptic) Soy Broth*; Center for Food Safety and Applied Nutrition. FDA 2018.
- (21) Fu, H.; Hopwood, D. A.; Khosla, C. *Chem. Biol.* 1994, 1, 205.
- (22) Robin, M. P.; Wilson, P.; Mabire, A. B.; Kiviaho, J. K.; Raymond, J. E.; **Haddleton, D. M.; O'Reilly, R. K.** *J. Am. Chem. Soc.* 2013, 135, 2875.
- (23) Hedir, G. G.; Pitto-Barry, A.; Dove, A. P.; O'Reilly, R. K. *J. Polym. Sci. Part Polym. Chem.* 2015, 53, 2699.
- (24) Castañeda, L.; Wright, Z. V. F.; Marculescu, C.; Tran, T. M.; Chudasama, V.; Maruani, A.; Hull, E. A.; Nunes, J. P. M.; Fitzmaurice, R. J.; Smith, M. E. B.; Jones, L. H.; Caddick, S.; Baker, J. R. *Tetrahedron Lett.* 2013, 54, 3493.
- (25) Smith, M. E. B.; Caspersen, M. B.; Robinson, E.; Morais, M.; Maruani, A.; Nunes, J. P. M.; Nicholls, K.; Saxton, M. J.; Caddick, S.; Baker, J. R.; Chudasama, V. *Org. Biomol. Chem.* 2015, 13, 7946.



## **Chapter 6:** Peptide functionalized macro-CTAs for mediating and templating aqueous polymerization-induced self-assembly

## 5.1 Abstract

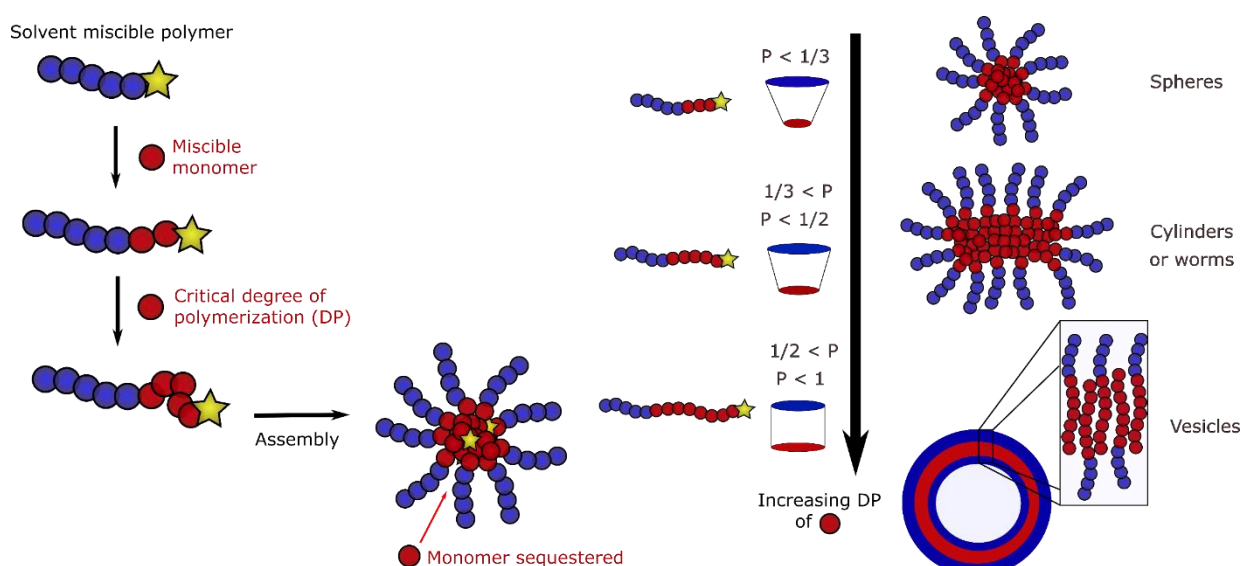
The primary driving force for polymerization-induced self-assembly (PISA) is well known to be hydrophobicity, however, little work has focused on tuning or templating the assembly of polymers during this process through interactions such as hydrogen bonding. We hypothesized that by utilizing peptide-based intramolecular interactions, for example hydrogen bonding pairs in  $\beta$ -sheets, we could template the assembly of polymers during PISA to encourage the formation of higher-order morphologies, such as vesicles and ribbons.

Towards this aim,  $\alpha$ -helix,  $\beta$ -sheet and random coil peptides were synthesized as macro-CTAs for RAFT polymerization of PISA monomers diacetone acrylamide (DAAm) and *N*-hydroxypropyl methacrylate (HPMA). While synthesis of the macro-CTAs was successful and polymerization could be achieved, aggregation of assemblies was universally encountered. Calculation of the  $\text{Log}P_{\text{oct}}/\text{SA}$  of the CTAs suggested they were very polar in nature, and should make good stabilizing blocks, which confused results. Several design changes were investigated with no success at preventing aggregation until it was decided to functionalize the core-forming monomer with peptide instead of CTA. In this case a PEG macro-CTA was used as a solvophilic block and used to graft through a peptide acrylamide monomer to create stable particles through RAFT mediated PISA. The assembly of particles was observed by DLS, whereas none was observed without peptide, confirming that the peptides are driving assembly through a process which is not hydrophobicity driven. Future work will investigate this further with a range of peptide-functionalized monomers.

## 5.2 Introduction

### 5.2.1 Polymerization-induced self-assembly (PISA)

Block copolymer self-assembly is a well-understood phenomenon dating back over half a century,<sup>1</sup> as discussed in the introduction to this thesis. This assembly is typically driven post-polymerization, with methods such as solvent switching and direct dissolution in a selective solvent. However, a relatively new and rapidly growing field of self-assembly is polymerization induced self-assembly (PISA). PISA under dispersion conditions, occurs when a stabilizing, or solvophilic block, is extended with a monomer that is solvent miscible. Upon reaching a particular degree of polymerization this block becomes solvophobic (Scheme 6.1).<sup>2</sup> This block, forms the core of the forming assembly and can continue to grow upon the addition of more monomer. Typically, the onset of assembly is followed by a marked increase in polymerization kinetics as monomer can be sequestered into the solvophobic domain, leading to an increase in the local concentration of monomer.<sup>3</sup>



**Scheme 6.1:** Illustrated representation of the dispersion PISA process.



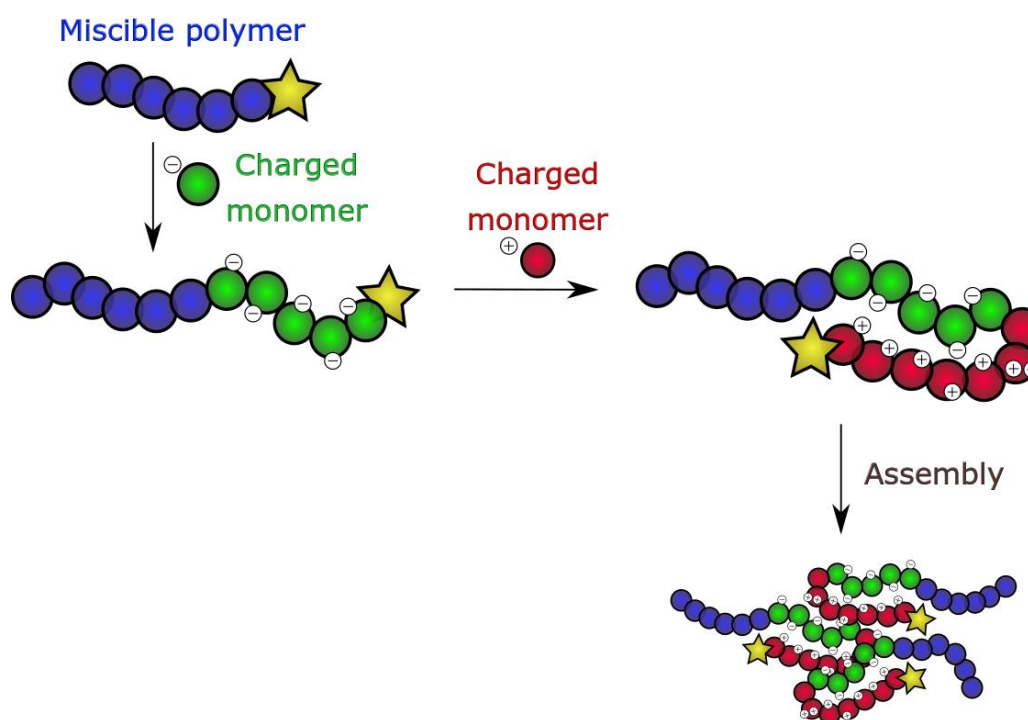
There are numerous advantages of PISA over traditional self-assembly methods, especially for industrial applications. In particular this includes reducing the steps in synthesis, assembly and purification, as quantitative monomer conversion is usually achieved and no dilute scale assembly steps are required - as PISA can be conducted at very high percentage solids (typically 5-50 w%, compared to <1 w% for conventional self-assembly methodologies).<sup>4</sup>

These advantages have led to a rapid growth in the technique, with many different reported types and applications. A vast array of morphologies can be accessed *via* PISA, determined primarily by the packing parameter ( $P$ ), comparable to traditional self-assembly methods. Examples range from the traditional spheres and worms,<sup>5,6</sup> to higher-order morphologies such as multilamellar vesicles and tubular vesicles.<sup>7</sup> Applications range from cell preservation and storage;<sup>8,9</sup> drug delivery through encapsulation during or post-PISA;<sup>10-13</sup> to PISA in oil for lubrication applications.<sup>4</sup>

Using PISA for peptide-based applications has been previously explored. In our group, work has focused on the entrapment and encapsulation of enzymes and peptides within vesicles,<sup>11,14</sup> and within polymer membranes during PISA.<sup>15</sup> Entrapment of enzymes was shown to provide effective protection from immunogenicity and proteolysis,<sup>11</sup> problems typically associated with peptide-based therapeutics.<sup>16</sup> Gianneschi and co-workers have demonstrated a peptide based-monomer that can undergo ring-opening metathesis polymerization (ROMP) mediated PISA.<sup>17</sup> While a range of morphologies were obtained, the peptide was modified with protecting groups to increase hydrophobicity, thus allowing aqueous phase PISA, but limiting therapeutic applications.

Near universally, PISA is regarded to proceed as a consequence of solvophobicity, which in aqueous media is the hydrophobicity of the growing

polymer chain.<sup>5,18</sup> However, one report of polymerization induced electrostatic self-assembly (PIESA) has recently been published, which details the induction of assembly through ionic interactions in the case of a histamine acrylamide polymerization by a poly(HPMA)-*co*-poly(AMPS) macro-CTA (Figure 6.2).<sup>19</sup> As the length of ionic blocks increased, larger assemblies from spheres, to worms to films were observed. Hydrogen bonding is another intermolecular interaction that has been well-known to affect self-assembly behaviour,<sup>20-22</sup> and work by Reiger and co-workers has shown how urea functionalized seeds can template the assembly of fibres through PISA of HPMA.<sup>23</sup> It is hypothesized that peptides can utilize both effects, allowing greater control over hydrogen bonding and ionic effects to template the formation of therapeutic nanoparticles *via* PISA.



**Scheme 6.2:** Illustration of PIESA reported by Cai *et al.*<sup>19</sup>

### 5.2.2 Reversible addition-fragmentation chain-transfer (RAFT) polymerization

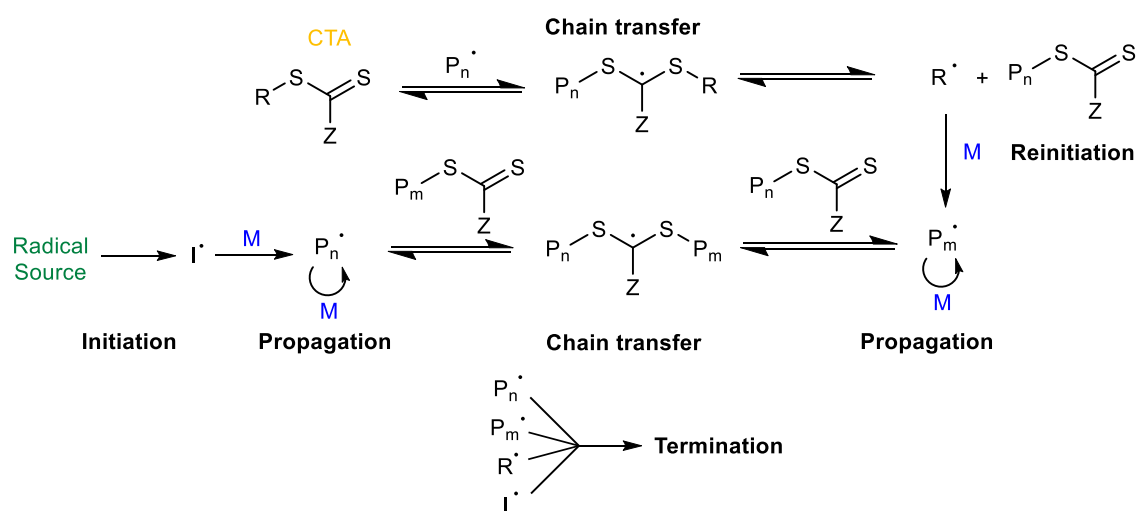
The requirement for well-defined diblock copolymer synthesis for PISA necessitates the use of a controlled polymerization technique. The majority of

literature examples, therefore, employ reversible-addition fragmentation chain-transfer (RAFT) polymerization to achieve this.<sup>12,21–25</sup> Other methodologies have been reported, including other radical polymerizations, such as ATRP-PISA,<sup>26</sup> and non-radical polymerizations, for example, ROMP-PISA.<sup>27</sup>

For this chapter, RAFT will be relied upon to synthesize peptide-polymer conjugates. RAFT is a type of reversible-deactivation radical polymerization (RDRP) or controlled radical polymerization technique, as presented in the introduction to this thesis. RAFT relies on the use of a chain transfer agent (CTA), specifically, a thiocarbonylthio compound for example dithiocarbamates,<sup>27</sup> or used in this Chapter, trithiocarbonates. This CTA transfers the activity of a growing polymer chain to another polymer chain, thus averaging the molecular weight of polymer chains in the environment through giving equal probability to all chains to grow.<sup>28</sup> It also provides a dormant species which reduces the concentration of active radicals in solution, therefore reducing termination and increasing propagation lifetime. By reducing initiator concentration, thereby keeping radical concentration low (< 1 mol%), Perrier and co-workers have shown termination can effectively be eliminated enabling end-group fidelity of 97 % and a  $\bar{D}_M$  close to 1.1.<sup>29</sup>

The mechanism of RAFT (Scheme 6.3) starts with activation through initiation and generation of radicals, typically created through thermal initiation of a radical initiator. These radicals ( $I^\bullet$ ) can then react with monomers ( $M$ ) to form propagating chains ( $P_n^\bullet$ ) and can then be captured by a CTA, entering into an equilibrium between the active and dormant states.<sup>29,30</sup> This dormant state can fragment to produce a new initiating group ( $R^\bullet$ ), which can re-initiate

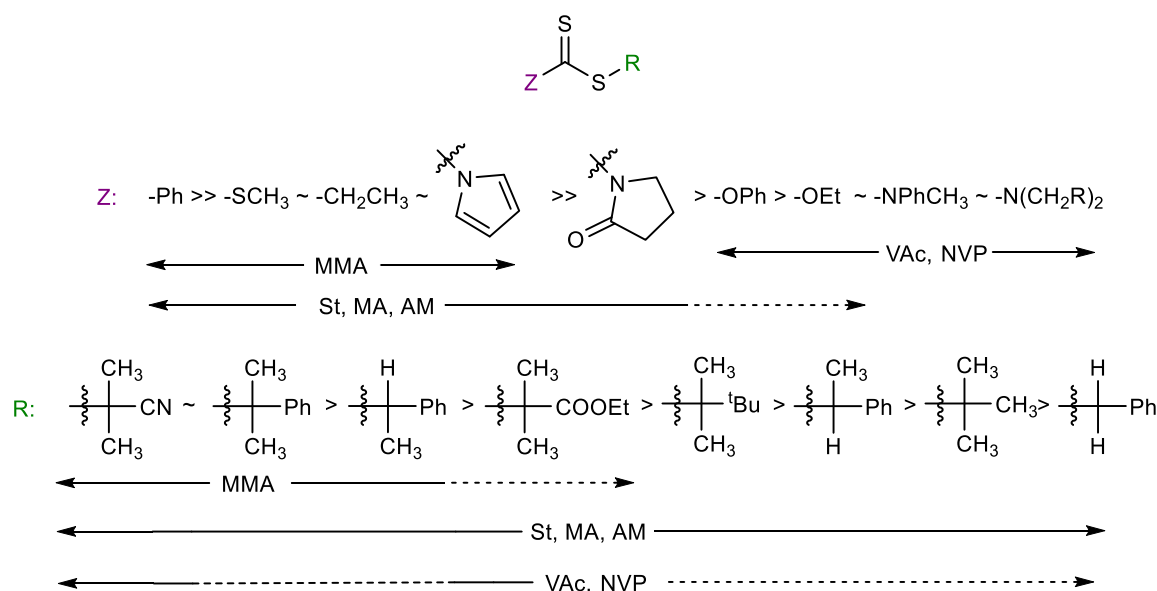
a propagating chain ( $P_m^\bullet$ ). Now a rapid equilibrium is formed in which  $P_m^\bullet$  or  $P_n^\bullet$  have an equal chance to fragment and propagate, leading them to exhibit similar degrees of polymerization over time. The termination reaction often is inevitable in a radical polymerization system, and this is still true with RAFT. It is noteworthy that as bimolecular termination does not lead to loss of CTA activity in RAFT, the amount of terminated chains in solution will be equal to the amount of initiator that has decomposed in that timeframe.<sup>30</sup>



**Scheme 6.3:** Proposed RAFT mechanism.

The success of RAFT polymerization is dependent upon the judicious choice of CTA. As seen in Figure 6.3, CTAs are variable in R and Z functionality, which each have different effects on the polymerization. The Z-group significantly affects stability of the radical intermediates in the chain transfer steps, thus affecting the rate of fragmentation of the CTA.<sup>32</sup> Furthermore, through activation of the C=S bond, it affects rate of addition of propagating radicals.<sup>32</sup> Specifically, the Z-group should be chosen so that the CTA is 10-100 times more reactive towards the propagating chain than the target monomer.<sup>33</sup> The R-group, in comparison, should be chosen to be a good

leaving group from the chain transfer radical intermediate and should undergo effective re-initiation with monomer.<sup>31</sup> A schematic representation to illustrate R and Z group reactivity is shown in Scheme 6.4 (adapted from Moad *et al.*).<sup>33</sup>



**Scheme 6.4:** Structure of generic RAFT agent, and empirical guide to R and Z-group selection for selected monomers, adapted from ref.<sup>33</sup>

## 5.2.3 Peptide synthesis

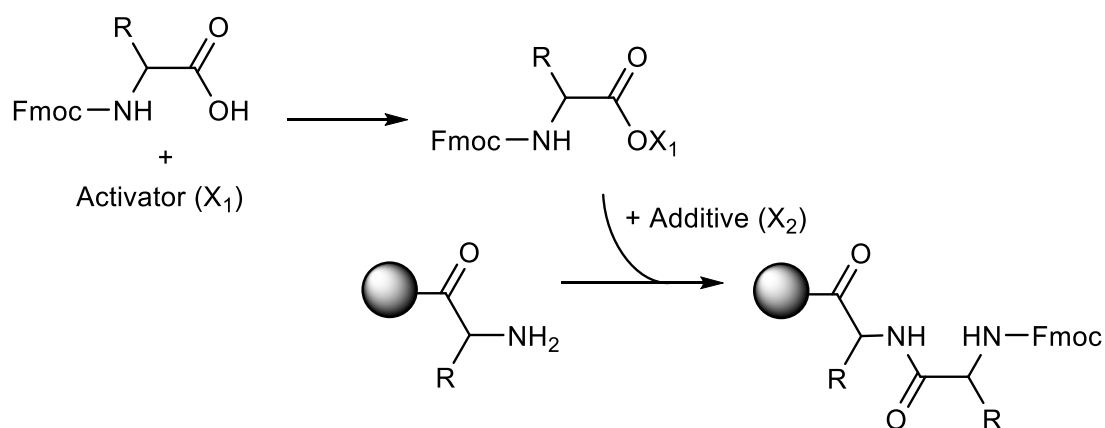
### 6.2.4.1 Preparation of synthetic peptides

Nature is well developed to synthesize peptide chains, with eukaryotes able to synthesize around 6 aa/sec per chain.<sup>34</sup> Synthetically, in contrast, chemists with the latest microwave-assisted methods can realistically achieve 3-4 aa/hour. In most labs, this is achieved with Fmoc protected, solid-phase peptide synthesis (SPPS).<sup>35</sup> In this the peptide bond formation occurs *via* activated carboxylic acid couplings to amines supported on a solid phase resin. This allows easy purification through removal of unbound side products and unused reagents, allowing large excesses to help achieve high conversion, and eliminating the laborious process of peptide isolation between each coupling. While Boc protected peptide coupling is used and has its advantages (for example all deprotection side products are

volatile), Fmoc SPPS has become the standard methodology due to its orthogonality with the other chemistries involved. In particular, the basic deprotection of Fmoc protected backbone amines is orthogonal to the acid labile chemistries used to protect side groups and to enact resin cleavage. While for Boc SPPS, HF is required for resin cleavage which has many issues associated with its use, including handling a low boiling point liquid (19.6 °C), the inability to use glassware, and handling an extremely toxic reagent.<sup>36</sup>

#### 6.2.4.2 Activation and amide bond formation

To achieve conversions in peptide couplings required for multistep peptide synthesis, very efficient amide coupling conditions are required.<sup>37</sup> The activation used to achieve this is a cause for many of the issues encountered in the synthesis including racemization issues at the chiral backbone carbon. Therefore, a range of specialized peptide coupling reagents have been developed from original carbodiimide based couplings to more recent uronium salt-based coupling agents (Scheme 6.5), which combine uronium activating chemistry with a racemization suppressing additive such as 1-hydroxy-benzotriazole (HOBt). If a carbodiimide based coupling agent is used (for example diisopropylcarbodiimide, DIC) a racemization reducing additive is also required, so triazoles such as HOBt are added separately. Recently, ethyl 2-Cyano-2-(hydroxyimino)acetate (OXYMA) has been developed as a safer and equally efficient racemization reducing additive,<sup>38</sup> and it will therefore be used in this study.



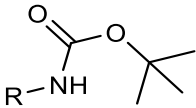
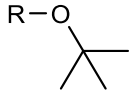
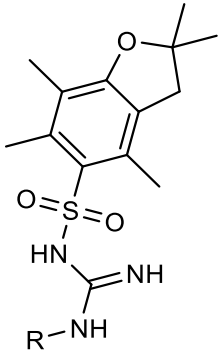
Activators		Additives	
	Carbodiimides e.g. diisopropyl- carbodiimide (DIC)		Tirazoles e.g. hydroxybenzotriazole (HOBt)
	Uronium salts e.g. HATU		Ethyl cyano- hydroxyiminoacetate (OXYMA)

**Scheme 6.5:** Simplified scheme of the coupling step and selection of example activators and racemization reducing reagents.

#### 6.2.4.3 Sidechain protection

The incoming amino acid may contain reactive moieties in the side chain, and these require protection orthogonally to the  $\alpha$ -amino Fmoc. Except for a few special circumstances (for example selective disulfide bridging),<sup>39</sup> side chain protection groups must be stable to coupling and Fmoc deprotection conditions, and should be cleaved effectively under the resin cleavage conditions (for example 95% TFA). This protecting group varies depending on the functionality but some groups encountered in this chapter include:  $N_\epsilon$ -Boc protection of lysine residues, and  $O$ -<sup>t</sup>Bu protection of aspartic acid residues (Table 6.1)

**Table 6.1:** Selected side chain protection strategies employed in this chapter.

Protecting group		Residues protected	Deprotection conditions
	N-Boc	Lysine and cysteine	>90% TFA
	O- <sup>t</sup> Bu	Aspartic acid, glutamic acid, tyrosine and serine	>90% TFA
	N-Pbf	Arginine	>90% TFA

#### 6.2.4.4 Resins used for SPPS

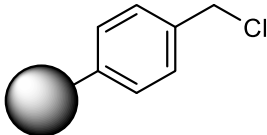
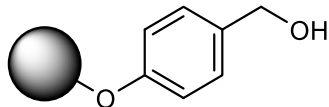
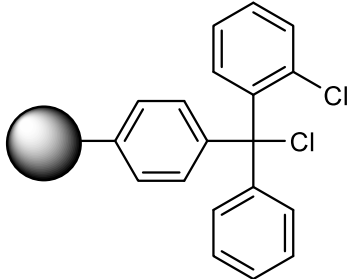
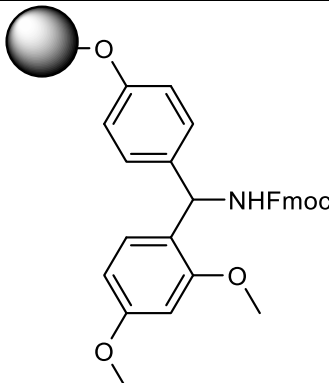
While the principle of a solid phase support for peptide synthesis may appear trivial, the resin used has to: be stable to all reaction conditions including high temperature in microwave-assisted synthesis; be selectively cleaved under suitable conditions; and swell with addition of reaction solvent to allow efficient diffusion, while not swelling to a degree which increases the already high solvent consumption of SPPS.<sup>40</sup>

The first resin reported by Merrifield was a polystyrene resin cross-linked with 2% 4-divinylbenzene, with a chloromethyl benzene linker for peptide attachment.<sup>41</sup> However issues are associated with its use, for example the resin is particularly hydrophobic leading to increased peptide-peptide chain interactions, and therefore lower coupling yields and poorer swelling as peptide weight increases.<sup>42</sup> The linker used in this resin also required HF cleavage, which is



undesirable as discussed earlier. More recently PEG-based resins have become popular as they exhibit better swelling properties.<sup>43</sup>

**Table 6.2:** Structure of selected resin linkers, with their cleavage conditions and produced C-terminus.

Resin linker		Cleavage	C-terminus
	Merrifield / chloromethyl benzene	HF	Acid
	Wang / 4-hydroxybenzyl ether	>90% TFA	Acid
	2-chlorotrityl chloride	1-5% TFA	Acid
	Rink amide	>90% TFA	Amide

Importantly, newer linkers have been developed which require milder cleavage conditions and can give specific C-terminus functionalization (Table 6.2). For example, Wang resins include a 4-hydroxybenzyl ether linker,<sup>44</sup> which are cleaved by TFA and leave a C-terminus acid. While Rink-Amide resins contain a 4-((2,4-dimethoxyphenyl)(Fmoc-amino)methyl)phenoxyalkyl linker that is cleaved by TFA to produce a C-terminus amide (Table 6.2).<sup>45</sup>

## 5.3 Results

### 5.3.1 Synthesis of peptide-functionalized chain transfer agents

Peptides are perfectly sequence controlled polymers that can assemble into distinct controllable assemblies dependent upon their sequence, for example barrels and ribbons,<sup>46,47</sup> as discussed in the introduction to this thesis. It was hypothesized that *de novo* peptides could be designed to template and direct the assembly of higher order morphologies during polymerization induced self-assembly (PISA). For example,  $\beta$ -sheet forming peptides could help template linear higher order morphologies such as ribbons through parallel hydrogen bonding interactions,<sup>46</sup> or alpha helices could template the formation of chiral vesicles through twisted stacking interactions,<sup>48</sup> that would also have other applications like enantiomer screening in supported stereoselective catalysis.<sup>49</sup>

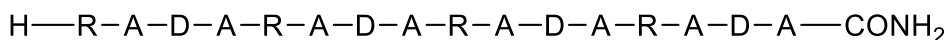
To investigate the effect of peptide secondary structure on the assembly of peptide-polymer conjugates, a series of peptides were selected for comparison. Based upon the two main types of secondary structure observed in nature, an  $\alpha$ -helix forming peptide and a  $\beta$ -sheet forming peptide were chosen to compare to a random coil control peptide sequence. Based on the work of Baldwin and co-workers, an  $(\text{ER})_{i+4}$   $\alpha$ -helix was targeted (Scheme 6.6), as this was shown to possess exceptional  $\alpha$ -helical character in solution.<sup>50,51</sup> For the  $\beta$ -sheet comparison an  $\text{RADA}_n$  repeating sequence was selected as it possesses a repeating unit of a strong  $\beta$ -sheet domain, shown to form  $\beta$ -sheet nanofibrils in aqueous solution.<sup>52</sup> Finally, for the control random coil a sequence was selected from a known non-assembling peptide subunit, the kinase-independent domain of the cAMP response element-binding protein (KID-CREB).<sup>53,54</sup> It is also a useful sequence as it contains

eight amino acids, including amino, alcohol, aromatic and acid functionality, a good test for the compatibility of this technique to a range of peptide functionality.

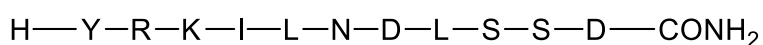
(ER)<sub>i+4</sub>  $\alpha$  Helical



RADA<sub>16</sub>  $\beta$  Sheet



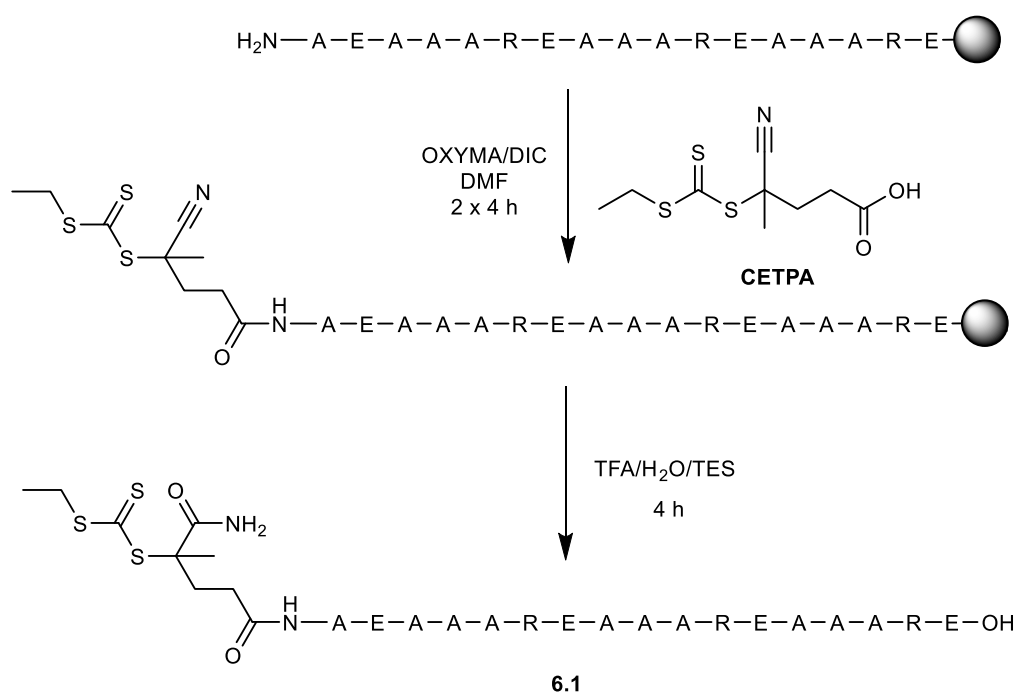
KID-CREB Random Coil



**Scheme 6.6:** Sequences of the three targeted peptide sequences.

Firstly, the helical peptide (ER)<sub>i+4</sub> was targeted for CTA functionalization, because of familiarity with its synthesis as a result of other projects and the ease of characterizing  $\alpha$ -helices *via* circular dichroism. The peptide was synthesized *via* Fmoc assisted solid-phase peptide synthesis (SPPS) using microwave-assisted couplings and an OXYMA/DIC reagent system. After synthesis of the main chain a small proportion of the resin (<5%) was taken and cleaved to assess success of the synthesis. LCMS of this confirmed good purity, so the remaining resin bound peptide was derivatized with the appropriate acid functionalized CTA *via* DIC mediated coupling. For this coupling, a nitrile derivatized trithiocarbonate CTA (CETPA) was targeted as it was suitable for polymerizing the most ubiquitous PISA monomer *N*-hydroxypropyl methacrylate (HPMA). This acid functionalized CTA was coupled to the synthesized peptide *via* solid-phase mediated amide coupling (Scheme 6.7). The resin-bound CTA-peptide was then cleaved using trifluoroacetic acid to give CTA **6.1**. While HPLC results suggested good purity, mass spectroscopy gave an *m/z* of 1997, 18 *m/z* higher than expected, indicative of hydrolysis or adduct formation upon ionization. Also, an initial test polymerization

of HPMA with this CTA, to a degree of polymerization (DP) of 50, showed poor control ( $\bar{D}_M = 3.79$ ) by DMF size exclusion chromatography (SEC) (Figure 6.1). It is hypothesized that the nitrile group is hydrolyzed during the TFA deprotection step leading to the mass observed and the poor control of polymerization. Nitrile based CTAs have been reported to hydrolyze to the amide under acidic aqueous environments.<sup>55</sup> It is not reported why further hydrolysis to the amine is not observed, however it could be envisioned that this product would lead to CTA aminolysis. A test deprotection was re-attempted without water in the deprotection solution, however, hydrolysis was still observed.



**Scheme 6.7:** Unsuccessful synthesis of **CETPA** functionalized  $(ER)_{i+4}$  peptide CTA **6.1**.

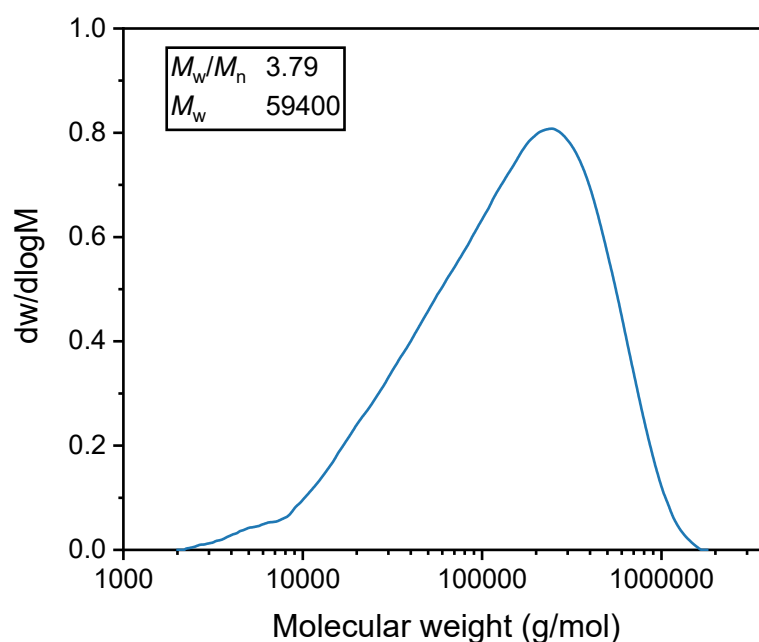
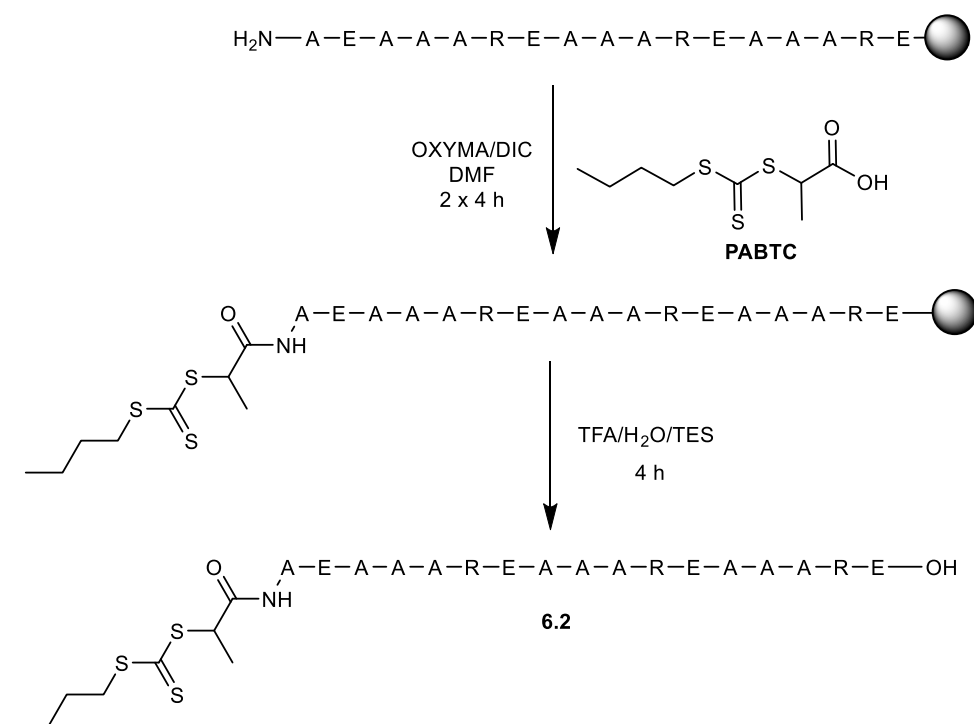


**Figure 6.1:** DMF SEC (DRI) molecular weight distribution of PHPMA (DP = 50) polymerized using macro-CTA **6.1**.

As a result of the nitrile hydrolysis seen in CETPA, a propanoic acid butyl trithiocarbonate (PABTC) CTA was targeted instead. PABTC can polymerize the aqueous PISA monomer DAAM with good control. Therefore, PABTC was synthesized as per Skey and O'Reilly<sup>56</sup> and coupled to the peptide using the OXYMA/DIC system employed for CTA **6.1**. This time HPLC and mass spectroscopy proved good purity and retention of structure in CTA **6.2**. Circular dichroism of this CTA was conducted (Figure 6.2), and good  $\alpha$ -helical character was observed at 222 nm compared to a random coil peptide **6.5**.



**Scheme 6.4:** Synthesis of **PABTC** functionalized  $(\text{ER})_{i+4}$  peptide CTA **6.2**.

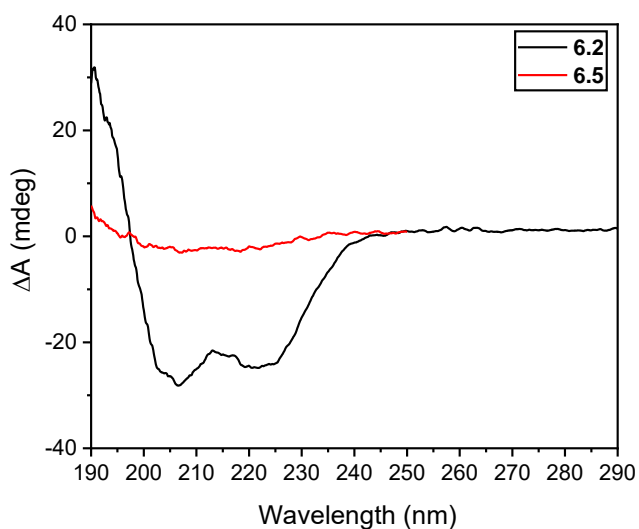


**Figure 6.2:** Circular dichroism spectra of  $(\text{ER})_{i+4}$  peptide CTA **6.2** and random coil peptide **6.5** conducted at 0.1 mg/mL in water.

Secondly, the  $\beta$ -sheet based  $\text{RADA}_{16}$  peptide was synthesized by this same method, followed by coupling to PABTC and subsequent cleavage to produce  $\beta$ -sheet forming CTA  $(\text{RADA})_{16}$ -PABTC **6.3** (Figure 6.3A). However, it was immediately apparent that **6.3** was not water-soluble, even after heating or

sonication. While in theory more polar than CTA **6.2**, this peptide is likely to have much stronger intermolecular interactions such as hydrogen bonding and ionic interactions. Based on literature precedent, it could be forming a  $\beta$ -sheet complex without the need for a hydrophobic block.<sup>51</sup> To confirm this the peptide was dispersed into solutions of guanidine, known to break apart  $\alpha$ -helix and  $\beta$ -sheet assemblies.<sup>57</sup> When dispersed into 8 M guanidine, solvation of the peptide at 1 mg/mL was achievable, confirming this hypothesis, and analysis of the denatured protein by HPLC confirmed fair purity exhibited by two peaks, as a consequence of diastereomer formation (Figure 6.3B), however noise attributable to the harsh conditions for solvation is present. As a result, only helical CTA **6.2** was chosen for initial investigations into peptide templated PISA.

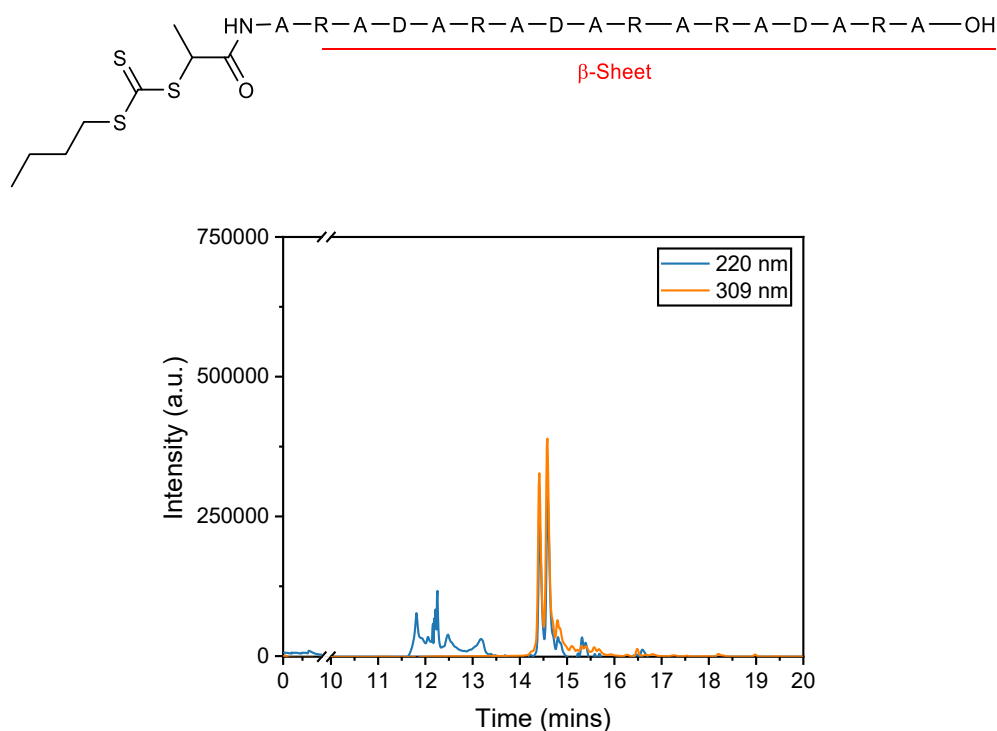


**Figure 6.3:** A) Structure of **PABTC** functionalized RADA<sub>16</sub> peptide CTA **6.3**. B) HPLC chromatogram after denaturing with 8 M guanidine.

### 5.3.2 Investigating aqueous PISA using a helical peptide-based PABTC macro-chain transfer agent

CTA **6.2** was investigated for aqueous PISA, using a water-soluble initiator, VA-044, and heating at 40 °C. Polymerizations were conducted at 10 and 15 w% solids concentration, targeting a DP of 50 and 100 of the PDDAm block. Solutions turned white and cloudy within 2 hours, indicative of polymerization-induced self-assembly. SEC analysis by DRI in DMF (Figure 6.4) indicated fair control of the polymerizations at 10 w% with molecular weight dispersities of 1.28 and 1.39 for DP = 50 (**P1**) and DP = 100 (**P2**) respectively. At 15 w% and DP = 100 (**P3**), analysis was complicated as SEC indicated a large population at very high molecular weight ( $\sim 80$  kDa), suggestive of association in the SEC eluent (DMF) or loss of polymerization control.

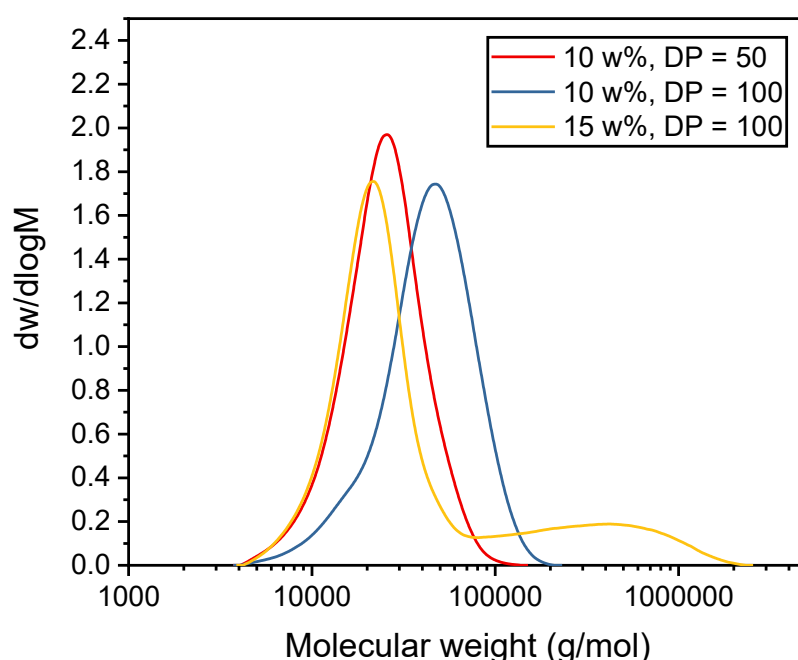


**Figure 6.4:** DMF SEC (DRI) molecular weight distribution of PDAAm polymerized using macro-CTA **6.2**.

$^1\text{H}$  NMR spectroscopy in  $\text{DMSO}-d_6$  indicated that the polymerizations proceeded to high conversion overnight ( $>99\%$  for the 10 w% polymerizations



and 82% for the 15 w% polymerization). As polymerization appeared to proceed well for **P1** and **P2**, DLS was conducted to establish whether stable assemblies were forming. However, DLS suggested aggregate formation (Table 6.3) with assemblies  $>1\ \mu\text{m}$  that had poor dispersity ( $>0.2$ ). Zeta potential was also measured to establish whether the peptide was providing charge stability, as theoretically each peptide-polymer should have a -1 charge. However, this indicated that only the DP = 50 sample exhibited a negative zeta potential (Table 6.3), suggesting that the peptide was not providing enough charge stability at longer PDAAm lengths.

**Table 6.3:** Summary of  $D_h$ , PD values and zeta potential values with deviation for assemblies formed *via* aqueous PISA, as determined by DLS analysis and microelectrophoretic analysis respectively.

#	Weight %	PDAAm DP	$D_h$ (nm)	PD	Zeta Potential (mV)
P1	10 w%	50	$1474 \pm 85$	$0.22 \pm 0.15$	$-19.03 \pm 0.15$
P2	10 w%	100	$346 \pm 57$	$0.54 \pm 0.07$	$6.32 \pm 0.29$
P3	15 w%	100	$3085 \pm 289$	$0.42 \pm 0.07$	$4.80 \pm 1.80$

Dry-state TEM imaging was conducted on **P2**, which suggested aggregated small spherical nanoparticle formation with diameters much shorter than observed by DLS (Figure 6.5). The aggregated nanoparticles observed by the TEM images strongly suggest aggregation of the assemblies in solution leading to the poor DLS observations. Based upon these observations it was decided to alter the peptide

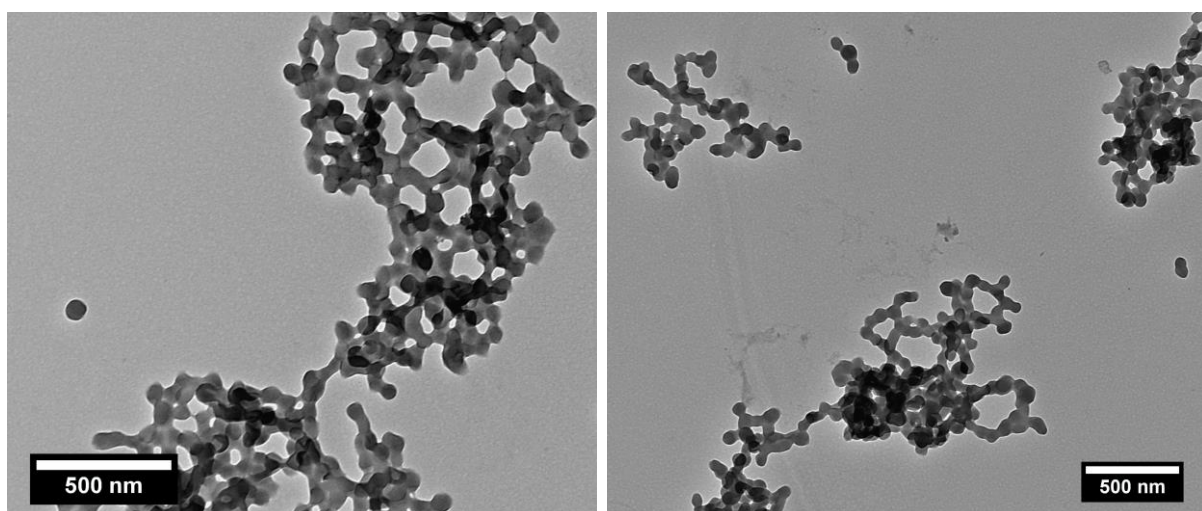


**Figure 6.5:** Dry-state TEM images of **P2**, stained with a 1 w% uranyl acetate solution on a formvar-carbon coated copper grid.

design to increase charge stabilizing characteristics. This was achieved by mimicking work on peptide amphiphiles which are often terminated by a tri-glutamic acid (EEE) tag. Thus, peptide CTA **6.4** was synthesized as previously, bearing a C-terminal EEE motif. Using this macro-CTA DAAM was again polymerized, targeting DP = 50 (**P4**) and DP = 100 (**P5**) at 10 w%. Both polymerizations proceeded to >99% conversion by  $^1\text{H}$  NMR spectroscopy ( $\text{DMSO-}d_6$ ) when left overnight at 40  $^\circ\text{C}$ . Nano-structure formation was observed for both samples by DLS in both THF and DMF preventing SEC characterization. DLS of **P4** under aqueous conditions showed aggregate formation, with zeta potential measurement of the crude solution indicating positively charged particles (Table 6.4). Dissolution into a range of buffers suggested that at neutral and basic pH the particles were negatively charged, however, aggregation was still observed by DLS. It is hypothesized that this may be a cause of chain entanglement. As RAFT is poorly suited to basic conditions as a result of CTA hydrolysis,<sup>52</sup> it was decided to switch to a tri-arginine (RRR) tag for stability under acidic conditions.

**Table 6.4:** Summary of  $D_h$ , PD values and zeta potential with deviation for **P4** in different pH buffers, as determined by DLS analysis and microelectrophoresis respectively.

#	Buffer	$D_h$ (nm)	PD	Zeta
P4	crude	$1666 \pm 239$	$0.72 \pm 0.12$	$14.1 \pm 2.42$
P4	pH 4 acetate	$4098 \pm 158$	$0.13 \pm 0.06$	$-0.06 \pm 0.23$
P4	pH 7 phosphate	$1623 \pm 45$	$0.49 \pm 0.05$	$-16.7 \pm 0.29$
P4	pH 10 carbonate	$2011 \pm 87$	$0.50 \pm 0.1$	$-14.4 \pm 0.56$
P5	crude	$3340 \pm 353$	$0.33 \pm 0.07$	$0.38 \pm 2.36$

### 5.3.3 Investigating aqueous photo PISA using a random coil peptide-based PABTC chain transfer agent

As a result of unstable assemblies observed with the helical peptide CTA, and lack of solubility of the  $\beta$ -sheet peptide, it was decided to switch to a random coil peptide (KID-CREB). This was terminated with a trimer of arginine (RRR) analogous to the EEE tag but potentially more suitable for low pH conditions that suit RAFT mediated PISA (Figure 6.6A). It was also decided to utilize photoinitiation by light (405 nm) irradiation, instead of thermal initiation, as there was success within the group with this negating the need for initiator.<sup>58</sup> RRR capped KID-CREB macro-CTA **6.5** was successfully synthesized and used for PISA at 40 °C in a pH 2 sodium phosphate solution (**P6**), in a photoreactor. A block of DP = 50 PDAAm was targeted at 10 w% and a conversion of 88% was reached in 4 hours by  $^1\text{H}$  NMR spectroscopy ( $\text{DMSO-}d_6$ ). SEC analysis was possible in THF which showed poor dispersity ( $\mathcal{D}_M = 1.56$ ) and an  $M_n$  higher than targeted (33600 g/mol versus targeted  $M_n$  of 9400 g/mol, Figure 6.6B), however, this is based off a PMMA standard.

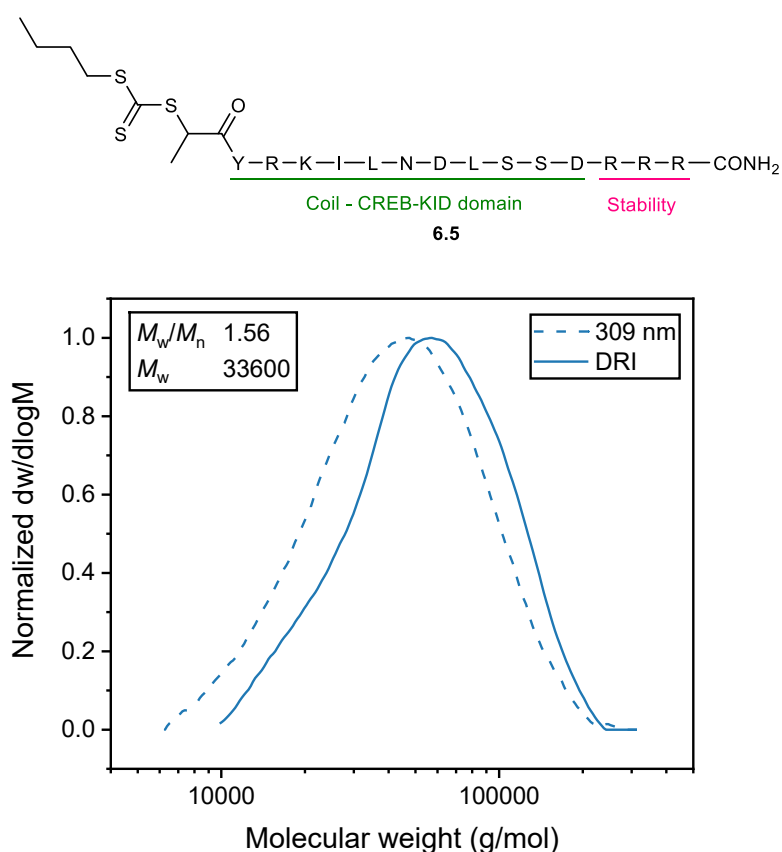


**Figure 6.6:** A) Structure of macro-CTA **6.5** B) SEC (dashed = UV 309 nm, line = DRI) of **P6** in THF.

DLS of **P6** suggested aggregate formation with assemblies over  $>1 \mu\text{m}$ . Treatment of the samples with a 0.5 M NaCl solution to screen charge interactions, did not improve assembly, with aggregates still observed. It is hypothesized that the peptide block is not large and hydrophilic enough to stabilize such high DPs of hydrophobic monomer. Therefore, CTA **6.5** was used to polymerize DAAM targeting 15 DP at 5 w% (**P7**) using photo-irradiation. Polymerization conversion was slower reaching only 75% as determined by  $^1\text{H}$  NMR spectroscopy ( $\text{DMSO-}d_6$ ), and THF SEC of the polymer suggested a broad ( $\mathcal{D}_M = 1.70$ ) unimodal distribution with a slight low molecular weight shoulder hypothesized to be unreacted macro-CTA (Figure 6.7A).

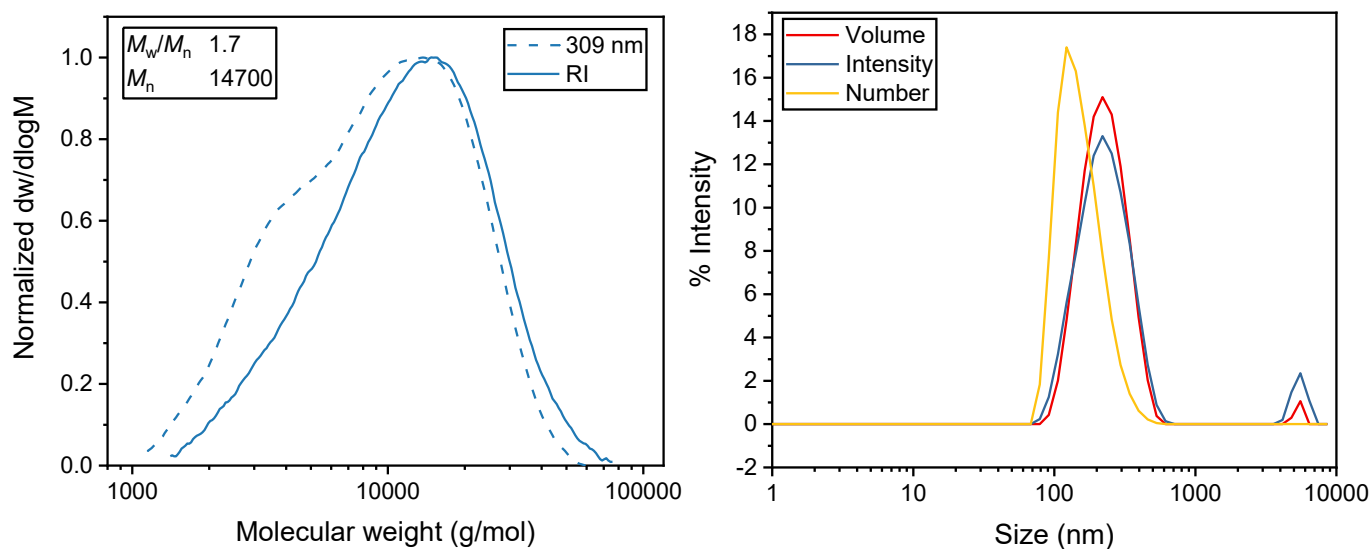


**Figure 6.7:** A) Normalized THF SEC  $M_w$  distribution of **P7** (dashed = 309 nm, line = DRI) B) crude DLS measurement of **P7**.

During the polymerization the solution went cloudy indicative of nanoscale assembly. DLS confirmed this with fairly large unstable assemblies still observed for the 15 DP polymer (Figure 6.7B). Zeta potential did confirm positively charged particles which was screened in 0.5 M NaCl, however aggregation was still observed in salt solution (Table 6.5). Atomic force microscopy (AFM) was conducted on **P7** to help confirm morphology. This showed sphere-like particles, the size of which were several fold smaller than that observed by DLS, which appeared to be clustered - although these observations may be driven by drying effects (Figure 6.8).

**Table 6.5:**  $D_h$ , PD values, zeta potentials and observed size with deviations for **P4**, as determined by DLS analysis, microelectrophoresis and AFM respectively.

	DLS		Zeta potential (mV)	AFM		
	$D_h$ (nm)	Dispersity		Mean	SD	Max/Min
P7	$208 \pm 6$	$0.16 \pm 0.04$	$18.9 \pm 3.0$	69 nm	21 nm	123 nm/44 nm
P7 + 0.5 M NaCl	$1222 \pm 117$	$1 \pm 0$	$-0.1 \pm 1.9$	-	-	-

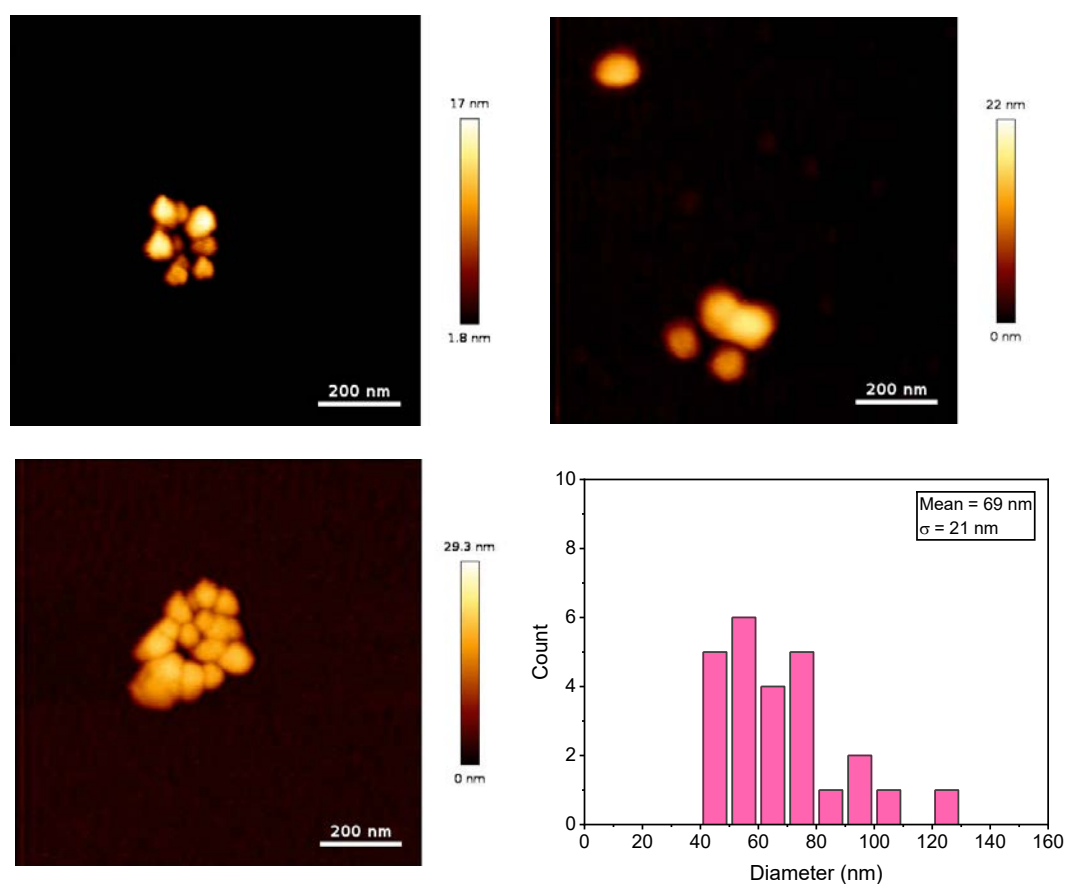


**Figure 6.8:** Dry state AFM images of **P7**, and histogram of measured particle diameters (bottom right).

Work in the group has pioneered the use of  $\text{Log}P_{\text{oct}}/\text{SA}$  to establish the use of monomers for aqueous PISA.<sup>59,60</sup> We hoped to utilize this technique to establish whether the peptide macro-CTAs are polar enough to act as a stabilizing block for aqueous PISA. Using the previously reported methodology, the  $\text{Log}P_{\text{oct}}/\text{SA}$  was

calculated for both helical CTA **6.2** and coil CTA **6.5**, at various ionization states (Table 6.6). The calculated  $\text{Log}P_{\text{oct}}/\text{SA}$  values are negative and suggest the peptide CTAs would have good solubility in water. In fact, they have a lower  $\text{Log}P_{\text{oct}}/\text{SA}$  in comparison to a DP = 12 PEG; suggesting they theoretically should be a better stabilizing block than PEG-based off hydrophilicity effects alone.

**Table 6.6:** Atom based octanol-water partition coefficients (ALogP98), calculated Connolly solvent accessible surface area (SA) and surface area normalized  $\text{Log}P$  (ALogP98/SA) for CTAs **6.2** and **6.5**.

CTA	Approx. pH	ALogP98	Connolly SA	ALogP98/SA
6.2	2-4	-10.0478	1746.79	-0.0058
6.2	6-11	-15.943	1729.21	-0.0092
6.5	2-4	-11.082	1924.08	-0.0058
6.5	6-11	-14.0306	1924.2	-0.0073
PEG (DP = 12)	N/A	-1.449	754.72	-0.0024

### 5.3.4 Synthesis and aqueous PISA of peptide based acrylamide monomers

As a result of the poor behaviour of the peptide-based macro-CTAs, and difficulty in characterization, it was decided to study peptide-based monomers that can be grafted through. These can be polymerized with a PEG macro-CTA to give a PEG stabilizing block. Towards this aim, the random coil peptide KID-CREB was synthesized by SPPS with single couplings, and coupled to acrylic acid by OXYMA/DIC coupling on resin. This was then cleaved under standard TFA conditions, to give monomer **6.6** (Figure 6.9); HPLC and MS analysis confirmed structure and fair purity.

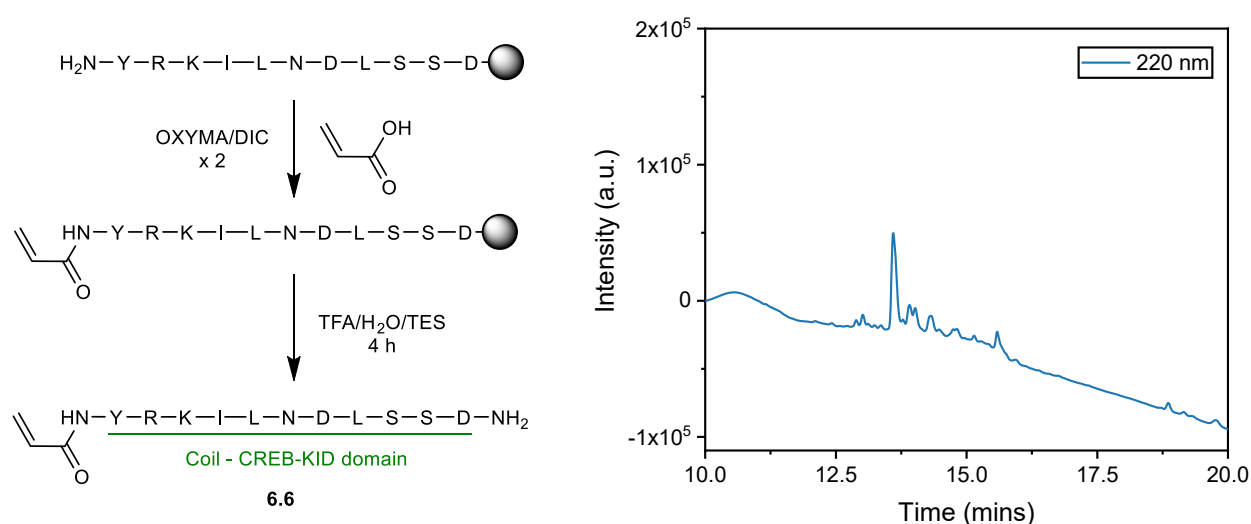


**Figure 6.9:** A) Synthesis of peptide side-chain monomer **6.6** B) HPLC of monomer **6.6** detected at 220 nm.

This was polymerized to DP = 3, using a PEG<sub>2k</sub>-CETPA macro-CTA, under aqueous photo PISA conditions, to give a PEG-poly(KID-CREB) diblock copolymer, with a short peptide block. This was subsequently chain extended with HPMa targeting DP = 10 (**P8**) or 25 (**P9**) to give a PEG-poly(KID-CREB)-HPMA triblock copolymer. As a control, the same CTA was also used to polymerize HPMa without an intermediate peptide block at DP = 10 (**P10**) and 25 (**P11**). After



polymerization, PHPMA-PEG (**P10-11**) standards were clear, while both **P8** and **P9** had turned slightly turbid, indicative of nanoparticle assembly. DLS of these solutions confirmed these observations with no assembly observed for both **P10** and **P11**, however, assemblies were observed for **P8** and **P9** (Table 6.7). Also, DLS of monomer **6.6** at 5 w% in water showed no assembly. This is highly suggestive that peptides are driving assembly during the polymerization and indicative that these peptides are not suitable for forming corona blocks as studied earlier in this chapter.

Unfortunately, DLS data for **P8** and **P9** showed aggregates in both DMF and THF, so SEC analysis could not be completed, however, <sup>1</sup>H NMR analysis suggested good conversion for the PHPMA controls and peptide blocks (>99%). However, only fair conversion for the PHPMA chain-extension of the peptide diblock copolymers was realized (**P8**: 67%; **P9**: 81%), hypothesized to be a result of assembly formation in the peptide block step or CTA degradation from photo irradiation.

**Table 6.7:** Summary of  $D_h$  and PD values with deviation for **P8-11**, as determined by DLS analysis. \*Signal too weak for analysis.

	Peptide DP	HPMA DP	DLS	
			$D_h$ (nm)	Dispersity
<i>P8</i>	3	10	$49 \pm 0.7$	$0.15 \pm 0.01$
<i>P9</i>	3	25	$221 \pm 1.3$	$0.02 \pm 0.005$
<i>P10</i>	0	10	*	*
<i>P11</i>	0	25	*	*

The assembly of such hydrophilic peptides with hydrophilic PEG polymer suggests that the assembly is not hydrophobicity driven, which corroborates previous LogP<sub>oct</sub>/SA calculations. It is hypothesized that hydrogen bonding and ionic interactions are playing an important role in the assembly process, and future

work will investigate the mechanism and formation of therapeutic assemblies *via* peptide-monomer based PISA.

## 5.4 Conclusions

A range of peptide-based macro-CTAs were synthesized *via* SPPS exhibiting different secondary structures. CETPA based CTAs hydrolyzed during solid-phase cleavage so PABTC based CTAs were synthesized for polymerization of PISA monomer DAAM. While polymerizations with such CTAs proceeded to good conversion, aggregation and unstable assemblies were universally encountered, some to such a degree that SEC characterization was not possible.  $\text{Log}P_{\text{oct}}/\text{SA}$  calculation of the CTAs suggested this was not caused by hydrophobicity. As a result of these issues, the experimental design was switched from a peptide-CTA to a peptide-based monomer for graft through polymerization using a PEG macro-CTA. Assembly was noted during the graft through polymerization, analyzed by DLS, whereas none was observed for the non-peptide controls. This indeed confirms that the peptides were not suitable as stabilizing blocks for PISA, and thus future work will study the apparent PISA behaviour of various peptide-based monomers.

## 5.5 Experimental

### 5.5.1 Materials and instrumentation

#### 5.5.1.1 Materials

Fmoc amino acids were received from Novabiochem or Iris Biotech. All other chemicals were obtained from either: Sigma Aldrich, Fisher Chemicals, Acros Chemicals, Carbosynth or Alfa Aesar and used as received. CEPTA was kindly donated by Mr Zachary Coe, and PEG<sub>2k</sub>-CETPA was kindly donated by Dr Turgay Yildirim.

#### 5.5.1.2 Instrumentation

<sup>1</sup>H NMR spectra were recorded on a Bruker Advance 300, a Bruker Advance III HD 400 or a Bruker Advance III HD 500 spectrometer at 300, 400 and 500 MHz respectively. Shifts are quoted in  $\delta$  in parts per million (ppm) relative to the solvent peak.

Infrared spectra were recorded on neat samples using a Perkin Elmer Spectrum 100 FT-IR Spectrometer.

Reverse phase high pressure liquid chromatography (HPLC) analysis was performed on a modular Shimadzu instrument with the following modules: CBM-20A system controller, LC-20AD solvent delivery module, SIL-20AC HT autosampler, CTO-20AC column oven, SPD-M20A photodiode array UV-Vis detector, RF-20A spectrofluorometric detector (not used) and a FRC-10 fraction collector (not used). Chromatography was performed on a Shim-pack GISS 5  $\mu$ m C18 (4.6 $\times$ 125mm) reverse phase column heated at 30 °C. Flow rate was set at 0.8 mL/min and the products were eluted using a gradient of gradient of 18.2 M $\Omega$ -cm water and acetonitrile. A typical elution gradient is shown in Figure 6.10.

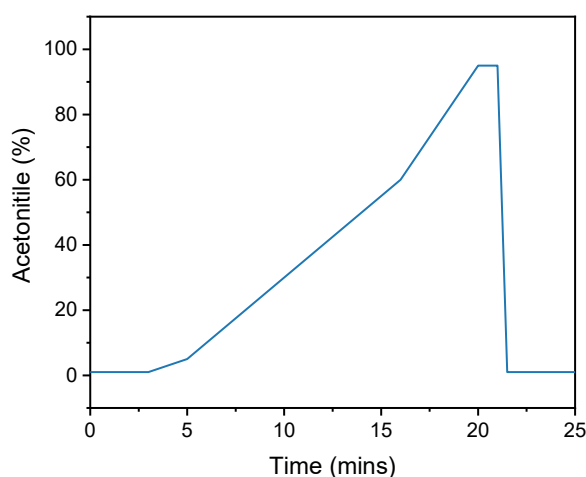


**Figure 6.10:** Typical elution gradient for peptide chromatography.

Peptide mass spectra were conducted on either a Thermofischer LCQ fleet Ion Trap Mass Spectrometer or a Waters Xevo G2-XS QToF Mass Spectrometer, in positive or negative ionization mode respectively.

Size exclusion chromatography (SEC) in DMF was performed on an Agilent 1260 Infinity II LC system equipped with a Wyatt DAWN HELEOS II multi-angle laser light scattering (MALLS) detector, a Wyatt Optilab T-rEX differential refractive index detector, an Agilent 1260 Infinity II WR diode array detector, an Agilent guard column (PLGel 5  $\mu$ M, 50  $\times$  7.5 mm) and two Agilent Mixed-C columns (PLGel 5  $\mu$ M, 300  $\times$  7.5 mm). The mobile phase was DMF (HPLC grade) containing 5 mM  $\text{NH}_4\text{BF}_4$  and was ran at 50  $^\circ\text{C}$  at a flow rate of 1.0 mL/min. Number average molecular weights ( $M_n$ ), weight average molecular weights ( $M_w$ ) and dispersities ( $\mathcal{D}_M = M_w/M_n$ ) were determined using Wyatt ASTRA v7.1.3 software against poly(methyl methacrylate) (PMMA) standards ( $M_w$  range = 1,160 – 6,025,000).

SEC in THF was performed on an Agilent 1260 Infinity II LC system equipped with an Agilent guard column (PLGel 5  $\mu$ M, 50  $\times$  7.5 mm) and two Agilent Mixed-C columns (PLGel 5  $\mu$ M, 300  $\times$  7.5 mm). The mobile phase used was THF (HPLC grade) containing 2% v/v triethylamine at 40  $^\circ\text{C}$  at a flow rate of 1.0 mL/min.

Number average molecular weights ( $M_n$ ), weight average molecular weights ( $M_w$ ) and dispersities ( $\mathcal{D}_M = M_w/M_n$ ) were determined using Agilent SEC software against polystyrene (PS) standards used for calibration ( $M_w$  range = 925 – 3647000).

DLS analysis of the crude PISA solutions was conducted using a Malvern Zetasizer Nano S instrument with a 4 mW He-Ne 633 nm laser module at 25 °C and at a detection angle of 173°. Samples were diluted with 18.2 M $\Omega$ ·cm water. Z-average hydrodynamic diameters ( $D_h$ ) were calculated from three repeat measurements using Malvern DTS 6.20 software.

Dry-state stained TEM analysis was performed on a JEOL JEM-1400 microscope operating at 80 kV. Purified samples were diluted with 18.2 M $\Omega$ ·cm water then deposited onto formvar-coated copper grids. After roughly 1 min, excess sample was blotted from the grid and the grid stained with an aqueous 1 w% uranyl acetate (UA) solution for 1 min prior to blotting, drying and microscopic analysis. TEM images were collected by Mr Spyridon Varlas (O'Reilly Group, University of Birmingham).

Atomic Force Microscopy (AFM) was performed on a JPK Nanowizard 4 system at room temperature in the supplied acoustic enclosure and vibration isolation using Nanosensor PPP-NCHAuD tips with a force constant of around 42 N/m. For data acquisition and handling Nanowizard Control and Data Processing Software V.6.1.117 in QI mode with a setpoint of 25 nN was used. Samples were prepared on freshly cleaved mica by drop-casting a solution of 0.5 mg/mL crude sample, and spin-drying the cast sample.

### 5.5.1.3 Photoreactor

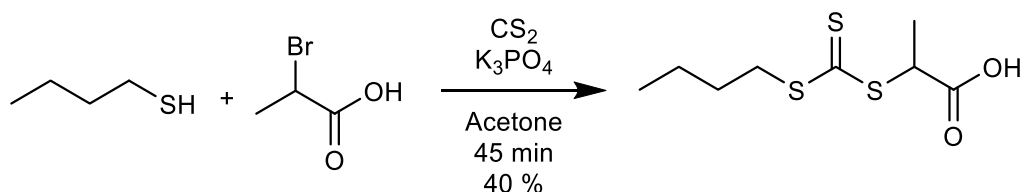


**Figure 6.11:** Photo of photoreactor set-up used for photoinitiated polymerizations in this chapter.

The photoreactor set up used included an LED source for the visible-light irradiation (TruOpto OSV5X3CAC1E, 4.5 W - purchased from Rapid Electronics), and had a radiant flux of 800 mW@400 mA at 12V DC operating at a wavelength of 400–410 nm. This was fitted to a custom-built setup equipped with a dimmer switch for controlling the output light intensity (Figure 6.11). The vials are positioned 19 mm above the LED, giving 76% light intensity at the base perimeter of the vial. The base of each vial holder contains a magnetic stirring mechanism for sample stirring.

## 5.5.2 Small molecule synthesis

### 6.5.2.1 PABTC



The synthesis was based off a previously reported protocol.<sup>52</sup> Butanethiol (5 g, 55 mmol) was added to a stirred suspension of  $\text{K}_3\text{PO}_4$  (11.6 g, 55 mmol) in acetone (100 mL). Carbon disulfide (3.9 mL, 55 mmol) was added to this solution and left to stir for 10 minutes, the solution went bright yellow. After, ethyl-2-bromopropionate (8.3 mL, 55 mmol) was added and the precipitation of KBr was observed. After stirring for 45 minutes, the solution was filtered and the precipitate washed with acetone. The filtrate was taken and the solvent removed *in vacuo*. This crude solid was purified by silica column chromatography (50% ethyl acetate in petroleum ether as the eluent) to give a white solid (5.4 g, 41%).

$^1\text{H}$  NMR ( $\text{CDCl}_3$ , 300MHz, ppm)  $\delta$  = 4.80 (q,  $^3J_{\text{HH}}$  = 7.4 Hz, 1H, CH), 3.41 – 3.20 (m, 2H,  $\text{CH}_2$ ), 1.70 – 1.59 (m, 2H,  $\text{CH}_2$ ), 1.56 (d,  $^3J_{\text{HH}}$  = 7.4 Hz, 3H,  $\text{CH}_3$ ), 1.37 (dq,  $J_{\text{HH}}$  = 14.3, 7.3 Hz, 2H,  $\text{CH}_2$ ), 0.87 (t,  $^3J_{\text{HH}}$  = 7.3 Hz, 3H,  $\text{CH}_3$ ).

$^{13}\text{C}$  NMR ( $\text{CDCl}_3$ , 300MHz, ppm)  $\delta$  = 222.0 ( $\text{CS}_3$ ), 176.4 (CO), 47.4 (CH), 37.2 ( $\text{CH}_2$ ), 29.9 ( $\text{CH}_2$ ), 22.1 ( $\text{CH}_2$ ), 16.6 ( $\text{CH}_3$ ), 13.6 ( $\text{CH}_3$ ).

MS (ESI) -  $[\text{M}+\text{H}]^+$ : calculated m/z 238.0, observed m/z 238.1

Matches literature data.<sup>52</sup>



### 5.5.3 Peptide synthesis

#### 5.5.3.1 General synthesis

Peptide synthesis was conducted on a CEM liberty blue automated microwave-assisted peptide synthesizer.

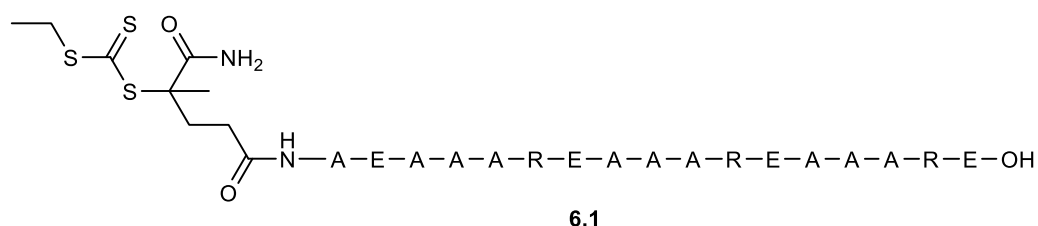
For coupling steps in DMF, the activator *N,N'*-diisopropylcarbodiimide (DIC) was used in 10 equivalents and oxyma was used in 5 equivalents to reduce racemization issues associated with DIC coupling. The Fmoc L-amino acids for synthesis were added as a 0.2 M solution in DMF, with the following protection chemistry: arginine-*N*<sub>ω</sub>-Pbf; aspartic acid-*O*<sub>ε</sub>-*t*Bu; glutamic acid-*O*<sub>ε</sub>-*t*Bu; lysine-*N*<sub>ε</sub>-Boc; serine-*O*<sub>γ</sub>-*t*Bu; asparagine-*N*<sub>ε</sub>-Trt and tyrosine-*O*-*t*Bu.

For arginine, coupling steps were conducted at 75 °C for 5 minutes, to minimize  $\gamma$ -lactam formation.<sup>62</sup>

For deprotection, a solution of 10% piperidine in DMF was utilized. The resin was washed with this solution twice for 2 mins at 90 °C under microwave irradiation. If aspartate was part of the peptide sequence 0.1 M OXYMA was added to the piperidine solution to prevent aspartimide formation.<sup>63</sup>

Resin cleavage was conducted after coupling of the CTA. To achieve this the resin was first washed thoroughly on a fritted funnel with DMF (10 mL) and then methanol (~10 mL) several times. The resin was subsequently dried *in vacuo* to remove residual methanol. This resin was then added to 5 - 10 mL of cleavage solution, of 95% v/v trifluoroacetic acid (TFA), 2.5% v/v water and 2.5% v/v triethylsilane. After 4 hours, the solution was filtered through glass wool, and the eluent was concentrated and precipitated into cold diethyl ether. The precipitate was isolated through centrifugation and re-washed with diethyl ether three times. The final precipitate was dried *in vacuo*, solubilized in water and freeze-dried.

### 5.5.3.2 Synthesis of CEPTA functionalized (ER)<sub>i+4</sub> peptide (6.1)



The synthesis was conducted according to the general synthesis outlined in 6.5.3.1. A Wang resin (0.6 mmol/g, 0.417 g) was used for synthesis at a 0.25 mmol scale. For the final coupling, CEPTA was used instead of amino acid at the same 0.2 M concentration. Subsequent cleavage and precipitation was conducted to give CTA **6.1**. Prep-HPLC was not conducted to ensure enough peptide was available for investigation, however purity is fair.

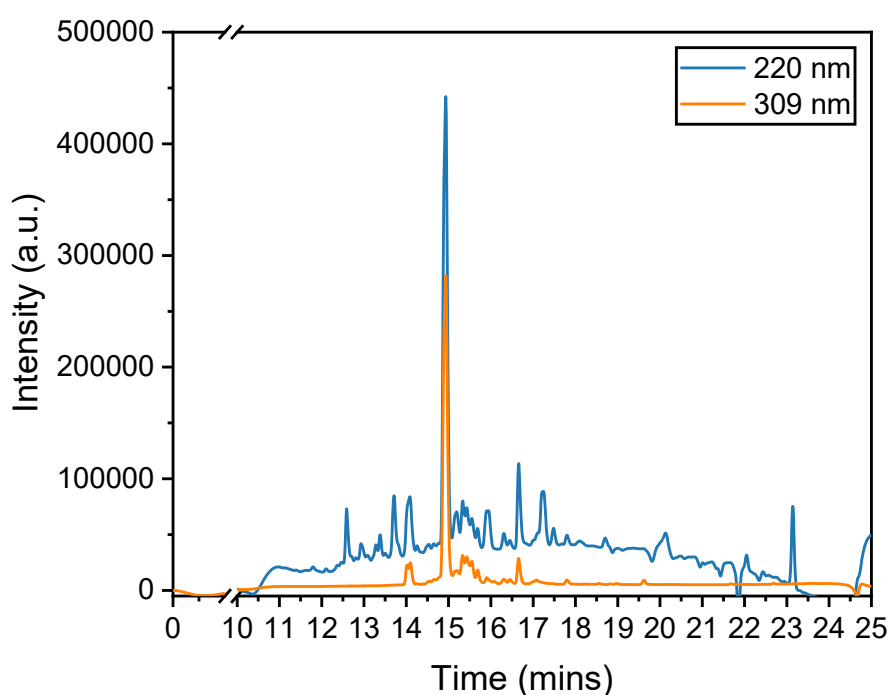
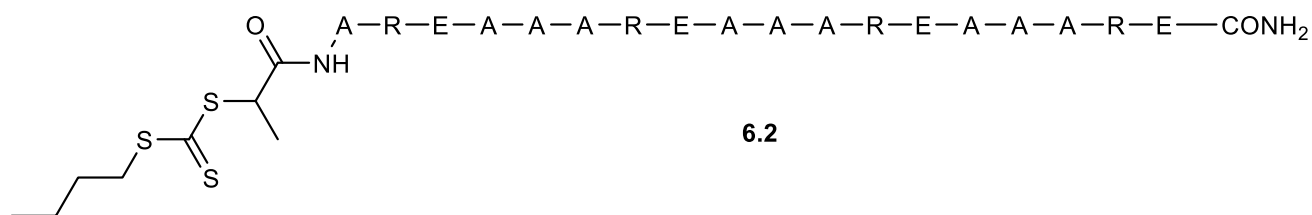


**Figure 6.12:** HPLC chromatogram of **6.1**.

MS (Thermofischer LCQ fleet): (M+Na<sup>+</sup>) Observed m/z 1997.12, calculated m/z 1997.87

### 5.5.3.3 Synthesis of PABTC functionalized (ER)<sub>i+4</sub> peptide (6.2)



The synthesis was conducted according to the general synthesis outlined in 6.5.3.1. A rink amide resin (0.7 mmol/g, 0.357 g) was used for synthesis at a 0.25 mmol scale. For the final coupling, PABTC was used instead of amino acid at the same 0.2 M concentration. Subsequent cleavage and precipitation was conducted to give CTA **6.2**, which was obtained in very good purity without further purification (Figure 6.13); it should be noted the product is diastereotopic resulting in the two peaks by HPLC.

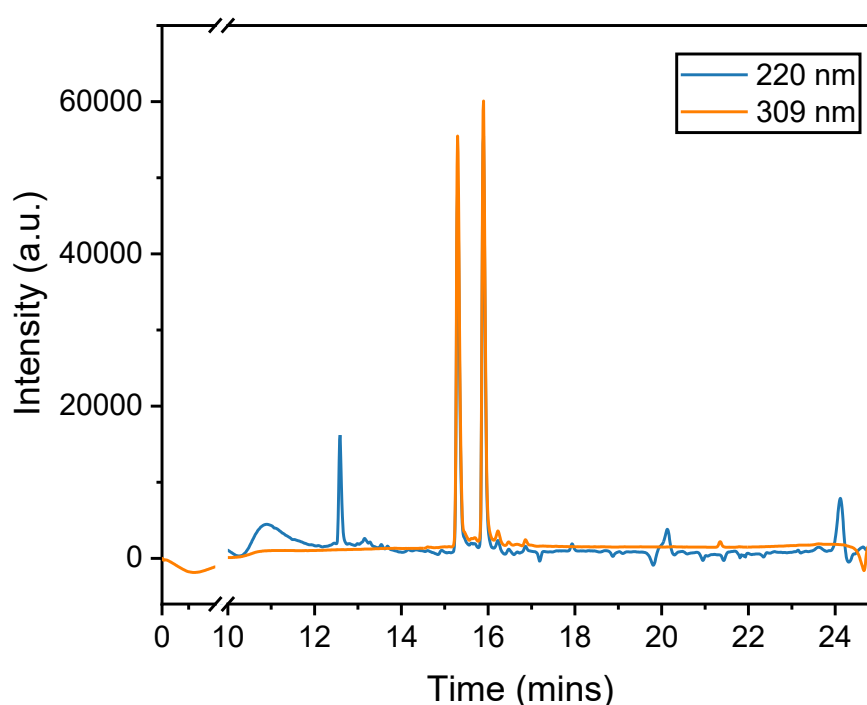
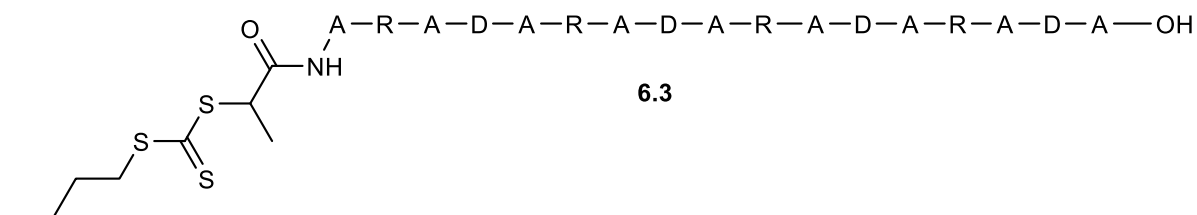


**Figure 6.13:** HPLC chromatogram of **6.2**.

MS (Waters):[M+3H<sup>+</sup>] Observed m/z 697.70, calculated m/z 697.70

#### 5.5.3.4 Synthesis of PABTC functionalized (RADA)<sub>4</sub> peptide (6.3)



The synthesis was conducted according to the general synthesis outlined in 6.5.3.1. An alanine-Wang resin (0.7 mmol/g, 0.357 g) was used for synthesis at a 0.25 mmol scale. For the final coupling, PABTC was used instead of amino acid at the same 0.2 M concentration. Subsequent cleavage and precipitation was conducted to give CTA **6.3**.

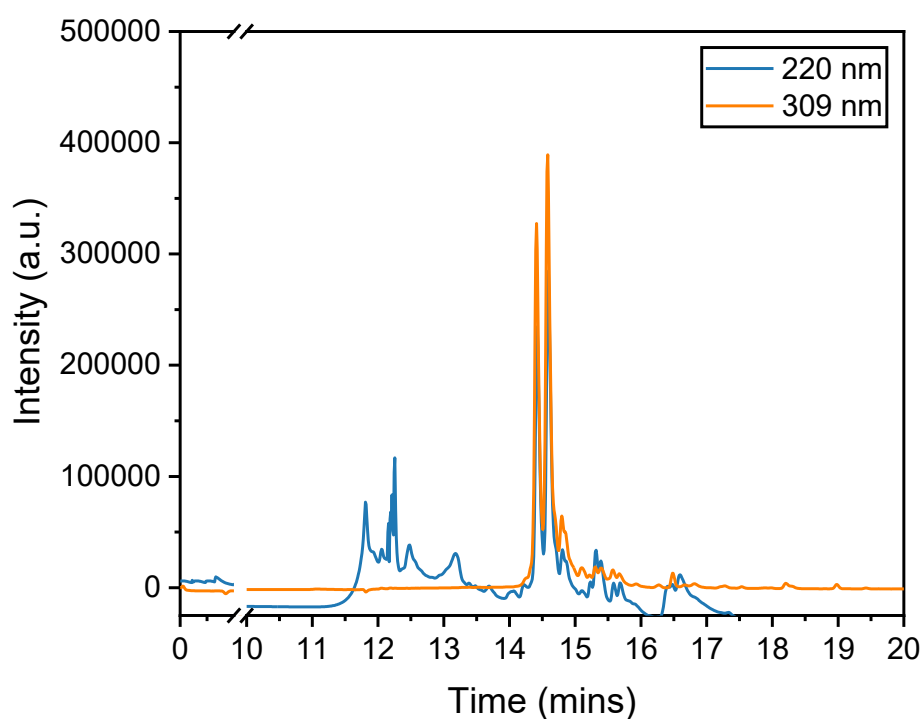
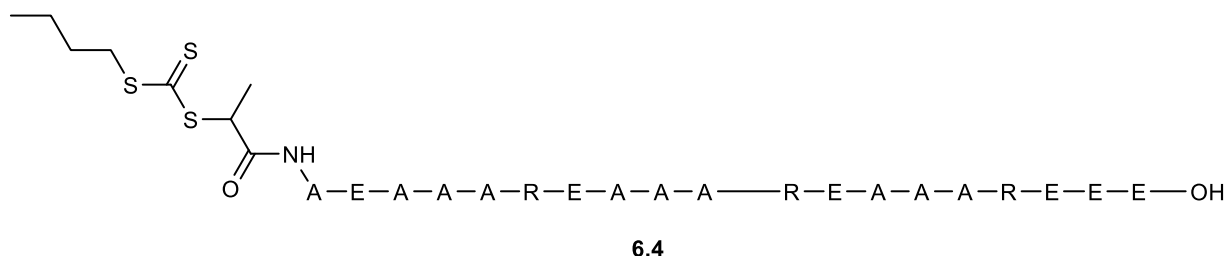


**Figure 6.14:** HPLC chromatogram of **6.3** (conducted in an 8M guanidine solution to ensure solubility).

LCMS: Not obtained due to high concentration of salt required for dissolution

#### 6.5.3.5 Synthesis of PABTC functionalized EEE tagged (ER)<sub>i+4</sub> peptide (6.4)



The synthesis was conducted according to the general synthesis outlined in 6.5.3.1. A Wang resin (0.6 mmol/g, 0.417 g) was used for synthesis at a 0.25 mmol scale. For the final coupling, PABTC was used instead of amino acid at the same 0.2 M concentration. Subsequent cleavage and precipitation was conducted to give 80 mg of CTA **6.4**, HPLC indicated significant presence of uncapped peptide (~20% by integration).

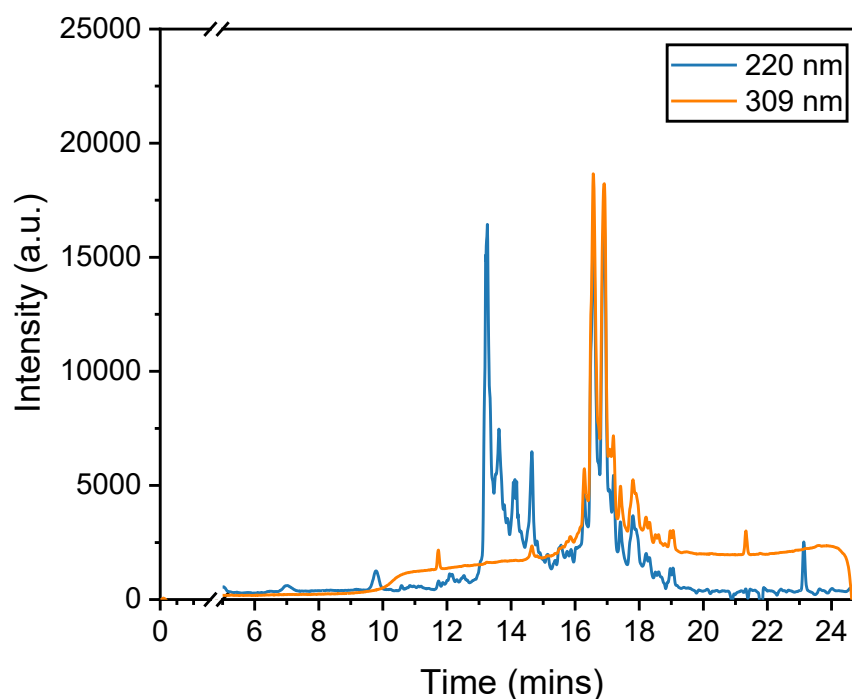
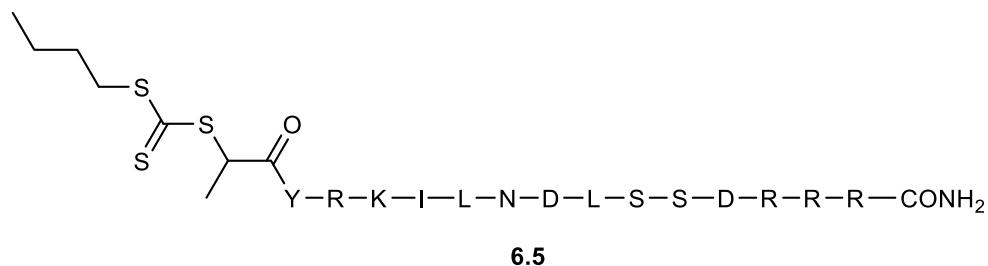


**Figure 6.15:** HPLC chromatogram of **6.4**.

LC-MS - Thermofischer LCQ fleet: (M+Na<sup>+</sup>) Observed m/z 1997.12, calculated m/z 1997.87

#### 6.5.3.6 Synthesis of PABTC functionalized RRR tagged KID-CREB peptide (6.5)



The synthesis was conducted according to the general synthesis outlined in 6.5.3.1. A rink amide resin (0.7 mmol/g, 0.357 g) was used for synthesis at a 0.25 mmol scale. For the final coupling, PABTC was used instead of amino acid at the same 0.2 M concentration. Subsequent cleavage and precipitation was conducted to give 121 mg of CTA **6.5** which was obtained in very good purity without further purification (Figure 6.16); again the product is diastereotopic resulting in the two peaks by HPLC.

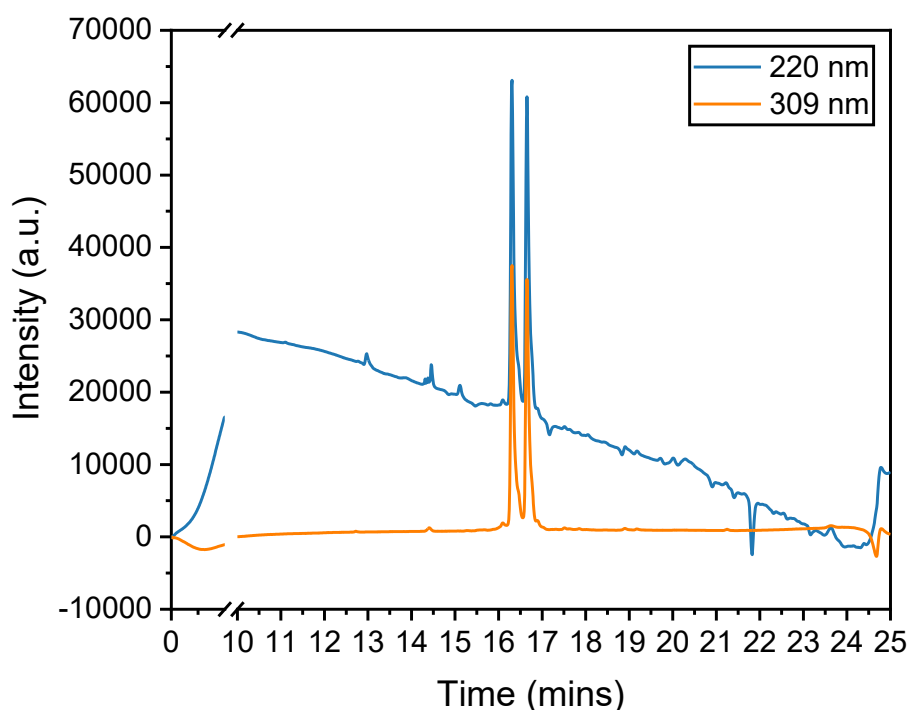
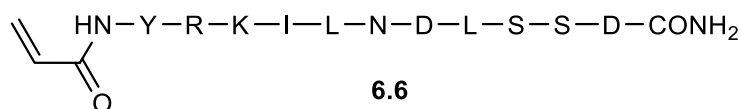


**Figure 6.16:** HPLC chromatogram of **6.5**.

LC-MS - Xevo: (M-H<sup>+</sup>) Observed m/z 2009.94, calculated m/z 2010.01.

#### 5.5.3.5 Synthesis of KID-CREB acrylamide monomer (6.6)



The synthesis was conducted according to the general synthesis outlined in 6.5.3.1. A rink amide resin (0.7 mmol/g, 0.357 g) was used for synthesis at a 0.5 mmol scale. For the final coupling, acrylic acid was used instead of amino acid at the same 0.2 M concentration. Subsequent cleavage and precipitation was conducted to give 140 mg of monomer **6.6**. The purity was <90% by HPLC integration, however, it was determined for initial investigations this was sufficient.

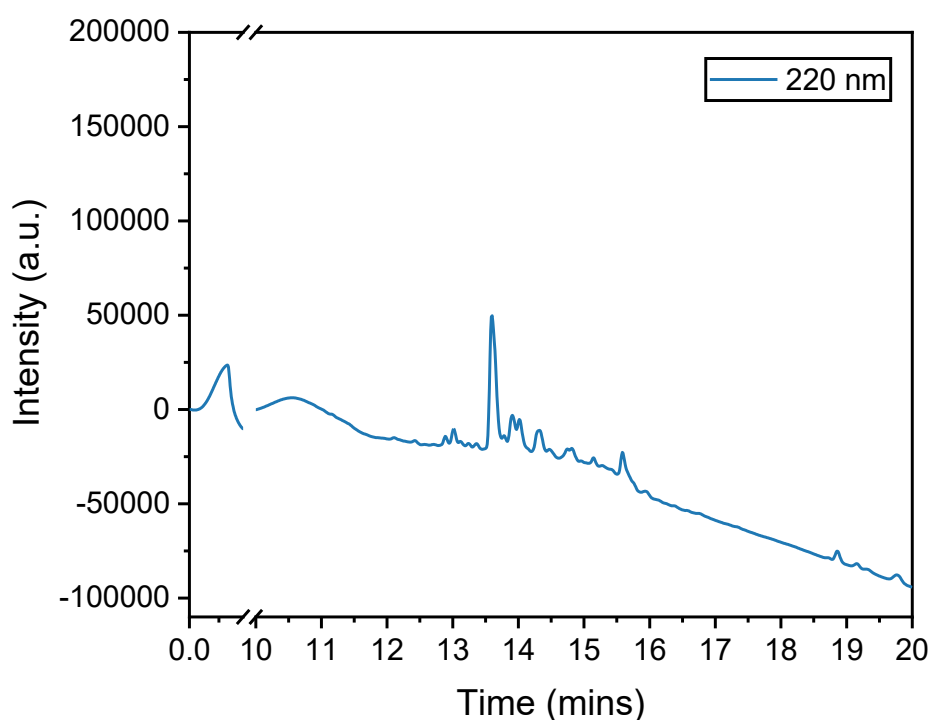


**Figure 6.17:** HPLC chromatogram of 6.6

MS (ESI) – Observed  $m/z$  1790.1, calculated  $m/z$  1790.0

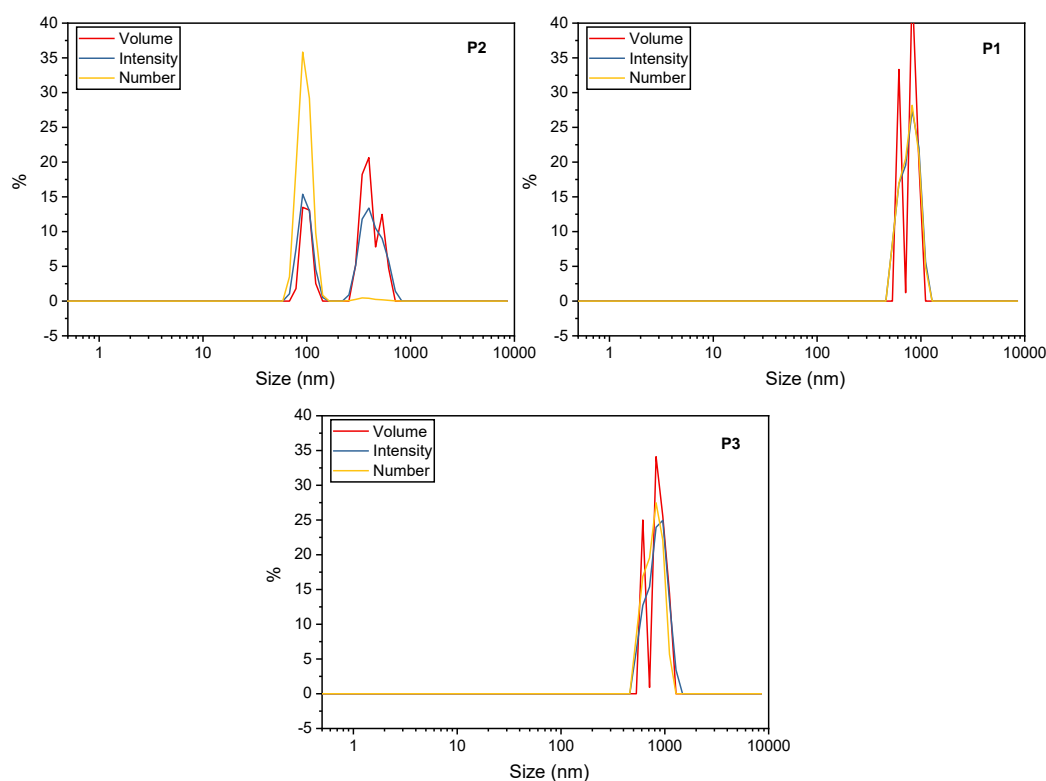
## 5.5.4 Aqueous PI SA using peptide macro-CTAs

### 5.5.4.1 CTA 6.2 mediated polymerization of DAAM (P1-3)

CTA **6.2** (1 equiv., 8 mg) and DAAM (**P1** and **P3**: 50 equiv., 35 mg; **P2**:100 equiv., 69 mg) were dissolved in deionized water (**P1-2**: 0.69 mL; P3: 0.386 mL) containing VA-044 initiator (0.13 mg), in a 3 mL scintillation vial containing a magnetic stirrer. The mixture was degassed by bubbling N<sub>2</sub> through the solution for 10 min. This sealed vial was incubated at 40 °C and stirred. After leaving overnight, the vial was opened to air and allowed to cool to room temperature before the conversion was measured by <sup>1</sup>H NMR spectroscopy (DMSO-*d*<sub>6</sub>) and SEC (DMF) analysis was collected.

	NMR (DMSO- <i>d</i> <sub>6</sub> )		SEC (DMF)		
	Conversion (%)	M <sub>n</sub> (theor)	M <sub>n</sub> (kDa)	M <sub>w</sub> (kDa)	Đ <sub>M</sub>
P1	>99	10.9	21.8	27.7	1.28
P2	>99	19.3	35.6	49.6	1.39
P3	82	15.8	23.8	117.6	4.94

DLS graphs for P1-3:



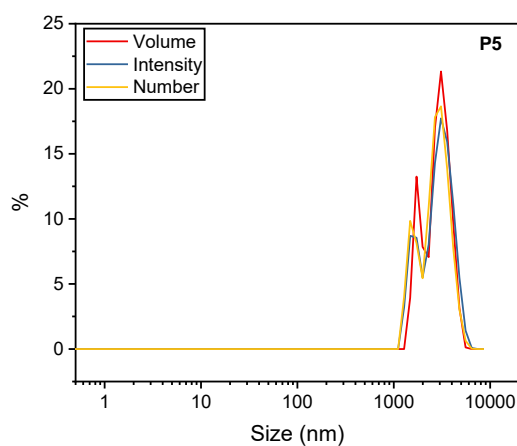
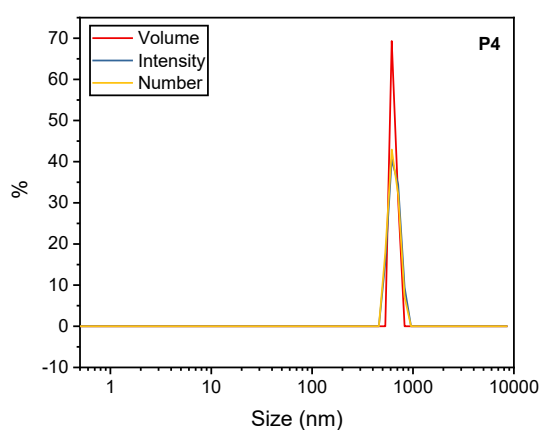


#### 5.5.4.2 CTA 6.4 mediated polymerization of DAAM (P4-5)

CTA **6.4** (1 equiv., 6 mg) and DAAM (**P4**: 50 equiv., 20.5 mg; **P5**:100 equiv., 41 mg) were dissolved in deionized water (0.423 mL) containing VA-044 initiator (0.08 mg), in a 3 mL scintillation vial containing a magnetic stirrer. The mixture was degassed by bubbling N<sub>2</sub> through the solution for 5-10 min. This sealed vial was incubated at 40 °C and stirred. After leaving overnight, the vial was opened to air and allowed to cool to room temperature before the conversion was measured by <sup>1</sup>H NMR spectroscopy (DMSO-*d*<sub>6</sub>). SEC data could not be collected as aggregation was observed by DLS in DMF, THF and water.

	NMR (DMSO- <i>d</i> <sub>6</sub> )	
	Conversion (%)	M <sub>n</sub> (theor)
P4	>99	10.4
P5	>99	18.9

DLS graphs for **P4** and **P5**:

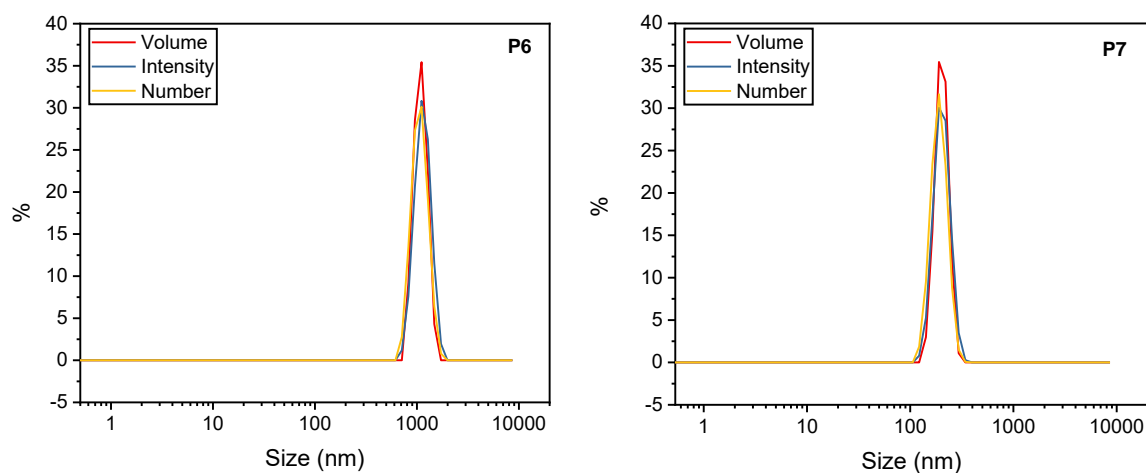


#### 6.5.4.3 CTA 6.5 mediated photo-polymerization of DAAM (P6-7)

CTA **6.5** (1 equiv., 5 mg) and DAAM (**P6**: 50 equiv., 21 mg; **P7**: 15 equiv., 6.3 mg) were dissolved in pH 2 phosphate solution (0.42 mL), in a 3 mL scintillation vial containing a magnetic stirrer. The mixture was degassed by bubbling N<sub>2</sub> through the solution for 5-10 min. This sealed vial was incubated in a photoreactor at 40 °C and stirred. After leaving overnight, the vial was opened to air and allowed to cool to room temperature before the conversion was measured by <sup>1</sup>H NMR spectroscopy (DMSO-*d*<sub>6</sub>) and SEC (THF) analysis was collected.

	NMR (DMSO- <i>d</i> <sub>6</sub> )		SEC (THF)		
	Conversion (%)	M <sub>n</sub> (theor)	M <sub>n</sub> (kDa)	M <sub>w</sub> (kDa)	Đ <sub>M</sub>
P6	88	9,400	33.6	52.3	1.56
P7	75	3,900	8.6	14.7	1.7

DLS graph for **P6-7**:



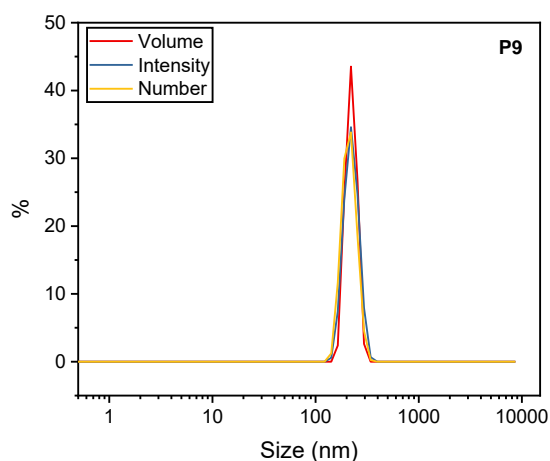
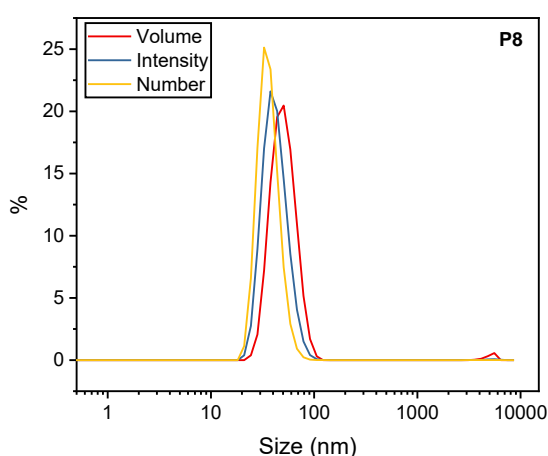
#### 5.5.4.3 Aqueous photo-PISA of peptide-monomer using PEG<sub>2k</sub>CETPA macro-CTA

PEG<sub>2k</sub>-macro-CTA (1 equiv., 8 mg) and monomer **6.6** (**P8-9**: 3 equiv., 20 mg; **P10-11**: none) were dissolved in deionized water (**P8/10**: 0.450 mL; **P9/11**: 0.580 mL), in a 3 mL scintillation vial containing a magnetic stirrer.

For **P8** and **P9** the mixture was degassed by bubbling N<sub>2</sub> through the solution for 5-10 min, and these sealed vials were incubated at 40 °C in a photoreactor and stirred. After leaving for 4 hours, vials of P8/9 were opened to air and allowed to cool to room temperature. To all solutions, HPMA (**P8/10**: 10 equiv., 5.1 mg; **P9/11**: 25 equiv., 12.6 mg) was added, and all solutions were degassed again with N<sub>2</sub>, followed by sealing and incubation at 40 °C with stirring in the photoreactor. These were left for 4 hours, after which they were opened to air and left to cool, before conversion was measured by <sup>1</sup>H NMR spectroscopy (DMSO-*d*<sub>6</sub>) and SEC analysis was collected for **P10-11**.

	NMR (DMSO- <i>d</i> <sub>6</sub> )		SEC (THF)		
	Conversion (%) Peptide, PHPMA	M <sub>n</sub> (theor)	M <sub>n</sub> (kDa)	M <sub>w</sub> (kDa)	Đ <sub>M</sub>
P8	>99%, 81%	8.8	n/a	n/a	n/a
P9	>99%, 67%	11.0	n/a	n/a	n/a
P10	N/A, >99%	3.0	8.8	10.6	1.21
P11	N/A, >99%	5.6	11.5	13.9	1.21

DLS graph for **P8-9**:



## 5.6 References

- (1) Beecher, J. F.; Marker, L.; Bradford, R. D.; Aggarwal, S. L. *J. Polym. Sci. Part C Polym. Symp.* 1969, 26, 117.
- (2) Canning, S. L.; Smith, G. N.; Armes, S. P. *Macromolecules* 2016, 49, 1985.
- (3) Jones, E. R.; Semsarilar, M.; Wyman, P.; Boerakker, M.; Armes, S. P. *Polym. Chem.* 2016, 7, 851.
- (4) Derry, M. J.; Fielding, L. A.; Armes, S. P. *Polym. Chem.* 2015, 6, 3054.
- (5) Warren, N. J.; Mykhaylyk, O. O.; Mahmood, D.; Ryan, A. J.; Armes, S. P. *J. Am. Chem. Soc.* 2014, 136, 1023.
- (6) Blanazs, A.; Ryan, A. J.; Armes, S. P. *Macromolecules* 2012, 45, 5099.
- (7) **Varlas, S.; Keogh, R.; Xie, Y.; Horswell, S. L.; Foster, J. C.; O'Reilly, R. K.** *J. Am. Chem. Soc.* 2019.
- (8) Mitchell, D. E.; Lovett, J. R.; Armes, S. P.; Gibson, M. I. *Angew. Chem. Int. Ed.* 2016, 55, 2801.
- (9) Canton, I.; Warren, N. J.; Chahal, A.; Amps, K.; Wood, A.; Weightman, R.; Wang, E.; Moore, H.; Armes, S. P. *ACS Cent. Sci.* 2016, 2, 65.
- (10) Wright, D. B.; Proetto, M. T.; Touve, M. A.; Gianneschi, N. C. *Polym. Chem.* 2019, 10, 2996.
- (11) Blackman, L. D.; Varlas, S.; Arno, M. C.; Houston, Z. H.; Fletcher, N. L.; **Thurecht, K. J.; Hasan, M.; Gibson, M. I.; O'Reilly, R. K.** *ACS Cent. Sci.* 2018, 4, 718.
- (12) Zhang, W.-J.; Hong, C.-Y.; Pan, C.-Y. *Biomacromolecules* 2017, 18, 1210.
- (13) Karagoz, B.; Esser, L.; Duong, H. T.; Basuki, J. S.; Boyer, C.; Davis, T. P. *Polym. Chem.* 2013, 5, 350.
- (14) Blackman, L. D.; Varlas, S.; Arno, M. C.; Fayter, A.; Gibson, M. I.; **O'Reilly, R. K.** *ACS Macro Lett.* 2017, 6, 1263.
- (15) Varlas, S.; Blackman, L. D.; Findlay, H. E.; Reading, E.; Booth, P. J.; **Gibson, M. I.; O'Reilly, R. K.** *Macromolecules* 2018, 51, 6190.
- (16) Lau, J. L.; Dunn, M. K. *Bioorg. Med. Chem.* 2018, 26, 2700.
- (17) Wright, D. B.; Touve, M. A.; Adamiak, L.; Gianneschi, N. C. *ACS Macro Lett.* 2017, 6, 925.
- (18) Six, J.-L.; Ferji, K. *Polym. Chem.* 2018, 10, 45.
- (19) Cai, M.; Ding, Y.; Wang, L.; Huang, L.; Lu, X.; Cai, Y. *ACS Macro Lett.* 2018, 7, 208.
- (20) Tsai, S.-C.; Lin, Y.-C.; Lin, E.-L.; Chiang, Y.-W.; Kuo, S.-W. *Polym. Chem.* 2016, 7, 2395.
- (21) Kang, Y.; Pitto-Barry, A.; Rolph, M. S.; Hua, Z.; Hands-Portman, I.; **Kirby, N.; O'Reilly, R. K.** *Polym. Chem.* 2016, 7, 2836.
- (22) Warren, N. J.; Armes, S. P. *J. Am. Chem. Soc.* 2014, 136, 10174.
- (23) Mellot, G.; Guigner, J.-M.; Bouteiller, L.; Stoffelbach, F.; Rieger, J. *Angew. Chem. Int. Ed.* 2019, 58, 3173.
- (24) Lansalot, M.; Rieger, J. *Macromol. Rapid Commun.* 2019, 40, 1800885.
- (25) Cheng, G.; Pérez-Mercader, J. *Macromol. Rapid Commun.* 2019, 40, 1800513.
- (26) Wang, G.; Schmitt, M.; Wang, Z.; Lee, B.; Pan, X.; Fu, L.; Yan, J.; Li, S.; Xie, G.; Bockstaller, M. R.; Matyjaszewski, K. *Macromolecules* 2016, 49, 8605.
- (27) Varlas, S.; **Foster, J. C.; O'Reilly, R. K.** *Chem. Commun.* 2019, 55, 9066.

- (28) Moad, G. J. *Polym. Sci. Part Polym. Chem.* 2019, *57*, 216.
- (29) Perrier, S. *Macromolecules* 2017, *50*, 7433.
- (30) Gody, G.; Barbey, R.; Danial, M.; Perrier, S. *Polym. Chem.* 2015, *6*, 1502.
- (31) Chiefari, J.; Chong, Y. K.; Ercole, F.; Krstina, J.; Jeffery, J.; Le, T. P. T.; Mayadunne, R. T. A.; Meijs, G. F.; Moad, C. L.; Moad, G.; Rizzardo, E.; Thang, S. H. *Macromolecules* 1998, *31*, 5559.
- (32) Moad, G.; Rizzardo, E.; Thang, S. H. *Polymer* 2008, *49*, 1079.
- (33) Keddie, D. J.; Moad, G.; Rizzardo, E.; Thang, S. H. *Macromolecules* 2012, *45*, 5321.
- (34) Darzacq, X.; Shav-Tal, Y.; Turris, V. de; Brody, Y.; Shenoy, S. M.; Phair, R. D.; Singer, R. H. *Nat. Struct. Mol. Biol.* 2007, *14*, 796.
- (35) *Fmoc Solid Phase Peptide Synthesis: A Practical Approach*; Chan, W.; White, P., Eds.; Practical Approach Series; Oxford University Press: Oxford, New York, 1999.
- (36) Murata, H.; Carmali, S.; Baker, S. L.; Matyjaszewski, K.; Russell, A. J. *Nat. Commun.* 2018, *9*, 845.
- (37) El-Faham, A.; Albericio, F. *Chem. Rev.* 2011, *111*, 6557.
- (38) Subirós-Funosas, R.; Prohens, R.; Barbas, R.; El-Faham, A.; Albericio, F. *Chem. – Eur. J.* 2009, *15*, 9394.
- (39) Dürrenberger, F.; Abbate, V.; Ma, Y.; Arno, M. C.; Jaiash, D.; Parmar, A.; Marshall, V.; Latunde-Dada, G. O.; Zimmermann, T.; Senn, D.; Altermatt, P.; Manolova, V.; Hider, R. C.; Bansal, S. S. *Bioconjug. Chem.* 2013, *24*, 1527.
- (40) Lopez, J.; Pletscher, S.; Aemissegger, A.; Bucher, C.; Gallou, F. *Org. Process Res. Dev.* 2018, *22*, 494.
- (41) Merrifield, R. B. *J. Am. Chem. Soc.* 1963, *85*, 2149.
- (42) Palomo, J. M. *RSC Adv.* 2014, *4*, 32658.
- (43) Zalipsky, S.; Chang, J. L.; Albericio, F.; Barany, G. *React. Polym.* 1994, *22*, 243.
- (44) Wang, S.-Sun. *J. Am. Chem. Soc.* 1973, *95*, 1328.
- (45) Albericio, F.; Kneib-Cordonier, N.; Biancalana, S.; Gera, L.; Masada, R. I.; Hudson, D.; Barany, G. *J. Org. Chem.* 1990, *55*, 3730.
- (46) J. Dou, A. A. Vorobieva, W. Sheffler, L. A. Doyle, H. Park, M. J. Bick, B. Mao, G. W. Foight, M. Y. Lee, L. A. Gagnon, L. Carter, B. Sankaran, S. Ovchinnikov, E. Marcos, P.-S. Huang, J. C. Vaughan, B. L. Stoddard and D. Baker, *Nature*, 2018, *561*, 485–491.
- (47) H. Cui, T. Muraoka, A. G. Cheetham and S. I. Stupp, *Nano Lett.*, 2009, *9*, 945–951.
- (48) R. Baumgartner, H. Fu, Z. Song, Y. Lin and J. Cheng, *Nat. Chem.*, 2017, *9*, 614–622.
- (49) X. Chen, Y. Wang, H. Wang, Y. Kim and M. Lee, *Chem. Commun.*, 2017, *53*, 10958–10961.
- (50) Marqusee, S.; Robbins, V. H.; Baldwin, R. L. *Proc. Natl. Acad. Sci.* 1989, *86*, 5286.
- (51) Marqusee, S.; Baldwin, R. L. *Proc. Natl. Acad. Sci.*, 1987, *84*, 8898.
- (52) Arosio, P.; Owczarz, M.; Wu, H.; Butté, A.; Morbidelli, M. *Biophys. J.* 2012, *102*, 1617.
- (53) Ganguly, D.; Chen, J. *J. Am. Chem. Soc.* 2009, *131*, 5214.
- (54) Liu, J.; Perumal, N. B.; Oldfield, C. J.; Su, E. W.; Uversky, V. N.; Dunker, A. K. *Biochemistry* 2006, *45*, 6873.
- (55) Fuchs, A. V.; Thurecht, K. J. *ACS Macro Lett.* 2017, *6*, 287.

- (56) **Skey, J.; O'Reilly, R. K. Chem. Commun.** 2008, 4183.
- (57) Camilloni, C.; Rocco, A. G.; Eberini, I.; Gianazza, E.; Broglia, R. A.; Tiana, G. *Biophys. J.* 2008, *94*, 4654.
- (58) Thomas, D. B.; Convertine, A. J.; Hester, R. D.; Lowe, A. B.; McCormick, C. L. *Macromolecules* 2004, *37*, 1735.
- (59) Blackman, L. D.; Doncom, K. E. B.; Gibson, **M. I.; O'Reilly, R. K. Polym. Chem.** 2017, *8*, 2860.
- (60) Foster, J. C.; Varlas, S.; Couturaud, B.; Jones, J. R.; Keogh, R.; Mathers, **R. T.; O'Reilly, R. K. Angew. Chem. Int. Ed.** 2018, *57*, 15733.
- (61) Varlas, S.; Foster, J. C.; Arkinstall, L. A.; Jones, J. R.; Keogh, R.; **Mathers, R. T.; O'Reilly, R. K. ACS Macro Lett.** 2019, *8*, 466.
- (62) Cezari, M. H.; Juliano, L. *Pept. Res.* 1996, *9*, 88.
- (63) Subirós-Funosas, R.; El-Faham, A.; Albericio, F. *Pept. Sci.* 2012, *98*, 89.



## Conclusions and future work

This thesis investigated the use of maleimide fluorophores for use in peptide-based applications. Initially, this was investigated through developing bromomaleimides for enzyme conjugations to reduced disulfides and lysine residues. Poor fluorescence of the conjugates was observed, attributed to poor protection of the dye from interactions with water.

Two routes were then investigated in an attempt to overcome this: through developing improved dyes through steric shielding and through the synthesis of maleimide derived amino acids for genetic expression in peptides, in solvent shielded locations. While synthesis of sterically shielded dyes did realize better emission in protic solvents, the increase was small and solubility issues prevented aqueous applications. However serendipitously, a novel solid-state emission phenomenon was discovered, shown to be different to that seen in an aggregation-induced emission dye. This compound could provide a better dye for solid-state applications where a low weight percentage of dye may be preferential.

Regarding the fluorescent amino acids, synthesis of activated amino acids was successful and studies into the expression of these is ongoing. In particular, N- and C-terminal expression of ACM-containing amino acids has been realized, and future work will look at the incorporation mid-chain for expression deeper into enzymes where solvent interactions should not occur in the native state; suggested examples are given in Chapter 4. Such enzymes could then be responsive to denaturing or protein-protein interactions, for example.

The synthesis of a range of alkyne containing maleimide fluorophores was then undertaken for coupling to enzyme intermediate probes. The coupled fluorescent probes were successfully realized and initial tests have shown successful capture of polyketide intermediates. The stability of the dyes to the



expression media used for such experiments was also proven through test incubations and extensive chromatographic characterization. Future work will focus on using the fluorescence of the dyes to aid identification of off-loaded intermediates, and potentially using the dye to measure the kinetics of these pathways.

Finally, the investigation into templation of assembled nanostructures was investigated through the synthesis of peptide-functionalized RAFT agents and monomers. Universally, peptide-based RAFT agents used for PISA led to aggregated assemblies, attributed to hydrogen bonding and ionic interactions. However, peptide-based monomers were shown to be PISA active, paving the way for a universal one-pot synthesis and encapsulation of peptide-based therapeutics. Peptide therapeutics are particularly sensitive to proteolysis and immunogenicity, and therefore such encapsulation could be a commercially viable method for creating peptide therapeutics without the need for complex, high molecular weight separation associated with traditional peptide conjugates. A greater understanding of the driving forces behind this phenomenon are also required to aid future project design.